Staurolite-kyanite-amphibolites: Calculated phase relations with application to amphibolites from the Harts Range, central Australia and the Zillertaler Alpen, Austria.

Joanne Lee Arnold

Thesis submitted for the degree of Doctor of Philosophy in

Department of Geology and Geophysics,

Faculty of Science,

The University of Adelaide

July 1994

Table of Contents

Abstract

The mineralogy of amphibolites is dominated by relatively high variance assemblages involving calcium amphibole, chlorite, epidote, plagioclase, quartz ± garnet ± K-, Ti- and CO_2-phases (i.e. the "common assemblage" of Laird (1980) over a wide range of metamorphic conditions including amphibolite, greenschist and blueschist facies metamorphism

In recent years a number of unusual amphibolite assemblages, involving kyanite, staurolite or other aluminous phases which occur more typically in rocks of pelitic affinity, have been reported from all over the world (e.g. Gibson, 1978; Spear, 82; Humphries, 1993). There are two possible reasons for the rarity of this type of assemblage: (1) the bulk compositions required to develop these assemblages are atypical, or (2) the metamorphic conditions under which the assemblages formed are unusual and so may provide useful information about the pressure-temperature distribution of certain tectonic environments. Several workers have suggested that kyanite–staurolite–hornblende and related assemblages have developed in rocks of typical mafic igneous compositions (e.g. Gibson, 1978; Helms et al., 1987) and that their formation results from metamorphism at pressures in excess of those appropriate to the "common" amphibolite assemblage (e.g. Selverstone et al., 1984; Helms et al., 1987). Other workers have suggested that although more magnesium-rich rocks may develop kyanite–staurolite–hornblende assemblages under high pressure conditions, more Fe-rich samples may not require such unusually high pressures of equilibration (e.g. Ward, 1984a). This thesis attempts to develop an understanding of the phase relations in natural kyanite–staurolite-amphibolites and related rocks and to develop phase diagram to explain their P-T significance.

Equilibrium thermodynamics calculations using the dataset of Holland and Powell (1985, 1990) are used to determine the phase relations in the FMASH model sub-system and later the CFMASH system involving aluminosilicates, staurolite, cordierite, garnet, chlorite, orthoamphibole and hornblende with anorthite, quartz and aqueous vapour in excess. The resulting phase diagram predicts that hornblende will be stable with staurolite in a very restricted P-T field at pressures of 8.2-9.5 kbar and 600-680°C. Kyanite may co-exist with hornblende under a wider range of conditions, at pressures greater than about 8.2 kbar and temperatures up to about 800°C. The predictions of the phase diagram are largely in accordance with the pressure and temperature estimates made from natural examples and their reaction relations (e.g. Selverstone et al., 1984; Grew & Sandiford, 1985; Helms et al., 1987; Humphries, 1993). The effects of sodium are considered and the resulting NCFMASH phase equilibria are consistent with many natural kyanite- and staurolite-amphibolite assemblages.

A new example of kyanite–staurolite amphibolites is reported from the Harts Range of central Australia where a large variety of mineral assemblages provides good relatively comprehensive constraints on the compatibility relations of the aluminous amphibolites. The

equilibrium associations and reaction textures observed in these samples, together with the theoretical phase relations calculated in earlier sections constrains the P-T history for the otherwise poorly constrained Harts Range region. The multiple-episode heating and cooling (broadly clock-wise) history determined from these studies is consistent with the geochronological data available from the region.

The compatibility relations of kyanite–staurolite amphibolites from the Zillertaler Alpen in western Austria and those reported in the literature allow the phase relations in amphibolites to be constrained independently of the equilibrium thermodynamics calculations and provide a useful comparison with the calculated phase relations. The observed compatibility relations confirm that the calculated petrogenetic grids are at least partly consistent with those in natural amphibolites and that they may be a useful tool in understanding the metamorphic history of amphibolite-dominated terrains.

Information from natural kyanite–staurolite amphibolites and from the calculated equilibria suggest that the paucity of kyanite–staurolite-bearing amphibolites in comparison to the "common" amphibolite assemblage is due to the confined P-T-X widow appropriate to their formation. The stability fields of staurolite–hornblende and kyanite–hornblende in the CFMASH system occupy only a small, high P/T, pressure-temperature window for rocks of intermediate to magnesian compositions. As a result, although the stability fields of kyanite and staurolite-amphibolites may often be intersected, they may be easily overprinted by higher temperature assemblages during the normal thermal evolution of a convergent orogen. Thus, although kyanite–hornblende and staurolite–hornblende assemblages are stable under relatively unremarkable P-T conditions, their preservation is strongly dependent on their specific composition and P-T history and so they will only be rarely preserved in convergent orogens.

This work contains no material which has been accepted for the award of any other degree or diploma in any university or other tertiary institution and, to the best of my knowledge and belief, contains no material previously published or written by another person, except where due reference is made in the text.

I give consent to this copy of my thesis, when deposited in the University Library being made available for loan and photocopying.

signed date 1/7/94

Acknowledgements

Most obviously and most deservedly, my sincere thanks must go to my supervisor, Mike Sandiford, who not only gave me the opportunity to visit Austria and Europe but also beautiful central Australia. Mike also provided support at various trying times and a spur (not so appreciated at the time) when I most needed it. He has been most patient with my attempts at scientific writing and thinking and has been instrumental in the progress which I hope I have made during the candidature of my PhD and has been a source of inspiration since 1988.

Mike Sandiford, Simon Turner and Alan Purvis all provided the early encouragement which saw me embark on my honours project and thus begin this rather epic journey into the land of metamorphic geology.

The Commonwealth Government provided an Australian Post-graduate Research Award, and the University of Adelaide provided funding through a DR Stranks Travelling Fellowship for field work in the Harts Range.

In order of appearance I must also thank Kurt, Karin, Mike, John and Johnny for the wonderful time we all had during the petrological pilgrimage. Andy Barnicoat and his wife, Christine, and daughter, Rachel, are thanked for their hospitality and for acting as geological tour guides in the Zermatt-Saas Fee area, southern Switzerland and northern Italy. Dr Barnicoat also kindly provided samples of some kyanite–staurolite–garnet amphibolites which he had collected from Frodalera in Switzerland. Neil Manktelow provided very welcome hospitality in Zurich when I was there in 1990 and the Familie at Grawand Hütte, Zillertal, Austria looked after me very well when I used their home as a field base.

During my central Australian field season in 1991, in addition to the Stranks Travelling Fellowship, field support for myself and two honours students, Jo Mawby and Simon Wetherley, was provided by the Department of Geology and Geophysics at the University of Adelaide. Geoff Fraser provided field assistance in the Harts Range. The Cavenagh family allowed us access to their property and were most hospitable for the period of our stay. The Northern Territory Geological Survey also provided a Flying Doctor radio in case of emergency.

During the course of my candidature I have had assistance from many people and I thank all of them heartily: Huw Rosser and other staff at CEMMSA, the University of

Adelaide, for assistance with the electron micro-probe, sample coating, SEM and questions in general; Rick Barrett who assisted with photography, repros and with computer problems and who really was a great help; Sherry Proferes advised on both computer drafting, using a pen and ink and other computer questions; Wayne Mussared and Geoff Trevelyan prepared lots of normal and polished thin sections; Sophie Craddock and Mary Odlum provided help with all sorts of things, from photocopiers and faxes to organising the financial side of things, and for being a mine of all sorts of information; Nick Spencer helped with various computing problems, notably setting up a back-up of my hard disk on Jaeger; Don Creighton was most helpful in the closing stages, helping to solve problems with printing; John Stanley helped with sample preparation and did some XRF analyses and Phil McDuie and Jo Mawby also helped with sample preparation.

More academically, Mike Sandiford, Ian Scrimgeour, John Foden, Jo Mawby, Kurt Stüwe, Karin Ehlers, Simon Wetherley and Annette Bingemer are thanked for comments and discussions on my work and theirs. I also enjoyed helpful discussions with Ian Williams, Mark Fanning, Ian MacDougall, Bill Collins, Gladys Warren, Russell Shaw and other participants at the SGGMP conference "Application of Geochronology to Field Related Geological Problems" in Alice Springs July, 1992.

Bill Collins, Geoff Clarke, Ben Goscombe, Ian Scrimgeour, Jo Mawby, Simon Wetherley, Annette Bingemer, John Foden and Mike Sandiford all read various parts and versions of the thesis and are thanked for their input.

Thankyou very much to Thomas Flöttmann for the seemingly constant use of that wonderful piece of literature, the thesaurus and to Frau Stüwe for obtaining the base for my Zillertal locality map and sending it so promptly.

Roger Powell was patient and helpful with the many aspects of my problems (and CFMASH's problems) with THERMOCALC and the associated datafiles, activity expressions, a-X relations, and provided me with more new versions of the dataset and the program than I could cope with. I must also thank him for his help during those frustrating periods we spent hunched over a monstrous phase diagram. Thomas Will also provided much appreciated advice over activity expressions and amphiboles in particular.

I am also very grateful for the unfailing support that I received early in my academic career (including when I was way out of sight on the other side of the world) from the late John Lock and his family.

And so to more social things: thanks very much to Kurt and Karin and Thomas Will for a place to lay my head during various sojourns to Melbourne; Annette, Thomas, Fran, John and Di, Mike and Bridget, Simon and Kathy, Bunge, Graham, Soph and Andy for many dinners, lunches, bar sessions, visits to the Exeter, Cafe Michael and, of course, Fasta Pasta which provided a much appreciated break from sitting at my desk. Duncan has been a wonderful source of entertainment, inspiration and happiness and I am extremely grateful for the friendship and support provided by him and his family, Diana, Ian and Jo over the last couple of years.

Finally, I wish to sincerely thank my parents for their moral and financial support during my education. They never doubted that I would be the first of my family to attend university, and though they may have been surprised at how long I stayed, they were never anything but proud.

List of Figures

List of Tables

Chapter 1: Introduction

1.1 Introduction

Metamorphic rocks provide a unique opportunity to constrain the processes acting in the interior of the earth. They act as time capsules, preserving information about the physical and chemical conditions which operated during metamorphism and about the deformational processes which acted during and after equilibration. Detailed study of the mineral equilibria, textures and mineral chemistry in metamorphic rocks are especially important for constraining the physical conditions (pressure, P and temperature, T) during metamorphism and the way they change with time. Since rocks of different composition may preserve different aspects of the metamorphic evolution, data from a number of different rocks in a small area have the potential to constrain the way P-T conditions evolve over time (e.g. Droop & Bucher-Nurminen, 1984; Schumacher & Robinson, 1987). Thus metamorphic rocks contain evidence of the tectonic processes involved in orogenesis (e.g. England & Thompson, 1984; Thompson & England, 1984; Hodges, 1991).

The best rock-types for evaluating metamorphic conditions are those which are reactive under a wide range of metamorphic conditions. Pelites provide a classic example and their common occurrence in metamorphic belts has made them the focus of many studies (e.g. Thompson, 1976a,b). However pelites are neither ubiquitous nor reactive over the entire metamorphic spectrum and other rock-types may also provide useful records of metamorphism. This thesis evaluates the potential of amphibolites as a vehicle for constraining metamorphic evolution.

1.2 Background

The protoliths of amphibolites are relatively common in many types of crustal settings as the products of vulcanism, magmatism and sedimentary processes. Although their chemical complexity permits a range of mineralogy (e.g. Eskola, 1914, 1915), over a wide range of metamorphic conditions, they are often characterised by the relatively high variance assemblage calcium-amphibole, chlorite, epidote, plagioclase, quartz ± Fe^{3+}-oxides, carbonates, K-bearing and Ti-bearing phases. This assemblage occurs in greenschist, amphibolite and blueschist grade rocks and has been called the "common" assemblage (e.g. Laird, 1980). Several studies have documented the chemical and modal variation of the phases in these "common" amphibolites with evolving pressure and temperature conditions (e.g. Laird, 1980; Thompson et al., 1982) however these factors (especially modal variation) are extremely sensitive to the bulk-rock chemistry as well as the physical conditions of metamorphism.

There are several reported occurrences of less typical amphibolites which contain more aluminous phases such as kyanite, staurolite, cordierite, garnet and orthoamphibole in addition to more typical amphibolite phases such as hornblende, plagioclase, quartz and oxides (e.g. Gibson, 1978; Ward, 1984a; Selverstone et al., 1984; Helms et al., 1987). The variance of these assemblages is generally lower than in the "common" amphibolites and this makes them an important target for constraining the equilibration conditions under which they developed.

As with all unusual assemblages, it is important to establish if their rarity is due to unusual bulk composition or due to rarely attained conditions of metamorphism. Mass balance calculations and comparative bulk chemical analyses, suggest that these unusual amphibolites may develop in rocks of "typical" mafic igneous composition and that the same rocks are capable of producing the "common" amphibolite assemblage (e.g. Helms et al., 1987). Several workers have suggested that kyanite–staurolite–hornblende assemblages are in a reaction relationship with the "common" assemblage and that they result from metamorphism at higher pressures than is typical for the "common" assemblage (e.g. Selverstone et al., 1984; Helms et al., 1987). However Laird (1980) has commented that the "common" assemblage occurs under a wide range of metamorphic conditions (including high pressure blueschist facies) and thus it is likely that the stability and preservation of kyanite–staurolite–hornblende and related assemblages is dependent on factors other than simple pressure variation. Variation in bulk composition (especially Fe-, Mg- and Al-content) is likely to have a significant effect on the stability of kyanite–staurolite–hornblende assemblages (Ward, 1984a).

1.3 Calculated phase relations in amphibolites

Previous investigations of kyanite–staurolite-amphibolites have dealt principally with a description of the mineralogy and chemistry of individual low variance assemblages together with their higher variance subsets (e.g. Gibson, 1978, 1979; Purtscheller & Mogessie, 1984; Ward, 1984a; Grew & Sandiford, 1985; Grew et al., 1988). Several publications have dealt with a small number of low variance assemblages (e.g. Selverstone et al., 1984; Spear, 1978, 1979, 1982; Humphreys, 1993), however few authors have attempted to understand the phase relations which relate these different occurrences. This may be partly due to the small range of of physical conditions under which kyanite–staurolite–hornblende and related assemblages appear to form (e.g. Robinson et al., 1982), the compositional complexity of amphibolites and the often poor constraints on the P-T conditions at which the assemblages equilibrated.

Froese and Hall (1983) attempted to develop a qualitative P-T grid for kyanite–staurolite amphibolites by linking published data from mafic and pelitic rocks using Schreinemakers analysis. They used generalised phase compositions to write reactions in the linking system, however, the variability of the phase compositions both within and between real assemblages suggests that while this may have been a necessary simplification, the resulting phase relations are unlikely to be valid for all natural occurrences. The P-T grid constructed by Froese and Hall (1983) deals only with univariant reactions in the CaO-FeO-MgO-Al_2O_3-SiO_2-H_2O (CFMASH) system, and no attempt was made to understand the

continuous reactions which are important for most real rocks. Moreover, they have not applied the completed grid to either their own assemblages or those of other workers.

Spear (1978) and Spear and Rumble (1986) have constructed P-μ_{H_2O} petrogenetic grids for amphibolites involving fixed composition aluminous phases. The slopes of the reactions were determined using the ΔV and stoichiometric co-efficients of H_2O for each fixed composition reaction. Although they have the advantage of encompassing sodic plagioclase and amphiboles, their grids also deal specifically with discontinuous reactions and neither Spear (1978) nor Spear and Rumble (1986) discuss continuous reactions. The phase relations in their calculated grids correspond with the compatibility relations reported from the Post Pond and Ammonoosuc Volcanics but do not explicitly address relationships with other known occurrences.

One of the major aims of this thesis is to determine the phase relations in kyanite- and staurolite- amphibolites and related rocks for phases of variable composition, and to determine the continuous reactions which act upon them. As a result of the paucity of direct experimental data for such chemically complex assemblages equilibrium thermodynamics calculations are the most potentially useful method of determining the phase relations between the relevant solid-solution phases. Equilibrium thermodynamics calculations were carried out using the computer program THERMOCALC (Powell & Holland, 1985, 1988) and the internally consistent dataset of Holland and Powell (1985, 1990, pers. comm., 1992).

1.4 Applications

In addition to outlining the theoretical phase relations of kyanite- and staurolite-amphibolites, this thesis presents a review of important occurrences as well as reporting a new world-class locality for kyanite–staurolite amphibolites from the Harts Range region of the eastern Arunta Inlier, central Australia (Chapter 4).

1.4.1 Amphibolites from the Harts Range

The wide compositional variety of the Harts Range amphibolites, especially in regard to X_{Fe}, has resulted in the development of several low-variance assemblages, including kyanite–staurolite–gedrite–hornblende, staurolite–garnet–gedrite–hornblende and kyanite–cordierite–anthophyllite–hornblende (+ plagioclase–quartz). The presence of kyanite- and staurolite-amphibolites suggests that the Harts Range region and the eastern Arunta Inlier have experienced an unusual metamorphic history and the variety of observed amphibolite assemblages are an ideal vehicle for understanding this metamorphic history.

Previous workers have, almost without exception, noted the high temperature-low pressure metamorphic style which is dominant over large areas of the Arunta Inlier and other northern Australian Proterozoic terrains (e.g. Clarke et al., 1990; Etheridge et al., 1987; Sandiford & Powell, 1991). These high grade regions are typically cut by narrow kyanite-bearing retrograde shear zones, however Goscombe (1992a,b) has reported that the

metamorphic history of the Strangways Range in the eastern Arunta Inlier involved an early high temperature history, but also later, widespread metamorphism under high P/T ratios. The mineral assemblages and metamorphic textures from the Harts Range area confirm that high P/T metamorphism also occurred in this area as part of a multiple phase heating and deformational sequence.

An important aspect of understanding the metamorphic history of the Harts Range region relates to a long-standing disagreement over the relative importance of Proterozoic and Phanerozoic (Alice Springs) deformation in the region (e.g. Ding & James, 1988; James & Ding, 1988; Collins & Teyssier, 1989a,b). The metamorphic pressure-temperature-time (P-T-t) history of the Harts Range region is not sufficiently well constrained to discern between these alternatives, and further (mainly geochronological) work is required before this question can be adequately addressed.

1.4.2 Amphibolites and related rocks from the literature

Kyanite–staurolite–hornblende and related assemblages have been reported from several different localities. Among the best of these in terms of variety of low variance assemblages are those from the Zillertal in western Austria. The much studied and relatively young nature of metamorphism in the European Alps mean that the equilibration conditions and metamorphic history of the kyanite–staurolite-amphibolites from this region should be far better constrained than those from other world-wide occurrences. Consequently, these samples form the basis of a comparison of the compatibility relations in similar assemblages from around the world. The kyanite–staurolite-amphibolites from the Zillertaler Alpen contain four different low variance assemblages, involving similar phases to those reported from the Harts Range region. However, there are significant differences in the compatibility relations for the Austrian and Australian rocks despite the small differences in their equilibration conditions (approximately 560°C, 7 kbar and 650-700°C, 7 kbar) implying that the phase relations in this segment of P-T space must be complex, involving at least five univariant reactions. Similar information about the changing compatibility relations over P-T space can be determined from other sets of equilibria, e.g. those from the Post Pond Volcanics, Vermont, USA (Spear, 1982), the M_1 and M_2 assemblages from the Copperton Formation in South Africa (Humphreys, 1993) and the New Hampshire amphibolites (Schumacher & Robinson, 1987). The compatibility relations from many other reported kyanite–staurolite and related amphibolites (e.g. from New Zealand (Gibson, 1978; Ward, 1984a; Cooper, 1980), Antarctica (Grew & Sandiford, 1985), the former USSR(Grew et al., 1988)) encompass only restricted compositional ranges and as a consequence they provide only relatively poor constraints on the changing phase relations over P-T space. However, the relatively small P-T range spanned by this wide variety of assemblages is consistent with the complex phase relations apparent from the Harts Range and Zillertal amphibolites. A broad view of the phase relations in amphibolites has been developed from a comparison of those from many localities.

The final aim of this investigation is to compare the natural amphibolite mineral assemblages with the calculated phase relations in order to obtain a better understanding of kyanite–hornblende, staurolite–hornblende and similar amphibolite assemblages and the rocks in which they occur.

One of the most interesting questions regarding these kyanite- and staurolite-amphibolites is the reason for their rarity, given the apparent abundance of rocks which are chemically suitable for their development. The complexity of the calculated and observed phase relations in kyanite–staurolite amphibolites and related rocks in only a small area of P-T space suggests that their paucity in relation to the "common" amphibolite assemblage results from the small P-T-X (pressure-temperature-composition) window appropriate to each assemblage. The stability fields for these assemblages lie in an area of P-T space which may be intersected in a variety of orogenic settings and correspond to conditions often attained in Barrovian style terrains (Fig. 1.1). However, because of the complexity of especially the sub-system reactions, inappropriate bulk composition (e.g. X_{Fe}), slight overstepping of the reactions, or small increases in temperature during later or continuing metamorphism may be sufficient to allow different assemblages to overprint the rare kyanite- and staurolite–hornblende assemblages. Thus kyanite–staurolite–hornblende assemblages are only rarely preserved.

1.5 Aims of the thesis

The aims of this thesis are: to develop phase diagrams relevant to kyanite- and staurolite-bearing amphibolites from equilibrium thermodynamics calculations; to describe a new occurrence of these assemblages from the Harts Range and to use the calculated phase relations to constrain the metamorphic evolution of the area; to develop an understanding of the phase relations in real amphibolites and to compare the calculated phase relations with those determined from petrological observations.

1.6 Outline of the thesis

A major aim of this project has been to develop a pressure-temperature projection for chemical model systems appropriate to amphibolites. Because amphibolites typically contain a wide variety of elements, reflecting in part the diverse mineralogy of the amphibole group, this is not a trivial problem. Thus, I begin with a well understood, simpler compositional sub-system which is closely related to the more complex amphibolites. Chapter 2 deals with the calculated phase relations in the FeO-MgO-Al_2O_3-SiO_2-H_2O (FMASH) system which approximate the chemistry of cordierite–orthoamphibole-type, K- and Ca-poor rocks. The calculated phase relations are compared with those from well understood natural occurrences of this rock-type.

The good correspondence between the calculated and observed phase relations in cordierite–orthoamphibole-type rocks permits optimism in proceeding to the more complex

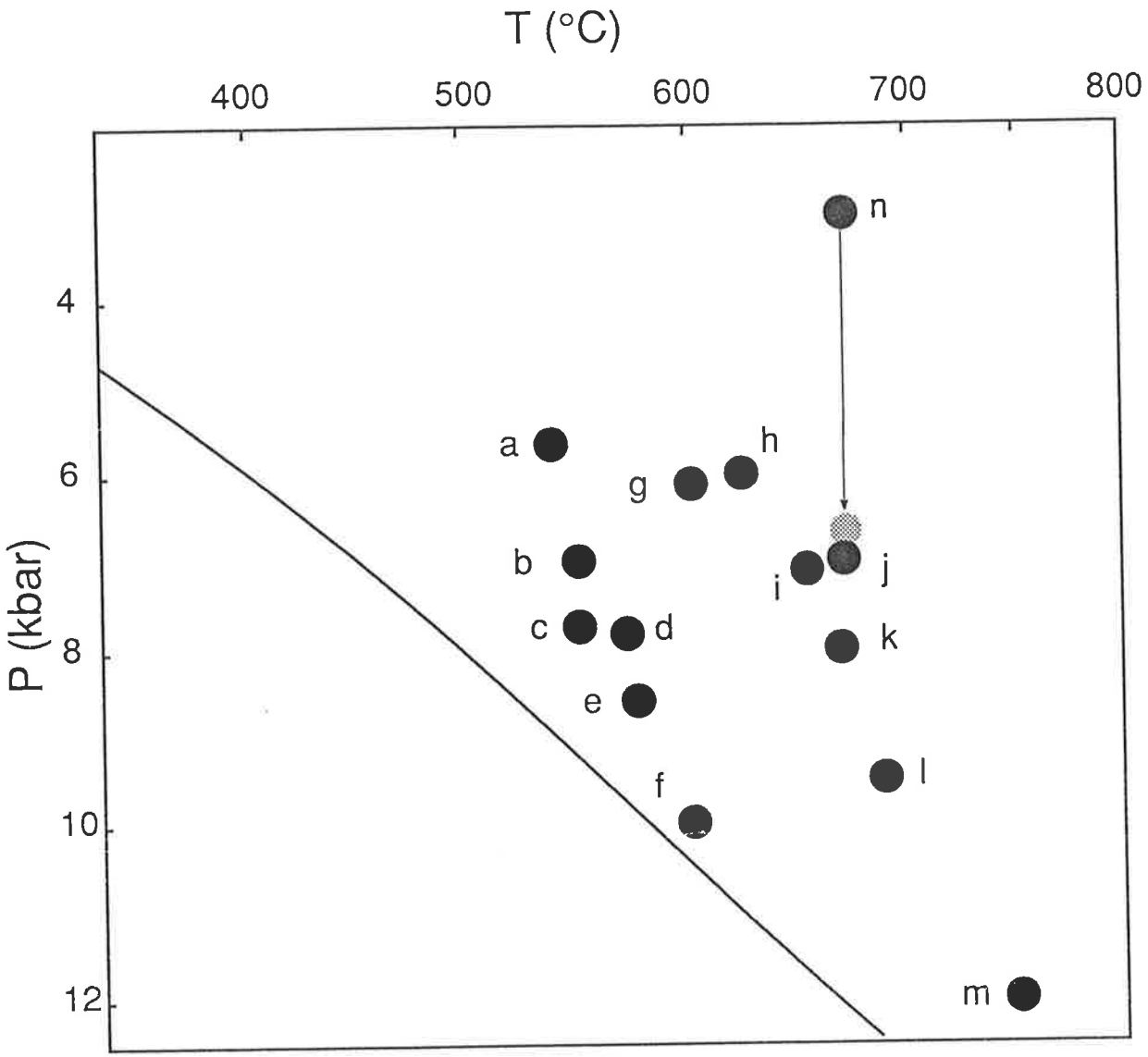

Figure 1.1. The estimated P-T conditions under which reported kyanite-, staurolite- and related amphibolites equilibrated (see Chapter 6 for more detail) in comparison to the stable crustal geotherm of England & Thompson (1984) calculated assuming a thermal conductivity of 2 $Wm^{-1}K^{-1}$. P-T data from a) Spear, 1982; b) Selverstone et al., 1984; c) Chapter 6 (Frodalera); d) Helms et al., 1987; e) Grew & Sandiford, 1985; f) Cooper, 1980; g) Humphreys, 1993; h) Schumacher & Robinson, 1987; i) Grew et al., 1988; j) Chapter 4 (Harts Range); k) Ward, 1984a; l) Gibson, 1978, 1979; m) Ward, 1984a; n) Purtscheller & Mogessie, 1984 (the shaded circle denotes more appropriate conditions).

CFMASH (CaO-FeO-MgO-Al_2O_3-SiO_2-H_2O) system. The connection between the FMASH and CFMASH systems and the justification and reasoning behind simplifying the complex amphibolite chemistry to the chemically simple CFMASH model system are discussed in Chapter 3. The calculated phase relations involving aluminosilicates, staurolite, cordierite, garnet, orthoamphibole, hornblende, anorthite, quartz and an aqueous vapour are developed and the resulting petrogenetic grid is presented in Chapter 3. The calculated equilibria are consistent with many similar amphibolite assemblages reported in the literature. To determine more realistically the limitations on low temperature assemblages and to allow comparisons between the equilibration conditions required for the assemblages of particular interest here and those of the "common" assemblage, chlorite was also included in the model system. This revealed significant problems with the calculated phase relations in the more complex system. The inconsistency between the calculated phase relations and the natural assemblages cannot be explained by variation in chemical factors and thus, the problems seem to result from uncertainties in the thermodynamic data for one or more of the endmember phases *gedrite*, *Mg-staurolite*, *Fe-staurolite* or perhaps the activity-composition (a-X) relations in garnet or chlorite. The correspondence achieved between the reaction relations in rocks from the Harts Range region (Chapter 5) and other reported chlorite-absent kyanite- and staurolite-amphibolites and the calculated phase relations suggests that these problems are not critical in the chlorite-absent CFMASH system. Thus, phase relations calculated for the chlorite-absent CFMASH system apply at least qualitatively to chlorite-free amphibolites. A new chlorite-bearing CFMASH grid, constructed using modified thermodynamic data for *Mg-staurolite* and *Fe-staurolite* provides a much closer approximation of the phase relations in amphibolites. Thus suggests that the phase diagram for real amphibolites will have the same form as this calculated P-T projection and that mainly the *absolute* positions of the invariant points in P-T space will change as less uncertain data are obtained.

Chapter 4 deals with the mineral assemblages, textures and compositions of the amphibolites from the Harts Range region (samples and thin sections are housed in the collection of the Department of Geology and Geophysics at the University of Adelaide, and are prefixed by the sample numbers 962-, 950-, 890-, 891-, HR91-, 85-, 852- and 853-) and implications of these assemblages in terms of constraining the metamorphic history of the area.

Chapter 5 describes the mineral assemblages, textures and compositions of kyanite–staurolite amphibolites and associated rocks from the Austrian Zillertaler Alpen (accession number 938-). The compatibility relations of the hornblende garbenschiefer are also discussed. Chapter 6 deals with the compatibility relations determined from reported kyanite- and staurolite-amphibolites and those described in this thesis. The relationships between the different amphibolite assemblages are discussed and the P-T constraints on the amphibolite assemblages determined from petrological observation are compared with those calculated by Spear & Rumble (1986) and determined from equilibrium thermodynamics calculations in Chapter 3. The final chapter is a summary of the findings of the thesis and presents some ideas about how to improve the calculated phase relations in order that they provide a more widely relevant basis for the interpretation of amphibolites.

Chapter 2: Phase relations in aluminous schists: the FMASH model system

2.1 Aluminous rock-types and their constituent phases

Rocks with bulk compositions essentially restricted to the FMASH (FeO-MgO-Al_2O_3-SiO_2-H_2O) compositional system show an extraordinary diversity in mineral assemblages over a wide range of pressure temperature conditions. Consequently they have been subject to a large number of petrological investigations (e.g. Hudson & Harte, 1985; Robinson & Jaffe, 1969a, Harley, 1985). The rock-types encompassed by the FMASH model system include cordierite–orthoamphibole rocks, aluminous schists, "whiteschists" (Schreyer, 1973, 1974) and sapphirine granulites. They will be collectively termed here "aluminous schists". World-wide occurrences of these rock-types show them to be particularly reactive in a broad cross-section of orogenic settings. Their phase relations are well constrained from natural occurrences and this, together with their unusual chemical simplicity, means they may be used to constrain the phase relations in the FMASH model system.

In amphibolite and granulite facies "aluminous schists", the phases commonly present include the aluminosilicates (kyanite, andalusite, sillimanite), staurolite, cordierite, garnet, chlorite, orthoamphiboles, orthopyroxene, quartz, sapphirine, corundum, Fe-Mg spinels and less commonly, chloritoid, talc and yoderite. Biotite, plagioclase and a Ti-phase (rutile or ilmenite) are often present in minor proportions. The rocks of particular interest in this study are medium grade (amphibolite facies) rocks which contain sufficient silica to stabilise free quartz. Consequently, not all of the above-mentioned FMASH phases will be considered. Chloritoid is typically a low temperature phase in pelites (Albee, 1972) and is only rarely reported from the aluminous schists under consideration here. Orthopyroxene typically occurs in anhydrous rocks appropriate to the granulite facies, while talc and yoderite are stable in high pressure parageneses (Schreyer & Seifert, 1969a, 1969b). Corundum, Fe-Mg spinels and sapphirine do not occur with free quartz under amphibolite facies conditions. The minor phases biotite, plagioclase and rutile or ilmenite are stabilised by the additional components K, Ca and Na and Ti, respectively and thus can be excluded from the FMASH system. Our interest is therefore restricted to the aluminosilicates, staurolite, cordierite, garnet, chlorite, orthoamphiboles and quartz and an aqueous vapour. The general formulae and abbreviations used for the phases of interest in this thesis are listed in Appendix A1.

This chapter deals with the phase relations in aluminous schists under quartz saturated, medium grade conditions. The chemographic relations of the phases and their implications for the univariant reactions in FMASH are discussed and the mineral equilibria and compatibility relations in natural aluminous schists are used to constrain the stable FMASH equilibria.

Equilibrium thermodynamics calculations are used to determine a quantitative P-T projection for the FMASH model system, which is tested by comparison with the natural phase relations.

2.2 Chemographic relations in the FMASH system and the concept of singularities

For FMASH rocks with quartz and an aqueous vapour phase in excess, phase relations may be conveniently represented on an AFM compatibility diagram, as in Fig. 2.1a and 2.1b. The ferromagnesian phases of interest may have widely variable composition in rocks from different localities, however they typically display a consistent order of Fe-enrichment: Grt ≥ St > Oam > Chl > Crd (e.g. Hudson & Harte, 1985; James et al., 1978; Sharma & MacRae, 1981; Baker et al., 1987; Harley, 1985; Arnold & Sandiford, 1990). Garnet is typically more Fe-rich than co-existing staurolite (e.g. Percival et al., 1982; Harley, 1985; Hudson & Harte, 1985; Baker et al., 1987; Arnold & Sandiford, 1990) however the Fe/Mg contents (X_{Fe} = Fe/(FeO+MgO)) of these phases are often very close and in some samples a reversal of the "usual" trend is observed, so that $X_{Fe,St} > X_{Fe,Grt}$ (Sharma & MacRae, 1981; Purtscheller & Mogessie, 1984; Grew & Sandiford, 1985; Visser & Senior, 1990). The majority of the phases of interest show relatively little Al-substitution and only orthoamphibole and chlorite allow appreciable variation in Al-content due to tschermakite substitution ($Mg_{-1}Si_{-1}Al_1Al_1$) toward the *gedrite* and *amesite* end-members, respectively. The effects of this variability in the chemographic relations are discussed below.

The variation in relative X_{Fe} of staurolite and garnet as well as the range of A/AFM in chlorite and orthoamphibole has the potential to cause significant complexity in the phase relations. Figure 2.1a represents the tie-lines apparent in the AFM projection assuming that (i) garnet is more Fe-rich than co-existing staurolite and that (ii) chlorite occurs on the Mg-rich side of the cordierite–orthoamphibole tie-line (e.g. Percival et al., 1982; Hudson & Harte, 1985). A significantly different array of tie-lines will result if either of these assumptions is untrue. An alternative AFM diagram, assuming that $X_{Fe,St} > X_{Fe,Grt}$ and chlorite plots *inside* the cordierite–orthoamphibole–garnet tie-triangle is presented in Fig. 2.1b.

2.2.1 Singularities

In real rocks it is likely that the compositions of the phases in a univariant reaction will evolve with the intensive variables (e.g. P, T), allowing the possibility that the compatibility relations may change with the developing physical conditions. Changes in the relative Fe-Mg-Al partitioning will occur gradually as the G-X relations evolve and at some intermediate stage, a colinearity involving three of the four phases will develop. In the case of a Mg-rich assemblage involving aluminosilicate, cordierite and chlorite ± one other phase, this intermediate stage will be marked by the intersection of the univariant reaction, e.g.

aluminosilicate + chlorite ⇒ cordierite + orthoamphibole,

Figure 2.1. AFM diagram with quartz and an aqueous vapour in excess. (a) assuming that garnet is more Fe-rich than co-existing staurolite, and that chlorite occurs on the Mg-rich side of the cordierite-orthoamphibole tie-line, (b) assuming that staurolite is more Fe-rich than co-existing garnet, and that chlorite plots inside the cordierite-orthoamphibole-garnet tie-triangle.

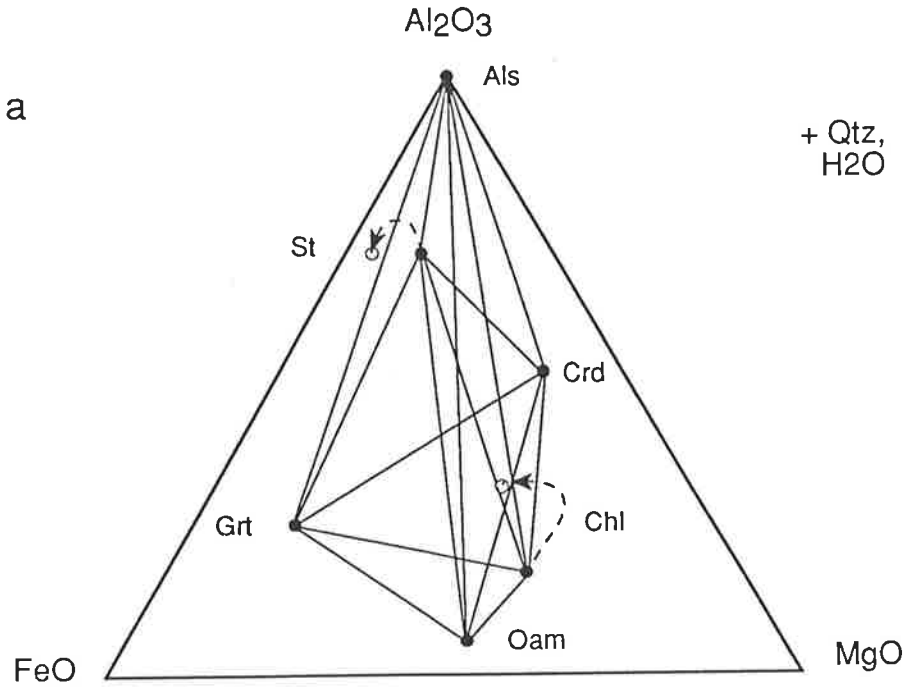
a
Al2O3
Als
+ Qtz,
H2O
St
Crd
Grt
Chl
Oam
FeO
MgO

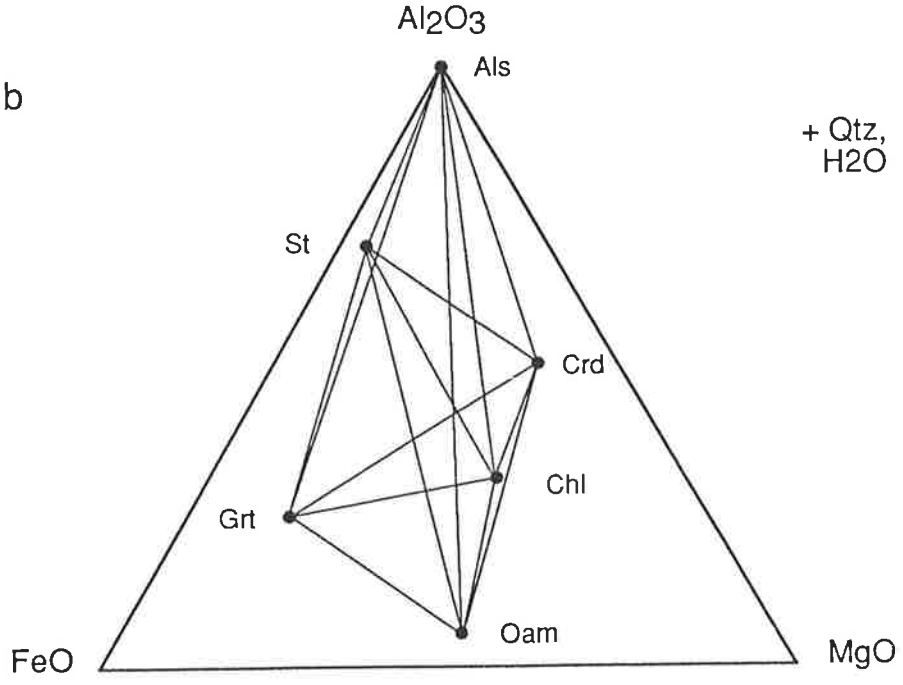
b
Al2O3
Als
+ Qtz,
H2O
St
Crd
Chl
Grt
Oam
FeO
MgO

with the degenerate reaction,

chlorite + aluminosilicate ⇒ cordierite

(Fig. 2.2) as the pressure and temperature increase. As the intensive variables continue to evolve, the co-linearity (degenerate reaction) will be crossed and a new tie-line topology will result. In the current example cordierite becomes interior to the tie-triange aluminosilicate–chlorite–orthoamphibole so that

aluminosilicate + chlorite + orthoamphibole ⇒ cordierite.

Similarly, the topology of the Fe-rich portion of the compatibility diagram will evolve via a singularity involving the aluminosilicate + garnet ⇒ staurolite degenerate reaction. The point at which the degenerate (n phase) reaction intersects the univariant (n+1) reaction is known as a singularity (Guiraud et al., 1990; Will et al., 1990a).

2.3 Phase relations from real mineral assemblages

2.3.1 Stability of univariant reactions and invariant points

As determined above, the FMASH (n = 5) model system appropriate to "aluminous schists" involves 10 (n+5) phases. The effective number of components can be reduced to 3 and the number of phases to 8 by considering that quartz and aqueous vapour are in excess. If we further consider that in general only one aluminosilicate polymorph (either kyanite, andalusite *or* sillimanite) is stable at a given P-T co-ordinate, then the FMASH system consists of a total of 6 (n+3) phases. This implies that there are 6 possible invariant points, some of which will be stable while others will be metastable.

The reaction textures and equilibria observed in natural rocks with compositions approaching the FMASH system can be used to establish which of the six possible invariant points are stable. For example, the presence of sillimanite in the core of staurolite–cordierite coronas in a gedrite–quartz-bearing sample from southwestern New Hampshire (Robinson & Jaffe 1969a; Schumacher & Robinson, 1987) implies that the reaction

gedrite + aluminosilicate = cordierite + staurolite (Chl, Grt)

is seen by real rocks and that it is a reaction appropriate to the sillimanite stability field. (In this thesis, the conventional notation will be followed for labelling invariant and univariant equilibria i.e., the phase(s) which is *not* involved in a particular equilibrium will appear as its label in either brackets [invariant points] or parentheses (univariant lines).) Similarly, the presence of several other univariant (four-phase) assemblages in real FMASH rocks confirm that the reactions

garnet + sillimanite ⇒ cordierite + staurolite (Chl, Oam),

garnet + cordierite ⇒ sillimanite + gedrite (Chl, St)

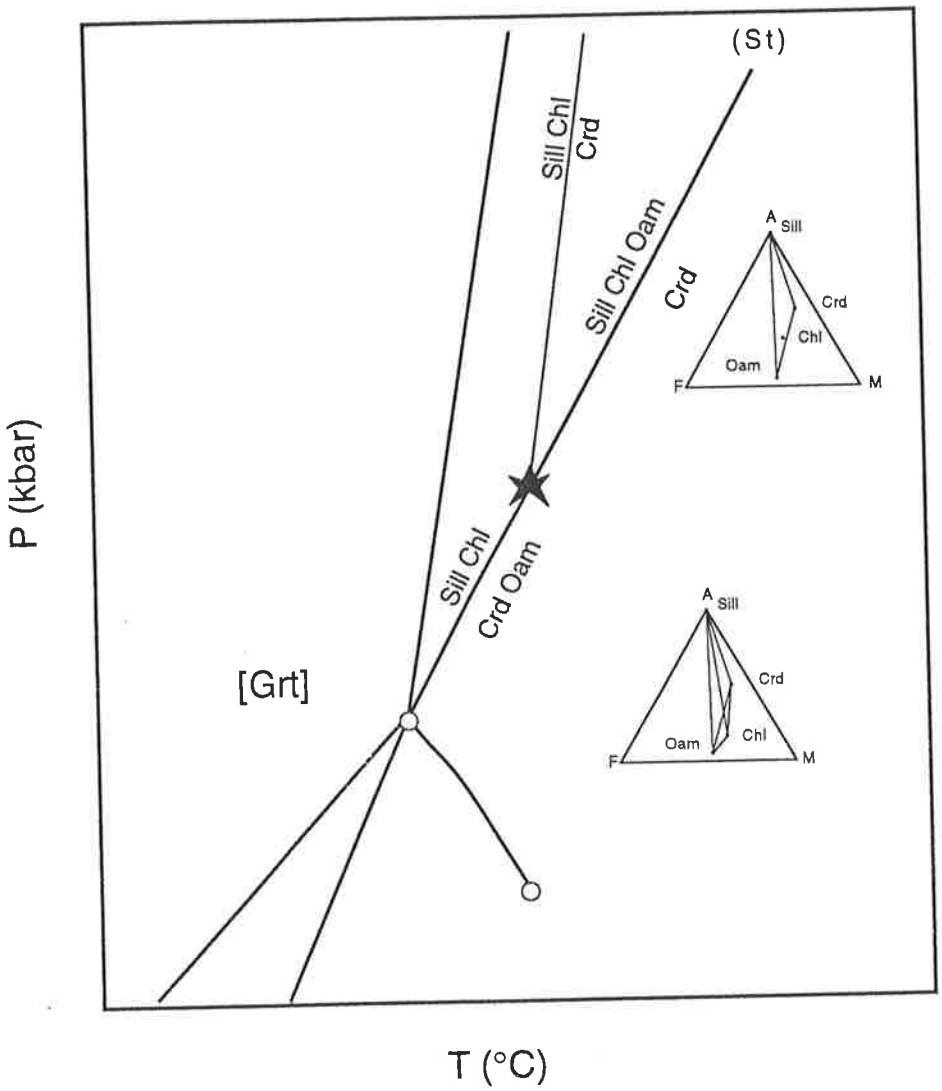

Fig. 2.2. A singularity in the FMASH (+ Qtz, H_2O) system. Chlorite becomes more Al-rich and more Mg-rich with increasing pressure and temperature along the FMASH univariant reaction (Grt,St); sillimanite + chlorite ⇒ cordierite + orthoamphibole. When the composition of chorite is co-linear with sillimanite and cordierite in the AFM plane, the univariant (Grt,St) intersects the FMASH degenerate reaction sillimanite + chlorite ⇒ cordierite to form a singularity, marked by the star. As pressures and temperatures increase further, chlorite moves to the Mg-rich side of the cordierite, so that the FMASH reaction (Grt,St) becomes sillimanite + chlorite + orthoamphibole ⇒ cordierite.

(Sharma & MacRae, 1981) and

staurolite = garnet + sillimanite (kyanite)+ gedrite (Chl, Crd)

(Robinson & Jaffe, 1969b) are also observed in real rocks. The existence of these four reactions (and their sub-assemblages) in natural rocks approximating the FMASH system suggest that the invariant point from which these reactions emanate is stable in real rocks, providing that the critical assemblages are not stabilised by small amounts of additional components. The stability of the invariant point [Chl] involving aluminosilicates, staurolite, cordierite, garnet and orthoamphibole, here termed Ip_1, is taken as the starting-point for the construction of the FMASH P-T grid.

2.3.2 Topology of univariant reactions around FMASH invariant points

Information about the topology of the univariant reactions around Ip_1 can also be determined from published descriptions of aluminous schists. For example, staurolite–cordierite assemblages occur at lower pressures than the orthoamphibole–aluminosilicate stability field (Schumacher & Robinson, 1987) and at lower temperatures than the garnet–cordierite stability field (Vallance, 1967; James et al., 1978; Sharma & MacRae, 1981; Stoddard & Miller, 1990; Arnold & Sandiford, 1990). Staurolite–orthoamphibole is a low temperature assemblage in comparison to garnet–cordierite and staurolite–cordierite (Arnold & Sandiford, 1990).

Chlorite is observed in equilibrium assemblages in lower temperature aluminous schists. These include the "notable" appearance of kyanite–chlorite in greenschists (Schreyer & Seifert, 1969a; Schumacher & Robinson, 1987) and staurolite–chlorite in the sillimanite stability field (Stoddard & Miller, 1990). Orthoamphibole co-exists with cordierite to somewhat higher temperatures than most of these assemblages (Vallance, 1967; Robinson & Jaffe, 1969a, 1969b; Schreyer & Seifert, 1969a; Green & Vernon, 1974; James et al., 1978; Sharma & MacRae, 1981, Harley, 1985; Stoddard & Miller, 1990; Arnold & Sandiford, 1990).

2.3.3 Location of Ip_1 in P-T space

Sillimanite and kyanite (but not andalusite) are the dominant aluminosilicate pseudomorphs in (or associated with) many of the three- and four-phase assemblages reported from aluminous schists (e.g. kyanite–garnet–gedrite (Hietanen, 1959), kyanite–cordierite–gedrite (Vernon, 1972), kyanite–garnet–orthoamphibole, cordierite–garnet–orthoamphibole (Harley, 1985), sillimanite–cordierite–orthoamphibole (Schumacher & Robinson, 1987)). This suggests that the invariant point which relates these assemblages is surrounded by the sillimanite and kyanite stability fields and the above information about the relative stabilities of the assemblages (section 2.3.2) restricts the location of Ip_1 to the sillimanite stability field.

Aluminosilicate–orthoamphibole-bearing samples also almost invariably occur in either the kyanite or sillimanite stability field. Two possible exceptions, in which *andalusite* is associated with orthoamphibole, are reported from South Australia and Japan:

(1) In the Springton region of South Australia aluminous schists preserve evidence of a progressing sequence of reactions; staurolite–orthoamphibole or andalusite–sillimanite–orthoamphibole to staurolite–cordierite to cordierite–garnet (Arnold & Sandiford, 1990). The andalusite involved in these reaction textures is typically rimmed by sillimanite, suggesting that the andalusite is relict.

(2) Andalusite–cordierite–garnet–orthoamphibole assemblages from Japan have been reported by Seki and Yamasaki (1957) and these are also at odds with the perception that Ip_1 must occur in the sillimanite field. However, the original authors have commented on the fine grain-size of the samples in which this assemblage occurs, and the difficulty in distinguishing the various phases. From some of these samples Seki and Yamasaki (1957) also report very low variance parageneses (including 5 different invariant assemblages), sometimes involving corundum and/or spinel with quartz. This suggests that the equilibrium volumes in these samples were extremely small and that the association of andalusite with orthoamphibole, which is thought by most workers to be metastable (e.g. Robinson & Jaffe, 1969b), may not be an equilibrium assemblage.

Several other workers also report orthoamphibole and andalusite from the same sample, however, the two minerals typically occur in discrete, separate layers (e.g. Visser & Senior, 1990). Thus these two exceptions to the general rule that aluminosilicate–orthoamphibole assemblages occur entirely (or at least predominantly) in the kyanite and sillimanite stability fields can be accounted for as the result of local disequilibrium and the position of Ip_1 in real rocks can be safely placed in the sillimanite field.

2.4 A calculated FMASH grid

The P-T position of each of the invariant points and univariant reactions involving andalusite, sillimanite, kyanite, staurolite, cordierite, garnet, chlorite and orthoamphibole (with quartz and an aqueous vapour in excess) has been calculated using the computer program THERMOCALC. The thermodynamic data used for the calculations in this thesis are listed in Appendix A2. Appendix A3 contains the permanent datafiles used in this chapter for the FMASH calculations and Appendix A4 is an explanation of the permanent datafiles. Appendix A5 is an example output file for the FMASH invariant point Ip_1 or [Chl]. Ideal mixing has been assumed for all solid solution phases, as this assumption was used to extract many of the data (Holland & Powell, 1990). The resulting P-T grid (constructed using Schreinemakers analysis, Zen, 1966) is presented in Fig 2.3.

Both Schreinemakers analysis and the empirical data outlined in section 2.3 suggest that only two ([Chl] and [Grt]) of the six possible univariant points in the FMASH system are stable. [St] is metastable with respect to these and [Crd], [Oam] and [Als] are all metastable with respect to FASH subsystem invariant points. Both [Grt] and [Chl] occur at moderate

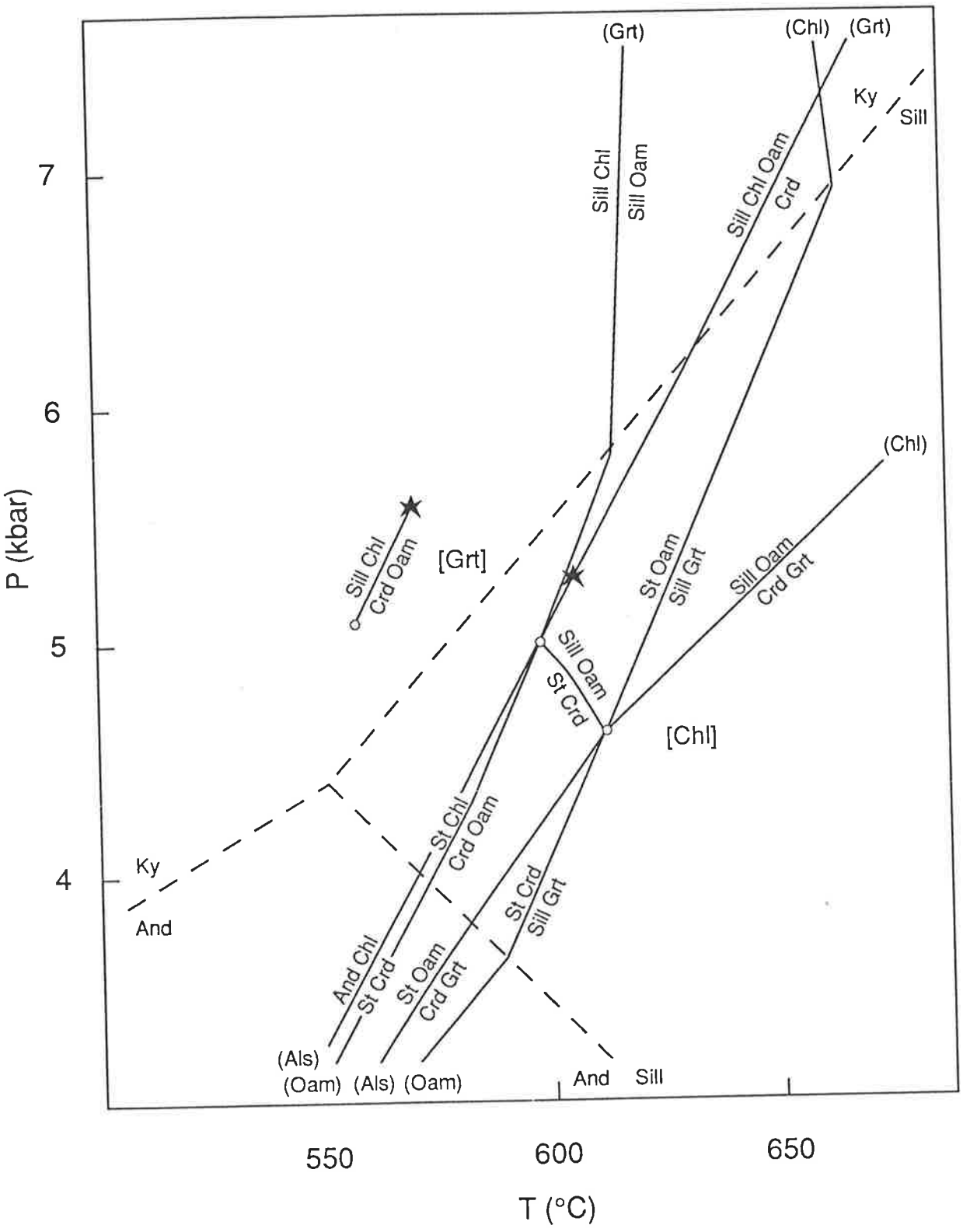

Fig. 2.3 P-T projection calculated for the FMASH system involving the phases andalusite, sillimanite, kyanite, staurolite, cordierite, garnet, chlorite and orthoamphibole (with quartz and an aqueous vapour in excess).

pressures and temperatures and so may be expected to have a strong influence on the phase relations observed in many natural rocks. For example, according to Fig. 2.3, assemblages involving orthoamphibole with an aluminosilicate phase are limited to elevated pressures and orthoamphibole should never occur in equilibrium with the andalusite polymorph. Cordierite–garnet and cordierite–orthoamphibole are both restricted to high temperatures whereas staurolite–orthoamphibole, staurolite–chlorite and aluminosilicate–chlorite occur only under low to moderate temperatures. Assemblages involving co-existing cordierite and staurolite will be observed only in low pressure aluminous schists.

2.5 Uncertainties in the calculated P-T projection

The internally consistent nature of the data used to calculate the phase diagram (Fig. 2.3) allows some confidence in the predictions of these diagrams (especially in the relative positions of the stability fields and the slopes of the univariant reactions which separate them). However, there are still substantial uncertainties in the data themselves and these may have a significant effect on the loci of the equilibria in P-T space. For example, the slopes of most of the reactions involved in the mid-pressure, mid-temperature invariant points, [Grt] and [Chl], are fairly similar and their sub-parallel nature means that the positions of [Grt] and [Chl], marked by the intersection of these univariants, will not be well defined. However, both of these bundles of reactions also involve the near-perpendicular reaction;

orthoamphibole + sillimanite ⇒ staurolite + cordierite (Grt, Chl).

The high angle at which this reaction intersects the other reactions means that it effectively controls the position of both of the invariant points. It follows that any error in the position of the reaction (Grt, Chl) may have a considerable effect on the absolute position of the critical assemblages in P-T space.

Although many of the data required for equilibrium thermodynamics calculations are relatively well characterised from experimental work, standard molal enthalpies of formation are notoriously difficult to determine to an acceptable level of accuracy (Helgeson et al., 1978; Powell & Holland 1985). The uncertainties on standard molal enthalpies of formation determined from both molten salt calorimetry and low temperature heat by solution in HF are high and may cause errors in the calculated position of a reaction of as much as 100°C (Helgeson et al., 1978). For this reason it is assumed that the enthalpy data of the mineral end members will be the major contributors to uncertainties in the P-T conditions of the calculated mineral equilibria.

The uncertainties on the thermodynamic data used in the calculation of Fig. 2.3 are listed in Appendix A2. Although the aluminosilicates, quartz and water vapour all have fairly insignificant uncertainties on ΔH_f, and those for the end members *clinochlore*, *amesite*, *almandine* and *pyrope* are also quite low (3.21, 2.98, 2.78, 2.33 kJ mol^{-1} respectively), the uncertainties for the enthalpies of formation of the other end-members are comparatively high. The most uncertain data are those for *Mg-staurolite*, *Fe-staurolite*, *gedrite*, *ferro-anthophyllite*

and *anthophyllite* (8.31, 8.17, 6.55, 6.44, 5.58 kJ mol^{-1} respectively). It is unfortunate that the reaction controlling the position of both [Chl] and [Grt] involves phases with significant uncertainties. Figure 2.4 illustrates the uncertainty in the P-T position of the invariant point [Chl] due to altering the ΔH of *gedrite* and both *Fe-* and *Mg-staurolite* within the limits of their uncertainties.

Another source of potential problems in the calculated equilibria is in the relative Fe-Mg partitioning exhibited by staurolite and garnet which, in natural rocks, may have overlapping X_{Fe} (see section 2.2). Small changes in the enthalpy of one of the staurolite end members (or in the thermodynamic data or a-X (activity-composition) relations of garnet) may cause an exaggeration (or, less likely, a reversal) of the differences in the calculated compositions of staurolite or garnet.

2.6 A comparison between observed and calculated phase relations in aluminous schists

The positions of the invariant points in the calculated P-T projection (Fig. 2.3) correspond quite well with the relative positions of the real assemblages in P-T space and with the estimated temperatures of equilibration of these rocks (see sections 2.3 & 2.4). The calculated pressures of the invariant points in Fig. 2.3 also seem to correspond reasonably well with the information obtained from the natural rocks, however the presence of additional components is likely to have a significant effect on this conformity.

Most natural aluminous schists contain at least a small proportion of plagioclase, a titanium phase and sometimes a small amount of biotite (e.g. Harley, 1985; Arnold & Sandiford, 1990). While rutile (or ilmenite), biotite and anorthite are each stabilised by an additional component which is not easily incorporated into other phases, albite is stabilised by the presence of sodium which may also be partitioned into the structure of orthoamphiboles. This means that for *nearly all* natural examples, the phase relations in aluminous schists are more properly described in the NFMASH rather than the FMASH system. If the phase diagram is projected from plagioclase (as it is effectively for the other additional components, K and Ti) then the orthoamphibole-bearing assemblages will be stabilised with respect to the other phases and those stability fields will be expanded along (down) the [Oam] reactions. Because it is the *model* system FMASH which is of primary interest here (a system which can later be used to explain the effects of minor additional components such as Na), the calculated equilibria in Fig.2.3 are considered to occur at excessively low pressures. Of most significance is the likelihood that with the addition of Na to the phase diagram in Fig. 2.3, the invariant point Ip_1 is likely to move to lower pressures, thus allowing orthoamphibole to be stable with andalusite and thus contradicting the observed phase relations.

As mentioned previously, the uncertainties in the thermodynamic data used to calculate the P-T projection in Fig. 2.3 are quite considerable, especially for the *mst, fst, ged, fath* and *anth* end members. Therefore it is possible to adjust the ΔH data for these endmember phases without invalidating the results of the calculations. Because of the old and inaccurate nature of

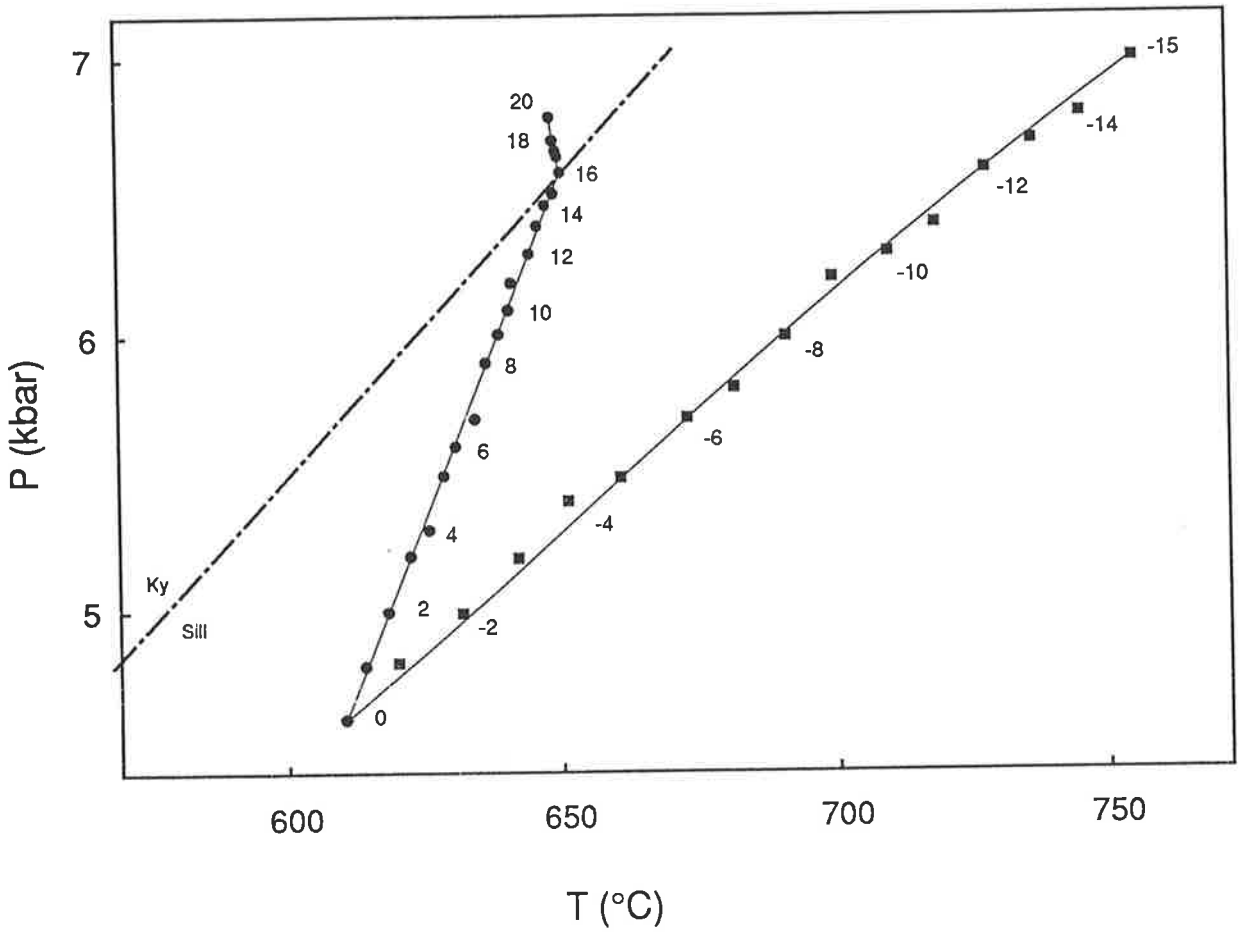

Figure 2.4. The changing location of the FMASH invariant point [Chl] or Ip_1, with increasing ΔH_{ged} from 0 to 20 kJmol^{-1} (circles) and decreasing $\Delta H_{mst} = \Delta H_{fst}$ 0 to -15 kJmol^{-1} (squares).

the thermodynamic data for the *gedrite* endmember which was generated from the experimental data of Schreyer and Seifert (1969b; see also Howell, 1991), altering the enthalpy of *gedrite* is considered to be the most appropriate adjustment to make to the data set. In order to better represent the phase relations in the FMASH model system, the enthalpy of *gedrite* (ΔH_{ged}) should be altered by a factor which places Ip_1 high up in the sillimanite stability field (Howell, 1991; Xu et al., 1993). For rocks containing sodium, Ip_1 may then move down pressure, along the [Oam] FMASH univariant reaction, without leaving the sillimanite stability field.

2.7 FMASH grid with adjusted thermodynamic data

A second P-T projection (Fig 2.5) has been calculated for the FMASH system (with quartz and aqueous vapour in excess) involving aluminosilicates, staurolite, cordierite, garnet, chlorite and orthoamphibole, using the permanent datafile in Appendix A3 in with the enthalpy of *gedrite* (ΔH_{ged}) adjusted by + 10 $kJmol^{-1}$.

2.8 Applications of the FMASH P-T projection

Recent applications of the FMASH P-T projections calculated in this section have included an investigation of the metasomatic evolution of pelites and semi-pelites to K-depleted aluminous schists during prograde metamorphism (Arnold & Sandiford, 1990) and an estimate of the changing metamorphic field gradient in a thermal aureole (Sandiford et al., in prep.). Both of these are reproduced in Appendix A6 and a brief outline of the latter follows.

The metamorphic sequence outcropping in the eastern Mt Lofty Ranges (southern Adelaide Fold Belt) comprises a large proportion of psammitic material with minor pelites, semi-pelites, K-depleted aluminous schists, calc-silicates and marbles. Various aspects of the metamorphism of an area East of Springton have been recently described by Sandiford et al. (1990), Arnold and Sandiford (1990) and Dymoke and Sandiford (1992). In comparison to the dominantly biotite grade observed elsewhere in the Mt Lofty Ranges, metamorphism in the eastern Mt Lofty Ranges area is significantly higher grade. This is thought to result from contact metamorphism around a suite of syn-tectonic granites (Sandiford et al., 1991; Sandiford et al., 1992).

The metamorphic grade preserved in the rocks gradually increases from NE to SW where the pelites progress from biotite-, through andalusite–staurolite- and sillimanite-schists to migmatites. In aluminous schists the mineral assemblages: staurolite–cordierite–orthoamphibole, cordierite–orthoamphibole, cordierite–garnet–orthoamphibole and garnet–orthoamphibole describe a prograde sequence over a distance of approximately 5 km. The sequence of divariant and trivariant assemblages preserved in the aluminous schists provides an excellent record of the peak conditions reached in the different parts of the area, and with the aid of compositional information, the opportunity to determine the metamorphic field gradient across the area, documented by the changing mineralogy. P-T pseudosections (e.g. Fig. 2.6)

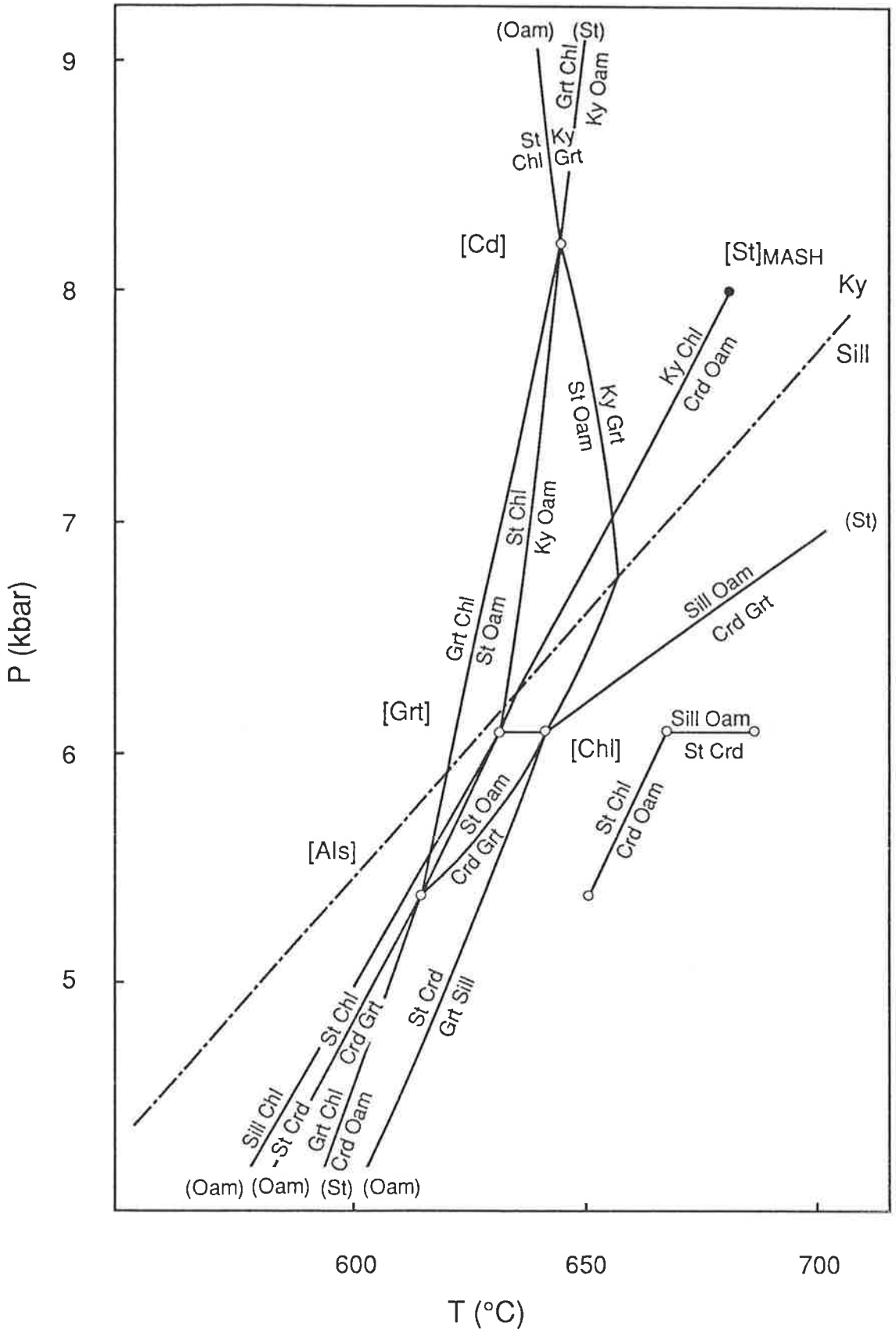

Fig. 2.5 P-T projection calculated for the FMASH system involving the aluminosilicates, staurolite, cordierite, garnet, chlorite and orthoamphibole (with quartz and aqueous vapour in excess). In which the enthalpy of *gedrite* (ΔHged) has been adjusted by + 10 kJmol^{-1}.

Figure 2.6. P-T pseudosections calculated around the [Chl] invariant point) for bulk compositions of Al_2O_3: FeO: MgO (a) 20: 64 :16 (X_{Fe} = 0.8) and (b) 20: 72 : 8 (X_{Fe} = 0.9) with quartz, aqueous vapour and orthoamphibole in excess. Pseudosections such as these may be used to estimate the metamorphic field gradient across a prograde metamorphic sequence.

a

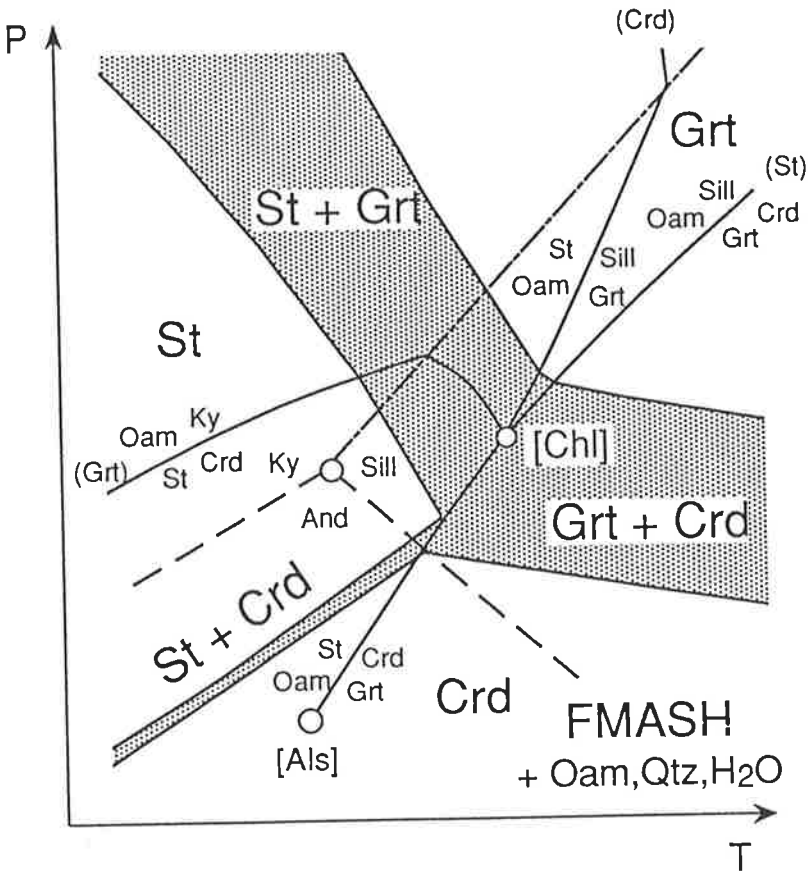
P
T
(Crd)
Grt
(St)
Sill
Oam
Crd
Grt
St + Grt
St
Sill
Oam
Grt
Oam
Ky
(Grt)
St
Crd
Ky
Sill
[Chl]
And
Grt + Crd
St + Crd
St
Crd
Oam
Grt
Crd
FMASH
[Als]
+ Oam,Qtz,H2O

b

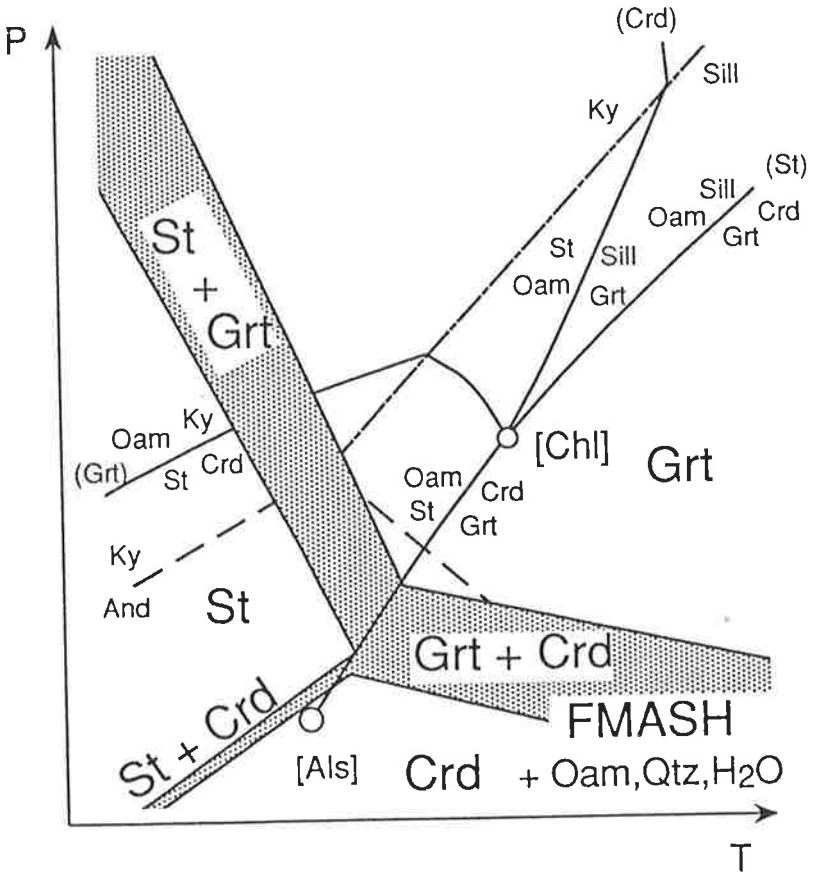
P
T
(Crd)
Sill
Ky
(St)
Sill
Oam
Crd
Grt
St
+
Grt
St
Sill
Oam
Grt
Oam
Ky
(Grt)
St
Crd
[Chl]
Grt
Oam
Crd
St
Grt
Ky
And
St
Grt + Crd
FMASH
St + Crd
[Als]
Crd
+ Oam,Qtz,H2O

constructed for the specific bulk compositions observed should allow quantitative estimates of the changing peak conditions and thus the metamorphic field gradient.

2.9 Discussion

The success of the calculated P-T projections in explaining the mineral equilibria observed in FMASH-type rocks suggests that despite the necessary simplifications of both the compositional system and the a-X and mixing relations of the phases, the construction of phase diagrams from thermodynamic data is essentially a good method. Some problems remain, the most obvious being the substantial uncertainties in some of the data and a lack of both thermodynamic data for minor-component end-members and mixing data between solid-solution end-members.

One potentially serious problem with the P-T projections calculated thus far is that they do not take account of Na. This problem, relating to the position of invariant point Ip_1 (and related invariants) in real rocks containing Na, may be addressed to some extent by including a sodic-orthoamphibole endmember phase, "*ortho-edenite*" (Will & Powell, 1992) and *albite* plagioclase in the grid. While the thermodynamic data for *albite* are readily available, those for edenitic orthoamphibole are not. However, Will and Powell (1992) have recently suggested that difficult-to-obtain thermodynamic data may be determined from a combination of natural mineral pair data and thermodynamic data for better constrained end-members. These workers suggest that Darken's quadratic formalism may be utilised to express the thermodynamic data for a particular phase as an ideal mixing solution between a real (well determined) endmember and a fictive (un-determined) endmember with the same structure. The chemical potential for "*ortho-edenite*" can be written as a linear combination of edenite, anthophyllite and tremolite so that

$$\mu oed \text{ in Oam} = \mu ed \text{ in Oam} + \mu anth \text{ in Oam} - \mu tr \text{ in Oam.}$$

Will and Powell (1992) suggest that it is possible to combine the thermodynamic data of these phases in a similar way, in order to obtain the data of interest for *orthoedenite*. In order to account for the non-ideality in mixing between these real and fictive phases, the authors have determined Darkens quadratic formalism (DQF) terms (or "I-values") which relates data for a known real endmember to a fictive endmember. In the case of the above mixing scheme, $I_{ed,Oam}$ (I*edenite* in Oam) = 44.3, $I_{anth,Oam} = 0$ and $I_{tr,Oam} = 34.5$. Therefore the I-value for *orthoedenite* in orthoamphibole = 44.3 + 0 - 34.5 = 9.8 (see Appendix A4 for the coding of DQF terms). Thus, although the experimental data for the sodic-orthoamphibole endmember are not available, it can be estimated for the purposes of equilibrium thermodynamics calculations.

The end-members *albite* and *orthoedenite* were incorporated into the permanent data files listed in Appendix A3 (NFMASH) and a P-T projection for the NFMASH system was calculated (Fig. 2.7). As expected, the invariant points equivalent to those in Figs. 2.3 & 2.5 moved along the (Oam) univariant reactions to expand the orthoamphibole-bearing fields (see Fig. 2.7). However, contrary to expectations (Howell, 1991; Xu et al., 1993), only a tiny

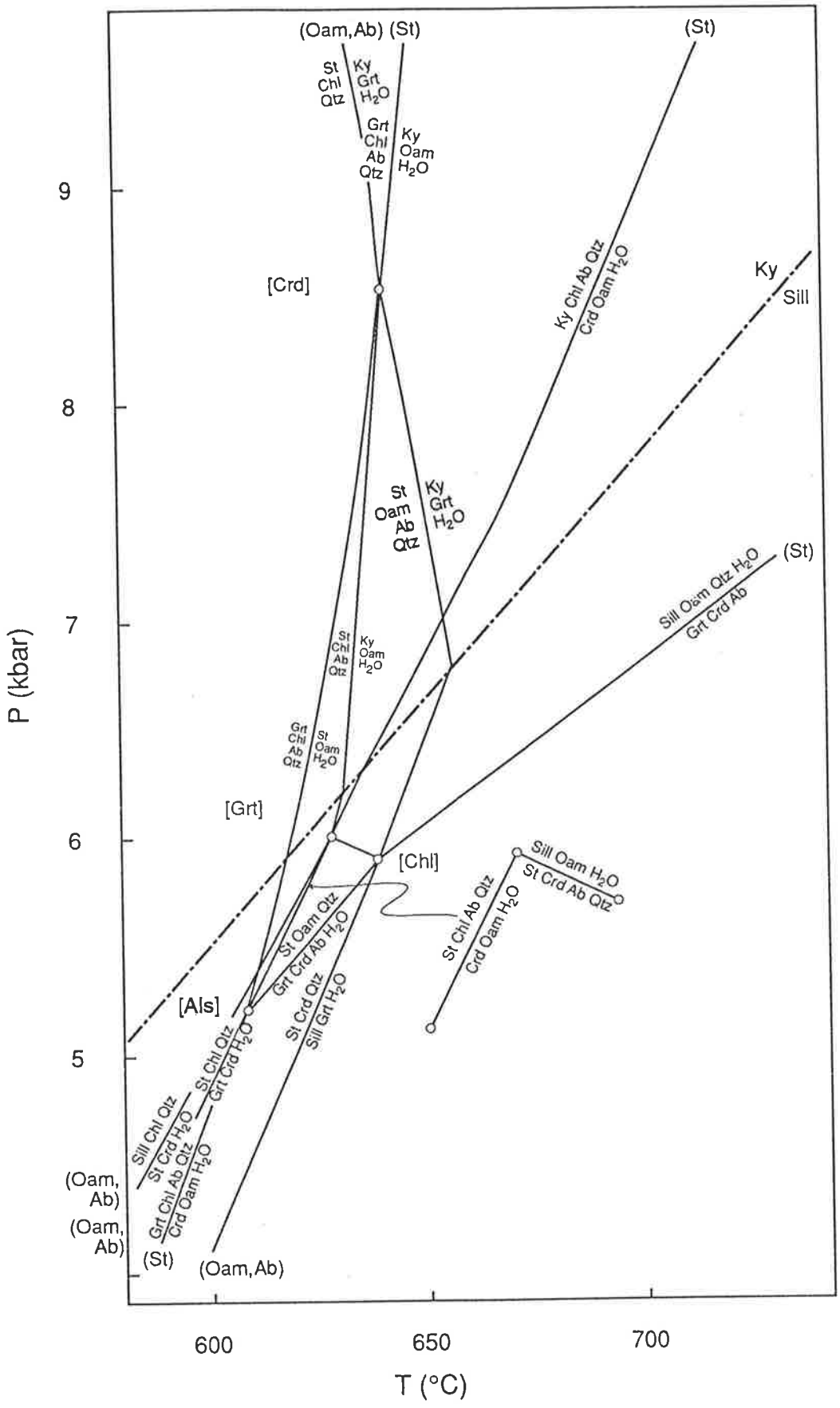

Figure 2.7. NFMASH phase diagram drawn with quartz, and aqueous vapour in excess. ΔH_{ged}= 0 kJmol^{-1}.

amount of Na (a maximum of $X_{Na,A}$ = 0.032-0.063 for ΔH_{ged}=0) was partitioned into the orthoamphibole before a new Na-bearing phase, albite, was stabilised. The calculated positions of corresponding FMASH and NFMASH invariant points varied by only 0.1-0.3 kbar. This result is very much contrary to the general opinion as to the effect of Na on the FMASH model system (R Powell pers. comm., 1993), and it implies that sodium has only a minimal effect on the stability field of orthoamphibole. Further, this suggests that our neglect of Na in the "aluminous schists" may not introduce very significant errors.

This small change in the positions of the invariant points with the addition of *orthoedenite* and *albite* to the constituent phases suggests that the adjustments made to the thermodynamic data in order to move the invariant point Ip_1 high into the sillimanite stability field may not be necessary. Therefore it seems likely that the P-T projection most applicable to real FMASH-type rocks is the original, un-adjusted P-T projection portrayed in Fig. 2.3.

Chapter 3: Calculated phase relations in amphibolites: the CFMASH system

3.1 Introduction

The main aim of this thesis is to develop an understanding of the phase relations in amphibolites with particular emphasis on those containing aluminous phases, such as kyanite and staurolite, which are not typically present in meta-igneous rocks. Reported examples of this type of amphibolite from the Eastern European Alps (Selverstone et al., 1984; Purtscheller & Mogessie, 1984), Central European Alps (Frey et al., 1980), New Zealand (Gibson, 1978; Cooper, 1980; Ward, 1984), USA (Spear, 1982; Helms et al., 1987), Antarctica (Grew & Sandiford, 1985) and the southwestern Pamirs in Tajikistan (former USSR, Grew et al., 1988) include both ortho- and para-amphibolites and in this thesis I describe an important new occurrence from the Harts Range in central Australia (Chapter 4). An important aspect of previous work on these rocks is that the bulk-rock chemistry of the unusual assemblages has been shown to be very similar to that of more common amphibolite assemblages (Helms et al., 1987), suggesting that pressure and temperature may be important factors in the stabilisation of the unusual assemblages. If this is the case it may engender considerable tectonic significance for these assemblages.

A number of previous workers (e.g. Selverstone et al., 1984; Helms et al., 1987) have proposed that assemblages involving an aluminous phase with hornblende are in a reaction relationship with the "common" amphibolite assemblage (calcium-amphibole, chlorite, epidote, plagioclase, quartz ± Fe^{3+}-oxides, carbonates, K-bearing and Ti-bearing phases (Laird, 1980)) and that they occur as a result of high pressure metamorphism (≥ 6 kbar) at intermediate temperatures. Despite this, only preliminary attempts have been made to constrain the important univariant and divariant reactions relating these aluminous assemblages to the more common amphibolite assemblage, and their positions in P-T space. Froese and Hall (1983) developed a P-T grid with which they hoped to evaluate the phase relations in these amphibolites. They combined data from published accounts of the assemblages in potassium-poor pelitic rocks and mafic rock-types and used Schreinemakers analysis to construct a linking CFMASH grid which involved phases observed in both rock-types. Spear (1978) and Spear and Rumble (1986) constructed schematic P-μ_{H_2O} and P-T petrogenetic grids for the NCFMASH system. Their calculations involved determining the ΔV and the stoichiometric coefficients of H_2O of reactions between generalised (fixed composition) phases to determine the slope of the univariant reactions. Although these grids provide a useful insight into the phase relations in rocks which are intermediate between pelitic and mafic rocks, it is clearly desirable to quantify the phase relations in terms of P and T, and to determine the significance and

location of the continuous reactions which are likely to control the appearance of the relevant assemblages.

In contrast to the FMASH system, in which the natural phase relationships are relatively well documented, aluminous amphibolites are relatively poorly described and poorly understood. Thus, a theoretical approach is more appropriate to these rock-types, and equilibrium thermodynamics calculations will be used to develop a P-T projection for the amphibolites in the model system CFMASH. In order to evaluate the applicability of the calculated grid to natural amphibolites, the predicted phase relations will be compared to the reaction textures and assemblages which have been described in the literature. The final sections discuss the continuous reactions discerned from the calculated CFMASH phase diagrams and the effect of sodium on the equilibria. Later chapters discuss the metamorphic history preserved in reaction textures in newly described amphibolites from central Australia (Chapter 4), the Zillertal Alps in Austria (Chapter 5), and the phase relations in world wide amphibolite occurrences (Chapter 6) from the point of view of the phase diagrams constructed here.

3.2 An appropriate model system for calculations

The phases involved in the aluminous amphibolites reported in the literature include "typical" mafic meta-igneous phases, such as clinopyroxene, orthopyroxene, hornblende, plagioclase, garnet, chlorite, quartz, spinel, biotite, epidote, rutile, ilmenite, magnetite and titanite with aluminosilicates (mainly kyanite), staurolite, cordierite, orthoamphibole (both gedrite and anthophyllite), cummingtonite, corundum, calcite and dolomite. The primary motivation of this study was to address the metamorphic record of aluminous amphibolites from the Harts Range (see Chapter 4) and the Zillertaler Alpen in Austria (Chapter 5). These rocks are dominantly quartz-saturated, precluding the stability of Mg-Fe-spinel or corundum and do not contain equilibrium clinopyroxene or orthopyroxene. Although chlorite is observed in the Zillertal rocks, it is absent from the Harts Range amphibolites and so is neglected in the first instance. Cummingtonite does not occur with the aluminous phases kyanite, staurolite or cordierite in the Harts Range amphibolites and so has also been neglected. Several of the observed phases (e.g. ilmenite, magnetite, biotite, epidote, calcite and dolomite) contain considerable amounts of an otherwise minor components (such as, Ti, Fe^{3+}, K, CO_2) and these are thus excluded from the analysis presented here. Epidote typically contains a significant proportion of the pistacite molecule ($Ca_2Fe^{3+}Al_2O_{12}(OH)$) and, as such, is stabilised by the presence of ferric iron. The major element chemistry of the remaining phases can be described in the model system Na_2O-CaO-FeO-MgO-Al_2O_3-SiO_2-H_2O (NCFMASH).

In view of the complexity and fundamental uncertainties in of the activity-composition (a-X) relations in plagioclase feldspar (e.g. Holland & Powell, 1992), there seems little point in making quantitative thermodynamic calculations in the full NCFMASH system and I will begin by neglecting Na_2O. Additional justification for neglecting the effect of Na on the phase relations in CFMASH is provided in Chapter 2 where the addition of sodium to the FMASH

system caused negligible change (of the order of 0.2 kbar) in the P-T positions of invariant equilibria in the FMASH (NFMASH) system. Moreover, in the Harts Range aluminous amphibolites, Na_2O is a relatively minor component (e.g. coronas of staurolite and plagioclase around kyanite involve calcium-rich bytownite-anorthite plagioclase, Chapter 4) and thus many of the important equilibria should be evident in the CFMASH system. Thus, the CFMASH compositional system seems an appropriate model for calculating the phase relations of the aluminous assemblages in amphibolites. A qualitative extension into NCFMASH is considered in a later section.

As mentioned above, the rocks of interest here are quartz-saturated, medium grade samples which are generally considered to have equilibrated with aqueous vapour. Considering quartz, anorthite and aqueous vapour to be in excess (a_{H_2O} =1), the components required to graphically represent the compositional relationships between the phases in the amphibolites can be reduced to the ternary system Al_2O_3-FeO-MgO (AFM). The generalised chemographic relations of the phases in AFM are presented in Fig. 3.1. The relative compositions in the CFMASH system are similar to those in FMASH (See Chapter 2), with the exception that hornblende (projected from quartz, anorthite and aqueous vapour) is also present. In natural occurrences, hornblende typically has X_{Fe} intermediate between orthoamphibole and cordierite (Hietanen, 1959; James et al, 1978; Spear, 1982; Froese & Hall, 1983; Schumacher & Robinson, 1987; Helms et al., 1987) and plots at a negative A/AFM value due to the projection from anorthite. Hornblende and orthoamphibole both show significant tschermakite substitution. Depending on the extent of the Mg_1Fe_{-1}, tschermakite and Mg_1Ca_{-1} substitutions in the relevant phases, orthoamphibole may occur on either side of the staurolite–hornblende tie-line (Fig. 3.1). As mentioned in Chapter 2, the relative X_{Fe} of staurolite and garnet may comply with the usual trend, that is $X_{Fe,Grt} > X_{Fe,St}$ (e.g. Spear, 1982; Froese & Hall, 1983; Selverstone et al., 1984, Chapter 6) or may be "reversed" (e.g. Purtscheller & Mogessie, 1984; Grew & Sandiford, 1985; Arnold et al., 1994; Chapter 4). These variations in the chemographic relations allow the possibility of two degenerate reactions (co-linearities in AFM + An + Qtz, + aqueous vapour):

orthoamphibole $\Rightarrow$ staurolite + hornblende

and

staurolite $\Rightarrow$ garnet + aluminosilicate

which may result in singularities in the P-T projection (e.g. Fig. 3.2).

3.3 A CFMASH phase diagram

As a starting point from which to develop the CFMASH phase diagram, I consider the effect of a small amount of CaO on the FMASH equilibria discussed in the previous chapter. The FMASH invariant point, Ip_1 (see Chapter 2) involves many of the phases of interest in the CFMASH system and will form the basis of this discussion. Qualitatively incorporating a small amount of a new component into existing phases increases the variance of all of the

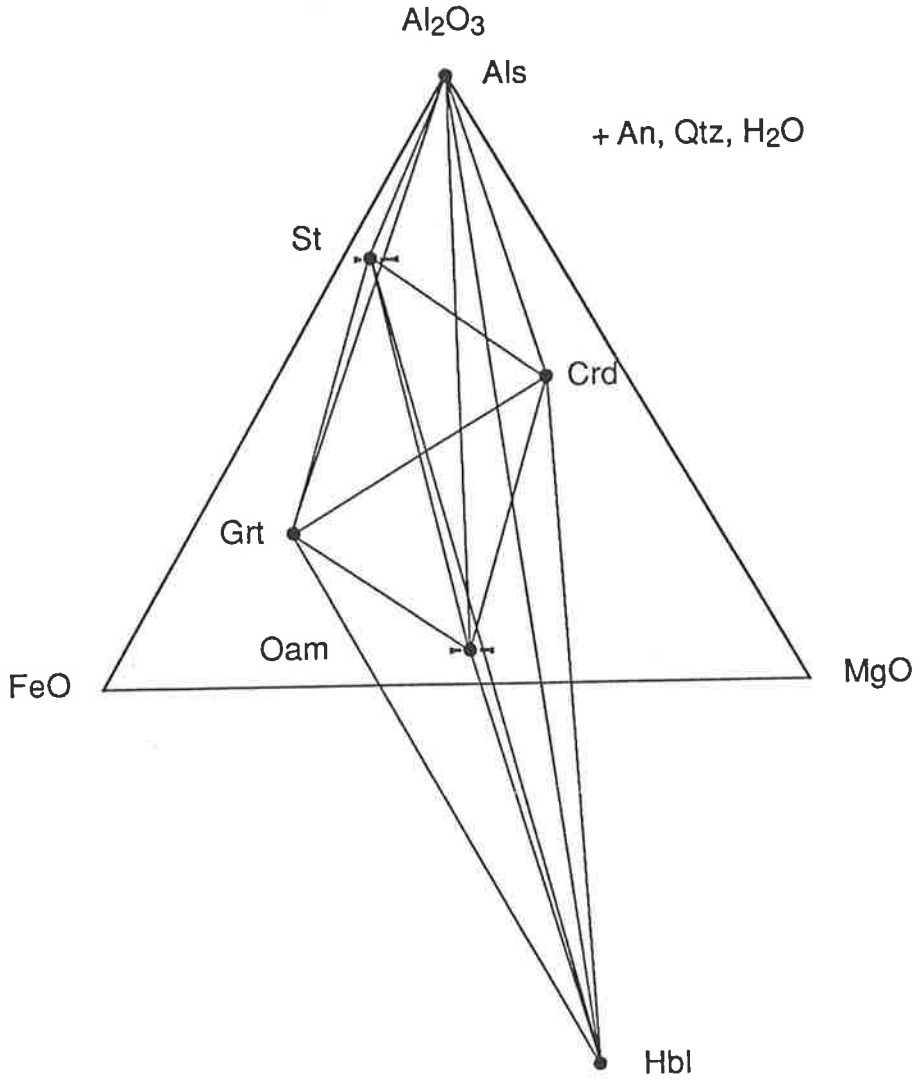

Figure 3.1. AFM diagram illustrating the generalised compositions of the phases of interest in the CFMASH model system, projected from anorthite, quartz and aqueous vapour onto the AFM plane.

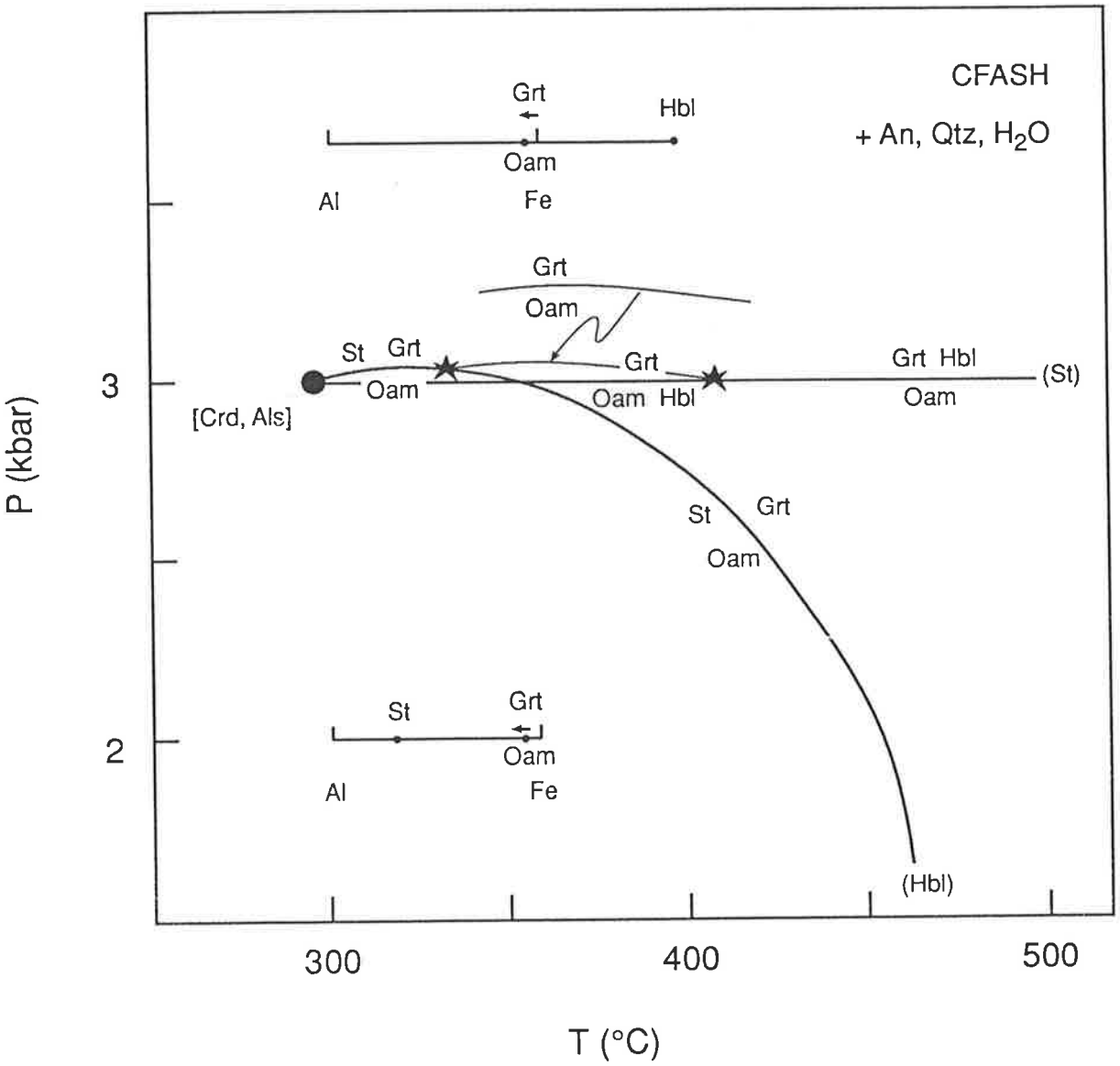

Figure 3.2. An example of singularities in the relatively simple CFASH (+ An, Qtz, H_2O) system. The close proximity of orthoamphibole and garnet on the AF plane allows singularities to develop if the chemistry of one changes more rapidly than that of the other along a reaction. For example, as the grossular content of garnet decreases with increasing temperature, the composition of garnet moves towards the "A" end of the binary (due to its projection from anorthite) while the composition of orthoamphibole becomes more aluminous at a much slower rate. The composition of garnet approaches and gradually overtakes that of orthoamphibole, resulting in the degenerate reaction garnet ⇒ orthoamphibole (light line). This degenerate reaction intersects both of the illustrated CFASH reactions in a singularity and causes the third CFASH phase to swap to the opposite side of the reaction.

equilibria and expands the stability fields involving phases that preferentially accommodate the new component. Garnet is the only FMASH phase able to accommodate significant CaO, therefore the addition of CaO to the FMASH system stabilises garnet-bearing assemblages with respect to others, as illustrated in Fig. 3.3. The garnet-bearing assemblages are stabilised (Fig. 3.3a, b) until at some critical composition, the amount of CaO in the system exceeds the solubility of grossular in garnet, and a new phase, such as anorthite or hornblende, will be stabilised (Fig. 3.3d). The appearance of a new phase along the trace of the CFMASH univariant must reduce the variance of the assemblage by one, thus defining a new CFMASH invariant point (Fig. 3.3c). For the case where anorthite is stabilised, this invariant point, labelled [Hbl], can be used as a basis from which to develop the CFMASH P-T projection.

Excluding invariant points due to Al_2SiO_5 polymorph reactions and assuming that quartz, anorthite and an aqueous vapour are in excess, then six (stable or metastable) invariant points exist in the CFMASH system involving aluminosilicates, staurolite, cordierite, garnet, orthoamphibole and hornblende with plagioclase, quartz and aqueous vapour in excess.

Pressure, temperature and compositional information for reactions in the CFMASH model system has been calculated from the internally consistent thermodynamic data set of Holland and Powell (1990; pers. comm., 1992), modified to increase the enthalpy of *gedrite* (ΔH_{ged}=10) as in Chapter 2, using the computer program THERMOCALC (version 2.2b1 Powell & Holland, 1988). Application of Schreinemakers principles to the calculated reactions reveals that only 3 of the 6 possible invariant points are stable. The predicted stable invariant points, [Hbl], [Crd], and [Grt], all occur at intermediate P-T conditions (Fig. 3.4). The divergent orientation of the stable parts of the (Grt, Als) and (Crd, Als) univariants and the (Grt, Oam) and (Crd, Oam) univariants imply the metastability of [Als] and [Oam]. However, the near parallelism of the (Als) univariants allows the possibility that the invariant point [Als] may be stable in the CFMASH model system. Although the (St) univariants are convergent, indicating the possible stability of [St], each is terminated in a CMASH invariant point. Each of the stable univariant reactions in CFMASH terminates in either a CFMASH invariant or a subsystem (e.g. CFASH or CMASH) invariant point and it is emphasised that it is these subsystem invariant and univariant equilibria that control the continuous reactions which are important for most rocks (e.g. Chapter 4).

The important aspects of the calculated CFMASH equilibria are as follows; CFMASH rocks containing aluminosilicate–orthoamphibole (with anorthite, quartz and vapour in excess) will be limited to pressures higher than ~4.5 kbar and may occur in only a narrow temperature range (Fig. 3.5). Staurolite–orthoamphibole and staurolite–cordierite are also limited to low to medium temperature bands (300-550°C) for pressures less than ~6.5 and 5.5 kbar respectively. Orthoamphibole-bearing and cordierite–garnet assemblages are restricted to the high temperature side of reactions with steep slopes (> 300°C, > 450°C respectively) while the assemblage aluminosilicate–hornblende occurs over a wide range of elevated pressures up to temperatures approaching the kyanite-sillimanite inversion (Fig. 3.5). Hornblende–staurolite and aluminosilicate–garnet assemblages are limited by several reactions which form a strongly curved stability limit, convex to the temperature axis. The maximum pressure for hornblende-

Figure 3.3. (a) The effect of adding Ca to the FMASH system (b). Garnet takes up a small amount of Ca and garnet-bearing assemblages are stabilised with respect to the others. The FMASH univariant reactions would become divariant and move along a univariant line in the CFMASH system, stabilising successively more Ca-rich phases (c) until the amount of Ca in the system was sufficient to stabilise a new phase, anorthite, (e). This causes the variance of the assemblage to be reduced by one, forming a new invariant point in CFMASH (d).

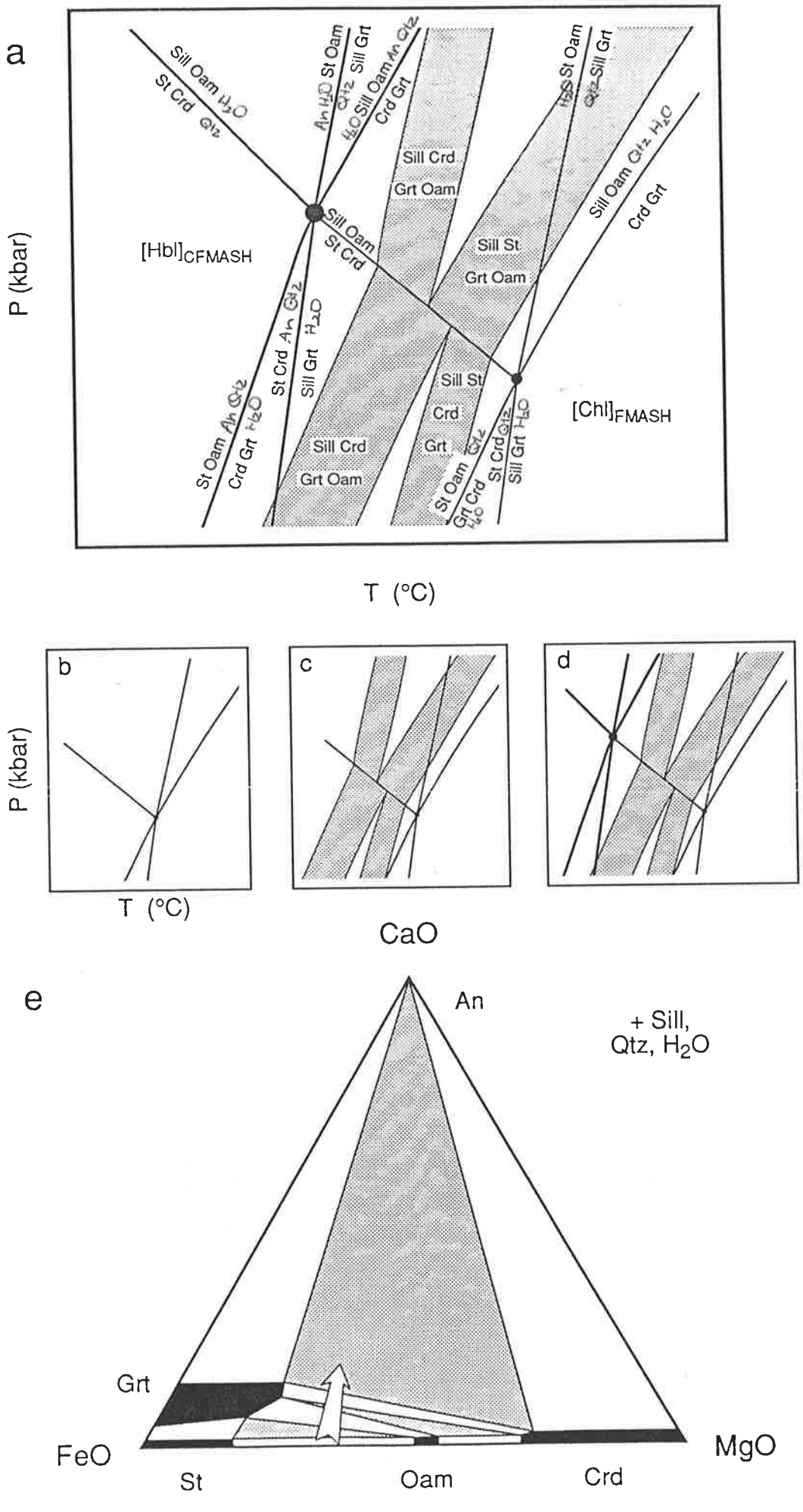
a
P (kbar)
T (°C)
[Hbl]CFMASH
[Chl]FMASH
Sill Oam H2O
St Crd Qtz
An H2O St Oam
Qtz Sill Grt
H2O Sill Oam An Qtz
Crd Grt
H2O St Oam
Qtz Sill Grt
Sill Oam Qtz H2O
Crd Grt
Sill Crd
Grt Oam
Sill St
Grt Oam
Sill Oam
St Crd
St Crd An Qtz
Sill Grt H2O
St Oam An Qtz
Crd Grt H2O
Sill Crd
Grt Oam
Sill St
Crd
Grt
St Oam Qtz
Grt Crd H2O
St Crd Qtz
Sill Grt H2O
b
c
d
P (kbar)
T (°C)
CaO
e
An
+ Sill,
Qtz, H2O
Grt
FeO
MgO
St
Oam
Crd

Figure 3.4. A P-T projection in the CFMASH model system involving aluminosilicates, staurolite, cordierite, garnet, orthoamphibole and hornblende calculated for anorthite, quartz and aqueous vapour in excess. Calculated from the internally consistent thermodynamic data set of Holland and Powell (1990; pers comm., 1992), adjusted for *gedrite*, using the computer program THERMOCALC (Powell & Holland, 1988). Heavy lines and large unfilled circles are CFMASH equilibria, light lines and small unfilled circles are CFASH equilibria, light lines with filled small circles are CMASH equilibria. Stars indicate the locations of singularities.

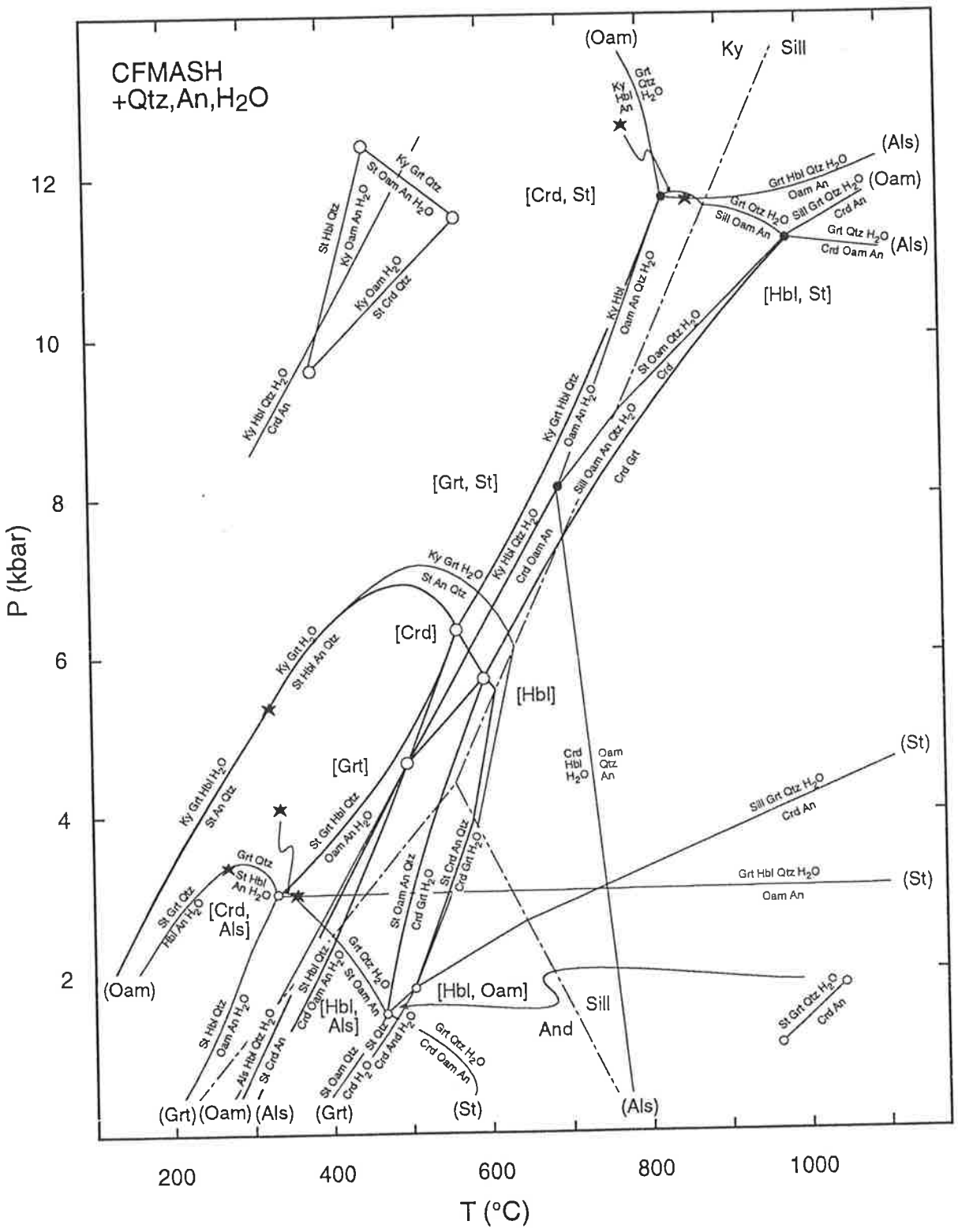
CFMASH
+Qtz,An,H2O
P (kbar)
T (°C)
12
10
8
6
4
2
200
400
600
800
1000
(Oam)
Ky
Sill
(Als)
(Oam)
(Als)
[Crd, St]
[Hbl, St]
[Grt, St]
[Crd]
[Hbl]
[Grt]
[Crd, Als]
[Hbl, Oam]
[Hbl, Als]
(St)
(St)
(St)
Sill
And
(Grt)
(Oam)
(Als)
(Grt)
(St)
(Als)

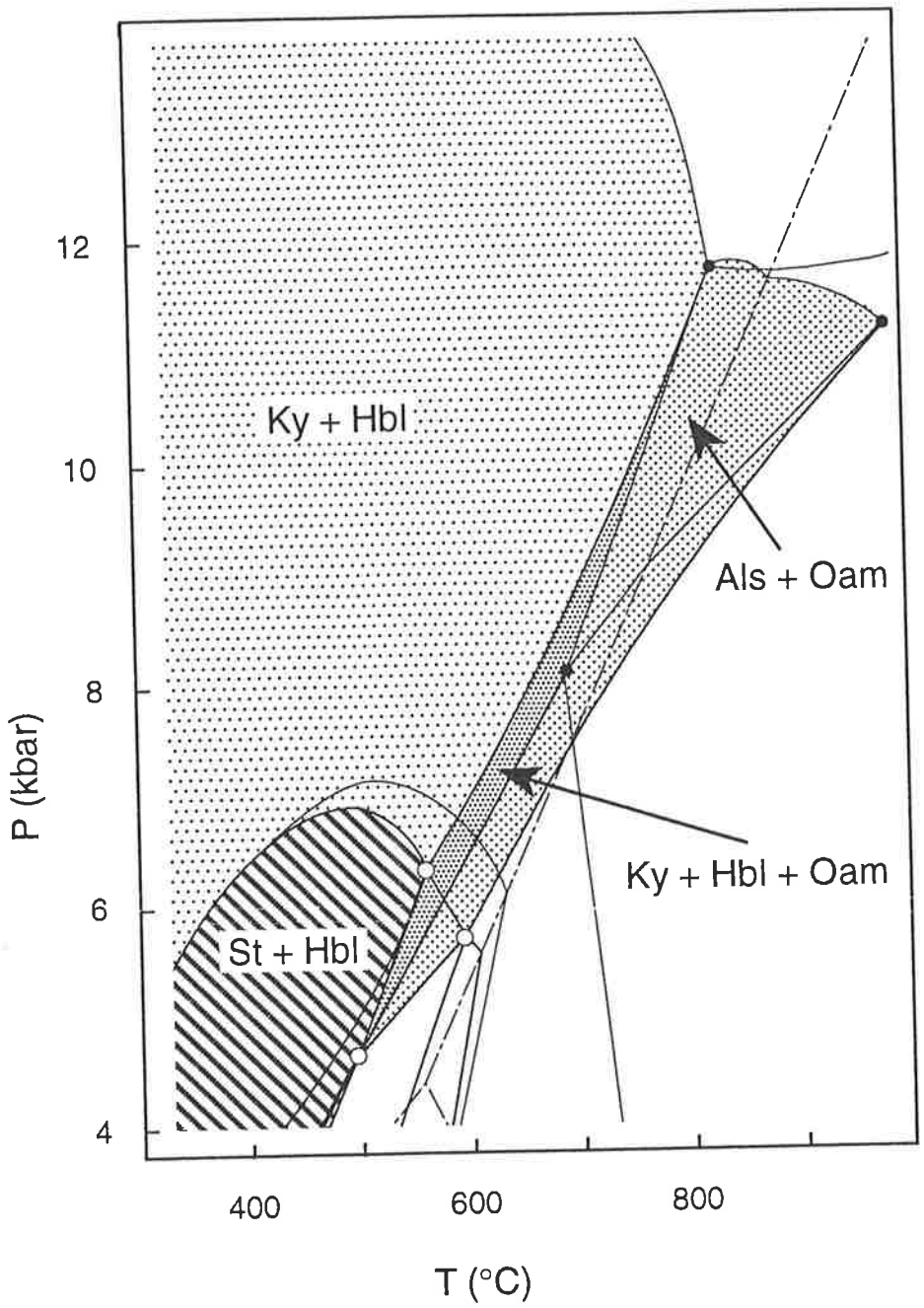

Figure 3.5. The stability fields of the assemblages kyanite-hornblende, staurolite-hornblende, kyanite-staurolite-hornblende and aluminosilicate-orthoamphibole (+ plagioclase, quartz and aqueous vapour) on the CFMASH phase diagram portrayed in Fig. 3.4.

staurolite stability is 7 kbar, above which aluminosilicate–garnet becomes stable. Hornblende-staurolite assemblages are also limited to temperatures of less than ~ 550°C (Fig. 3.5).

As in the FMASH system, there is significant uncertainty attached to the thermodynamic data used to calculate the P-T projection in Fig. 3.4 and these may have a considerable effect on the calculated positions of reactions and their intersections. Staurolite, orthoamphibole and hornblende are the least well-characterised phases (see Appendix A2) and as a consequence of the relatively steep slopes of many of the CFMASH reactions, errors in the thermodynamic data for these phases may effect a substantial shift in the calculated pressure of the invariant points. Similarly, uncertainties in the hornblende endmember data may cause the phase diagram's interior triangle (the lower part of the kyanite–orthoamphibole stability field) to either expand away from, or contract toward, [Hbl].

3.4 Testing the calculated phase relations

Although they are internally consistent, the uncertainties in the thermodynamic calculations outlined above imply that caution is needed in the application of the phase relations determined from equilibrium thermodynamics calculations to amphibolites. The relevance of the calculated phase diagrams can be determined from comparison of the predicted phase relations with those determined in natural assemblages. The comparison here comprises three parts: identifying the likely stable CFMASH invariant points and univariant reactions from natural low-variance assemblages; constraining the location of the invariants and univariants in P-T space; and comparing the calculated phase diagram to those determined by previous authors.

3.4.1 CFMASH invariant points and univariant reactions

There are several reported instances of low-variance amphibolites and although these correspond more closely to the NCFMASH system, they are closely related to CFMASH and FMASH sub-system equilibria. These assemblages may be used to infer, independent of the calculations, which of the six CFMASH invariant points are likely to be relevant to real rocks i.e. which CFMASH invariant points are stable. (A fuller account of the relevant occurrences is given in Chapter 6.)

As shown in the previous chapter, rocks with low Ca-, K- and Na-contents can be approximated by the FMASH model system. Examples of these reported from the literature include the assemblages (with co-existing quartz):

sillimanite/kyanite–staurolite–garnet–orthoamphibole (Hbl, Pl, Crd)
Robinson & Jaffe (1969b),

sillimanite/kyanite–staurolite–cordierite–orthoamphibole (Hbl, Pl, Grt)
Schumacher & Robinson (1987),

sillimanite–staurolite–cordierite–garnet (Hbl, Pl, Oam)
Sharma & MacRae (1981),

sillimanite–cordierite–garnet–orthoamphibole (Hbl, Pl, St)
Sharma & MacRae (1981).

These univariant assemblages intersect in an FMASH invariant assemblage involving aluminosilicate, staurolite, cordierite, garnet and orthoamphibole with quartz, which suggests that the [Hbl, Pl] invariant point is stable in the FMASH system.

In Ca-rich rocks hornblende and plagioclase are commonly equilibrium phases. Examples of four-phase assemblages involving hornblende include (with plagioclase and quartz):

staurolite–garnet–orthoamphibole–hornblende (Crd, Als)
(Spear, 1977; 1982; Chapter 4)

kyanite–staurolite–garnet–hornblende (Crd,Oam)
(Purtscheller & Mogessie, 1984; Selverstone et al., 1984; Chapters 4 & 5),

kyanite–staurolite–orthoamphibole–hornblende (Crd, Grt)
(Chapter 4),

sillimanite–staurolite–cordierite–hornblende (Grt, Oam)
(Schumacher & Robinson, 1987),

kyanite–cordierite–orthoamphibole–hornblende (Grt, St)
(Chapter 4) and

cordierite–garnet–orthoamphibole–hornblende (Als, St)
(Humphreys, 1993).

Apart from the last, all of these four phase assemblages are consistent with the stability of the CFMASH invariant points [Crd] and [Grt]. Thus the phase relations observed in real rocks suggest that the three invariant points, [Hbl], [Crd] and [Grt] are potentially stable (cf. Fig. 3.4). However, the occurrence of cordierite–garnet–orthoamphibole–hornblende–plagioclase–quartz (Als, St) is inconsistent with the CFMASH grid and seems to indicate that either [Als] or [St] is stable.

3.4.2 P-T constraints

Information from natural amphibolite assemblages and the rocks with which they are associated can also provide an independent constraint on the pressures and temperatures of the CFMASH equilibria. In particular, the aluminosilicate polymorphs associated with individual assemblages might be expected to provide broad constraints on the location of the stability

fields of the relevant aluminosilicate-bearing assemblages and here I briefly describe examples of these.

The calculated phase diagram predicts that the assemblages aluminosilicate–hornblende and aluminosilicate–orthoamphibole will be restricted to elevated pressures in the kyanite and kyanite and sillimanite stability fields, respectively (Fig. 3.5). This is in accord with most recorded assemblages. For example, hornblende is generally observed in equilibrium with kyanite rather than sillimanite or andalusite, whereas orthoamphibole is typically observed with either sillimanite or kyanite but only rarely with andalusite.

As discussed in Chapter 2, the rare examples of andalusite–orthoamphibole rocks reported in the literature (e.g. Seki & Yamasaki, 1957) probably reflect problems associated with very small scale equilibrium volumes, rather than equilibrium associations, however the discrepancies involving aluminosilicates with hornblende are more problematic. There are two instances of hornblende reported in association with sillimanite, neither of which can be easily dismissed. Schumacher and Robinson (1987) report corroded sillimanite in the cores of aluminous enclaves separating sillimanite from the hornblende–orthoamphibole–plagioclase matrix. They suggest that sillimanite–hornblende–gedrite–plagioclase defined a relatively early equilibrium assemblage which later became metastable with respect to cordierite–plagioclase ± other aluminous phases. Similarly, Humphreys (1993) reports equilibrium assemblages including sillimanite–staurolite–cordierite–hornblende–plagioclase–quartz. Since, there is no indication that either of these authors are in error this discrepancy between the calculated phase relations and those observed in natural amphibolites probably reflects the relatively large uncertainties attached to the thermodynamic data from which the phase diagram was calculated. The calculated uncertainties on the reactions bounding the hornblende–aluminosilicate field (Grt, St), (Grt, Oam) are of the order of 150°C and thus allow the possibility that the aluminosilicate–hornblende stability field may extend as far as 100°C into the sillimanite stability field.

Further constraints on the relevance of the calculated CFMASH phase diagram to natural amphibolites might be expected from the evolving compatibility relations of amphibolites in a prograde metamorphic sequence. The only well-documented example of this type of field setting involves four separate outcrops of the Post Pond and Ammonoosuc Volcanics (Spear, 1978). However, the compatibility diagrams constructed for each outcrop do not detail the full sequence of reactions and the assemblages are thought to have equilibrated with fluids of variable composition (Spear, 1982). Thus even these relatively well described amphibolites are unlikely to provide a complete enough record to enable comparison with the calculated phase relations.

Similarly, reaction textures might be expected to yield information about the applicability of the calculated grid to the phase relations in natural rocks. Later in this thesis I discuss a set of low-variance reaction textures from amphibolites in the Harts Range area of central Australia (Chapter 4). These rocks provide evidence of the reactions:

kyanite + hornblende ⇒ staurolite + anorthite,

kyanite + orthoamphibole ⇒ cordierite + plagioclase,

kyanite + hornblende ⇒ cordierite + plagioclase

and

staurolite + hornblende ⇒ garnet + orthoamphibole.

However, the multi-phase metamorphic history and the complexity of the structural relations between the compositional units in the area mean that the interpretation of the pressure-temperature history of these rocks is by no means trivial. Later in this thesis the calculated CFMASH grid will be used to interpret these reaction textures and thus the P-T history of the area (Chapter 4).

3.4.3 Phase diagrams developed by other workers

An appealing aspect of the calculated grid is that it is essentially topologically equivalent to that of Froese and Hall (1983) which was developed for aluminous amphibolites. The Froese and Hall (1983) grid was constructed from a combination of published pressure-temperature information for stable invariant points in potassium-poor pelites and in mafic rocks which were then linked by CFMASH reactions and invariant points using Schreinemakers analysis. Slight inconsistencies between the two grids stem from Froese and Hall's (1983) assumptions that the phases involved have fixed compositions, that garnet is more Fe-rich than co-existing staurolite and that orthoamphibole is more Fe-rich than the staurolite–hornblende tie-line. These assumptions are contrary to the phase relations in some observed assemblages (e.g. Purtscheller and Mogessie, 1984; Schreyer et al., 1984).

Spear and Rumble (1986; see also Spear, 1978) constructed an NCFMASH P-T Schreinemakers net for the phases observed in the Post Pond and Ammonoosuc Volcanics. They used fixed composition phases and the ΔV and ΔS of the reactions to determine the slopes of the discontinuous reactions. The invariant points were positioned by comparison with peak metamorphic conditions determined from natural assemblages (Spear & Rumble, 1986). Because the grid calculated here and the NCFMASH grid of Spear and Rumble (1986) involve different compositional systems, they are not directly comparable (however, see section 3.6 for a qualitative extension into NCFMASH).

A problem encountered in the comparison of the calculated phase relations and those determined from natural amphibolites is the continued assertion that staurolite–hornblende assemblages occur under high pressure conditions of $\geq$ 6 kbar (e.g. Selverstone et al., 1984; Grew & Sandiford, 1985). The calculated phase diagram (Fig. 3.4) suggests that staurolite–hornblende may be stable under high P/T ratios, but only at limited pressures, up to approximately 7 kbar. The P-T grids of Froese and Hall (1983) and Spear and Rumble (1986) also predict that hornblende–staurolite assemblages will be limited to a high P/T stability field which is closed to higher pressure by a reaction involving staurolite, garnet, hornblende, aluminosilicate ($\pm$ chlorite or orthoamphibole for Spear & Rumble, 1986) with anorthite, quartz and aqueous vapour in excess. However, there is a large discrepancy in the maximum

pressure at which staurolite–hornblende is stable. Spear and Rumble (1986) predict that staurolite–hornblende will be a stable assemblage at pressures up to ~14 kbar, whereas the grid calculated here predicts a maximum pressure of ~ 7 kbar (Fig. 3.4). This problem is addressed in later sections.

3.4.4 Summary

The comparison between calculated phase equilibria and those observed in real rocks or predicted by other methods is largely encouraging, suggesting that, topologically, the calculated grid provides a reasonable approximation of natural rock systems. However, some problems are difficult to reconcile. The estimates of equilibration conditions from natural aluminous amphibolites are in general higher than predicted by the calculated P-T projection (e.g. for hornblende–staurolite stability) and the occurrence of sillimanite–hornblende assemblages in natural amphibolites is also in contrast to the calculated phase relations. Another notable problem relates to the existence of cordierite–garnet–hornblende assemblages from South Africa. Such discrepancies are probably not surprising in view of the uncertainties attached to the positions of the calculated reactions

3.5 Extending the CFMASH system to include chlorite

Several workers (e.g. Spear, 1978; Helms et al., 1987) have reported amphibolites which contain chlorite in addition to the phases dealt with in the previous section, suggests that chlorite may be stable in the lower temperature amphibolites. Thus, in order to better constrain the phase relations in low and medium temperature amphibolites, chlorite-bearing reactions are considered in this section. The inclusion of chlorite is also useful from the point of view of understanding the relationships between amphibolites which contain kyanite–hornblende or similar assemblages and those which contain the "common assemblage"; that is, calcium-amphibole, chlorite, epidote, plagioclase, quartz ± Fe^{3+}-oxides, carbonates, K-bearing and Ti-bearing phases (Laird, 1980).

In view of the problems which may be caused by the large uncertainty in H_{ged} (see section 2.6; Howell, 1991; Xu, 1994), the complexities of (n+4) systems and the restricted stability of co-existing chlorite and orthoamphibole (reported only by Spear, 1982), chlorite-bearing, orthoamphibole absent reactions will be investigated as a starting point. Consequently, the phases of concern are aluminosilicates, staurolite, cordierite, garnet, chlorite and hornblende with anorthite, quartz and aqueous vapour considered to be in excess. The activity of water (a_{H_2O}) is assumed to be 1. The compatibility relations are, of course, similar to those described in section 3.2, with the additional phase chlorite (Fig. 3.6). Chlorite is typically more Fe-rich than co-existing cordierite and less Fe-rich than hornblende, garnet and staurolite (Spear, 1982; Selverstone et al., 1984; Helms et al., 1987). When projected from anorthite, quartz and aqueous vapour, chlorite has higher A/AFM than hornblende and lower A/AFM than garnet, cordierite, staurolite and aluminosilicate. It may occur on either side of

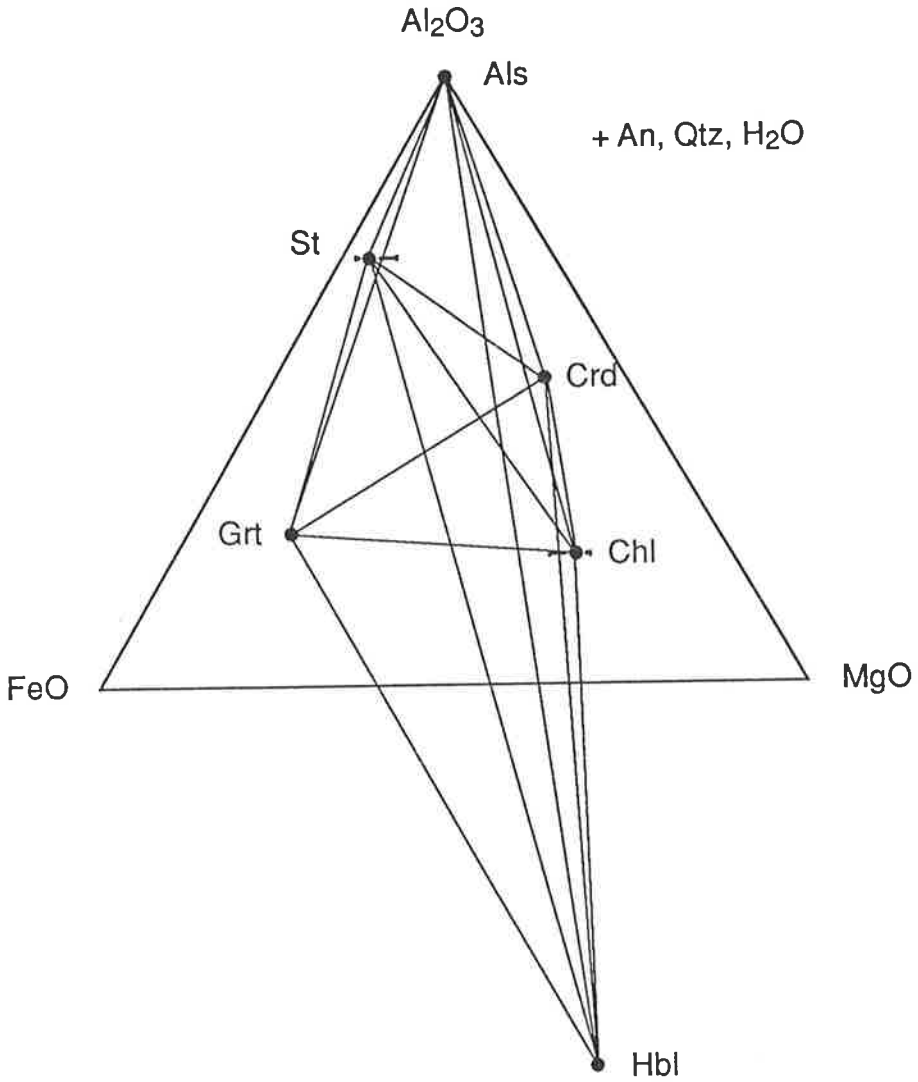

Figure 3.6. AFM diagram with anorthite, quartz and aqueous vapour in excess, illustrating the generalised compositions of the phases of concern in the chlorite-bearing, orthoamphibole-absent CFMASH model system.

the cordierite–hornblende tie-line, allowing the possibility of singularities in any reactions which contain the phases, cordierite, chlorite and hornblende with anorthite, quartz and aqueous vapour.

The positions of the univariant reactions and invariant points in the (orthoamphibole-absent) CFMASH system involving these phases have been determined using the internally consistent data set of Holland and Powell (1990, 1992 pers. comm.), the computer program THERMOCALC (version 2.2b1 Powell & Holland, 1988) and the method of Schreinemakers. Note that, of the 6 possible invariant points, only [St] and [Hbl] are stable (Fig. 3.7).

The petrogenetic grid determined for the chlorite-bearing, orthoamphibole-absent CFMASH system differs significantly from the chlorite-absent grid discussed in previous sections and the information determined from natural assemblages. For example, the invariant point [Hbl, Chl] (which is apparently stable in real rocks (Hudson & Harte, 1985; Arnold & Sandiford, 1990; section 3.4.1) occurs on the high pressure, metastable side of the stable invariant point [Hbl, Oam] (Fig. 3.8). Similarly the invariant point [Grt, Chl], which is also inferred to be stable in real rocks, is equally stable as [Hbl, Oam] which is metastable with respect to [St, Oam].

This discrepancy between the natural and calculated phase relations may result from any one of a number of causes. The assemblages in real amphibolites may (a) be stabilised by the presence of an additional component, (b) have formed under reduced activity of water, or (c) result from inaccurate thermodynamic data for one or more of the end-members, or inappropriate activity models for one or more of the phases. These possibilities are discussed below.

3.5.1 The effect of additional components

In order for the observed amphibolite phase relations to be correctly represented in the chlorite-bearing CFMASH system, at least one of the invariant points [St] and [Hbl] must become metastable with respect to other invariant points. The required inversion of topology (similar to that caused by the influence of oxygen fugacity on the phase relations in sapphirine granulites, as demonstrated by Hensen, 1986 and Powell & Sandiford, 1988) might be achieved by adding a new component which preferentially stabilises some phases. Such an effect may be induced by the presence of Na_2O or other minor components such as ZnO, MnO, or Fe_2O_3.

The addition of a small amount of Na_2O to the CFMASH model system expands the stability fields of plagioclase-, orthoamphibole- and hornblende-bearing assemblages and increases the variance of the CFMASH equilibria (i.e. CFMASH invariants would become NCFMASH univariants and univariant lines would become divariant fields). The calculated orthoamphibole-absent NCFMASH univariants describe weakly divergent lines in P-T space (see Fig. 3.9), implying that even in very Na-rich systems, no topological inversion would occur.

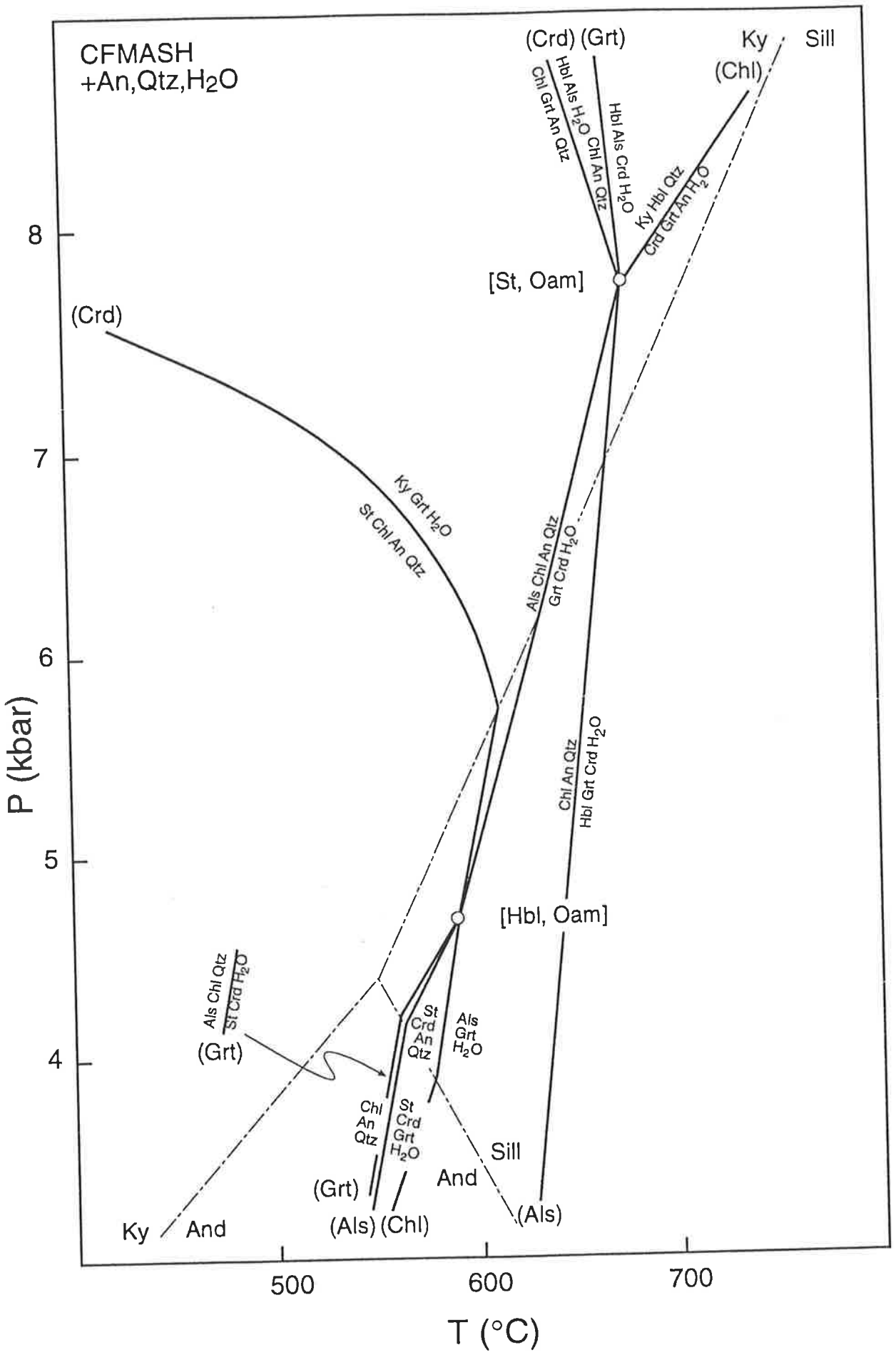
CFMASH
+An,Qtz,H2O
(Crd) (Grt)
Ky
Sill
(Chl)
Chl Grt An Qtz
Hbl Als H2O Chl An Qtz
Hbl Als Crd H2O
Ky Hbl Qtz
Crd Grt An H2O
[St, Oam]
(Crd)
Ky Grt H2O
St Chl An Qtz
Als Chl An Qtz
Grt Crd H2O
Chl An Qtz
Hbl Grt Crd H2O
[Hbl, Oam]
Als Chl Qtz
St Crd H2O
(Grt)
St Crd An Qtz
Als Grt H2O
Chl An Qtz
St Crd Grt H2O
(Grt)
(Als) (Chl)
Sill
And
(Als)
Ky
And
8
7
6
5
4
P (kbar)
500
600
700
T (°C)

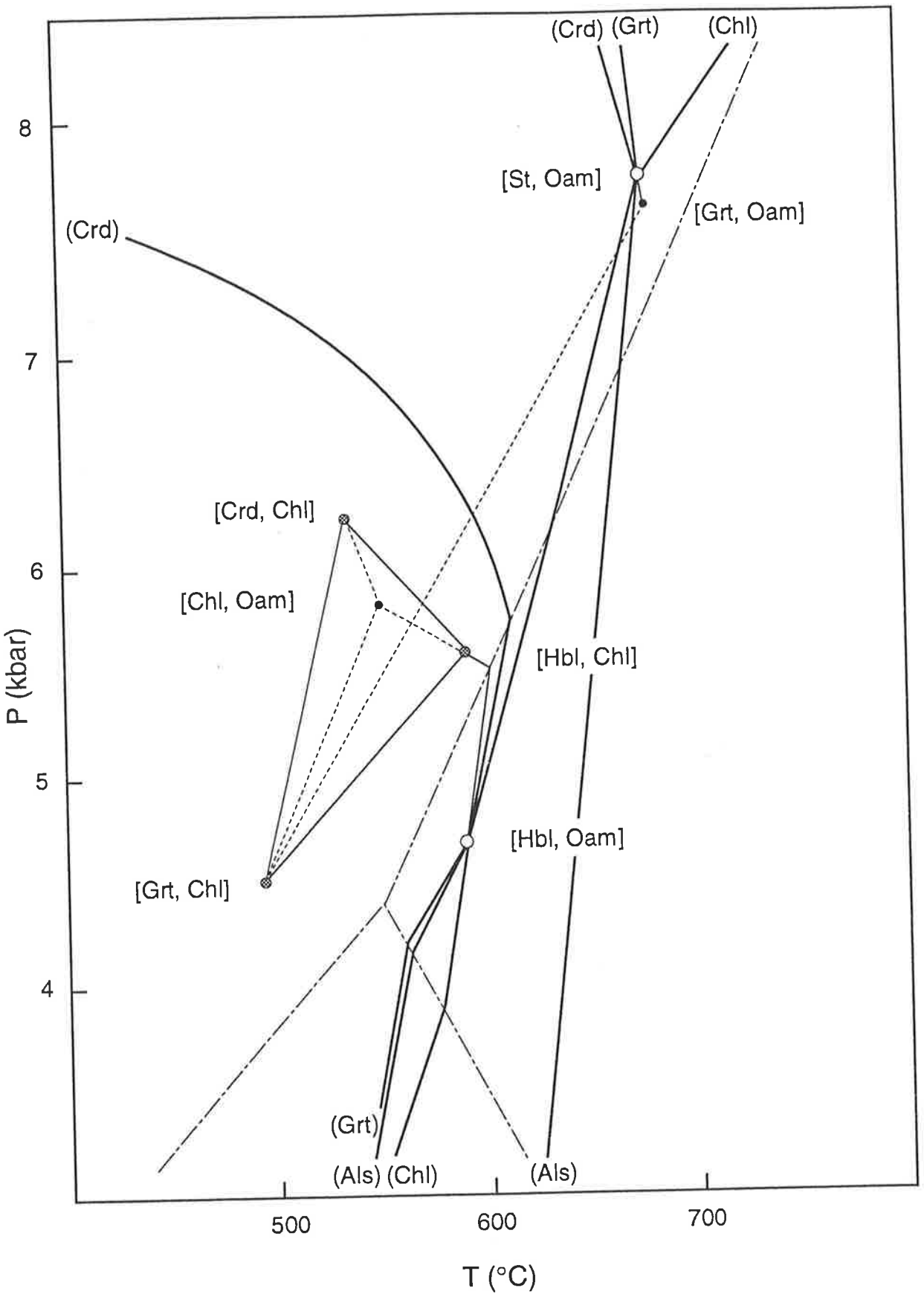

Figure 3.8. A P-T diagram showing the relative locations and stability (heavy lines, unfilled circles) and metastability (light and dashed lines, filled circles) between chlorite absent and chlorite-bearing invariant points in CFMASH relations.

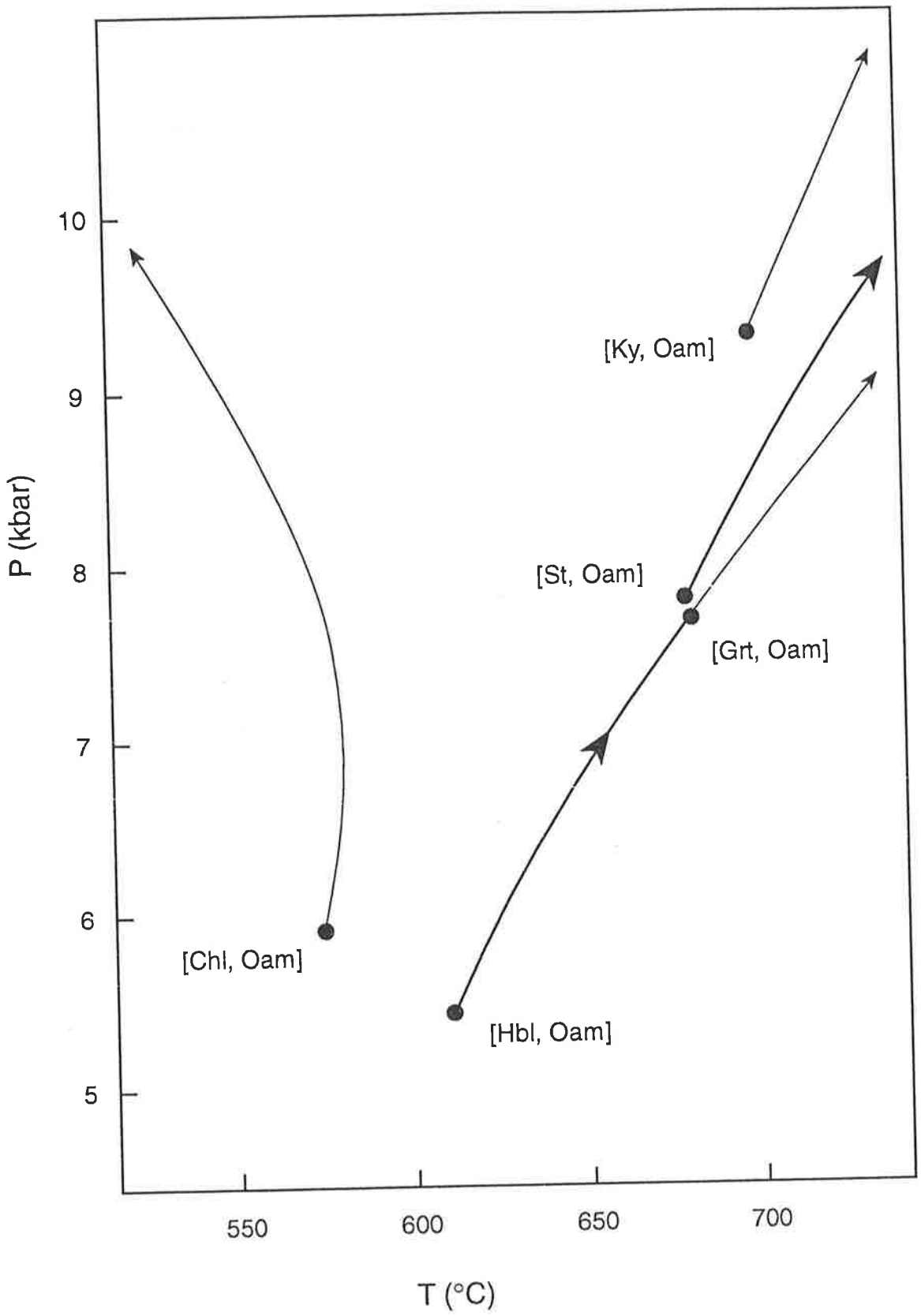

Fig. 3.9. NCFMASH univariant curves for the orthoamphibole free-system, with plagioclase, quartz and aqueous vapour in excess. Arrows show the direction in which the NaO_2 content of the assemblages (i.e. plagioclase and hornblende) increase. Heavy lines are stable univariant curves, light lines are metastable.

With the addition of MnO, which is preferentially accommodated in garnet, garnet-bearing stability fields would expand with respect to the other assemblages. Because of the divergent nature of the (Grt) univariant reactions emanating from the invariant points, and thus the related MnCFMASH univariants (Fig. 3.10), the addition of a *spessartine* component can not invert the topology.

The effect of additional components on a phase diagram (i.e. the P-T shift) can be estimated by considering that the end-member phase involving the new component effectively dilutes the other end-members in the solid solution phase. Thus the effect of incorporating ZnO into staurolite can be approximated by reducing the activities of *Fe-staurolite* (*fst*) and *Mg-staurolite* (*mst*) (Fig. 3.10). A new activity expression could be written for each of the end-members;

$$a_{fst}' = a_{fst}^{\circ} (1 - a_{znst}) = (X_{Fe})^4 (1 - X_{Zn})^4$$

and

$$a_{mst}' = a_{mst}^{\circ} (1 - a_{znst}) = (1 - X_{Fe})^4 (1 - X_{Zn})^4,$$

where a_{fst}' is the activity of the end-member *Fe-staurolite* in staurolite with zinc present, a_{fst}° is the activity of the end-member *Fe-staurolite* in staurolite with no zinc present, a_{znst} is the activity of the end-member *Zn-staurolite*, X_{Fe} = FeO / (FeO + MgO) and X_{Zn} = ZnO / (ZnO + FeO + MgO). The significant changes in the pressures and temperatures of the CFMASH equilibria which would be required to cause the inversion of topology might be achieved by the addition of ZnO to the extent that $X_{Zn} = 0.64$ (R.Powell, pers comm., 1993). While this may seem to provide an appropriate solution to the problem, all analyses from the staurolite–hornblende rocks reported in the literature have low ZnO-contents (see Table 3.1). Thus it would appear that ZnO does not provide an adequate explanation of the discrepancy between observed and calculated P-T phase relations.

As a first approximation, Fe_2O_3 is considered more likely to replace Al in hornblende than to substitute into other phases (e.g. Powell & Holland, 1990; Will et al., 1990b). Thus the addition of Fe_2O_3 is expected to stabilise hornblende-bearing assemblages with respect to others. As mentioned above, the displacement of the invariant assemblages across P-T space due to the presence of an additional component may be estimated by assuming that the relevant end-member, in this case, *ferri-hornblende* ($VCa_2Mg_3(MgFe^{3+})Si_4[Si_3Al]O_{22}(OH)_2$), effectively dilutes the other amphibole end-members, e.g.

$$a_{tr}' = a_{tr}^{\circ} (1 - a_{F3hb}),$$

$$a_{ftr}' = a_{ftr}^{\circ} (1 - a_{F3hb})$$

and

$$a_{hb}' = a_{hb}^{\circ} (1 - a_{F3hb}).$$

Thus, the effect of the new end-member may be estimated by reducing the activity formulation of each of the hornblende end-members in proportion to the amount of ferric iron present. (For a full explanation see Appendix A4, section A4.7.) An important factor in determining the effect of Fe_2O_3 on the locations of the equilibria corresponding to the CFMASH invariant points is that the substitution of Fe^{3+} into hornblende would occur via a

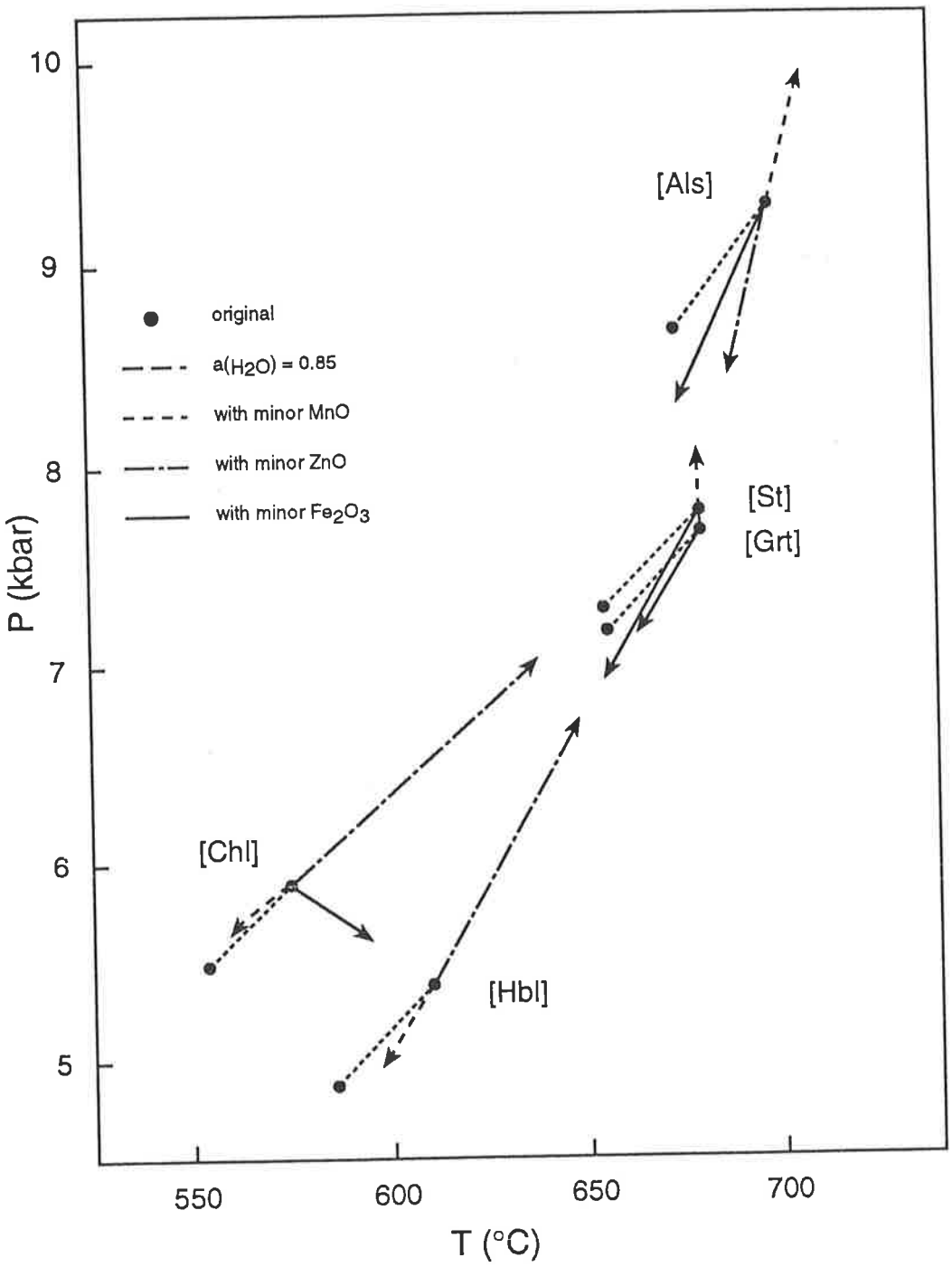

Figure 3.10. The trajectories of the CFMASH invariant points with decreasing activity of water (a_{H_2O}=0.85) and the directions the CFMASH invariant points would be displaced with the addition of MnO_2 which would be partitioned into garnet, ZnO partitioned into staurolite and Fe_2O_3 partitioned into hornblende.

Table 3.1. Zinc contents of staurolite in atoms per formula unit, calculated to 46 oxygens (44(O) + 4(OH), reported from hornblende-staurolite amphibolites in the literature.

	ZnO pfu (46 oxygens)
Gibson, 1978	0.099 – 0.205
Spear, 1982	0.088 – 0.639
Putscheller & Mogessie, 1984	0.037
Selvertone et al., 1984	0.024 – 0.188
Ward, 1984	0.00 – 0.026
Grew & Sandiford, 1985	0.567
Helms et al, 1987	0.00 – 0.056
Chapters 4 and 5	0.02 – 0.15

modified tschermakite substitution. Therefore the mole fraction of Si and Al on the tetrahedral sites will be related to the amount of Fe^{3+} on the M2 site and the effect of Fe_2O_3 will vary with the different aluminium contents.

Figure 3.11 shows the hornblende compositional range over which an inversion of the topology of the phase diagram will occur and compares the compositions of hornblendes reported in the literature. Although some reported hornblendes (in both aluminous-phase-bearing assemblages and more typical amphibolites) contain sufficient Fe_2O_3 to cause such an inversion of topology, (i.e. $X_{Fe3+,M2} \geq 0.3$ or $Fe^{3+} \geq 0.6$ moles per formula unit, 23O), this is not true for the majority of hornblendes from aluminous and typical amphibolites (Fig. 3.11). Thus, although many reported hornblendes (and presumably also those for which Fe_2O_3 levels are not estimated) contain significant Fe_2O_3, this does not appear to be sufficient to cause an inversion of the topology of the P-T projection. It is also anticipated that although a small amount of Fe_2O_3 may be incorporated into hornblende (or some of the other phases of interest), before the system becomes significantly oxidised, epidote and perhaps magnetite would become stable, preventing high levels of Fe_2O_3 in hornblende.

In summary, none of the chemical variations described above result in sufficiently large, appropriately oriented shifts of the invariant equilibria to cause the required inversion of topology.

3.5.2 The effect of variable activity of water

The effect of reducing the a_{H_2O} on the CFMASH phase diagram is to cause the stable and metastable invariant points portrayed in Fig. 3.7 to slide to lower pressures and temperatures without changing the topology of the CFMASH equilibria (Fig. 3.11). Thus, a_{H_2O} does not appear to be responsible for the discordance between observed and calculated phase relations.

3.5.3 The effect of uncertainties in the data and activity models

As discussed previously, low variance assemblages from natural amphibolites suggest that the phase diagram for amphibolites is likely to involve the three invariant points represented in Fig. 3.4 (i.e. [Chl, Hbl], [Chl,Crd], and [Chl, Grt]) and possibly also [Als, Chl] or [St,Chl] which contrasts with the calculations summarised in Fig. 3.7. Since the discrepancy appears unlikely to be due to the effects of additional minor components or reduced a_{H_2O}, it seems likely that some of the thermodynamic data may be in error. Note that a similar conclusion was reached by Howell (1991) and also by Xu (1994) who made adjustments to the enthalpy value for end-member *gedrite* in the FMASH system until the calculated phase relations matched those known from petrological observation.

In the case of the chlorite-bearing, orthoamphibole absent CFMASH model system, the least well constrained thermodynamic data are those for the end-members, *Fe-staurolite, Mg-staurolite , tremolite, Fe-tremolite* and *hornblende* (see Appendix A2). Another factor which

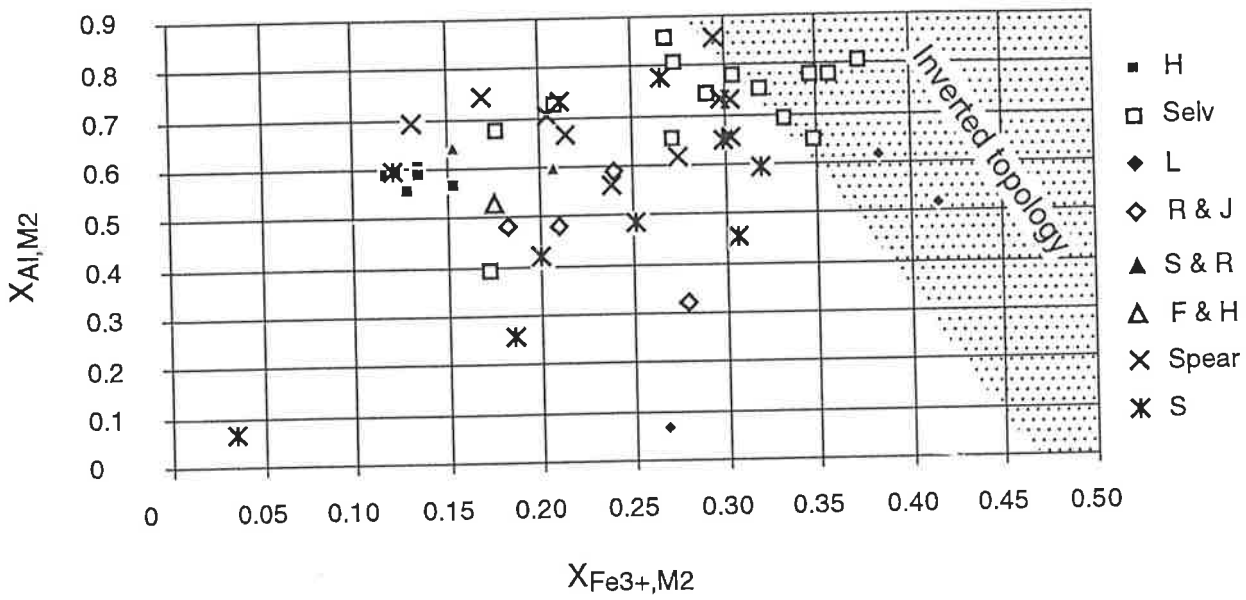

Figure 3.11. A plot of the tschermakite substitution ($Mg_{-1}Si_{-1}Al_1Al_1$) and modified tschermakite substitution ($Mg_{-1}Si_{-1}Fe^{3+}{}_1Al_1$) in hornblende required to cause an inversion of the topology of Fig. 3.7. The compositions of hornblendes from both normal and aluminous-phase amphibolites are plotted for reference. Abbreviations: H, Helms et al. (1987); Selv, Selverstone et al. (1984); L, Laird (1980); R & J, Robinson & Jaffe (1969); S & R, Schumacher & Robinson (1987); F & H, Froese & Hall (1983); Spear, cabonate-absent amphibolites, Spear (1982) ; S, carbonate-bearing amphibolites Spear (1982) .

may cause problems in the calculations is departure in the real minerals from the a-X relations assumed in formulating the data and the permanent datafiles. The most likely sources of such discrepancies are in the mixing of end-members in which some of the cations are of significantly different size. For example, garnet in the CFMASH system has been considered to be an ideal solid solution of *pyrope, almandine* and *grossular*. However, given the differences in the size of calcium, iron and magnesium ions, mixing between these end-members is likely to be non-ideal. In the case of the aluminous chlorite endmember, *amesite*, the experiments used to derive the thermodynamic data were based on solid-solution chlorite which did not closely approach the *amesite* endmember. Thus the thermodynamic data are strongly dependent on the (possibly suspect) activity model used to derive them (R. Powell, pers. comm., 1993). The effect of the non-ideality of a-X relations in garnet, and of adjusting the thermodynamic data within error for the less well constrained end-members, are discussed below.

Garnet

Non-ideality of mixing may be modelled using activity coefficients which relate the activity of the ideal end-member to that of its non-ideal, more realistic counterpart (Powell, 1978; Wood & Fraser, 1984). (See Appendix A4, section A4.3.2 for the formulation of activity-composition (a-X) relations for THERMOCALC permanent data files.) Activity coefficients (γ) are a function of the composition of the phase ($RT ln\ \gamma = w^{A}_{ij}\ f(X)$ where w^{A}_{ij} are interaction parameters for the mixing of the end-members i and j in the phase A). Powell (pers. comm., 1993) has suggested two models for non-ideality in the mixing relations of *pyrope*, *almandine* and *grossular* in garnet (R. Powell, pers. comm., 1993); one for Ca-rich and the other for low-Ca garnets. The garnets of interest in hornblende-staurolite amphibolites typically fall in the low-Ca region where the interaction parameters have determined as:

$$w^{Grt}_{FeMg} = 190R = 1.6\ kJ\ K^{-1}$$

$$w^{Grt}_{CaFe} - w^{Grt}_{CaMg} = -1100R = -9.1\ kJ\ K^{-1}$$

(R. Powell, pers. comm., 1993). A range of values for w^{Grt}_{CaFe} and w^{Grt}_{CaMg} were used to formulate activity models of garnet and the effects of these are illustrated in Fig. 3.12. For significant non-ideality in garnet (i.e. large interaction parameters e.g. $w^{Grt}_{CaFe} = 5\ kJ\ K^{-1}$ and $w^{Grt}_{CaMg} = 14.1\ kJ\ K^{-1}$), the CFMASH invariants [Hbl, Oam] and [Chl, Oam] move a significant distance toward [Grt, Oam], implying that non-ideality in garnet activity-composition (a-X) relations may be part of the reason for the difficulties encountered in the chlorite-bearing CFMASH grid. However, the effect of the non-ideality in garnet is insufficient to allow the predicted phase relations to correspond with those observed petrologically.

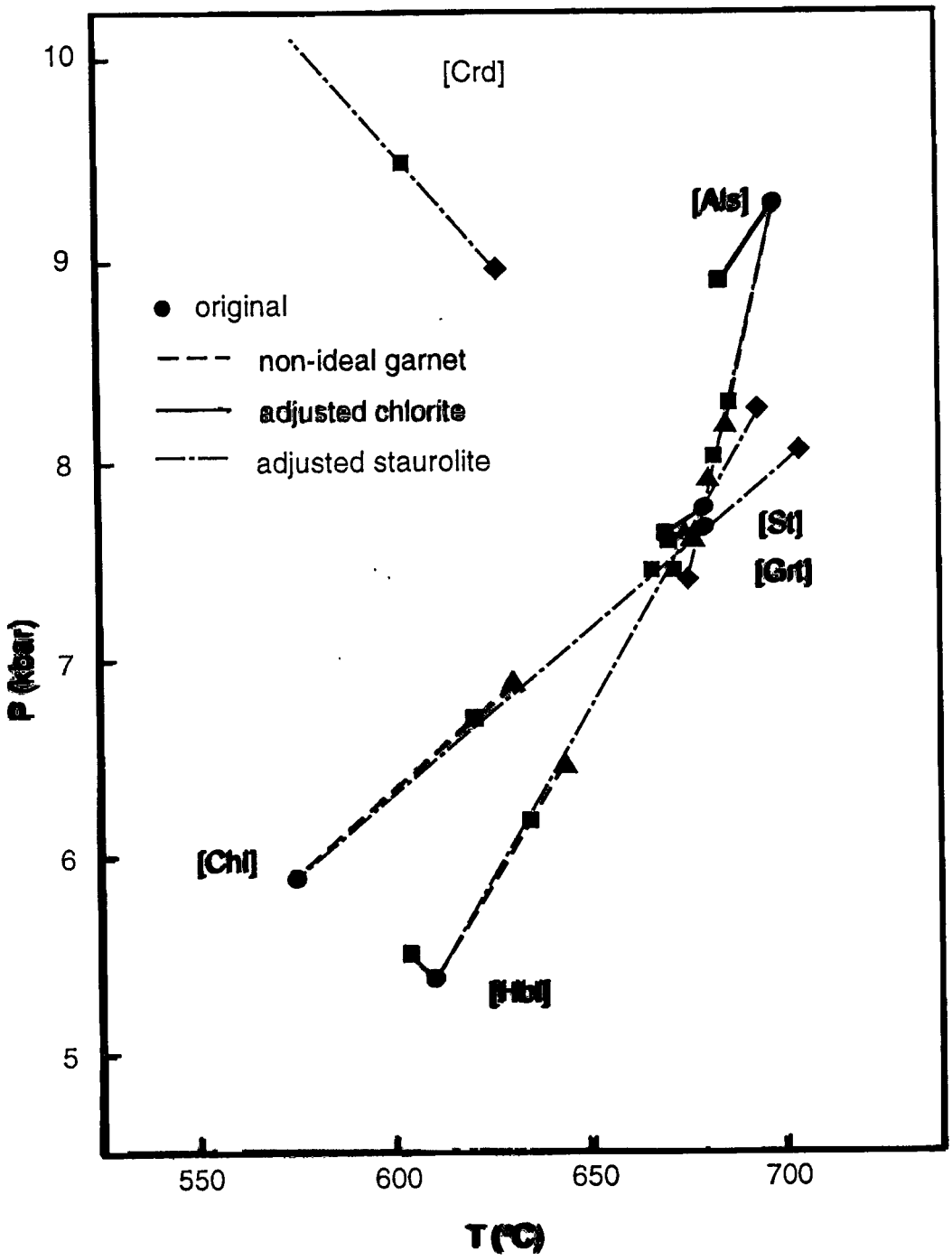

Figure 3.12. The effects of non-ideality in the mixing relations of pyrope, almandine and grossular in garnet for low-Ca garnets (solid squares indicate w^{Grt}_{CaFe} = 0 kJ mol^{-1}, w^{Grt}_{CaMg} = 9.1 kJ mol^{-1} and triangles w^{Grt}_{CaFe} = 5 kJ mol^{-1}, w^{Grt}_{CaMg} = 14.1 kJ mol^{-1}), uncertainty in the a-X relations for chorite reflected in the enthalpy of amesite (squares indicate ΔH_{ames} = 6 kJ mol^{-1}) and uncertainty in enthalpy values for the staurolite end-members (triangles ΔH_{fst} = (-17) kJ mol^{-1}), squares $\Delta H_{fst} = \Delta H_{mst}$ = (-10) kJ mol^{-1}), diamonds) $\Delta H_{fst} = \Delta H_{mst}$ = (-15) kJ mol^{-1}).

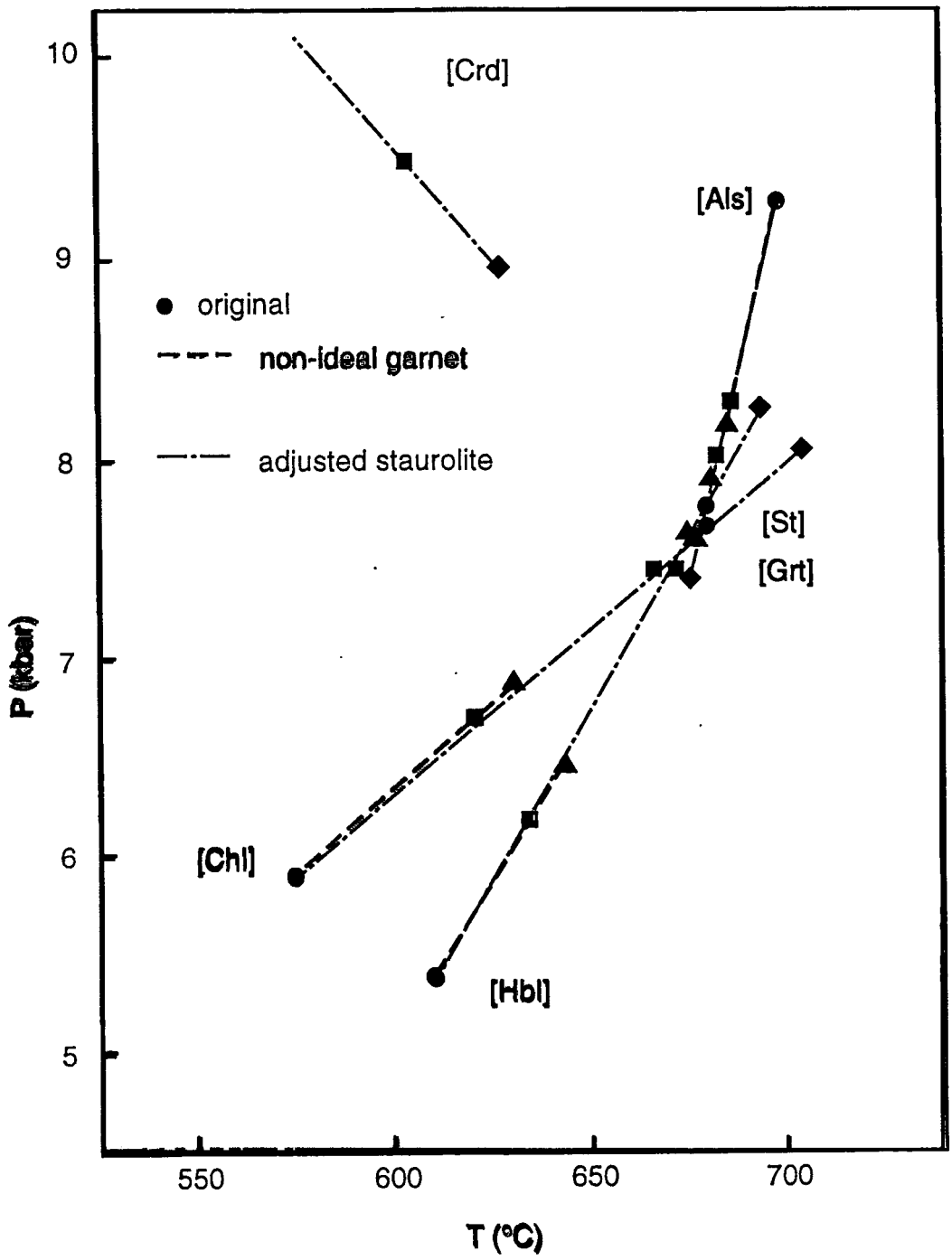

Figure 3.12. The effects of non-ideality in the mixing relations of pyrope, almandine and grossular in garnet for low-Ca garnets (solid squares indicate w^{Grt}_{CaFe} = 0 kJ mol^{-1}, w^{Grt}_{CaMg} = 9.1 kJ mol^{-1} and triangles w^{Grt}_{CaFe} = 5 kJ mol^{-1}, w^{Grt}_{CaMg} = 14.1 kJ mol^{-1}), uncertainty in the a-X relations for chorite reflected in the enthalpy of amesite (squares indicate ΔH_{ames} = 6 kJ mol^{-1}) and uncertainty in enthalpy values for the staurolite end-members (triangles ΔH_{fst} = (-17) kJ mol^{-1}), squares $\Delta H_{fst} = \Delta H_{mst}$ = (-10) kJ mol^{-1}), diamonds) $\Delta H_{fst} = \Delta H_{mst}$ = (-15) kJ mol^{-1}).

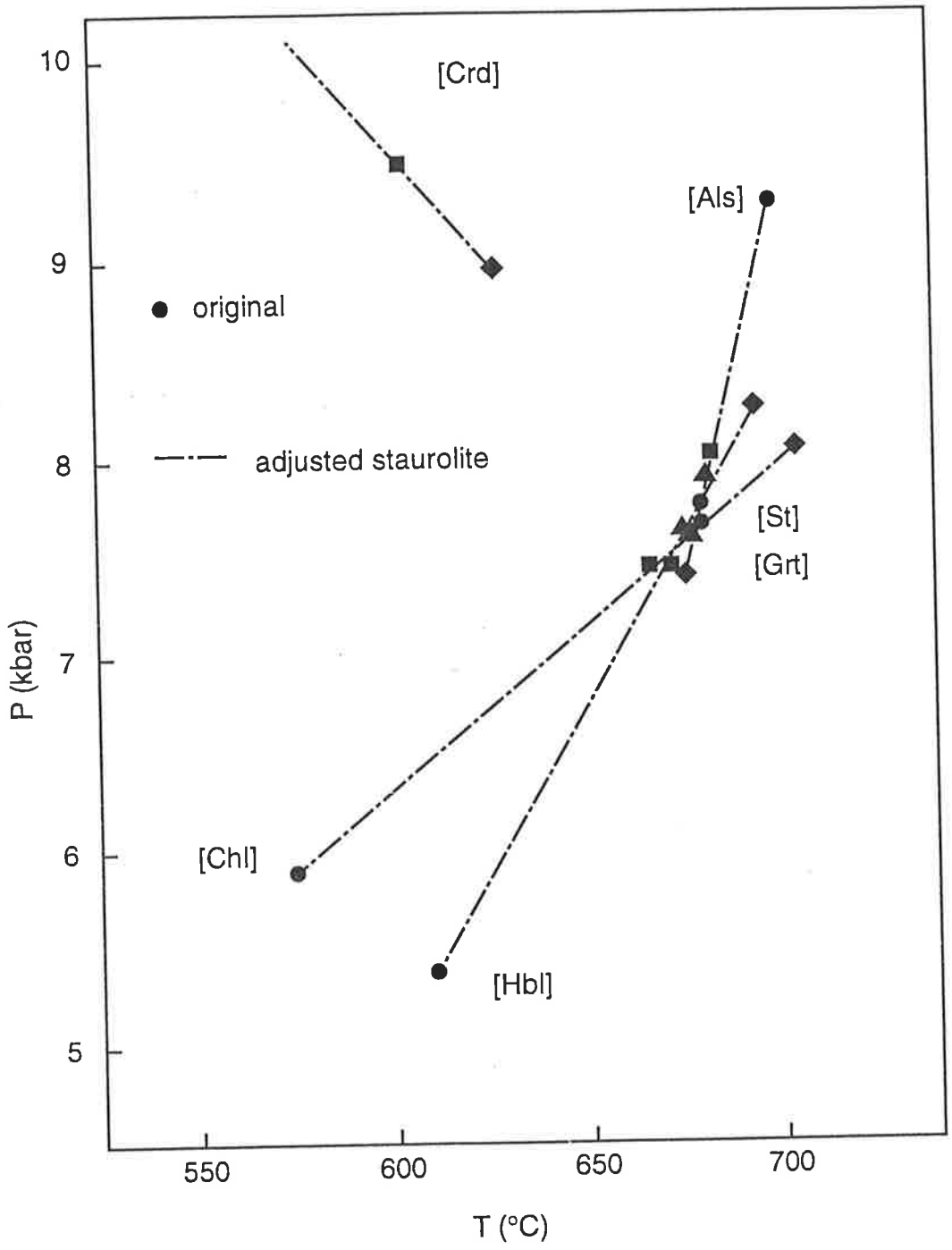

Figure 3.12. The effects of non-ideality in the mixing relations of pyrope, almandine and grossular in garnet for low-Ca garnets (solid squares indicate w^{Grt}_{CaFe} = 0 kJ mol^{-1}, w^{Grt}_{CaMg} = 9.1 kJ mol^{-1} and triangles w^{Grt}_{CaFe} = 5 kJ mol^{-1}, w^{Grt}_{CaMg} = 14.1 kJ mol^{-1}), uncertainty in the a-X relations for chorite reflected in the enthalpy of amesite (squares indicate ΔH_{ames} = 6 kJ mol^{-1}) and uncertainty in enthalpy values for the staurolite end-members (triangles ΔH_{fst} = (-17) kJ mol^{-1}), squares $\Delta H_{fst} = \Delta H_{mst}$ = (-10) kJ mol^{-1}), diamonds) $\Delta H_{fst} = \Delta H_{mst}$ = (-15) kJ mol^{-1}).

Chlorite

Although the ideal mixing model assumed in the derivation of the thermodynamic data of *amesite* is probably an over-simplification, the resulting data are strongly dependent on the activity model used to derive them (R. Powell, pers. comm., 1993). Thus, the uncertainty associated with the enthalpy of *amesite* is probably larger than the listed sd(H) (see Appendix A3). To determine whether the assumption of the ideal mixing allows sufficiently uncertainty to cause an inversion of the phase diagram topology, the enthalpy of *amesite* (ΔH_{ames}) was varied within the full range of its 2σ error bar (+6 kJ mol^{-1}). This caused all of the CFMASH invariant points involving chlorite to move toward the [Chl] invariant (which as it does not involve the end-member *amesite*, obviously is not affected by changes in the data for *amesite*), (Fig. 3.12). The degree of movement experienced by each of the invariant points ΔH_{ames} was slight and certainly insufficient to cause an inversion of the topology.

Hornblende

The enthalpy of the hornblende end-members hornblende, tremolite and Fe-tremolite are associate with considerable uncertainties (sd (H) = 4.55, 5.08 and 6.25 kJ mol^{-1} respectively, see Appendix A2) which could be partly responsible for the inadequacies of the calculated phase diagram. The effect of varying the enthalpy of either *hornblende* or both *tremolite* and *Fe-tremolite* to the full extent of their uncertainties is to cause the stable and metastable CFMASH invariant points to converge, however, the shifts are insufficient to cause an inversion of topology (Fig. 3.13).

Staurolite

The large uncertainties in the enthalpy values for the staurolite end-members suggest that staurolite may be a potential source for the inadequacies of the calculated chlorite-bearing grid (see Appendix A2). If the least well defined enthalpy, ΔH_{fst}, is adjusted to the full extent of its uncertainty (by ΔH_{fst} = -17 kJ mol^{-1}) the CFMASH invariant points draw very close together (Fig. 3.12). However, in doing so, the predicted compositions of the phases became unrealistic, with staurolite calculated as significantly more Fe-rich than garnet. A more satisfactory result was obtained by adjusting ΔH_{fst} and ΔH_{mst} by equal, smaller amounts (e.g. ΔH_{fst}, ΔH_{mst} = - 15 kJ mol^{-1}). This adjustment allows the topology of the calculated phase diagram to invert so that the [Hbl, Oam] and [St, Oam] CFMASH invariant points become metastable with respect to the remaining orthoamphibole-absent points, [Chl, Oam], [Crd, Oam], [Als, Oam], [Grt, Oam] (Fig. 3.14). This topology would then allow the orthoamphibole-bearing invariant points [Crd, Chl], [Grt, Chl] and [Hbl, Chl] to be stable, in agreement with the phase relations determined from natural rocks.

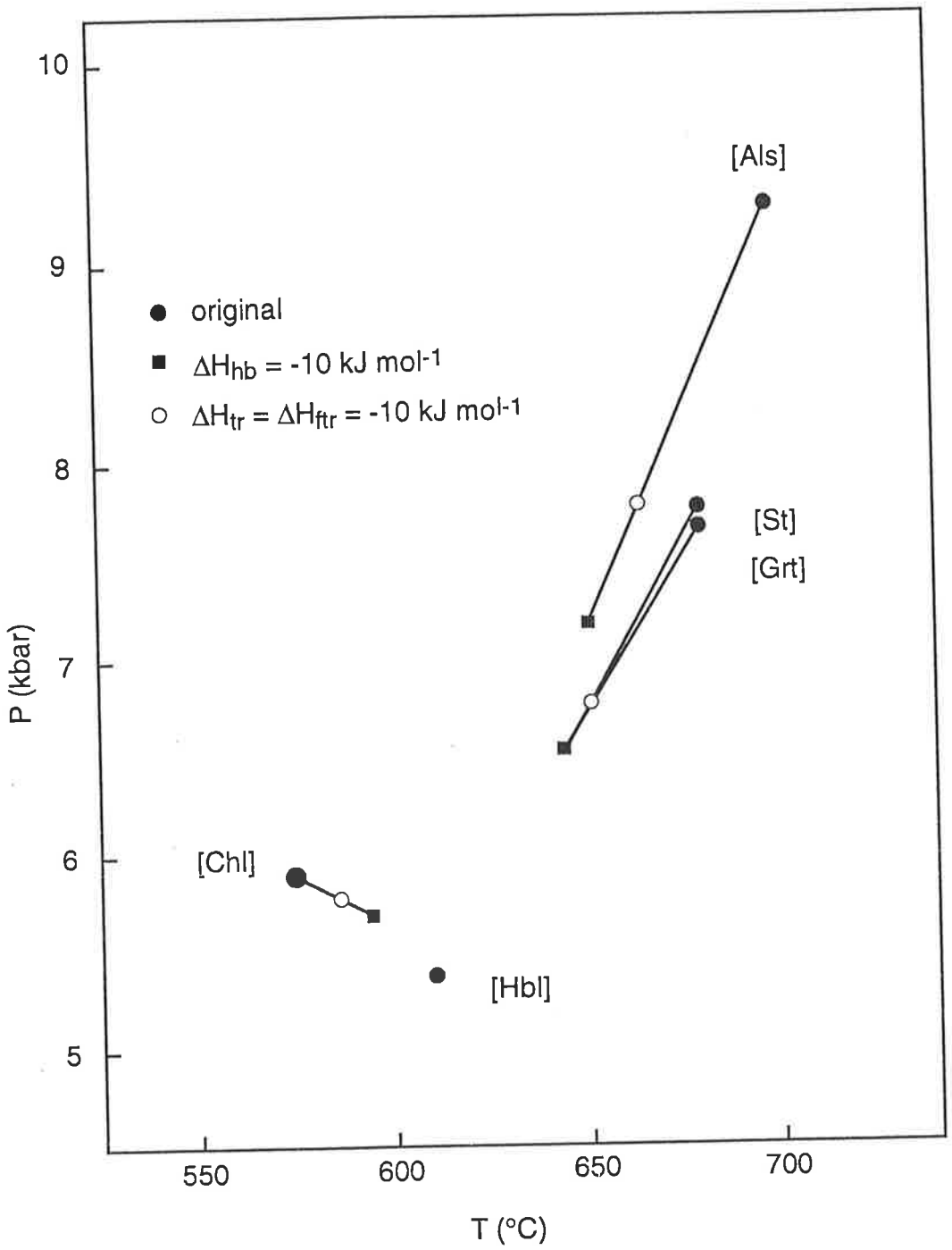

Figure 3.13. The effects of the uncertainty in the enthalpy of hornblende ΔH_{hb} = -10 kJ mol^{-1} and $\Delta H_{tr} = \Delta H_{ftr}$ = (-10) kJ mol^{-1} on the locations of the orthoamphibole-absent CFMASH univariant points.

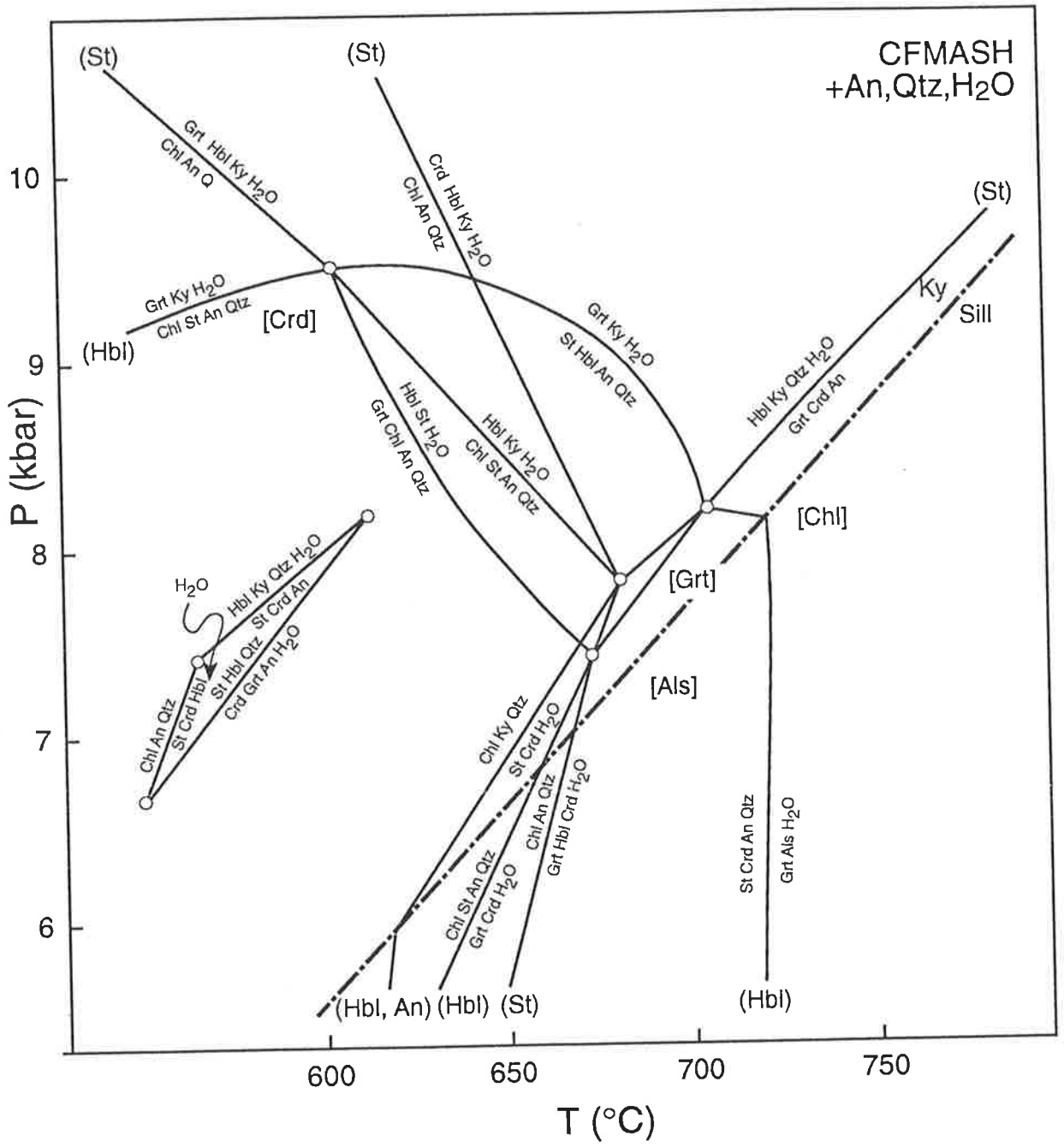

Figure 3.14. P-T projection for the CFMASH involving aluminosilicates, staurolite, cordierite, garnet, chlorite, hornblende with anorthite, quartz and aqueous vapour in excess. Calculated from the internally consistent thermodynamic data set of Holland and Powell (1990; pers comm., 1992), adjusting the enthalpy data for staurolite (ΔH_{fst}, ΔH_{mst} = - 15 kJ mol^{-1}) and using the computer program THERMOCALC (Powell & Holland, 1988).

3.5.4 A new CFMASH grid

Figure 3.15 is a P-T projection constructed for the CFMASH system involving aluminosilicates, staurolite, cordierite, garnet, chlorite, orthoamphibole, anorthite, quartz and aqueous vapour in excess using adjusted thermodynamic data for staurolite ($\Delta H_{fst} = \Delta H_{mst} = -15$ kJ mol^{-1}). The enthalpy of gedrite has been returned to its un-adjusted value as the effect of ΔH_{fst} and $\Delta H_{mst} = -15$ kJ mol^{-1} is similar to that of $\Delta H_{ged} = +10$ kJ mol^{-1} (see Fig. 2.4). Figure 3.15 predicts that the aluminosilicate–orthoamphibole stability field will extend into both the kyanite and sillimanite fields and will be restricted to a P-T range of 6.5-12.5 kbar ([Grt, Hbl, An]$_{FMASH}$ to [St, Crd, Chl]$_{CMASH}$) and 650-1070°C ([Crd, Grt] and [St, Chl, Hbl]$_{CMASH}$). Hornblende is expected to be stable only with the kyanite polymorph at pressures greater than ~ 8.2 kbar [St, Grt] and only up to temperatures of ~ 800°C ([St,Crd,Chl]$_{CMASH}$). Staurolite may coexist with hornblende in a small P-T window in the kyanite field at P-T conditions 8.2-9.5 kbar ([Crd, Grt] and [Crd, Oam]) and 600-680°C ([Crd, Oam] and [Crd, Chl]). Kyanite–staurolite–hornblende is expected to be stable in an even smaller region 8.5-9.5 kbar, 600-680°C [Crd, Grt]. Aluminosilicate–garnet is restricted to high temperatures with sillimanite and high pressures with kyanite (e.g [Crd, Chl], [Chl, Hbl]). Staurolite–cordierite is restricted to temperatures greater than ~500°C and less than 650°C and pressures of ~7 kbar [Chl, Hbl]. Chlorite is stable up to a maximum of ~ 630°C [Als, St, Grt]$_{CMASH}$.

The upper pressure limit of Laird's (1980) "common assemblage" Ca-amphibole–chlorite–epidote–plagioclase–quartz ± Fe^{3+}-phases, carbonates, K-bearing and Ti-bearing phases is also constrained by Fig. 3.15. The "common assemblage" is limited to pressures less than ~10 kbar [Crd, Oam] where chlorite–anorthite–quartz becomes metastable with respect to kyanite–garnet–hornblende and temperature less than ~630°C [Als, St, Grt]$_{CMASH}$ where chlorite–anorthite–quartz becomes metastable with respect to cordierite–orthoamphibole–hornblende, or chlorite–quartz goes to kyanite–cordierite–orthoamphibole. Thus the "common assemblage" becomes unstable to both higher pressure and temperature with respect to assemblages which contain more aluminous phases.

Despite the apparent similarity of some of the features in the grid with those expected from petrological observation, some problems remain. The most important of these involves the metastability of the CFMASH invariant points [Grt, Chl] and [Als, Chl], both of which appear to be stable from natural assemblages (see section 3.4.1). Thus, the adjustments made to the thermodynamic data for Fig. 3.15 do not remedy all of the discrepancies, indicating that not all of the problems of CFMASH are due to uncertainties the thermodynamic data for staurolite.

As can be seen from the above discussion, a number of factors could theoretically result in the inversion of topology required for the predicted assemblages to correspond to those observed in natural rocks. In practice, the problems of conflicting calculated and natural phase relations may lie in any one of non-ideal mixing in calcium-bearing garnet, non-ideal solution between chlorite end-members or the poorly constrained enthalpy data for staurolite or

Figure 3.15. P-T projection for the CFMASH involving aluminosilicates, staurolite, cordierite, garnet, chlorite, orthoamphibole, clinopyroxene and hornblende with anorthite, quartz and aqueous vapour in excess. Calculated from the internally consistent thermodynamic data set of Holland and Powell (1990; pers comm., 1992), with adjusted enthalpy data for staurolite (ΔH_{fst}, ΔH_{mst} = - 15 $kJmol^{-1}$) using the computer program THERMOCALC (Powell & Holland, 1988).

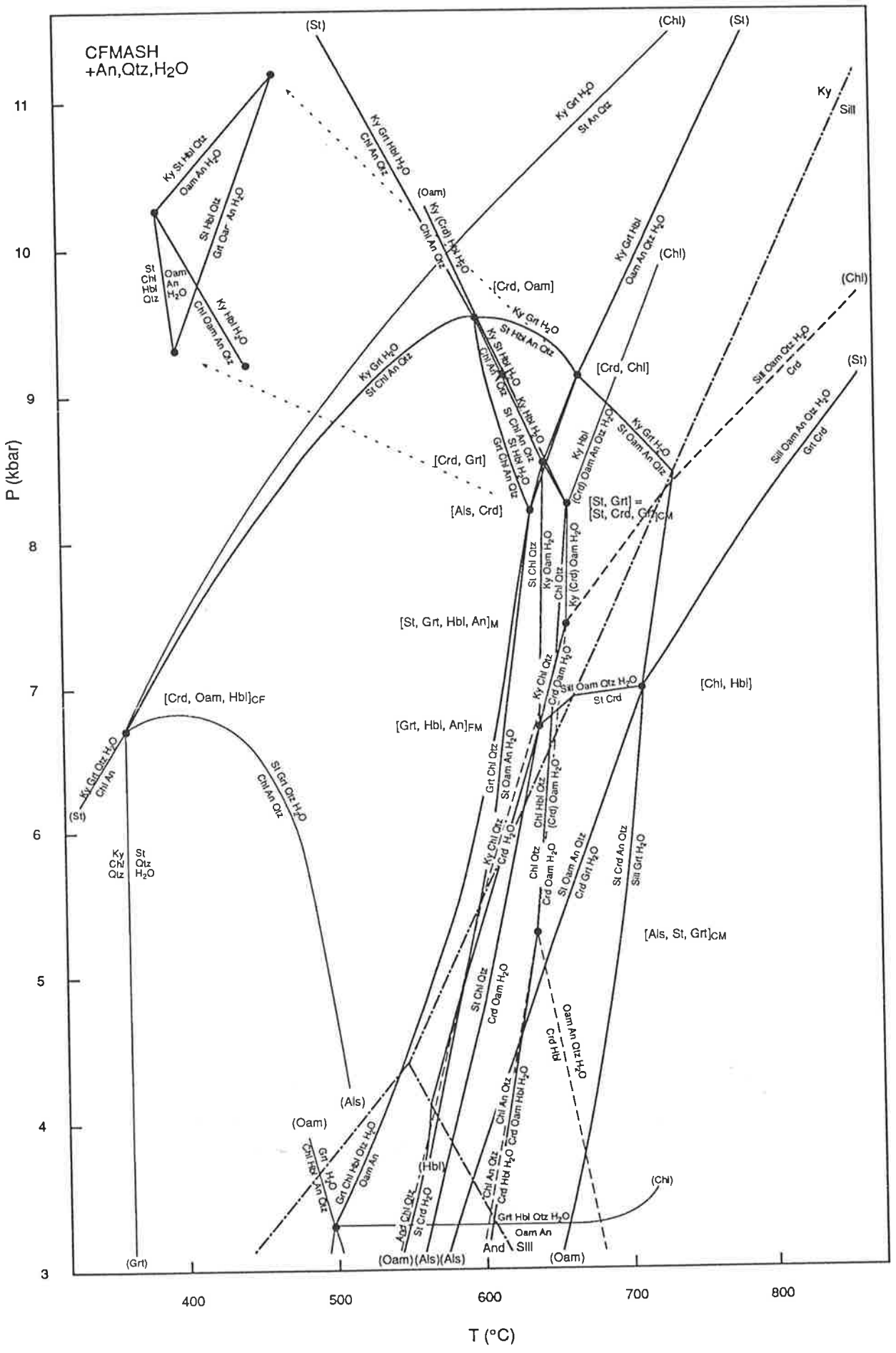
CFMASH
+An,Qtz,H2O
P (kbar)
T (°C)
[Crd, Oam]
[Crd, Chl]
[Crd, Grt]
[Als, Crd]
[St, Grt] = [St, Crd, Qtz]CM
[St, Grt, Hbl, An]M
[Crd, Oam, Hbl]CF
[Grt, Hbl, An]FM
[Chl, Hbl]
[Als, St, Grt]CM
Ky
Sill
And
(St)
(Chl)
(Oam)
(Als)
(Hbl)
(Grt)

hornblende. Precise resolution of this problem is impossible given the poor constraints on currently available thermodynamic data. For example, the combined effects of poorly constrained thermodynamic data for staurolite and hornblende *and* non-ideality in garnet, with or without the presence of ZnO or Fe_2O_3 might allow a P-T projection which is an adequate approximation of the natural amphibolites. As an example, Fig. 3.16 shows the effect of the uncertainty in the enthalpy of hornblende on the CFMASH grid presented earlier (in Fig. 3.15). Decreasing the enthalpy of hornblende (e.g. by specifying that $\Delta H_{hb} = -10$ kJmol^{-1} or $\Delta H_{tr} = \Delta H_{ftr} = -10$ kJmol^{-1}) expands the stability field of staurolite–hornblende. Neither of these adjustments is sufficient to alter the topology of the phase diagram.

Although the problems of resolving the inconsistencies in the chlorite-bearing CFMASH grid are insurmountable, there is relatively good correspondence between the calculated, adjusted grid and the higher temperature (chlorite-free) natural assemblages. The similarities between the chlorite-free grid and the adjusted chlorite-bearing grid are striking and consequently, except for relatively low-temperature chlorite bearing assemblages, either grid may provide a basis for interpreting natural amphibolites and their reaction textures. In order to facilitate this, the discussion below concerns the divariant (continuous) reactions appropriate to both of these grids.

3.6 Pseudosections and continuous reactions in the CFMASH system

P-T projections are useful in understanding the assemblages which *may* occur when a rock is subjected to particular P-T conditions. However, they are projections of *all possible reactions* in their respective compositional systems onto the P-T plane and, thus, not all of the reactions on the diagram would be seen for a rock of a particular composition, nor necessarily by any rocks of typical composition. Another problem with P-T projections is that they do not explicitly deal with the continuous reactions which are most important in controlling the reaction histories of most rocks. To determine what information the assemblages and mineral textures preserved in metamorphic rocks contain in terms of changing physical conditions, it is important to understand the forms of the continuous reactions and their locations in P-T-X space.

The assemblages formed, and reactions seen, by a particular rock are strongly influenced not only by the pressure and temperature conditions it experiences, but also its bulk composition. Thus, it is important to also consider the effects of bulk composition on the phase relations of a particular system. As phase diagram information can only be easily represented in two dimensions, one of the three parameters must be presumed to be either: (1) changing over the diagram (i.e. projected from that variable as a P-T projection is projected from the compositional variable) or (2) equal over the whole diagram (so that the three-dimensional diagram is *sectioned* with respect to that variable). Examples of sectioned phase diagrams include T-X (constant P) and P-X (constant T) diagrams. To be strictly valid, sections may only be made for constant values of intensive variables (e.g. P, T, chemical potential, molar Gibbs Energy) which are independent of the amount of material in the system

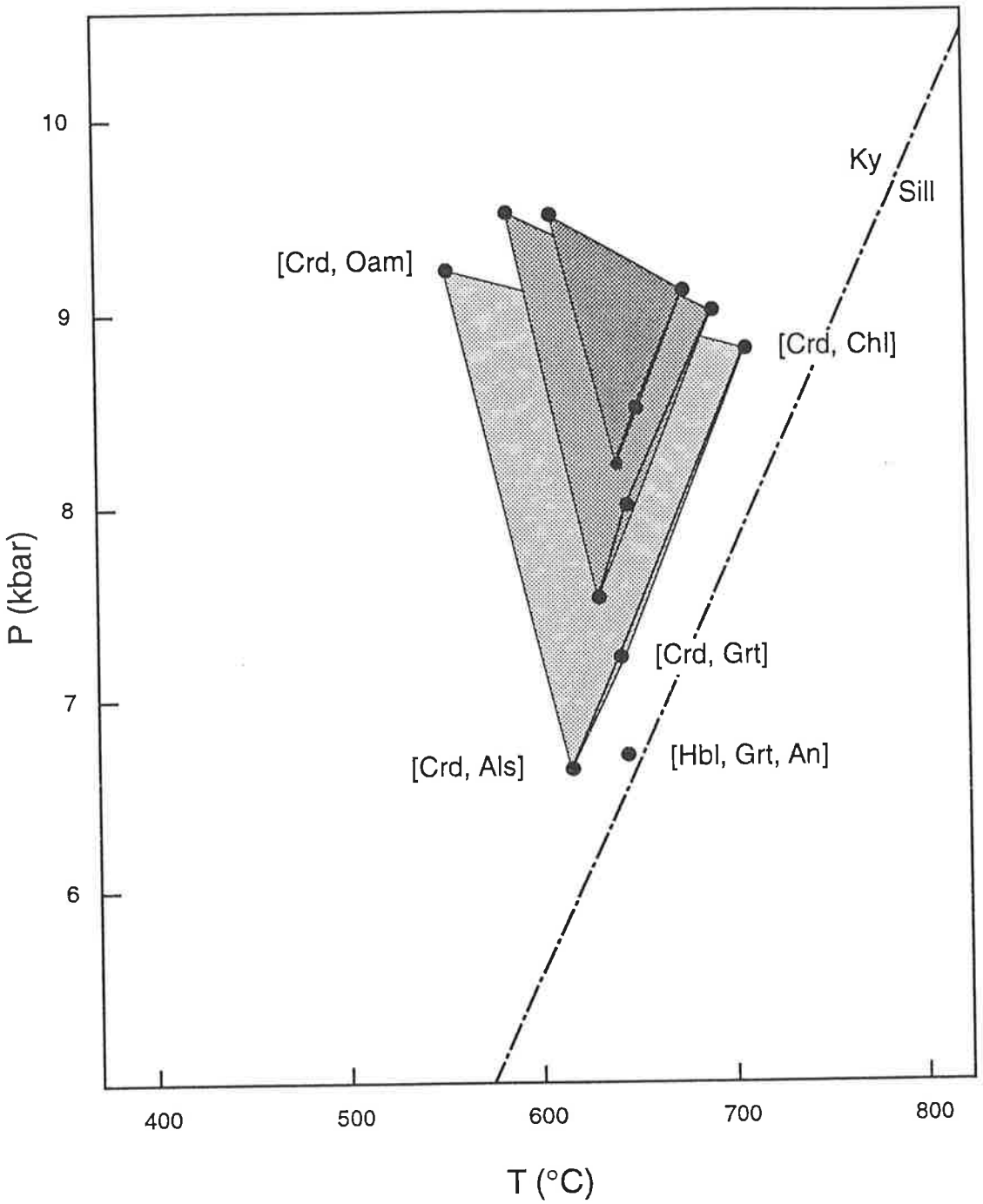

Figure 3.16. The effect of uncertainty in the enthalpy of hornblende on the stability field of staurolite-hornblende (+ plagioclase, quartz, H_2O). The dark region represents the stability field of staurolite-hornblende as shown in Fig. 3.15, with $\Delta H_{fst} = \Delta H_{mst} = -15$ kJ mol^{-1}. The lighter regions were calculated with $\Delta H_{fst} = \Delta H_{mst} = -15$ and $\Delta H_h b = -5$, and -10 kJ mol^{-1}, respectively. The lightest region maximises the stability of staurolite-hornblende by reducing the enthalpies of both hornblende and staurolite to full extent of their uncertainties.

(Powell, 1991). The way the mineralogy changes with physical conditions is of primary interest here. Thus the most petrologically useful phase diagram is one that is sectioned with respect to a compositional variable. However, bulk composition terms such as X_{Fe} are extensive, not intensive, variables as they do not have the same value for all phases in an equilibrium assemblage. These phase diagrams which are sectioned for bulk composition are known as pseudosections.

The divariant and trivariant fields which dominate the CFMASH pseudosections are related to the subsystem CFASH and CMASH univariant reactions in a similar way to which CFMASH divariant reactions are related to the FMASH subsystem reactions in Figs. 3.3 and 3.4). The orientations of the divariant reactions can be estimated from those of the corresponding subsystem reactions. The continuous nature of G-X relations means that the compositions of phases will change consistently along the univariant lines and so can be calculated using equilibrium thermodynamics (e.g. THERMOCALC, version 2.2b1, Powell & Holland, 1988). However, as the adjustments made to the thermodynamic data have a significant effect on the compositions of the phases at a given point on a univariant curve or at an invariant point, the continuous reactions seen by a given bulk composition will also vary with the thermodynamic data. As a result of this, schematic pseudosections are presented here.

Two series of schematic pseudosections are presented here; one for the chlorite-absent CFMASH system (Fig. 3.17) and one for the chlorite-bearing equilibria (Fig. 3.18). They were both constructed for a range of compositions (X_{Fe}) for the CFMASH system with hornblende, anorthite, quartz and aqueous vapour in excess. The major difference in the topology of the pseudosections developed for the chlorite-absent and the chlorite-bearing phase relations lies in the low temperature equilibria. In the chlorite-absent system, kyanite–hornblende appears to be stable over a wide range of compositions down to very low pressures and temperatures. In contrast, the chlorite-bearing equilibria restrict kyanite–hornblende to a small P-T window and the low temperature-low pressure field is dominated by the trivariant field, chlorite–hornblende. The assemblages predicted for other P-T ranges are similar except that the complex central portion of the chlorite-bearing CFMASH system (enlarged in Fig. 3.19) occurs about 3 kbar higher than that in the chlorite-absent system, as a result of the different locations of the invariant equilibria in the two systems (See Figs. 3.4 and 3.15). The diagrams predict that assemblages involving garnet–hornblende will dominate the intermediate to high pressure and temperature field for rocks with high X_{Fe} and will contract to successively higher conditions with increasing Mg-content. Cordierite–hornblende assemblages are stable up to pressures of about 5 kbar for low X_{Fe} rocks but retreat to very low pressures with increasing Fe-content. Orthoamphibole–hornblende is limited to relatively high temperatures and occur over a wide range of X_{Fe}. Staurolite–hornblende is only stable under high P/T ratios, and is most stable in a small P-T range in rocks of intermediate X_{Fe}.

Figure 3.17. Schematic pseudosections for the chlorite-absent CFMASH system (Fig. 3.4) with hornblende, anorthite, quartz and aqueous vapour in excess, showing the changing topology of the divariant and trivariant fields with decreasing X_{Fe}. a) Fe-rich assemblages; b, c and d are for successively lower X_{Fe} bulk compositions; e) Mg-rich rocks; f) CMASH endmember system.

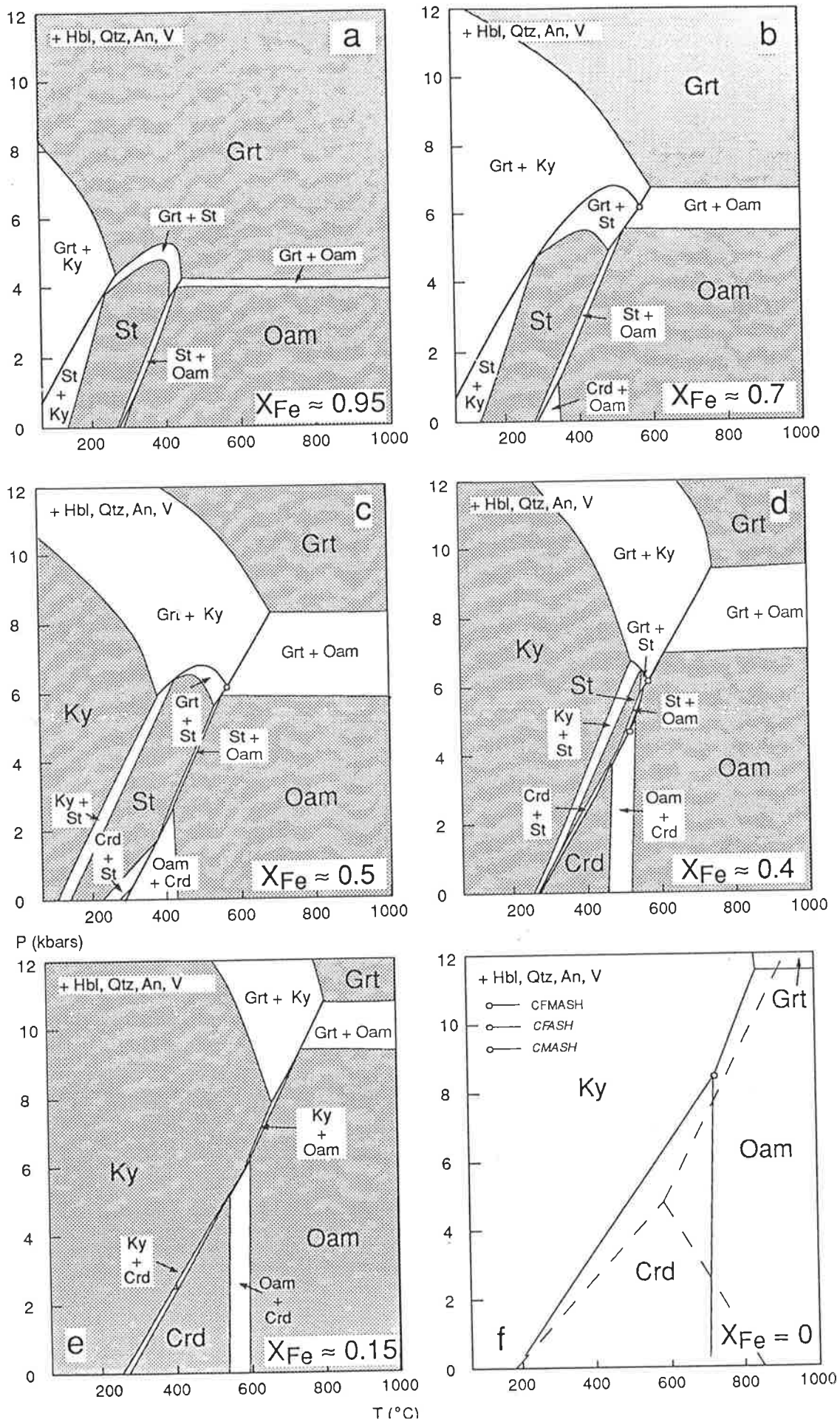
a
+ Hbl, Qtz, An, V
Grt
Grt + St
Grt + Ky
Grt + Oam
St
St + Oam
St + Ky
Oam
XFe ≈ 0.95
b
+ Hbl, Qtz, An, V
Grt
Grt + Ky
Grt + St
Grt + Oam
Oam
St
St + Oam
St + Ky
Crd + Oam
XFe ≈ 0.7
c
+ Hbl, Qtz, An, V
Grt
Grt + Ky
Grt + Oam
Ky
Grt + St
St + Oam
Ky + St
St
Oam
Crd + St
Oam + Crd
XFe ≈ 0.5
d
+ Hbl, Qtz, An, V
Grt
Grt + Ky
Grt + Oam
Ky
Grt + St
St
St + Oam
Ky + St
Oam
Crd + St
Oam + Crd
Crd
XFe ≈ 0.4
P (kbars)
e
+ Hbl, Qtz, An, V
Grt
Grt + Ky
Grt + Oam
Ky
Ky + Oam
Ky + Crd
Oam
Oam + Crd
Crd
XFe ≈ 0.15
T (°C)
f
+ Hbl, Qtz, An, V
CFMASH
CFASH
CMASH
Grt
Ky
Oam
Crd
XFe = 0

Figure 3.18. Schematic pseudosections for the chlorite-bearing CFMASH system (Fig. 3.15) with hornblende, anorthite, quartz and aqueous vapour in excess, showing the changing topology of the divariant and trivariant fields with decreasing X_{Fe}. a) Fe-rich assemblages; b, c, d and e are for successively lower X_{Fe} bulk compositions; f) Mg-rich rocks.

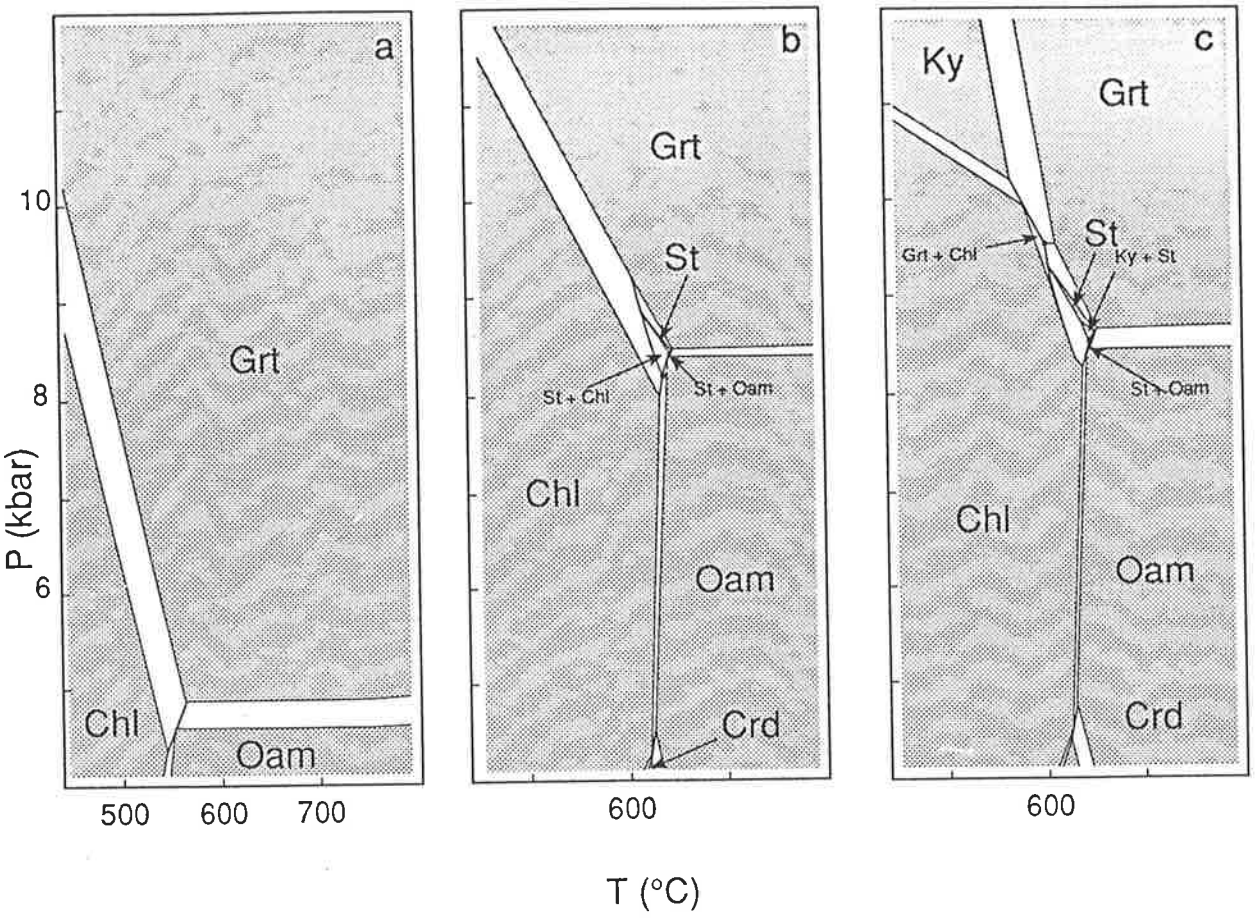
a
b
c
Ky
Grt
St
Grt + Chl
Ky + St
St + Chl
St + Oam
Chl
Oam
Crd
10
8
6
P (kbar)
500
600
700
T (°C)

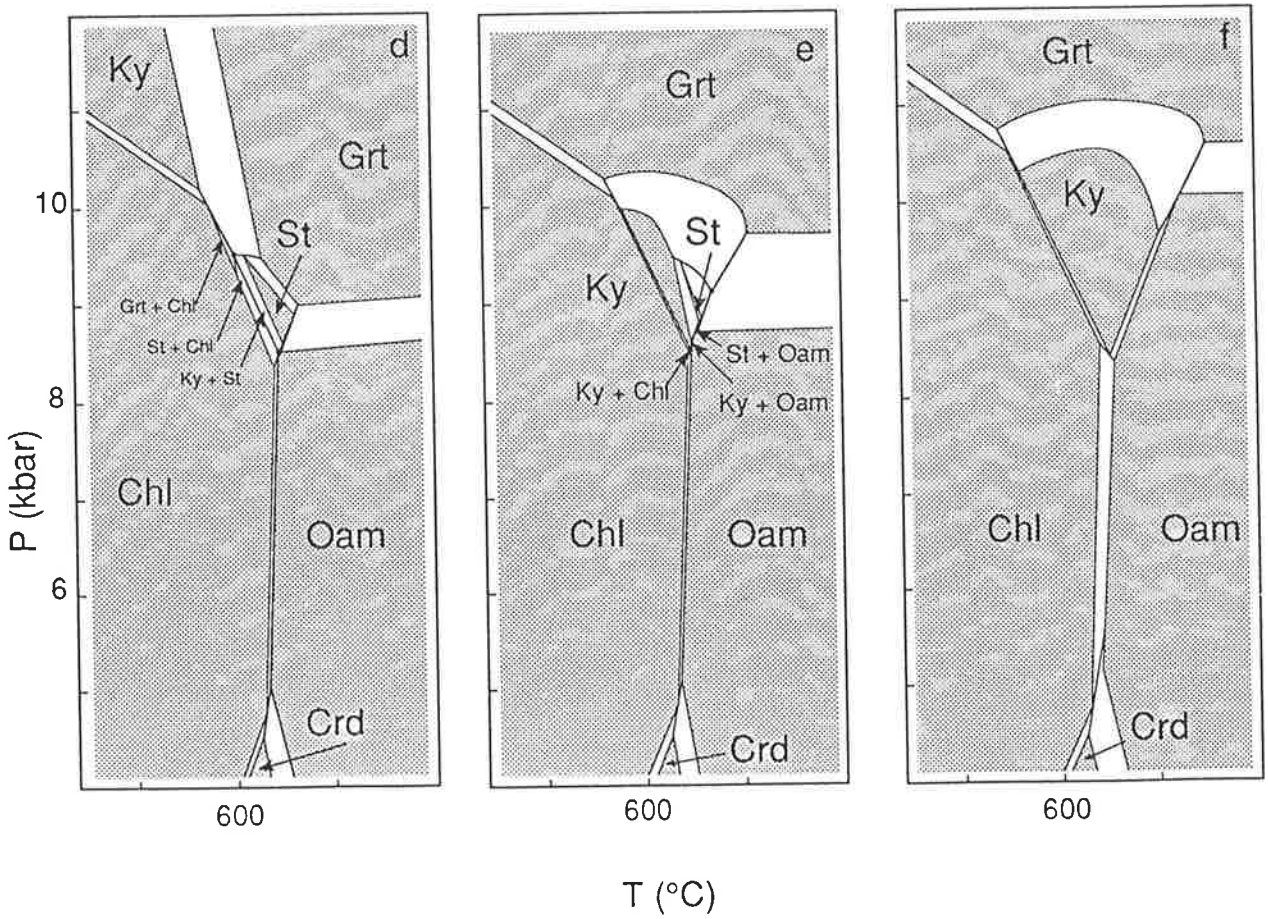
d
e
f
Ky
Grt
St
Grt + Chl
St + Chl
Ky + St
Ky + Chl
St + Oam
Ky + Oam
Chl
Oam
Crd
10
8
6
P (kbar)
600
T (°C)

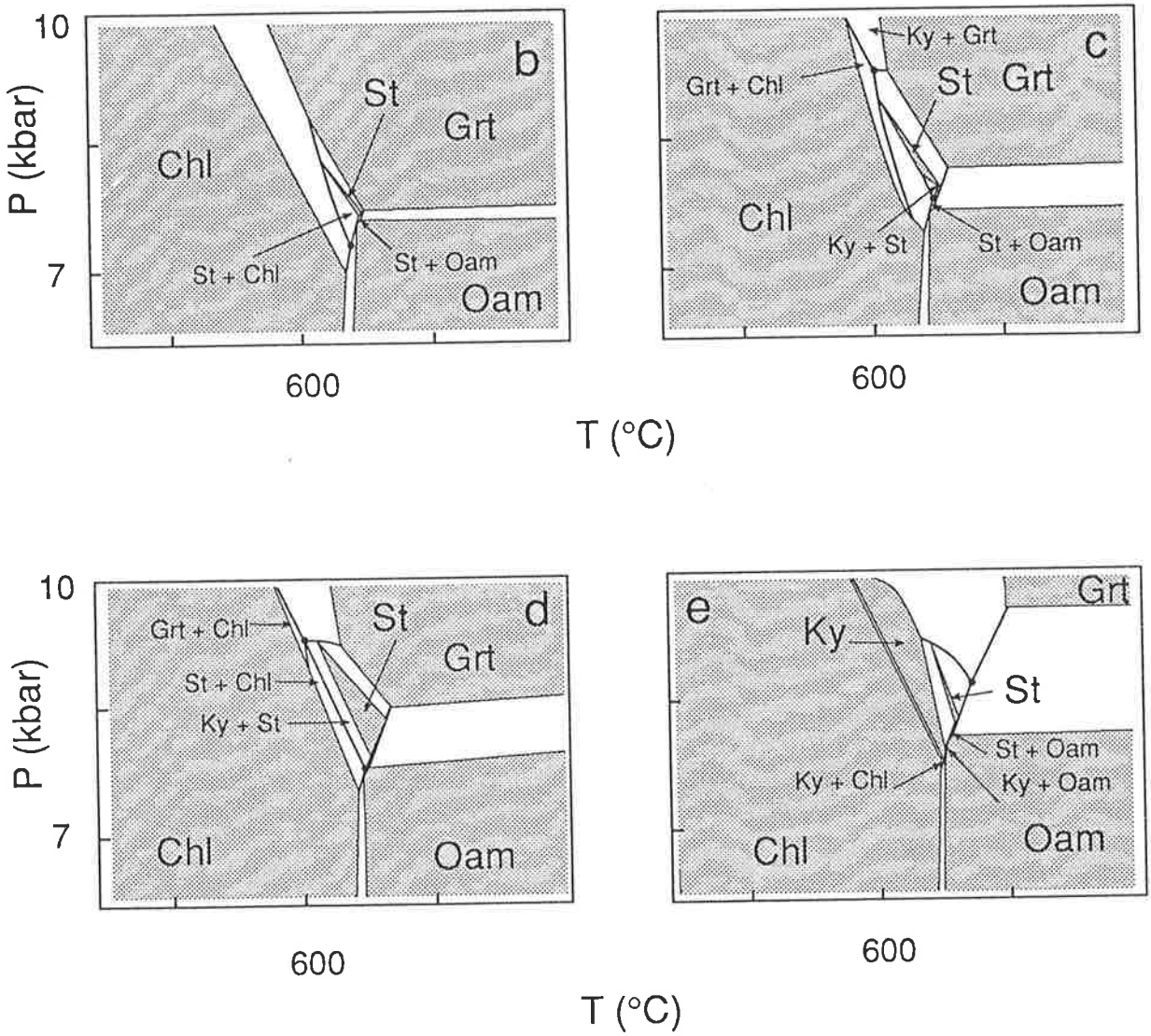

Figure 3.19. Blow-up of the complex central portion of the chlorite-bearing CFMASH pseudosections in Fig. 3.18.

3.7 A qualitative extension into NCFMASH

This section discusses the qualitative extension of the CFMASH phase diagrams into NCFMASH. The addition of Na to the CFMASH equilibria is assumed to increase the variance of a given assemblage, without causing a new phase to be stabilised. The relative proportions of sodium in natural amphibolite phases gives an indication of the extent to which the different phases accommodate sodium; plagioclase is typically more Na-rich than hornblende, which is more Na-rich than orthoamphibole, and the remaining phases contain negligible sodium. Thus, the addition of Na to the CFMASH equilibria is assumed to stabilise plagioclase over hornblende, hornblende over orthoamphibole, and orthoamphibole over all other phases. Hornblende and anorthite generally occur on opposite sides of CFMASH equilibria, so expanding the stability field of plagioclase often reduces that of hornblende. As a result, the NCFMASH equilibria emanating from the univariants in Fig. 3.15 are located between the anorthite-absent (An) and orthoamphibole-absent (Oam) CFMASH univariants, effectively expanding the stability fields of those phases. With hornblende, plagioclase, quartz and aqueous vapour in excess, these univariants intersect in an NCFMASH invariant point; [Crd] (Fig. 3.20).

The topology and reactions in Fig. 3.20 are broadly consistent with those of Spear's (1978; Spear & Rumble, 1986) corresponding invariant point. However, as mentioned earlier, the CFMASH and thus NCFMASH phase relations are not entirely consistent with the phase relations observed in natural amphibolites. In NCFMASH, the stability of only a single invariant point [Crd] in NCFMASH implies that cordierite–hornblende will never be a stable assemblage in amphibolites, however, this assemblage is observed from several localities including the Harts Range (see Chapter 4), South Africa (Humphreys (1993), southwestern New Hampshire (Schumacher & Robinson, 1987) and the Pamirs in the former USSR (Grew et al., 1988). Thus the NCFMASH invariant and univariant equilibria will be discussed further in Chapter 6, in terms of the phase relations in natural amphibolites.

In the following chapters the calculated CFMASH grids and qualitative NCFMASH phase diagrams developed here will be used to interpret the significance of aluminous amphibolite assemblages from a wide variety of localities, beginning with the Harts Range, central Australia.

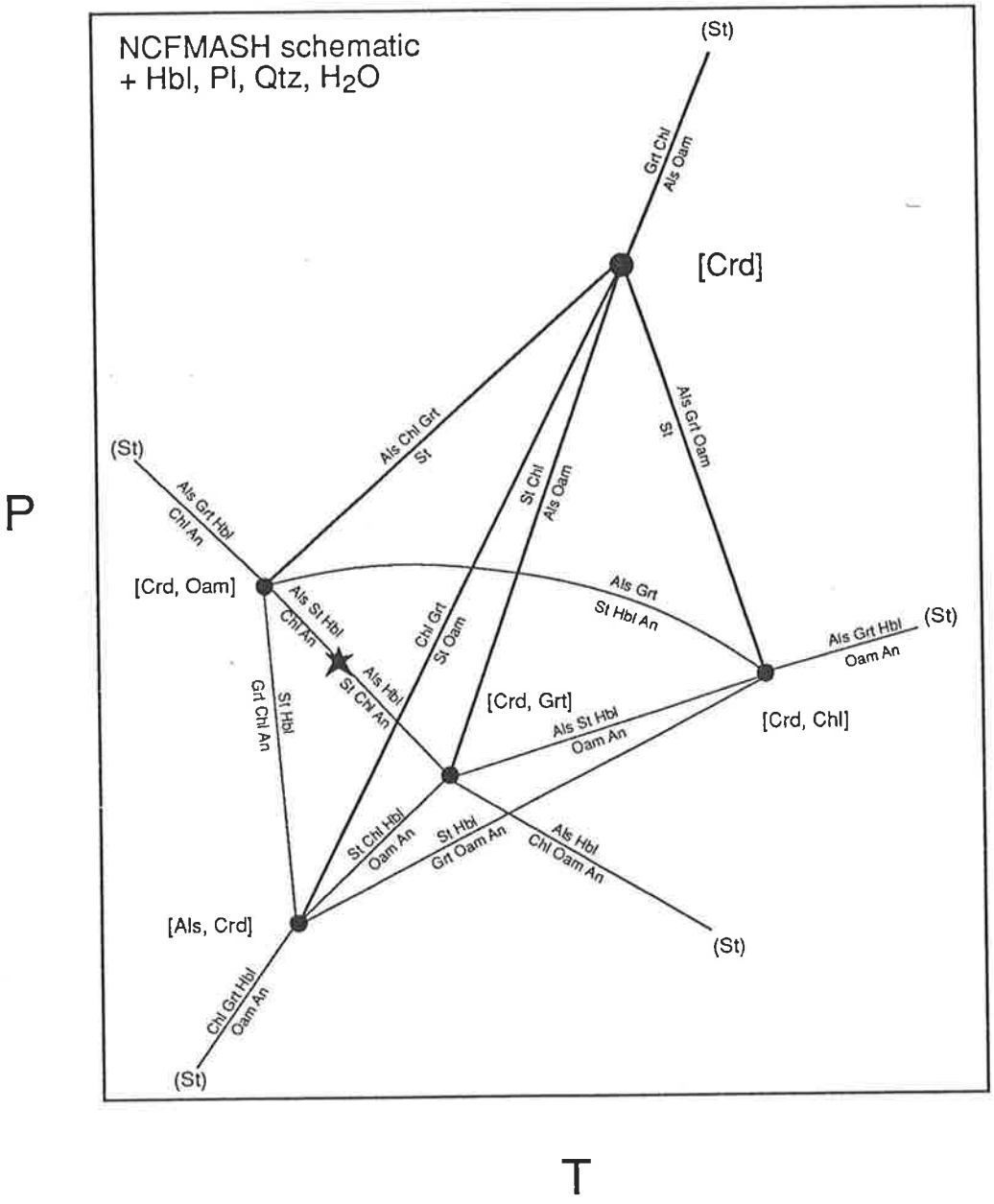

Figure 3.20. Schematic NCFMASH phase diagram (heavy lines, large circles) and their CFMASH terminae (small circles, light lines) with hornblende, plagioclase, quartz and aqueous vapour in excess. Extended from the CFMASH equilibria in Fig. 3.15 assuming that sodium stabilises plagioclase over hornblende, hornblende over orthoamphibole and orthoamphibole over other phases.

Chapter 4: Metamorphism in the Harts Range region, eastern Arunta Inlier.

4.1 Introduction

Previous chapters have dealt with the theoretical phase relations in amphibolites, with the aim of developing quantitative P-T phase diagrams for the FMASH and CFMASH model systems. In this chapter these phase relations will be used in the interpretation of the reactions and mineral equilibria observed in natural amphibolites. The phase diagrams are applied to the problem of discerning the metamorphic history of the Entia Dome which forms part of Harts Range in central Australia, using the phase relations in kyanite-, staurolite-, cordierite-, garnet- and gedrite-amphibolites.

A brief summary of the geological setting and field relations of these rocks from the Arunta Inlier will be followed by an account of their petrography (described more fully in Appendix A8) and the constraints the mineral assemblages and reaction textures place on the P-T evolution of the area using the phase relations developed in previous chapters. The final section discusses the implications of this P-T evolution with respect to the available geochronological data. A slightly modified version of this chapter is currently in press in Precambrian Research (Arnold et al., 1994).

4.2 Geological setting and background

The Arunta Inlier is one of a number of Proterozoic crustal blocks exposed in northern and central Australia, and outcrops over approximately 200 000 km^2 in the Alice Springs region (Fig. 4.1). It has been extensively mapped to the 1:100 000 scale by the BMR (now AGSO, e.g. Shaw et al., 1990) who proposed the stratigraphic divisions and structural provinces which have formed the basis of the knowledge of the Inlier (Stewart et al., 1984; Shaw et al., 1984). The Entia Dome is situated at the eastern end of the Arunta Inlier, approximately 180 km ENE of Alice Springs, in the Harts Range. The core of the 25 km wide dome comprises mainly felsic orthogneisses (Entia gneiss complex), interlayered with amphibolite bands and bodies which are of basaltic and intrusive origin (Foden et al., 1988). This is structurally overlain by a mylonitised granitic gneiss (the Bruna Gneiss) and a metamorphosed supracrustal sequence (the Irindina Supracrustal assemblage, Ding & James, 1985).

The Entia gneiss complex consists of a supracrustal assemblage including interlayered amphibolites, calc-silicates, carbonates, pelitic and other metasedimentary rocks which were

Figure 4.1 A geological map of the north-east portion of the Entia Dome, after Foden et al. (1988). Samples were collected from the "Supracrustal rocks" in the north-east of the area.

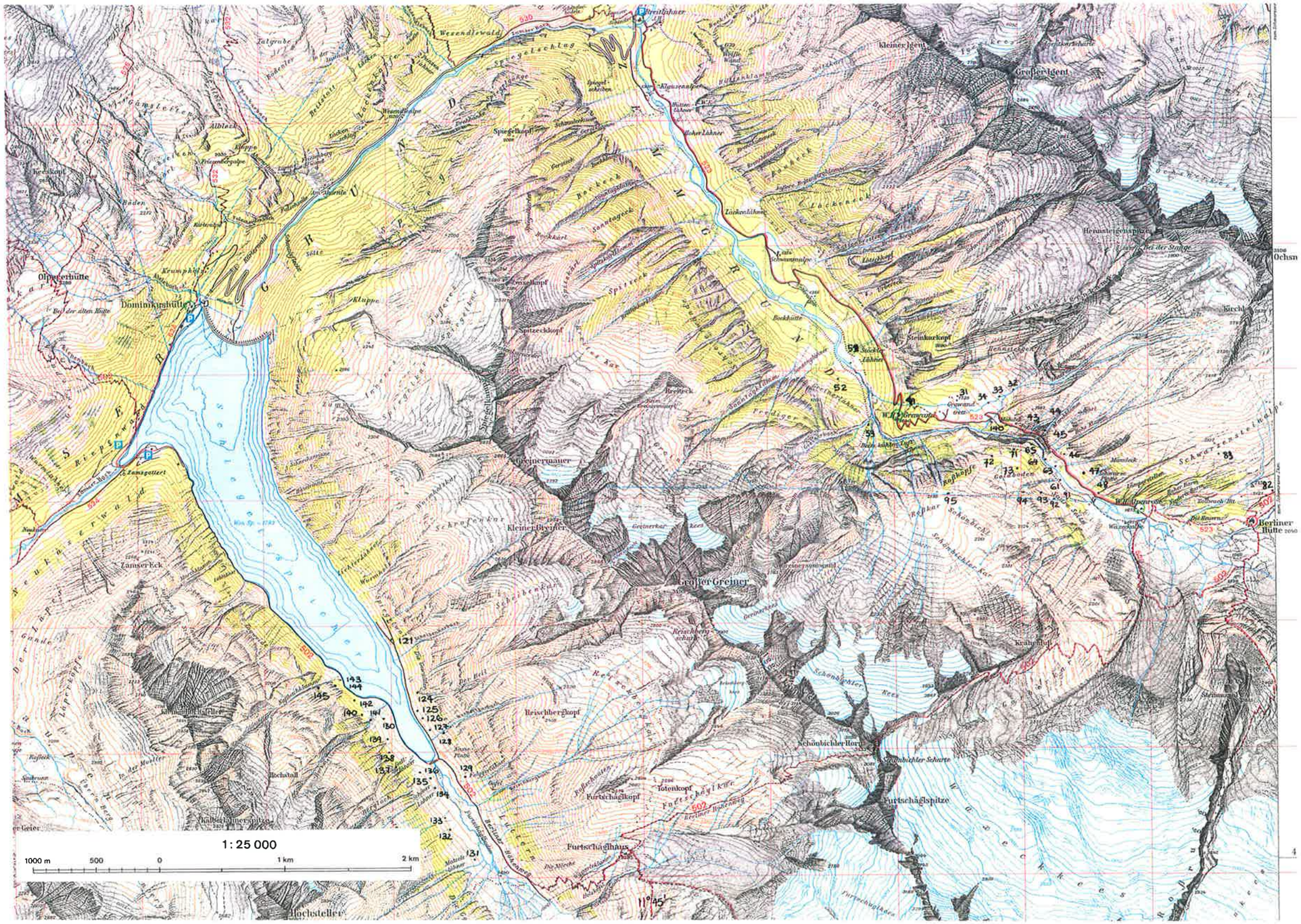
1: 25 000
1000 m
500
0
1 km
2 km
Breitlahner
Wesendlewald
Spiegelkopf
Kleiner Igent
Großer Igent
Hennsteigenspitze
Ochsn
Olpererhütte
Dominikushütte
Zamsgatterl
Schlegeisspeicher
Zamser Eck
Steinkarkopf
Breiteck
Greinermauer
Kleiner Greiner
Großer Greiner
Berliner Hütte
Reischbergkopf
Schönbichler Horn
Schönbichler Scharte
Furtschaglspitze
Furtschaglkopf
Totenkopf
Furtschaglhaus
Hochsteller
Kalbenlahnerspitze
Hochstall
11°45'
121
124
125
126
127
123
129
130
131
132
133
134
135
136
137
138
139
140
141
142
143
144
145
31
32
33
34
41
43
44
45
46
47
48
51
52
53
61
63
64
65
71
72
73
82
83
91
92
93
94
95

fragmented and dismembered by the intrusion, in a high temperature (granulite facies) environment, of large granitoid sheets at ~1767 ±2 Ma (Cooper et al., 1988). These granitoids consist of three main bodies, the Huckitta Granodiorite Gneiss, the Huckitta Tonalite Gneiss and the Inkamulla Granite Gneiss (Buick, 1983, 1985; Foden et al., 1988), which have been intruded by a younger set of amphibolite dykes and associated small layered intrusions (Foden et al., 1988).

The Entia gneiss complex contains a pervasive amphibolite facies foliation and mineral lineation (Ding & James, 1985; James & Ding, 1988), the retrogressive nature of which is evident from the occasional preservation of granulite facies assemblages in the cores of mafic boudins which are present at a range of scales (see Foden et al., 1994, and Appendix A8, section A8.3). Ding and James (1985) proposed that the dominant amphibolite fabric developed synchronously with compositional layering and is folded by a number of later fold generations which, however, did not cause new foliations to develop. It is the petrology and P-T history of these amphibolite facies assemblages which are the focus of this chapter. The isotopic characteristics of the area are discussed by Foden et al. (1994).

Earlier workers have proposed that the Entia gneiss complex forms the basement complex (observed as the core of the dome) to a cover sequence (the Irindina Supracrustal assemblage) both of which had experienced separate metamorphic and deformational histories (Ding & James, 1985). These two units are thought to have been juxtaposed in thrust complexes co-incident with the intrusion of the syn-tectonic, mylonitised Bruna Gneiss at 1747 ±3 Ma (Cooper et al., 1988). However, other workers (Teyssier, 1985; Collins & Teyssier, 1989) have proposed that much of the strain evident in the Entia Dome was taken up in smaller scale shear zones which are continuous with those in the Arltunga Nappe Complex to the south. This implies that the majority of the deformation experienced by the Entia gneiss complex occurred during the Palaeozoic Alice Springs Orogeny (Collins & Teyssier, 1989).

The structurally overlying (according to both Ding & James, 1985 and Collins & Teyssier, 1989) Irindina supracrustal assemblage comprises the Harts Range meta-igneous complex and pelitic, semi-pelitic, carbonate and other minor lithologies. These rocks show evidence of repeated fold generations, the first of which resulted in the formation of a micaceous schistosity in amphibolite-grade pelites and tectonic layering and a mineral lineation in amphibolite, quartzite and calcareous lithologies (Ding & James, 1985). The common nature of the amphibolite metamorphism to both the Entia gneiss and the Irindina supracrustal assemblage suggests that these sequences may have been juxtaposed prior to or during amphibolite facies metamorphism (Ding & James, 1985).

Supracrustal assemblages are found as lenses within the volumetrically dominant intrusive felsic magmas of the Entia Dome. These provide suitably reactive compositions for the development of the array of metamorphic assemblages which form the basis for this study. Of particular interest is a band of supracrustals occurring in the north-eastern quadrant of the Entia Dome (Fig. 4.1). This discontinuous layer (up to ~20 m thick) of supracrustal material exhibits a relatively consistent internal stratigraphy involving an association of calc-silicates

(including a distinctive pink-coloured manganiferous epidote rock), porphyroblastic garnet amphibolites, garnet–kyanite–biotite schists, and gedrite gneisses over a distance of several kilometres, suggesting that some semi-continuous character is retained. Although strongly boudinaged within and disrupted by the intrusive felsic gneisses, such supracrustal layers form mappable horizons which provide evidence of multiple fold generations (e.g. Ding & James, 1985 and Fig. 4.1). The whole-rock chemistry, petrography and mineral chemistry of these supracrustal rocks are discussed below (Tables 4.1, 4.2 and 4.3 respectively). (Mineralogical abbreviations are listed in Appendix A1 and detailed descriptions of selected Harts Range amphibolites are summarised in Appendix A8).

4.3 Rock chemistry, petrography and mineral chemistry

Bulk rock chemistry plays an important role in determining which assemblages are stable in particular rock samples. Beyond the obvious factors such as K and Ca content, Na, Al, Fe and Mg contents also appear to be important for determining which mineral assemblages are formed. In the following sections the bulk rock chemistry of the different assemblages is discussed and compatibility diagrams are constructed to clarify these compositional effects. As a consequence of their compositional complexity, assumptions and simplifications are required in order to graphically represent the chemistry of amphibolites. As discussed in Chapters 3 and 6, the chemistry of amphibolites can be simplified to the NCFMASH (Na_2O-CaO-FeO-MgO-Al_2O_3-SiO_2-H_2O) system from which, assuming that hornblende, plagioclase, quartz and an aqueous vapour are in excess, AFM-type compatibility diagrams can be constructed. (The projections were carried out using the computer program outlined in Appendix A9.) AFM diagrams (+ hornblende, plagioclase, quartz and aqueous vapour) will be used to illustrate the compositional variation of the amphibolites and their phases and the compatibility relations of the amphibolite assemblages.

4.3.1 Biotite-rich rocks

Bulk rock analyses of porphyroblastic kyanite–biotite schists from the Entia Dome (Table 4.1, e.g. sample 853-76) show that these rocks are SiO_2 and K_2O poor, but Al_2O_3 rich in comparison to true pelitic rocks (cf. Hudson & Harte, 1985). The association of this rock type with migmatites adjacent to intrusive units (Buick, 1983) suggests that they may be restitic material associated with partial melting of pelitic or quartzo-feldspathic rocks in the kyanite stability field. Elongate kyanite grains contain straight inclusion trails and are sub-parallel to the biotite foliation which wraps around them. This implies that the kyanite is syn-deformational. In some samples kyanite is pseudomorphed by fibrous sillimanite. Garnet porphyroblasts are wrapped by the biotite foliation and in several examples garnet is in contact with kyanite (Fig. 4.2a). Minor proportions of quartz, plagioclase hornblende and muscovite are observed. Biotite and garnet compositions show significant variation. Biotite is most magnesian in association with kyanite and more Fe-rich with garnet or hornblende with a wide

Table 4.1. Whole rock analyses.§

Sample #	Ky-Bt-schist 853-76	u.m. cum 950-081	u.m. cum 950-089	Crd-Oam 853-30	amphibolite 962-017r	amphibolite 853-180	amphibolite 962-155	Ky-St-Hbl-Ep HR91-4	St-Grt-Hbl-Ep HR91-8	St-Grt-Hb-Bt 853-16
%										
SiO2	42.93	48.77	48.73	47.18	47.78	49.28	46.42	38.14	37.92	67.04
TiO2	0.31	0.12	0.34	0.65	0.57	0.61	1.06	1.47	2.37	1.01
Al2O3	34.84	5.71	7.62	26.53	23.99	14.62	16.29	19.41	20.78	11.05
Fe2O3*	5.23	7.86	14.13	7.57	6.83	9.59	13.59	16.45	17.25	9.03
MnO	0.05	0.16	0.21	0.12	0.10	0.16	0.20	0.24	0.16	0.12
MgO	11.8	27.41	22.19	15.9	5.33	9.91	7.67	8.29	6.37	3.26
CaO	0.55	4.19	3.96	0.43	9.11	14.02	11.90	11.60	11.04	6.17
Na2O	1.05	0.37	0.83	0.91	3.47	1.75	2.20	1.86	1.36	1.09
K2O	2.68	0.03	0.06	0.73	1.12	0.32	0.48	0.76	0.50	0.27
P2O5	0.2	0.01	0.05	0.07	0.42	0.04	0.16	0.43	0.04	0.38
LOI	3.09	5.01	2.53	2.93	1.59	0.71	0.64	1.60	0.91	0.35
Total	99.64	94.63	98.12	100.09	100.31	101.01	100.61	100.25	98.70	99.77
ppm										
Cr	nd	4945	2641	5.0	118.0	-	156	311.0	38.0	nd
Ni	20.0	1025.7	961.2	13.0	37.0	194.0	82	115.0	40.0	2.0
Sc	9.8	24.9	16.9	26.0	22.3	55.0	47.6	47.4	54.7	26.0
V	75.0	73.9	132.4	78.0	170.6	271.0	281.5	242.9	262.0	107.0
Pb	-	nd	2.3	-	11.7	-	9.2	8.8	5.6	-
Rb	75.0	0.9	0.1	21.7	41.5	4.4	4	20.9	14.1	4.9
Sr	34.0	28.4	8.1	14.0	524.1	90.0	507.2	197.5	363.6	442.0
Ba	412.0	532	7	91.0	67.0	43.0	113	103.0	162.0	95.0
Ga	28.0	5.9	7.1	27.0	29.1	15.0	18	22.5	27.2	13.0
Nb	7.7	0.8	2.3	14.4	7.2	1.2	3.4	6.9	14.3	5.4
Zr	190.0	13.8	13.3	264.0	116.6	24.4	57.9	162.1	241.8	161.0
Y	12.9	13.9	10.9	14.0	30.5	12.6	23.3	33.2	52.1	20.1
Th	-	nd	1.2	-	11.1	-	1.1	6.4	4.5	-
U	-	nd	nd	-	2.4	-	nd	2.5	3.1	-
ppm										
La	-	8	16	2.0	41.0	3.0	4.0	32.0	46.0	46.0
Ce	2.0	nd	11	20.0	78.0	-	10.0	69.0	87.0	92.0
Nd	-	7	1	5.0	33.0	4.0	4.0	33.0	46.0	36.0
Cu	-	17.8	24.9	-	9	-	123	67	529	-
Zn	-	95.6	185.7	-	44	-	105	129	96	-
Co	-	59.2	96.9	-	62.5	-	67	77.6	61.8	-

§ Analysis by X-Ray Fluorescence in the University of Adelaide on a Philips PW 1480 X-ray spectrometer.
Major element analysis after Norrish & Hutton (1969).
Trace element analysis: unignited powder mixed with binder and pressed into a pellet.
Elements not analysed are marked (-) those with concentrations below detection limits are marked (nd) and have detection limits of approximately 3.5, 2, 2, 5, 5.5 ppm for Pb, Th, U, Ce, Cr respectively.
Fe2O3* total iron represented as Fe2O3. Analyses from: 853- Sullivan, 1985; 857- Aouker, 1985; 950-, 962-, HR91- this study.
u.m. cum = ultramafic cumulate

Table 4.2. Selected brief petrographic descriptions of supracrustal rocks of the Entia Gneiss complex.

	Qtz	Pl	Cpx	Hbl	Oam	Ms	Bt	Grt	St	Ky	Ep	Chl	Rt	Opaques	Crd	Misc
890-8	X	Z		X	X	1°	X		P	P		Rbt	X	1		
853-93	X	Z		X	X		X		X	P	X	R	X			apatite
890-16	X	Z		X	X				P	X			X	X		
HR91-2	X	Z		X		2°	X		X	P		Rhbl	X			allanite
891-11		Z		X					P	P		Rhbl	X	X		
890-5A	X	Z		X		2°			X	X	X	Rhbl	X	X		zircon, apatite
853-97	X	Z		X			X			P		Rbt	X			
85-72	X	Z		X		2°			P		X	Rhbl	X	X		zircon
962-131m	X	Z		X					X					X		
891-8		Z		X		2°			P				X	X		corundum, zircon, apatite
950-077	X	Z		X	X			P	X				X	X		
HR91-8	X	Z		X		2°		P	X		X	Rhbl	X	X		
HR91-22	X	Z		X	X			X						X		apatite
NA-6	X	Z		X				P				Rhbl		X		
853-180	X	Z	X	X				P						X		apatite
HR91-20	X	Z		X				P						X		allanite, apatite
HR91-21	X	Z		X				P				R		X		apatite
853-16	X	Z		X				P					X	X		zircon, apatite
HR91-10	X	Z		X			X	P				Rbt		X		apatite
962-17	X	Z		X	X								X	1		
962-017r		Z		X							X	X	X	X		
853-180	X	Z	X	X							X			X		titanite
853-27	X	Z					X	P						X		zircon
85-75	X	Z				1°	X	P		P			X	X		zircon
962-11	X	Z					X			fibrolite						
962-017b	X	Z				2°	X			P			X			
853-77		Z				1°	X		P	P		Rbt	X	X		corundum
853-102		Z		X		2°	X	P				R		X		
85-77	X	Z				1°, 2°		X	P				X			zircon, apatite
950-47	X	Z		X	X	2°						R	X		X	zircon, allanite
950-047a	X	Z		X	X	2°				P			X		X	
950-84	X	Z			X					P		R	X		X	titanite, zircon
853-74	X	Z			X		X			P		Rbt			X	zircon
853-30	X	Z			X		X			X		Rbt	X	1	X	zircon
950-00A	X	Z								X			X		X	apatite
950-098	X	Z				2°	X			P			X	X	X	zircon
950-081					X							X	X	X		talc, apatite
950-089				X	X							X	X	X		talc, apatite

Abbreviations: X phase present, Z zoned, 1° primary phase, 2° secondary phase, P porphyroblastic, R retrograde, Rbt retrograde after biotite, Rhbl retrograde after hornblende, 1 one oxide only (i.e. not the usual exsolved ilmenite/titaniferous magnetite-ulvöspinel).

Table 4.3. Selected analyses of phases from the Harts Range.

	NA-06					HR91-5							HR91-8								HR91-20			HR91-21		
	Hbl	Hbl	Pl	Grt	Grt	Cpx,core	Cpx	Cpx	Hbl	Hbl	Grt	Grt	Hbl	Hbl	Hbl	Pl	St	Grt	Grt	Grt	Pl	Hbl	Grt	Grt	Pl	Hbl
	11:04	11:38	11:19	11:21	11:28	11:33	11:42	11:57	12:09	12:15	12:07	12:13	12:57	1:04	1:43	1:20	14:02	12:58	1:01	1:46	4:01	4:20	4:19	10:49	10:39	11:01
	*	*		*	*		@	@	*	*	*@	*@	*	*	*			*	*	*		*	*	*		*
SiO2	43.33	43.15	56.89	38.77	38.73	48.87	50.24	50.67	39.74	40.18	38.14	38.06	41.16	40.66	40.47	46.02	27.58	39.45	39.51	39.16	48.34	39.75	38.87	38.96	62.19	43.00
TiO2	0.76	0.82	0.00	0.09	0.00	0.05	0.00	0.06	0.12	0.05	0.00	0.01	0.65	0.16	0.42	0.07	0.78	0.02	0.00	0.01	0.05	0.20	0.08	0.00	0.00	0.18
Al2O3	15.53	15.55	28.15	22.29	22.63	0.15	0.70	0.87	12.84	12.16	22.72	21.90	18.39	18.86	18.97	35.14	51.84	23.18	23.21	23.01	33.56	19.97	22.33	23.02	21.40	15.95
FeO	17.22	17.16	0.14	25.83	26.08	42.06	20.35	20.67	26.98	26.44	30.80	32.77	15.40	15.83	15.10	0.00	12.86	27.80	26.31	25.94	0.18	18.09	28.01	29.66	0.00	15.50
MnO	0.42	0.27	0.22	2.23	4.23	0.39	0.20	0.53	0.41	0.34	1.88	2.23	0.16	0.29	0.34	0.00	0.13	1.81	1.84	2.09	0.02	0.36	2.12	1.70	0.22	0.18
MgO	9.14	8.96	0.00	2.72	2.55	8.29	7.25	7.35	3.89	4.38	1.17	1.12	9.86	8.70	9.87	0.00	3.40	6.80	6.73	5.95	0.00	7.51	3.53	5.98	0.00	10.96
CaO	11.42	11.52	9.72	9.69	9.36	1.05	20.96	20.40	10.69	10.76	7.49	6.95	10.17	10.72	10.65	18.08	0.02	4.02	5.42	5.59	16.32	10.66	6.99	3.64	3.21	9.64
Na2O	1.40	1.36	6.16	0.00	0.27	0.00	0.00	0.08	1.50	1.33	0.00	0.00	0.92	1.04	1.43	0.83	0.04	0.00	0.00	0.00	2.25	1.50	0.00	0.00	2.17	1.28
K2O	0.72	0.70	0.00	0.00	0.00	0.03	0.02	0.08	1.97	1.82	0.00	0.04	0.24	0.14	0.31	0.00	0.03	0.00	0.05	0.00	0.00	0.29	0.00	0.00	9.46	0.19
Cr2O3																	0.03									
ZnO																	0.71									
Total	99.95	99.49	101.27	101.61	103.83	100.88	99.71	100.70	98.13	97.45	102.20	103.08	96.95	96.40	97.56	100.14	97.4	103.09	103.07	101.75	100.72	98.33	101.93	102.96	98.65	96.88
Si	6.32	6.32	2.52	3.00	2.96	1.99	1.98	1.98	6.29	6.38	2.98	2.98	6.09	6.07	5.98	2.11	7.710	2.97	2.97	2.99	2.20	5.91	3.00	2.96	2.86	6.35
Ti	0.08	0.09	0.00	0.01	0.00	0.00	0.00	0.00	0.01	0.01	0.00	0.00	0.07	0.02	0.05	0.00	0.164	0.00	0.00	0.00	0.00	0.02	0.00	0.00	0.00	0.02
Al	2.67	2.68	1.47	2.03	2.04	0.01	0.03	0.04	2.40	2.28	2.09	2.02	3.21	3.32	3.30	1.90	17.082	2.06	2.06	2.07	1.80	3.50	2.03	2.07	1.16	2.78
Fe2+	2.10	2.10	0.01	1.67	1.67	1.43	0.67	0.67	3.57	3.51	2.01	2.14	1.91	1.98	1.86	0.00	3.007	1.75	1.66	1.65	0.01	2.25	1.81	1.89	0.00	1.92
Mn	0.05	0.03	0.01	0.15	0.27	0.01	0.01	0.02	0.05	0.05	0.12	0.15	0.02	0.04	0.04	0.00	0.030	0.12	0.12	0.14	0.00	0.04	0.14	0.11	0.01	0.02
Mg	1.99	1.96	0.00	0.31	0.29	0.50	0.43	0.43	0.92	1.04	0.14	0.13	2.17	1.94	2.17	0.00	1.416	0.76	0.75	0.68	0.00	1.66	0.41	0.68	0.00	2.41
Ca	1.78	1.81	0.46	0.80	0.77	0.05	0.89	0.85	1.81	1.83	0.63	0.58	1.61	1.72	1.68	0.89	0.006	0.32	0.44	0.46	0.80	1.70	0.58	0.30	0.16	1.53
Na	0.40	0.39	0.53	0.00	0.04	0.00	0.00	0.01	0.46	0.41	0.00	0.00	0.27	0.30	0.41	0.07	0.020	0.00	0.00	0.00	0.20	0.43	0.00	0.00	0.19	0.37
K	0.13	0.13	0.00	0.00	0.00	0.00	0.00	0.00	0.40	0.37	0.00	0.00	0.04	0.03	0.06	0.00	0.009	0.00	0.00	0.00	0.00	0.05	0.00	0.00	0.56	0.04
Cr																	0.006									
Zn																	0.146									
Total	15.53	15.51	5.00	7.98	8.04	4.00	4.00	4.00	15.92	15.86	7.97	8.01	15.39	15.41	15.56	4.97	29.596	7.99	8.00	7.98	5.00	15.57	7.98	8.00	4.93	15.44
XFe	0.51	0.52	-	0.84	0.85	0.74	0.61	0.61	0.80	0.77	0.94	0.94	0.47	0.51	0.46	-	0.68	0.70	0.69	0.71	-	0.57	0.82	0.74	-	0.44

Footnote: Analyses carried out at CEMMSA, using a JEOL 733 Electron Probe Microanalyser with the support of Mr Huw Rosser.
Labelled analyses used in geothermometry using the mineral pair: * hbl-gt , # gt-bt, @ cpx-gt (for results for geothermometry see Table 4).
Analyses used in average P calculations using the method of Powell and Holland (1988): t1, t2

Table 4.3 Continued.

	HR91-22							853-16				853-55											HR91-10		
	Hbl	Hbl	Hbl	Pl	Grt	Grt	Oam	Hbl	Pl	Grt	St	Hbl	Hbl	Hbl	Hbl	Pl	Grt	Grt	Grt	Grt	Bt	Bt	Bt	Pl	Grt
	9:16	9:21	9:34	10:07	9:26	9:29	10:13	12:40	13:01	12:38	12:50	1:36	1:42	2:04	2:47	12:54	1:29	1:39	1:52	2:43	3:19	3:30	8:42	8:18	8:43
	*	*	*		*	*		*		*		*	*	*	*		*	*	*	* #	#	#	#		#
SiO2	43.97	42.57	42.99	59.26	39.43	39.15	47.35	42.06	52.64	38.83	28.07	39.35	39.98	39.41	39.58	47.78	38.39	38.56	38.37	38.21	35.78	35.06	36.90	62.54	38.61
TiO2	0.49	0.69	0.50	0.03	0.00	0.00	0.24	0.49	0.19	0.12	0.72	0.23	0.31	0.21	0.57	0.14	0.00	0.10	0.03	0.05	2.31	2.73	1.45	0.00	0.10
Al2O3	14.66	15.23	15.43	25.62	22.70	23.00	11.47	16.70	30.73	22.82	53.46	17.74	17.05	16.73	16.89	31.84	22.22	22.15	22.33	22.14	18.56	18.84	18.52	23.49	22.72
FeO	15.00	14.13	14.85	0.04	28.34	28.48	19.40	17.17	0.09	29.92	13.05	19.23	18.61	20.72	20.08	0.21	23.82	27.09	27.59	27.55	19.99	18.80	14.19	0.00	28.43
MnO	0.37	0.34	0.45	0.05	1.67	1.98	0.35	0.32	0.17	1.11	0.10	0.77	0.42	0.52	0.57	0.00	7.11	4.36	4.30	3.55	0.13	0.18	0.34	0.17	5.55
MgO	12.28	11.24	10.89	0.00	7.31	7.17	16.71	9.41	0.00	6.00	2.86	6.74	7.47	6.50	6.90	0.86	2.41	3.28	3.71	3.86	9.79	9.96	13.95	0.00	5.31
CaO	9.47	10.05	9.81	6.92	2.92	2.86	0.78	11.08	12.69	4.82	0.04	11.32	11.04	11.09	11.32	15.45	7.31	6.32	6.19	6.54	0.22	0.33	0.32	4.60	1.42
Na2O	1.43	1.36	1.26	7.19	0.00	0.00	0.20	1.20	4.09	0.00	0.01	0.54	0.98	0.76	0.99	3.04	0.00	0.00	0.00	0.00	0.00	0.00	0.00	8.60	0.00
K2O	0.10	0.20	0.14	0.00	0.00	0.00	0.00	0.47	0.00	0.03	0.02	1.07	0.83	1.09	1.06	0.00	0.07	0.00	0.00	0.00	9.46	8.77	7.23	0.03	0.00
											0.03														
											0.61														
Total	97.76	95.81	96.33	99.10	102.39	102.63	96.51	98.89	100.59	103.65	99.0	95.92	95.85	95.93	96.91	99.32	101.33	101.85	102.52	101.91	96.23	94.67	92.90	99.42	102.14
Si	6.43	6.35	6.38	2.66	2.99	2.97	6.90	6.19	2.37	2.94	7.706	6.01	6.09	6.06	6.02	2.21	3.00	3.00	2.97	2.97	2.70	2.67	2.77	2.78	2.98
Ti	0.05	0.08	0.06	0.00	0.00	0.00	0.03	0.05	0.01	0.01	0.149	0.03	0.04	0.02	0.06	0.00	0.00	0.01	0.00	0.00	0.13	0.16	0.08	0.00	0.01
Al	2.53	2.68	2.70	1.35	2.03	2.06	1.97	2.90	1.63	2.04	17.301	3.20	3.06	3.03	3.03	1.74	2.05	2.03	2.04	2.03	1.65	1.69	1.64	1.23	2.07
Fe2+	1.83	1.76	1.84	0.00	1.80	1.81	2.36	2.11	0.00	1.90	2.996	2.46	2.37	2.67	2.55	0.01	1.56	1.76	1.78	1.79	1.26	1.20	0.89	0.00	1.84
Mn	0.05	0.04	0.06	0.00	0.11	0.13	0.04	0.04	0.01	0.07	0.023	0.10	0.05	0.07	0.07	0.00	0.47	0.29	0.28	0.23	0.01	0.01	0.02	0.01	0.36
Mg	2.68	2.50	2.41	0.00	0.83	0.81	3.63	2.06	0.00	0.68	1.170	1.53	1.70	1.49	1.56	0.06	0.28	0.38	0.43	0.45	1.10	1.13	1.56	0.00	0.61
Ca	1.48	1.61	1.56	0.33	0.24	0.23	0.12	1.75	0.61	0.39	0.012	1.85	1.80	1.83	1.85	0.77	0.61	0.53	0.51	0.54	0.02	0.03	0.03	0.22	0.12
Na	0.41	0.39	0.36	0.63	0.00	0.00	0.06	0.34	0.36	0.00	0.006	0.16	0.29	0.23	0.29	0.27	0.00	0.00	0.00	0.00	0.00	0.00	0.00	0.74	0.00
K	0.02	0.04	0.03	0.00	0.00	0.00	0.00	0.09	0.00	0.00	0.008	0.21	0.16	0.21	0.21	0.00	0.01	0.00	0.00	0.00	0.91	0.85	0.69	0.00	0.00
											0.006														
											0.123														
Total	15.47	15.45	15.41	4.98	7.99	8.00	15.11	15.53	4.99	8.03	29.499	15.55	15.57	15.61	15.65	5.05	7.98	7.98	8.01	8.01	7.79	7.75	7.68	4.98	7.98
XFe	0.41	0.41	0.43	-	0.68	0.69	0.39	0.51	-	0.74	0.72	0.62	0.58	0.64	0.62	-	0.85	0.82	0.81	0.80	0.53	0.51	0.36	-	0.75

Table 4.3 Continued.

	853-27				85-72			950-077					950-047					950-081				853-30	
	Grt	Grt	Bt	Bt	Hbl	St	Pl	St	Hbl	Oam	Grt	Pl	Tcl	Crd	Pl	Hbl	Chl	Chl	Hbl	Tlc	Oam	Oam	Crd
	12:10	12:26	12:12	12:29	3:49	14:50	4:15	pladj gt	6:45	6:58	7:00	6:41	SW	SW	SW	SW	SW	SW	SW	SW	SW	11:35	11:38
	#	#	#	#				t2	t1,2	t1	t1,2	t1,2											
SiO2	38.71	38.73	36.98	36.03	40.18	26.62	47.02	29.20	42.02	41.72	38.47	57.88	57.90	50.65	47.31	47.04	25.99	31.37	55.80	57.68	57.82	44.68	49.56
TiO2	0.00	0.00	1.20	1.04	0.80	0.46	0.00	0.47	0.57	0.03	0.01	0.09	0.00	0.02	0.03	0.47	0.00	0.18	0.20	0.00	0.00	0.20	0.00
Al2O3	22.43	22.31	17.04	17.07	19.70	53.10	34.75	54.46	16.00	17.94	22.58	25.86	3.86	33.74	39.00	14.97	21.72	16.20	0.68	0.24	0.52	19.23	34.02
FeO	24.94	25.80	11.43	10.48	13.91	11.75	0.13	12.47	14.68	19.62	29.31	0.28	3.65	2.15	0.02	6.72	7.15	3.63	2.35	3.95	8.08	13.41	2.61
MnO	4.38	2.64	0.11	0.10	0.48	0.28	0.12	0.12	0.16	0.34	1.74	0.06	0.21	0.00	0.00	0.23	0.21	0.00	0.15	0.07	0.75	0.43	0.16
MgO	9.63	9.45	18.89	17.40	10.37	3.16	0.00	3.00	10.69	14.20	6.10	0.00	28.55	11.65	0.00	16.16	28.58	30.84	22.63	26.54	28.90	18.75	11.36
CaO	2.23	2.62	0.41	1.12	10.59	0.02	16.99	0.02	9.81	0.70	3.16	7.48	0.22	0.17	0.30	11.21	0.00	0.20	12.38	0.32	0.50	0.74	0.29
Na2O	0.93	0.48	1.94	1.61	2.29	0.01	1.52	0.01	1.35	1.09	0.00	6.68	0.00	0.00	7.19	0.75	1.73	0.00	0.00	0.00	0.00	1.13	0.00
K2O	0.00	0.02	7.63	7.00	0.29	0.01	0.00	0.02	0.09	0.00	0.00	0.00	0.00	0.22	0.35	0.06	0.00	0.00	0.00	0.03	0.00	0.00	0.00
						0.04		0.02															
						0.19		0.39															
Total	103.25	102.05	95.63	91.84	98.60	95.6	100.53	100.2	95.37	95.64	101.38	98.33	94.4	98.6	94.2	97.6	85.37	82.42	94.19	88.83	96.57	98.6	98.0
Si	2.92	2.94	2.70	2.72	5.86	7.520	2.14	7.867	6.30	6.20	2.97	2.62	3.78	5.05	2.21	6.60	2.58	2.67	7.91	3.99	7.94	6.23	4.93
Ti	0.00	0.00	0.07	0.06	0.09	0.098	0.00	0.095	0.06	0.00	0.00	0.00	0.00	0.00	0.00	0.05	0.00	0.01	0.02	0.00	0.00	0.02	0.00
Al	1.99	2.00	1.46	1.52	3.39	17.686	1.87	17.295	2.83	3.14	2.06	1.38	0.30	3.97	2.15	2.48	2.55	1.63	0.11	0.02	0.08	3.16	4.04
Fe2+	1.57	1.64	0.70	0.66	1.70	2.777	0.00	2.808	1.84	2.44	1.89	0.01	0.20	0.18	0.00	0.79	0.59	0.26	0.28	0.23	0.93	1.56	0.22
Mn	0.28	0.17	0.01	0.01	0.06	0.068	0.00	0.027	0.02	0.04	0.11	0.00	0.01	0.00	0.00	0.03	0.02	0.00	0.02	0.00	0.09	0.05	0.01
Mg	1.08	1.07	2.05	1.96	2.25	1.330	0.00	1.204	2.39	3.14	0.70	0.00	2.78	1.73	0.00	3.38	4.24	3.92	4.78	2.74	5.91	3.89	1.70
Ca	0.18	0.21	0.03	0.09	1.66	0.006	0.83	0.005	1.58	0.11	0.26	0.36	0.02	0.02	0.02	1.69	0.00	0.02	1.88	0.02	0.07	0.11	0.03
Na	0.14	0.07	0.27	0.24	0.65	0.004	0.13	0.003	0.39	0.31	0.00	0.59	0.00	0.00	0.65	0.20	0.33	0.00	0.00	0.00	0.00	0.31	0.00
K	0.00	0.00	0.71	0.67	0.05	0.003	0.00	0.005	0.02	0.00	0.00	0.00	0.00	0.03	0.02	0.01	0.00	0.00	0.00	0.00	0.00	0.00	0.00
						0.008		0.004															
						0.040		0.078															
Total	8.16	8.10	8.00	7.92	15.71	29.539	4.99	29.31	15.43	15.39	8.00	4.97	7.07	10.98	5.05	15.220	10.310	8.503	15.009	7.003	15.021	15.327	10.994
XFe	0.59	0.61	0.25	0.25	0.43	0.68	-	0.70	0.44	0.44	0.73	-	0.07	0.09	-	0.19	0.12	0.06	0.06	0.08	0.14	0.286	0.114

Figure 4.2a. Sketch of euhedral garnet and kyanite poikiloblasts in a muscovite biotite schist (85/75) . Scale bar = 2 mm.

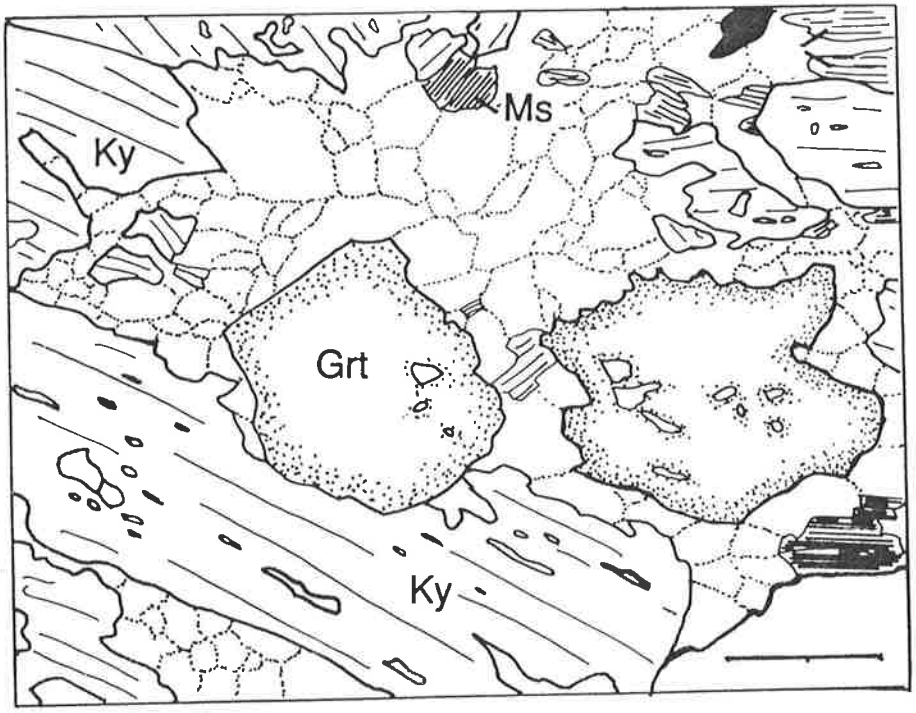
Ms
Ky
Grt
Ky

range of X_{Fe} (= Fe/(Fe+Mg) 0.13-0.45) and has tschermakite substitution ($Mg_{-1}Si_{-1}Al_1Al_1$, from phlogopite) in the range 0.25-0.33. Garnet (X_{Fe} 0.63-0.77) is also more Fe-rich in hornblende-bearing biotite schists. Plagioclase is calcium rich andesine (An_{31-32} =Ca/(Ca+Na) 0.31-0.32).

4.3.2 Magnesium-rich rocks

Two types of magnesium-rich rocks occur in the Entia Dome, both typified by low CaO and alkali contents (Table 4.1), but distinguishable by their relative aluminium bulk-rock contents. Low alumina magnesium-rich rocks occur as isolated pods and have bulk rock chemistry (including trace element chemistry; e.g. samples 950-081, 950-089, Table 4.1) broadly consistent with mafic or ultramafic intrusive, cumulate or xenolithic origins. Their low CaO and Al_2O_3 contents and high FeO, MgO, Cr and Ni (cf. Sivell et al., 1985) imply an orthopyroxene cumulate protolith. The hydrated mineral associations occurring in these rocks involve magnesio-anthophyllite–tremolite (or magnesio-hornblende)–talc–chlorite with minor biotite, plagioclase, magnetite, rutile and zircon (amphibole nomenclature after Leake, 1978). Anthophyllite (X_{Fe} 0.12-0.27, Table 4.3), tremolite (X_{Fe} 0.06-0.1) or magnesio-hornblende (X_{Fe} 0.24-0.25) form euhedral diamond shaped grains or laths which are surrounded by acicular to fine talc (X_{Fe} 0.07-0.1, Al^{vi} 0.01-0.04) and chlorite (X_{Fe} 0.06-0.16, Al^{vi} 0-0.22) which tend to form radiating sheaves. Rare intergrown biotite occurs in minor proportions.

The more aluminous Mg-rich rocks are dominated by cordierite and have bulk chemistry which is comparable to that of the "whiteschists" described by Schreyer (1973) (Table 4.1, sample 853-39). As noted by previous authors (e.g. McKie, 1959; Robinson & Jaffe, 1969a; Chinner & Fox, 1974) these rocks are compositionally unlike any common sedimentary or igneous rock-type (having high Al-content but comparatively very low Ca, K and Fe). Chemically similar sedimentary rocks may result from the deposition of sediments in an evaporitic environment (Schreyer, 1977). Alternative sources for "whiteschist" type rocks include hydrothermal alteration (Vallance, 1967), metasomatism (Tilley, 1937; Arnold & Sandiford, 1990), erosion (with a chemical weathering component) of mafic igneous rocks (Robinson & Jaffe, 1969a) or partial melting of a more typical rock-type (Robinson & Jaffe, 1969a). The sporadic occurrence of these bodies suggests that their protoliths were not originally laterally extensive and, with the lack of associated shallow water meta-sediments, is not consistent with deposition in an evaporitic environment. They are not generally associated with igneous bodies, nor do they contain evidence of high temperature metamorphism or partial melts and thus a restitic origin can be discounted. The cordierite-bearing rocks contain variable amounts of rounded zircon grains and coarse apatite (0.5-2%) and they typically contain abundant rutile. The high apatite and zircon contents and relatively low Cr- and Ni-contents (Table 4.1) of these rocks is consistent with a felsic rather than mafic origin. Sapphirine granulites from the Strangways Range to the West of this area have a similar chemistry (Windrim et al., 1984). The field relations and widely variable REE concentrations

of those rocks have been correlated with an abundance of minor phases such as zircon, sphene and apatite which were attributed to precipitation during hydrothermal alteration (Windrim et al., 1984). In the Entia Dome this association of cordierite-bearing Mg-Al-rich rocks is also consistent with an origin involving hydrothermally altered felsic rocks, which may have experienced chloritisation (addition of magnesium, removal of silica, calcium and alkalis) and, by correlation with the Strangways examples, possible mobilisation of trace elements before metamorphism.

The classification of the bulk chemistry of these rocks as "whiteschists" does not extend to their mineralogy which, by definition, should involve the assemblage kyanite–talc (Schreyer, 1973). Although kyanite is present as elongate, skeletal porphyroblasts (Fig. 4.2b) sub-parallel to the orthoamphibole, biotite or hornblende foliation, it is never observed with similarly oriented talc. Kyanite and amphibole (hornblende and anthophyllite) are never observed in contact and kyanite is corroded with optically-continuous relic grains surrounded by coarse, relatively fresh cordierite (Fig. 4.2b,c). Although kyanite, hornblende and orthoamphibole define a weak foliation, cordierite is coarse grained, randomly oriented and undeformed. Fine intergrowths of talc and chlorite are randomly oriented among corroded amphiboles and cross cut the coarse cordierite grains (Fig. 4.2c). Quartz, plagioclase, rutile and apatite are subordinate and zircons are relatively coarse and abundant (up to 0.3 mm). All of the ferro-magnesian minerals occurring in these cordierite rocks are very Mg-rich ($X_{Fe,Hbl}$ 0.16-0.27, $X_{Fe,Oam}$ 0.07-0.1, $X_{Fe,Crd}$ 0.07-0.08, $X_{Fe,Tlc}$ 0.07-0.17, Table 4.3, see Fig. 4.3) and the amphiboles show limited edenite substitution in contrast to associated rock types. The proportion of tschermakite molecule in both clino- and ortho-amphiboles is high in comparison to those in other assemblages. The hornblende–plagioclase-bearing Mg-rich rocks are of an appropriate composition to be included in the following discussion of amphibolite assemblages and they are described in more detail in Appendix A8.

4.3.3 Amphibolites

Amphibolites in the Entia Dome span a wider range in bulk composition and mineralogy (the mineral textures and their compatibility relations are described in more detail in Appendix A8). The most common amphibolite assemblage, hornblende–plagioclase–epidote (± clinopyroxene ± garnet) typifies basaltic compositions (e.g. Cox et al., 1980) and contains significant Na_2O (≥ 1.3 wt%, e.g. samples 962-017r, 853-180, 962-155). More unusual assemblages occur in rocks which are relatively depleted or enriched in various other elements when compared with typical basalts (Table 4.1). Staurolite- and kyanite-bearing amphibolites (e.g. samples HR91-4, HR91-8, 853-16) in particular, have high Si- and Al-contents in comparison to mafic igneous rocks and high Ca- and Mg-contents relative to felsic rocks. These compositions are also inconsistent with typical intermediate igneous rocks (e.g. Cox et al., 1980) suggesting that they have experienced some sort of chemical evolution. The relatively high rare earth elements (REE) contents of these unusual high-Si-Al-Ca-Mg

Figure 4.2b. Sketch of corroded anthophyllite and kyanite in cordierite with talc and chlorite (853-74). Scale bar = 2 mm.

Figure 4.2c Sketch of corroded hornblende and kyanite in cordierite (950-100). Width of view 2mm.

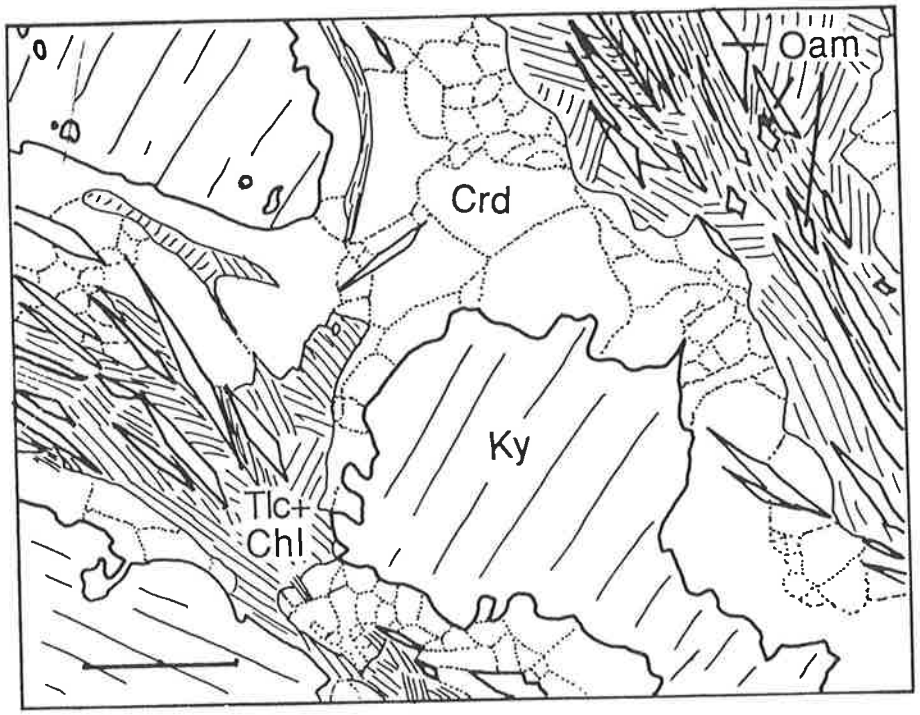
Oam
Crd
Ky
Tlc+
Chl

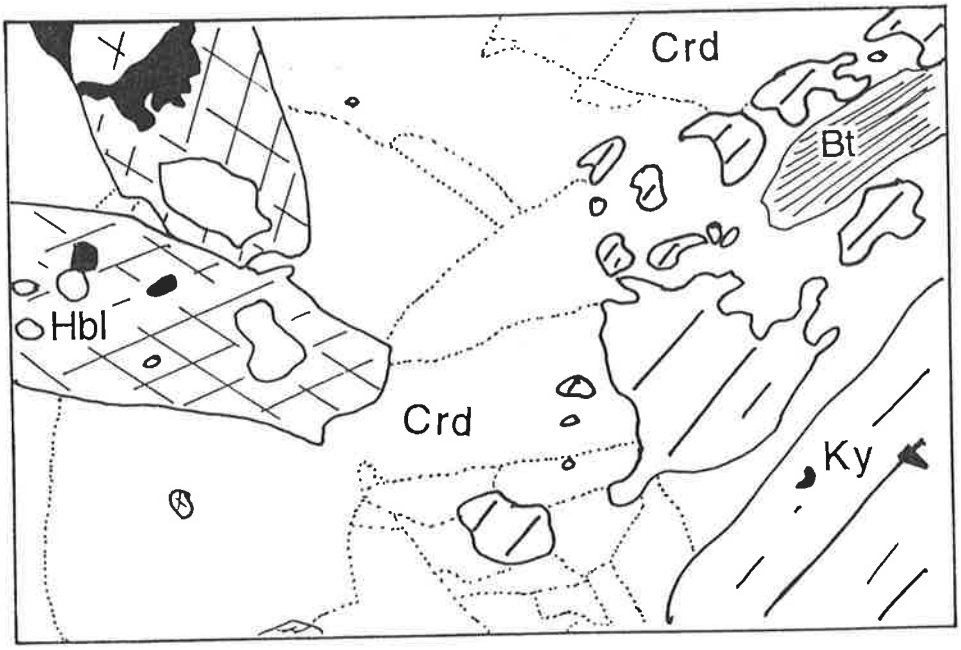
Crd
Bt
Hbl
Crd
Ky

Figure 4.3. The compatibility relations of cordierite-amphibolites, projected from hornblende, plagioclase, quartz and aqueous vapour onto the AFM ($AlO_{3/2}$- FeO-MgO) plane.

Figure 4.4. The compatibility relations of kyanite–staurolite-amphibolites, projected from hornblende, plagioclase, quartz and aqueous vapour onto the AFM ($AlO_{3/2}$- FeO-MgO) plane. The crossing of the tie-lines results from the different stages of reaction preserved in the different samples.

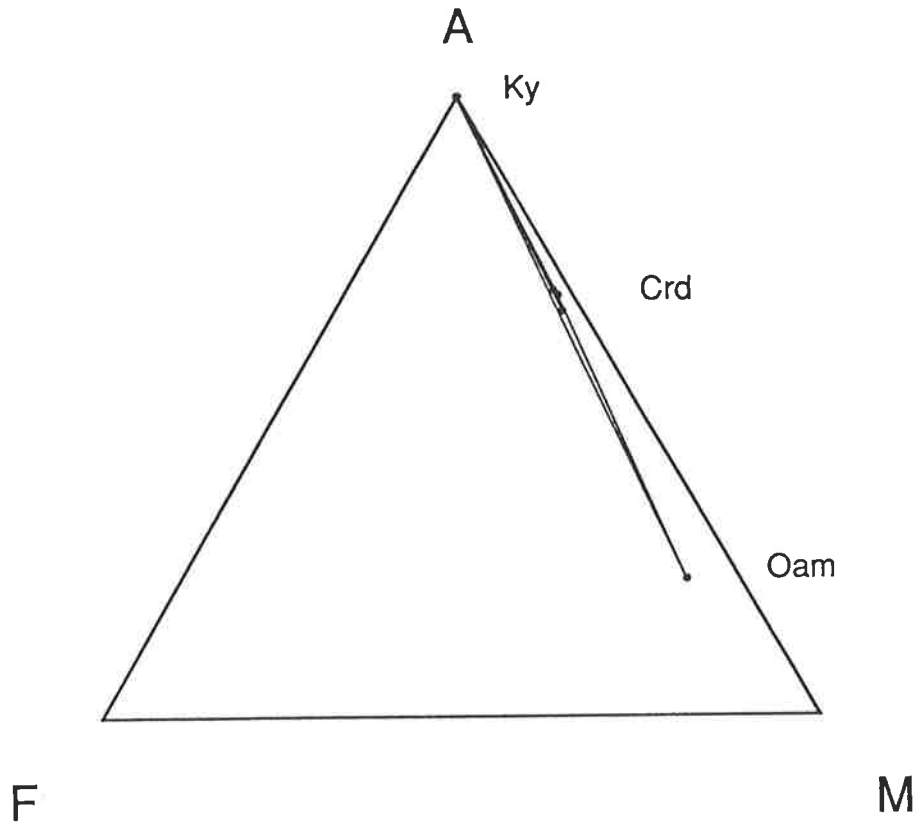
A
Ky
Crd
Oam
F
M

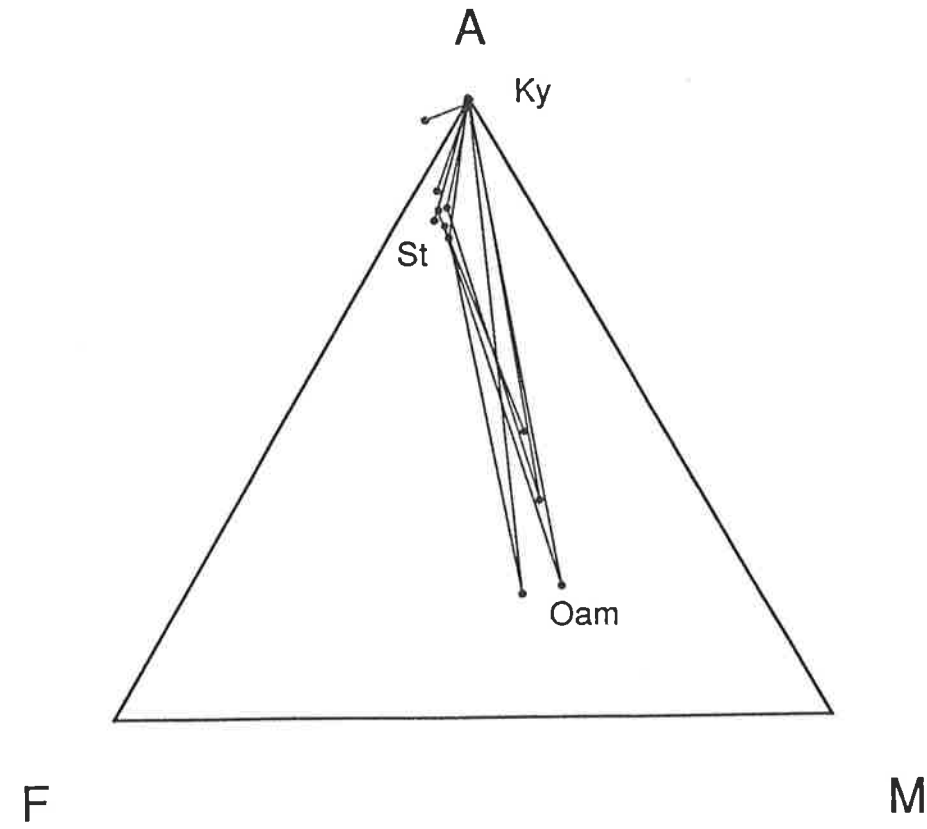
A
Ky
St
Oam
F
M

amphibolites in comparison to the 'basaltic' types suggests that they do not have a cumulate origin. This is because the incompatible REE would be expected to partition into the melt fraction of a solid-liquid system, depleting the cumulates in REE in comparison to the undifferentiated "basalts". It is more likely that the rocks have experienced some chemical alteration. Because the reaction textures observed in these samples may be simply interpreted in terms of closed system divariant equilibria in CFMASH, they probably do not reflect syn-amphibolite facies metasomatism and it is considered likely that the chemical modification was diagenetic in nature.

The bulk chemistry of these unusual amphibolites exerts considerable control on their mineralogy. Lower Na_2O and CaO contents allow unusual assemblages involving hornblende–staurolite–kyanite–orthoamphibole ± quartz or corundum. The more Fe-rich samples contain hornblende–garnet assemblages and none of the samples collected contain the "common" assemblage (calcium-amphibole, chlorite, epidote, plagioclase, quartz ± garnet, Fe^{3+}-oxides, carbonates, K-bearing and Ti-bearing phases, Laird, 1980) which is often observed in basaltic rocks.

The less calcic and sodic staurolite- and kyanite-bearing amphibolites often preserve evidence of incomplete reactions in the form of coronas and overgrowths and thus are potentially useful in determining the metamorphic history of the rocks. Kyanite typically forms embayed porphyroblasts which are surrounded by a moat of staurolite inside a rim of anorthitic plagioclase (see Appendix A8, section A8.5.3). These coronas separate the weakly aligned kyanite from the generally well foliated hornblende–plagioclase ± orthoamphibole mosaic which makes up the bulk of the rock (Fig. 4.2d). Commonly kyanite is not present and large subhedral grains of staurolite are rimmed by anorthite-bytownite plagioclase in a hornblende–plagioclase ± orthoamphibole mosaic. Unlike kyanite, staurolite is observed in contact with hornblende. Figure 4.4 illustrates the compositions of the assemblages in kyanite–staurolite-bearing amphibolites. In rocks which do not contain quartz, corundum rarely occurs in optically-continuous poikiloblastic aggregates rimmed with anorthite and in contact with staurolite in an amphibolite matrix (Fig. 4.2e).

Coarse, euhedral orthoamphibole is observed in contact with hornblende, often cross cutting both the hornblende-defined foliation and also the hornblende grains themselves (Fig. 4.2f). Only in very Mg-rich rocks is orthoamphibole included in another phase (Fig. 4.2c).

In a number of Fe-rich amphibolites garnet occurs as euhedral porphyroblasts typically 0.25-20 mm in diameter (see Appendix A8, sections A8.5.1 and A8.5.2) however large (up to metre scale) porphyroblasts are also observed. The porphyroblasts often contain large inclusions of plagioclase, quartz, hornblende and titanium phases which define straight to slightly curved inclusion trails (Fig. 4.2h). Rutile occurs in the cores of euhedral garnet porphyroblasts but decreases in abundance as ilmenite increases toward the rims. Anhedral garnet grains are generally elongate parallel to the foliation direction (Fig. 4.2i). Staurolite and garnet co-exist in several samples (see Appendix A8, section A8.5.2). Amoeboid inclusions of staurolite occur in the core of very coarse garnet (Fig. 4.2g) which has weak inclusion trails

Figure 4.2d. Sketch of corroded kyanite porphyroblast separated by a staurolite-calcic plagioclase corona from the hornblende-plagioclase-quartz matrix (890-11). Scale bar = 2 mm.

Figure 4.2e Sketch of corroded corundum with staurolite and plagioclase in a hornblende-plagioclase-quartz matrix (890-005a). Width of view 2mm.

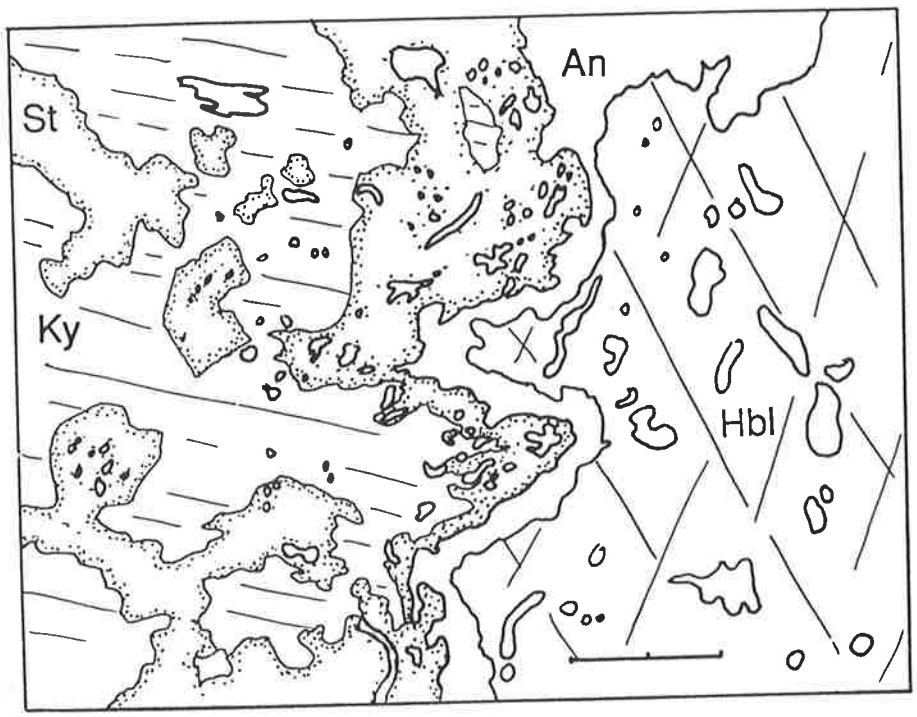
An
St
Ky
Hbl

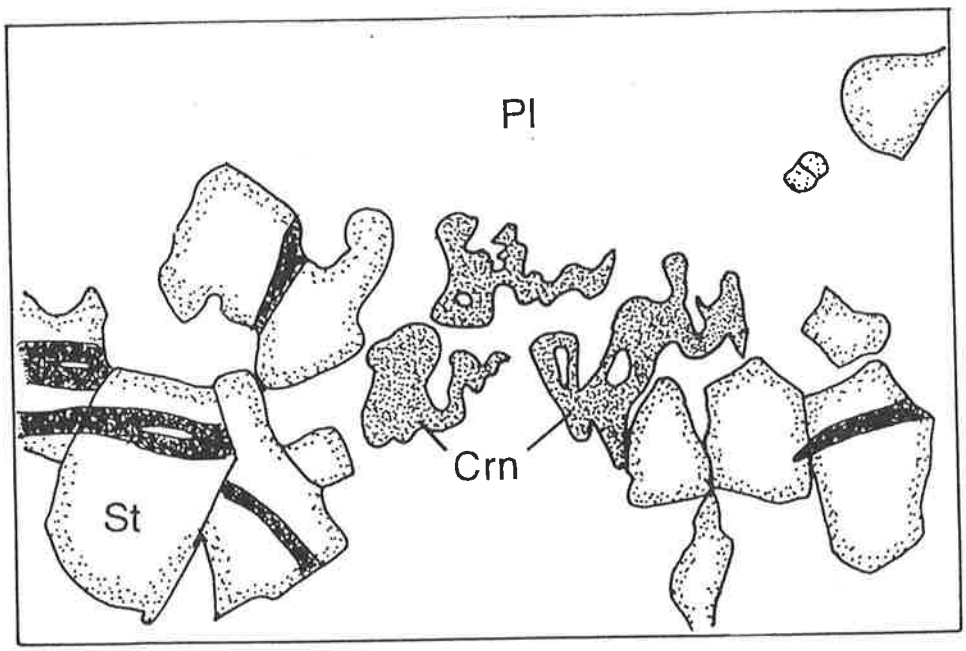
Pl
Crn
St

Figure 4.2f. Sketch of gedrite cross cutting hornblende foliation and hornblende grains (890-014). Width of view 2mm.

Figure 4.2g Sketch of garnet porphyroblast containing straight inclusion trails (950-105). Width of view 2mm.

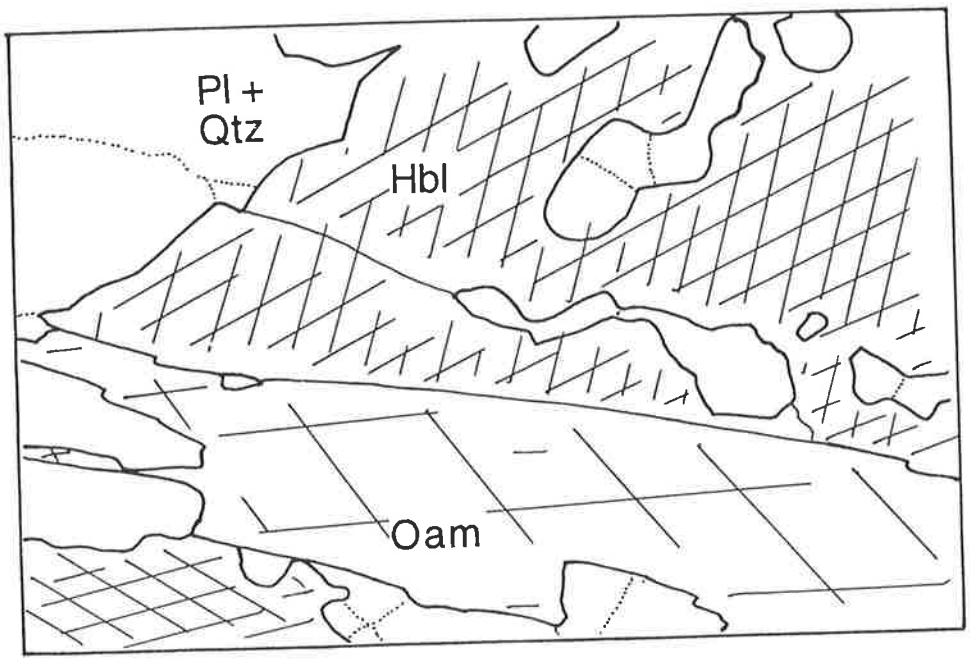
Pl +
Qtz
Hbl
Oam

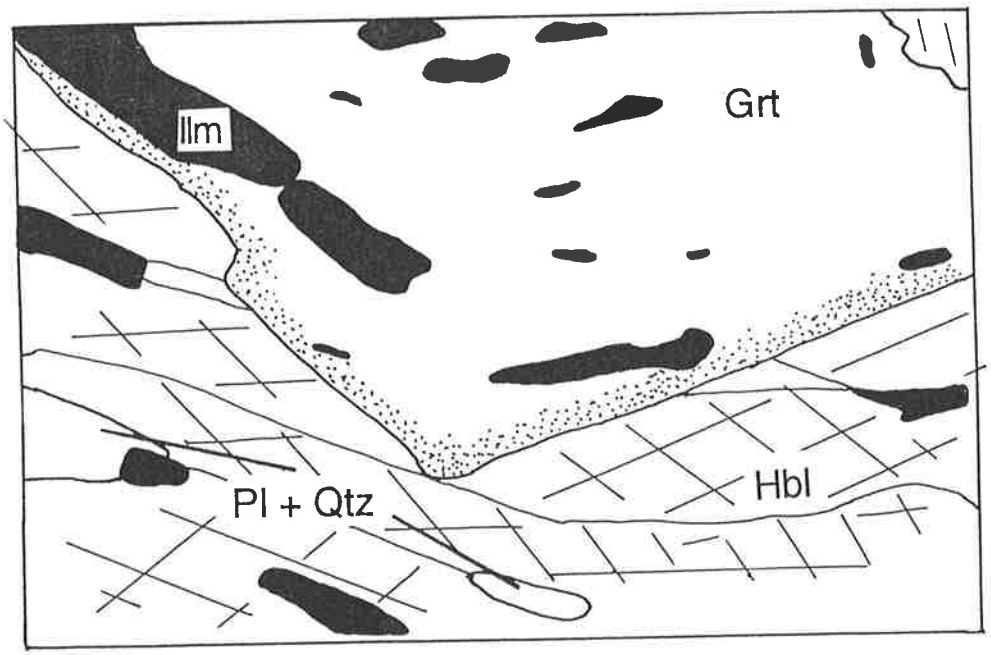
Ilm
Grt
Hbl
Pl + Qtz

Figure 4.2h. Sketch of anhedral garnet porphyroblast with coarse inclusions (962-214). Width of view 2mm.

Figure 4.2i Sketch of garnet porphyroblast containing staurolite inclusions (950-077). Scale bar = 2 mm.

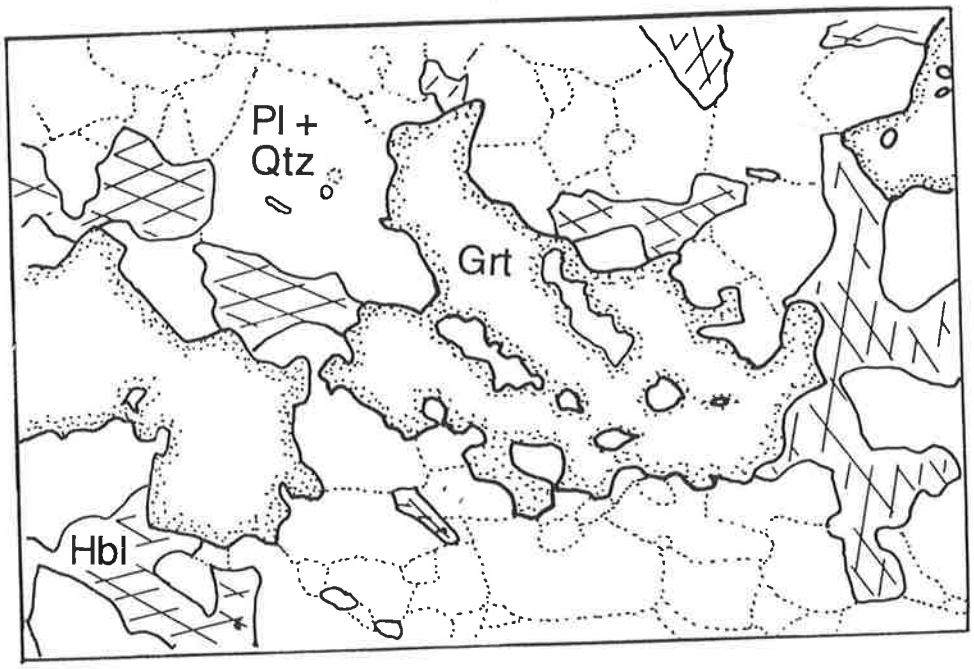
Pl +
Qtz
Grt
Hbl

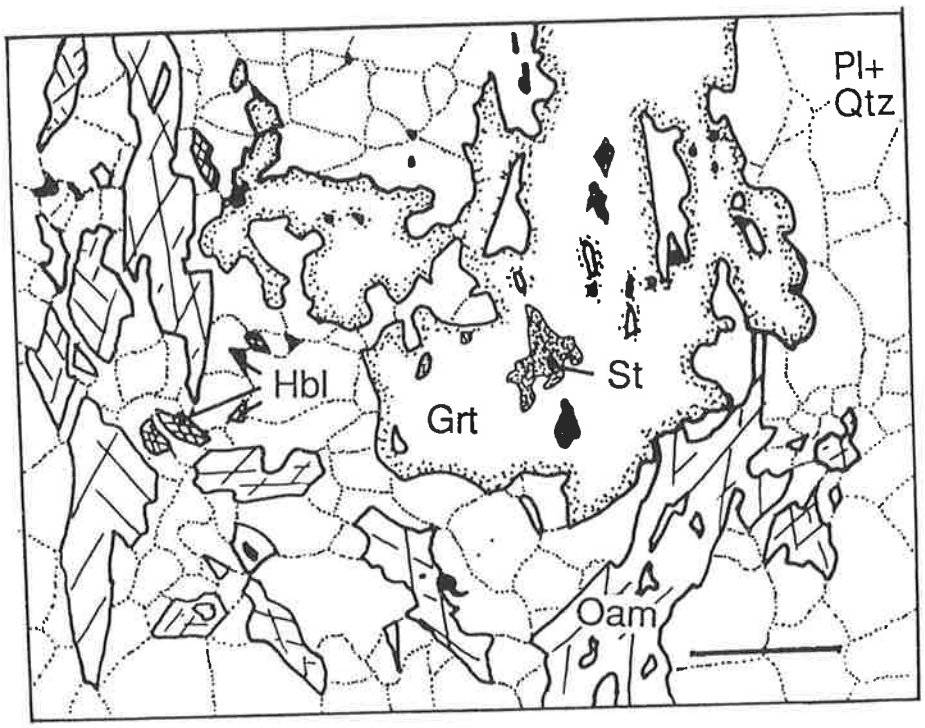
Pl+
Qtz
Hbl
Grt
St
Oam

parallel to its external garnet–orthoamphibole–hornblende–plagioclase foliation in sample 950-077. Staurolite also forms inclusions in garnet an orthoamphibole-free sample (853-16), is partly included in garnet in sample 950-105 (Fig. 4.2j) and occurs in the matrix in contact with plagioclase and garnet but not hornblende of sample HR91-8 (Fig. 4.2k). The compositional variation of the staurolite–garnet amphibolites is illustrated in Fig. 4.5. Chlorite and biotite pseudomorph and rim hornblende, chlorite grows over biotite and hornblende may be replaced by the low temperature assemblage titanite–epidote–prehnite in garnet amphibolites.

Microprobe analyses (WDS) of staurolites suggest that Zn does not play a role in the stabilisation of staurolite in the amphibolites (staurolites contain 0.12-0.77 wt% ZnO ≡ 0.02-0.15 ZnO per formula unit with 44O+4(OH), Table 4.3 and A8.5) and the mineral chemistry of the staurolites corresponds fairly closely with the "normal" ranges reported by Ribbe (1982). These relatively low Zn-contents imply that the presence of staurolite in this rare assemblage must be related to the phase relations of mafic rocks and varying physical conditions rather than unusual chemistry. Staurolite in these amphibolites is unzoned and has well defined compositions. It is more Fe-rich with garnet (X_{Fe} 0.69-0.83) and more magnesian in rocks which contain hornblende and/or gedrite (X_{Fe} 0.52-0.71,).

Garnet in these amphibolites is generally almandine-rich, (X_{alm} 0.51-0.7, X_{prp} 0.1-0.36, X_{sps} 0.04-0.16, X_{grs} O.04-0.22 Table 4.3 and A8.4 and A8.5) individual grains are unzoned and their compositions are consistent from grain to grain. The analyses show no evidence of substitution of Fe^{3+}, Ti or Cr for Si or Al. Coexisting garnet and staurolite show reversed Fe-Mg partitioning (i.e. $X_{Fe,St}$ (0.69-0.83) > $X_{Fe,Grt}$ (0.66-0.74)) in comparison to typical rocks of pelitic affinity (e.g. Sharma & MacRae, 1981; Spear, 1982; Arnold & Sandiford, 1990). This may be due to the changing distribution co-efficient of iron and magnesium in garnet and staurolite with increasing pressure (A. Purvis, pers. comm., 1991; see Chapter 6) or possibly the continued reaction of one phase in isolation from the other (e.g. Grew & Sandiford, 1985).

Hornblende is pargasitic to tschermakitic (Leake, 1978) and contains up to 0.9 atoms of Na per 23 oxygens. It generally has an X_{Fe} less than that of co-existing garnet and staurolite, similar to orthoamphibole and greater than coexisting biotite and chlorite, in the range 0.21-0.77 (Table 4.3 and A8.1-7). The orthoamphibole in the Harts Range amphibolites is generally gedrite (Except for the cordierite-rich samples which contain anthophyllite), which exhibits substantial edenite and tschermakite substitution (0-0.53 Na per formula unit, Al^{iv} 0.62-1.56 Table 4.3 and A8.3,4,5,6,7). Gedrite shows no evidence of exsolution lamellae (even at the micron scale) and there is only one orthoamphibole present in any given sample.

The composition of plagioclase in amphibolites from the Entia Dome shows systematic variation with the nature of the assemblage in which it occurs. Typically matrix plagioclase is weakly zoned, with cores several percent richer in albite than the rims (i.e. reverse zoning). The most calcic plagioclase (anorthite-bytownite) co-exists with staurolite, while plagioclase occurring with hornblende, orthoamphibole or epidote tends to be andesine. The most sodic plagioclases (oligoclase) occur with garnet. Epidote is generally a solid solution between

Figure 4.2j. Sketch of staurolite partly included in a garnet porphyroblast (950-105). Width of view 2mm.

Figure 4.2k Sketch of staurolite in the matrix of a garnet-amphibolite (950-105). Width of view 2mm.

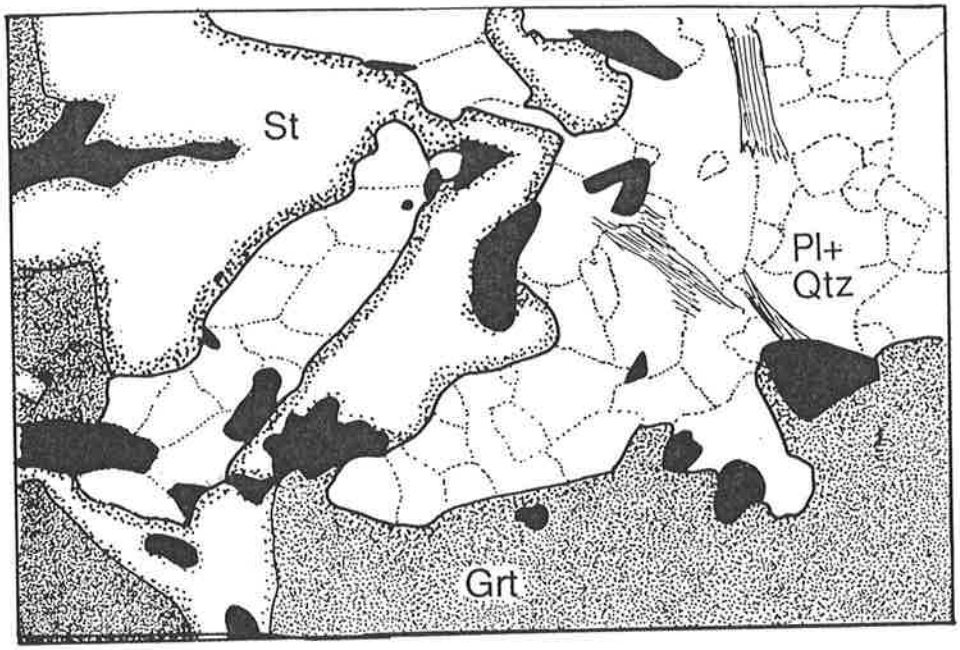
St
Pl+
Qtz
Grt

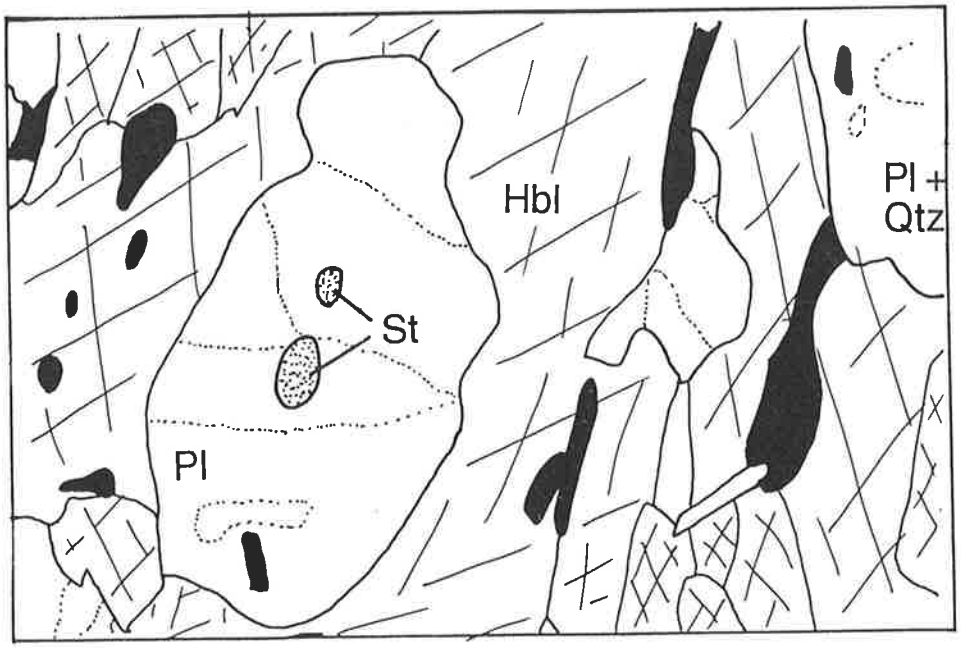
Hbl
Pl +
Qtz
St
Pl

Figure 4.5. The compatibility relations of staurolite-garnet-amphibolites, projected from hornblende, plagioclase, quartz and aqueous vapour onto the AFM ($AlO_{3/2}$- FeO-MgO) plane. The crossing of the tie-lines and unusual plotting location of garnet result from the variable sodium contents of plagioclase and hornblende and from the different stages of reaction preserved in the different samples.

Figure. 4.6. Compatibility diagram showing the low variance assemblages in the Harts Range amphibolites, projected from hornblende, plagioclase, quartz and aqueous vapour onto the AFM (Al_2O_3-FeO-MgO) plane.

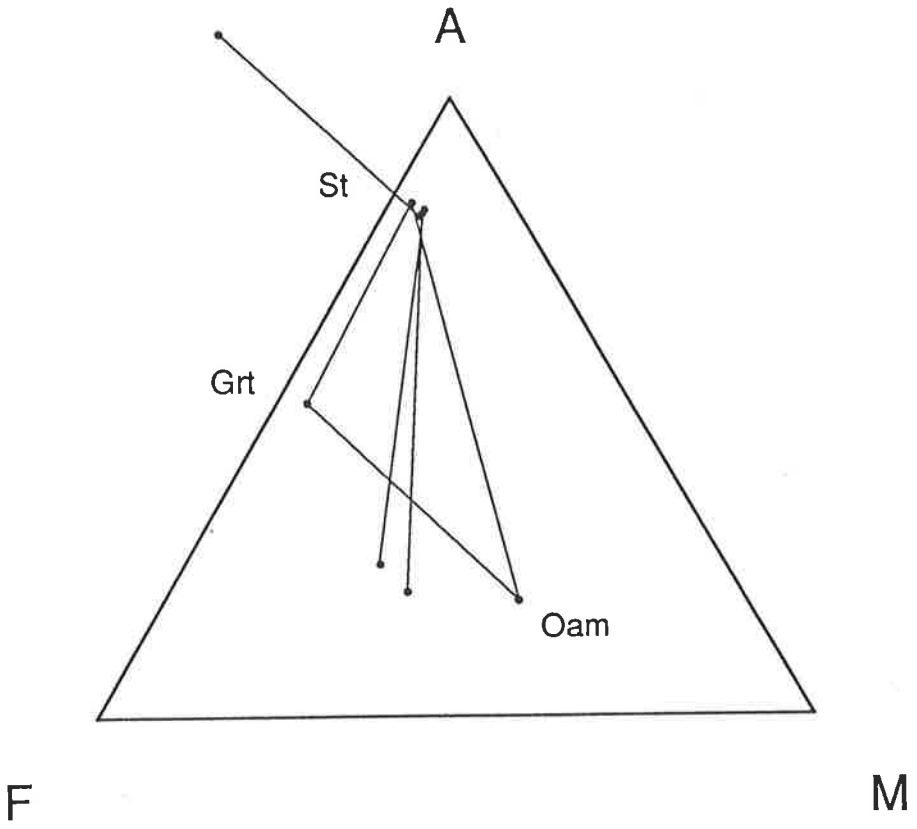
A
St
Grt
Oam
F
M

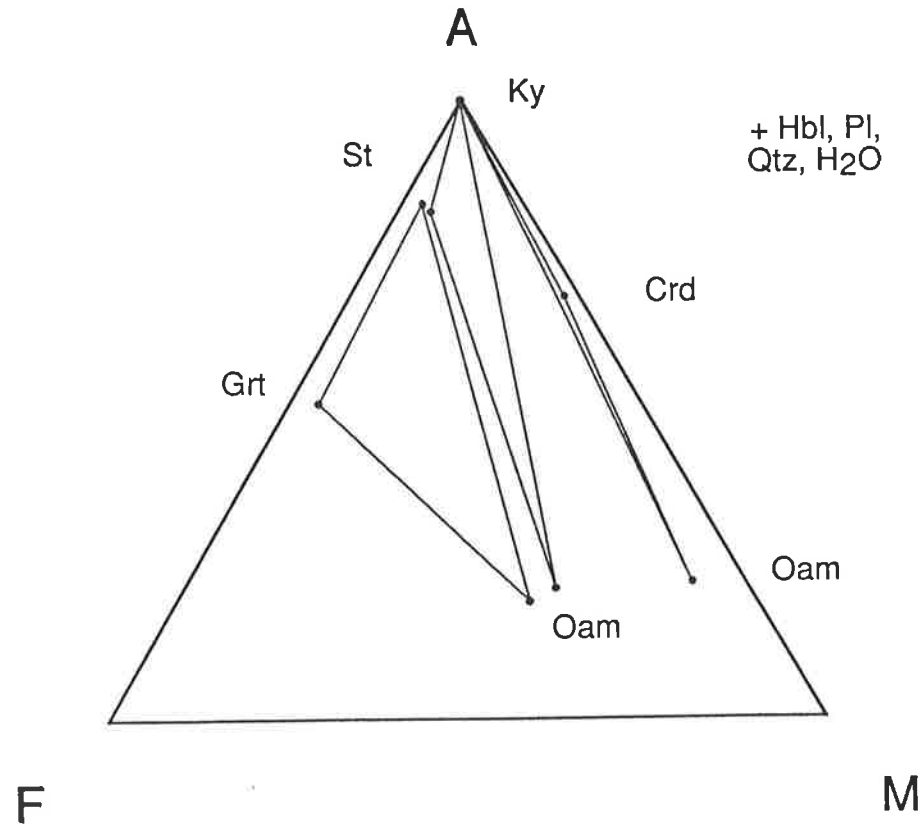
A
Ky
+ Hbl, Pl,
Qtz, H2O
St
Crd
Grt
Oam
Oam
F
M

clino-zoisite and epidote, with 30-90% epidote endmember (or Ps_{10-30}, see Table 4.3) in amphibolites bearing other aluminous phases such as staurolite, kyanite or gedrite. Kyanite from the Entia Dome amphibolites contains < 0.64% Fe_2O_3 and < 0.1% MnO.

The order of Fe-enrichment in amphibolites is staurolite > garnet > hornblende ≥ gedrite > biotite > chlorite. Figure 4.6 shows the compatibility relations of quartz-bearing amphibolites from the Harts Range.

4.4 Conditions of metamorphism

The variety of assemblage preserved in the Entia gneiss complex allows several different methods of P-T estimation to be employed. Conventional geothermometry, average pressure estimation and phase equilibria are used here to estimate the conditions at which the rocks equilibrated. The following section will deal with the information contained in the amphibolite reaction textures and their implications for the P-T evolution of the Hart Range region.

4.4.1 Geothermometry

The wide variety of rocks occurring in the supracrustal assemblage of the Entia gneiss complex provides an opportunity to constrain its thermal history using a number of different geothermometers. A selection of calibrations of Fe-Mg cation exchange in garnet–hornblende (Graham & Powell, 1984; Powell, 1985), garnet–biotite (Thompson, 1976; Ferry & Spear, 1978; Hodges & Spear, 1982) and garnet–clinopyroxene (Powell, 1985) pairs have been used to constrain the peak metamorphic conditions of equilibria in rocks from the Entia Dome. Calculated temperatures were in the range 570-710°C at an assumed pressure of 5 kbar (see Table 4.4) and somewhat higher in samples which showed signs of retrogression. These are considered to be minimum estimates for peak amphibolite facies metamorphism temperatures, and show substantial variation (14-99°C) between different pairs of analyses in the same sample. This may be a function of the different assemblages samples equilibrating at different times and hence different temperatures due to variations in grainsize.

4.4.2 Average pressure calculations

The results of average pressure calculations by the method of Powell and Holland (1988) are presented in Table 4.5 for the adjacent core (staurolite–garnet–hornblende) and matrix (hornblende–garnet–gedrite) assemblages in sample 950-077. Compositions of staurolite and hornblende inclusions in garnet and the garnet core compositions were used to establish average pressures for the core assemblage at 5.4 kbar for an assumed temperature of 600°C. The matrix assemblage hornblende–garnet–gedrite equilibrated at a calculated pressure of 6.7 kbar for an assumed temperature of 650°C. These conditions are consistent with the occurrence of kyanite.

Table 4.4. Temperature estimates made using Fe-Mg partitioning for garnet-hornblende, garnet-biotite and garnet-clinopyroxene.*

Grt-Hbl	NA-6	NA-6	853-16	HR91-5	HR91-5	HR91-8	HR91-8
XFeHbl	0.51	0.52	0.51	0.80	0.77	0.47	0.46
XFeGrt	0.84	0.85	0.74	0.94	0.94	0.70	0.71
XCaGrt	0.29	0.28	0.13	0.23	0.20	0.11	0.16
ln Kd	1.618	1.678	1.005	1.332	1.575	0.963	1.049
T(°C) G&P2	647	628	665	664	585	660	685
T(°C) G&P	673	654	692	690	614	688	710

Grt-Hbl	HR91-20	HR91-21	HR91-22	HR91-22	HR91-22	HR91-22
XFeHbl	0.57	0.44	0.41	0.41	0.43	0.43
XFeGrt	0.82	0.74	0.69	0.69	0.69	0.69
XCaGrt	0.21	0.10	0.08	0.08	0.08	0.08
ln Kd	1.192	1.253	1.179	1.150	1.046	1.071
T(°C) G&P2	685	571	569	576	602	595
T(°C) G&P	711	602	607	607	632	626

Grt-Bt	HR91-10	853-27	853-27
Xann	0.36	0.25	0.25
Xalm	0.63	0.51	0.53
Xpy	0.21	0.35	0.35
Xgrs	0.04	0.06	0.07
Xsps	0.12	0.09	0.05
ln K(ideal)	-1.661	-1.454	-1.512
T(°C) F&S	602	683	659
T(°C) T	597	639	625
T(°C) H&S	618	706	687

Grt-Cpx	HR91-5	HR91-5
XFeCpx	0.61	0.61
XFeGrt	0.94	0.94
XCaGrt	0.23	0.20
ln Kd	2.236	2.338
T(°C) P	621	581

* Temperature estimates are near independent of pressure (varying by ~5°C/kbar).
Abbreviations: Garnet-hornblende (G&P2) the updated method of Graham & Powell (1984) (Powell, 1985); (G&P) Graham and Powell (1984); Garnet-biotite: (F&S) Ferry and Spear (1978); (T) Thompson (1976); (H&S) Hodges and Spear (1982); Clinopyroxexe-garnet (Powell, 1985). Calculated for 5 kbar.

Table 4.5. Average pressure calculations*

(a) 950-077 (inside gt) (for x(H2O) = 1.0)

	q	H2O	ilm	ru	an	ab	tr	ftr
a	1	1	1	1	0.377	0.62	0.0003	3.6E-05
sd(a)/a	0		0	0	0.11644	0.05	1.1547	1.13707

	hb	parg	ed	gl	cumm
a	0.0264	0.0148	0.00095	9.5E-06	5.2E-06
sd(a)/a	0.42086	0.50889	0.84708	6.47524	8.77903

	gr	py	alm	fst	mst
a	0.00064	0.0125	0.244	0.232	0.009
sd(a)/a	0.75127	0.53073	0.15	0.2	0.57463

T°C	500	525	550	575	600	625	650
av P	4.5	4.7	4.9	5.2	5.4	5.6	5.9
sd	1.14	1.1	1.09	1.12	1.17	1.15	1.23
f	2.1	2	1.9	1.9	1.9	1.9	2

(b) 950-077 (outside gt) (for x(H2O) = 1.0)

	q	H2O	ilm	ru	an	ab	ftr
a	1	1	1	1	0.377	0.62	3.6E-05
sd(a)/a	0		0	0	0.11644	0.05	1.13707

	hb	parg	ed	gl	cumm	anth
a	0.0264	0.0148	0.00095	9.5E-06	5.2E-06	0.00012
sd(a)/a	0.42086	0.50889	0.84708	6.47524	8.77903	1.7999

	ged	gr	py	alm
a	0.0171	0.00064	0.0125	0.244
sd(a)/a	0.46515	0.75127	0.53073	0.15

T°C	500	525	550	575	600	625	650
av P	4.8	5.1	5.4	5.9	6.2	6.4	6.7
sd	0.84	0.83	0.84	0.81	0.82	0.85	1.03
f	1.6	1.6	1.5	1.4	1.4	1.4	1.6

* made using THERMOCALC v 2.2ß1 Powell & Holland (1988) and the enlarged and updated dataset of Holland & Powell (1990). Activities calculated using mixing on sites. For amphiboles activity calculations ignore substitution on the tetrahedral sites (as suggested by R Powell, pers. comm. 1992)
For 95% confidence, fit (= sd(fit)) should be less than 1.39

4.4.3 Theoretical phase relations

The theoretical phase relations in model compositional systems provide another avenue for interpreting complex textural relations in metamorphic rocks. Here we use phase diagrams from the literature and earlier chapters to constrain the nature of changes in P-T conditions recorded as reaction textures in the Harts Range rocks. The constraints imposed by the simple KFMASH (K_2O-FeO-MgO-Al_2O_3-SiO_2-H_2O) and FMASH (FeO-MgO-Al_2O_3-SiO_2-H_2O) systems appropriate to pelites and rocks of "whiteschist" character are discussed here.

KFMASH

The KFMASH phase diagrams of Powell and Holland (1990) and Dirks et al. (1991) may be used to place a limit upon the prevailing conditions during foliation development by comparing the equilibrium assemblages with those represented in the phase diagram. The presence of garnet in kyanite-biotite schists with muscovite, quartz and vapour implies temperatures must have been greater than 660°C at pressures greater than the sillimanite-kyanite univariant reaction i.e. > 6.5 kbar as the foliation developed. The subsequent replacement of kyanite by randomly oriented sillimanite suggests that higher temperatures and/or lower pressure conditions were intersected at some time after deformation.

(F)MASH

The broadly similar chemistry of the cordierite bearing rocks in the Entia gneiss complex to "whiteschists" (Schreyer, 1973, 1974) suggests that theoretical phase diagrams for the MASH system may be appropriate to the phase relations of these real rocks. Experimental work with emphasis on the stability of cordierite under changing physical conditions (Schreyer & Seifert, 1969a) has been used to construct phase diagrams for the MASH system appropriate to "whiteschists" (Schreyer, 1973, 1974) and chemically similar rock types. The original work of Schreyer and Seifert (1969a) suggested that a reaction, involving the breakdown of anthophyllite and kyanite to produce cordierite, takes place as a result of decreasing pressure from greater than about 10 kbar at temperatures > 800°C. That information has been superseded by newer data suggesting that the appropriate pressure for this reaction is approximately 6 kbar (Massone & Schreyer, 1983). The equilibrium thermodynamics calculations earlier in this thesis (Chapter 2) suggest that kyanite–orthoamphibole is not stable below about 6 kbar and that cordierite–orthoamphibole is stable only at temperatures ≥ 500°C. Thus the breakdown of kyanite–orthoamphibole occurred at pressures less than about 6 kbar at elevated temperatures.

4.5 The determination of changing physical conditions from metamorphic reaction textures in amphibolites

The wide variety of amphibolite assemblages and the reaction textures preserved in them should provide additional information about the P-T evolution of the area. The Harts Range amphibolites described above (section 4.3) contain evidence of three distinct divariant NCFMASH equilibria and their higher variance subsets. Garnet–staurolite–orthoamphibole (+ hornblende, plagioclase, quartz and aqueous vapour) is stable in Fe-rich amphibolites, kyanite–staurolite–orthoamphibole is stable in aluminous and intermediate X_{Fe} assemblages and Mg-rich rocks contain kyanite–cordierite–orthoamphibole. As illustrated in Fig. 4.6, these assemblages do not define crossed tie-lie relations and thus do not provide evidence of any discontinuous reactions during the area's P-T evolution. On the contrary, they suggest that the preserved assemblages all equilibrated within a single stability field, confined by several NCFMASH univariant reactions which prohibit assemblages involving staurolite–cordierite, cordierite–garnet and aluminosilicate–garnet. The absence of equilibrium chlorite in any of the Harts Range samples suggests that chlorite may also be metastable in this field, even for very magnesian samples.

The reaction textures observed in the Fe-rich, aluminous and Mg-rich amphibolites will be interpreted in terms of the chlorite absent CFMASH phase relations developed in Chapter 3.

4.5.1 Fe-rich amphibolites

The presence of foliation-parallel staurolite inclusions in garnet porphyroblasts suggests that staurolite–garnet was a stable assemblage in the early stages of foliation development but that staurolite became metastable as deformation continued. As hornblende occurs as inclusions in garnet in some amphibolites (e.g. samples HR91-8, 853-16, 950-105), the inclusion assemblage is likely to have been staurolite–garnet–hornblende (+ plagioclase, quartz and aqueous vapour). This assemblage is trivariant in NCFMASH, and can be described in terms of the equivalent CFMASH divariant reaction:

staurolite + hornblende $\Rightarrow$ garnet (+plagioclase, quartz, aqueous vapour),

illustrated in Fig. 4.7. The different stages at which samples 853-16, 950-105 and HR91-8 ceased reacting (i.e. with staurolite completely, partly and not included in garnet, respectively) is probably due to slight differences in the compositions of the bulk rocks (see Appendix A8.5). According to the pseudosections constructed in previous chapter (e.g. Fig. 3.17), with increasing temperature and pressure, the very Fe-rich rocks pass through the divariant CFMASH field, staurolite–garnet, and staurolite becomes decreasingly stable with respect to garnet (+ hornblende, anorthite, quartz, vapour) (Fig. 4.8). Staurolite inclusions are also preserved in garnet porphyroblasts in contact with a variably foliated gedrite–hornblende–

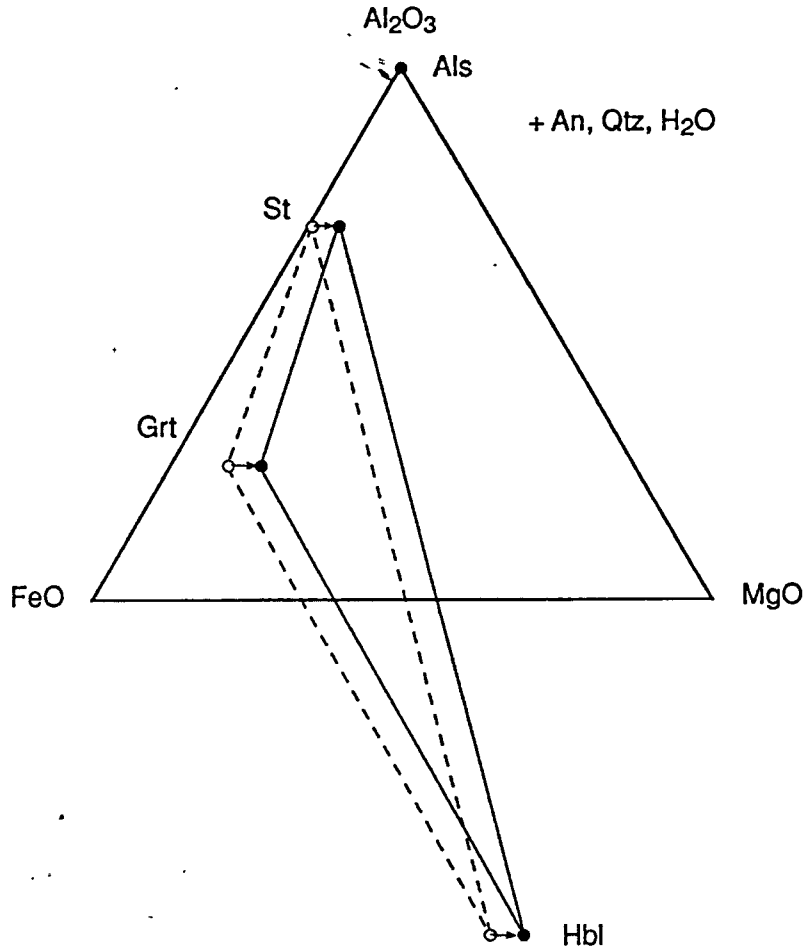
Al_2O_3
Als
+ An, Qtz, H_2O
St
Grt
FeO
MgO
Hbl

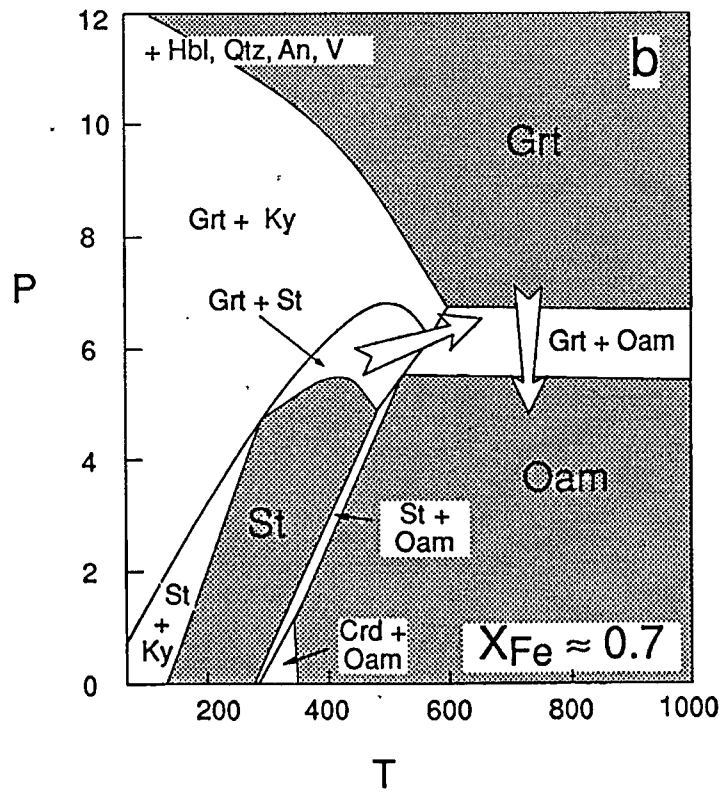
12
10
8
6
4
2
0
P
+ Hbl, Qtz, An, V
b
Grt
Grt + Ky
Grt + St
Grt + Oam
Oam
St
St + Oam
St + Ky
Crd + Oam
$X_{Fe} \approx 0.7$
200
400
600
800
1000
T

Figure 4.7. A compatibility diagram illustrating the CFMASH divariant reaction staurolite + hornblende ⇒ garnet, projected from anorthite, quartz and aqueous vapour onto the AFM (Al_2O_3-FeO-MgO) plane.

Figure 4.8. CFMASH pseudosections appropriate to Fe-rich amphibolites (with hornblende, anorthite, quartz, vapour in excess) showing the changes in pressure and temperature required to cause staurolite to become metastable with respect to garnet and for orthoamphibole to become stable with respect to garnet.

plagioclase–quartz matrix (sample 950-077). It is likely that the included staurolite was part of the NCFMASH divariant assemblage staurolite–garnet–gedrite–hornblende–plagioclase–quartz, which formed during deformation. The cross-cutting nature of some of the matrix gedrite grains and the lack of any dis-equilibrium textures suggest that gedrite became increasingly stable as deformation waned. This corresponds in the CFMASH pseudosections to a decrease in pressure toward the orthoamphibole (+ hornblende, plagioclase, quartz, vapour) trivariant field (Fig. 4.8). The presence of co-existing staurolite–orthoamphibole limits the NCFMASH assemblage (see Fig. 4.5) to the region bounded by the NCFMASH univariants [Crd, Als] and [Crd,Chl] in Fig. 3.20.

4.5.2 Aluminous, intermediate X_{Fe} amphibolites

High surface energy coronas of anorthite and staurolite separate foliated kyanite and hornblende in the hornblende–plagioclase–quartz matrix of aluminous samples (e.g. HR91-2, HR91-4, 890-5A, 890-12). The preservation of these textures suggests that the relevant NCFMASH trivariant (or CFMASH divariant) reaction:

kyanite + hornblende ⇒ staurolite + anorthite (+ quartz, aqueous vapour)

(Fig. 4.9) occurred after significant deformation had ceased. This reaction would be most simply achieved by an increase in temperature, however the pressure change associated with the reaction is unconstrained from this reaction texture (Fig. 4.10). Gedrite is observed in the matrix of some aluminous samples (e.g. 853-93, 890-8, 890-9). Thus the NCFMASH divariant assemblage kyanite–staurolite–gedrite–hornblende–plagioclase–quartz–vapour was probably stable in some rocks (see Fig. 4.4), however it is not clear from the textures what part gedrite played in the reaction. The assemblage kyanite–staurolite–gedrite–hornblende–plagioclase–quartz limits the amphibolites to the the P-T region bounded by the [Crd, Grt] and [Crd, Chl] NCFMASH equilibria in Fig. 3.20. In some samples (e.g. 890-14, 890-15) the reactions have gone to completion and all kyanite has been consumed.

4.5.3 Magnesium-rich amphibolites

The reaction textures in the cordierite-amphibolites are relatively clear-cut petrographically. Weakly foliated kyanite, hornblende and anthophyllite, kyanite and hornblende or kyanite and anthophyllite are corroded and are never observed in contact. They are surrounded and separated by undeformed cordierite and plagioclase, implying the CFMASH reactions:

kyanite + anthophyllite + hornblende ⇒ cordierite (+ plagioclase, quartz, vapour)

kyanite + hornblende ⇒ cordierite (+ plagioclase, quartz, vapour)

Figure 4.9. A compatibility diagram illustrating the CFMASH divariant reaction kyanite + hornblende ⇒ staurolite, projected from anorthite, quartz and aqueous vapour onto the AFM (Al_2O_3-FeO-MgO) plane.

Figure 4.10. CFMASH pseudosections appropriate to intermediate X_{Fe} amphibolites (with hornblende, anorthite, quartz, vapour in excess) showing the changes in pressure and temperature required to cause staurolite to become stable with respect to kyanite.

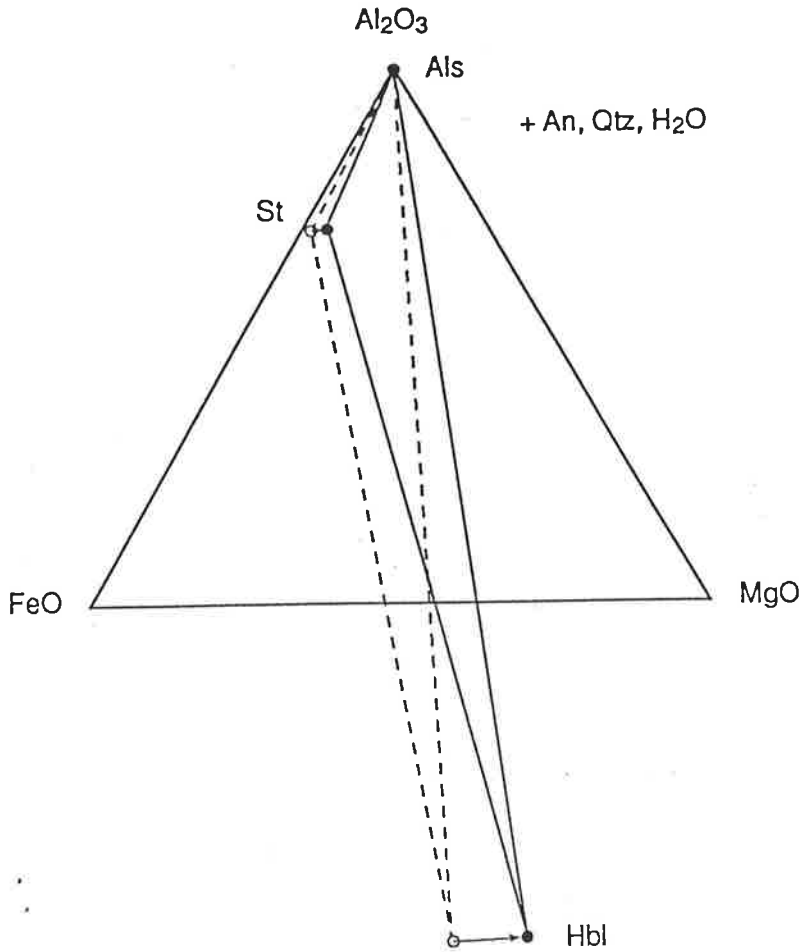
Al_2O_3
Als
+ An, Qtz, H_2O
St
FeO
MgO
Hbl

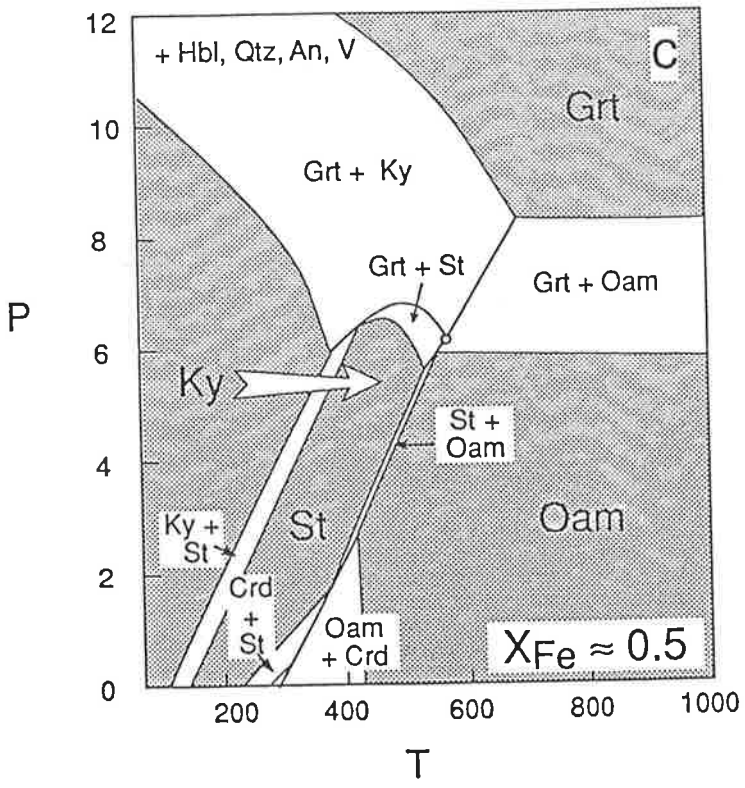
12
10
8
6
4
2
0
P
200
400
600
800
1000
T
+ Hbl, Qtz, An, V
C
Grt
Grt + Ky
Grt + St
Grt + Oam
Ky
St + Oam
Ky + St
St
Oam
Crd + St
Oam + Crd
$X_{Fe} \approx 0.5$

and the FMASH univariant reaction:

kyanite + anthophyllite ⇒ cordierite (+ quartz, vapour).

These assemblages are presented in Fig. 4.11 and result from decreasing pressure (Fig. 4.12). As a consequence of the cordierite-absent nature of the NCFMASH equilibria in Fig. 3.20, these Mg-rich assemblages are not represented in the phase diagram. Thus, as suggested in Chapter 3, the NCFMASH phase relations must involve more than one invariant point, the univariants of which allow rocks in the stability field appropriate to the Harts Range region to contain cordierite.

4.5.4 Temporal sequence of reactions

The deformation observed in each of the Harts Range amphibolite samples can be used as a scale against which to estimate the timing of mineral growth. This sequence of mineral growth can then be compared to other samples and, providing that the same deformation features are preserved in all samples, a regional chronology of the mineral growth can be developed. To that end, Table 4.6 presents the temporal sequence of amphibolite phases and assemblages with respect to the foliation formation in the individual amphibolite types. The foliation-parallel nature of the staurolite inclusions in garnet, together with the strength of the foliation in the surrounding garnet–gedrite–hornblende–plagioclase–quartz matrix suggest that staurolite–garnet was stable in the earliest-preserved stages of the deformational history (Table 4.6). The strongly foliated to slightly cross-cutting nature of gedrite in the staurolite–garnet-amphibolites, garnet amphibolites and gedrite-amphibolites suggests that gedrite developed syn-deformationally and continued to be stable until after deformation ceased.

The weakly foliated nature of kyanite, gedrite and hornblende in the Mg-rich and aluminous, intermediate X_{Fe} amphibolites and their often parallel fine inclusions of quartz or plagioclase indicate that these phases equilibrated during a period of deformation. However, the poorly developed nature of the foliation in these samples suggests that these phases developed during relatively weak deformation, in the declining stages of an intense deformation or as strain began to be partitioned into surrounding rocks. It is not clear whether the foliation preserved in the less Fe-rich rocks developed synchronously with that in the Fe-rich amphibolites. Coarse-grained plagioclase and cordierite which make up the matrix of the Mg-rich amphibolites are undeformed and contain random inclusion trails, suggesting that the cordierite grew subsequent to any pervasive deformation (Table 4.6). Similarly, the preservation of the high surface energy configuration of the coronas in the intermediate X_{Fe} amphibolites suggests that although the coronas are consuming foliated phases, significant deformation had ceased when staurolite–anorthite became stable (Table 4.6).

Figure 4.11. Compatibility diagrams illustrating (a) the CFMASH divariant reaction kyanite + hornblende ⇒ cordierite, projected from anorthite, quartz and aqueous vapour and (b) the FMASH divariant reaction kyanite + orthoamphibole ⇒ cordierite, projected from quartz and aqueous vapour. Both projected onto the AFM (Al_2O_3-FeO-MgO) plane.

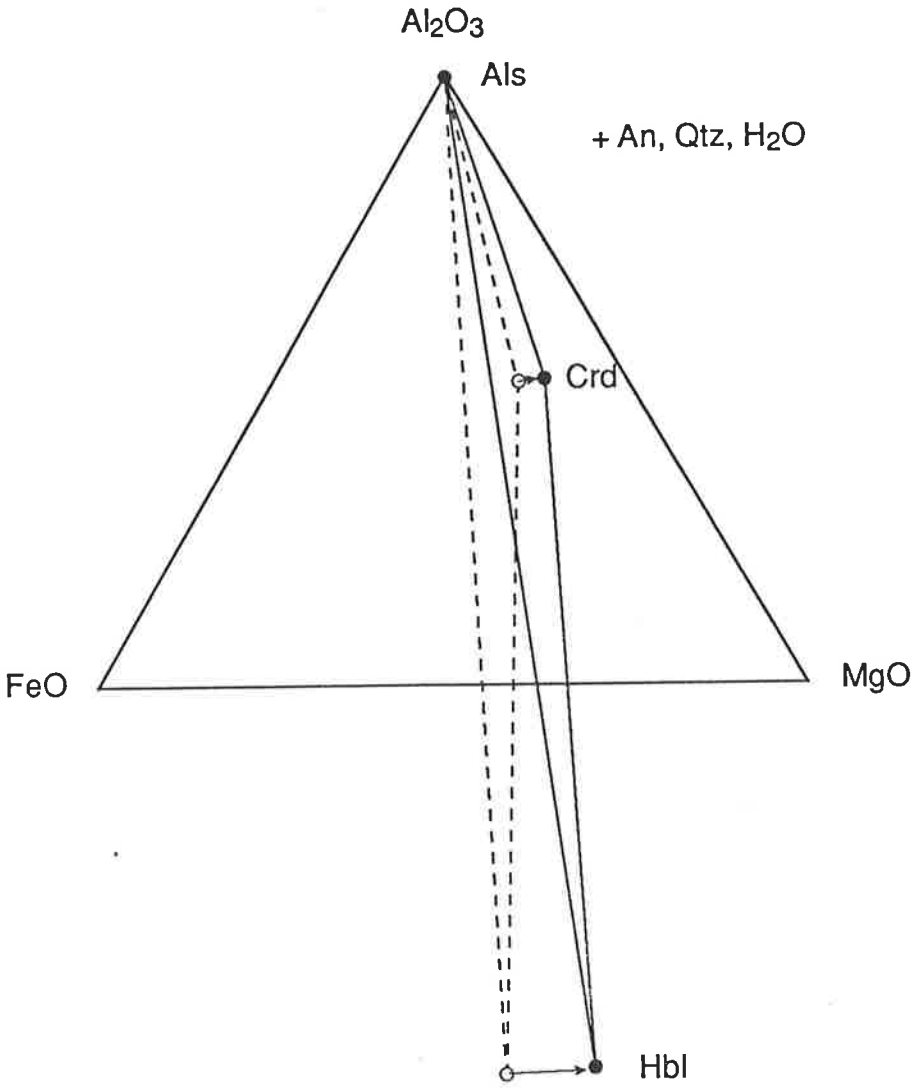
Al_2O_3
Als
+ An, Qtz, H_2O
Crd
FeO
MgO
Hbl

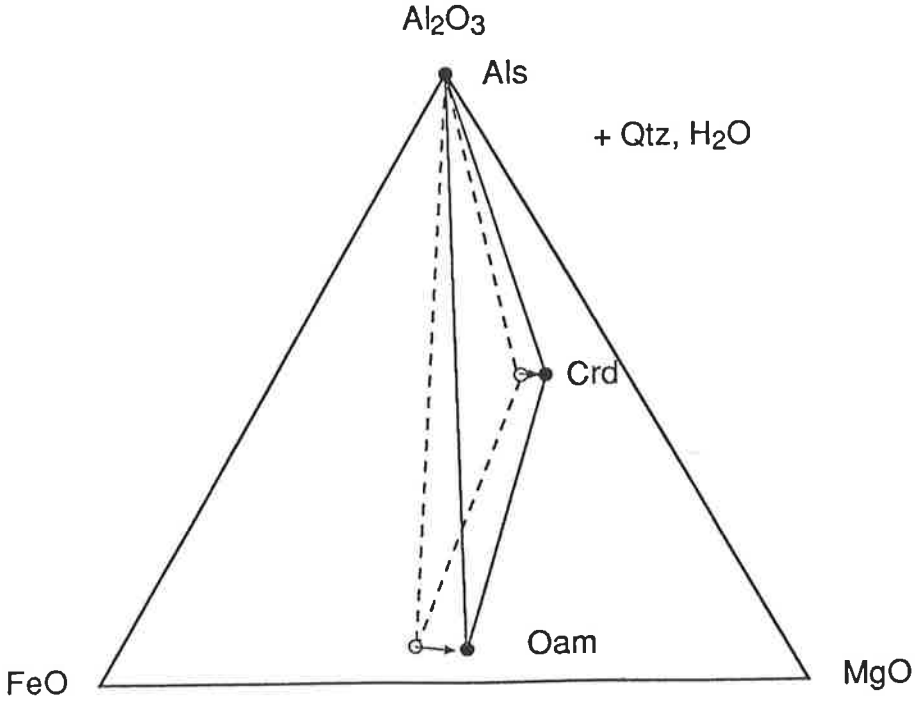
Al_2O_3
Als
+ Qtz, H_2O
Crd
Oam
FeO
MgO

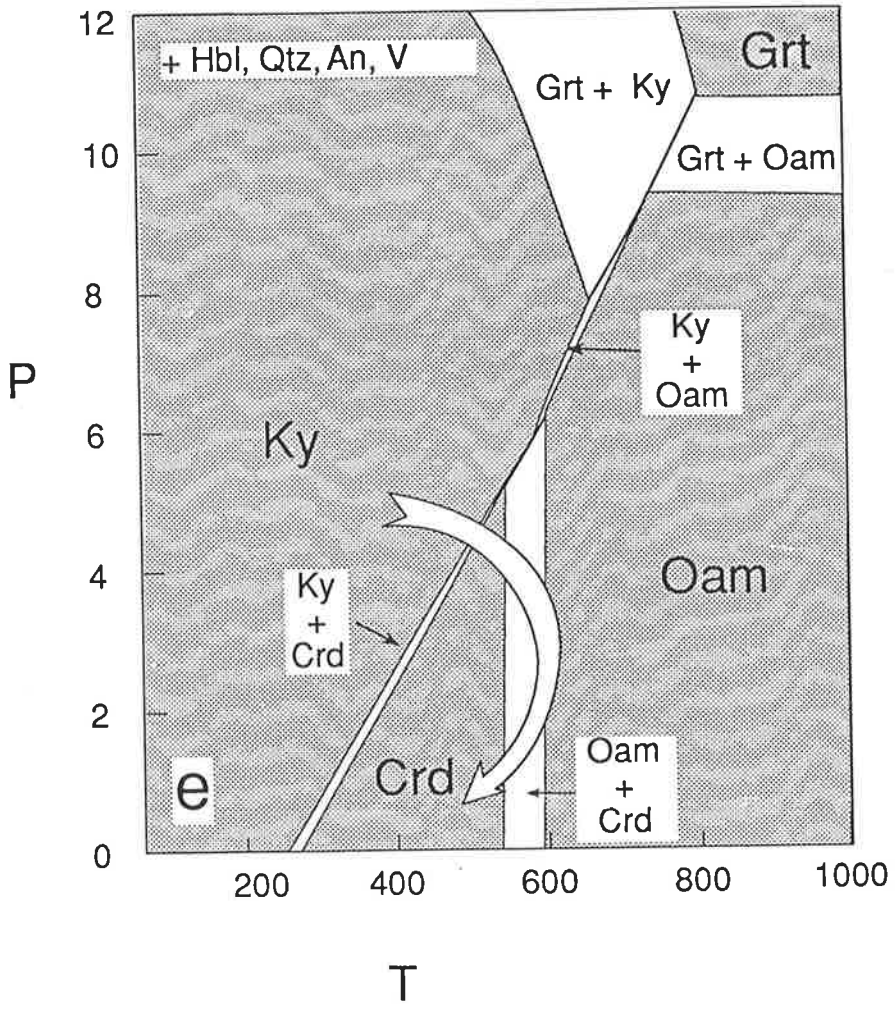

Figure 4.12. CFMASH pseudosections appropriate to Mg-rich amphibolites (with hornblende, anorthite, quartz, vapour in excess) showing the changes in pressure and temperature required to cause cordierite to become stable with respect to kyanite, orthoamphibole and hornblende.

Table 4.6. The timing of mineral growth in the different amphibolite types with respect to foliation.

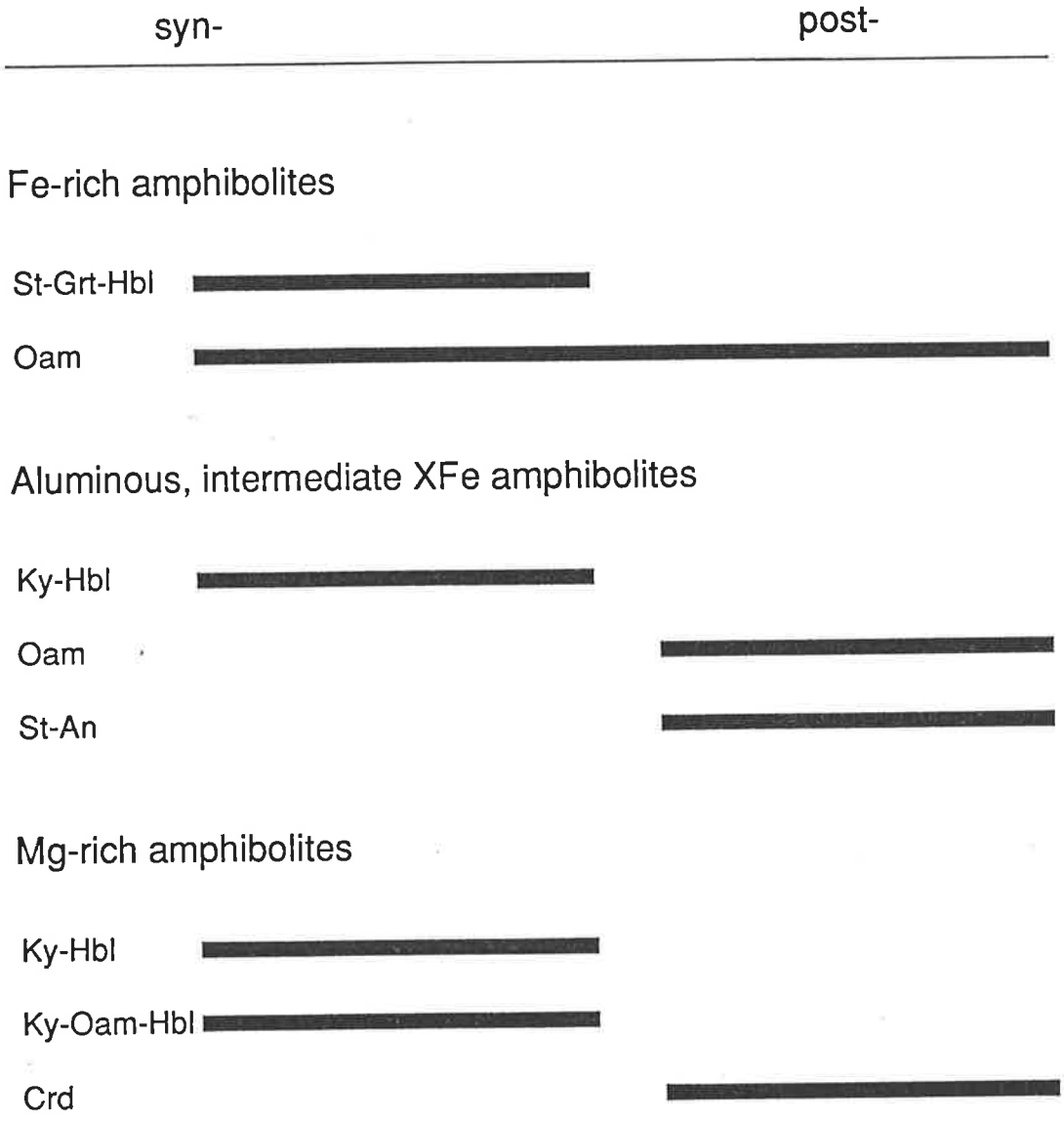

4.5.5 P-T evolution of the Harts Range amphibolites

The metamorphic history of the Harts Range region appears to have involved an intense period of deformation and foliation formation as the pressure and temperature of the rocks increased (staurolite ⇒ garnet ⇒ orthoamphibole) through ~5.5 to 6.5 kbar (Table 4.5) and to temperatures as high as 700°C (Table 4.4 and from kyanite–garnet pelites). There is also evidence of decreasing pressure as the effects of deformation declined (increasing orthoamphibole). The formation of weakly foliated kyanite and hornblende occurred under lower temperatures than garnet, garnet–orthoamphibole and orthoamphibole assemblages and there is no evidence of deformation in the subsequent higher temperature (staurolite) and lower pressure (cordierite) phases.

It is difficult to reconcile the above pressure, temperature and chronological information with a single pervasive foliation forming event. The strong foliation preserved in the garnet and garnet–gedrite amphibolites occurred under relatively high temperature conditions and thus any late-forming, and thus weakly deformed, equilibria could also be expected to be relatively high temperature assemblages. Any assemblages formed early (at low P-T) in this part of the P-T evolution might have developed under only weak stress, however, as metamorphism progressed the assemblages would probably become more strained, thus obliterating the weak deformational features and probably also the lower temperature mineral assemblage. Thus, if the kyanite–hornblende rocks formed early in the foliation-forming deformation that co-incided with garnet growth, the deformation must have been strongly partitioned among different structural regimes, thus preserving both the texture and the mineralogy of the samples. Alternatively, the kyanite–hornblende rocks may have equilibrated during a separate stage of metamorphism during active, but fairly weak deformation.

Independent of the question regarding the timing of kyanite–hornblende growth, the formation of staurolite–anorthite and cordierite assemblages occurred subsequent to deformation, at significantly lower temperatures and pressures than garnet–orthoamphibole (Fig. 4.13). Thus, the metamorphic evolution of the Harts Range region involved a period of heating and increasing pressure, followed by a period of decompression and cooling to pressures less than about 6 kbar. Further reaction was then initiated in rocks which were not undergoing active deformation. In absence of evidence for other mechanisms to provide the activation energy to allow reaction (e.g. deformation or an increase in the fluid content of the rocks), it seems likely that the activation energy required to initiate reaction was provided by heat input associated with increasing temperatures. This increase may have been essentially isothermal and followed by a period of decreasing pressure or may have involved a contemporaneous pressure decrease (Fig. 4.14).

From the above discussion, it seems likely that the Harts Range amphibolites provide evidence of at least two periods of prograde metamorphism. The lack of strong deformational features associated with the second, lower temperature stage and the lack of crossed tie-lines in the NCFMASH compositional system implies that this second phase may have been only a

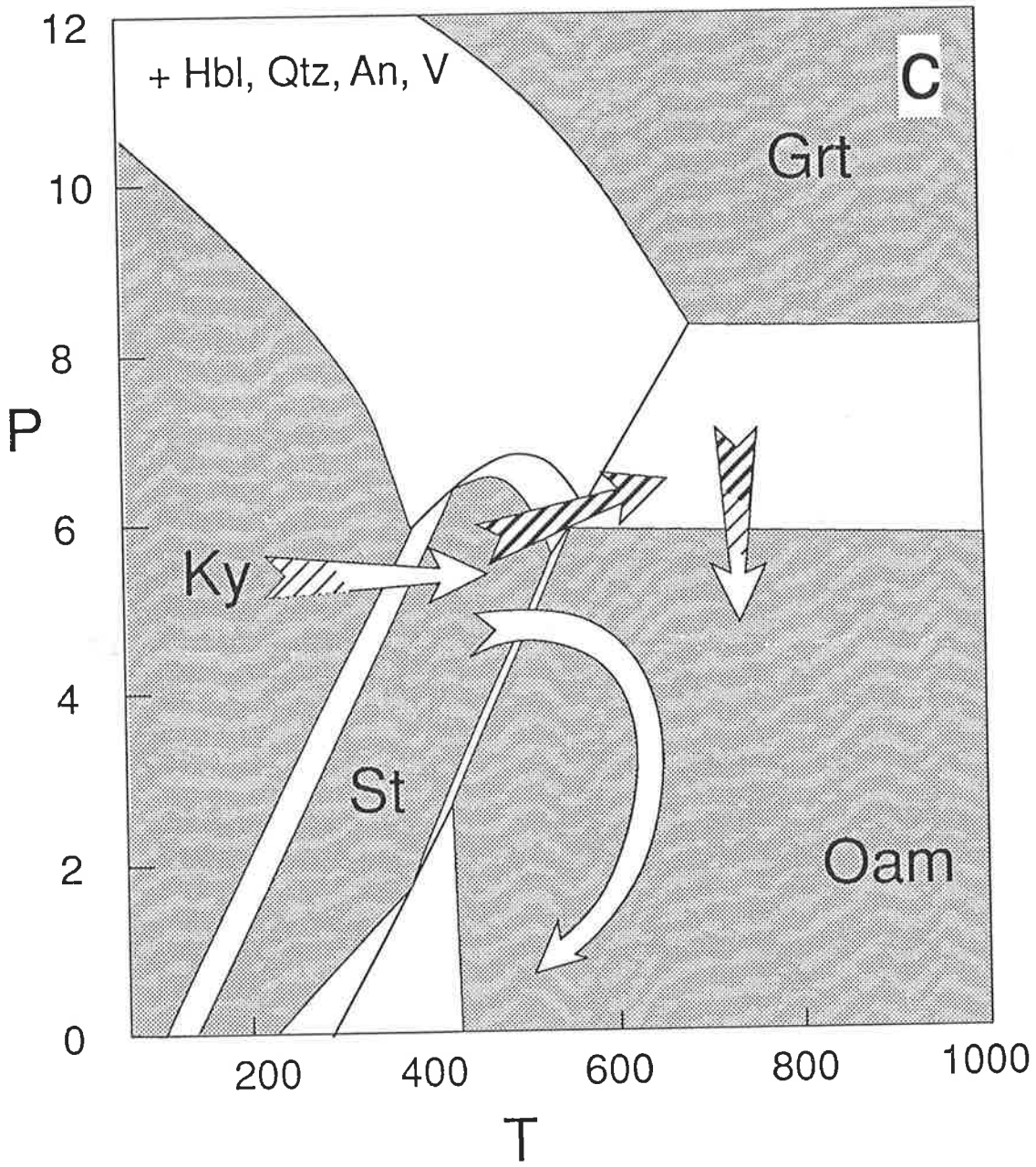

Figure 4.13. Pseudosection constructed for intermediate X_{Fe} amphibolites (with hornblende, anorthite, quartz, aqueous vapour in excess) illustrating the paths recorded in the Harts Range amphibolites. Heavy stripes are strongly foliated, light stripes are weakly foliated and unpatterned portions show no evidence of deformation.

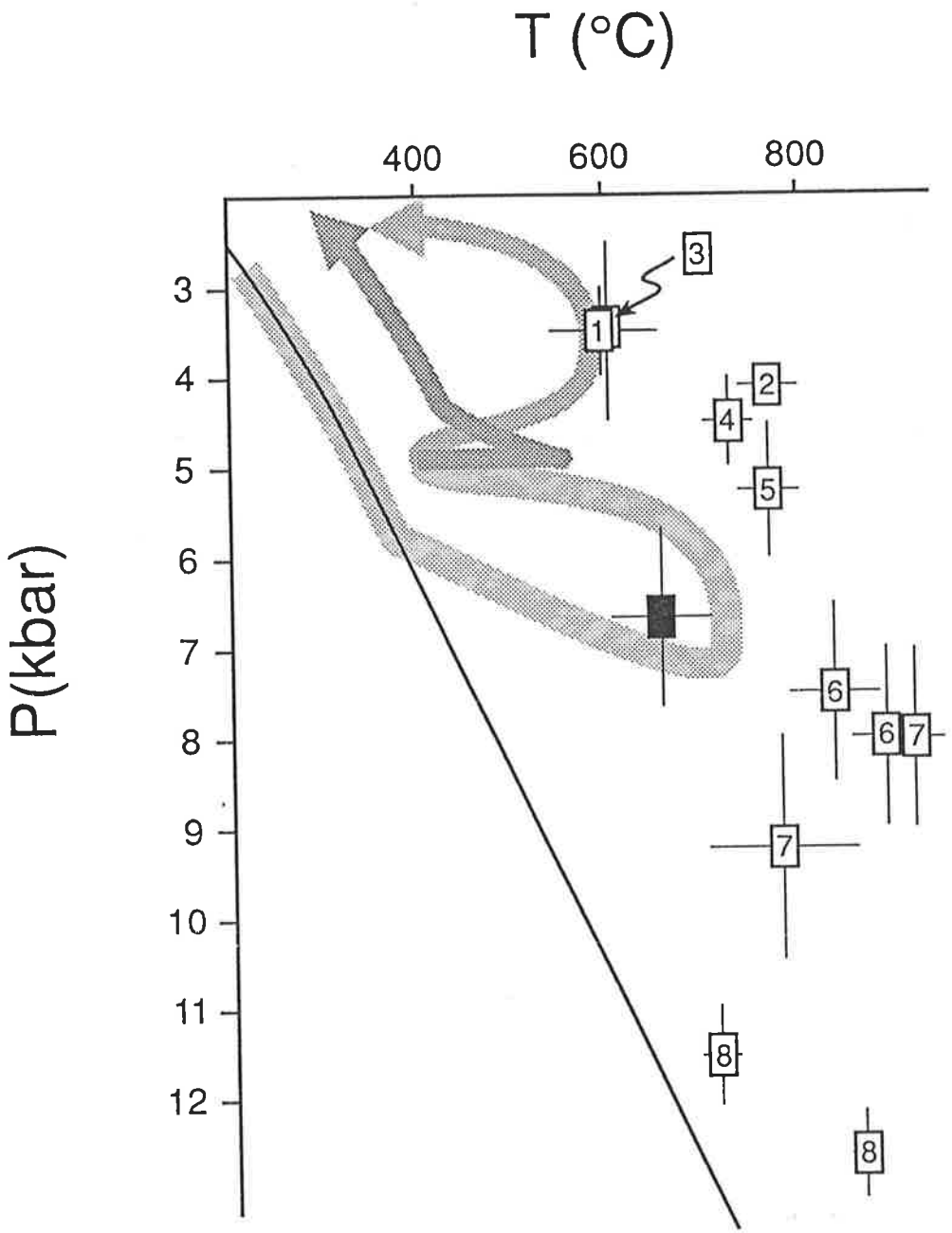

Figure. 4.14. A comparison of peak metamorphic conditions recorded in various central and northern Australian Proterozoic terranes and two possible P-T paths for the Entia Dome plotted with reference to the stable continental geotherm of England and Thompson (1984) calculated for a thermal conductivity of 2 $Wm^{-1}K^{-1}$. Results from this paper shown in black, other areas: 1) Granites Tanami Block, Scrimgeour & Sandiford, 1993; 2) Reynolds Range, Arunta Inlier, Dirks et al., 1991; 3) Mary Kathleen Fold Belt, Mt Isa Inlier, Oliver et al., 1991; 4) Anmatjira Range, Arunta Inlier, Hand et al., 1992; 5) Broken Hill Block, Phillips, 1980; 6) Strangways Range, Arunta Inlier, Warren, 1983; 7) Strangways Range, Arunta Inlier, Goscombe, 1992b; 8) Musgrave Range, Maboko et al., 1991.

relatively minor effect (perhaps a transient thermal perturbation) which allowed the activation energy of the assemblages to be overcome without significantly disrupting the overall evolution of the region. However, the low temperatures required for these undeformed assemblages are little higher than those appropriate to a stable continental geotherm (Fig. 4.14) and it is possible that the two parts of the P-T evolution were separated by a long period of time, during which the P-T conditions of the area were essentially stable.

4.6 Discussion

A small number of the mineral assemblages observed in the Entia Gneiss Complex provide evidence that the Harts Range region experienced granulite grade metamorphism early in its history, in common with the eastern Arunta Inlier (Goscombe, 1992a,b) and the remainder of the Arunta Inlier and other northern Australian Proterozoic terranes. However, the amphibolite grade assemblages which dominate the samples indicate that its later evolution involved crustal reworking under much cooler thermal regimes (Fig. 4.14). The most notable feature of this retrogressive kyanite-grade reworking is its regional extent which contrasts with the metamorphic reworking in other areas of the Arunta Inlier in which higher temperature assemblages are overprinted by very restricted kyanite-bearing retrograde shear zones (e.g. Warren, 1983; Clarke et al., 1990).

Clearly the full significance of the amphibolite facies metamorphism in the Harts Range awaits detailed a evaluation of the mineral isotopic systems. A preliminary study of this is presented by Foden et al. (1994). A brief discussion of the petrological data as it bears on the isotopic results of Foden et al. (1994) follows.

Foden and co-workers (1992, 1994) have identified four distinct isotopic closure "events" in the eastern Arunta Inlier. The first of these relates to an episode of significant crustal growth involving the intrusion of both felsic and mafic magmas at granulite facies conditions at 1765-1735 Ma, which is recorded in U-Pb zircon systematics (Mortimer et al., 1987; Cooper et al., 1988) and in some Sm-Nd whole rock isochrons, at 1780-1740 Ma. Foden et al. (1994) report that some Sm-Nd and Rb-Sr whole rock isochrons and Sm-Nd mineral isochrons yield ages in the vicinity of 1463 ±170 Ma. Similar ages have been determined from the Strangways region and Goscombe (1992a) has proposed that high grade crustal reworking at this time caused re-equilibration of the isotopic systems. $^{40}Ar/^{39}Ar$ age spectra from muscovite porphyroclasts in the Ruby Gap duplex, immediately south of the Harts Range on the northern margin of the Amadeus Basin, may also be correlated with this mid-Proterozoic resetting of the isotopic systems (> 1100 Ma, Dunlap et al., 1991). Sm-Nd systematics of garnet–hornblende pairs from the assemblages described here indicate that this assemblage either cooled through its closure temperature (~500-650°C, Foden et al., 1994) or formed at about 450 Ma. Rb-Sr isochrons in micas (closing at lower temperatures, approximately 500°C, Foden et al., 1994) preserve ages of 400-300 Ma. Similar ages have been reported from $^{40}Ar/^{39}Ar$ spectra for neocrystallised phengites (311-413 Ma) from Ruby

Gap (Dunlap et al., 1991).

The time intervals between the various isotopic closure "events" obtained from the Entia gneiss complex (i.e. 240, 900 and 50 or more million years) are generally long in comparison to the thermal time constant of the lithosphere (the time required for a perturbed geotherm to relax, which is thought to be of the order of 80 million years). Therefore it is unlikely that any of these geochronological "events" are causally related by a single cooling event affecting the whole region. It is probable that at least some of these isotopic events reflect distinct thermal episodes. Since the isotopic systems with high closure temperatures retain ages of about 1400 Ma and are correlated with the regional penetrative fabric, this age probably corresponds to the peak pressure and temperature conditions represented by garnet–hornblende equilibria. A further thermal perturbation at 450 Ma sufficient to reset Sm-Nd mineral systematics may be recorded in the mineral assemblages in the staurolite–anorthite coronas developed between earlier hornblende and kyanite. It is also likely that the substantial uplift elsewhere ascribed to the Alice Springs Orogeny (Collins & Teyssier, 1989) at approximately 300 Ma (and preserved in Rb-Sr mica cooling ages) is recorded in the Entia Dome amphibolites. This uplift may correspond to the growth of coarse grained cordierite developed between kyanite and hornblende and/or orthoamphibole and sillimanite replacing kyanite in pelites.

4.7 Conclusion

Petrographic evidence from the Harts Range amphibolites suggests that the region has experienced a complex metamorphic history. This involved early, granulite facies metamorphism which was followed and largely overprinted by strongly foliated high P/T metamorphism assemblages. Later thermal perturbation(s?) allowed re-equilibration under lower P-T conditions which may have accompanied or been followed by significant decompression

The petrographic evidence supporting repeated metamorphic heating episodes suggests that the isotopic "events" recorded in the Harts Range region may be correlated with the development of one or more of the observed mineral textures. If this is the case it suggests that the eastern Arunta Inlier experienced a granulite facies history during the early Proterozoic in common with other northern Australian inliers, but that it was subjected to substantial thermal perturbation and possibly crustal reworking in the late Proterozoic and maybe into the Palaeozoic.

The metamorphic history of the the Harts Range area and the Arunta Inlier in general has important implications for understanding Proterozoic tectonics in northern Australia and world-wide. Part of its significance is due to the contrast it offers to the remainder of the Arunta Inlier and the other northern Australian inliers. In general, the northern Australian Proterozoic terranes are dominated by high P-low T granulite facies metamorphism (e.g. Clarke et al., 1990; Dirks et al., 1991; Hobbs et al., 1984; Scrimgeour & Sandiford, 1994)

and lower temperature, higher pressure metamorphism is restricted to discrete kyanite-bearing retrograde shear-zones (e.g. Warren, 1983). This seeming ubiquity of low P- high T metamorphism in northern Australia has lead several workers to suggest that the tectonics of the individual inliers was inter-related and strongly dependent on intraplate rather than interplate interactions (e.g. Loosveld & Etheridge, 1990; Etheridge et al., 1987). However, recent work in the Strangways Range has revealed widely distributed high P/T metamorphism which overprinted the high T-low P granulite facies metamorphism (e.g. Goscombe, 1992b). Thus, the eastern Arunta Inlier (e.g. the Strangways and Harts Ranges) has experienced a metamorphic history at least partly distinct from many other northern Australian terranes and this engenders considerable significance for the Harts Range in future interpretations of the northern Australian Proterozoic terranes.

Chapter 5: Kyanite–staurolite–bearing amphibolites from the Zillertaler Alpen, Austria

5.1 Introduction

Earlier chapters have developed quantitative phase diagrams for model systems which approximate the composition of amphibolites (Chapter 3) and described a new occurrence of kyanite–staurolite–hornblende assemblages from the Harts Range of central Australia (Chapter 4). The assemblages and phase relations observed in the Harts Range amphibolites are rather different to those from kyanite- and staurolite-bearing amphibolites reported in the literature (e.g. Spear, 1977, 1978, 1982; Selverstone et al., 1984; Ward, 1984a; Spear & Rumble, 1986; Schumacher & Robinson, 1987). In order to better understand the phase relations in kyanite- and staurolite-amphibolites, the many different occurrences should all be considered and this chapter deals with the compatibility relations of kyanite–staurolite–hornblende garben schiefer from western Austria. The following chapter summarises the compatibility relations of kyanite- and staurolite-amphibolites reported in the literature and discusses their relationships to each other and the calculated phase relations calculated in Chapter 3.

Kyanite–staurolite amphibolites from the Zillertaler Alpen in western Austria make up part of a near-complete P-T path determined for the south-western Tauern Window (Selverstone et al., 1984). As a consequence of the variety of low variance assemblages reported from the area and their location in the relatively well-characterised metamorphic terrain of the Tauern Window (e.g. Miller, 1974; Droop, 1982; Selverstone et al., 1984; Selverstone, 1993), the Austrian samples provide an excellent opportunity for comparing the phase relations in kyanite–staurolite-bearing amphibolites.

Selverstone et al. (1984) briefly describe the petrography of the kyanite–staurolite–hornblende-bearing garbenschiefer of the Zillertaler Alpen and construct a P-T path for these rocks. However neither this paper, nor any of the associated publications (e.g. Selverstone & Spear, 1985; Selverstone & Munoz, 1987), adequately describe the textural and chemical relations of these rocks. Thus, this chapter includes a summary of the petrography (Table 5.1) and mineral chemistry (Table 5.2) of the low variance kyanite–staurolite–hornblende garbenschiefer (described in detail in Appendix A5.10) and related amphibolites and a discussion of their compatibility relations.

Table 5.1. Selected brief petrographic descriptions of rocks from the Zillertaler Alpen, samples 938-

	Qtz	Pl	Px	Hbl	Ms	Bt	Grt	St	Ky	Ep	Chl	Rt	Ilm	Ank
33b	X	Z		P & Cumm		1°, Rh	P				Rh,g		X	
51	X	Z		P		1°		X	X	Z	Rb	X	X	X
52a	X	Z		P						X	X	X	X	X
52b	X	Z		P		1°			X	X	Rb,h	X	X	
52c		Z		P	Rb	1°	P		P	Z				
72	X	Z			Rb	1°	P				Rb		X	
72a	X	Z				1°	P					X		
81	X	Z			X	X				X	Rb	X	X	
82	X	Z			1°	1°	1°	X			R	X	X	
82a														
83	X	Z			X	X	P		P			X	X	
83a	X	Z		P						X	Rh		X	X
83b	X	Z		P						X	Rh		X	X
91a	X	Z		P	1°	1°	P	X			X	X	X	
91b	X	Z		P	1°	1°	X				Rb	X	X	
92a	X	Z		P & Cumm		1°	P				X,Rb		X	
92b	X	Z		P		X				X			X	X
93	X	Z		P			X			H	R	X	X	Cal
94	X	Z		X								X	X	
94a	X	Z			X	X	P	P	P	X	Rb			X
94b	X	Z		X		X					Rb		X	
95	X	Z		P	Rb	Rh							X	
127	X	Z		P	2°	1°	P	X	X	G	Rh,b	X	X	
128	X	Z		P						X	Rb	X	X	X
128a	X	Z		X		X				X	X	X		
129	X	Z		X						X		X		
129a	X	Z			1°	1°				X	Rb	X	X	
129b	X	Z			1°						Rb		X	
129c	X	Z				1°			X		Rb	X	X	
129d	X	Z			X	X					Rb		X	
137b	X	Z		P & Cumm		1°, Rh	P				Rh		X	
140	X	Z			1°					X			X	
140a	X	Z			1°					X	1°			X
141	X	Z			1°	1°	P						X	
141a	X	Z		P		1°				X	Rb	X		X
141b	X				1°	1°				X			X	X
141c	X	Z		P	1°	1°				X		X	X	X

Abbreviations: X phase present, Z zoned, 1° primary phase, 2° secondary phase, P porphyroblastic, Cal calcite, Rb, retrograde after biotite, Rh retrograde after hornblende, Rg retrograde after garnet, H in hornblende, G in garnet

Table 5.2. Selected probe data from sample 938-127 recalculated according to Appendix A1

938-127

	Grt	St	Ky	Hbl	Pl	Bt	Grt core	Grt	Grt rim	Bt	St	Grt	Pl	Ep	Pl	Pg	Hbl	Hbl core
SiO2	39.62	29.90	37.50	41.52	58.34	35.17	37.13	34.83	37.19	36.26	28.14	37.43	59.09	36.78	57.93	44.50	41.08	41.07
TiO2	0.03	0.46	0.08	0.48	0.05	1.58	0.10	6.41	0.09	2.09	0.36	0.07	0.03	0.05	0.00	0.16	0.47	0.70
Al2O3	21.66	53.19	59.39	16.12	23.71	17.55	21.80	19.97	21.63	17.47	53.50	21.70	23.69	26.37	24.37	39.27	14.32	15.30
FeO	30.77	12.72	1.83	16.10	0.25	16.49	27.42	26.50	30.21	14.44	12.70	30.98	0.53	8.55	0.14	0.86	16.63	16.27
MnO	3.51	0.21	0.03	0.13	0.03	0.22	4.74	3.46	3.63	0.00	0.24	3.43	0.13	0.15	0.12	0.10	0.15	0.56
MgO	3.82	2.22	0.57	8.93	0.00	12.66	1.78	2.26	4.16	14.76	2.16	4.07	0.00	0.08	0.16	0.29	8.03	7.54
CaO	2.82	0.03	0.04	10.13	6.02	0.19	8.46	7.01	3.47	0.19	0.03	2.89	5.66	23.23	6.31	0.59	10.51	10.38
Na2O	0.00	0.05	0.05	1.33	7.66	0.00	0.05	0.00	0.00	0.00	0.42	0.00	7.86	0.24	7.74	6.56	1.04	1.07
K2O	0.01	0.01	0.02	0.37	0.00	8.49	0.00	0.00	0.00	8.86	0.00	0.03	0.02	0.04	0.00	1.01	0.48	0.28
Cr2O3	0.02	0.03	0.06	n.a.	n.a.	n.a.	n.a.	n.a.	n.a.	n.a.	n.a.	n.a.	n.a.	n.a.	n.a.	0.19	0.09	0.20
ZnO	0.08	0.18	0.13	n.a.	n.a.	n.a.	n.a.	n.a.	n.a.	n.a.	n.a.	n.a.	n.a.	n.a.	n.a.	n.a.	n.a.	n.a.
Total	102.3	99.0	99.7	95.1	96.1	92.4	101.5	100.4	100.4	94.1	97.5	100.6	97.0	95.5	96.7	93.5	92.8	93.4
Si	3.066	8.141	1.026	6.302	2.701	2.720	2.937	2.775	2.955	2.723	7.798	2.968	2.711	3.009	2.669	2.918	6.432	6.377
Ti	0.002	0.094	0.002	0.054	0.002	0.092	0.006	0.384	0.005	0.118	0.076	0.004	0.001	0.003	0.000	0.008	0.056	0.081
Al	1.975	17.074	1.915	2.885	1.294	1.600	2.033	1.876	2.026	1.547	17.479	2.028	1.281	2.543	1.323	3.036	2.643	2.801
Fe2+	1.991	2.897	0.042	2.044	0.010	1.067	1.814	1.766	2.007	0.907	2.944	2.054	0.020	0.585	0.005	0.047	2.178	2.113
Mn	0.230	0.049	0.001	0.016	0.001	0.015	0.318	0.233	0.244	0.000	0.057	0.231	0.005	0.011	0.004	0.005	0.020	0.074
Mg	0.441	0.900	0.023	2.020	0.000	1.460	0.210	0.269	0.493	1.652	0.890	0.481	0.000	0.010	0.011	0.028	1.875	1.745
Ca	0.234	0.008	0.001	1.647	0.299	0.016	0.717	0.599	0.295	0.015	0.008	0.246	0.278	2.036	0.311	0.041	1.764	1.726
Na	0.000	0.029	0.003	0.390	0.688	0.000	0.008	0.000	0.000	0.000	0.224	0.000	0.699	0.038	0.692	0.834	0.316	0.323
K	0.001	0.004	0.001	0.072	0.000	0.838	0.000	0.000	0.000	0.849	0.000	0.003	0.001	0.004	0.000	0.084	0.097	0.055
Cr	0.001	0.007	0.001	-	-	-	-	-	-	-	-	-	-	-	-	0.010	0.011	0.024
Zn	0.004	0.036	0.003	-	-	-	-	-	-	-	-	-	-	-	-	-	-	-
Total	7.945	29.240	3.016	15.432	4.994	7.807	8.044	7.902	8.027	7.810	29.476	8.015	4.997	8.237	5.015	7.011	15.391	15.318
An					0.303								0.285		0.310			
XFe	0.819	0.763		0.503		0.422	0.896	0.868	0.803	0.354		0.810					0.537	0.548
Aliv				1.698		1.280				1.277						1.082	1.568	1.623
Alvi				1.187												1.953	1.076	1.177
Xalm	0.688						0.593	0.616	0.660			0.682						
Xpy	0.152						0.069	0.094	0.162			0.160						
Xgrs	0.081						0.234	0.209	0.097			0.082						
Xsps	0.079						0.104	0.081	0.080			0.077						
ps														15.236				

Table 5.2. Selected probe data from samples 938-91a, 938-52c recalculated according to Appendix A1

938-91a

	Ep	Chl	Pl	Hbl	Pl	Bt	Grt rim	St	Hbl	Bt	Pl
SiO2	37.53	25.14	56.87	41.42	56.42	35.52	37.57	27.20	41.64	35.49	57.23
TiO2	0.00	0.05	0.14	0.49	0.08	1.86	0.13	0.57	0.49	1.69	0.00
Al2O3	25.41	18.11	22.62	14.24	22.68	15.59	19.67	46.97	14.80	15.88	21.75
FeO	6.78	22.02	0.35	15.82	0.11	17.00	32.37	11.14	16.32	17.27	0.21
MnO	0.08	0.03	0.01	0.08	0.12	0.13	1.56	0.09	0.10	0.09	0.11
MgO	0.20	16.13	0.00	8.36	0.00	10.92	3.49	1.36	7.54	11.02	.0.00
CaO	24.11	0.00	7.64	10.47	7.82	0.16	4.08	0.07	10.66	0.25	6.96
Na2O	0.13	0.00	6.90	1.37	6.92	0.00	0.04	1.59	1.16	0.13	7.71
K2O	0.00	0.00	0.00	0.41	0.06	9.42	0.00	0.00	0.30	9.33	0.00
Cr2O3	0.15	0.07	0.30	0.18	0.36	0.00	0.06	0.08	0.08	0.08	0.04
ZnO	n.a.	n.a.	n.a.	n.a.	n.a.	n.a.	n.a.	n.a.	n.a.	n.a.	n.a.
Total	94.4	81.5	94.8	92.8	94.6	90.6	99.0	89.0	93.1	91.2	94.0
Si	3.082	2.817	2.684	6.458	2.674	2.827	3.043	8.263	6.471	2.809	2.722
Ti	0.000	0.004	0.005	0.057	0.003	0.112	0.008	0.129	0.058	0.101	0.000
Al	2.461	2.393	1.259	2.617	1.267	1.463	1.878	16.822	2.712	1.481	1.220
Fe2+	0.466	2.063	0.014	2.063	0.004	1.131	2.192	2.829	2.121	1.143	0.008
Mn	0.006	0.003	0.000	0.011	0.005	0.009	0.107	0.023	0.013	0.006	0.005
Mg	0.025	2.694	0.000	1.942	0.000	1.295	0.421	0.613	1.746	1.300	0.000
Ca	2.122	0.000	0.387	1.749	0.397	0.014	0.354	0.022	1.776	0.021	0.355
Na	0.021	0.000	0.631	0.414	0.636	0.000	0.007	0.935	0.351	0.021	0.711
K	0.000	0.000	0.000	0.082	0.003	0.956	0.000	0.000	0.058	0.942	0.000
Cr	0.010	0.006	0.011	0.022	0.014	0.000	0.004	0.018	0.009	0.005	0.002
Zn	-	-	-	-	-	-	-	-	-	-	-
Total	8.193	9.980	4.991	15.414	5.003	7.807	8.012	29.655	15.315	7.828	5.023
An			0.380		0.385						0.333
XFe		0.434		0.515		0.466	0.839	0.822	0.549	0.468	
Aliv		1.183		1.542		1.173			1.529	1.191	
Alvi		1.210		1.075		0.291			1.183	0.290	
Xalm							0.713				
Xprp							0.137				
Xgrs							0.115				
Xsps							0.035				
Ps	17.968										

938-52c

	Chl	Pl	Bt	Grt	Hbl	Grt	Hbl
SiO2	25.76	59.45	34.92	36.92	42.23	37.59	38.75
TiO2	0.00	0.00	0.86	0.00	0.26	0.00	0.28
Al2O3	20.33	25.25	17.65	20.19	15.75	20.13	16.12
FeO	17.21	0.00	13.90	30.53	16.38	29.74	18.09
MnO	0.35	0.00	0.15	2.59	0.43	2.64	0.00
MgO	21.41	0.00	15.59	3.68	8.53	3.92	9.82
CaO	0.00	7.42	0.00	4.83	9.75	5.21	8.72
Na2O	0.18	7.19	0.30	0.22	1.24	0.34	1.40
K2O	0.00	0.07	8.43	0.00	0.29	0.00	0.28
Cr2O3	0.00	0.00	0.00	0.00	0.00	0.00	0.00
ZnO	n.a.	n.a.	n.a.	n.a.	n.a.	n.a.	n.a.
Total	85.2	99.4	91.8	99.0	94.9	99.6	93.5
Si	2.686	2.664	2.686	2.991	6.419	3.014	6.060
Ti	0.000	0.000	0.050	0.000	0.030	0.000	0.033
Al	2.500	1.334	1.601	1.928	2.822	1.903	2.972
Fe2+	1.501	0.000	0.894	2.068	2.082	1.995	2.366
Mn	0.031	0.000	0.010	0.178	0.055	0.179	0.000
Mg	3.328	0.000	1.787	0.444	1.932	0.468	2.289
Ca	0.000	0.356	0.000	0.419	1.588	0.448	1.461
Na	0.036	0.625	0.045	0.035	0.365	0.053	0.425
K	0.000	0.004	0.827	0.000	0.056	0.000	0.056
Cr	0.000	0.000	0.000	0.000	0.000	0.000	0.000
Zn	-	-	-	-	-	-	-
Total	10.082	4.983	7.900	8.063	15.351	8.060	15.661
An		0.363					
XFe	0.311		0.333	0.823	0.519	0.810	0.508
Aliv	1.314		1.314		1.581		1.940
Alvi	1.186		0.287		1.241		1.032
Xalm				0.665		0.645	
Xprp				0.143		0.152	
Xgrs				0.135		0.145	
Xsps				0.057		0.058	
Ps							

Table 5.2. Selected probe data from samples 938-52c (continued) and 938-124c recalculated according to Appendix A1

938-52c (continued)

	Grt	Hbl	Hbl	St	Hbl	St	Ep rim	Ep core
SiO2	37.01	40.01	39.90	27.21	41.38	27.64	36.71	36.28
TiO2	0.33	0.31	0.34	0.50	0.31	0.43	0.00	0.12
Al2O3	19.15	14.86	15.17	47.64	14.55	47.66	23.47	20.65
FeO	31.12	13.86	15.98	11.28	14.26	10.92	9.17	12.02
MnO	1.88	0.30	0.32	0.38	0.32	0.26	0.25	0.17
MgO	2.78	8.85	7.86	1.61	9.09	1.99	0.25	0.00
CaO	5.44	11.81	10.38	0.15	10.97	0.06	23.31	22.90
Na2O	0.00	1.51	1.58	0.26	1.42	0.62	0.00	0.14
K2O	0.00	0.31	0.31	0.00	0.33	0.00	0.00	0.01
Cr2O3	0.09	0.26	0.25	0.00	0.24	0.10	0.37	0.18
ZnO	n.a.	n.a.	n.a.	n.a.	n.a.	n.a.	n.a.	n.a.
Total	97.8	92.1	92.1	89.0	92.9	89.7	93.5	92.5
Si	3.041	6.285	6.302	8.235	6.417	8.294	3.088	3.142
Ti	0.020	0.037	0.041	0.113	0.036	0.097	0.000	0.008
Al	1.855	2.751	2.824	17.000	2.660	16.860	2.328	2.108
Fe2+	2.138	1.820	2.111	2.855	1.849	2.741	0.646	0.871
Mn	0.130	0.040	0.043	0.097	0.042	0.066	0.018	0.012
Mg	0.340	2.072	1.849	0.728	2.101	0.888	0.031	0.000
Ca	0.479	1.988	1.757	0.048	1.822	0.019	2.101	2.125
Na	0.000	0.461	0.484	0.153	0.428	0.358	0.000	0.023
K	0.000	0.062	0.063	0.000	0.065	0.000	0.000	0.002
Cr	0.006	0.032	0.031	0.000	0.029	0.023	0.024	0.012
Zn	-	-	-	-	-	-	-	-
Total	8.009	15.548	15.504	29.228	15.449	29.346	8.236	8.302
An								
XFe	0.863	0.468	0.533	0.797	0.468	0.755		
Aliv		1.715	1.698		1.583			
Alvi		1.036	1.126		1.077			
Xalm	0.692							
Xprp	0.110							
Xgrs	0.155							
Xsps	0.042							
Ps							22.409	29.733

938-124c

	Hbl	Pl	Grt rim	Ky	Ep	Ep	Bt	Hbl
SiO2	42.37	55.68	38.69	38.41	39.18	39.26	38.43	43.52
TiO2	0.30	0.00	0.11	0.01	0.12	0.09	0.80	0.38
Al2O3	18.66	29.05	21.64	61.98	28.56	26.96	18.56	17.07
FeO	15.32	0.13	27.85	0.30	5.97	8.34	16.13	15.35
MnO	0.11	0.00	1.23	0.03	0.03	0.14	0.05	0.11
MgO	8.43	0.00	2.45	0.00	0.04	0.02	13.70	9.34
CaO	10.42	11.09	8.31	0.04	23.27	23.43	0.06	10.58
Na2O	1.49	5.01	0.00	0.04	0.00	0.01	0.16	1.37
K2O	0.41	0.05	0.02	0.00	0.01	0.03	8.77	0.37
Cr2O3	0.05	0.01	0.03	0.02	0.04	0.03	0.08	0.00
ZnO	0.17	0.00	0.00	0.08	0.15	0.13	0.07	0.05
Total	97.7	101.0	100.3	100.9	97.4	98.4	96.8	98.1
Si	6.219	2.480	3.040	1.028	3.076	3.092	2.803	6.352
Ti	0.033	0.000	0.006	0.000	0.007	0.005	0.044	0.041
Al	3.229	1.525	2.004	1.955	2.643	2.503	1.596	2.937
Fe2+	1.881	0.005	1.830	0.007	0.392	0.549	0.984	1.874
Mn	0.014	0.000	0.082	0.001	0.002	0.010	0.003	0.014
Mg	1.843	0.000	0.287	0.000	0.005	0.002	1.489	2.032
Ca	1.639	0.529	0.700	0.001	1.958	1.978	0.005	1.655
Na	0.425	0.432	0.000	0.002	0.000	0.002	0.023	0.388
K	0.076	0.003	0.002	0.000	0.001	0.003	0.816	0.069
Cr	0.006	0.000	0.002	0.000	0.002	0.002	0.004	0.000
Zn	0.019	0.000	0.000	0.002	0.009	0.007	0.004	0.005
Total	15.38	4.975	7.952	2.996	8.095	8.153	7.772	15.37
An		0.550						
XFe	0.505		0.865				0.398	0.480
Aliv	1.781						1.197	1.648
Alvi	1.448						0.400	1.289
Xalm			0.631					
Xprp			0.099					
Xgrs			0.241					
Xsps			0.028					
Ps					11.887	16.555		

Table 5.2. Selected probe data from samples 938-124c recalculated according to Appendix A1

938-124c (continued)

Grt core	Grt	Grt	Grt	Grt	Grt rim	Bt	St	Hbl	Bt	Pl	Ms	Hbl	Grt rim	Hbl	Grt	Bt	Grt	Bt
38.27	38.52	38.56	38.99	38.13	38.59	37.84	28.95	42.28	37.13	60.46	45.39	41.17	37.18	46.73	37.68	36.13	37.79	44.28
0.10	0.09	0.04	0.05	0.00	0.03	1.11	0.53	0.37	1.15	0.00	0.45	0.35	0.16	0.34	0.00	1.12	0.00	0.35
21.74	21.59	21.87	21.84	21.48	21.75	19.76	53.87	17.20	18.58	24.69	29.92	15.61	19.57	7.33	19.16	14.14	19.40	28.11
29.89	29.79	29.46	29.34	30.76	31.18	16.30	12.44	16.34	15.66	0.29	1.23	15.21	30.92	14.15	30.38	21.80	29.33	1.69
0.64	0.70	0.68	0.70	2.11	1.90	0.01	0.12	0.03	0.06	0.04	0.00	0.00	0.94	0.14	1.22	0.08	0.80	0.03
3.18	3.22	3.34	3.77	2.87	3.29	13.13	2.04	8.20	13.50	0.01	0.91	8.14	3.52	11.08	3.28	9.60	3.03	0.97
6.55	6.27	6.25	5.96	3.67	4.03	0.07	0.04	10.00	0.11	6.73	0.12	10.56	5.63	11.33	6.20	0.30	8.24	0.35
0.05	0.07	0.00	0.07	0.09	0.06	0.24	0.01	1.34	0.21	7.41	0.97	1.35	0.00	0.44	0.17	0.00	0.19	0.67
0.00	0.01	0.03	0.00	0.01	0.04	8.79	0.00	0.46	8.53	0.09	8.99	0.51	0.00	0.07	0.00	8.35	0.00	8.64
n.a.	n.a.	n.a.	n.a.	n.a.	n.a.	n.a.	0.00	0.00	0.02	0.02	0.08	0.11	0.12	0.30	0.11	0.06	0.08	0.10
n.a.	n.a.	n.a.	n.a.	n.a.	n.a.	n.a.	1.55	0.04	0.09	0.04	n.a.	n.a.	n.a.	n.a.	n.a.	n.a.	n.a.	n.a.
100.4	100.2	100.2	100.7	99.1	100.9	97.3	99.5	96.3	95.0	99.8	88.1	93.0	98.0	91.9	98.2	91.6	98.9	85.2
3.012	3.032	3.029	3.041	3.049	3.032	2.749	7.893	6.324	2.760	2.697	3.249	6.380	3.030	7.244	3.065	2.895	3.049	3.284
0.006	0.005	0.002	0.003	0.000	0.002	0.061	0.110	0.042	0.064	0.000	0.024	0.040	0.010	0.039	0.000	0.068	0.000	0.020
2.017	2.003	2.026	2.008	2.025	2.016	1.692	17.316	3.032	1.628	1.298	2.526	2.853	1.880	1.340	1.837	1.336	1.846	2.457
1.967	1.961	1.935	1.914	2.057	2.049	0.990	2.836	2.043	0.974	0.011	0.074	1.971	2.107	1.834	2.067	1.461	1.980	0.105
0.043	0.046	0.045	0.046	0.143	0.127	0.001	0.028	0.004	0.004	0.002	0.000	0.000	0.065	0.018	0.084	0.005	0.055	0.002
0.373	0.378	0.391	0.438	0.341	0.386	1.422	0.830	1.827	1.496	0.001	0.097	1.881	0.427	2.561	0.398	1.147	0.364	0.107
0.553	0.529	0.526	0.498	0.315	0.340	0.006	0.011	1.602	0.009	0.322	0.010	1.753	0.491	1.882	0.540	0.026	0.713	0.028
0.007	0.010	0.000	0.011	0.014	0.009	0.034	0.005	0.388	0.030	0.641	0.135	0.407	0.000	0.132	0.026	0.000	0.030	0.096
0.000	0.001	0.003	0.000	0.001	0.004	0.815	0.001	0.088	0.809	0.005	0.821	0.100	0.000	0.014	0.000	0.853	0.000	0.817
-	-	-	-	-	-	-	0.000	0.000	0.001	0.001	0.004	0.014	0.008	0.037	0.007	0.004	0.005	0.006
-	-	-	-	-	-	-	0.312	0.005	0.005	0.001	-	-	-	-	-	-	-	-
7.978	7.966	7.957	7.958	7.945	7.964	7.768	29.342	15.36	7.780	4.977	6.939	15.400	8.017	15.101	8.026	7.794	8.040	6.921
										0.334								
0.841	0.839	0.832	0.814	0.858	0.842	0.411	0.774	0.528	0.394			0.512	0.831	0.417	0.839	0.560	0.845	0.495
						1.251		1.676	1.240		0.751	1.620		0.756		1.105		0.716
						0.441		1.357	0.389		1.775	1.233		0.584		0.231		1.741
0.670	0.673	0.668	0.661	0.720	0.706								0.682		0.669		0.636	
0.127	0.130	0.135	0.151	0.120	0.133								0.138		0.129		0.117	
0.188	0.181	0.182	0.172	0.110	0.117								0.159		0.175		0.229	
0.015	0.016	0.016	0.016	0.050	0.044								0.021		0.027		0.018	

Table 5.2. Selected probe data from samples 938-51 and 938-92a recalculated according to Appendix A1

938-51

	Hbl	St	Hbl	Pl	Pl	St	Ank	Hbl	Bt	Chl	Ep	Ep
SiO2	40.53	27.08	41.27	57.90	63.27	29.13	0.04	43.97	36.43	25.21	36.33	36.56
TiO2	0.32	0.64	0.00	0.00	0.00	0.39	0.06	0.35	0.63	0.10	0.35	0.15
Al2O3	16.74	50.70	16.33	25.30	24.88	52.90	0.01	17.30	14.54	19.60	22.06	22.76
FeO	14.29	12.29	13.34	0.00	0.23	11.71	11.26	14.66	12.57	14.12	9.75	9.33
MnO	0.14	0.17	0.00	0.00	0.00	0.16	0.36	0.16	0.17	0.26	0.02	0.00
MgO	9.44	2.54	9.93	0.00	0.00	2.39	19.08	9.94	14.11	19.69	0.06	0.22
CaO	10.92	0.00	11.06	7.74	6.60	0.01	30.25	10.64	0.18	0.13	23.31	23.10
Na2O	0.25	0.49	1.41	7.06	7.74	0.03	0.05	1.58	0.00	0.00	0.00	0.00
K2O	0.00	0.00	0.21	0.10	0.08	0.03	0.01	0.27	8.71	0.04	0.03	0.00
Cr2O3	0.00	0.16	0.00	0.00	0.01	0.16	0.04	0.09	0.05	0.14	0.24	0.37
ZnO	n.a.	n.a.	n.a.	n.a.	0.07	0.18	0.02	0.00	n.a.	n.a.	n.a.	n.a.
Total	92.6	94.1	93.6	98.1	102.9	97.1	61.2	99.0	87.4	79.3	92.2	92.5
Si	6.247	7.802	6.298	2.636	2.730	8.058	0.001	6.342	2.925	2.780	3.116	3.111
Ti	0.037	0.139	0.000	0.000	0.000	0.081	0.001	0.038	0.038	0.009	0.023	0.010
Al	3.042	17.221	2.938	1.358	1.265	17.255	0.000	2.942	1.376	2.548	2.231	2.283
Fe2+	1.842	2.961	1.702	0.000	0.008	2.710	0.266	1.768	0.844	1.303	0.699	0.664
Mn	0.018	0.041	0.000	0.000	0.000	0.037	0.009	0.019	0.011	0.024	0.002	0.000
Mg	2.168	1.091	2.258	0.000	0.000	0.987	0.803	2.136	1.688	3.237	0.007	0.027
Ca	1.803	0.000	1.808	0.378	0.305	0.003	0.915	1.644	0.015	0.015	2.142	2.106
Na	0.075	0.274	0.417	0.623	0.648	0.017	0.003	0.443	0.000	0.000	0.000	0.000
K	0.000	0.000	0.041	0.006	0.004	0.009	0.000	0.049	0.892	0.005	0.003	0.000
Cr	0.000	0.037	0.000	0.000	0.000	0.035	0.001	0.010	0.003	0.012	0.016	0.025
Zn	-	-	-	-	0.002	0.036	0.000	0.000	-	-	-	-
Total	15.233	29.567	15.463	5.000	4.963	29.229	1.999	15.390	7.793	9.934	8.240	8.226
XAn				0.377	0.320							
XFe	0.459	0.731	0.430			0.733	0.249	0.453	0.333	0.287		
Aliv	1.753		1.702					1.658	1.075	1.220		
Alvi	1.289		1.235					1.284	0.301	1.328		
Xalm								-				
Xprp								-				
Xgrs												
Xsps												
Ps											25.637	23.892

938-92a

	Cum	Grt	Chl 2°	Chl 1°	Pl	Hbl	Cum	Hbl
SiO2	51.70	37.37	23.83	25.02	60.11	42.03	51.95	41.31
TiO2	0.10	0.00	0.19	0.15	0.11	0.24	0.00	0.45
Al2O3	0.85	19.77	18.04	19.03	20.05	13.01	0.44	14.34
FeO	23.25	33.84	35.57	24.02	0.24	16.40	25.15	15.53
MnO	0.42	1.01	0.37	0.30	0.05	0.13	0.23	0.00
MgO	16.04	3.58	8.04	14.80	0.00	8.81	14.94	9.19
CaO	0.49	3.64	0.12	0.10	4.22	9.75	0.60	10.10
Na2O	0.00	0.00	0.00	0.00	8.71	1.73	0.00	1.86
K2O	0.03	0.00	0.00	0.00	0.04	0.19	0.00	0.35
Cr2O3	0.00	0.00	0.04	0.18	0.00	0.14	0.18	0.18
ZnO	n.a.	n.a.	n.a.	n.a.	n.a.	n.a.	n.a.	n.a.
Total	92.9	99.2	86.2	83.6	93.5	92.4	93.5	93.3
Si	7.965	3.028	2.733	2.766	2.844	6.586	8.017	6.403
Ti	0.011	0.000	0.017	0.012	0.004	0.028	0.000	0.052
Al	0.153	1.889	2.440	2.480	1.119	2.402	0.081	2.621
Fe2+	2.995	2.294	3.411	2.221	0.009	2.149	3.246	2.013
Mn	0.054	0.069	0.036	0.028	0.002	0.017	0.030	0.000
Mg	3.683	0.432	1.374	2.438	0.000	2.058	3.436	2.122
Ca	0.081	0.316	0.014	0.011	0.214	1.637	0.099	1.677
Na	0.000	0.000	0.000	0.000	0.799	0.524	0.000	0.558
K	0.007	0.000	0.000	0.000	0.003	0.039	0.000	0.068
Cr	0.000	0.000	0.004	0.015	0.000	0.018	0.022	0.023
Zn	-	-	-	-	-	-	-	-
Total	14.950	8.028	10.028	9.973	4.994	15.458	14.932	15.536
An					0.211			
XFe	0.448	0.842	0.713	0.477		0.511	0.486	0.487
Aliv	0.035		1.267	1.234		1.414	-0.017	1.597
Alvi	0.118		1.173	1.247		0.988	0.098	1.024
Xalm		0.737						
Xprp		0.139						
Xgrs		0.102						
Xsps		0.022						
Ps								

5.2 Petrography and mineral chemistry of the low variance kyanite–staurolite–hornblende garbenschiefer

Large regions of the European Alps are dominated by high pressure mineral assemblages attributable to blueschist and eclogite facies metamorphism (Barnicoat & Fry, 1986; Dal Piaz & Lombardo, 1986; Pognante, 1991; Bowtell et al., 1994). In some cases (e.g. the Dora Maira massif) very high pressure pyrope–coesite-bearing assemblages are thought to have equilibrated at pressures up to and exceeding 30 kbar (Chopin, 1984). However, high pressure parageneses are largely restricted to the Western Alps. In the Eastern Alps, metamorphism is generally low-medium pressure greenschist to amphibolite facies, however the sparsely exposed Penninic units and Austroalpine complexes (e.g. the Koralm and Ötztal) provide some evidence of higher pressure metamorphism in the Eastern Alps (e.g. Miller, 1977; England & Holland, 1979; Droop et al., 1990). Ernst (1973) has suggested that the paucity of high pressure assemblages in the Eastern Alps may be due to the severe (and often complete) thermal overprinting experienced by the region as the terrain evolved. However the lower pressure greenschist to amphibolite facies metamorphism observed in the Tauern Window is significantly younger than that in the surrounding Austroalpine rocks (Frank et al., 1992), suggesting that the problem is more complex. Frank et al. (1992) suggest that the earlier phase of metamorphism observed in the Penninic units may be the high pressure phase associated with widespread medium pressure metamorphism observed in the Austroalpine units. The kyanite–staurolite–hornblende assemblages which have been described from rocks of basaltic composition in the southwestern Tauern Window may provide evidence of this early high pressure phase which has since been almost entirely obliterated (Selverstone et al., 1984).

5.2.1 Geological setting

The Tauern Window is one of few tectonic windows in the Eastern Alps where the Penninic basement is observed beneath the structurally overlying Austroalpine nappes. This basement comprises three tectonic slices (Fig. 5.1); (i) the pre-Mesozoic Zentralgneis (Cliff, 1981), a felsic orthogneiss at the base of the section, (ii) the Palaeozoic Lower (Inner) Schieferhülle and (iii) the Permo-Mesozoic Upper (Peripheral) Schieferhülle (Ackermand et al., 1978). The Lower Schieferhülle consists mainly of paragneisses, mica schists, quartzites and amphibolites, whereas the Upper Schieferhülle is composed of calc-mica schists, and intercalated greenstones (Morteani, 1974; Ackermand et al., 1978). The relationships between these tectonic slices is somewhat unclear, especially with respect to the status of the intervening Lower Schieferhülle, which has been interpreted as either an autochthonous section, into which the felsic magma which is now the Zentralgneis intruded (Selverstone & Munoz, 1987), or as an allochthonous sheet, either grouped with the Upper Schieferhülle (Bickle et al., 1975) or separately emplaced between the Penninic Basement and the Austroalpine nappes

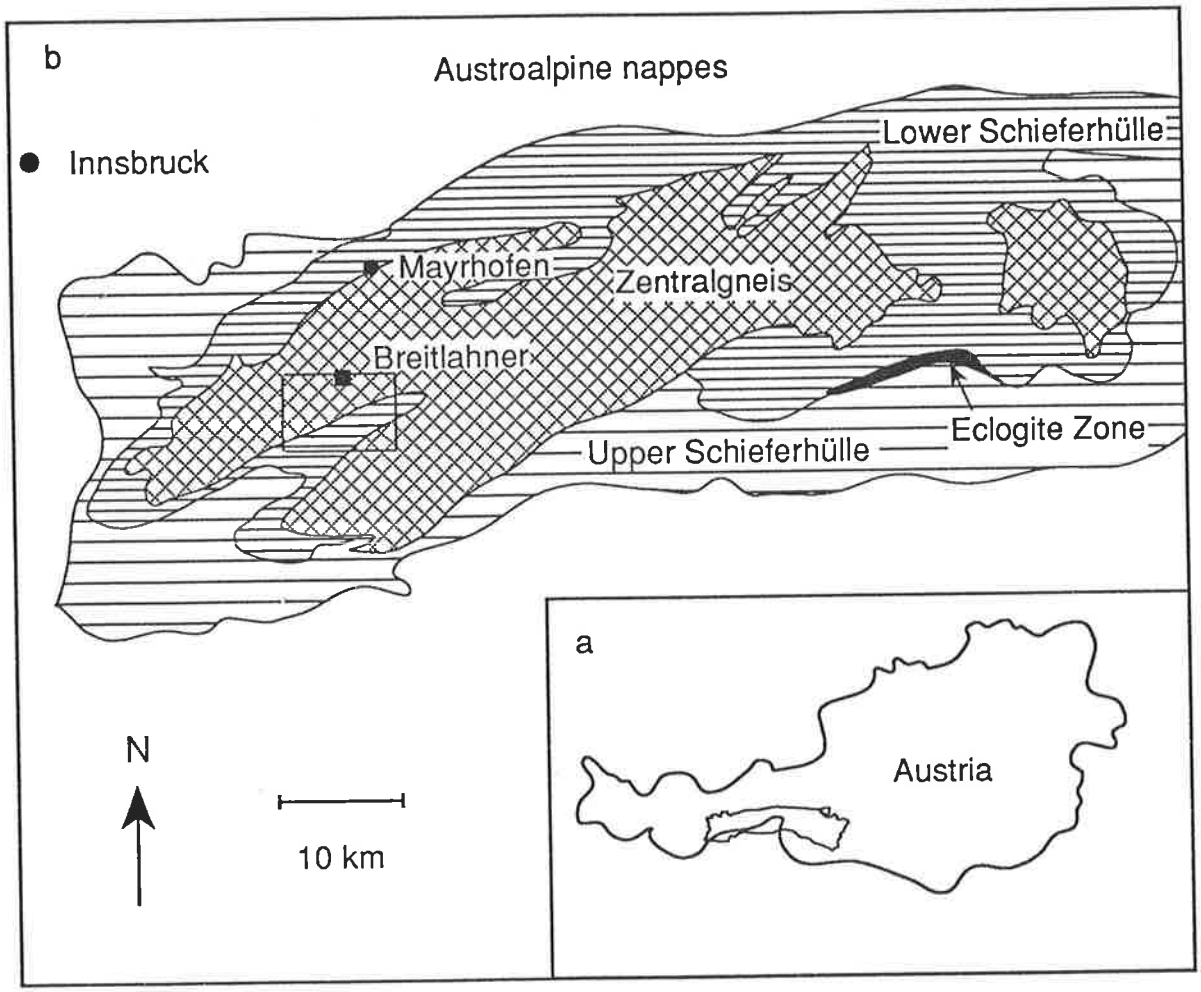

Figure 5.1a Sketch map showing the location of the Tauern Window. b, Geological sketch map of the western Tauern Window, after Selverstone and Spear, 1985.

(Selverstone et al., 1984). A number of workers have also suggested that the Lower Schieferhülle plays a somewhat intermediate role as an autochthonous to parautochthonous nappe over the Zentralgneis basement (Morteani, 1974; Selverstone & Spear, 1985).

In the southwestern Tauern Window (Zillertaler Alpen), in a region sectioned by the Schlegeis and Zummgrund glacial valleys, a narrow parcel of Lower Schieferhülle is exposed between two tongues of Zentralgneis. These rocks belong to the Greiner series (Morteani, 1974) and consist of garnet, kyanite and staurolite mica-schists, amphibolites and spectacular hornblende garbenschiefer. Samples were collected from this parcel of the Lower Schieferhülle on either side of both valleys over two profiles approximately 4 km in length (see Appendix A10, Fig. A10.1).

5.2.2 Petrography and mineral chemistry

The rocks of the Lower Schieferhülle are compositionally layered on a centimetre to metre scale with different layers varying in mineralogy, grainsize and the degree of foliation development and overprinting. The rock-types present may be broadly divided into hornblende gneisses (± staurolite, garnet, kyanite, ankerite, calcite), mica-schists (± staurolite, garnet, kyanite) and combinations of these. The hornblende gneisses (garbenschiefer) of the Lower Schieferhülle are of interest here.

The majority of samples collected from the Schlegeis and Zummgrund valleys contain a strong foliation defined by white mica, biotite, hornblende, epidote, rutile, ilmenite, quartz ribbons and plagioclase aggregates. Garben of hornblende may be aligned in the foliation plane but also may cross-cut it (e.g. Selverstone, 1993). Many samples also contain evidence of a second foliation manifest as a crenulation of the main foliation. Evidence of further deformation is often preserved as extensive micro-boudinage and fracturing of garnet and hornblende grains. In addition to their occurrence in the foliation, chlorite, white mica, hornblende and biotite all occur as coarse, cross-cutting grains.

Detailed study of the textural relationships in the hornblende garbenschiefer reveals that kyanite, staurolite, garnet, hornblende, ankerite and epidote are syn- and post-kinematic with respect to *both* foliation forming events. Neither the timing, nor the order of mineral growth is consistent between samples and the paragenesis is not progressively developed from one location to another. The consistency of mineralogy between the garbenschiefer samples, despite their textural variation, suggests that the samples contain equilibrium assemblages which were formed under similar pressure and temperature. As such, they define subsets of a single compatibility diagram which will be compared to those from other regions in Chapter 6. As no clear, consistent petrogenetic sequence can be determined, it is not possible to discern reaction relations from the samples. (The petrography (Table 5.1) and mineral chemistry (Table 5.2) of the hornblende garbenschiefer which are summarised here are described more fully in Appendix. A10. For a list of abbreviations and mineral formulae see Appendix A1.)

The hornblende garbenschiefer are generally dominated by fine aggregates of zoned

plagioclase, large, undulose quartz grains or aggregates and hornblende which may lie parallel to quartz and plagioclase aggregates and/or, across it, either randomly oriented or defining a second foliation (e.g. Fig. 5.2). The cores of randomly oriented hornblende often contain straight (or rarely crenulated) inclusion trails of plagioclase, epidote, ankerite or quartz which are parallel to those in other porphyroblasts (e.g. garnet) and to the matrix foliation. Hornblende which is parallel to the foliation typically contains relatively few, randomly oriented inclusions. Hornblende is generally tschermakitic or ferro-tschermakitic in composition (Table 5.2) and may be slightly zoned with a slightly Na-rich core and Na-poor rim. It is commonly surrounded by a rim of greenish, Fe-rich biotite and Fe-rich, dark green chlorite (e.g. Fig. 5.2).

Plagioclase (typically oligoclase to andesine) often exhibits normal optical zoning, both as a matrix phase and as inclusions in porphyroblasts, however differences in composition from cores to rims of plagioclase are typically less than 2 percent (Table 5.2). Good twinning is rarely developed (partly due to the generally small grain size), however in coarse grains cleavage planes parallel to the twin lamellae are often the site of sericitisation..

Abundant inclusions are concentrated in the cores of coarse garnet grains with almost totally inclusion-free, euhedral rims. The inclusion trails (e.g. Figs. 5.3, 5.4) are generally continuous with the matrix foliation. Garnet porphyroblasts are often wrapped by the foliation and are occasionally surrounded by well developed pressure shadows. Anhedral garnets both with or without inclusion trails are generally elongate parallel to the foliation (Fig. 5.5). The almandine-rich (X_{alm} 0.58-0.74, see Appendix A1 for abbreviations) garnet grains are compositionally homogeneous or only weakly zoned, most noticeably in the grossular end-member contents, by about 7 mol % (e.g. Fig. 5.6, Table 5.2). The general lack of a strong zoning profile suggests that all but the coarsest grains have re-equilibrated during and after the high-temperature part of their metamorphic history.

Staurolite is observed in contact with most phases with no obvious reaction relationships (e.g. Fig. 5.7). It is commonly subhedral to euhedral and either aligned with or cross-cutting the foliation. Staurolite is generally Zn poor with a maximum of 0.36 moles of Zn per unit formula (44 O+ 4 (OH)) in amphibolites (Table 5.2). Kyanite forms weakly aligned, random and crenulated optically continuous aggregates in the quartz–plagioclase matrix, near hornblende and garnet grains and also in mica-rich portions (e.g. Figs. 5.8, 5.9). It occasionally forms very coarse aggregates with staurolite which may be aligned with or cross-cut the foliation. Staurolite is associated with biotite and chlorite, hornblende and plagioclase (Fig. 5.10) and kyanite forms crenulated sheaves in the biotite-rich part of some samples (Fig. 5.11).

Biotite occurs in varying proportions, both as a primary, foliation-forming phase (e.g. Fig. 5.11) and as an alteration product (with chlorite) of hornblende (e.g. Figs. 5.2 and 5.12) and early biotite. Where two generations of biotite are present they are distinguishable by greenish, Fe-rich nature of late biotite as well as by their textural relationships with the foliation phases. Chlorite also developed during at least two stages. Mats of chlorite define the

Figure 5.2. Cross-cutting hornblende with weak straight inclusion trails which are parallel to the weak matrix foliation (parallel to the staurolite elongation direction). Hornblende is rimmed by finer grained Fe-rich biotite (938-127) width of view 2 mm.

Figure 5.3. S-shaped inclusion trails in the core of garnet. Note that rims are relatively inclusion-free and euhedral and that garnet overgrows the foliated matrix (938-52c) scale bar = 2mm.

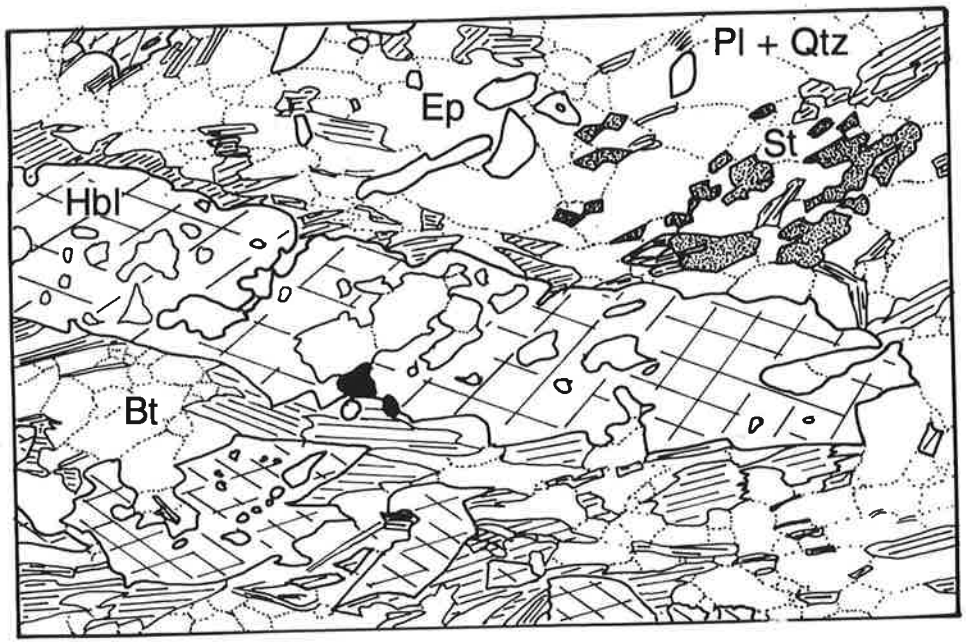
Pl + Qtz
Ep
St
Hbl
Bt

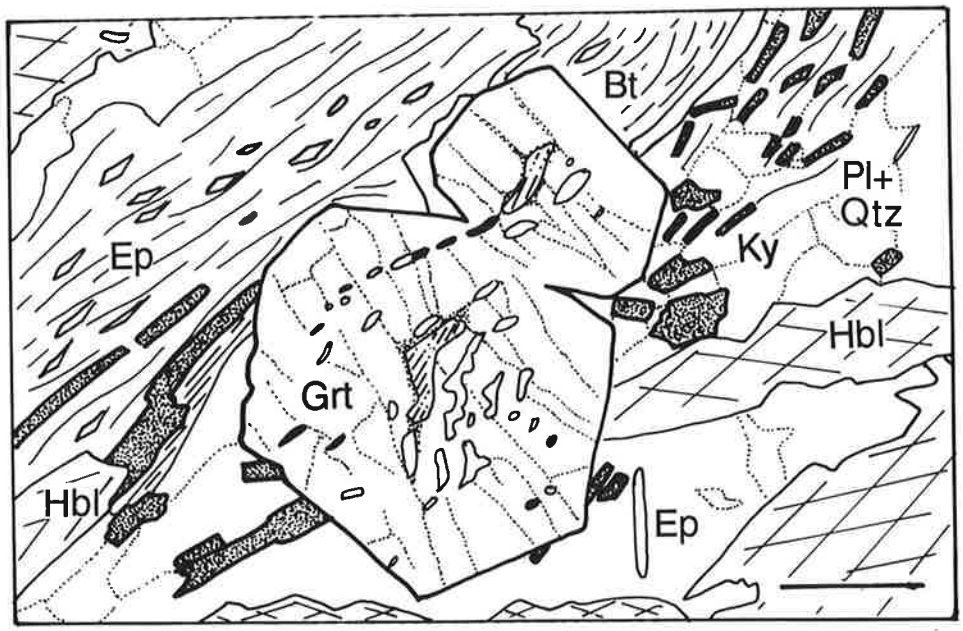
Bt
Pl+
Qtz
Ky
Ep
Hbl
Grt
Hbl
Ep

Figure 5.4. Euhedral garnet with straight inclusion trails in a hornblende-quartz-plagioclase matrix (938-33b). Inclusion trails are parallel to the weak matrix foliation, shown in this view by the orientation of rutile and ilmenite grains (in black). Width of view 2 mm.

Figure 5.5. Hornblende, anhedral garnet and elongate plagioclase defining a weak foliation which is parallel to the weakly defined straight inclusion trails in garnet (938-33b) and parallel to the short edge of the diagram, width of view 2 mm.

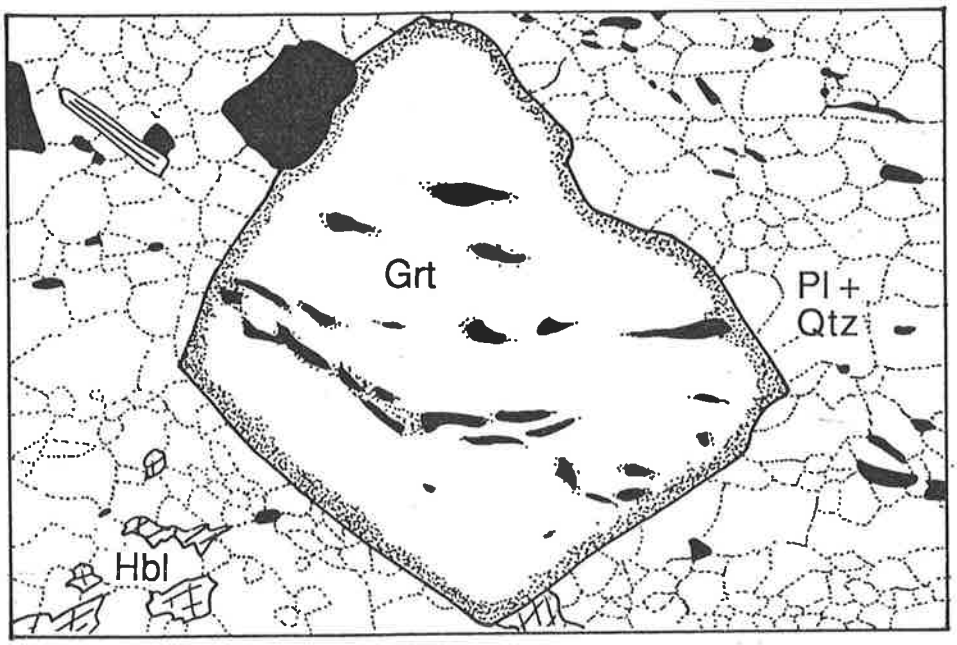
Grt
Pl +
Qtz
Hbl

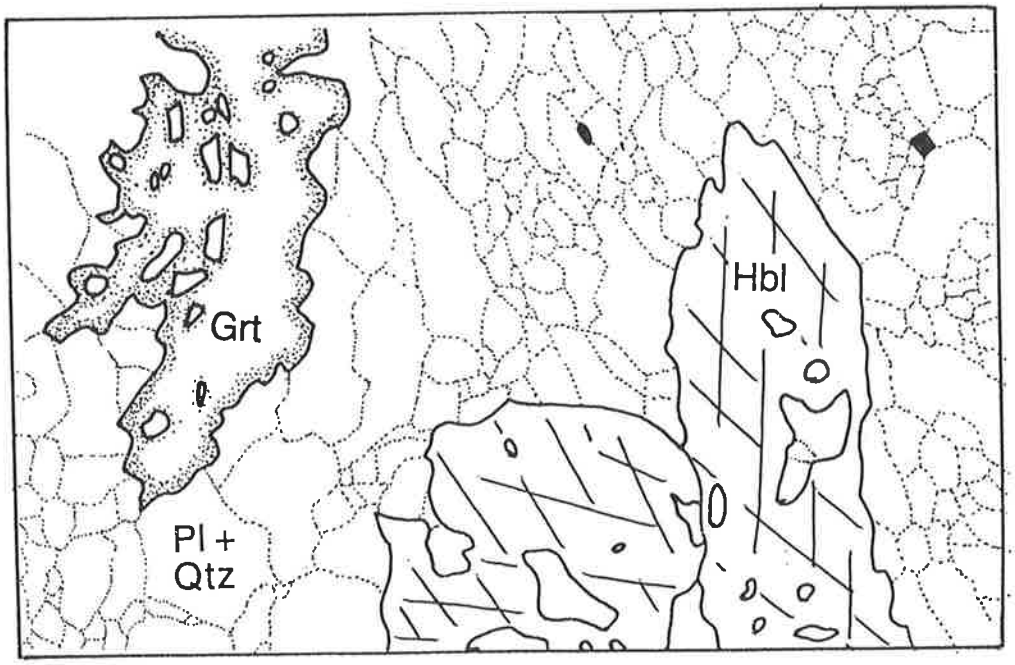
Grt
Hbl
Pl +
Qtz

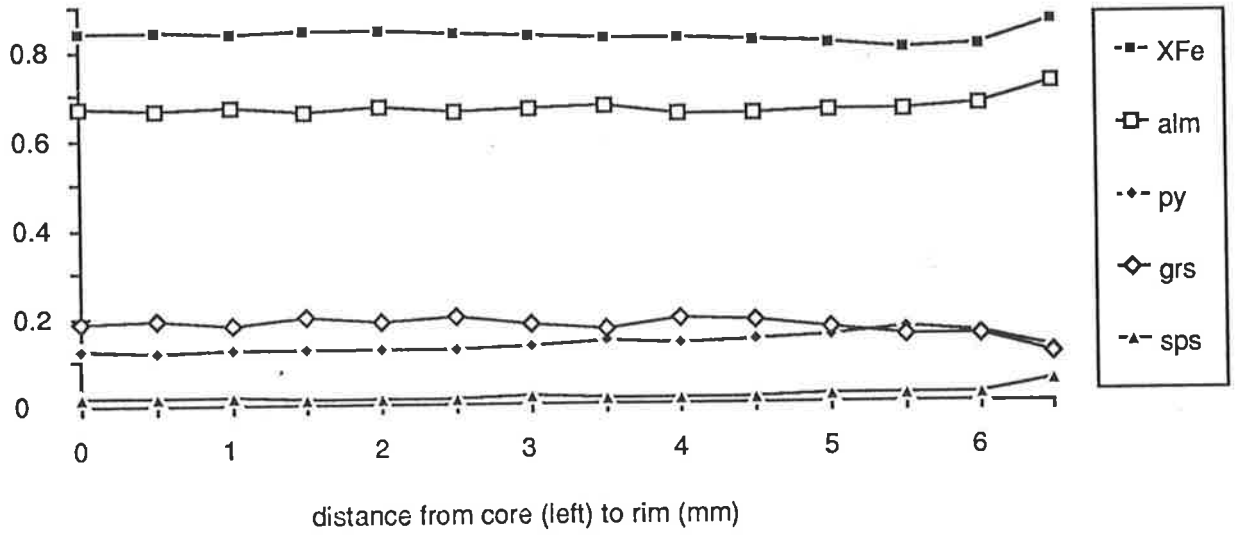

Figure 5.6. Compositional variation across a very weakly zoned garnet, note the small discontinuity at the rim. Sample 938-124c.

Figure 5.7. Staurolite-hornblende equilibrium in a quartz-plagioclase matrix (938-51), width of view 2 mm.

Figure 5.8. Kyanite-hornblende in contact in a quartz-plagioclase matrix (938-51). The fine lines represent contorted fine, linear inclusion trails of paragonite, width of view 2 mm.

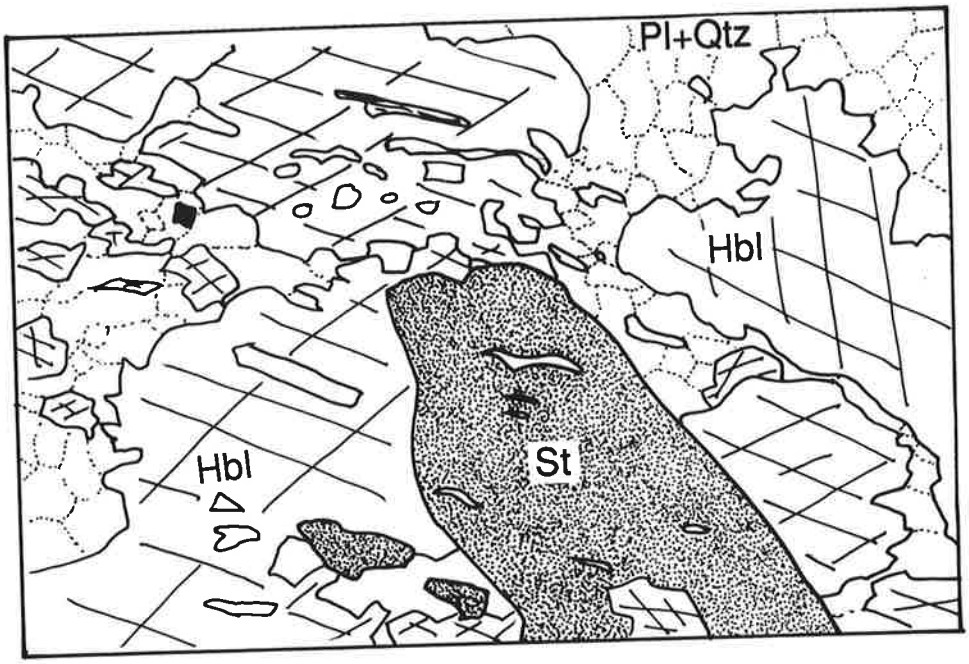
Pl+Qtz
Hbl
St
Hbl

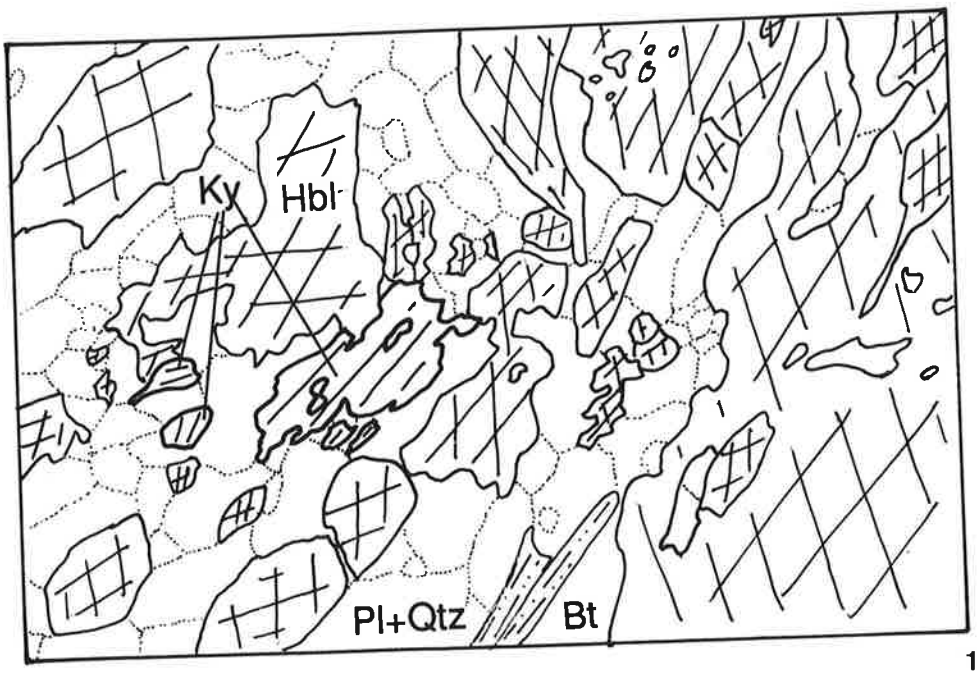
Ky
Hbl
Pl+Qtz
Bt

Figure 5.9. Kyanite, hornblende and biotite in a quartz-plagioclase matrix in which plagioclase contains convoluted inclusion trails of white mica (938-52c) width of view 2 mm.

Figure 5.10. Aggregate of staurolite with chlorite biotite, plagioclase and hornblende hornblende (938-91a) width of view 2 mm.

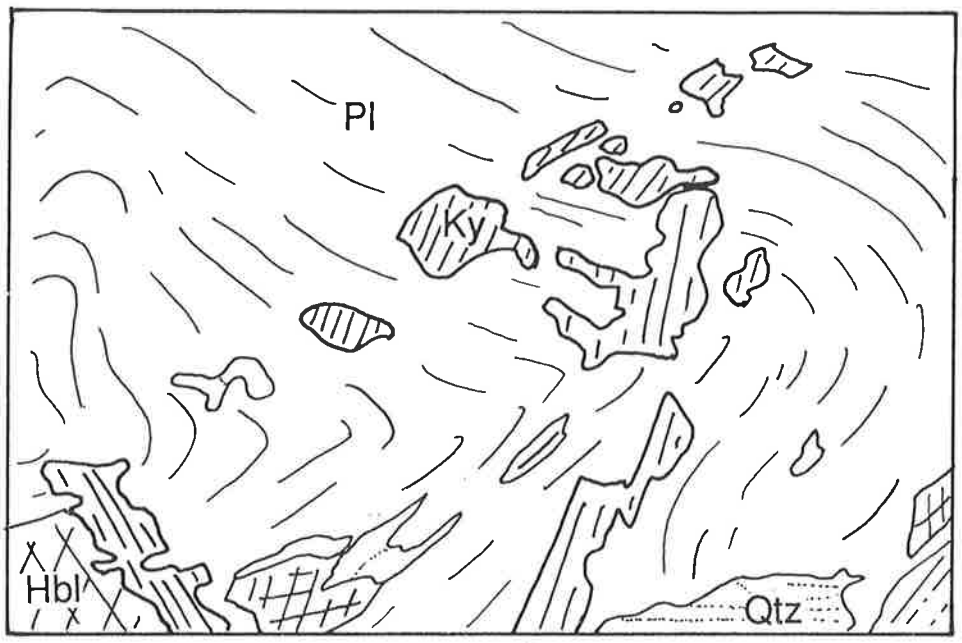
Pl
Ky
Hbl
Qtz


Hbl
Chl
St
Pl +
Qtz
Bt

Figure 5.11. Crenulated kyanite and biotite with quartz and plagioclase (938-61e) width of view 2 mm.

Figure 5.12. Fractured hornblende in which the fracture is infilled with chlorite–biotite–white mica–plagioclase–quartz (938-124c) width of view 2 mm.

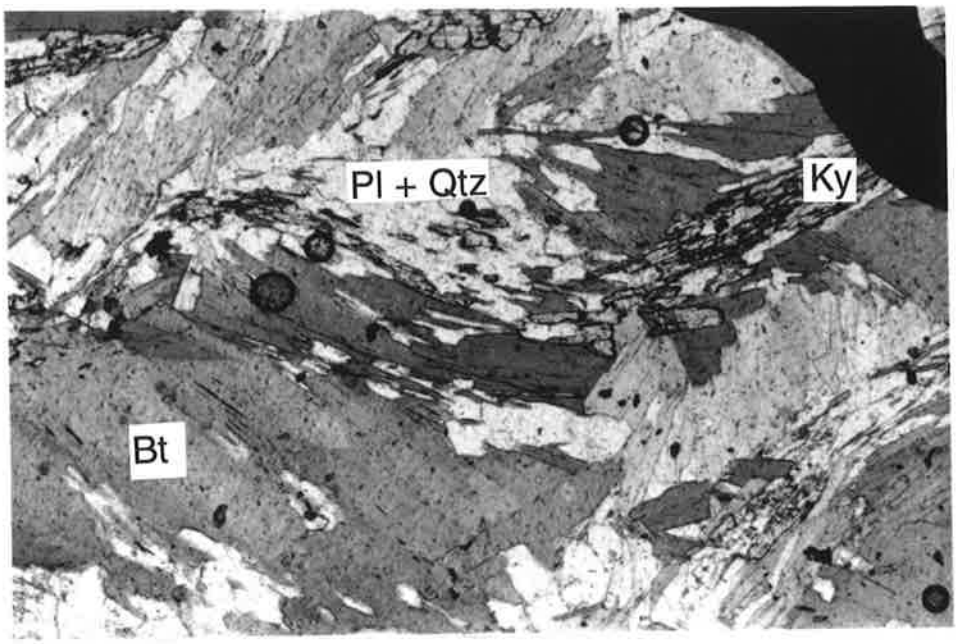
Pl + Qtz
Ky
Bt

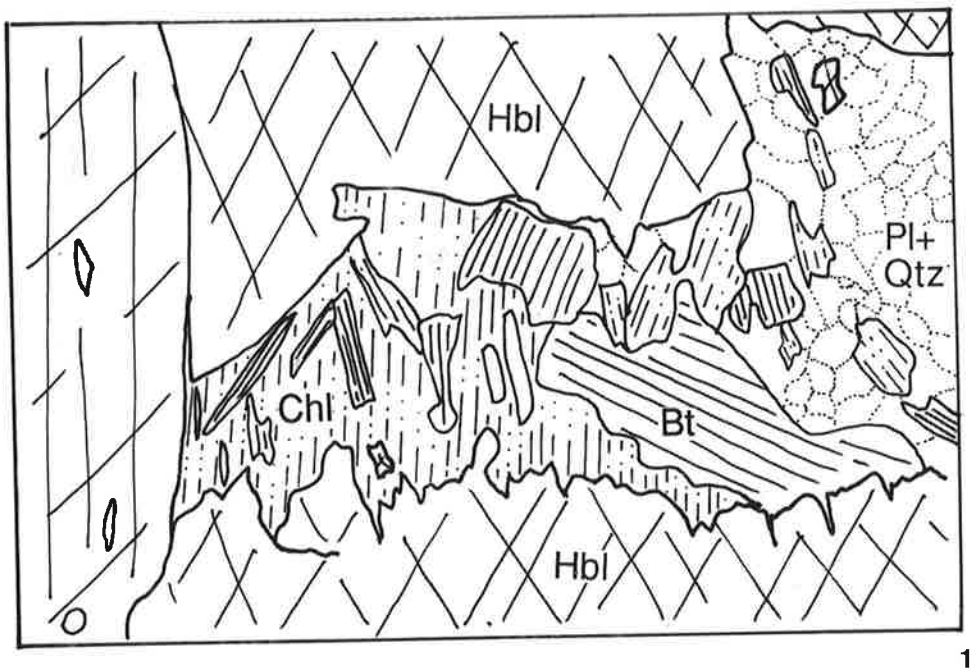
Hbl
Pl+
Qtz
Chl
Bt
Hbl

foliation direction in some samples whereas later, cross-cutting or infilling chlorite is associated with altered or fractured hornblende (e.g. Fig. 5.12), biotite or garnet or in cross-cutting quartz veins. Fine grained white mica (either muscovite, or more often a paragonite-dominated solid solution, Table 5.2) defines the foliation direction in a number of samples. It also occurs as acicular inclusions in plagioclase which may exhibit a very contorted geometry (Fig. 5.9). Coarser grained white mica may be parallel to the foliation or, more commonly, cross-cuts the foliation.

Cummingtonite generally forms fine to medium epitaxial grains on hornblende (Fig. 5.13). Epidote (Ps_{8-30}) occurs as inclusions in most phases and forms part of most matrix associations as relatively coarse, euhedral grains or very fine anhedral grains in large aggregates. It is generally parallel to the foliation and shows zonal birefringence due to compositional zoning and slight to strong pleochroism. Coarse epidote grains are discontinuously zoned, from pale green, high birefringence epidote in the core to colourless, lower birefringence (less Fe-rich) epidote in the rim (Table 5.2). Chemical variation in epidote due to zonation (from clinozoisite-rich cores to epidote-rich rims) may be as much as 20 molar %. Ilmenite often defines inclusion trails in garnet and hornblende, however the dominant oxide in the matrix is rutile. Euhedral magnetite is very rarely present in the matrix and as inclusions. Ankerite or, rarely, calcite occurs in the matrix as relatively coarse subhedral to anhedral grains. It is generally the most Mg-rich phase present with $X_{Fe,Ank}$ in the range 0.19-0.27 (Table 5.2). The order of Fe-enrichment amongst the phases in these assemblages is consistent and increases in the order ankerite ($X_{Fe,Ank}$ 0.19-0.27) < chlorite ($X_{Fe,Chl}$ 0.24-0.46) < biotite ($X_{Fe,Bt}$ 0.31-0.56) < cummingtonite ($X_{Fe,Cum}$ 0.45-0.49) hornblende ($X_{Fe,Hbl}$ 0.30-0.58) < staurolite ($X_{Fe,St}$ 0.70-0.82) < garnet ($X_{Fe,Grt}$ 0.78-0.90, Table 5.2).

The garbenschiefer appear to fall into an aluminous and a less aluminous classification; the mineralogy of the more aluminous hornblende garbenschiefer involves kyanite, staurolite, garnet, hornblende, chlorite, plagioclase, quartz, biotite, white-mica, ankerite, epidote and rutile, whereas less aluminous assemblages involve garnet, cummingtonite, hornblende, chlorite, plagioclase, quartz, biotite, ankerite, epidote and rutile. The following sections deal with the compatibility relations defined by these assemblages.

5.3 Representation of amphibolites in compositional space

Graphical representation is an important tool for developing an understanding of the phase relationships in metamorphic rocks. The following sections devise a graphical representation for amphibolites (which is also used in Chapters 4 and 6) and discusses the compatibility relations of the mineral assemblages in terms of this representation.

The chemical complexity of amphibolites and amphiboles themselves has been noted frequently in the past. Robinson et al. (1982, pp. 2) commented that amphibole acted as a "mineralogical shark in an sea of unsuspecting elements". Amphibolites typically contain significant amounts of Na_2O, CaO, FeO, MgO, Al_2O_3, SiO_2, H_2O as well as lesser, but often

Figure 5.13. Fine grained cummingtonite in an epitaxial relationship to foliation-forming hornblende (938-92a) width of view 2 mm.

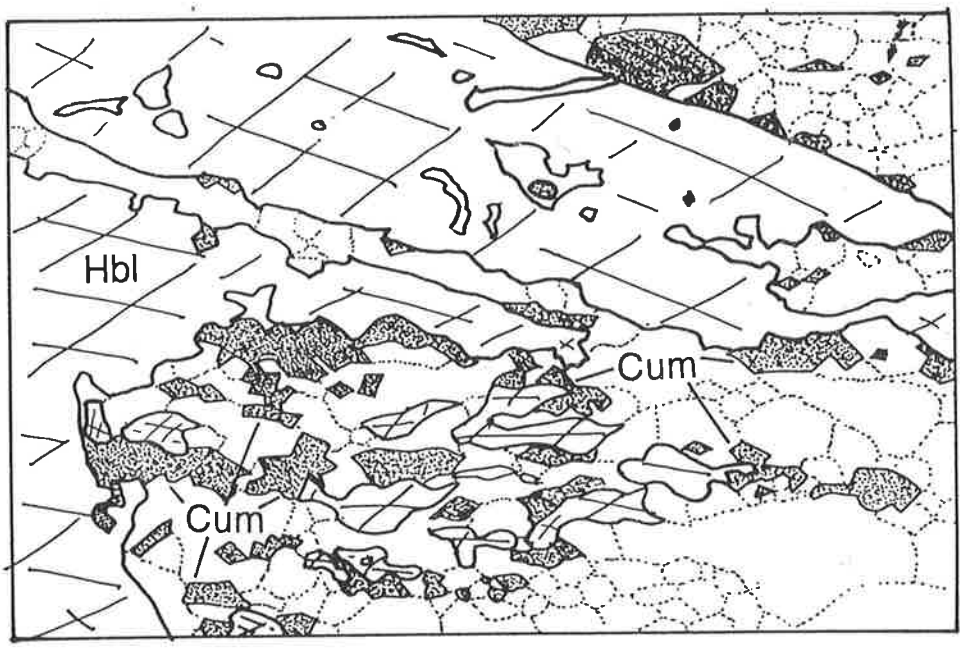
Hbl
Cum
Cum

significant proportions of K_2O, Fe_2O_3, MnO, TiO_2, CO_2 and minor ZrO_2, ZnO, Cr_2O_3 and P_2O_5. In order to graphically represent the chemistry of the phases and the compatibility relations of amphibolites, this list of components must be significantly reduced to include only those which are likely to have an important bearing on the observed phase relations. Some components (e.g. ZrO_2 and P_2O_5, TiO_2, CO_2, K_2O and Fe_2O_3) are generally present in significant proportions in a single phase (e.g. zircon, apatite, ilmenite or rutile, a carbonate phase, biotite or muscovite and magnetite, respectively). As each additional component stabilises only one phase, the variance of a given assemblage is not affected by their presence and they may be neglected. Other components such as MnO, ZnO and Cr_2O_3, often occur in minor proportions in phases which can otherwise be described by the major elements Na_2O, CaO, FeO, MgO, Al_2O_3, SiO_2. Where these components occur in significant amounts they increase the stability of the phases they occur in with respect to the major element compositional system. In order to simplify the compatibility relations, phases which are stabilised by a minor component are generally neglected (e.g. Thompson, 1954) and are considered to be metastable in the major-element-defined model system. Thus we are left with a list of major components: Na_2O, CaO, FeO, MgO, Al_2O_3, SiO_2, H_2O (NCFMASH).

Although this is a significant simplification of the components, the compositional system remains too complex for graphical representation (requiring 6 dimensions to represent the seven components). The list of components may be further simplified by assuming that other phases are "in excess", that is, they are always present in sufficient proportions that their abundance is never a limiting factor on any reaction. In the case of many amphibolites, quartz and plagioclase may be considered to be in excess, while an aqueous vapour is also considered to be present (or μ_{H_2O} may be generally considered to be constant). This reduces the number of components to four, i.e. CAFM. Although four-component, three-dimensional compatibility diagrams may be represented in two dimensions, they are generally difficult to read. As calcic amphibole is also consistently present in amphibolites, it is considered to be a further "excess" phase (cf. Spear, 1978; Spear & Rumble, 1986), further reducing the components to AFM. It must be noted that the composition of hornblende and plagioclase vary over the compatibility diagram for a particular set of P-T conditions. Thus, the phase relations in kyanite–staurolite-bearing amphibolites from the Zillertal and amphibolites from other localities will be represented on compatibility diagrams with apices $AlO_{3/2}$, FeO and MgO (AFM) with hornblende, plagioclase, quartz and an aqueous vapour in excess. Each assemblage is plotted separately due to the variation in the composition of both hornblende and plagioclase between assemblages and the results have been combined to form compatibility diagrams for the Zillertal amphibolites (Fig.5.14).

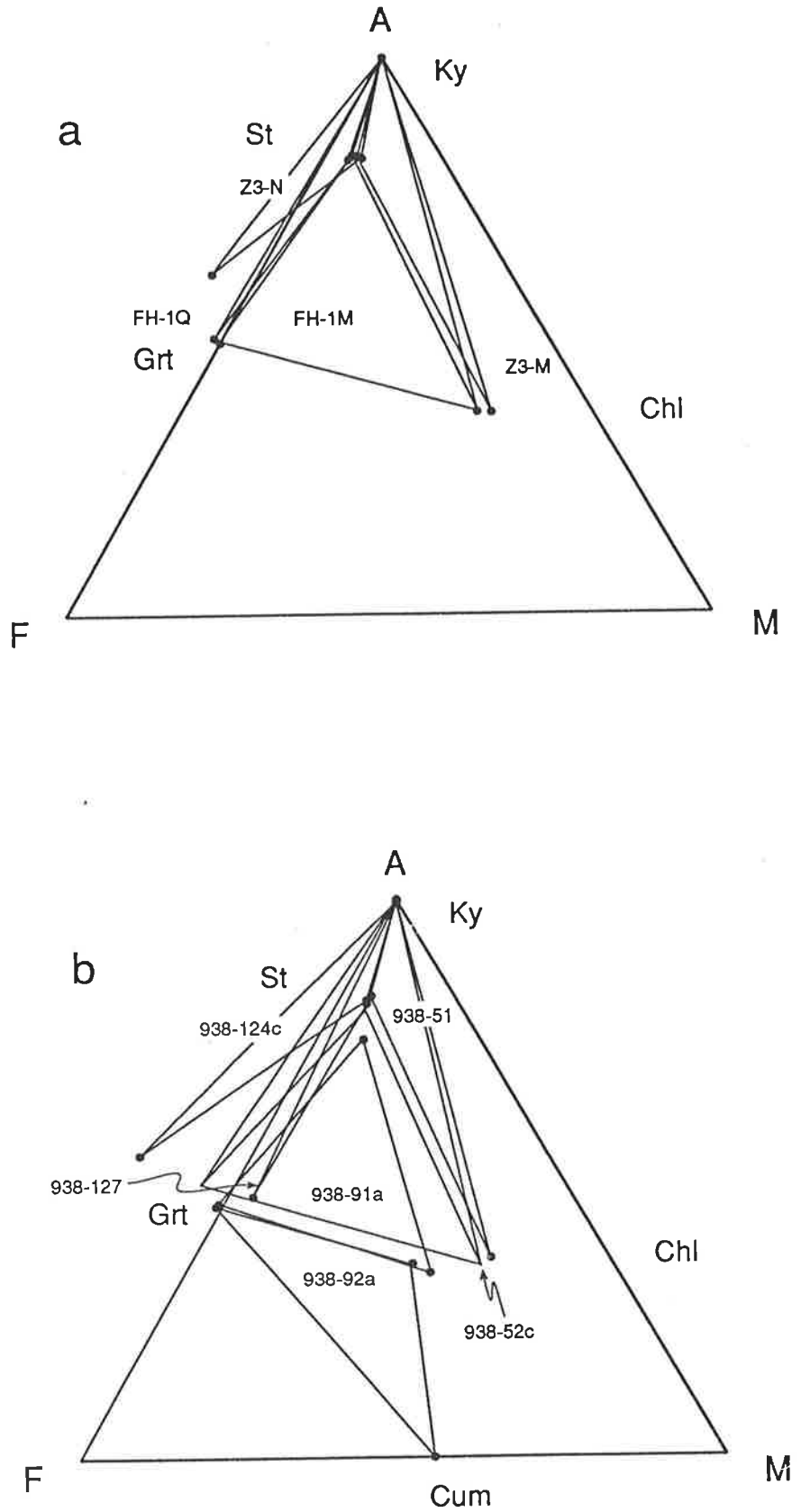

Figure. 5.14. The compatibility relations in amphibolites from the Zillertaler Alpen represented in AFM (AlO3/2, FeO, MgO with hornblende, plagioclase, quartz and an aqueous vapour in excess). a) data repored by Selverstone et al. (1984) b) from this study.

5.4 Compatibility relations in amphibolites from the Zillertal

Figures 5.14a and 5.14b depict the compatibility relations of the Zillertal amphibolites. Figure 5.14a illustrates the divariant (in NCFMASH) assemblages kyanite–staurolite–garnet and kyanite–staurolite–chlorite (+hornblende, plagioclase, quartz, vapour) and the univariant assemblage kyanite–staurolite–garnet–chlorite reported by Selverstone et al. (1984). Figure 5.14b illustrates the divariant (in NCFMASH) assemblages found in this study including the new assemblages staurolite–garnet–chlorite and garnet–chlorite–cummingtonite (+hornblende, plagioclase, quartz, vapour). The low variance hornblende garbenschiefer define four distinct assemblages. Fe-rich, aluminous amphibolites contain kyanite–staurolite–garnet–hornblende–plagioclase–quartz–vapour, whereas Mg-rich rocks contain kyanite–staurolite–chlorite–plagioclase–quartz–vapour assemblages. Less aluminous samples may contain cummingtonite with garnet or chlorite and hornblende, plagioclase, quartz and vapour and intermediate composition samples contain subsets of the assemblage staurolite–garnet–chlorite–hornblende–plagioclase–quartz–vapour.

The equilibrium tie-triangles determined from the Zillertal equilibria, are schematically consistent, however, they overlap each other slightly and are also overlapped by a four phase assemblage; kyanite–staurolite–garnet–chlorite (samples 938-52c from this study and FH-1M from Selverstone et al., 1984). According to the phase rule, crossed tie-lines may not occur in compatibility diagrams drawn for rocks which formed under the same intensive variables and this implies that either:

(1) the garbenschiefer assemblages formed under the same intensive variables but involved additional components which stabilised some phases out of their model system stability fields (in a larger compositional system), or

(2) the individual assemblages did not all equilibrate with the same intensive variables (P-T-μ_{H_2O}-f_{O_2} etc).

Selverstone et al. (1984) suggested that garnet was stabilised in some of the Zillertal assemblages by the presence of manganese, however the majority of their reported analyses and those from this study do not contain a noticeably high spessartine content. Similarly, staurolite contains only a small amount of Zn (0.02-0.36 moles of Zn per formula unit (pfu) i.e. 44O + 4(OH), Selverstone et al. (1984) and this study) and Cr (0-0.05 moles of Cr pfu from this study) and so is probably not stabilised by these components. Kyanite is also virtually contaminant-free (e.g. 0-0.003 moles of Cr, 0.006-0.042 moles of Fe^{2+}). Thus, the slightly overlapping compatibility relations in amphibolites from the Zillertaler Alpen do not seem to result from the presence of a minor component, but stem rather from some difference in the intensive variables experienced by the different assemblages

Although pressure, temperature, μ_{H_2O}, μ_{CO_2} and a_{O_2} (f_{O_2}) are generally assumed to be constant over small areas, differences in these intensive variables between individual rocks may result in apparent disequilibrium between the preserved assemblages. Careful petrography and analysis of element partitioning shows that none of the phases in the

amphibolites from the Zillertaler Alpen are either relict or retrograde (other than Fe-rich biotite and chlorite which have been excluded from the equilibrium assemblage). The *almost* excellent fit of the compatibility relations in the Zillertal amphibolites suggests that none of the phases involved is in gross dis-equilibrium with others, but rather that the individual assemblages may have equilibrated sequentially under the influence of different intensive variables.

The close proximity of the Zillertal samples suggests that the pressure and temperature of equilibration is the same for all of the samples, and that a_{O_2}, μ_{H_2O} and μ_{CO_2} are more likely to vary between samples. Activity of oxygen controls the proportion of Fe^{3+} in amphibolite phases and thus could stabilise some phases outside their normal stability fields. However, hornblende is the silicate phase most likely to contain Fe^{3+} (e.g. Powell & Holland, 1990; Will et al., 1990b) and it is unlikely that increasing the stability of hornblende would have any effect on the equilibrium assemblage of amphibolites.

Spear (1977, 1982) suggested that crossed tie-lines from the Post Pond and Ammonoosuc Volcanics resulted from the internal buffering of fluid composition (μ_{H_2O}-μ_{CO_2}) within different layers. The presence of carbonate in some, but not all, samples from the Zillertal suggests that the activity of CO_2 may have varied between samples and that the activity of water in the different assemblages may also be variable. This may have allowed the assemblages to equilibrate under slightly different conditions, resulting in the slight crossing of tie-lines and the preservation of both divariant and univariant assemblages, as illustrated in Fig. 5.14.

Despite crossed tie-lines in the compatibility relations determined for the hornblende garbenschiefer from the Zillertaler Alpen, (Fig. 5.14) the small angles between the tie-lines suggest that the assemblages represent equilibration in a relatively small portion of intensive variable space. Thus the preserved assemblages may be ascribed to a single compatibility diagram. The schematic compatibility relations illustrated in Fig. 5.15 describe a complete or near-complete range of assemblages at the conditions of equilibration (~7 kbar and ~550°C, Selverstone et al., 1984). The compatibility relations are dominated by four three-phase divariant assemblages: kyanite–staurolite–garnet (+ hornblende, plagioclase, quartz, aqueous vapour) for Fe-rich compositions, kyanite–staurolite–chlorite in Mg-rich rocks, garnet–chlorite–cummingtonite in less aluminous rocks and staurolite–garnet–chlorite in rocks with intermediate Fe-Mg and Al-contents.

The relatively complete nature of the compatibility diagram allows speculation on the way the compatibility relations may change under the influence of different equilibration conditions. For example, the absence of orthoamphibole(s) and cordierite from Fig. 5.15 suggests that a significantly different array of tie-lines will result when these phases become stable. The stabilisation of orthoamphibole will allow new tie-lines to develop involving garnet, chlorite and cummingtonite, whereas the growth of cordierite in Mg-rich assemblages would result in the break-down of the kyanite–chlorite, staurolite–chlorite and perhaps garnet–chlorite tie-lines. A change in the relative Fe-Mg partitioning between garnet and staurolite would also cause a rearrangement of the tie-lines. The following chapter (Chapter 6) discusses

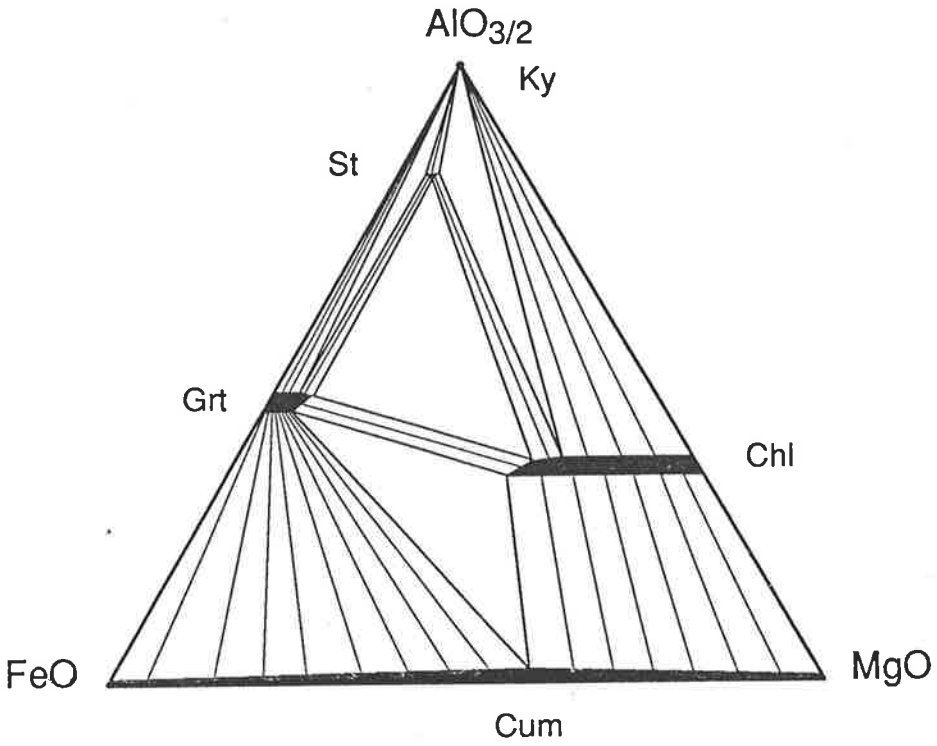

Figure 5.15. A schematic compatibility diagram for the amphibolites from the Zillertaler Alpen represented in AFM ($AlO_{3/2}$, FeO, MgO with hornblende, plagioclase, quartz and an aqueous vapour in excess).

the equilibria and the compatibility relations of kyanite–staurolite amphibolites and related amphibolites reported in the literature and the constraints these provide on the phase relations of kyanite–staurolite amphibolites.

Chapter 6: Review of compatibility relations in kyanite- and staurolite-amphibolites

6.1 Introduction

In addition to the specific locations discussed in Chapters 4 and 5, kyanite–staurolite-amphibolites and related rocks have been reported from a number of other areas. Examples occur in New Zealand (Gibson, 1978, 1979; Ward, 1984a,b; Cooper, 1980), Antarctica (Grew & Sandiford, 1985), North America (Spear, 1977, 1978, 1982; Helms et al., 1987; Schumacher & Robinson, 1987), Europe (Purtscheller & Mogessie, 1984; Frey et al., 1980), South Africa (Humphreys, 1993) and the former USSR (Grew et al., 1988). These many different occurrences span a variety of compositions from very Mg-rich, "whiteschist"-style rocks (Grew et al., 1988) to those analogous to mafic volcanics (e.g. Helms et al., 1987). They contain a variety of assemblages formed under a range of pressure-temperature conditions and hence provide an opportunity to constrain the compatibility relations of these unusual amphibolites.

This chapter briefly describes the mineral equilibria and compatibility relations of the individual assemblages reported from kyanite–staurolite amphibolites and related rocks from around the world and discusses their relationships to each other and to the petrogenetic grids determined in this study and by Spear and Rumble (1986). The most potentially useful occurrences, involving more than one equilibrium assemblage (for example, in both Fe-rich and Mg-rich samples, Spear, 1982; Selverstone et al., 1984; Helms et al., 1987; Humphreys, 1993; Chapters 4 and 5) are described first, in order of increasing equilibration temperature. The occurrences which involve only one low variance assemblage are presented from most Fe-rich to most Mg-rich. Abbreviations used to describe the chemistry of the amphibolite phases are listed in Appendix A1. Compatibility diagrams are presented as AFM ternary plots projected from hornblende, plagioclase, quartz and vapour as outlined in Chapter 5, where A = $AlO_{3/2}$, F = FeO, M = MgO. For completeness, the occurrences from the Harts Range and Zillertaler Alpen, discussed in Chapters 4 and 5, are also briefly summarised here.

6.2 Amphibolites from the Post Pond Volcanics, Vermont, USA

The Post Pond Volcanics described by Spear (1982) provide a wide variety of low variance amphibolite assemblages including garnet–hornblende, garnet–staurolite–chlorite–gedrite–hornblende, garnet–staurolite–chlorite–hornblende and three- and four-amphibole assemblages with or without garnet and chlorite (all plus plagioclase and quartz). The phase relations developed in the Post Pond Volcanics in the Mt Cube Quadrangle are thought to result

from metamorphism to approximately 535 ± 40°C and 5.5 kbar (Spear, 1982). The relative Fe-enrichment of ferromagnesian phases in the carbonate-absent amphibolites described by Spear (1982) decreases in the order garnet > staurolite > gedrite > anthophyllite ≈ cummingtonite ≈ hornblende > biotite > chlorite > cordierite > talc.

Although Spear (1982) does not report any reaction textures from the carbonate-absent amphibolites of the Post Pond Volcanics, crossed-tie line relations and apparent univariant equilibria are evident in the chemographic projection used to portray their equilibria (Fig. 6.1). Spear (1982) suggests that these result from variable μ_{H_2O} (and μ_{CO_2}) between the samples, reflecting internal buffering of fluid composition. It is therefore inappropriate to assume constant μ_{H_2O} and Spear (1982) constructed two separate compatibility diagrams, for high and low μ_{H_2O}, which are separated by at least three univariant reactions:

anthophyllite + garnet ⇒ gedrite + cummingtonite

gedrite + cummingtonite ⇒ anthophyllite + chlorite

garnet + chlorite ⇒ staurolite + gedrite,

(all plus hornblende, plagioclase, quartz and vapour). Many of the equilibria observed in the Post Pond Volcanics are intermediate to these two compatibility diagrams.

Spear (1978) and Spear and Rumble (1986) have constructed P-μ_{H_2O} and P-T Schreinemakers nets, respectively, for the phases observed in the Post Pond and Ammonoosuc Volcanics. The later investigation (Spear & Rumble, 1986) found that, according to Schreinemakers analysis, Spear's (1982) original reaction, anthophyllite + garnet ⇒ gedrite + cummingtonite, occurs with *decreasing* temperature or increasing μ_{H_2O}, that is, in the opposite sense to that initially proposed (Spear, 1982; Spear & Rumble, 1986). Thus, the compatibility diagrams constructed by Spear (1982) have been corrected to include the high μ_{H_2O} assemblage gedrite–cummingtonite and the low μ_{H_2O} assemblage anthophyllite–garnet, and are presented in Fig. 6.2.

Although the compatibility relations reported by Spear (1982) for more aluminous bulk compositions are similar to those from other kyanite–staurolite and related amphibolites (Fig. 6.2), less aluminous assemblages containing cummingtonite or two orthoamphiboles are very rare. The presence of co-existing orthoamphiboles in the Post Pond Volcanics rocks is in contrast to the single orthoamphibole reported from the Harts Range and Zillertaler Alpen (Chapters 4 & 5), suggesting that the Post Pond Volcanics equilibrated at lower temperatures (or perhaps higher μ_{H_2O}) than these occurrences (cf. Spear, 1980).

6.3 Kyanite, staurolite and garnet amphibolites from the Zillertaler Alpen, Austria

The compatibility relations in variable composition amphibolites from the Zillertaler Alpen in western Austria are discussed in detail in Chapter 5 (see also Appendix A10).

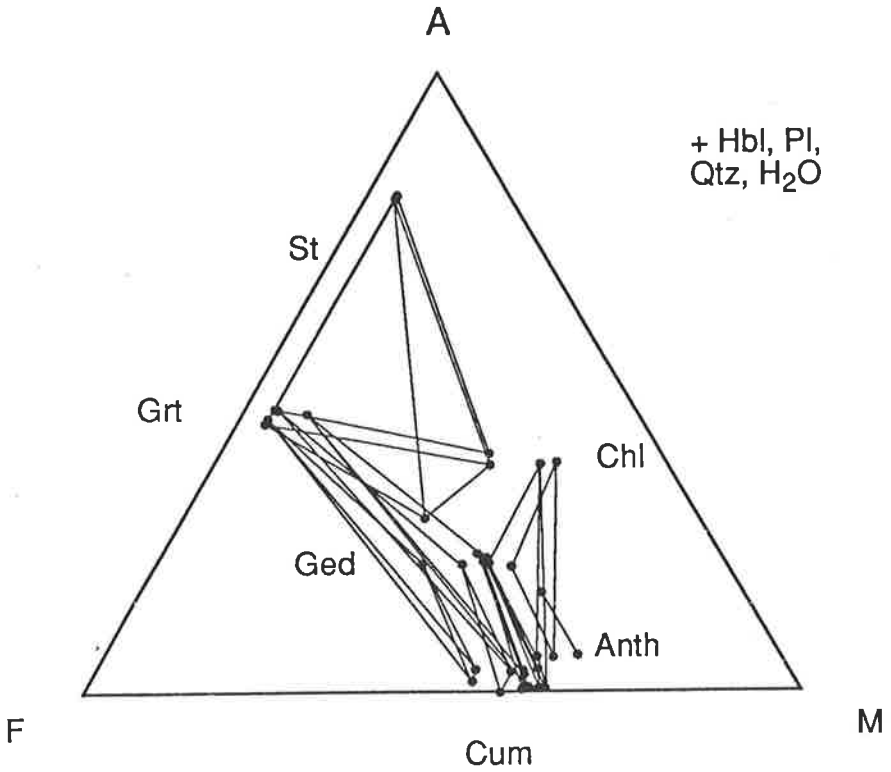

Figure 6.1. Compatibility relations for assemblages from the Post Pond Volcanics, Vermont, USA (+ hornblende, plagioclase, quartz and aqueous vapour). Equilibration conditions ~535°C, 5.5 kbar. Data from Spear (1982).

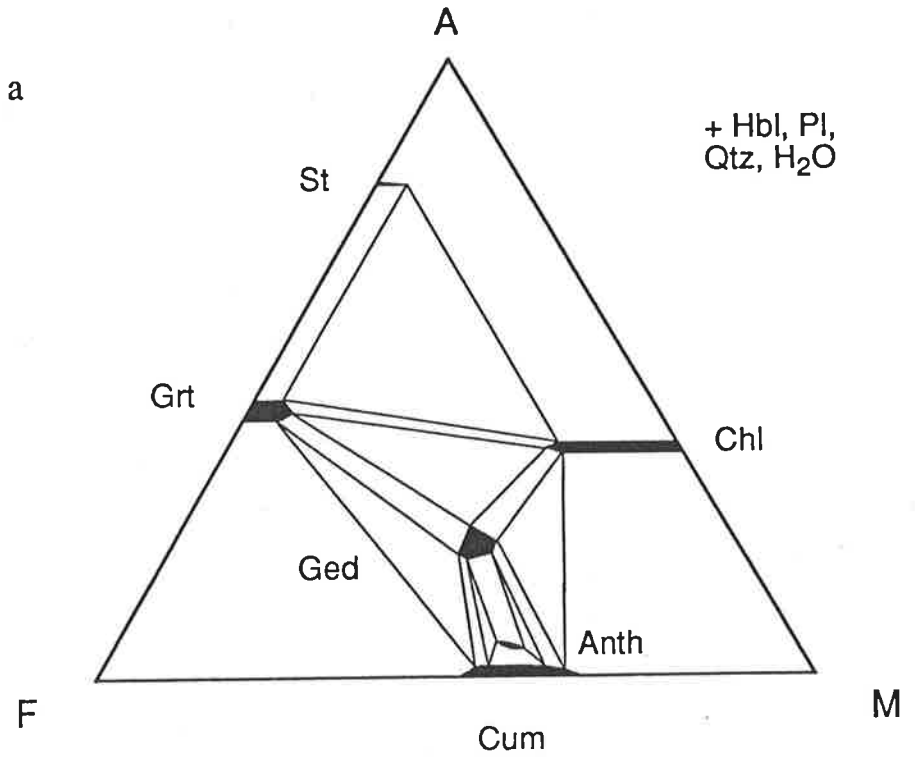

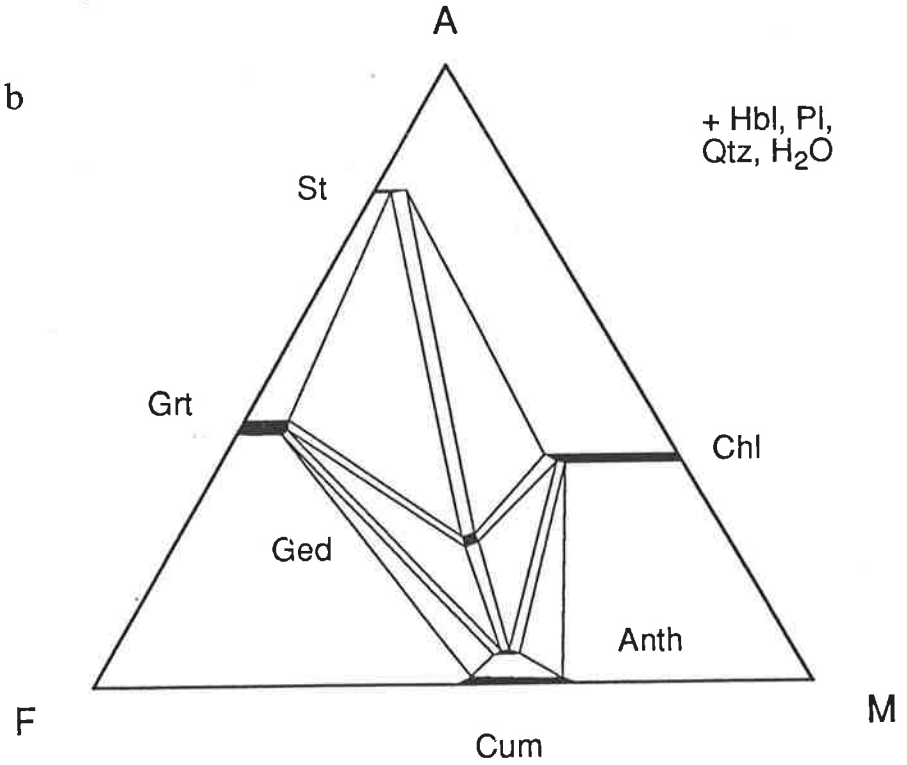

Figure 6.2. High μ_{H_2O} (or low T) (a) and low μ_{H_2O} (or high T) (b) compatibility diagrams for assemblages from the Post Pond Volcanics, Vermont, USA (+ hornblende, plagioclase, quartz and aqueous vapour). Equilibration conditions ~535°C, 5.5 kbar. Data from Spear (1980), corrected in accordance with Spear and Rumble (1986).

Selverstone et al. (1984) estimates that the Zillertal samples equilibrated at approximately 550°C, 7 kbar. The hornblende garbenschiefer contain four distinct divariant equilibria in the NCFMASH system: kyanite–staurolite–garnet in Fe-rich rocks, kyanite–staurolite–chlorite in more Mg-rich samples, garnet–chlorite–cummingtonite in less aluminous rocks and staurolite–garnet–chlorite in intermediate composition amphibolites (all plus hornblende, plagioclase, quartz and vapour, Fig. 6.3). Overlapping tie-triangles and the presence of the univariant assemblage kyanite–staurolite–garnet–chlorite suggest that, like the Post Pond Volcanics, these assemblages may have equilibrated under the influence of variable fluid compositions (Chapter 5).

6.4 Kyanite-, staurolite- and gedrite-amphibolites from Georgia, USA

A mafic-ultramafic slice (the Laurel Creek amphibolite) outcropping in the Blue Ridge metamorphic province of the Southern Appalachians contains several low variance assemblages. These include: kyanite–staurolite–chlorite–gedrite–hornblende–biotite–plagioclase (+ quartz and rutile ± pyrrhotite, sample L-112-N, Helms et al., 1987), garnet–chlorite–gedrite–hornblende–plagioclase (sample L-112-D), staurolite–garnet–chlorite–hornblende–plagioclase (sample L-100), staurolite–garnet–chlorite–gedrite–hornblende (sample L-79), kyanite–chlorite–hornblende–biotite–plagioclase (sample L-75) and kyanite–staurolite–garnet–biotite–plagioclase (sample L-36). These assemblages include univariant, divariant and trivariant associations (when considered as part of the NCFMASH system) which have developed in samples which have Mg-rich olivine-normative basaltic compositions. According to the results of mass balance calculations, chemically, the samples are capable of producing Laird's (1980)"common" amphibolite assemblage, i.e. calcium-amphibole, chlorite, epidote, plagioclase, quartz ± garnet ± Fe^{3+}-oxides, carbonates, K-bearing and Ti-bearing phase, given the appropriate metamorphic conditions. The relatively wide-spread occurrence of these otherwise rare aluminosilicate-bearing amphibolites in the Laurel Creek amphibolite was attributed by Helms et al. (1987) to the rocks being exposed to unusual metamorphic conditions. Helms et al. (1987) suggest that the assemblages reported from the Laurel Creek amphibolite equilibrated at 540-625°C and a minimum pressure of 7.7 kbar, possibly under conditions of variable μ_{H2O}.

The compositions of phases reported from the Laurel Creek amphibolite are relatively Mg-rich with Fe-partitioning decreasing in the order: $X_{Fe,St}$ (0.61-0.73) > $X_{Fe,Grt}$ (0.63-0.73) > $X_{Fe,Oam}$ (0.32-0.35) > $X_{Fe,Hbl}$ (0.30-0.37) > $X_{Fe,Chl}$ (0.2). The hornblende is typically tschermakitic hornblende or tschermakite and has a variable Na-content (0.09-0.49 moles per formula unit). Orthoamphibole typically contains less Al and less Na than co-existing hornblende (Helms et al., 1987) and the low aluminium content places them at the boundary of the anthophyllite and gedrite compositional fields (Leake, 1978).

As seems typical in very low variance aluminous amphibolites (e.g. Spear, 1982; Selverstone et al., 1984; Chapter 5), there are no obvious reaction textures and it must be

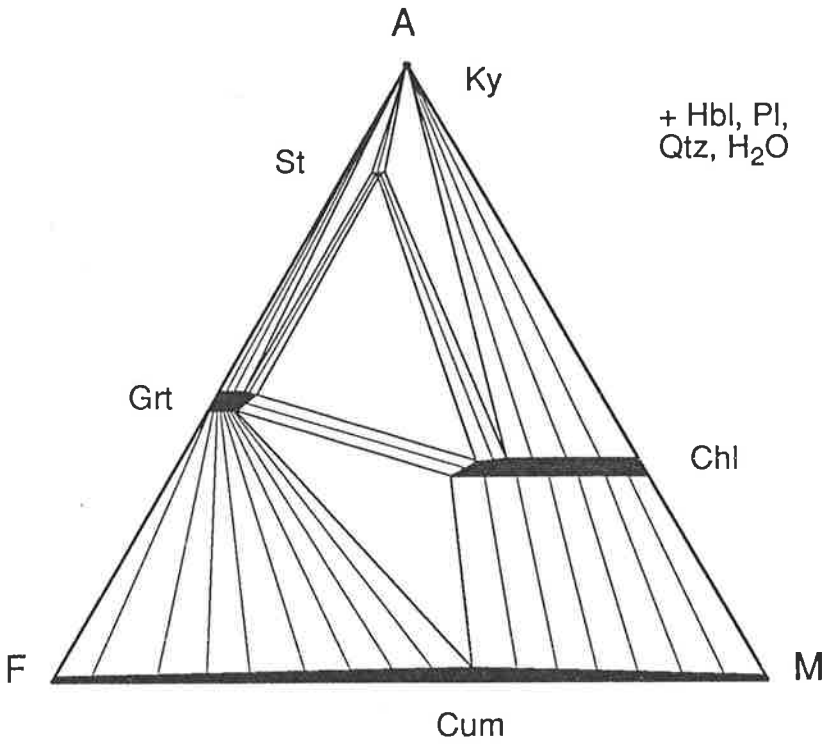

Figure 6.3. A schematic compatibility diagram for amphibolites from the Zillertaler Alpen (with hornblende, plagioclase, quartz, and aqueous vapour in excess), from Chapter 5. The Zillertal samples are thought to have equilibrated at approximately 550°C, 7 kb (Selverstone et al., 1985).

assumed that the mineral assemblages observed at the thin section scale represent equilibrium associations. The compatibility relations for the hornblende-, plagioclase- and quartz-bearing Georgia Blue Ridge amphibolites are illustrated in Fig. 6.4. As noted by Helms et al. (1987), the compatibility relations of some of these assemblages cross-cut the others. It is possible that small but significant amounts of ZnO or Cr_2O_3 in staurolite or kyanite, MnO in garnet or perhaps Fe_2O_3 in hornblende or chlorite might have caused one of these phases to be stable outside its model system stability field and thus appear in an anomalously low variance assemblage. Staurolite in the Laurel Creek amphibolite typically contains little ZnO (< 0.05 mol per formula unit), Cr_2O_3 content not reported and no kyanite analyses were given (Helms et al., 1987). The low spessartine content of garnet (X_{sps} 0.02) suggests that garnet is not stabilised by MnO. These low concentrations of potentially stabilising components suggest that none of the phases are stabilised outside their normal stability fields and that crossed-tie lines defined by the Laurel Creek assemblages rocks may, like those of Spear (1978; 1982), result from variable μ_{H_2O} between the samples.

The assemblages described from samples L-112-D (garnet, chlorite, gedrite) and L-100 (staurolite, garnet, chlorite) are compatible with each other, but not with the univariant assemblage in sample L-112-N (kyanite, staurolite, gedrite, chlorite), suggesting that these assemblages span at least two univariant NCFMASH reactions which bound the garnet–chlorite and staurolite–chlorite stability fields. Figure 6.5 displays the sequence of schematic compatibility diagrams which must relate the assemblages observed in the Laurel Creek amphibolite. Figure 6.5a displays what is expected to be the lower temperature configuration which is bounded to higher temperature (as chlorite is a very hydrous phase it is likely to occur on the high μ_{H_2O}, low temperature side of a reaction) by the reaction,

garnet + chlorite ⇒ staurolite + gedrite (+ hornblende, plagioclase, quartz, vapour).

With decreasing μ_{H_2O} or increasing temperature another chlorite-bearing reaction,

staurolite + chlorite ⇒ kyanite + gedrite (+ hornblende, plagioclase, quartz, vapour)

would be encountered. The assemblage in sample L-75, kyanite–chlorite, may be stable in any of these compatibility diagrams. The low variance assemblage in sample L-70 (staurolite–garnet–chlorite–gedrite) which reportedly lacks plagioclase corresponds to the lower temperature reaction between Fig. 6.5a and b, implying that if (as seems likely given the calcic nature of the garnet and the presence of hornblende, Helms et al., 1987) a small amount of plagioclase was, this assemblage would fit sensibly into the compatibility relations illustrated here.

The intermediate X_{Fe} of the Laurel Creek amphibolite and its abundance of low-variance assemblages with complex phase relations make the Georgia Blue Ridge amphibolites a potentially useful tool for understanding the compatibility relations in kyanite- and staurolite-amphibolites.

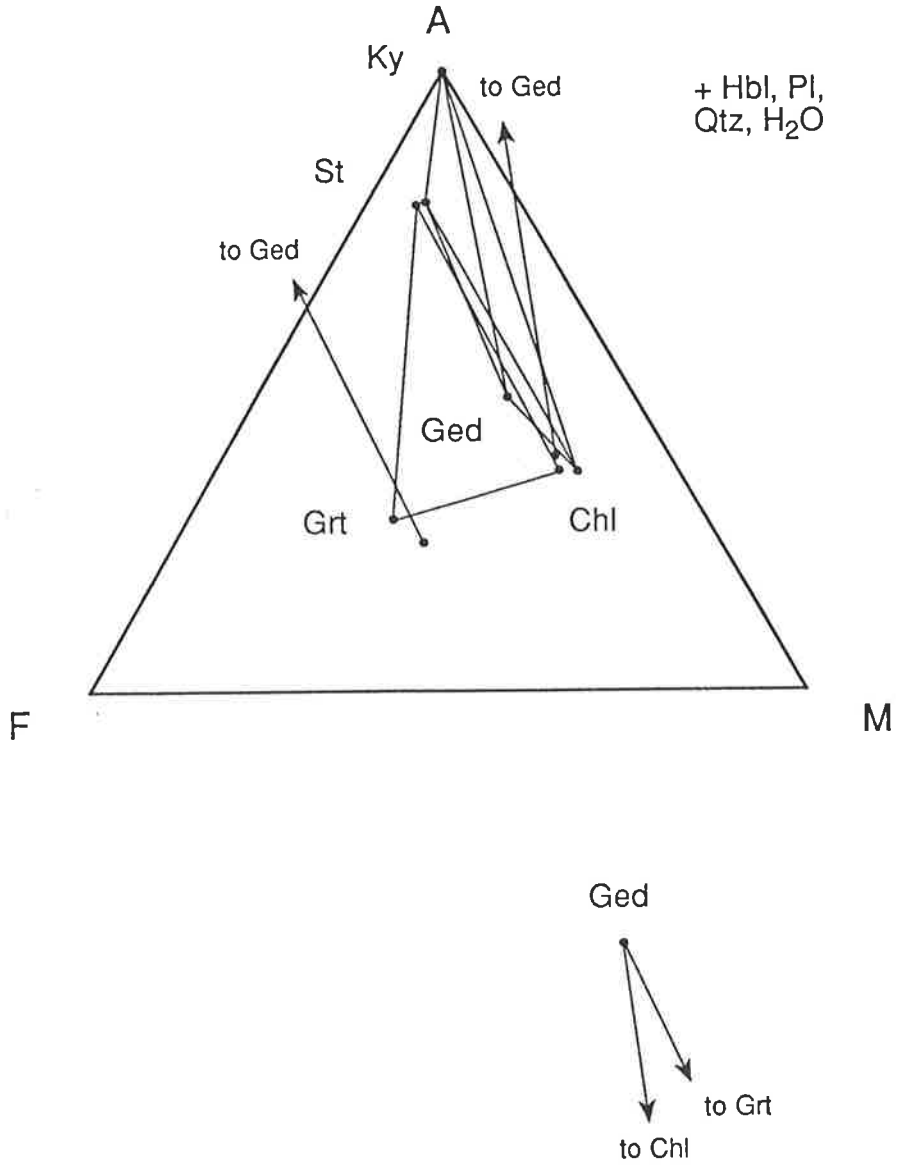

Figure 6.4. Low variance assemblages from the Blue Ridge metamorphic province, Georgia, USA; kyanite–staurolite–chlorite–gedrite; garnet–chlorite–gedrite; staurolite–garnet–chlorite; staurolite–garnet–chlorite–gedrite (+ hornblende, plagioclase, quartz and aqueous vapour). Equilibration conditions 540-625°C, ≥ 7.7 kbar . Data from Helms et al. (1987). The variation in plotting positions of garnet and gedrite result from the variable compositions of the co-existing projecting phases plagioclase and hornblende. Crossed tie-lines may result from variable a_{H_2O} between the samples, see text.

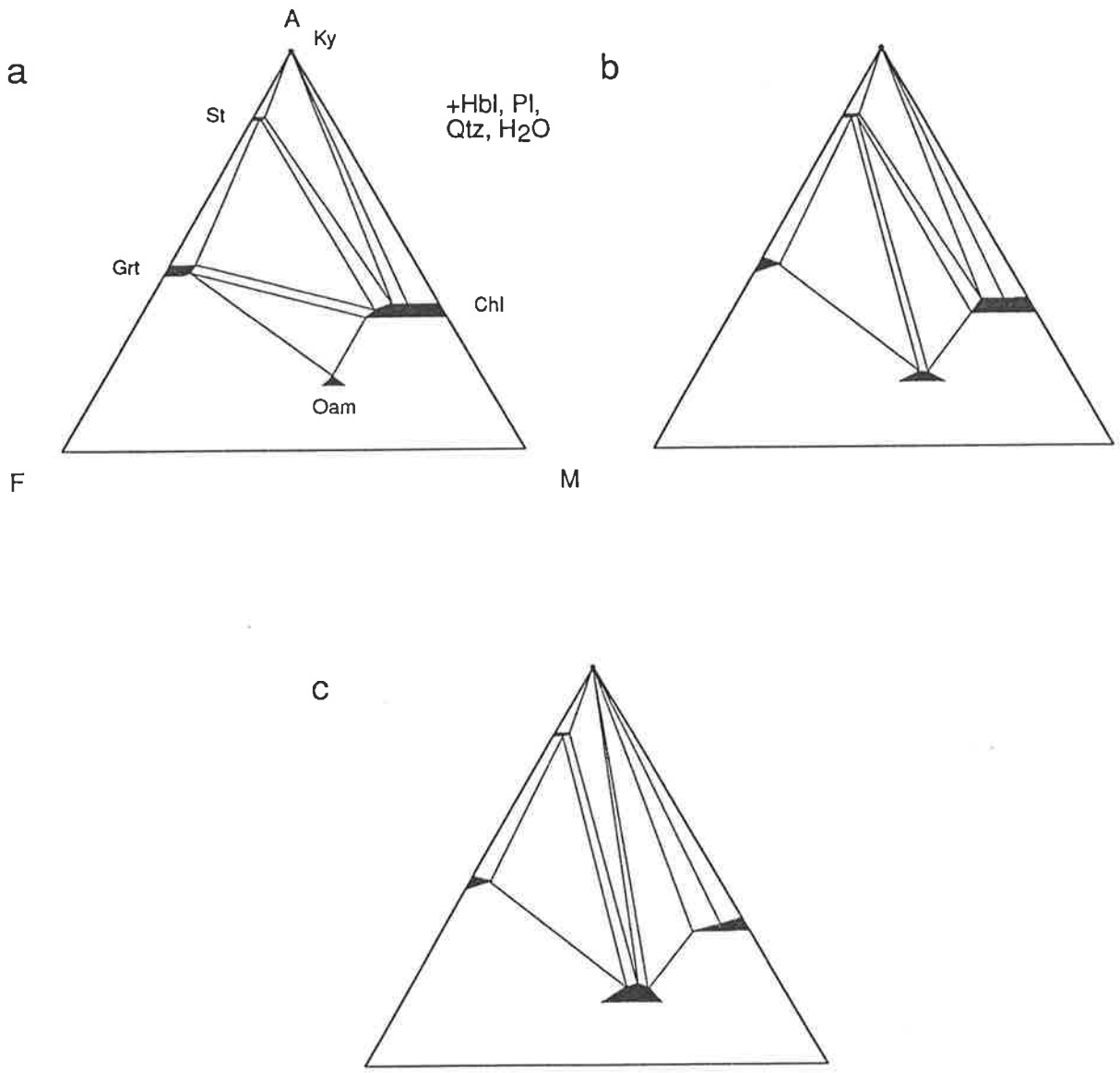

Figure 6.5. Schematic compatibility diagrams illustrating the three compatibility diagrams which describe the phase relations from the Laurel Creek amphibolite. Temperature increases (or μ_{H_2O} decreases) from a to c.

6.5 Aluminous gneisses from South Africa

The Copperton Formation is a poly-metamorphosed Meso-Proterozoic island-arc sequence (Humphreys, 1993) in the western part of central South Africa. It consists of granulite and amphibolite grade gneisses and schists which include aluminous orthoamphibole and hornblende amphibolites. Of particular interest here are the rare sillimanite–staurolite–cordierite–hornblende and cordierite–garnet–gedrite–hornblende assemblages. The co-existence of sillimanite (rather than kyanite) with hornblende has been reported previously only from amphibolites in south western New Hampshire (Schumacher & Robinson, 1987) and the cordierite–garnet–gedrite–hornblende association appears to be unique to this locality. The relative Fe-enrichment of the amphibolite phases decreases in the order garnet > staurolite > orthoamphibole ≥ hornblende > chlorite > cordierite (note that hornblende is more Fe-rich than orthoamphibole in some samples, but that the trend is reversed in others).

Although Humphreys (1993) considers that these sillimanite–staurolite–hornblende assemblages are not related to those of Selverstone et al. (1984) or Helms et al. (1987), their similar mineralogy suggests that the reactions which control the stability of the Copperton assemblages will also be appropriate to less aluminous assemblages (cf. Selverstone et al., Fig. 5, 1984). Humphreys (Table 2, 1993) reports three separate sets of mineral equilibria, the first of which formed under intermediate pressures and temperatures resulting in the amphibolite assemblages sillimanite–staurolite–cordierite–hornblende–plagioclase–quartz and cordierite–garnet–orthoamphibole–hornblende–plagioclase–quartz (Fig. 6.6a). Upon cooling and rehydration (at similar pressures) these assemblages became metastable and were replaced by assemblages involving kyanite–staurolite–chlorite and containing the staurolite–orthoamphibole, staurolite–chlorite and sillimanite–chlorite tie-lines, respectively (all with hornblende, plagioclase and quartz, Fig 6.6b). Later reheating resulted in the growth of staurolite after chlorite and garnet after staurolite and orthoamphibole. This latter stage seems poorly constrained and will not be discussed further.

Humphreys (1993) has obtained estimates of ~580-620°C and > 6.1 kbar from conventional geothermobarometry on peak metamorphic assemblages, however in the discussion of the P-T evolution of the area, he quotes significantly different peak conditions (600-625°C and 4 kbar), derived from the FMASH grid of Hudson and Harte (1985). The relevant assemblages are limited to a maximum pressure and temperature by the position of the FMASH invariant point [Chl] (Hudson& Harte, 1985; Humphreys, 1993). Earlier sections of this thesis and other similar works (Xu et al., 1993) have placed this invariant point (Ip_1, [Chl]) at conditions of about 6 kbar and 650°C (Chapter 2). These conditions are similar to those determined from geothermobarometry and thus, the original estimates are considered to be more appropriate for the purposes of this discussion.

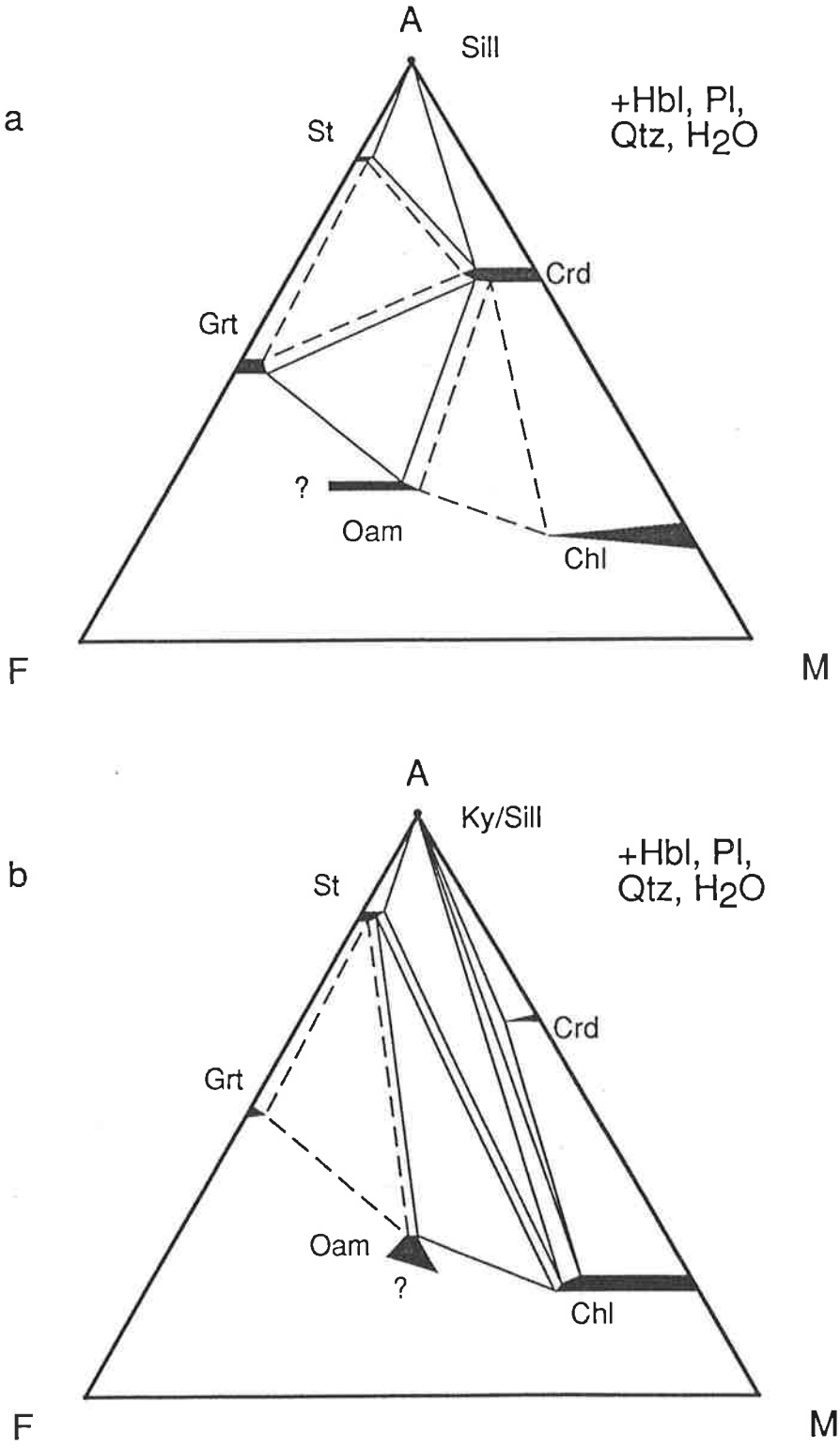

Figure 6.6. (a) High temperature (M_1) and (b) low temperature (M_2) (b) compatibility diagrams for assemblages from the Copperton Formation, South Africa (+ hornblende, plagioclase, quartz and aqueous vapour). Equilibration conditions for M_1: ~580-620°C and > 6.1 kbar. Data from Humphreys (1993). Dashed tie-lines are implied from the observed compatibility diagrams.

6.6 Amphibolites from the Harts Range, central Australia

Kyanite-, staurolite-, garnet-, cordierite-, and orthoamphibole-bearing amphibolites have been reported from Proterozoic supracrustal rocks in the Harts Range region of central Australia (Chapter 4, Appendix A8). These phases define a number of equilibria which span a relatively broad segment of compositional space, and thus provide good constraints on the compatibility relations of the amphibolites and on their reaction relations and pressure-temperature history. The amphibolite grade rocks have been metamorphosed to an estimated maximum pressure of 7 kbar and to temperatures up to 650-700°C.

Poikiloblasts of garnet preserve weakly aligned inclusions of more Fe-rich staurolite, hornblende, plagioclase, quartz and ilmenite, suggesting that these phases once defined an equilibrium assemblage. The matrix assemblage contains foliated garnet, gedrite, hornblende, plagioclase, quartz and ilmenite. Staurolite is not a matrix phase in samples containing gedrite, implying that the early foliated assemblage staurolite–garnet became metastable with respect to gedrite–hornblende in garnet-bearing samples. For detailed descriptions and interpretation, see Chapter 4 (See also Appendix A8).

Other samples contain porphyroblasts of kyanite and hornblende which define a weak foliation in a plagioclase, quartz ± gedrite (+ accessories) matrix. Kyanite is typically rimmed by moats of staurolite and anorthitic plagioclase and is never observed in contact with hornblende. The matching shapes of the boundaries of both kyanite and hornblende with the enclaves as a whole suggests that these two phases defined an equilibrium assemblage form an equilibrium assemblage which later became metastable with respect to staurolite and anorthite. The corona textures preserved in these samples (see Chapter 4 & Appendix A8) suggests that the samples have experienced minimal deformation and metamorphic overprinting since their formation.

Less calcic, more magnesian samples are preserved in rare outcrops of "whiteschist"-like rocks which contain small amounts of hornblende and plagioclase. A foliation assemblage of porphyroblastic kyanite, hornblende and anthophyllite is overprinted and corroded by coarse-grained, randomly oriented cordierite and plagioclase (Appendix A8). This suggests that subsequent to deformation, kyanite–hornblende–gedrite became metastable with respect to cordierite–plagioclase.

Cummingtonite has been observed in less aluminous rocks, co-existing with hornblende, garnet , relict clinopyroxene and orthopyroxene and minor plagioclase.

The amphibolites from the Harts Range define a relatively complete compatibility diagram, portrayed in Fig. 6.7 in which the X_{Fe} of the phases decreases in the order staurolite > garnet > cummingtonite > hornblende ≥ orthoamphibole > cordierite. The observed mineral textures may be interpreted in terms of continuous reactions and do not violate the NCFMASH compatibility relations (Fig. 6.7, see Chapter 4). Fe-rich samples are dominated by staurolite–garnet–gedrite, intermediate X_{Fe} samples contain subsets of kyanite–staurolite–gedrite and Mg-rich samples contain kyanite–cordierite–anthophyllite. Very Mg-rich rocks might be expected

Figure 6.7. Compatibility diagram for the Harts Range amphibolites; (+ hornblende, plagioclase, quartz and aqueous vapour). Equilibration conditions up to 650-700°C, 7 kbar. Data from Chapter 4 (and Appendix A4). Dotted tie-lines are implied only.

Figure 6.8. Staurolite and garnet from the Lanterman Range, Antarctica (+ hornblende, plagioclase, quartz and aqueous vapour) equilibrated at > 6 kbar, 500-650°C. Data from Grew & Sandiford (1985).

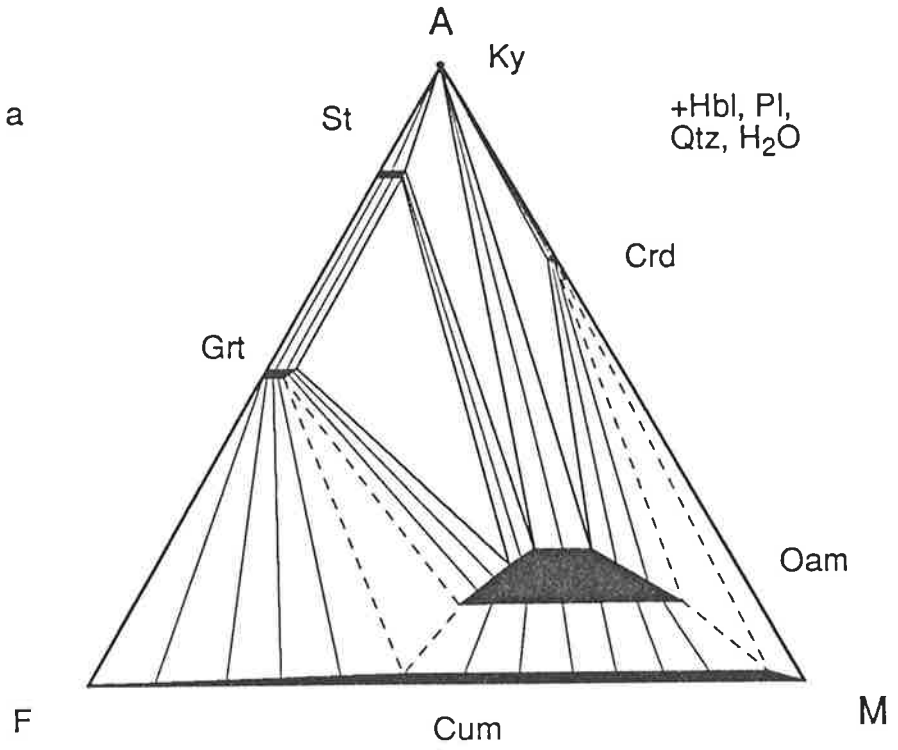
a
A
Ky
St
+Hbl, Pl,
Qtz, H2O
Crd
Grt
Oam
F
Cum
M

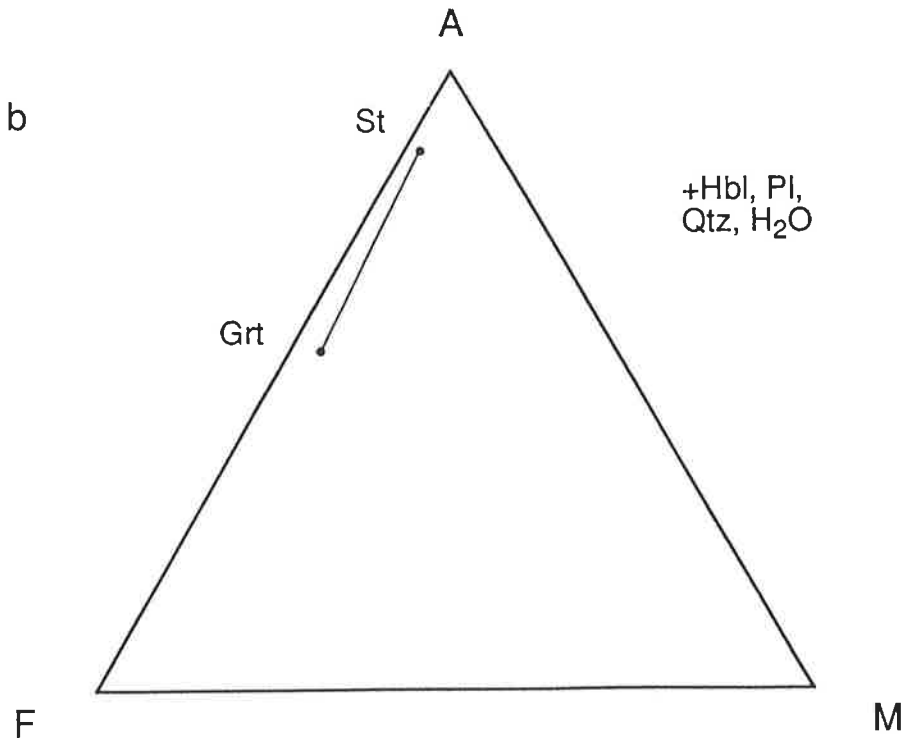
b
A
St
+Hbl, Pl,
Qtz, H2O
Grt
F
M

to contain chlorite or talc, perhaps with cordierite and anthophyllite, however it is possible that these phases are not stable under these conditions. Cummingtonite is observed in only one trivariant assemblage (garnet–cummingtonite), however this assemblage, and the presence of cummingtonite in the similar grade amphibolites from the Zillertaler Alpen suggests that other lower variance assemblages, such as garnet–gedrite–cummingtonite or chlorite–gedrite–cummingtonite (if chlorite is stable) or cordierite–gedrite–cummingtonite may be stable at similar P-T conditions.

6.7 Staurolite–garnet–hornblende biotite schist from the Lanterman Range, Antarctica

Staurolite inclusions in margarite enclosed by garnet were reported from hornblende–biotite schists in the Lanterman Range of northern Victoria Land, Antarctica (Grew & Sandiford, 1985). The staurolite has been interpreted as a relic of the previous assemblage, staurolite–garnet–hornblende. The relationship between the matrix phases and the inclusion assemblage is not clear. The grossular-rich garnet porphyroblasts (X_{grs} 0.16) are generally less Fe-rich (X_{Fe} 0.61-0.67) than the coexisting staurolite (X_{Fe} 0.8) (Fig. 6.8) and Grew and Sandiford (1985) suggest that this results from the continuing reaction of the small staurolite grains in isolation from garnet. The equilibration conditions for this assemblage are thought to be at least 6 kbar at intermediate temperatures, that is, similar to the 500-650°C, 7-10 kbar proposed for the nearby Mt Burnsen rocks (Grew & Sandiford, 1984, 1985). The Fe-rich nature of this sample (Fig. 6.8) means that is unlikely to show crossed tie-line relations with the assemblages discussed above, however the relative X_{Fe} of garnet and staurolite may provide an important indication of P-T conditions.

6.8 Kyanite–staurolite–garnet amphibolites from the Ötztal, Austria

Purtscheller and Mogessie (1984) report that relatively calcium-poor amphibolites in the Sölden region of the Austrian Ötztal contain equilibrium assemblages including kyanite–staurolite–garnet–hornblende. Staurolite needles occur predominantly along grain boundaries common to hornblende and garnet grains and also as fine inclusions in both of these phases. Kyanite also appears as inclusions in garnet and at grain boundaries of garnet with hornblende. The compatibility relations corresponding to the equilibria involving ferroan pargasite, almandine- and grossular-rich garnet, kyanite and staurolite are depicted in Fig. 6.9 and were constructed on the assumption that quartz and plagioclase were probably present in these samples, although the authors omitted to mention them (no corundum was described from the samples). Staurolite (X_{Fe} 0.68) is more Fe-rich than co-existing garnet (X_{Fe} 0.59) and both are poor in the potentially stabilising minor components zinc, chromium and manganese. Purtscheller and Mogessie (1984) suggest that this assemblage may have equilibrated at a

Figure 6.9. Kyanite–staurolite–garnet from the Sölden region of the Ötztal, Austria (+ hornblende, plagioclase, quartz and aqueous vapour) apparently equilibrated at 3-4 kbar, < 670°C (Purtscheller and Mogessie, 1984). Independent information from the presence of kyanite and the association of contemporary eclogites suggest at least intermediate pressures of formation. Data from Purtscheller and Mogessie (1984).

Figure 6.10. Compatibility relations from Frodalera near the Lukmanier Pass area of south-eastern Switzerland (+ hornblende, plagioclase, quartz and aqueous vapour) equilibrated at 7.7 kbar, 530-580°C. Data from Table 6.3.

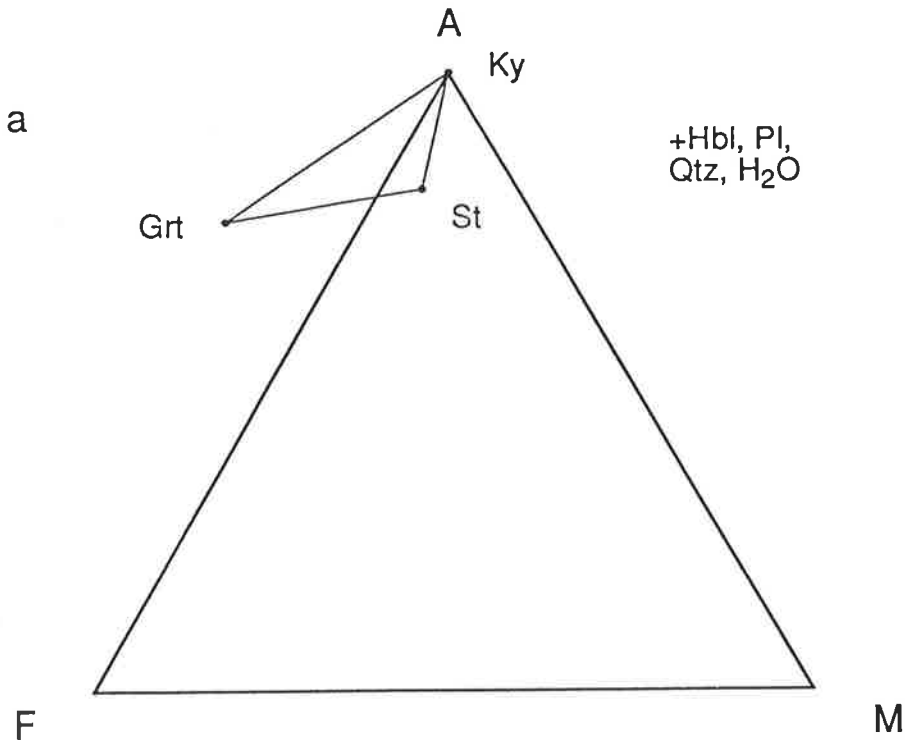
a
A
Ky
+Hbl, Pl,
Qtz, H_2O
Grt
St
F
M

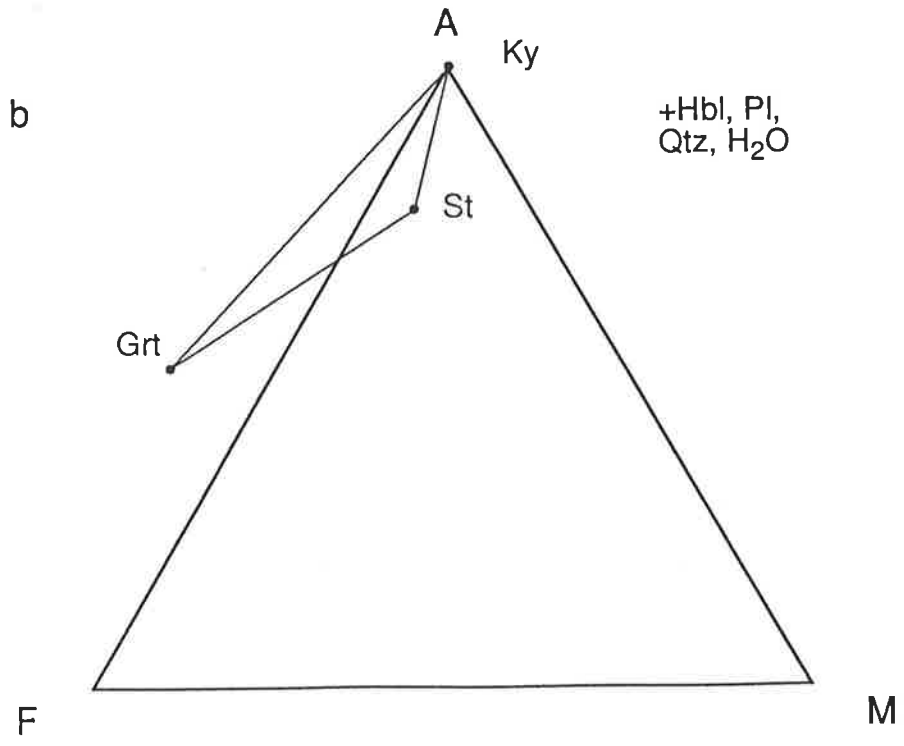
b
A
Ky
+Hbl, Pl,
Qtz, H_2O
St
Grt
F
M

maximum temperature of 670°C at a pressure of 3-4 kbar, however this is at odds with both the presence of kyanite in the equilibria and associated eclogites of the same age (Purtscheller & Mogessie, 1984, pp. 230) which both suggest *at least* intermediate pressure metamorphism.

6.9 Kyanite–staurolite–garnet amphibolites from Frodalera, Switzerland

Frey et al. (1980) report kyanite–staurolite–garnet-bearing hornblende garbenschiefer from Frodalera near Lukmanier Pass in south-eastern Switzerland. These Upper Triassic Quartenschiefer occur in a narrow zone south of the Gotthard massif and were collected by Dr Andy Barnicoat who has kindly made the samples available for this study. Frey et al. (1980) reports that the Quartenschiefer often contain coarse hornblende which are sheaf-like (garben) in habit and are part of the assemblage: hornblende–kyanite–staurolite–garnet–biotite–chlorite–plagioclase–epidote–quartz–ilmenite. The Hornblende garbenschiefer are thought to be the high grade equivalents of dolomite and calcite-bearing chlorite mica schists found to the north at Lukmanier Pass (Frey et al., 1980).

The garbenschiefer commonly contain hornblende poikiloblasts with a finer, strongly foliated biotite–epidote–plagioclase–quartz ± white mica ± rutile ± ilmenite ± hornblende matrix. The foliation often wraps around the coarse, randomly oriented to subparallel hornblende and slightly elongate garnet. Subhedral to euhedral garnet, hornblende and kyanite often contain straight inclusion trails of epidote, plagioclase, quartz, ilmenite and rutile. Dolomite is restricted to isolated inclusions in coarse hornblende grains and hornblende is often surrounded by a biotite selvage. Staurolite and kyanite occur in several samples as small (≤ 0.5 mm in length) elongate grains subparallel to the foliation direction and in contact with biotite, white mica, plagioclase, quartz and hornblende and both kyanite and staurolite may be corroded. Petrographic summaries of the Frodalera hornblende garbenschiefer are given in Table 6.1 and selected mineral composition information is summarised in Table 6.2.

The phases analysed from the Frodalera amphibolites are broadly similar to those from other areas. Tschermakite to tschermakitic hornblende and andesine to labradorite plagioclase (An_{31-49}) dominate the matrix. More calcic plagioclase (bytownite, An_{76-87}) is observed in association with staurolite and kyanite plagioclase and more sodic oligoclase (An_{24-44}) is observed in association with garnet. Garnet is the most Fe-rich phase analysed ($X_{Fe,Grt}$ 0.86-0.87), followed in decreasing order by staurolite ($X_{Fe,St}$ 0.74-0.79), hornblende ($X_{Fe,Hbl}$ 0.45-0.56), chlorite ($X_{Fe,Chl}$ 0.37-0.48 after primary biotite, 0.74 with secondary biotite) and biotite ($X_{Fe,Bt}$ 0.34-0.45 for primary biotite, 0.69 for secondary grains). Epidote is a solid solution mixture of pistacite and clinozoisite (Ps_{11-21}) and garnet is dominated by the almandine and grossular end-members (X_{alm} 0.63-68, X_{prp} 0.09-0.11, X_{grs} 0.16-0.21, X_{sps} 0.05-0.06).

The lowest variance assemblages observed in the samples include kyanite–staurolite–garnet–hornblende (+ plagioclase–quartz–epidote–biotite ± ilmenite ± rutile) (51773b);

Table 6.1. Selected brief petrographic descriptions of the Hornblende Garbenschiefer from Frodlera, Switzerland

	Qtz	Pl	Hbl	Ms	Bt	Grt	St	Ky	Ep	Chl	Rt	Ilm	Ank
51773a	X	X	P	1°	R		X	X	Z	Rb			H
51773b	X	X	P	X	X	P	X	X	X	Rb	X	X	G
51774	X	Z	P		X			X	Z	Rh			
51775	X	Z	P	X	X			P	Z	Rb	X		
51775b	X	Z	P	X	X	P		P	Z	R		X	
51776a	X	Z	P	X	X	P			Z		X	X	
51776b	X	Z	1°		X	P			Z	Rh			H
51777	X	Z	P	P		X			X	Rh,b	X	X	

Abbreviations: X phase present, Z zoned, 1° primary phase, 2° secondary phase, P porphyroblastic, R retrograde, Rb retrograde after biotite, Rh retrograde after hornblende, H in hornblende, G in garnet

Table 6.2. Selected mineral composition data from the Frodalera amphibolites. n.a. = not analysed.

	Pl	Ep	Pl	St	Ky	Ep rim	Ep core	Ms	Bt	Hbl	Chl	Pl	Hbl	Ilm	Rt	Bt
SiO2	48.07	38.86	47.88	27.42	37.16	38.67	38.96	46.85	38.28	43.54	24.65	59.32	42.80	2.57	0.34	37.78
TiO2	0.00	0.00	0.00	0.64	0.00	0.00	0.12	0.38	1.70	0.37	0.00	0.00	0.24	58.78	100.00	1.64
Al2O3	32.82	26.77	33.19	51.58	62.40	26.34	26.90	32.42	17.81	16.82	20.84	26.13	17.06	1.25	0.32	16.42
Fe2O3																
FeO	0.00	7.69	0.35	12.73	0.27	7.77	7.56	2.18	16.12	14.60	21.02	0.33	15.57	31.11	0.60	14.70
MnO	0.00	0.00	0.00	0.15	0.00	0.00	0.00	0.00	0.00	0.00	0.00	0.00	0.00	0.00	0.00	0.00
MgO	0.00	23.49	0.00	2.51	0.18	0.00	0.00	1.01	11.02	10.08	18.58	0.00	9.70	0.77	0.17	14.37
CaO	16.33	0.33	16.73	0.00	0.00	23.76	23.56	0.12	0.00	11.27	0.00	8.31	10.99	0.30	0.30	0.25
Na2O	2.21	0.11	2.19	0.82	0.21	0.30	0.38	0.62	0.14	1.43	0.15	6.74	1.45	0.26	0.00	0.15
K2O	0.00	0.00	0.06	0.00	0.05	0.00	0.07	9.62	9.20	0.34	0.00	0.00	0.33	0.12	0.00	9.34
Cr2O3	0.00	0.00	0.00	0.13	0.00	0.14	0.00	0.00	0.00	0.00	0.00	0.00	0.00	0.00	0.00	0.00
ZnO	n.a.	n.a.	n.a.	n.a.	n.a.	n.a.	n.a.	n.a.	n.a.	n.a.	n.a.	n.a.	n.a.	n.a.	n.a.	n.a.
Total	99.4	97.3	100.4	96.0	100.3	97.0	97.5	93.2	94.3	98.5	85.2	100.8	98.1	95.2	101.7	94.7
Si	2.212	2.909	2.191	7.763	1.002	3.092	3.089	3.185	2.874	6.326	2.623	2.628	6.270	0.062	0.004	2.824
Ti	0.000	0.000	0.000	0.136	0.000	0.000	0.007	0.019	0.096	0.040	0.000	0.000	0.026	1.073	0.985	0.092
Al	1.781	2.363	1.790	17.216	1.984	2.483	2.515	2.598	1.576	2.881	2.614	1.365	2.946	0.036	0.005	1.447
Fe3+																
Fe2+	0.000	0.482	0.013	3.014	0.006	0.520	0.501	0.124	1.012	1.774	1.871	0.012	1.908	0.632	0.007	0.919
Mn	0.000	0.000	0.000	0.036	0.000	0.000	0.000	0.000	0.000	0.000	0.000	0.000	0.000	0.000	0.000	0.000
Mg	0.000	2.621	0.000	1.059	0.007	0.000	0.000	0.102	1.233	2.183	2.946	0.000	2.118	0.028	0.003	1.601
Ca	0.805	0.026	0.820	0.000	0.000	2.036	2.002	0.009	0.000	1.755	0.000	0.395	1.725	0.008	0.004	0.020
Na	0.197	0.016	0.194	0.450	0.011	0.047	0.058	0.082	0.020	0.403	0.031	0.579	0.412	0.012	0.000	0.022
K	0.000	0.000	0.004	0.000	0.002	0.000	0.007	0.834	0.881	0.063	0.000	0.000	0.062	0.004	0.000	0.891
Cr	0.000	0.000	0.000	0.029	0.000	0.009	0.000	0.000	0.000	0.000	0.000	0.000	0.000	0.000	0.000	0.000
Zn	-	-	-	-	-	-	-	-	-	-	-	-	-	-	-	-
Total	4.996	8.417	5.013	29.703	3.012	8.185	8.179	6.954	7.693	15.426	10.085	4.979	15.467	1.855	1.008	7.816
An	0.80		0.81									0.41				
XFe				0.74				0.55	0.45	0.45	0.39		0.47			0.36
Xalm																
Xprp																
Xgrs																
Xsps																
Ps		21.24				17.24	16.18									

	Bt	Pl	Ms	Ep	Hbl	Ky	Pl
SiO2	36.98	57.76	45.84	38.77	41.95	36.99	30.03
TiO2	1.63	0.00	0.44	0.00	0.22	0.00	0.00
Al2O3	17.53	27.02	33.83	26.56	17.24	62.30	49.77
Fe2O3							
FeO	13.12	0.27	1.73	7.02	14.84	0.48	0.55
MnO	0.00	0.00	0.00	0.00	0.00	0.00	0.00
MgO	14.04	0.00	0.69	0.00	9.37	0.10	0.30
CaO	0.15	9.35	0.00	23.47	10.82	0.00	11.48
Na2O	0.16	6.27	0.72	0.23	1.68	0.32	1.62
K2O	9.33	0.13	9.98	0.00	0.43	0.00	0.09
Cr2O3	0.00	0.00	0.00	0.00	0.14	0.00	0.10
ZnO	n.a.	n.a.	n.a.	n.a.	n.a.	n.a.	n.a.
Total	92.9	100.8	93.2	96.1	96.7	100.2	93.9
Si	2.794	2.571	3.118	3.112	6.235	1.000	1.474
Ti	0.093	0.000	0.023	0.000	0.025	0.000	0.000
Al	1.562	1.418	2.713	2.513	3.021	1.985	2.879
Fe3+							
Fe2+	0.829	0.010	0.098	0.471	1.845	0.011	0.023
Mn	0.000	0.000	0.000	0.000	0.000	0.000	0.000
Mg	1.581	0.000	0.070	0.000	2.075	0.004	0.022
Ca	0.012	0.446	0.000	2.018	1.723	0.000	0.604
Na	0.023	0.541	0.095	0.036	0.484	0.017	0.154
K	0.899	0.007	0.866	0.000	0.082	0.000	0.006
Cr	0.000	0.000	0.000	0.000	0.016	0.000	0.004
Zn	-	-	-	-	-	-	-
Total	7.794	4.994	6.983	8.150	15.505	3.016	5.165
An		0.45					0.80
XFe	0.34				0.47		
Xalm							
Xprp							
Xgrs							
Xsps							
Ps				16.23			

kyanite–staurolite–hornblende (51775a, 51773a) staurolite–garnet–hornblende (51776b) or kyanite–garnet–hornblende (51775b) and garnet–hornblende (51777). The compatibility relations of these samples are illustrated in Fig. 6.10. Garnet is typically more Fe-rich than staurolite, the same relationship which is preserved in the samples from the Eastern European Alps and other areas where metamorphism has apparently not exceeded about 7 kbar. The assemblages are similar to the Fe-rich samples from the Austrian Zillertal (Chapter 5), and the equilibration temperature estimated from garnet-biotite and garnet–hornblende geothermometry are also similar (530-580°C, Table 6.3). However, pressures determined from average pressure calculations are higher (7.7 kbar, Table 6.4) than those from the Zillertal.

6.10 Staurolite-amphibolites in the Black Giants Complex, central Fiordland, New Zealand

Staurolite has been reported from amphibolite and hornblendite sheets which form part of a large metamorphosed layered intrusion, the Black Giants Complex in Fiordland, New Zealand (Gibson, 1978). This was one of the earliest reported occurrences of staurolite in a rock of unquestioned igneous origin. Staurolite is common in these poly-metamorphosed rocks and occurs over a wide area, typically as part of the early metamorphic assemblage, M_1: kyanite–staurolite–hornblende–plagioclase ± minor corundum. It is disseminated throughout the samples or occurs as small euhedral grains in the rims of hornblende porphyroblasts where they are in contact with plagioclase. Garnet is also present in a corundum-bearing sample and is partially replaced by M_2 margarite and chlorite (Gibson, 1978). It seems likely that garnet was stable in the early, M_1, stage of metamorphism, with kyanite, staurolite and hornblende. Further work which should document these rocks more thoroughly is currently in progress (George Gibson, pers comm., 1992).

Gibson (1979) suggests that the second stage of metamorphism evident in these samples resulted in the consumption of hornblende and kyanite to form margarite, chlorite and plagioclase at ~ 550-720°C, with pressures up to 9.5 kbar. As margarite assemblages are stable at lower pressures than kyanite–clinozoisite and lower temperatures than corundum–anorthite (Gibson, 1979), it is likely that the kyanite–hornblende-bearing assemblages formed at temperatures and pressures higher than 550-720°C and 9.5 kbar.

Compositionally, the staurolites reported by Gibson (1978) are less Fe-rich ($X_{Fe,St}$ 0.65-0.68) than other examples of hornblende-staurolite rocks (e.g., Chapters 4 & 5) and they do not contain a high proportion of ZnO. Hornblende is relatively Al-rich, sodic and Mg-rich (X_{Fe} 0.27-0.29) pargasite, pargasitic or tschermakitic hornblende (Leake, 1978) and plagioclase is bytownite to anorthite in composition (An_{84-96}, Gibson, 1979). Garnet analyses are unavailable.

The trivariant assemblage kyanite–staurolite (in corundum-absent, presumably silica saturated rocks) is represented on a compatibility diagram similar to that developed in the previous chapter, with quartz, plagioclase, hornblende and vapour in excess (Fig. 6.11).

Table 6.3. Equilibration temperature estimated from garnet-biotite and garnet - hornblende geothermometry, using the methods of Ferry & Spear, 1978 and Graham & Powell (1984) respectively and the calibrations of Hodges & Spear, 1982 (H&S), and Powell,1985 (P).

garnet-hornblende geothermometry			garnet-biotite geothermometry		
P	51777	51777	H&S	51777	51777
	5.12.16	5.12.31		5.12.31	5.12.19
	5.12.17	5.12.34		5.12.32	5.12.20
XFehbl	0.536	0.549	Xann	0.378	0.359
XFegt	0.857	0.873	Xph/Xann	1.164	1.340
XCagt	0.155	0.173	Xpy	0.097	0.104
			Xalm	0.667	0.626
			Xgross	0.173	0.210
			Xspess	0.062	0.060
ln Kd	1.645	1.727	Rln K	-4.126	-4.149
			P (bar)	6000	6000
T(K)	802	800	T(K)	814	824
T(°C)	529	527	T(°C)	541	551

Table 6.4. Results of average pressure estimates for the Fodalera sample 51777 made using the method of Powell & Holland (1988) and the internally consistent dataset of Holland and Powell (1990). THERMOCALC v2.2b1 run at 15.30 on 3.5.94, thermodynamic dataset produced at 10.27 on 1.4.92. Calculated with hornblende 5.12.34 and plagioclase 15.12.35, with a_{an} = Xan * 1.28 (Orville, 1972), x(H2O) = 1.0 and omitting fgl, gr to improve the statistics.

	tr	ftr	hb	parg	ed	gl	cumm
a	8.05e-5	9.56e-5	0.0107	0.00653	2.76e-4	3.29e-5	3.00e-8
sd(a)/a	2.22911	1.06580	0.48229	0.61473	0.97404	3.48684	1.2e+2
	an	ab	gr	py	alm	phl	ann
a	0.307	0.756	0.00905	0.00111	0.209	0.0130	0.0823
sd(a)/a	0.14407	0.05000	0.56398	0.72328	0.15000	0.52652	0.39490
	east	ilm	ru	q	H2O		
a	0.0134	1.00	1.00	1.00	1.00		
sd(a)/a	0.52324	0	0	0			

Rock : average pressures(for x(H2O) = 1.0)

T°C	500	525	550	575	600	625	650	675	700
av P	7.0	7.4	7.7	8.0	8.4	8.7	9.0	9.4	9.7
sd	1.12	1.13	1.14	1.16	1.19	1.22	1.25	1.29	1.33
f	1.9	1.9	1.8	1.8	1.8	1.8	1.8	1.8	1.9

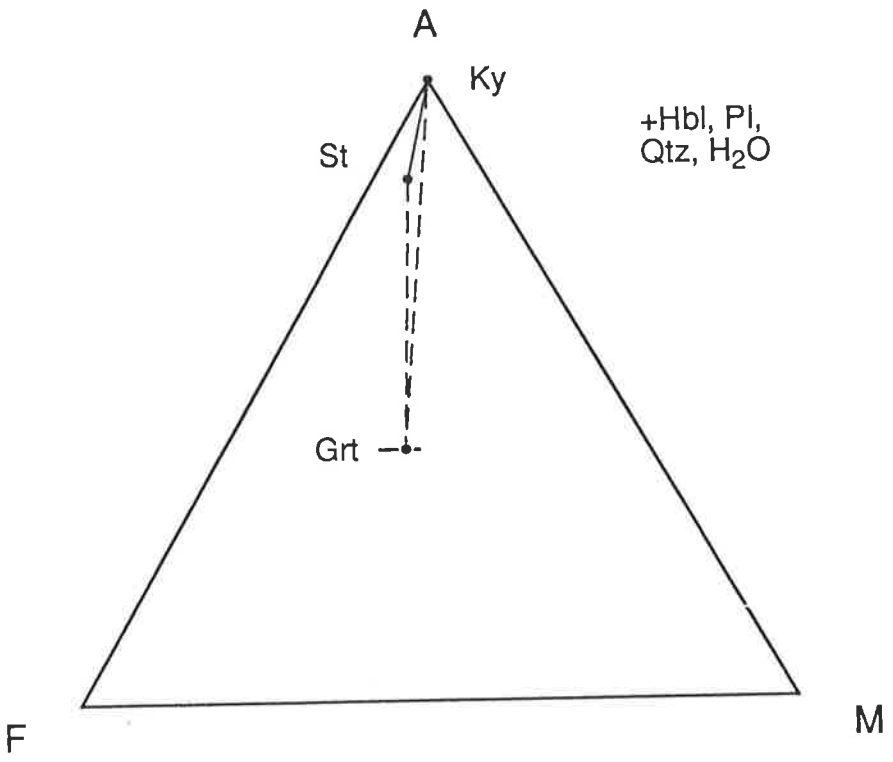

Figure 6.11. Staurolite–kyanite ± garnet from the Black Giants Complex, Fiordland, New Zealand (+ hornblende, plagioclase, quartz and aqueous vapour) equilibrated at > 9.5 kbar, 550-720°C. Data from Gibson (1978, 1979), however the location of garnet is schematic only.

Note that the dotted divariant assemblage kyanite–staurolite–garnet, may be stable but was not specifically reported.

6.11 Aluminous amphibolites from the Dusky Sound area of Fiordland, New Zealand

Ward (1984a,b) has reported staurolite in andalusite-pelites, kyanite–garnet pelites, meta-gabbro, meta-troctolite, mafic meta-tuffs and a "meta-basalt dyke" from Fiordland (20-40 km southwest of those described by Gibson, 1978). In the metabasites staurolite is fine grained and paler than is usual (probably due to its low Ti-content (Ward, 1984b)) and occurs both as "typical" staurolite (cf. Ribbe, 1982) and the extreme varieties (magnesium staurolite and chromian staurolite) which are the emphasis of Ward's work (1984a). Spinel, early (Type 1) staurolite or corundum are intergrown with hornblende enclosing plagioclase (An_{79-82}). Later (Type 2) staurolite occurs with garnet which is replacing hornblende–spinel ± orthopyroxene symplectites or as separate adjacent grains. Chlorite is present in garnet-bearing samples only. Ward (1984a) suggests that the early association (with Type 1 staurolite) results from the reaction of igneous orthopyroxene and plagioclase to form hornblende, an aluminous phase (spinel, staurolite or corundum) and plagioclase. The subsequent consumption of the hornblende–spinel symplectites with some additional orthopyroxene appears to have produced hornblende, garnet ± staurolite, chlorite and corundum. Ward (1984a) estimates that this latter reaction occurred at a temperature of ~ 750°C, and a pressure of ~12 kbar.

The staurolites ($X_{Fe,St}$ 0.45-0.55), garnet ($X_{Fe,Grt}$ 0.41-0.46), tschermakitic- and pargasitic-hornblende, spinel ($X_{Fe,Sp}$ 0.43) and chlorite ($X_{Fe,Chl}$ 0.09) are all particularly Mg-rich in these samples. Although the assemblages are thought to have formed under conditions of high pressure metamorphism, Ward (1984a, pp 538) suggests that "high pressure is not a necessary condition for the formation of staurolites in general in metabasites" and that staurolites may develop at lower pressures in more Fe-rich metabasites. The assemblage involving Type 2 staurolite, garnet and chlorite is depicted in Fig. 6.12a with the assumption that silica is "sufficiently mobile that spatial variation in silica is not a significant factor" (Ward, 1984a, pp 534).

Ward (1984a) also reports that green chromian staurolite from a nearby meta-tuff exists in equilibrium with bluish-green kyanite, gedrite, chlorite, hornblende, quartz, phlogopite, rutile and allanite. Staurolite contains significant Cr_2O_3 and is likely to be stabilised outside its normal (Cr-free) stability field. Phlogopite, allanite and rutile are all stabilized by an additional component and thus do not affect the variance of the assemblage. Thus, this assemblage may correspond to the NCFMASH divariant assemblage, kyanite–chlorite–orthoamphibole (Fig. 6.12b). The compatibility relations in Fig. 6.12b formed at significantly lower pressure and temperature (~8 kbar, 670°C) than those described above and thus define crossed tie-line relationships with staurolite–garnet–chlorite (Fig. 6.12a).

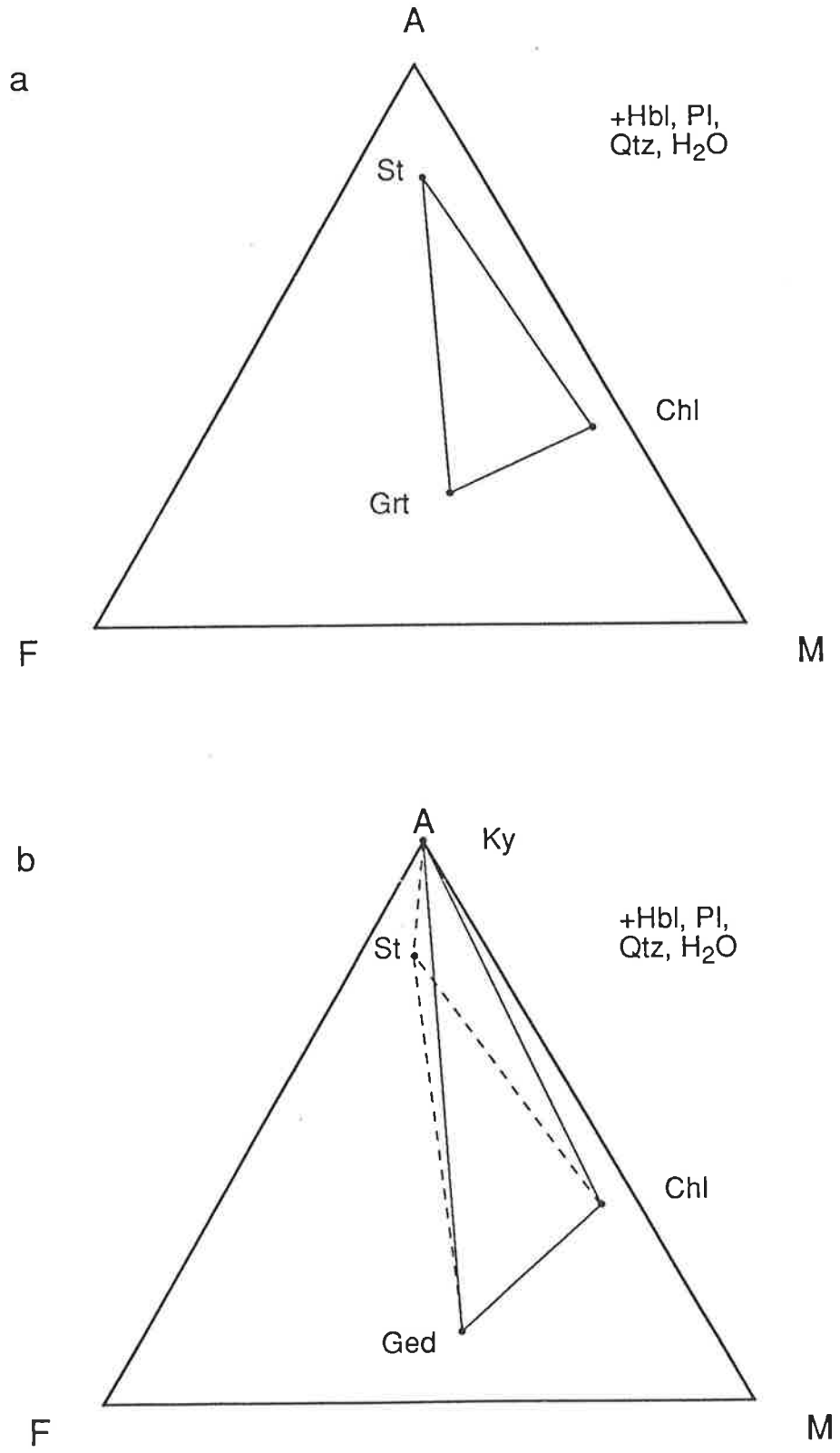

Figure 6.12. Compatibility diagrams for the Dusky Sound area of Fiordland, New Zealand (+ hornblende, plagioclase, quartz and aqueous vapour), data from (Ward, 1984a). (a) Staurolite, garnet and chlorite, equilibrated at 12 kbar, 750°C. (b) Kyanite, staurolite, gedrite and chlorite, equilibrated at 8 kbar, 670°C. Staurolite is likely to be stabilised by the effects of Cr_2O_3.

6.12 Hornblende amphibolites from New Hampshire

Aluminous enclaves of plagioclase and cordierite ± staurolite surround sillimanite in a gedrite–hornblende–plagioclase matrix in amphibolites from southwestern New Hampshire (Schumacher & Robinson, 1987). Corundum and/or sapphirine occur toward the centre of enclaves in less siliceous samples. In several samples Zn-bearing spinel occurs in the matrix or as part of the enclaves and it is likely that this phase is stabilised outside its normal stability field by the presence of Zn. Staurolite contains a variable proportion of zinc depending on its proximity to Zn-spinel and although it forms rims around Zn-spinel it is thought that staurolite would also be stable in the Zn-free system (Schumacher & Robinson, 1987, pp 1070).

The most common reaction texture in the amphibolites is a core of corroded sillimanite surrounded by a corona of staurolite and plagioclase. This is in turn rimmed by cordierite and plagioclase which separate the enclave phases from the hornblende–gedrite–plagioclase matrix. Schumacher and Robinson (1987) suggested that these enclaves result from the continuous reaction of once-stable hornblende and sillimanite to form staurolite, plagioclase and cordierite, however the high ratio of gedrite to hornblende in the samples implies that gedrite may also have been involved as a reactant in these rocks (as well as quartz and aqueous vapour). Thus the reaction would be discontinuous in NCFMASH. The spatial arrangement of the phases is thought to be due to the diffusion-controlled nature of the reaction, in which the location of mineral growth was determined by the relative mobilities of its released constituent components (Schumacher & Robinson, 1987). The diffusion-controlled nature of the reactions resulted in the attainment of *local* equilibrium while the sample as a whole retained up to several dis-equilibrium assemblages.

The reactions which resulted in these diffusion-controlled mineral assemblages were thought to correspond to a decrease in pressure with perhaps a small decrease in temperature during the waning of metamorphism from ~ 625°C, 6 kbar (Schumacher & Robinson, 1987). The compatibility relations of the assemblages before and after this decompression are depicted in Fig. 6.13a and b. The intermediate Fe-Mg nature of these samples makes them an important tool in understanding the phase relations of aluminous amphibolites and their compatibility relations differ significantly from those described from elsewhere.

6.13 Kyanite-bearing "amphibolite whiteschist" from south Westland, New Zealand

Cooper (1980) describes (amongst other assemblages) kyanite–chlorite–talc–hornblende–andesine plagioclase (An_{37})-quartz with later calcite, chlorite and muscovite, from the Jacobs River area of south Westland. Kyanite is partly retrogressed to margarite and hornblende is retrogressed to chlorite. Kyanite, hornblende and plagioclase are rimmed by bundles of fibrous kyanite. The primary ferro-magnesian phases involved in these assemblages are magnesium rich ($X_{Fe,Hbl}$ 0.16-0.20, $X_{Fe,Chl}$ 0.15-0.16, $X_{Fe,Tlc}$ 0.07), and

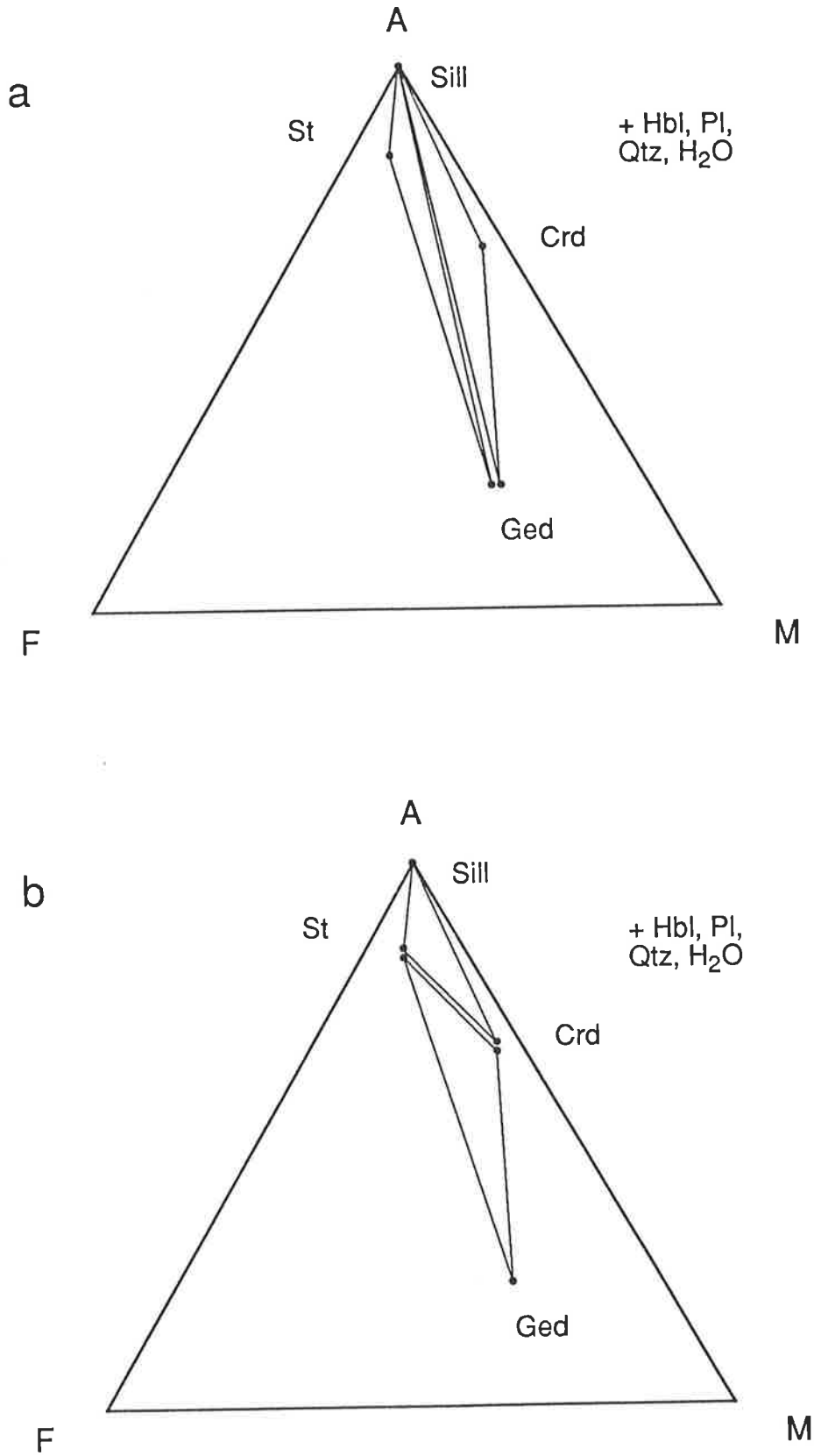

Figure 6.13. Compatibility diagrams for pressure and temperature above (a) and below (b) ~ 625°C, 6 kbar, i.e. before and after the reaction of sillimanite–orthoamphibole–hornblende to from staurolite–cordierite in southwestern New Hampshire (+ hornblende, plagioclase, quartz and aqueous vapour). Data from Schumacher & Robinson (1987).

kyanite contains significant Cr_2O_3 (0.71-1.44 wt %).

Cooper (1980) estimates a minimum temperature for amphibolite facies metamorphism of more than 600°C, at pressures of approximately 10 kbar. Retrogression to margarite assemblages occurred as a result of decreasing pressures (Cooper's Fig. 4, 1980).

The compatibility relations in Cooper's (1980) high pressure amphibolites apply to far more magnesian samples than those discussed previously (Fig. 6.14).

6.14 Cordierite–talc–kyanite-amphibolites from the Pamirs of Tajikistan (in the former USSR)

Very Mg-rich amphibolites from the southwestern Pamirs in Tajikistan include a variation on the "whiteschist" assemblage first reported by Schreyer (1973, 1974, 1977). Grew et al. (1988) describe inclusions of talc, cordierite, quartz and apatite in kyanite porphyroblasts which, along with hornblende, are separated from matrix talc by reaction rims of anorthite and cordierite ± corundum or sapphirine. The kyanite may be partly altered to sillimanite and/or andalusite. Anorthite and/or corundum and sapphirine are spatially associated with kyanite, and cordierite is adjacent to talc (X_{Fe} 0.004-0.007) and tremolitic- to magnesio-hornblende (X_{Fe} 0.013-0.018). Cordierite (X_{Fe} 0.005-0.013) and quartz were also identified from the matrix and as inclusions in hornblende, while minor retrograde chlorite is observed in kyanite and as veinlets in andalusite. Tourmaline, sulphides and apatite occur as accessory phases. Estimated equilibration conditions for the early kyanite–talc–hornblende ± quartz ± cordierite assemblage (Fig. 6.15) from the southwestern Pamirs are ≥ 650°C and ≥ 7 kbar while later sillimanite and the assemblage cordierite–anorthite–corundum probably developed at T ≤ 675°C and 6.2-6.5 kbar (Grew et al., 1988). The higher pressure assemblage reported from the Pamirs occurs at the Mg-rich extreme of the compatibility diagram in Fig. 6.15 and thus is difficult to compare to other kyanite–staurolite-bearing amphibolites.

6.15 Compatibility relations in kyanite–staurolite amphibolites

The variation of compatibility relations in kyanite–staurolite amphibolites with changing P-T conditions is a useful guide to the detailed phase relations of kyanite–staurolite amphibolites. The excellent range of assemblages displayed in low temperature-intermediate pressure amphibolites (550-650°C, 5.5-8 kbar) provides valuable information about the reactions which occur in this part of P-T space. Among the most useful compatibility relations are those presented by Spear (1982) from the Post Pond Volcanics. These amphibolites are internally buffered with respect to μ_{H_2O} (Spear, 1982) and the resulting range of assemblages has been resolved into two extremes; high and low μ_{H_2O}. The correlation of increasing temperature with decreasing μ_{H_2O} has been noted in many previous investigations (e.g., Spear, 1978; Schumacher & Robinson, 1987) and it is expected that high and low μ_{H_2O}

Figure 6.14. Kyanite–chlorite–talc from south Westland, New Zealand (+ hornblende, plagioclase, quartz and aqueous vapour) equilibrated at ~10 kbar, > 600°C. Data from Cooper (1980).

Figure 6.15. Kyanite–talc–cordierite from the Pamirs of Tajikistan in the former USSR (+ hornblende, plagioclase, quartz and aqueous vapour) equilibrated at ≥ 650°C and ≥7 kbar. Data from Grew et al. (1988).

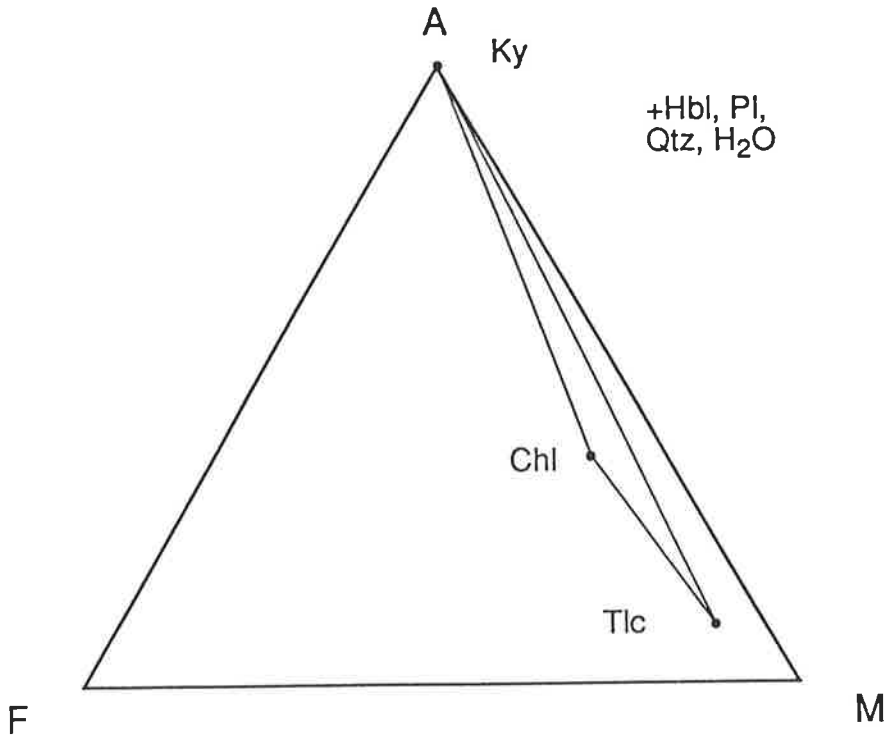
A
Ky
+Hbl, Pl,
Qtz, H_2O
Chl
Tlc
F
M

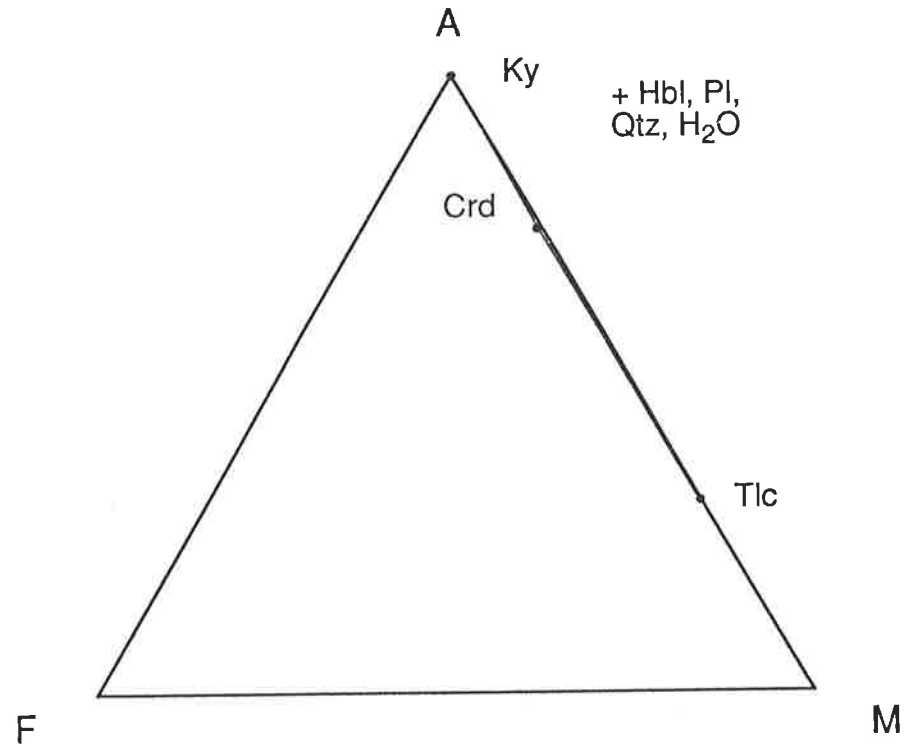
A
Ky
+ Hbl, Pl,
Qtz, H_2O
Crd
Tlc
F
M

compatibility relations from the Post Pond Volcanics would correspond to metamorphism at lower and higher temperatures, respectively and thus help define the phase relations at these conditions. Humphreys' (1993) amphibolite assemblages also define higher (M_1) and lower (M_2) temperature parageneses and similar information can be obtained from the comparison of the higher and lower pressure assemblages reported by Schumacher and Robinson (1987) or the compatibility relations reported from the Austrian Zillertal (Selverstone et al., 1984; Chapter 5) and the Harts Range in central Australia (Chapter 4) at higher pressures. Less complete compatibility diagrams for compositionally restricted rocks also provide some information about the generally magnesium-rich equilibria which have been observed from high pressure and temperature amphibolites.

Figure 6.16 displays the compatibility diagrams determined from the literature arranged in P-T space using the equilibration pressures and temperatures estimated by the original authors. For clarity the compatibility diagrams are drawn schematically. In the following section the relationships between the different compatibility diagrams and the assemblages they involve will be discussed. The resulting information will be compared to the NCFMASH phase diagram of Spear and Rumble (1986) and those calculated in this project (Chapter 3, Fig. 3.20).

6.15.1 Garnet–chlorite stability

Garnet–chlorite amphibolites are observed in regions which have experienced low temperature and low to intermediate pressure metamorphism (e.g. Spear, 1982; Selverstone et al., 1984; Helms et al., 1987; Chapter 5). The compatibility diagrams in Fig. 6.16 suggest that garnet–chlorite is stable only at temperatures less than about 550°C and in higher temperature amphibolites garnet–chlorite is metastable with respect to the staurolite–orthoamphibole tie-line (e.g. Spear, 1982; Schumacher & Robinson, 1987; Humphreys, 1993). At intermediate pressures ($\geq$ 7 kbar) the phase relations are more complex and the garnet–chlorite tie-line (stable in the Zillertal amphibolites, Selverstone et al., 1984; Chapter 5) breaks down to stabilise tie-lines joining orthoamphibole to staurolite, aluminosilicate or cordierite (e.g. Chapter 4) with increasing pressure. The breakdown of chlorite–garnet to stabilise the staurolite–orthoamphibole tie-line, as illustrated in Fig. 6.17, is only one of five reactions separating the compatibility relations of the Zillertaler Alpen (Selverstone et al., 1984; Chapter 5) from those of the only slightly higher temperature Harts Range amphibolites (Chapter 4). These other reactions are discussed in later sections.

An anomalous, high temperature, high pressure report of coexisting garnet and chlorite in amphibolites from Dusky Sound in New Zealand (750°C, 12 kbar, Ward, 1984a) may be due to either dis-equilibrium (perhaps retrograde) chlorite or an inaccurate temperature estimate (which Ward acknowledges is a possibility, 1984a, pp 535). Irrespective of the source of this problem, it seems clear from the other compatibility relations illustrated in Fig. 6.16 that garnet–chlorite is not stable at such elevated pressures and temperatures.

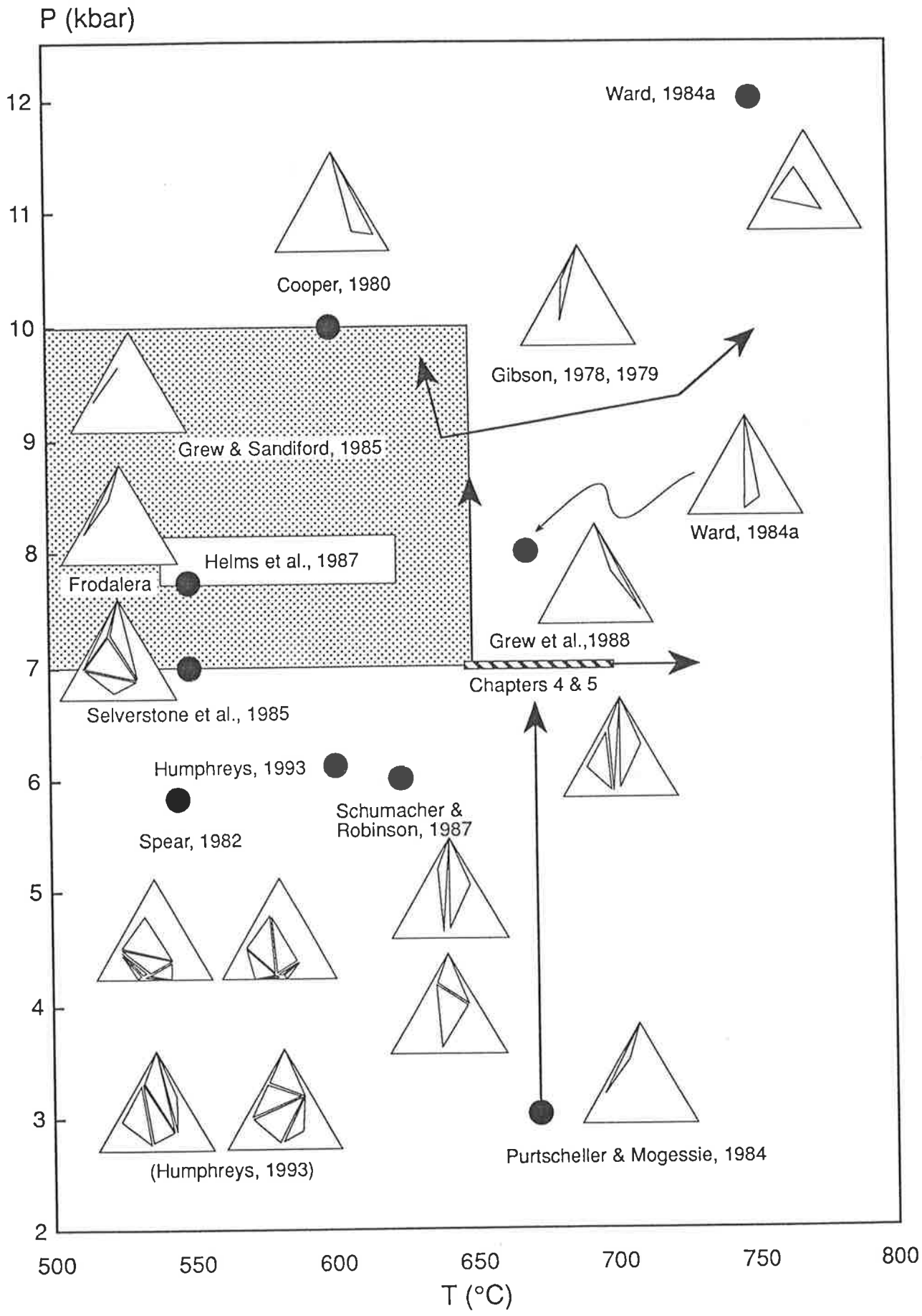

Figure 6.16. The compatibility diagrams determined from the literature arranged according to the equilibration pressures and temperatures estimated by the original authors. For clarity, the compatibility diagrams are schematic (+ hornblende, plagioclase, quartz and aqueous vapour). The estimates of Gibson (1978, 1979) and Grew et al., (1988) are minimum estimates, as indicated by the arrows. The estimates of Purtscheller & Mogessie (1984) are considered to be unreasonable and the arrow indicates a more appropriate pressure.

Figure 6.17. The compatibility diagrams and discontinuous reactions relating the lower temperature compatibility diagram from the Zillertaler Alpen (Selverstone et al., 1984; Chapter 6) to the higher temperature diagram from the Harts Range (Chapters 4 & 5), (+ hornblende, plagioclase, quartz and aqueous vapour). (a) to (b) Staurolite becomes more Fe-rich than garnet; (b) to (c) garnet–chlorite–cummingtonite ⇒ orthoamphibole; (c) to (d) garnet–chlorite ⇒ staurolite–orthoamphibole; (d) to (e) staurolite–chlorite ⇒ kyanite–gedrite; (e) to (f) kyanite–chlorite ⇒ cordierite–orthoamphibole.

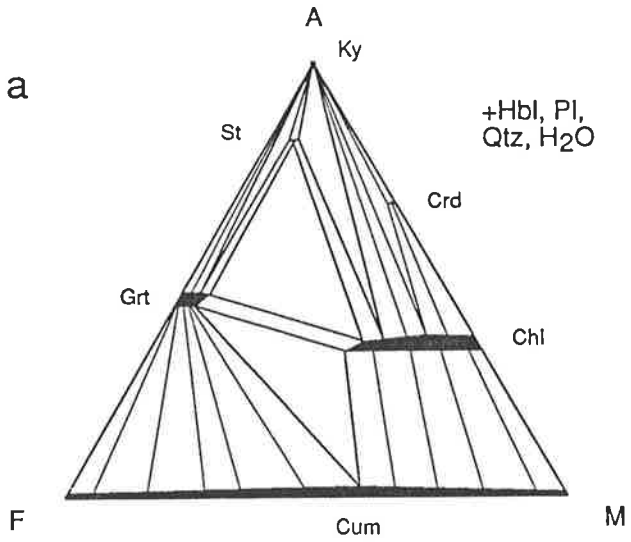
a
A
Ky
St
+Hbl, Pl,
Qtz, H_2O
Crd
Grt
Chl
F
Cum
M

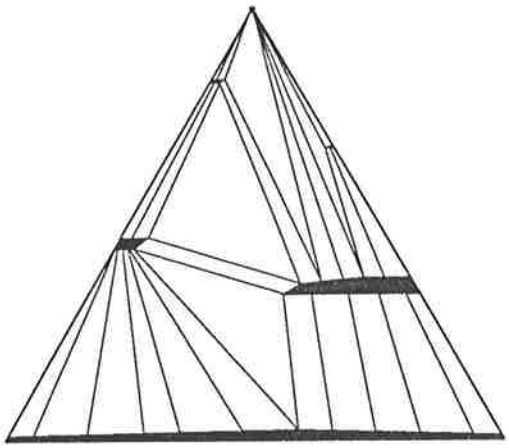
b

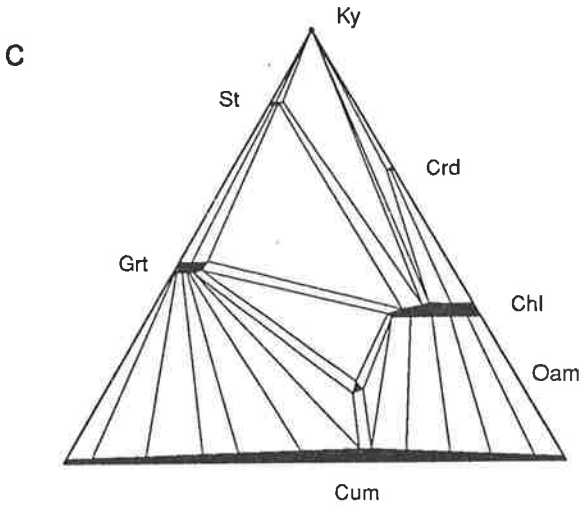
c
Ky
St
Crd
Grt
Chl
Oam
Cum

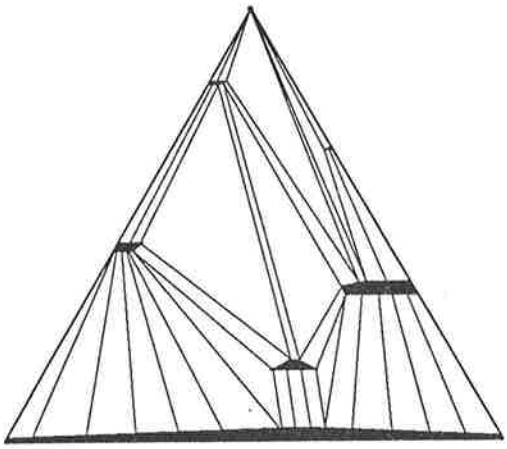
d

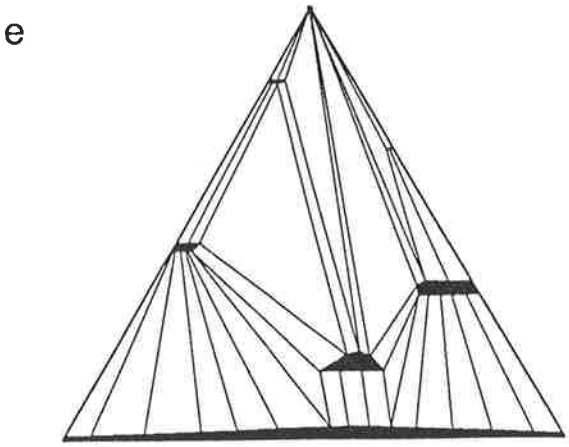
e

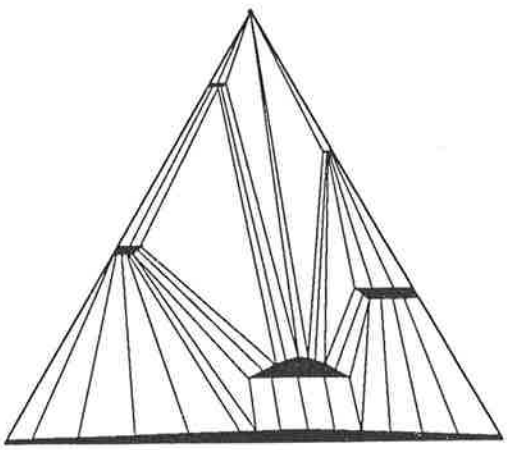
f

The amphibolite assemblages reported in the literature and summarised here do not impose an upper pressure limit on the stability of garnet–chlorite, however the (reliable) highest pressure occurrences equilibrated at 7 and 8 kbars (Selverstone et al., 1984 and Helms et al., 1987, respectively) suggest that the upper pressure limit may be about 8 kbar.

6.15.2 Staurolite–cordierite stability

Schumacher and Robinson (1987) and Humphreys (1993) provide the only reported instances of co-existing staurolite and cordierite in hornblende amphibolites. The P-T estimates made by these authors suggest that staurolite–cordierite is stable at 600-650°C and ~6 kbar. The compatibility relations of other workers suggest that the assemblage is stable in a relatively small pressure range and that at higher pressures staurolite–cordierite is metastable with respect to the aluminosilicate–chlorite (Selverstone et al., 1984; Ward, 1984a; Chapter 5), aluminosilicate–orthoamphibole (e.g. Ward, 1984a; Schumacher & Robinson, 1987; Chapter 4) or, possibly, aluminosilicate–garnet (Gibson, 1978, 1979) tie-lines, at successively higher temperatures. The low temperature limit of staurolite–cordierite stability occurs between the high (M_1) and lower (M_2) temperature metamorphic assemblages observed in the Copperton Formation (Humphreys, 1993) as illustrated in Fig. 6.18. Figure 6.18b depicts the first occurrence of staurolite–cordierite which becomes stable with respect to the sillimanite–chlorite tie-line with increasing temperature. The compatibility relations in Fig. 6.18c are similar to those from the New Hampshire amphibolite (Schumacher & Robinson, 1987) suggesting that the two compatibility diagrams characterise the same portion of P-T space.

6.15.3 Staurolite–garnet Fe-partitioning

One of the important differences between the compatibility diagrams for the Zillertal and Harts Range amphibolites (Fig. 6.17), is a reversal in the relative Fe-partitioning of staurolite and garnet. In general garnet appears to be more Fe-rich than staurolite in low pressure assemblages (< about 7 kbar, e.g. Spear, 1982; Selverstone et al., 1984; Chapter 5, Section 6.9) whereas in amphibolites which equilibrated at higher pressures, staurolite is generally more Fe-rich than garnet (e.g. Grew & Sandiford, 1985; Ward, 1984a; Gibson, 1978; Helms et al., 1987; Chapter 4). The chemical data from the Ötztal kyanite–staurolite–garnet amphibolites contradicts this general trend, and although the equilibration conditions estimated by Purtscheller & Mogessie (1984) are well below 7 kbar, staurolite is more Fe-rich than co-existing garnet (Purtscheller & Mogessie, 1984). However, as has been noted previously (Section 6.8; Grew & Sandiford, 1985), the pressure estimate provided by these authors (3-4 kbar) seems anomalously low considering that the rocks are kyanite-bearing and are associated with eclogites which are thought to be the same age. Despite these problems, the compositions of the projecting phases in this assemblage cause garnet to project to the Fe-rich side of staurolite so that at least the apparent Fe-enrichment corresponds to the general

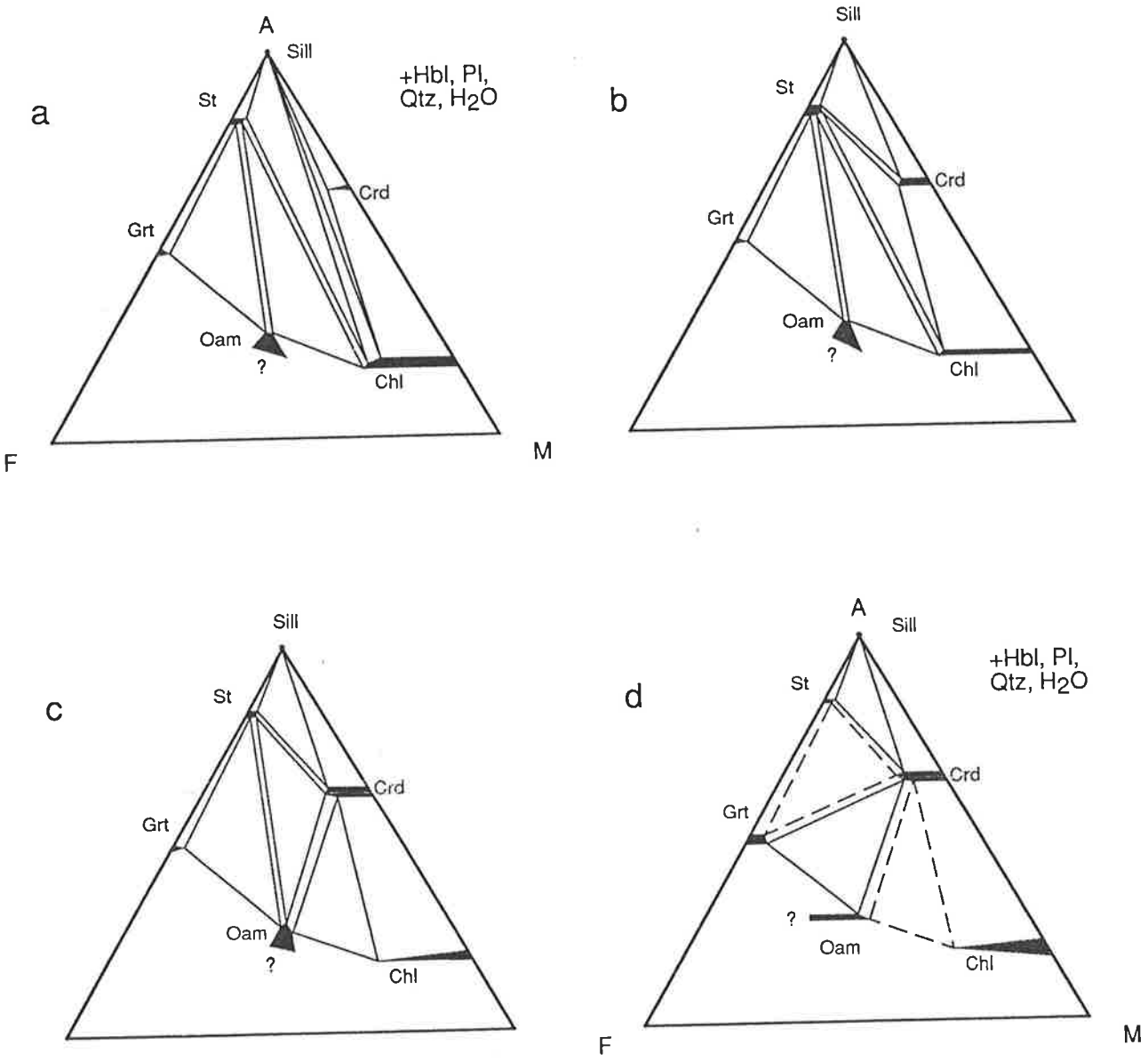

Figure 6.18. Compatibility diagrams and discontinuous reactions relating the lower temperature (M_2) compatibility diagram (a) to the higher temperature (M_1) compatibility diagram (b) from the Copperton Formation (Humphries, 1993), (+ hornblende, plagioclase, quartz and aqueous vapour). The discontinuous reactions separating these compatibility diagrams are: (a) to (b) Als + Chl ⇒ St + Crd; (b) to (c) St + Chl ⇒ Crd + Oam; (c) to (d) St + Oam ⇒ Crd + Grt.

trend.

The distribution co-efficient (K_D) of Fe-Mg partitioning between garnet and staurolite is reversed between the similar pressure assemblages from the Austrian Zillertal (Selverstone et al., 1984; Chapter 5) and Harts Range (Chapter 5), suggesting that the K_D may dependent on temperature as well as pressure and that at 7 kbar, the reversal occurs between 550 and 650°C.

6.15.4 Orthoamphibole-bearing assemblages

Gedrite is observed in many of the reported kyanite- or staurolite-amphibolites and is only explicitly excluded from the Zillertal hornblende garbenschiefer (Selverstone et al., 1984; Chapter 5). The relatively low temperature and elevated pressure of these orthoamphibole-absent rocks implies that this phase may be restricted to the high temperature side of a positively sloping reaction involving garnet–chlorite–cummingtonite. With increasing temperatures gedrite appears to become stable with respect to successively more aluminous phases (chlorite, staurolite, then kyanite) with increasing pressure (e.g. Figs. 6.16 and 6.17) and is stable with cordierite in the relatively low pressure, higher temperature Copperton (Humphreys, 1993) and New Hampshire (Schumacher & Robinson, 1987) amphibolites. Only the Post Pond Volcanics contain evidence of two co-existing orthoamphiboles (Spear, 1982), suggesting that the orthoamphibole solvus is exceeded in the higher pressure and temperature amphibolites.

6.15.5 Cordierite–gedrite stability

The important assemblage cordierite–gedrite is reported only from higher temperature amphibolites (> 550°C) at pressures up to ~7.5 kbar (e.g. Schumacher & Robinson, 1987; Humphreys, 1993; Chapter 4). At lower temperatures the cordierite–gedrite tie-line is metastable with respect to staurolite–chlorite and garnet–chlorite (e.g. Spear, 1982) and kyanite–chlorite (e.g. Selverstone et al., 1984, Fig. 6.17) while at higher pressures the kyanite–chlorite tie-line is stable (Helms et al., 1987; Ward, 1984a). The natural assemblages also reflect cordierite's instability at pressures greater than ~ 10 kbar (e.g. Cooper, 1980) when it becomes metastable with respect to the "whiteschist" (Schreyer, 1973, 1974) assemblage kyanite–chlorite–talc.

6.15.6 Staurolite–chlorite stability

The staurolite–chlorite tie-line appears to be stable at low temperatures, up to about 600-650°C (Spear, 1982; Selverstone et al., 1984; Humphreys, 1993; Chapter 5, Fig. 6.17). At higher temperatures staurolite–chlorite becomes metastable with respect to the cordierite–garnet and cordierite–orthoamphibole tie-lines (Humphreys, 1993) whereas kyanite–orthoamphibole (Ward, 1984a; Schumacher & Robinson, 1987; Chapter 4) and possibly

kyanite–garnet (Gibson, 1978, 1979) form stable tie-lines at higher pressures and temperatures. The natural assemblages do not provide a direct upper pressure limit to staurolite–chlorite stability in lower temperature amphibolites as the high pressure and high temperature assemblages reported by Grew & Sandiford (1985) and Cooper (1980) are extremely Fe-rich and Mg-rich, respectively, and thus care unlikely to influence the stability of staurolite–chlorite-bearing assemblages.

6.15.7 Al-poor assemblages

For less aluminous amphibolites, the assemblages described by Spear (1982) suggest that increasing temperature or decreasing μ_{H_2O} causes cummingtonite–gedrite to become metastable with respect to chlorite–anthophyllite in Mg-rich rocks, and garnet–anthophyllite in more Fe-rich samples at a temperature of about 600°C. Figure 6.19 shows the intermediate compatibility diagrams which may separate the high and low μ_{H_2O} (low and high temperature) compatibility diagrams of Spear (1982). The univariant reactions representing this sequence of compatibility diagrams must occur within a relatively small temperature range as assemblages from both high and low μ_{H_2O} extremes are observed in close proximity and appear to have been metamorphosed over a very small P-T range (Spear, 1982).

6.15.8 Summary

Despite the growing number of staurolite–kyanite amphibolites which have been described from around the world, the suite of compatibility diagrams they define remains incomplete. Many of the reported occurrences consist of only one low-variance assemblage, often in an extreme bulk composition, and even those which contain univariant assemblages are only incompletely understood. Of the several instances where a range of equilibria are preserved from a variety of bulk compositions, these often exhibit crossed tie-line relations which are only rarely adequately explained (cf. Spear, 1982 and Helms et al., 1987). The equilibration conditions of many of the assemblages are also poorly constrained. Further problems stem from variation and uncertainties in the relative compositions of phases (e.g. staurolite and garnet), the stability of sub-solidus or super-solidus orthoamphiboles and the stability of the aluminosilicate polymorphs. However, although the compatibility relations in kyanite–staurolite amphibolites are often restricted to extreme bulk compositions, especially at high pressures, and only rarely are there a range of assemblages represented from one locality, in combination they are a valuable source of information about the phase relations in amphibolites. The general features of the phase relations in amphibolites determined here from the natural assemblages will be used in the following section to construct an NCFMASH phase diagram which is consistent for the observed assemblages.

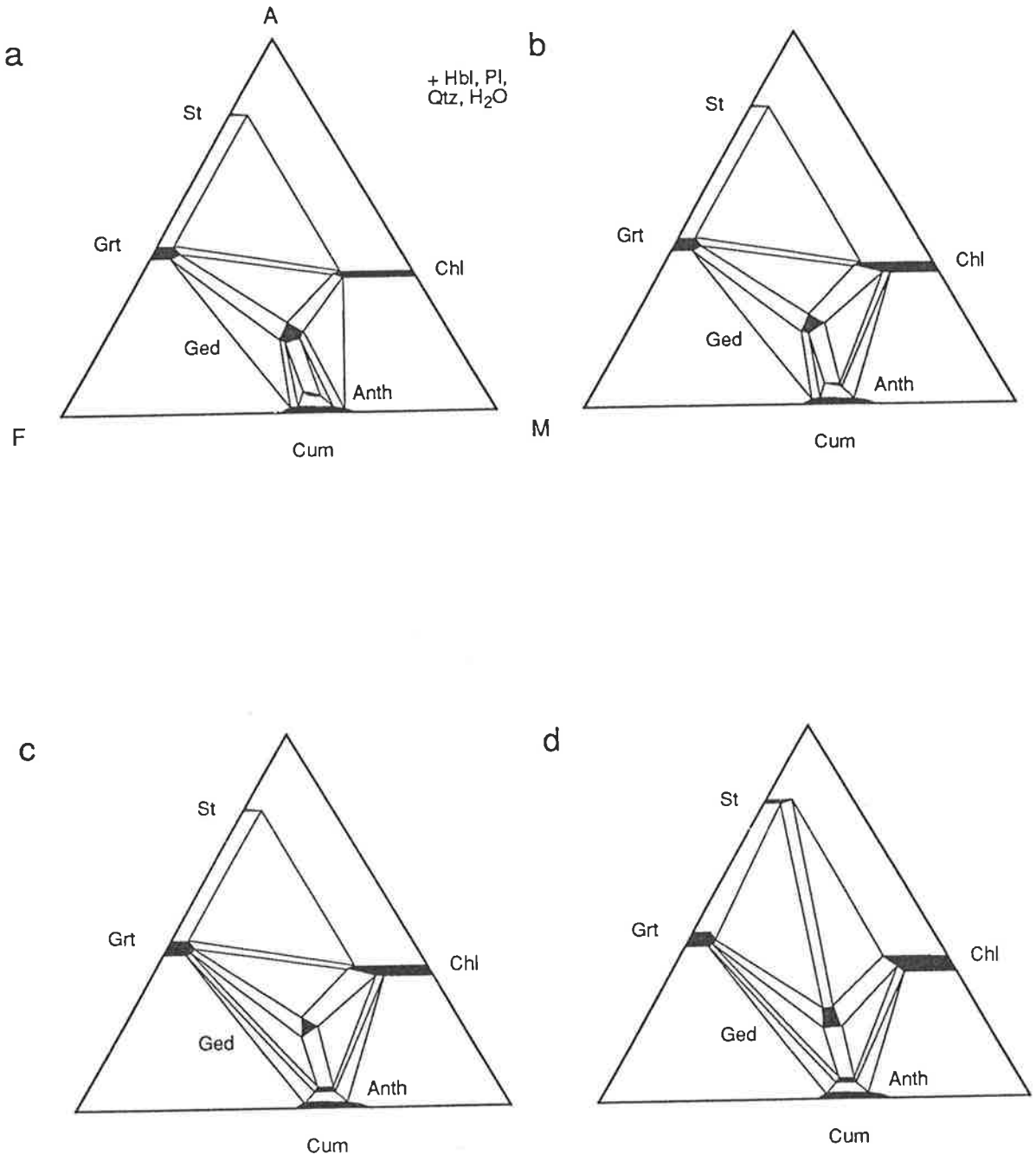

Figure 6.19. The compatibility diagrams which are intermediate between the high (a) and low (b) μH2O compatibility diagrams of Spear (1982), shown in Fig. 6.2, (+ hornblende, plagioclase, quartz and aqueous vapour).(a) to (b) Ged + Cum ⇒ Anth + Chl; (b) to (c) Ged + Cum ⇒ Anth + Grt; (c) to (d) Grt + Chl ⇒ St + Ged.

6.16 A petrogenetic grid based on natural amphibolite assemblages

The compatibility relations discussed in the previous sections provide valuable information about the stability fields of specific assemblages and the reactions which control the phase relations. In this section, this information is compiled and used to construct a P-T grid in the NCFMASH compositional system. Later, this grid will be compared to those determined by Spear and Rumble (1986), and constructed in earlier chapters from equilibrium thermodynamics calculations.

The univariant (in NCFMASH) assemblages observed in real amphibolites form a foundation on which to base the NCFMASH petrogenetic grid. Three distinct univariant equilibria have been reported in the literature (all plus hornblende, plagioclase, quartz, vapour):

kyanite–staurolite–garnet–chlorite (Crd, Oam)
from the Zillertaler Alpen (Selverstone et al., 1984; Chapter 5),

kyanite–staurolite–chlorite–gedrite (Crd, Grt)
from the Georgia Blue Ridge amphibolite (Helms et al., 1987) and

staurolite–garnet–chlorite–gedrite (Als, Crd)
from the Post Pond Volcanics (Spear, 1982) and

kyanite–staurolite–cordierite–gedrite (Grt, Chl)
from southwestern New Hampshire (Schumacher & Robinson, 1987).

It is likely that three of these univariant assemblages intersect in the cordierite-absent invariant point and that [Crd] is thus stable in NCFMASH, however, the presence of cordierite in several of the assemblages discussed above and the stability of the (Grt, Chl) univariant assemblage in New Hampshire suggests that at least one other invariant point, either [Grt] or [Chl] must also be stable.

Further information about which invariant points and univariant lines are likely to be stable may be obtained from the divariant NCFMASH assemblages. It is expected that many of the observed divariant assemblages will correspond to CFMASH sub-system univariant reactions (see the discussion of adding Ca to the FMASH compositional system, Section 3.3) and so may give an indirect indication of the stable phase relations in NCFMASH. The CFMASH phase relations implied from the divariant assemblages may be expanded into the NCFMASH system appropriate to amphibolites by making assumptions about the role of Na in amphibolite phases.

Table 6.5 lists the divariant assemblages reported from the literature as sets of reactions which intersect in the CFMASH invariant points [Crd, Chl], [Grt, Chl], [Grt,Oam], [Crd, Oam] and [Als, Chl], which are thus implied to be stable. Several of the observed NCFMASH divariant assemblages do not fit into this list. There are two likely explanations for this; a) they are involved in additional stable CFMASH invariant points or b) their divariant NCFMASH

Table 6.5. The amphibolite assemblages summarised in Chapter 6 divided according to the CFMASH invariant equilibria to which they are related.

CFMASH invariant assemblage label	phases	CFMASH univariant assemblage label	phases	references
[Crd, Chl]	Als St Grt Oam			
		[Crd,Chl,Oam]	Ky St Grt	Gibson, 1978[1], 1979; Selverstone et al., 1984; Chapter 5; Section 6.9
		[Crd,Grt,Chl]	Sill St Oam	Schumacher & Robinson, 1987; Chapter 4
		[Ky,Crd,Chl,Oam]	St Grt	Grew & Sandiford, 1985
		[Ky,Crd,Chl]	St Grt Oam	Spear, 1982; Chapter 4
[Grt, Chl]	Als St Crd Oam			
		[St,Grt,Chl]	Ky Crd Oam	Schumacher & Robinson, 1987; Chapter 4
		[Grt,Chl,Oam]	Sill St Crd	Humphreys, 1993, Schumacher & Robinson, 1987
		[Crd,Grt,Chl]	Sill St Oam	Schumacher & Robinson, 1987; Chapter 4
		[Ky,Grt,Chl]	St Crd Oam	Schumacher & Robinson, 1987
[Grt, Oam]	Als St Crd Chl			
		[St,Grt,Oam]	Ky Crd Chl	Humphreys, 1993
		[Grt,Chl,Oam]	Sill St Crd	Humphreys, 1993, Schumacher & Robinson, 1987
		[Grt,Chl,Oam]	Ky St Crd	Selverstone et al., 1984; Schumacher & Robinson, 1987; Helms et al., 1987; Humphreys, 1993; Chapter 5
[Crd,Oam]	Als St Grt Chl			
		[Crd,Grt,Oam]	Ky St Chl	Selvestone et al., 1984; Helms et al., 1987; Humphreys, 1993; Chapter 5
		[Crd,Chl,Oam]	Ky St Grt	Gibson[1], 1978, 1979; Selverstone et al., 1984; Chapter 5; Section 6.9
		[Ky,Crd,Chl,Oam]	St Grt	Grew & Sandiford, 1985
		[Ky,Crd,Oam]	St Grt Chl	Spear, 1982; Selverstone et al., 1984; Ward[1], 1984(A); Helms et al., 1987; Chapter 5
[Als, Chl]	St Crd Grt Oam			
		[Ky,St,Chl]	Crd Grt Oam	Humphreys, 1993
		[Ky,Grt,Chl]	St Crd Oam	Schumacher & Robinson, 1987
		[Ky,Crd,Chl,Oam]	St Grt	Grew & Sandiford, 1985
		[Ky,Crd,Chl]	St Grt Oam	Spear, 1982; Chapter 4
others		[Ky,St,Crd]	Grt Chl Oam	Spear, 1982; Helms et al., 1987
		[St,Crd,Grt]	Ky Chl Oam	Ward, 1984(B)
		[Ky,Crd,Grt]	St Chl Oam	Spear, 1982; Humphreys, 1993

[1] The stability of garnet is only *implied* by Gibson, 1978
[2] Doubtful reliability, see Section 6.15.1

assemblages occur in the interior of the NCFMASH phase diagram and so do not have stable CFMASH equivalents. Schreinemakers analysis of the CFMASH reactions is expected to reveal which of these alternatives is appropriate.

Figure 6.20 illustrates the schematic phase relations in the CFMASH system (projected from quartz and aqueous vapour) based on the assumption that the invariant points [Crd, Chl], [Grt, Chl], [Grt,Oam], [Crd, Oam] and [Als, Chl] are stable. The relative locations of the invariant points and the approximate slopes of the reactions are taken from Chapter 3 (where the calculated compositions of the phases place staurolite in the interior of the aluminosilicate–garnet–orthoamphibole and aluminosilicate–garnet–orthoamphibole–chlorite tie-triangles). Two of these invariant points, [Crd, Oam] and [Crd, Chl], were found to be stable in Chapter 3 (Fig. 3.15), however slight adjustments to the slopes of the reactions were required to stabilise [Grt, Chl] and hence the remainder of the invariant points. Schreinemakers analysis determines that two other invariant points, [Als, Oam] and [Hbl,Chl], are also stable. The invariant points and univariant lines represented in Fig. 6.20 include the hornblende- and anorthite-absent equilibria because these help to identify the effect of adding sodium to the compositional system. The absence of CFMASH invariant points which allow the unclassified assemblages, garnet–chlorite–orthoamphibole, aluminosilicate–garnet–chlorite, and staurolite–chlorite–orthoamphibole, (see Table 6.5) suggests that these phases must be stable in the interior of the NCFMASH petrogenetic grid.

In order to qualitatively extend the phase relations in Fig. 6.20 into the NCFMASH system, assumptions must be made about the effects of sodium on the stability of the phases and on the equilibria in general. Very sodium-rich phases are not typically observed in amphibolites. Thus, although the number of components increases with the addition of sodium, no new phase is likely to be stabilised and so the variance of a given assemblage will increase. The sodium content of natural amphibolite phases gives an indication of the ease with which the different phases accommodate sodium. Plagioclase is typically the most sodic phase, followed by hornblende and orthoamphibole. The remainder of the phases typically contain an insignificant amount of sodium. Thus, the addition of Na to the CFMASH equilibria causes plagioclase to be stabilised with respect to hornblende, hornblende with respect to orthoamphibole and orthoamphibole with respect to other phases. As a result of the calcium-rich nature of plagioclase and hornblende, these phases generally occur on opposite sides of CFMASH reactions and so increasing the stability field of plagioclase is likely to decrease that of hornblende. This means that the effective shift in the equilibria with the addition of sodium will stabilise plagioclase and orthoamphibole (often at the expense of hornblende) and the NCFMASH univariant reaction which emanates from each CFMASH invariant point will be close to the CFMASH [An] reaction, displaced toward [Oam]. The light, dotted arrows in Fig. 6.20 represent the orientation of the NCFMASH univariant emanating from each CFMASH invariant.

Figure 6.20. Schematic petrogenetic grid for the CFMASH compositional system, with quartz and vapour in excess. Constructed from the divariant assemblages listed in Table 6.5, considering only the kyanite aluminosilicte polymorph. Stars represent singularities (See Chapter 3) Light, dashed arrows mark the NCFMASH univariant curves which emanate from each CFMASH invariant point.

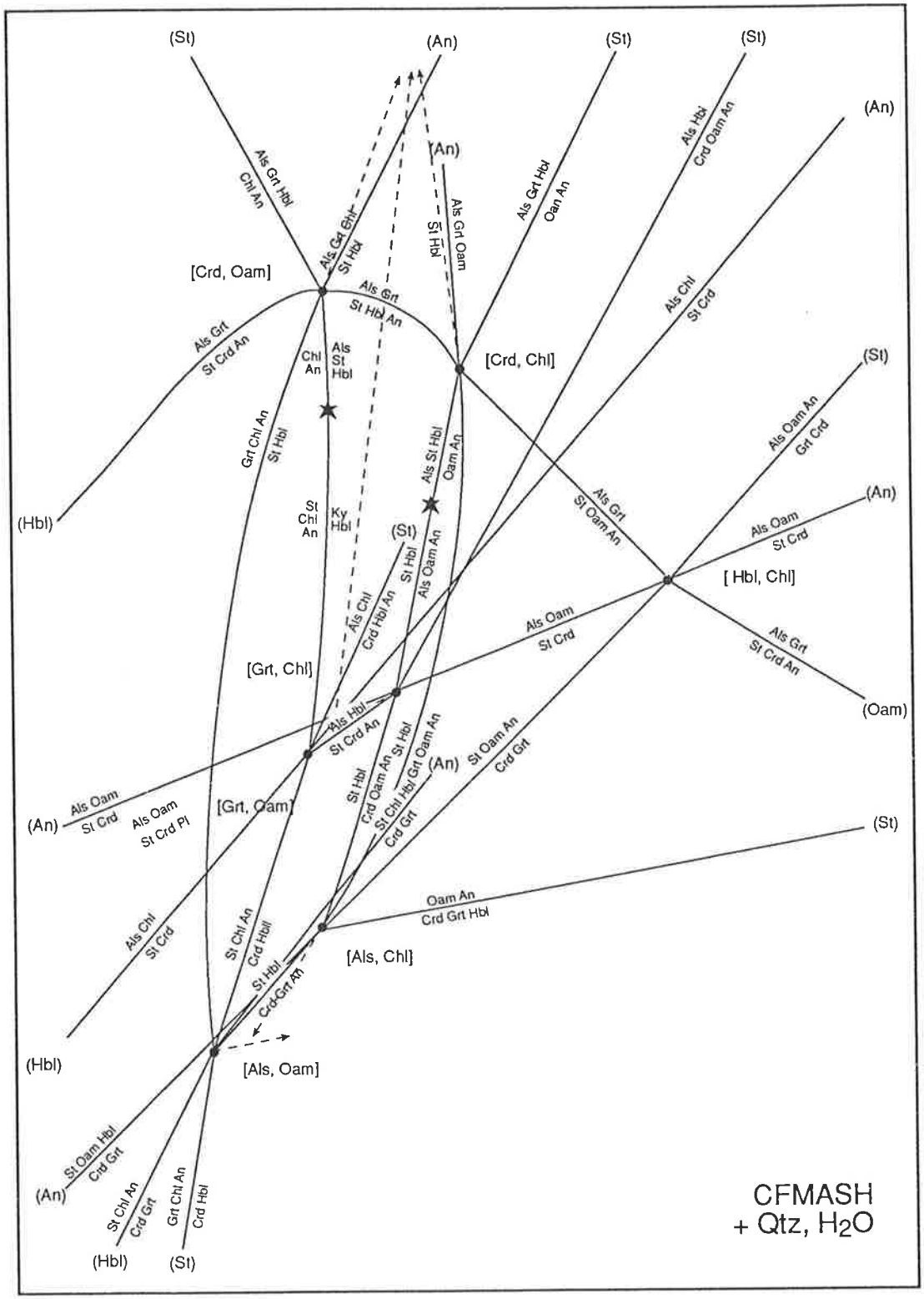
P
T
(St)
(An)
(St)
(St)
(An)
Als Grt Hbl
Chl An
Als Grt Ght
St Hbl
[Crd, Oam]
Als Grt
St Hbl An
Als Grt Oam
St Hbl
Als Grt Hbl
Oan An
Als Hbl
Crd Oam An
Als Chl
St Crd
Als Grt
St Crd An
Chl
An
Als
St
Hbl
[Crd, Chl]
(Hbl)
Grt Chl An
St Hbl
Als St Hbl
Oam An
(St)
Als Oam An
Grt Crd
St
Chl
An
Ky
Hbl
(St)
St Hbl
Als Oam An
(An)
Als Oam
St Crd
[Hbl, Chl]
Als Chl
Crd Hbl An
Als Grt
St Oam An
Als Oam
St Crd
[Grt, Chl]
Als Grt
St Crd An
(Oam)
Als Hbl
St Crd An
St Hbl
Crd Oam An
St Hbl
Grt Oam An
St Oam An
Crd Grt
(An)
Als Oam
St Crd
Als Oam
St Crd Pl
[Grt, Oam]
St Chl Hbl
Crd Grt
(St)
Als Chl
St Crd
St Chl An
Crd Hbl
Oam An
Crd Grt Hbl
St Hbl
Crd-Grt An
[Als, Chl]
(Hbl)
[Als, Oam]
St Oam Hbl
Crd Grt
(An)
St Chl An
Crd Grt
Grt Chl An
Crd Hbl
(Hbl)
(St)
CFMASH
+ Qtz, H2O

Figure. 6.21 illustrates the schematic phase relations in the NCFMASH system constructed from the assumptions outlined above. The grid consists of three invariant points [Crd], [Grt] and [Als] which are located at relatively high pressure conditions, in the vicinity of 9 kbar (from the calculated position of the CFMASH invariant point [Crd, Chl]). The grid allows all of the NCFMASH univariant (listed above) and divariant assemblages (in Table 6.5) to be stable. Although the univariant curves for [Chl], and perhaps [Oam], equilibria converge, both of these invariant points are metastable with respect to CFMASH invariant points.

The grid in Fig. 6.21 provides a more coherent representation of the phase relations in amphibolites than is available from the compatibility reactions alone. The grid also provides some information which was not previously available, most notably from the upper temperature and pressure regions. In brief, Fig. 6.21 limits cordierite–garnet to low pressures over a range of temperatures, garnet–chlorite is stable at low temperatures, over a range of pressures, and staurolite–chlorite is stable at low to intermediate temperatures and intermediate pressures. Aluminosilicate–orthoamphibole may only occur under conditions elevated pressures and temperatures and staurolite–cordierite, previously only poorly constrained, is a low pressure assemblage.

The phase relations in Fig. 6.21 reveal a slight inconsistency in the pressure-temperature estimates suggested by Spear (1982) and Humphreys (1983). Spear (1982) suggests that the Post Pond Volcanics contain either of the tie-lines staurolite–chlorite or staurolite–gedrite, depending on temperature, and that the amphibolites equilibrated at about 530°C, 5-6 kbar. Humphreys' (1993) assemblages imply that the assemblage garnet–cordierite will be stable for rocks of intermediate composition, metamorphosed at 600°C and pressures less than ~6 kbar. However, according to Fig. 6.21, cordierite–garnet assemblages are stable at lower pressures than staurolite–chlorite and staurolite–orthoamphibole and thus that there is an inconsistency (which is probably within error) in the estimated pressures.

A significant disparity between the observed assemblages and those presented in Fig. 6.21 relates to the Fe-Mg partitioning between staurolite in garnet. In higher pressure and temperature amphibolites staurolite is observed to be more Fe-rich than garnet, however the calculated compositions of the phases in CFMASH which were used to construct Fig. 6.21 predict that garnet is more Fe-rich for the P-T conditions of interest. This has a bearing on the phase relations, in that Fig. 6.21 predicts that staurolite–hornblende will become metastable at elevated pressures, whereas real staurolite-bearing amphibolites have been reported in rocks which have been metamorphosed at pressures up to about 9 (Gibson, 1978, 1979; Grew & Sandiford, 1985) and possibly 12 kbar (Ward, 1984a). This problem probably stems from the thermodynamic data and or activity-composition relations for garnet and staurolite, both of which are far from simple phases (see Chapter 3). The effect of assuming that staurolite is more Fe-rich than garnet would change the two univariant reactions [Crd, Oam] and [Crd, Chl] and the topology of the reactions around the [Crd] invariant point. It would also affect the compatibility relations of the divariant assemblages. The conditions under which this transition may occur was discussed above, in Section 6.15.3.

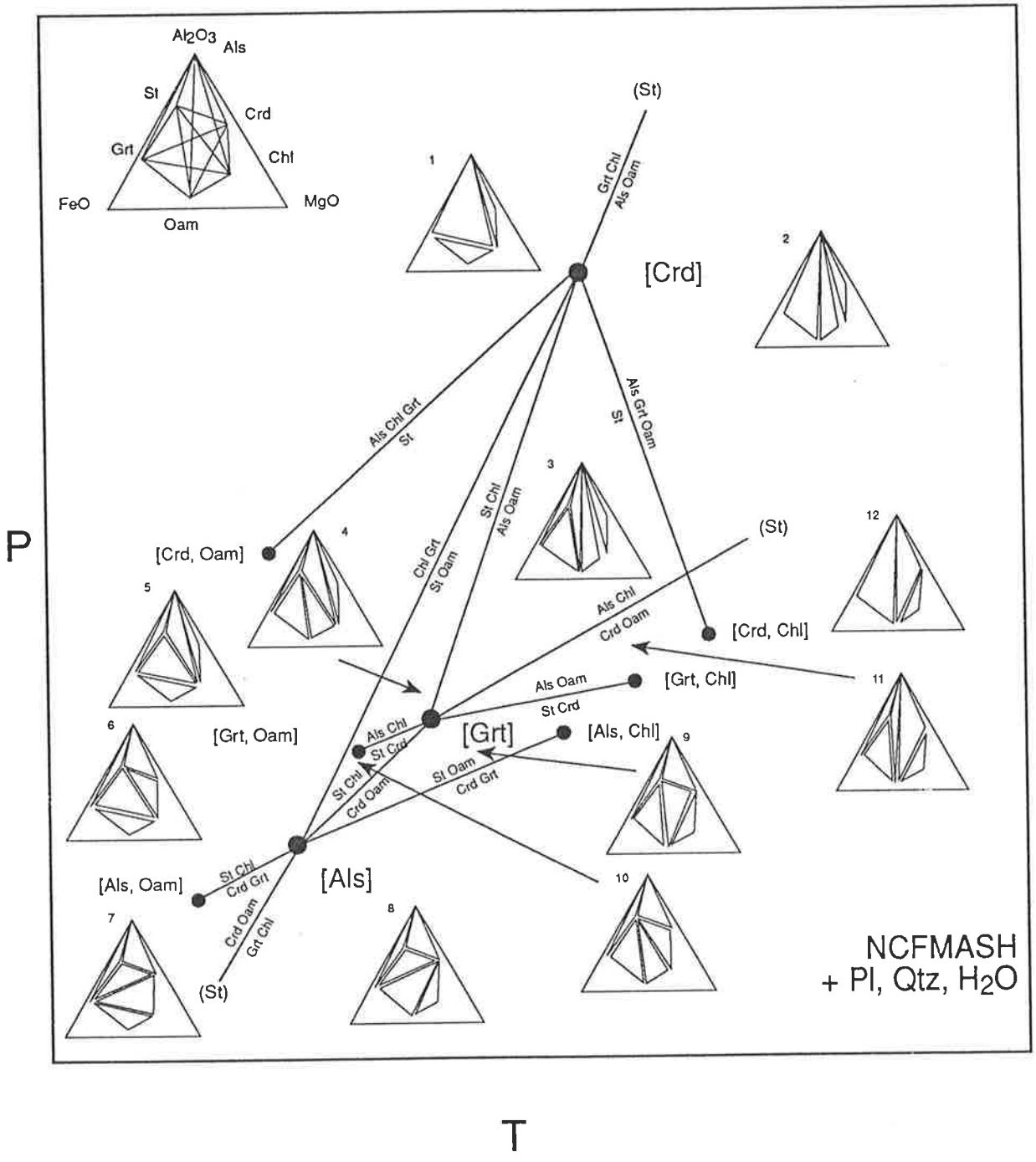

Figure 6.21. Schematic NCFMASH phase diagram, drawn for hornblende, plagioclase, quartz and aqueous vapour in excess, expanded from the CFMASH phase diagram in Fig. 6.20 and assuming and that sodium stabilises plagioclase over hornblende, hornblende over orthoamphibole and orthoamphibole over other phases.

6.16.1 A comparison with the phase relations of Spear and Rumble, 1986

The phase relations presented here are very similar to those of Spear and Rumble (1986). This is unsurprising given that both diagrams were constructed on the basis of compatibility relations observed in natural amphibolite assemblages. An obvious difference involves the inclusion of two orthoamphiboles and cummingtonite in Spear and Rumble's (1986) grid, however as a consequence of the aluminium-poor compositions of cummingtonite and anthophyllite, their inclusion or exclusion is unlikely to have a significant effect on the phase relations in most amphibolites. More important is the stable or metastable state of the invariant point which in Fig. 6.21 would be labelled [Chl]. Although Spear and Rumble (1986) found that this point is stable in the NCFMASH compositional system, according to the grid developed here, the invariant assemblage is metastable with respect to the CFMASH invariant points [Crd, Chl], [Grt, Chl] and [Als, Chl]. Although Spear (1978) considers that the [Chl] invariant point controls the stability of the assemblages reported by Stout (1972), in fact Stout (1972) does not report co-existing staurolite–hornblende from Telemark and as a result Stout's (1972) assemblages may be adequately described without recourse to the [Chl] invariant point. Thus there is no evidence from real amphibolites that the [Chl] invariant point is stable and no reason to doubt the topology of Fig. 6.21.

6.16.2 A comparison with the phase relations determined in Chapter 3

The NCFMASH petrogenetic grid constructed in this chapter is significantly different to that determined in Chapter 3 as an extension of the quantitative CFMASH phase diagram. Most important is the complete lack of cordierite-bearing amphibolites in Fig. 3.20. this is a consequence of the single NCFMASH invariant point which is allowed by the topology of the CFMASH sub-system reactions. This topology results from the metastability of the [Grt, Chl] invariant point with respect to [Crd, Grt] in CFMASH and if the [Crd, Grt] point could be stabilised, the incompatibility would be removed. The presence of cordierite-bearing amphibolite assemblages from New Hampshire (Schumacher & Robinson, 1987), the Pamirs (Grew et al., 1988), Copperton (Humphreys, 1993) and the Harts Range in central Australia (Chapter 4) indicates that cordierite-bearing assemblages are stable in at least some amphibolites. Thus, the NCFMASH phase relations determined in Chapter 3 are not entirely appropriate to real amphibolites.

Chapter 7: Summary

7.1 Introduction

The phase relations in kyanite- and staurolite-amphibolites have been investigated here from several distinct perspectives. In the first part of the thesis (Chapters 2 and 3), equilibrium thermodynamics calculations were used to develop petrogenetic grids for the FMASH, CFMASH and NCFMASH model systems. These grids were used to constrain the metamorphic history of the newly described occurrence of kyanite–staurolite-amphibolites from the Harts Range in central Australia (Chapter 4). Chapter 5 described the mineral textures in the staurolite- and kyanite-bearing hornblende garbenschiefer from the Zillertaler Alpen in Austria and summarised their compatibility relations. Chapter 6 summarised the equilibria reported from world-wide examples of kyanite- and staurolite-amphibolites and the compatibility relations they define and discussed the way in which compatibility relations change over P-T space. This information has been incorporated into an NCFMASH petrogenetic grid which is consistent with the reported assemblages, and, to varying degrees, with the phase diagrams developed by Spear and Rumble (1986) and in Chapter 3.

This final chapter serves as a summary of the main findings and presents some ideas on how to improve the match between the observed and calculated phase relations.

7.2 Calculated phase relations

Many of the phases contained within the FMASH compositional system are also observed in the kyanite- and staurolite-amphibolites which are the subject of this project. As a result of the relatively well understood nature of the phase relations in cordierite–orthoamphibole-type rocks, the FMASH system provides a sound basis for calculations in the more complex CFMASH and NCFMASH compositional systems. The phase relations determined by equilibrium thermodynamics calculations for the FMASH system are similar to those determined by Hudson and Harte (1985) and by and large are consistent with the reaction relationships observed in natural mineral assemblages (e.g. Robinson & Jaffe 1969a; Sharma & MacRae, 1981; Schumacher & Robinson, 1987; Arnold & Sandiford, 1990). In the process of calculating the phase relations for cordierite–orthamphibole-type rocks, the thermodynamic data for the *gedrite* end-member was adjusted within its uncertainty, reducing the size of the orthoamphibole field in the FMASH model system, and increasing the consistency between calculated and observed phase relations.

The phase relations in CFMASH were developed from the basis of the FMASH petrogenetic grid presented in Chapter 2, in the first instance, ignoring chlorite. They were found to be consistent with the phase relations observed in most chlorite-absent kyanite- and staurolite-amphibolites (e.g. Spear, 1977; 1982; Purtscheller & Mogessie, 1984; Selverstone et al., 1984; Schumacher & Robinson, 1987) and proved to be useful in constraining the metamorphic history of the Harts Range amphibolites (Chapter 4). Many of the observed kyanite- and staurolite-amphibolites contain chlorite in addition to the phases considered so far, however, calculations involving chlorite in the CFMASH system resulted in many of the previously stable equilibria becoming metastable with respect to chlorite-bearing assemblages. Compositional effects such as the influence of minor phases, oxygen fugacity and water activity do not provide an adequate explanation of the inconsistencies between the calculated and observed phase relations and thus it seems that uncertainties in the thermodynamic data or in the activity composition (a-X) relations of the phases are probably responsible. The uncertainties associated with several of the mineral end-members are significant, however only those for the staurolite end-members, *fst* and *mst* were sufficient to cause the topology of the calculated reactions to invert to one more appropriate to the observed assemblages. A similar effect might be achieved by a combination of the effects of uncertainties in the data for other mineral end-members, such as *tr*, *ftr*, *hb*, or for non-ideal mixing between the garnet end-members *alm*, *py*, and *grs*. Unfortunately some inconsistencies remain in the adjusted CFMASH system as a result of the large number of independent factors influencing the equilibrium relations. The exact cause of the CFMASH inadequacies are not reconcilable, however it is clear from the dramatic effects of uncertainties in the data, that in order to achieve better correspondence between the calculated and observed assemblages, not only the data, but also the uncertainties in the data must be improved.

The problems outlined above promote some scepticism over the quantitative aspect of the strongly data-dependent calculated phase relations. As a result, the univariant reactions in the NCFMASH system are dealt with only qualitatively here. An NCFMASH petrogenetic grid has been constructed from the phase relations in the adjusted CFMASH system, by assuming that Na did not stable any other phases, but rather increased the stability of plagioclase-, hornblende- and orthoamphibole-bearing assemblages. Some problems are obvious even from this qualitative approach. Most significant is the prediction that cordierite will not be stable under any pressure or temperature conditions in amphibolites which contain hornblende, plagioclase, quartz and an aqueous vapour. Despite this problem, the stable equilibria in the NCFMASH petrogenetic grid can account for many of the mineral assemblages and reaction relations observed in natural assemblages, implying that the calculated phase relations do contribute useful information for constraining the metamorphism of amphibolites.

7.3 Observed phase relations in amphibolites

7.3.1 Harts Range amphibolites

The mineralogy, textural relations and mineral chemistry of kyanite- and staurolite amphibolites from the Harts Range in central Australia have been described for the first time in this thesis (Chapter 4). The amphibolites show a range of compositions which allow development of several different divariant (and higher variance) assemblages during metamorphism to peak conditions of about 7 kbar and 650-700°C. As a consequence of the influence of composition on a rock's mineralogy for given physical conditions, this variable composition has resulted in a suite of assemblages which record different portions of the area's P-T evolution. Fe-rich amphibolites contain staurolite–garnet–gedrite–hornblende (+plagioclase, quartz and aqueous vapour), more Mg-rich samples have kyanite–cordierite–anthophyllite–hornblende and intermediate composition amphibolites contain kyanite–staurolite–gedrite–hornblende assemblages. Despite the temporal and compositional variation of the amphibolite assemblages, they do not define crossed tie-lines and thus do not violate the relevant NCFMASH compatibility diagram.

The NCFMASH divariant and trivariant reactions which are observed in the Harts Range are closely related to CFMASH univariant and divariant equilibria which were calculated in Chapter 3. They suggest that the area has experienced a period of syn-deformational up-pressure and up-temperature metamorphism, followed by a period in which pressure decreased and deformation waned. Cordierite-bearing amphibolites provide evidence of a further decrease in pressure at some later stage, which did not coincide with significant local deformation. The development of these cordierite-bearing assemblages as a result of decompression at some time after mineral growth had generally ceased, implies that the area experienced a period of at least localised heating which allowed mineral growth to resume. This two (or more) stage metamorphic history is consistent with geochronological information from the area which documents four separate "isotopic closure events" (Foden et al., 1994) The plausible P-T path determined from the amphibolite assemblages using the calculated phase diagrams and the consistency of this P-T history with the geochronological information provides support for the utility of the diagrams, at least for chlorite-absent amphibolites.

7.3.2 Zillertaler Alpen hornblende garbenschiefer

The hornblende garbenschiefer of the Austrian Zillertaler Alpen also contain a near-complete suite of mineral associations developed in amphibolites of variable composition. The phases observed in the garbenschiefer are similar to those in the Harts Range amphibolites, however the equilibrium assemblages are significantly different. The lower temperature (~7 kbar and ~550°C, Selverstone et al., 1984) hornblende garbenschiefer contain chlorite, rather

than cordierite in Mg-rich rocks and orthoamphibole is entirely absent. No reaction textures were observed in the garbenschiefer and the assemblages do not define crossed tie-lines.

7.3.3 Kyanite- staurolite and related amphibolite assemblages from around the world

Previous studies have focussed on individual occurrences of these unusual amphibolites, describing the mineralogy, textural relationships and mineral chemistry of the rocks, but largely without comparison to similar associations. Chapter 6 reviews the mineral assemblages and compatibility relations of reported kyanite-, staurolite- and related amphibolites, including those from the Harts Range, Zillertal and the little discussed examples from the Frodalera area of Switzerland. The intermediate pressure and temperature examples describe a wide range of compatibility diagrams both within and the relationships between the associations form the basis of an investigation of the phase relations of the amphibolites.

The prevalence of cordierite-absent NCFMASH univariant assemblages reported in the literature suggests that the NCFMASH invariant point [Crd] is stable whereas the presence of cordierite in some amphibolites and the observation of the reaction,

sillimanite + gedrite $\Rightarrow$ staurolite + cordierite [Grt, Chl]

(+ hornblende, plagioclase, quartz and vapour) in New Hampshire amphibolites (Schumacher & Robinson, 1987) implies that [Grt] or [Chl] may also be stable. All of the reported NCFMASH divariant reactions support the stability of [Crd], [Grt] and [Als] in NCMASH. The invariant points, [Chl] and perhaps [Oam] were found to be metastable with respect to CFMASH invariant points.

As expected, given their basis in the compatibility relations of natural amphibolite assemblages, the NCFMASH petrogenetic grid developed here is very similar to that presented by Spear and Rumble (1986) and with the observed assemblages. Important differences between the grids and the natural assemblages relate to the lack of two orthoamphiboles and cummingtonite from the NCFMASH grid determined here and the absence of talc from both this work and that of Spear and Rumble (1986). However, all three of these phases occur in relatively extreme parts of amphibolite compositional space and thus are unlikely to significantly influence the majority of amphibolites. A remaining problem with the CFMASH and NCFMASH grids calculated here and presented by Spear and Rumble (1986) concerns the relative X_{Fe} of staurolite and garnet. Observed assemblages suggest that garnet is more Fe-rich than staurolite at low to intermediate pressures and temperatures, however, with increasing pressure and temperature, staurolite becomes more Fe-rich. This reversal was encountered in the calculated CFMASH phase relations, however it is restricted to the metastable portion of the grid.

7.3 Ideas for future development

The problems encountered in the chlorite-bearing CFMASH model system when chlorite was incorporated are significant and indicate that the thermodynamic data is not yet as well constrained as we would like. This has important implications for phase relations in other rock-types as many of the phases of interest here also occur in pelites and semi-pelites and are important in the interpretation of these rocks. Specifically, the thermodynamic data for the staurolite and hornblende end-members are poorly constrained and the a-X relations in both of these phases and especially garnet, are poorly understood. In addition to achieving a better match between the topology of the observed phase relations and those calculated from thermodynamic data, improved information for staurolite and garnet may allow the reversal of X_{Fe} between these phases to be better characterised. The incorporation of compositional solvi in both orthoamphiboles and clinoamphiboles and the inclusion of talc will also add relevance to the calculated phase relations, once the above problems have been overcome.

As for most compositional systems, activity of oxygen may have a significant effect on the phase relations of amphibolites, and although the consideration of f_{O_2} would add another compositional variable to the already complex amphibolites, the availability of thermodynamic data for Fe^{3+}-bearing end-members of amphiboles and chlorite would allow the implications of epidote-bearing assemblages to be investigated. The inclusion of Fe^{3+}-bearing phases may allow a more comprehensive understanding of amphibolites in general, including the higher variance assemblages belonging to the common assemblage of Laird (1980).

7.4 Conclusion

In conclusion, the reaction textures, equilibrium associations and compatibility relations in kyanite-, staurolite- and related amphibolites are potentially a very useful tool in constraining the P-T evolution of metamorphic rocks. The investigation of the Harts Range amphibolites presented in Chapter 4 has outlined the possibilities for constraining not only the broad characteristics of a metamorphic terrain but also a relatively detailed picture of the evolution of the rocks based mainly on divariant and higher variance assemblages. Thus there is an impetus to improve our knowledge of the behaviour of minerals which are observed in amphibolites. In the light of more accurate thermodynamic data and mixing models, the phase relations observed here may be improved upon and extended, and may eventually prove a useful medium in which to evaluate metamorphic conditions.

Appendix A1: End-member and phase names, abbreviations and formulae

(a) Phase abbreviations

name	abbrev. (general)	abbrev. (THERMO -CALC)	formula
aluminosilicates	Als		
andalusite	And	*and*	Al_2SiO_5
sillimanite	Sill	*sill*	Al_2SiO_5
kyanite	Ky	*ky*	Al_2SiO_5
aqueous vapour	H_2O	*H2O*	H_2O
Biotite	Bt		$K(Fe,Mg)(Fe,Mg,Al)_2Si_2[Si,Al]_2O_{10}(OH)_2$
Muscovite	Ms		$VKAl_2Si_2[SiAl]O_{10}(OH)_2$
Paragonite	Pg		$VNaAl_2Si_2[SiAl]O_{10}(OH)_2$
calcite	Cal		$CaCO_3$
ankerite	Ank		$Ca(Fe,Mg)_2(CO_3)_2$
chlorite	Chl	*chl*	
clinochlore		*clin*	$Mg_4(MgAl)Si_2[AlSi]O_{10}(OH)_8$
daphnite		*daph*	$Fe_4(FeAl)Si_2[AlSi]O_{10}(OH)_8$
amesite		*ames*	$Mg_4(Al_2)Si_2[Al_2]O_{10}(OH)_8$
Clinopyroxene	Cpx		$Ca(Fe,Mg)Si_2O_6$
Orthopyroxene	Opx		$(Fe,Mg)_2Si_2O_6$
cordierite	Crd	*cd*	
cordierite		*crd*	$Mg_2Al_4Si_5O_{18}$
Fe-cordierite		*fcrd*	$Fe_2Al_4Si_5O_{18}$
hydrous cordierite		*hcrd*	$Mg_2Al_4Si_5O_{18}.H_2O$
Epidote	Ep		$Ca_2(Al,Fe^{3+})Al_2Si_3O_{12}(OH)_2$
garnet	Grt	*gt*	
almandine		*alm*	$Fe_3Al_2Si_3O_{12}$
pyrope	prp	*py*	$Mg_3Al_2Si_3O_{12}$
grossular		*gr*	$Ca_3Al_2Si_3O_{12}$
spessartine	sps		$Mn_3Al_2Si_3O_{12}$

name	abbrev. (general)	abbrev. (THERMO -CALC)	formula
hornblende	Hbl	*hbl*	
tremolite		*tr*	$VCa_2Mg_3(Mg_2)Si_4[Si_4]O_{22}(OH)_2$
ferro-tremolite		*ftr*	$VCa_2Fe_3(Fe_2)Si_4[Si_4]O_{22}(OH)_2)$
hornblende		*hb*	$VCa_2Mg_3(MgAl)Si_4[Si_3Al]O_{22}(OH)_2$
edenite		*ed*	$NaCa_2Mg_3(Mg_2)Si_4[Si_3Al]O_{22}(OH)_2$
ferri-hornblende	F3hb	*F3hb*	$VCa_2Mg_3(MgFe^{3+})Si_4[Si_3Al]O_{22}(OH)_2$
cummingtonite	Cum		$V(Fe,Mg)_2(Fe,Mg)_3(Fe,Mg)_2Si_4[Si_4]O_{22}(OH)_2$
Ilmenite	Ilm		$FeTiO_3$
orthoamphibole	Oam	*oa*	
anthophyllite		*anth*	$VMg_2Mg_3(Mg_2)Si_4[Si_4]O_{22}(OH)_2$
ferro-anthophyllite		*fath*	$VFe_2Fe_3(Fe_2)Si_4[Si_4]O_{22}(OH)_2$
gedrite		*ged*	$VFe_2Fe_3(Al_2)Si_4[Si_2Al_2]O_{22}(OH)_2$
ortho-edenite		*oed*	$NaMg_2Mg_3(Mg_2)Si_4[Si_3Al]O_{22}(OH)_2$
plagioclase	Pl		
C1 plagioclase			
albite		*ab*	$NaAlSi_3O_8$
fictive anorthite		*an*	$CaAl_2Si_2O_8$
I1 plagioclase			
anorthite		*an*	$CaAl_2Si_2O_8$
fictive albite		*ab*	$NaAlSi_3O_8$
anorthite	An	*an*	$CaAl_2Si_2O_8$
quartz	Qtz	*q*	SiO_2
rutile	Rt		TiO_2
staurolite	St	*st*	
Fe-staurolite		*fst*	$Fe_4Al_{18}Si_{7.5}O_{44}(OH)_4$
Mg-staurolite		*mst*	$Mg_4Al_{18}Si_{7.5}O_{44}(OH)_4$
Zn-staurolite		*znst*	$Zn_4Al_{18}Si_{7.5}O_{44}(OH)_4$
Talc	Tlc		$(Fe,Mg)_2(Fe,Mg,Al)Si_2[Si,Al]_2O_{23}(OH)_2$

(b) Compsitional abbreviations

Abbreviation	formula	comments
X_{Fe}	Fe / (Fe + MgO)	
$X_{Fe,Grt}$	Fe / (Fe + MgO)	in garnet
X_{alm}	Fe / (Fe + Mg + Ca + Mn)	in garnet
X_{prp}	Mg / (Fe + Mg + Ca + Mn)	in garnet
X_{grs}	Ca / (Fe + Mg + Ca + Mn)	in garnet
X_{sps}	Mn / (Fe + Mg + Ca + Mn)	in garnet
Ps_X	100 * Fe^{3+} / (Fe^{3+} + Al)	in epidote
An_X	100 * Ca / (Ca + Na)	in plagioclase
Al^{iv}	(Number of tetrahedral sites - Si)	Al on tetrahedral sites in hornblende, biotite, orthoamphibole, chlorite, talc
Al^{vi}	Al - Al^{iv}	Al on octahedral sites in hornblende, biotite, orthoamphibole, chlorite, talc

Appendix A2: Thermodynamic data

This appendix lists the thermodynamic data used in the calculation of FMASH and CFMASH phase diagrams. The data was obtained from the internally consistent dataset of Holland and Powell (1990, pers. comm., 1992), thermodynamic dataset produced at 10.27 on Wed 1 Apr, 1992) and is appropriate to the mineral end-member formulae in Appendix A1. H is the molar enthalpy (kJ); sd(H) is the standard deviation of the molar enthalpy; S is molar entropy (kJ K^{-1}), V is molar volume (kJ $kbar^{-1}$); a, b, c and d are molar heat capacity polynomial coefficients, where the heat capacity $C_p = a + bT + cT^{-2} + dT^{-1/2}$; α and β are the coefficients of thermal expansion and compressibility, multiplied by the molar volume. The factors underneath S, b, αV and βV are factors by which those data must be multiplied in order to obtain units of kJ, K and kbar.

A2.1 Standard data

Thermodynamic properties (units : kJ, K, kbar)

	H	sd(H)	S	V	a	b	c	d	αV	βV
			(x 10^{-3})			(x 10^{-5})			(x 10^{-5})	(x 10^{-3})
mst	-25120.82	8.31	890.00	44.260	2.8205	-5.9366	-13774.0	-24.1260	12.0	32.0
fst	-23750.30	8.17	1030.00	44.880	2.8800	-5.6595	-10642.0	-25.3730	13.0	36.0
py	-6283.62	2.33	266.30	11.318	0.5450	2.0680	-8331.2	-2.2830	29.8	6.3
alm	-5271.97	2.78	342.00	11.511	0.7230	-2.6775	-1992.1	-6.0436	28.3	6.6
gr	-6636.62	2.82	256	12.535	0.7286	-4.0986	-3128	-6.0774	31	7.9
crd	-9166.45	3.21	407.50	23.322	0.8213	4.3339	-8211.2	-5.0000	14.5	20.0
fcrd	-8463.43	3.39	458.00	23.710	0.8515	4.4724	-6645.0	-5.6234	13.0	20.0
hcrd	-9456.18	3.41	482.80	23.322	0.8614	5.1995	-7723.7	-5.2512	14.5	20.0
anth	-12064.24	5.58	537.00	26.540	1.2773	2.5825	-9704.6	-9.0747	74.0	33.0
fath	-9630.43	6.44	729.00	27.870	1.3831	3.0669	-4224.7	-11.2576	79.0	32.0
ged	-12313.69	6.55	515.00	25.800	1.3077	2.3642	-9307.4	-9.7990	72.0	32.0
clin	-8920.37	3.21	421.00	21.090	1.1618	1.0133	-7657.3	-9.6909	59.0	38.0
daph	-7156.15	4.38	559.00	21.340	1.2374	1.3594	-3743.0	-11.2500	59.0	38.0
ames	-9047.88	2.98	400.00	20.980	1.1770	0.9041	-7458.7	-10.0530	58.0	38.0
tr	-12302.4	5.08	550	27.27	1.2144	2.6528	-12362	-7.3885	84.5	36
ftr	-10530.12	6.25	705	28.28	1.29	2.9991	-8447.5	-8.947	88	37
hb	-12408.55	4.55	561	26.99	1.2296	2.5438	-12163.5	-7.7503	83	35
ed	-10530.12	6.25	705.00	28.280	1.2900	2.9991	-8447.5	-8.9470	88.0	37.0
an	-4232.45	1.57	199.3	10.079	0.3914	1.2556	-3036.2	-2.5832	14.3	10.7
ab	-3937.06	2.61	211.35	10.007	0.4520	-1.3364	-1275.9	-3.9536	28.7	14.3
and	-2590.96	0.89	91.40	5.153	0.2904	-1.0520	-1109.0	-2.6280	12.3	3.9
sill	-2586.40	0.90	96.20	5.003	0.2261	1.4070	-2440.0	-1.3760	6.7	3.8
ky	-2595.37	0.89	82.00	4.414	0.3039	-1.3390	-895.2	-2.9040	10.5	2.9
q	-910.83	0.52	41.50	2.269	0.0979	-0.3350	-636.2	-0.7740	8.0	5.4
H2O	-241.81	0.02	188.80	0	0.0401	0.8656	487.5	-0.2512	0	0

A2.2 Adjusted data

Thermodynamic properties (units : kJ, K, kbar)

	H	sd(H)	S (x 10^{-3})	V	a	b (x 10^{-5})	c	d	αV (x 10^{-5})	βV (x 10^{-3})
ged	-12303.69	6.55	515.00	25.800	1.3077	2.3642	-9307.4	-9.7990	72.0	32.0
mst	-25135.82	8.31	890.00	44.260	2.8205	-5.9366	-13774.0	-24.1260	12.0	32.0
fst	23765.30	8.17	1030.00	44.880	2.8800	-5.6595	-10642.0	-25.3730	13.0	36.0

Appendix A3: Permanent data files for FMASH

This appendix contains a listing of the permanent data files used in the calculation of pressure temperature projections in the FMASH, MASH, FASH and NFMASH model systems.

A3.1 FMASH

A3.1.1 Standard data

```
ky      and     sill

st  2           mst     1       1       1 1 -1 1 4
                fst     1       1       0 1 1 1 4
                2       1       1       0 1 1 1

x(st) 0.7

cd  3           crd     1       2       1 1 -1 1 2      1 1 -1 2 1
                fcrd    1       2       0 1 1 1 2       1 1 -1 2 1
                2       1       1       0 1 1 1
                hcrd    1       2       1 1 -1 1 2      0 1 1 2 1
                2       1       1       0 1 1 2

x(cd) 0.3
h(cd) 0.25

gt  2           py      1       1       1 1 -1 1 3
                alm     1       1       0 1 1 1 3
                2       1       1       0 1 1 1

x(gt) 0.65

chl 3           clin    16      3       1 1 -1 1 5      1 1 -1 2 2      0 1 1 2 2
                daph    16      3       0 1 1 1 5       1 1 -1 2 2      0 1 1 2 2
                2       0.2     2       0 1 2 1         3 1 -1 2
                ames    1       2       1 1 -1 1 4      0 1 1 2 4
                2       1       1       -1 1 2 2

x(chl) 0.4
y(chl) 0.6

oa  3           anth    0.0625  3       1 1 -1 1 7      1 1 -1 2 2      2 1 -1 2 4
                fath    0.0625  3       0 1 1 1 7       1 1 -1 2 2      2 1 -1 2 4
                2       0.1429  2       0 1 1 1         7 1 -2 2
                ged     1       3       1 1 -1 1 5      0 1 1 2 4       2 1 -1 2 2
                2       1       1       0 1 1 2
                3       0 0 0   % ged factor

x(oa) 0.5
y(oa) 0.55

q       H2O
```

A3.1.2 Orthoamphibole with ΔH_{ged} =+10 kJmol^{-1}

```
oa  3           anth    0.0625  3       1 1 -1 1 7      1 1 -1 2 2      2 1 -1 2 4
                fath    0.0625  3       0 1 1 1 7       1 1 -1 2 2      2 1 -1 2 4
                2       0.1429  2       0 1 1 1         7 1 -2 2
                ged     1       3       1 1 -1 1 5      0 1 1 2 4       2 1 -1 2 2
                2       1       1       0 1 1 2
                3       10 0 0          % ged factor

x(oa) 0.5
y(oa) 0.55
```

A3.2 MASH

```
ky      and     sill

mst

cd 2            crd     1       1       1 1 -1 1 1
                hcrd    1       1       0 1 1 1 1
                2       1       1       0 1 1 1
h(cd) 0.25

py

chl 2           clin    16      2       1 1 -1 1 2      0 1 1 1 2
                ames    1       1       0 1 1 1 4
                2       1       1       -1 1 2 1
y(chl) 0.7

oa 2            anth    0.0625  2       1 1 -1 1 2      2 1 -1 1 4
                ged     1       2       0 1 1 1 4       2 1 -1 1 2
                2       1       1       0 1 1 1
                3       5 0 0           % ΔHged fiddle
y(oa) 0.55

q       H2O
```

A3.3 FASH

```
ky      sill    and

fst

cd 2            fcrd    1       1       1 1 -1 1 1
                fhcd    1       1       0 1 1 1 1
                2       1       1       0 1 1 1
                4       3       1       hcrd 1   crd -1   fcrd 1
h(cd) 0.25

alm

chl     2       daph    16      2       1 1 -1 1 2      0 1 1 1 2
                fame    1       1       0 1 1 1 4
                2       1       1       -1 1 2 1
                4       3       5       ames 5  daph 4  clin -4 % makes fame
y(chl) 0.7

oa 2            fath    0.0625  2       1 1 -1 1 2      2 1 -1 1 4
                fged    1       2       0 1 1 1 4       2 1 -1 1 2
                2       1       1       0 1 1 1
                3       10 0 0                  % ΔHged fiddle
                4       3       7       ged 7  fath 5  anth 5  % makes fged
y(oa) 0.55

q       H2O
```

A3.4 NFMASH

```
ky      sill    and

st  2           mst     1       1       1 1 -1  1 4
                fst     1       1       0 1  1  1 4
                2       1       1       0 1  1  1
x(st) 0.7

cd  3           crd     1       2       1 1 -1  1 2     1 1 -1 2 1
                fcrd    1       2       0 1  1  1 2     1 1 -1 2 1
                2       1       1       0 1  1  1
                hcrd    1       2       1 1 -1  1 2     0 1  1 2 1
                2       1       1       0 1  1  2
x(cd) 0.3
h(cd) 0.8

gt  2           py      1       1       1 1 -1  1 3
                alm     1       1       0 1  1  1 3
                2       1       1       0 1  1  1
x(gt) 0.65

chl 3           clin    16      3       1 1 -1  1 5     1 1 -1 2 2      0 1 1 2 2
                daph    16      3       0 1  1  1 5     1 1 -1 2 2      0 1 1 2 2
                2       0.2     2       0 1  2  1       3 1 -1 2
                ames    1       2       1 1 -1  1 4     0 1  1 2 4
                2       1       1       -1 1  2 2
x(chl) 0.4
y(chl) 0.6

oa 4            anth    0.003906        4       1 1 -1  3 1      1 1 -1  1 7
                                                1 1 -1  2 2      4 2 -2  2 -1 3 4
                fath    0.003906        4       1 1 -1  3 1      0 1  1  1 7
                                                1 1 -1  2 2      4 2 -2  2 -1 3 4
                2       0.14286         2       0 1  1  1        7 1 -2  2
                ged     0.0625          5       1 1  -1 3 1      1 1 -1  1 5
                                                0 1  1  2 2      0 2 2 2 1 3 2
                                                4 2 -2  2 -1 3 2
                2       1               1       0 1  1  2
                3       0 0 0                   % DQF
                oed     0.0370          4       0 1  1  3 1      1 1 -1  1 7
                                                0 2  2  2 1 3 1          4 2 -2  2 -1 3 3
                2       1               1       0 1  1  2
                3       9.8 0  0                % DQF
                4       3               1       ed 1    anth 1  tr -1 % makes oed
x(oa) 0.5
y(oa) 0.55
n(oa) 0.4

ab      q       H2O
```

Appendix A4: Permanent data-file set up

A4.1 Introduction

Most of the information presented here about the permanent data-files which are required to run THERMOCALC is available in the THERMOCALC documentation. However, for convenience and clarity it is repeated and expanded upon here.

Using THERMOCALC it is possible to determine the positions of mineral equilibria in intensive variable space, including the compositions of the phases and a balanced reaction at a given P-T point, as well as compatibility diagram and pseudosection information. To carry out these calculations, coded information including mole fraction equations and compositional information, expressing the proportion of each end-member in terms of its compositional variables, are required. The iterative process used in THERMOCALC (Powell & Holland, 1988) means that starting guesses are required for the compositional variables for each of the phases. However, although a starting guess is required, the program actually calculates the compositions of the phases at each P-T point, so that, except for certain hard-to-find equilibria, the guesses need not be extremely accurate. Additional information may be incorporated to make adjustments to suspect thermodynamic data, to incorporate activity-composition information and Darken's quadratic formalism information (e.g. Will & Powell, 1992). End-members which are not included in the dataset can be incorporated as linear combinations of those which are in the data set.

The information in the permanent datafile must be set out in the consistent manner outlined below. The complete data file consists of a list of phase names, each of which is accompanied by the number of its constituent end-member phases, the end-member names, end-member information and a starting guess for the compositional variables for that phase.

{phase name} {number of end-members}
{end-member name} {end-member information}
{end-member name} {end-member information}
.
.
.
{variable name} {starting guess}
{variable name} {starting guess}
.
.
.

The end-member information is set out in the form

{thermodynamic mole fraction expression}
{activity-composition (a-X) expression}
{bulk compositional expression}
{Darken's quadratic formalism information}
{dependent end-member expression}

and the formulation of each of these will be dealt with in turn.

A4.2 Thermodynamic mole fraction expression

Thermodynamic mole fractions are typically represented as the product of a series of compositional terms e.g. $X_{fst,St} = (X_{Fe})^4$, where X_{Fe} = Fe/(Fe+Mg) (e.g. Powell, 1978). However, this is not a form which can be easily read by a computer program and, thus, a more general form is required. The different compositional terms, such as X_{Fe} can each be defined as a compositional variable (e.g. **x**) and, thus, may be more generally coded. The mole fraction formulations may include up to several terms, each of the form; bx_a, $n(c+bx)^a$ or $n(c+bx+dy)^a$, where **x** and **y** represent compositional variables; a, b, c and d are integers and n is a real number representing the constant term for the thermodynamic mole fraction. All three of these types terms may be described in the mole fraction formulations:

{normalisation factor} {number of terms}
{$const_1$} ($xterms_1$) {$mult_{11}$} {$index_{11}$} {$power_1$}
{$const_2$} ($xterms_2$) {$mult_{22}$} {$index_{22}$} {$power_2$}...

or

{normalisation factor} {number of terms}
{$const_1$} {$xterms_1$} {$mult_{11}$} {$index_{11}$} {$mult_{12}$} {$index_{12}$} {$power_1$}
{$const_2$} {$xterms_2$} {$mult_{21}$} {$index_{21}$} {$mult_{22}$} {$index_{22}$} {$power_2$}...

where {normalisation factor} is a factor by which the entire mole fraction equation is multiplied, comprising a factor to ensure that the mole fraction of a pure endmember is equal to 1, multiplied by the constant term for the mole fraction expression; {number of terms} is the number of different mole fraction terms; {$const_i$} is a constant; {$xterms_i$} is the number of compositional variables; {$mult_{ij}$} is the multiplier of the particular compositional variable; {$index_{ij}$} is the position of the compositional variable in the list of starting guesses and {$power_i$} is the power to which the entire term is raised (Powell and Holland, pers comm, 1991). The first example listed above is for terms in which {$xterms_i$} is equal to 1 (e.g. $(1-x)^2$), while the second is for {$xterms_i$} equal to 2 (e.g. $(x + y)^2$). As an example, the mole fraction of *Mg-staurolite* $X_{st} = (1-x)^4$ (see section A4.2.2), would be coded as

st 1 1 1 1 -1 1 4.

i.e., a normalisation factor of 1, 1 term, a constant of 1 ($(1-x)^4$), only one X-term (x),a multiplier of -1 ($(1-x)^4$), the first of the X-terms (x), all raised to the power 4 ($(1-x)^4$).

Mole fractions have been determined for this study assuming ideal solid solution for all phases (including garnet, though see section A4.3) and mixing on sites (e.g. Powell, 1978).

A4.2.1 Non-solid solution phases

The mole fraction calculation for non-solid-solution phases, is trivial, e.g. X_q in quartz = 1, and thus does not need to be coded. Thus, non-solid solution phases merely need to be listed in the data file;

q
an
H_2O
and
sill
ky.

A4.2.2 Simple solution phases

The mole fractions of end-members in phases which involve a single compositional variable, such as X_{Fe} are more complex. They involve a single compositional variable, such as X_{Fe}, are expressed as the proportion of the relevant element (of two possible) on each site on which substitution can occur, raised to the number of appropriate sites. In the case of staurolite, for which ideal substitution of $Fe_{-1}Mg_1$ is assumed, the mole fraction of the Fe-end-member (*fst*, $Fe_4Al_{18}Si_{7.5}O_{44}(OH)_4$) is simply the proportion of Fe on each of the four sites on which it may occur, raised to the power 4, i.e., $(X_{Fe})^4$.

If **x** is set to be X_{Fe} i.e., Fe/(Fe+Mg), then $X_{fst,st}$ may be coded as $\mathbf{x}^4$.
The mole fraction of the Mg-end-member (*mst*, $Mg_4Al_{18}Si_{7.5}O_{44}(OH)_4$) is the proportion of Mg on each site, raised to the power 4, i.e. X_{Mg}^4, $(1-X_{Fe})^4$ or $(1 - \mathbf{x}^4)$. The mole fraction of pure *fst* in staurolite is

$$X_{fst,st} = 1 = n * \mathbf{x}^4 = n * 1^4.$$

Therefore, the normalisation factor, n = 1. Thus the coded mole fraction information for *fst* is

fst 1 1 0 1 1 1 4.

That is, the normalisation factor = 1, there is one term, $(0-\mathbf{x})^4$, which has a constant of 0, one x-term which is multiplied by +1, the x-term is the first in the list (x) and the term is raised to the power 4.

$$X_{mst,st} = (1-\mathbf{x})^4,$$

so,

mst 1 1 1 1 -1 1 4

That is, the normalisation factor = 1, there is one term, $(1\text{-}x)^4$, which has a constant of 1, one x-term which is multiplied by -1, the x-term is the first in the list (x) and the term is raised to the power 4.

The coding for staurolite is

```
st      2       fst     1 1     0 1 1 1 4
                mst     1 1     1 1 -1 1 4
x(st) 0.8
```

A4.2.3 More complex solution phases

Similar formulation applies for more complex phases in which solid solution involves more than a single exchange vector (e.g. garnet, cordierite). In the case of garnet in the CFMASH system, the relevant end-members are almandine (*alm* $Fe_3Al_2Si_3O_{12}$), pyrope (*py* $Mg_3Al_2Si_3O_{12}$) and grossular (*gr* $Ca_3Al_2Si_3O_{12}$). Assuming ideal solid solution between these end-members the mole fraction of almandine in garnet is:

$$X_{alm,gt} = n * (X_{Fe,M})^3 = n^* [(X_{Fe})^* (1\text{-}X_{Ca})]^3.$$

If $\mathbf{x} = (X_{Fe})$ and $\mathbf{z} = X_{Ca} = Ca / (Ca + Fe + Mg)$, then

$$X_{alm,gt} = n * \mathbf{x}^3 * (1\text{-}z)^3.$$

Similarly,

$$X_{py,gt} = n * (X_{Mg,M})^3 = n^* [(1\text{-}X_{Fe}) * (1\text{-}X_{Ca})]^3, \text{ then}$$

$$X_{py,gt} = n * (1\text{-}\mathbf{x})^3 * (1\text{-}\mathbf{z})^3$$

and

$$X_{gr,gt} = n * (X_{Ca,M})^3 = n^* (X_{Ca})^3, \text{ so}$$

$$X_{gr,gt} = n * \mathbf{z}^3.$$

As **x**, (1-**x**) and **z** are equal to one for the pure end-members *alm*, *py* and *gr*, respectively, the normalisation factor, n = 1. Thus

```
gt      3       alm     1 2     0 1 1 1 3       1 1 -1 2 3
                py      1 2     1 1 -1 1 3      1 1 -1 2 3
                gr      1 1     0 1 1 2 3
```

A4.2.4 Solid solution phases with substitution on more than one site

The mole fractions of amphibole end-members are more complex again, because more than one type of site is involved in substitution. For hornblendes in the CFMASH system, the endmember phases are taken to be tremolite (*tr*, $VCa_2Mg_3(Mg_2)Si_4[Si_4]O_{22}(OH)_2$), ferro-tremolite (*ftr*, $VCa_2Fe_3(Fe_2)Si_4[Si_4]O_{22}(OH)_2$) and hornblende (*hb*, $VCa_2Mg_3(MgAl)Si_4[Si_3Al]O_{22}(OH)_2$). $X_{V,A}$, $X_{Ca,M4}$ and $X_{Si,T2}$ are all assumed to be 1, **x** = Fe/(Fe+Mg) and **y** = $X_{Al,M2}$, therefore,

$X_{Fe,M1,3} = \mathbf{x}$	The amount of Fe on a site which may have Fe and Mg
$X_{Mg,M1,3} = (1 - X_{Fe}) = (1 - \mathbf{x})$	The amount which is not Fe, on a site which may have Fe and Mg
$X_{Al,M1} = \mathbf{y}$	The amount of Al on each of two sites which may have Al, Fe and Mg
$X_{Fe,M2} = X_{Fe} * (1 - X_{Al,M2}) = \mathbf{x} * (1 - \mathbf{y})$	The amount which is not Al * the ratio of Fe/(Fe+Mg)
$X_{Mg,M2} = (1 - X_{Fe}) * (1 - X_{Al,M2}) = (1 - \mathbf{x}) * (1 - \mathbf{y})$	The amount which is not Al * the ratio of Mg/(Fe+Mg)
$X_{Al,T1} = (X_{Al,M2}) / 2 = \mathbf{y} / 2$	The amount of Al on each of 4 sites which may have Al and Si (twice as many sites as M2)
$X_{Si,T1} = (1 - (X_{Al,T1})) = (1 - (\mathbf{y} / 2)) = 0.5 * (2 - \mathbf{y})$	The amount which is not Al

so,

$$X_{tr,hbl} = n * (X_{Mg,M1,3})^3 * (X_{Mg,M2})^2 * (X_{Si,T1})^4$$
$$= n * (1 - \mathbf{x})^3 * (1 - \mathbf{x})^2 * (1 - \mathbf{y})^2 * (0.5)^4 * (2 - \mathbf{y})^4$$
$$= n / 16 * (1 - \mathbf{x})^5 * (1 - \mathbf{y})^2 * (2 - \mathbf{y})^4$$

for pure tr $X_{tr,hbl} = 1$, $\mathbf{x} = 0$, $\mathbf{y} = 0$ therefore $1 = n / 16 * 1 * 1 * 1$, so $n = 16$, and the normalisation factor = 16 / 16 = 1.

$$X_{tr,hbl} = (1 - \mathbf{x})^5 * (1 - \mathbf{y})^2 * (2 - \mathbf{y})^4$$

Similarly, $X_{ftr,hbl} = (\mathbf{x})^5 * (1 - \mathbf{y})^2 * (2 - \mathbf{y})^4$

$$X_{hb,hbl} = n * (X_{Mg,M1,3})^3 * (X_{Mg,M2}) * (X_{Al,M2}) * (X_{Si,T1})^3 * (X_{Al,T1})$$
$$= n * (1 - \mathbf{x})^3 * (1 - \mathbf{x}) * (1 - \mathbf{y}) * \mathbf{y} * (0.5 * (2 - \mathbf{y}))^3 * (\mathbf{y} / 2)$$
$$= n / 2^4 * (1 - \mathbf{x})^4 * (1 - \mathbf{y}) * \mathbf{y}^2 * (2 - \mathbf{y})^3$$

for pure hb $X_{hb,hbl} = 1$, $\mathbf{x} = 0$, $\mathbf{y} = 0.5$ therefore $1 = n / 2^4 * 1 * 1/2 * (1/2)^2 * (3/2)^3$

$$= n / 2^4 * (1/2)^6 * 3^3 = n\, 3^3 / 2^{10},$$

so $n = 2^{10} / 3^3$ and the normalisation factor = $(2^{10} / 3^3) / 2^4 = (2^6 / 3^3) = 2.3704$.

$X_{hb,hbl}$ $= 2.3704 * (1 - x)^4 * (1 - y) * y^2 * (2 - y)^3$

hbl	3	tr	0.0625 3	1 1 1 -1 5	1 1 -1 2 2	2 1 -1 2 4
		ftr	0.0625 3	0 1 1 1 5	1 1 -1 2 2	2 1 -1 2 4
		hb	2.3704 4	1 1 1 -1 4	1 1 -1 2 1	
				0 1 1 2 2	2 1 -1 2 3	

Appendices A3 and A7 list the permanent data files used in phase diagram calculations in this thesis.

A4.3 Activity-composition (a-X) formulation

An a-X facility in THERMOCALC allows calculations to be carried out on minerals which have non-ideal activity-composition relations, for example, solid solution garnets involving the end members *almandine*, *pyrope* and *grossular* or plagioclase which has different structures for the *anorthite* and *albite* end-members. Activity is related to thermodynamic mole fraction by the equation $a = \gamma X$, where γ is the activity coefficient of the end-member in the phase and X is the mole fraction of the end-member in the phase. Activity coefficients can be written as a function of a set of interaction parameters, and represent the difference between the two mineral end-members. The relations between the activity co-efficients and interaction parameters are described below, however, the interaction parameters themselves are functions of P and T, such that, $w_{ij} = a + bT + cP$, where a,b and c are constants. The permanent data files used in THERMOCALC may specify the a, b and c values for a particular end-member.

A4.3.1 a-X formulation for plagioclase

Although plagioclase is a chemically simple phase, structurally it is far more complex. The result of this is a number of miscibility gaps, one of which will be dealt with here. Holland and Powell (1992) modelled activity-composition relations in plagioclase using both Darken's quadratic formalism (DQF) (see Powell, 1987; section A4.5) and Landau theory, and found that the former appears more appropriate to phase diagram calculations (Holland & Powell, 1992). The method involves dividing plagioclase into two structurally distinct portions which are bridged by an imposed continuity. The model used in this formulation is Holland and Powell's (1992) model 4 in which plagioclase is (1) 4T-disordered in the C1 (*albite*-rich) field, in which there is random mixing on both the large ion cation site and the tetrahedral sites with Al and Si distributed evenly over all 4 tetrahedral sites and (2) ordered in the I1 (*anorthite*-rich) field where Al-Si mixing is assumed not to contribute to the entropy of mixing.

Each of the phases, C1 and I1 consists of a real end-member and a "fictive" endmember (see the DQF section (A4.5) below). In the case of C1 plagioclase, *albite* is the real end-member, however there is no *anorthite* end-member with C1 structure, so we use a

fictive endmember for C1 *anorthite* which is related to real I1 *anorthite* by Darken's quadratic formalism. In I1 plagioclase *anorthite* is the real end-member and $I1_{albite}$ is fictive. The C1 and I1 plagioclases are entered as separate phases which are used to calculate the P,T and X information for a given reaction involving first C1, and then I1 plagioclase. The transition composition (where C1 plagioclase becomes more stable than I1 plagioclase, X_b) can be determined for a given temperature from the linear equation

$$X_b = 0.12 + 0.00038T\ (K)$$

(Holland & Powell, 1992) and thus, either the C1 or the I1 plagioclase will be stable at a calculated P-T point.

The general formula for the activity coefficient of a multi-component system is

$$RT ln\gamma_{endmember} = - \Sigma_i \Sigma_{j>i} w_{ij} (x_i^\circ - x_i)(x_j^\circ - x_j)$$

where w_{ij} is the interaction parameter for a mixture of end-members i and j, x_i is the mole fraction of i in the phase, x_i° is the mole fraction of i in the pure endmember (R. Powell, pers. comm.) e.g., in anorthite,

$$x_{An}^\circ = 1,\ x_{Ab}^\circ = 0.$$

The general features of activity coefficients and interaction parameters are described in general texts such as Powell (1978) or Wood and Fraser (1977).

For the I1 simple region, for *anorthite*;

$$\begin{aligned} RT\ ln\ \gamma^{I1}_{An} &= -w^{I1}_{An} (X_{An}^\circ - X_{An}) (X_{Ab}^\circ - X_{Ab}) \\ &= -w^{I1}_{An} (1 - X_{An}) (0 - X_{Ab}) \\ &= w^{I1}_{An} (1 - X_{An}) X_{Ab}. \end{aligned}$$

If $X_{An} = x$ and $X_{Ab} = 1 - x$

$$RT\ ln\ \gamma^{I1}_{An} = w^{I1}_{An} (1-x) (1-x).$$

For fictive *albite*

$$\begin{aligned} RT\ ln\ \gamma^{I1}_{Ab} &= -w^{I1}_{Ab} (X_{Ab}^\circ - X_{Ab}) (X_{An}^\circ - X_{An}) \\ &= -w^{I1}_{Ab} (1 - X_{Ab}) (0 - X_{An}) \\ &= w^{I1}_{Ab} (1 - X_{Ab}) X_{An} \end{aligned}$$

if $X_{An} = x$ and $X_{Ab} = 1-x$

$$RT\ ln\ \gamma^{I1}_{Ab} = w^{I1}_{Ab}\ x\ x.$$

From Holland and Powell (1992), $w^{I1} = 9.8\ kJ\ K^{-1}$.

This information is coded in a similar format to the other permanent datafile information. First, the integer 1 to indicate the mode of information (i.e. a-X information), then the number of w terms, then each of the terms above is entered as (e.g. for (real) anorthite in the I^1 structured plagioclase w^{I1}_{An}):

(1) $w_{ij} = a + bT + cP$ 9.8 0 0

(2) a normalisation factor (number of sites for mixing) 1

(3) number of terms 1

(4) {const$_1$} (xterms$_1$) {mult$_{11}$} {index$_{11}$} {power$_1$} 1 1 -1 1 1

The THERMOCALC permanent datafile for plagioclase also requires DQF terms for both the $C\bar{1}$ and $I\bar{1}$ phases: relating the fictive albite endmember in the $I\bar{1}$ simple region to real albite in $C\bar{1}$ plagioclase (see section A4.5).

The full coding for Ca-Na-plagioclase with $I\bar{1}$ and $C\bar{1}$ structures is listed in Appendix A7.4 in the NCFMASH permanent datafile.

A4.3.2 a-X formulation for garnet

Experimental work constraining the mixing relations in garnets implies that different interaction parameters are required for Ca-rich and low-Ca garnets. The garnets which are observed in amphibolites typically fall into the low-Ca region of garnet compositional space. Powell (pers. comm., 1993) has determined interaction parameters for low-Ca garnet :

$$w^{Grt}_{FeMg} = 190R = 1.6 \text{ kJ K}^{-1}$$

and

$$w^{Grt}_{CaFe} - w^{Grt}_{MgCa} = -1100R = -9.1 \text{ kJ K}^{-1}.$$

The activity coefficient of each end-member can be determined using the general formula:

$$RT ln\gamma_{endmember} = - \Sigma_i \Sigma_{j>i} w_{ij} (x_i^\circ - x_i)(x_j^\circ - x_j)$$

where w are interaction parameters, x_i is the mole fraction of i in the phase, x_i° is the mole fraction of i in the pure endmember, for example in *almandine*,

$$x_{Fe}^\circ = 1, x_{Mg}^\circ = 0, x_{Ca}^\circ = 0.$$

Thus, the a-X expression for *almandine* takes the form:

$$\begin{aligned} RT\, ln\, \gamma_{Fe} &= -w_{FeMg} (X_{Fe}^\circ - X_{Fe}) (X_{Mg}^\circ - X_{Mg}) \\ &\quad -w_{FeCa} (X_{Fe}^\circ - X_{Fe}) (X_{Ca}^\circ - X_{Ca}) \\ &\quad -w_{MgCa} (X_{Mg}^\circ - X_{Mg}) (X_{Ca}^\circ - X_{Ca}) \\ &= -w_{FeMg} (1 - X_{Fe}) (0 - X_{Mg}) \\ &\quad -w_{FeCa} (1 - X_{Fe}) (0 - X_{Ca}) \\ &\quad -w_{MgCa} (0 - X_{Mg}) (0 - X_{Ca}) \\ &= + (1 - X_{Fe}) X_{Mg} w_{FeMg} \end{aligned}$$

$$+ (1-X_{Fe})\, X_{Ca}\, w_{FeCa}$$

$$- X_{Mg}\, X_{Ca}\, w_{MgCa}$$

$$= \quad + X_{Mg}\, w_{FeMg} - X_{Fe}\, X_{Mg}\, w_{FeMg}$$

$$+ X_{Ca}\, w_{FeCa} - X_{Fe}\, X_{Ca}\, w_{FeCa}$$

$$- X_{Mg}\, X_{Ca}\, w_{MgCa}$$

$X_{Fe} = \mathbf{x}\ (1-\mathbf{z})$, $X_{Mg} = (1-\mathbf{x})\ (1-\mathbf{z})$ and $X_{Ca} = \mathbf{z}$, so

$$RT\ ln\ \gamma_{Fe} = + (1-\mathbf{x})\ (1-\mathbf{z})\ w_{FeMg} - \mathbf{x}\ (1-\mathbf{x})\ (1-\mathbf{z})^2\ w_{FeMg}$$

$$+ \mathbf{z}\ w_{FeCa} - \mathbf{x}\ \mathbf{z}\ (1-\mathbf{z})\ w_{FeCa}$$

$$- (1-\mathbf{x})\ (1-\mathbf{z})\ \mathbf{z}\ w_{MgCa}.$$

The values w_{FeMg}, w_{FeCa} and w_{MgCa} are determined from the equations: $w^{Grt}_{FeMg} = 1.6$ kJ K^{-1} and $w^{Grt}_{CaFe} - w^{Grt}_{MgCa} = -9.1$ kJ K^{-1}, by assuming a value for w^{Grt}_{CaFe} or w^{Grt}_{MgCa}. Initially I assume that Fe-Ca mixing is more ideal than Mg-Ca mixing, with $w^{Grt}_{CaFe} = 5$ kJ K^{-1} so, $w^{Grt}_{MgCa} = w^{Grt}_{CaFe} + 9.1 = 14.1$ kJ K^{-1}.

This information is coded in the same format as for plagioclase. First, the integer 1 to indicate the mode of information (i.e. a-X information), then the number of w terms (for garnet there will be 3, one for each of *almandine*, *pyrope* and *grossular*), then each of the terms above is entered as (e.g. for the w^{Grt}_{MgCa} term: $-w_{MgCa}\ (1-\mathbf{x})\ (1-\mathbf{z})\ \mathbf{z}$:

(1) $w_{ij} = a + bT + cP$	-14.1 0 0
(2) a normalisation factor (number of sites with mixing)	3
(3) number of terms	3
(4) {const$_1$} (xterms$_1$) {mult$_{11}$} {index$_{11}$} {power$_1$}	1 1 -1 1 1
{const$_2$} (xterms$_2$) {mult$_{22}$} {index$_{22}$} {power$_2$}	1 1 -1 2 1
{const$_2$} (xterms$_2$) {mult$_{22}$} {index$_{22}$} {power$_2$}	0 1 1 2 1

The activity co-efficient information for the *almandine* endmember is:

1	1	1.6 0 0	3	2	1 1 -1 1 1	1 1 -1 2 1	
		-1.6 0 0	3	3	0 1 1 1 1	1 1 -1 1 1	1 1 -1 2 2
		5 0 0	3	1	0 1 1 2 1		
		-5 0 0	3	3	0 1 1 1 1	1 1 -1 2 1	0 1 1 2 1
		-14.1 0 0	3	3	1 1 -1 1 1	1 1 -1 2 1	0 1 1 2 1

A4.4 Bulk compositional formulation

Bulk compositional terms for each end-member are set out in a similar format to that of the mole fraction expression, except that they involve only four integers as the expressions are never raised to a power other than 1, and they are preceded by the integer 2, indicating that they are compositional formulations. The number of compositional terms required for each phase is one less than the necessary number of end-members as the remaining compositional term can be determined simply by difference. In the simplest case of phases with only one type of substitution, compositional formulations have the form:

2 1 1 0 1 1 1.

i.e. $X_{fst} = X_{Fe} = \mathbf{x}$.

Garnet is slightly more complex. The compositional variables, **x** and **z** were set in the mole fraction expression (section A4.2.3) to X_{Fe} = Fe / (Fe+Mg) and X_{Ca} = Ca / (Ca+Fe+Mg). If *alm*, *py* and *gr* are set to be the molar proportion of almandine, pyrope and grossular in garnet, then *alm* + *py* + *gr* = 1. The formulae of the end-members are used to write the compositional variables in terms of the end-member names and then simplify to obtain the proportion of each of the end-members in terms of compositional variables. To write **z** in terms of the end-members:

z = Ca / (Ca + Fe + Mg),

there are 3 Ca in *grossular*, so Ca = 3 *gr*, 3 Fe in *almandine*, so Fe = 3 *alm*, and 3 Mg in *pyrope*, so Mg = 3 *py*.

Thus,

z = Ca / (Ca + Fe + Mg) = 3*gr* (3 *gr* + 3*alm* + 3*py*) = 3 *gr* / 3

gr = **z**

x = Fe / (Fe + Mg) = 3*alm* / (3*alm* + 3*py*) = 3 *alm* / (3 - 3_{gr}) = *alm* / (1 - *gr*)

x = *alm* / (1 - z)

alm = **x** (1 - **y**).

This is represented as, for almandine, 2 1 2 0 1 1 1 1 1 -1 2

for grossular, 2 1 1 0 1 1 2.

The amphiboles are more complex again, with **x** = X_{Fe} = Fe / (Fe+Mg) and **y** = $X_{Al,M2}$.

y = *hb* / (2 *hb* + 2 *tr* + 2 *ftr*) = *hb* / 2

hb = 2 **y**

x = 5*ftr* / (5*ftr* + 5*tr* + 4*hb*) = 5*ftr* / (5 - *hb*) = *ftr* / (1 - (*hb* / 5))

x = ftr / (1 - (2 **y** / 5))

ftr = **x** (1 - (2 **y** / 5)) = (x / 5) * (5 - 2y) = 0.2 * **x** * (5-2y)

represented as, for Fe-tremolite,	2	0.2	2	0 1 1 1	5 1 -2 2
for hornblende,	2	2	1	0 1 1 2.	

A4.5 Darken's quadratic formalism

The poorly understood a-X relations of mineral end-members and the significant uncertainties associated with the thermodynamic data are large problems inherent in thermodynamic calculations. These problems are made even more difficult when the end-members of interest do not occur naturally (e.g. the edenite component in orthoamphibole). A method for dealing with such uncertainties has been suggested by Powell (1987) and Will and Powell (1992) after the method proposed by Darken for binary metallic solutions (Darken, 1967). In simple terms, Darken's quadratic formalism (DQF) is a model which divides the compositional range of a binary phase with inhomogeneous structure (or other features) into two terminal regions with an intermediate section between them (Powell, 1987). In each of the terminal regions there is ideal mixing between a real and a "fictive" end-member (Fig. A4.1) (Will and Powell, 1992). The difference in Gibbs energy between the real and the fictive end-members (e.g. between real monoclinic *tremolite* and fictive tremolite in the orthorhombic orthoamphibole structure), is denoted by I^{A}_{1} where A is the phase and 1 is the end-member of interest (e.g. I^{Oam}_{tr}). The method of Will and Powell (1992) uses co-existing amphibole pairs to constrain the properties of the fictive end-member and thus find I^{A}_{1}, whereas Holland and Powell (1992) determine I_{An} and I_{Ab} in terms of the difference in interaction parameters for the I1 and C1 structures.

The facility to incorporate Darken's quadratic formalism terms has been introduced into THERMOCALC and requires that the I-values (which will be of the form I = a + bT + cP, where a, b and c are constants) are entered into the permanent data set with the other endmember information in the form

3 {a} {b} {c},

where 3 indicates the use of the formulation, and {a},{b} and {c}correspond to the constants in the equation I = a + bT +cP. This information effectively adjusts the Gibbs energy for the end-member and, thus, can be used in defining linearly dependent end-members (see section A4.6). DQF may also be used to make corrections to incomplete, outdated or incorrect thermodynamic data where the results of thermodynamic calculations using the data are clearly in conflict with information from natural rocks. An example of this is the inaccuracy found in the position of the invariant point Ip1, discussed in Chapter 2 (section 2.6). This discrepancy is thought to result from the rather old and inaccurate data for gedrite (generated from the experimental data of Schreyer & Seifert, 1969b) and thus the thermodynamic data was adjusted using the provision in the program for Darken's quadratic formalism. Various values of {a} were tested and the most appropriate value was found to be +10 kJ mol^{-1}.

This is coded as; 3 10 0 0.

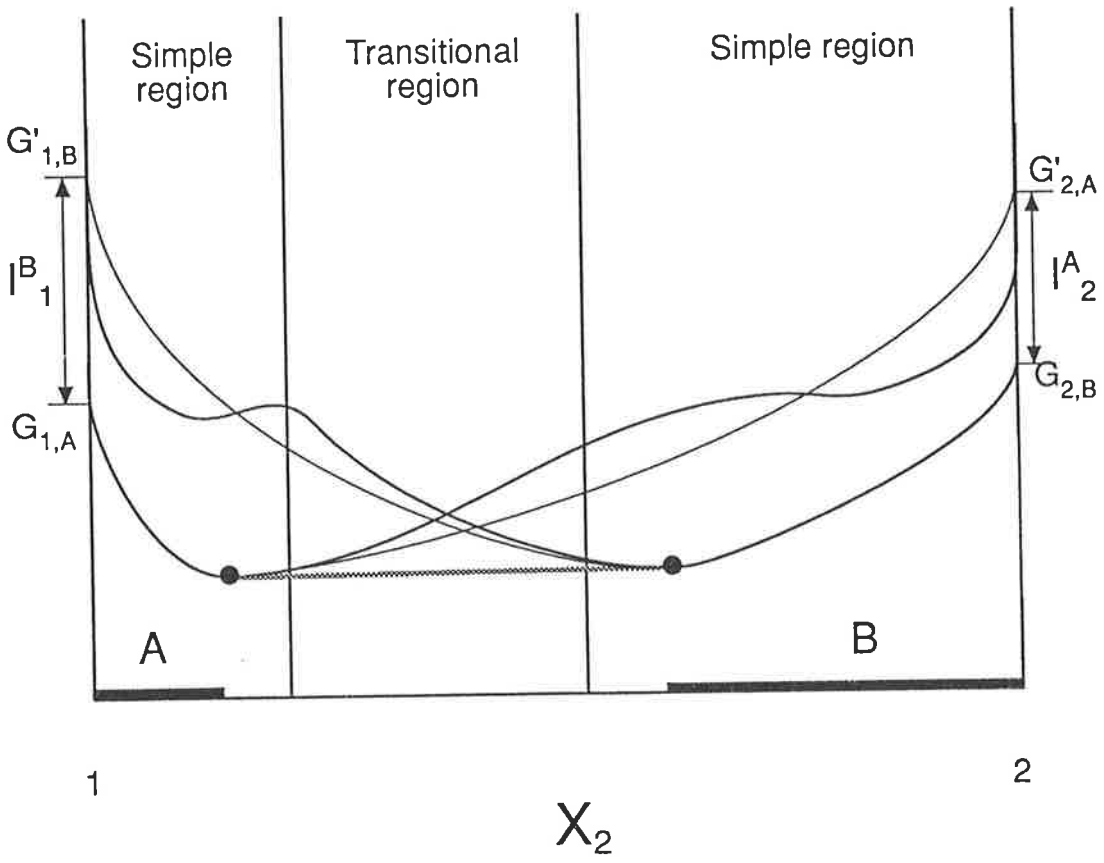

Figure A4.1. G-X diagram illustrating the relationships between the real and fictive end-members, A and B, in the compositional system 1-2. The heavy lines represent the real G-X curves for A and B (joined by a thick, shaded tie-line), whereas the light lines represent a model of the G-X relations in the simple regions only. The difference in the Gibbs energy of a real phase and the corresponding fictive phase is termed I.

DQF terms are also required for both the $\bar{C}1$ and $\bar{I}1$ phases of Ca-Na plagioclase, relating the fictive *albite* endmember in the $\bar{I}1$ simple region to real C1 *albite* (I = 1.72 - 0.00395T) and fictive *anorthite* in the $\bar{C}1$ simple region to real *anorthite* (I = 4.31 - 0.00217T) (R Powell, pers. comm., 1993). Thus for $\bar{C}1$ plagioclase, fictive anorthite has the DQF term

3 4.31 -0.00217 0

and for I1 plagioclase, fictive albite has the DQF term

3 1.72 -0.00395 0.

A4.6 Dependent end-member formulation

End-members which are not included in the data set may be included by writing an expression that will make up their thermodynamic data as a linear combination of end-members which are in the data set. Examples of this are the Fe-end-members of *hornblende* and *gedrite* (i.e. $VCa_2Fe_3(FeAl)Si_4[Si_3Al]O_{22}(OH)_2$ and $VFe_2Fe_3(Al)_2Si_4[Si_3Al]O_{22}(OH)_2$), for which there is no thermodynamic data listed, but which can be written as linear combinations of end-members which are in the data set. *Ferro-hornblende* (*fhb*) may be expressed as

$$VCa_2Fe_3(FeAl)Si_4[Si_3Al]O_{22}(OH)_2 = VCa_2Mg_3(MgAl)Si_4[Si_3Al]O_{22}(OH)_2 + 4/5\ (VCa_2Fe_3(Fe_2)Si_4[Si_4]O_{22}(OH)_2) - 4/5\ (VCa_2Mg_3(Mg_2)Si_4[Si_4]O_{22}(OH)_2)$$

or

$$fhb = (1/5) * (5hb + 4ftr - 4tr).$$

The factors 4 and 5 are due to the fact that *hornblende* has only 4/5 of the Mg content of *tremolite*, as one of the Mgs is replaced by Al. *Ferro-gedrite* (*fged*) may be similarly expressed as

$$fged = (1/7) * (7ged + 5\,fath - 5anth).$$

This dependent end-member formulation is denoted by a figure 4 (as Darken's Quadratic Formalism was denoted by the figure 2), which is followed by the number of end-members and a divider for the dependent end-member (so that there are no fractions). Thus that the appropriate coding has the form, for *fhb*,

4 3 5 hb 5 ftr -4 tr -4,

and for *fged*,

4 3 7 ged 7 fath 5 anth -5.

A4.7 Permanent datafile set-up for Fe_2O_3-bearing hornblendes

The effect of an additional end-member in a mineral can be modelled by assuming that it simply acts to dilute the other end-members. Thus, for any given Fe^{3+}-content in hornblende, the activity formulations may be multiplied by a factor which is equal to the

activity of the Fe_2O_3 end-member divided by the activity of the Fe_2O_3-free endmember. Because hornblende is a complex phase with several different types of substitution, the activity formulation for Fe_2O_3-bearing hornblende is also complex. An important factor in determining the effect of Fe_2O_3 on the positions of reaction equilibria is that Fe^{3+} is substituted into hornblende as part of a modified tschermakite substitution (Leake, 1978) and therefore the mole fractions of Si and Al on the tetrahedral sites will be related to the amount of Fe^{3+} on the M_2 site. Thus the effect of Fe_2O_3 will be different for hornblendes with different aluminium contents. The mole fraction information required to calculate the effect of Fe_2O_3 is outlined below. $X'_{tr,hbl}$ is the mole fraction of *tremolite* in Fe^{3+}-bearing hornblende.

sites:	M_2	M_4	$M_{1,3}$	M_2	T_1	T_2	
tr	V	Ca_2	Mg_3	(Mg_2)	Si_4	$[Si_4]$	$O_{22}(OH)_2$
ftr	V	Ca_2	Fe_3	(Fe_2)	Si_4	$[Si_4]$	$O_{22}(OH)_2$
hb	V	Ca_2	Mg_3	(MgAl)	Si_4	$[Si_3Al]$	$O_{22}(OH)_2$
F3hb	V	Ca_2	Mg_3	$(MgFe^{3+})$	Si_4	$[Si_3Al]$	$O_{22}(OH)_2$

$X_{V,A}$, $X_{Ca,M4}$ and $X_{Si,T2}$ are all taken to be 1,

$\mathbf{x}$ = Fe/(Fe+Mg), $\mathbf{y} = X_{Al,M2}$ = Al/(Al+Fe^{2+}+Mg) on M2,

$\mathbf{f} = X_{Al,M2} = Fe^{3+}/(Fe^{3+}+Al+Fe^{2+}+Mg)$ on M2.

Therefore,

$X_{Fe,M1,3} = \mathbf{x}$

$X_{Mg,M1,3} = (1 - \mathbf{x})$

$X_{F3,M2} = \mathbf{f}$

$X_{Al,M2} = \mathbf{y} * (1 - \mathbf{f})$

$X_{Fe,M2} = \mathbf{x} * (1 - \mathbf{y}) * (1 - \mathbf{f})$

$X_{Mg,M2} = (1 - \mathbf{x}) * (1 - \mathbf{y}) * (1 - \mathbf{f})$

$X_{Al,T1} = \mathbf{y} / 2 + \mathbf{f} / 2 = 0.5 * (\mathbf{y} + \mathbf{f})$

$X_{Si,T1} = 1 - (0.5 * (\mathbf{y} + \mathbf{f})) = 0.5 * (2 - \mathbf{y} - \mathbf{f})$

so, the mole fraction of *tremolite* in an Fe^{3+}-bearing hornblende is:

$$X'_{tr,hbl} = n * (X_{Mg,M1,3})^3 * (X_{Mg,M2})^2 * (X_{Si,T1})^4$$

$$= n * (1 - \mathbf{x})^3 * (1 - \mathbf{x})^2 * (1 - \mathbf{y})^2 * (1 - \mathbf{f})^2 * (0.5)^4 * (2 - \mathbf{y} - \mathbf{f})^4$$

$$= n / 16 * (1 - \mathbf{x})^5 * (1 - \mathbf{y})^2 * (1 - f)^2 * (2 - \mathbf{y} - f)^4$$

for pure *tr*, $X'_{tr,hbl} = 1$, $\mathbf{x} = 0$, $\mathbf{y} = 0$, $\mathbf{f} = 0$, therefore, $1 = n / 16 * 1 * 1 * 1 * 1$, so $n = 16$, and the normalisation factor = 16 / 16 = 1.

$$X'_{tr,hbl} = (1 - x)^5 * (1 - y)^2 * (1 - f)^2 * (2 - y - f)^4$$

Similarly,

$$X'_{ftr,hbl} = (x)^5 * (1 - y)^2 * (1 - f)^2 * (2 - y - f)^4$$

$$X'_{hb,hbl} = n * (X_{Mg,M1,3})^3 * (X_{Mg,M2}) * (X_{Al,M2}) * (X_{Si,T1})^3 * (X_{Al,T1})$$

$$= n * (1 - x)^3 * (1 - x) * (1 - y) * (1 - f) * y * (1 - f) * (0.5 * (2 - y - f))^3 * 0.5 * (y + f)$$

$$= n / 2^4 * (1 - x)^4 * (1 - y) * y^2 * (1 - f)^2 * (2 - y - f)^3 * (y + f)$$

for pure *hb* $X'_{hb,hbl} = 1$, $x = 0$, $y = 0.5$, therefore

$$1 = n / 2^4 * 1 * 1/2 * (1/2)^2 * (3/2)^3$$

$$= n / 2^4 * (1/2)^6 * 3^3 = n\, 3^3 / 2^{10},$$

so, $n = 2^{10} / 3^3$ and the normalisation factor $= (2^{10} / 3^3) / 2^4 = (2^6 / 3^3) = 2.3704$.

$$X'_{hb,hbl} = 2.3704 * (1 - x)^4 * (1 - y) * y^2 * (1 - f)^2 * (2 - y - f)^3 * (y + f).$$

In order to determine a multiplying factor with which to reduce the activities of the non-Fe^{3+}-bearing end-members we must divide each of the above activity expressions ($X'_{tr,hbl}$, $X'_{ftr,hbl}$, $X'_{hb,hbl}$) by its own activity expression with **f** set to 0.

So for *tr* and *ftr*

$$\text{mult factor} = \frac{(1 - x)^5 * (1 - y)^2 * (1 - f)^2 * (2 - y - f)^4}{(1 - x)^5 * (1 - y)^2 * (1)^2 * (2 - y)^4}$$

$$= \frac{(1 - f)^2 * (2 - y - f)^4}{(2 - y)^4}$$

and for *hb*

$$\text{mult factor} = \frac{2.3704 * (1 - x)^4 * (1 - y) * y^2 * (1 - f)^2 * (2 - y - f)^3 * (y + f)}{2.3704 * (1 - x)^4 * (1 - y) * y^2 * (2 - y)^3 * y}$$

$$= \frac{(1 - f)^2 * (2 - y - f)^3 * (y + f)}{(2 - y)^3 * (y)}$$

By substituting in the values of **y** and **f** of interest, multiplication factors can be determined with which the activity expressions for the Fe^{3+} absent end-members can be adjusted.

Appendix A5: Example output file

An example output file from THERMOCALC v2.2b1, calculated using the thermodynamic dataset of Holland & Powell (1990, pers. comm, 1992 produced at 10.27 on Wed 1 Apr, 1992, with ΔHged=10) for the FMASH invariant point Ip_1 or [Chl], and its associated univariant reactions.

[chl] phases :st, gt, cd, oa, sill (q, fluid)

P(kbar)	T(°C)	x(st)	x(gt)	x(cd)	h(cd)	x(oa)	y(oa)
6.1	641	0.846	0.783	0.342	0.741	0.527	0.322

univariants

[chl,gt] in sill phases :st, cd, oa, sill (q, fluid)

P(kbar)	T(°C)	x(st)	x(cd)	h(cd)	x(oa)	y(oa)
5.0	674	0.965	0.733	0.646	0.852	0.326
	10st + 19cd + 40q = 12oa + 120sill + 20H2O					
5.2	674	0.953	0.669	0.659	0.810	0.325
	10st + 20cd + 39q = 13oa + 122sill + 21H2O					
5.4	672	0.939	0.604	0.674	0.763	0.325
	10st + 22cd + 37q = 13oa + 126sill + 22H2O					
5.6	668	0.922	0.537	0.690	0.710	0.324
	10st + 24cd + 35q = 14oa + 130sill + 23H2O					
5.8	662	0.899	0.464	0.708	0.647	0.324
	10st + 27cd + 33q = 15oa + 135sill + 25H2O					
6.0	649	0.865	0.381	0.730	0.567	0.322
	10st + 32cd + 29q = 16oa + 143sill + 27H2O					

[chl,st] in sill phases :gt, cd, oa, sill (q, fluid)

P(kbar)	T(°C)	x(gt)	x(cd)	h(cd)	x(oa)	y(oa)
5.0	577	0.864	0.444	0.739	0.640	0.318
	39gt + 67cd = 40oa + 148sill + 14q + 10H2O					
5.5	606	0.829	0.393	0.741	0.586	0.320
	30gt + 57cd = 32oa + 123sill + 15q + 10H2O					
6.0	637	0.790	0.349	0.741	0.534	0.321
	25gt + 51cd = 28oa + 108sill + 16q + 10H2O					
6.5	669	0.747	0.309	0.740	0.486	0.323
	21gt + 47cd = 25oa + 99sill + 17q + 10H2O					
7.0	702	0.702	0.275	0.738	0.439	0.325
	19gt + 45cd = 23oa + 93sill + 18q + 10H2O					
7.5	737	0.653	0.243	0.735	0.396	0.327
	17gt + 43cd = 22oa + 89sill + 19q + 10H2O					
8.0	773	0.602	0.214	0.731	0.354	0.328
	16gt + 42cd = 21oa + 86sill + 19q + 10H2O					

[chl,als] phases :st, gt, cd, oa (q, fluid)

P(kbar)	T(°C)	x(st)	x(gt)	x(cd)	h(cd)	x(oa)	y(oa)
5.0	599	0.898	0.856	0.441	0.718	0.634	0.313
	10st + 21oa + 45q = 35gt + 34cd + 17H2O						
5.2	607	0.889	0.843	0.420	0.723	0.613	0.314
	10st + 21oa + 46q = 35gt + 34cd + 16H2O						
5.4	615	0.880	0.830	0.401	0.727	0.593	0.316
	10st + 21oa + 47q = 35gt + 34cd + 16H2O						
5.6	622	0.870	0.817	0.382	0.732	0.573	0.318
	10st + 21oa + 48q = 34gt + 34cd + 15H2O						
5.8	630	0.860	0.803	0.365	0.736	0.553	0.319
	10st + 21oa + 48q = 34gt + 35cd + 15H2O						
6.0	638	0.850	0.789	0.348	0.740	0.534	0.321
	10st + 20oa + 49q = 33gt + 35cd + 15H2O						
6.2	646	0.839	0.774	0.333	0.743	0.515	0.323
	10st + 20oa + 50q = 33gt + 35cd + 14H2O						
6.4	654	0.829	0.760	0.317	0.747	0.497	0.325
	10st + 20oa + 50q = 33gt + 35cd + 14H2O						
6.5	658	0.823	0.752	0.310	0.749	0.488	0.325
	10st + 20oa + 50q = 33gt + 35cd + 14H2O						

[chl,oa] in sill phases :st, gt, cd, sill (q, fluid)

P(kbar)	T(°C)	x(st)	x(gt)	x(cd)	h(cd)
3.0	573	0.987	0.981	0.868	0.602
	91st + 10cd + 365q = 129gt + 715sill + 189H2O				
3.5	585	0.971	0.958	0.751	0.629
	77st + 10cd + 306q = 110gt + 607sill + 161H2O				
4.0	597	0.954	0.932	0.649	0.654
	66st + 10cd + 258q = 95gt + 519sill + 138H2O				
4.5	608	0.933	0.903	0.559	0.677
	56st + 10cd + 218q = 82gt + 446sill + 120H2O				
5.0	619	0.909	0.869	0.481	0.699
	48st + 10cd + 185q = 71gt + 384sill + 104H2O				
5.5	630	0.882	0.832	0.412	0.719
	42st + 10cd + 157q = 62gt + 333sill + 91H2O				
6.0	640	0.851	0.790	0.351	0.738
	36st + 10cd + 133q = 55gt + 290sill + 79H2O				

[chl,oa] in and phases :st, gt, cd, and (q, fluid)

P(kbar)	T(°C)	x(st)	x(gt)	x(cd)	h(cd)
2.5	542	0.995	0.992	0.939	0.593
	112st + 10cd + 451q = 156gt + 873and + 230H2O				
3.0	563	0.983	0.976	0.836	0.613
	93st + 10cd + 370q = 131gt + 726and + 192H2O				
3.5	583	0.971	0.957	0.744	0.631
	78st + 10cd + 307q = 110gt + 609and + 162H2O				
4.0	603	0.956	0.935	0.664	0.647
	66st + 10cd + 256q = 94gt + 516and + 137H2O				

[chl,cd] in sill phases :st, gt, oa, sill (q, fluid)

P(kbar)	T(°C)	x(st)	x(gt)	x(oa)	y(oa)
5.0	617	0.884	0.835	0.604	0.322
	75st + 10oa + 288q = 121gt + 560sill + 160H2O				
5.5	629	0.867	0.812	0.567	0.322
	70st + 10oa + 267q = 115gt + 523sill + 150H2O				
6.0	640	0.849	0.787	0.532	0.322
	66st + 10oa + 249q = 109gt + 489sill + 141H2O				
6.5	651	0.830	0.762	0.499	0.322
	62st + 10oa + 232q = 103gt + 458sill + 133H2O				
7.0	661	0.810	0.736	0.467	0.322
	58st + 10oa + 217q = 99gt + 430sill + 126H2O				

[chl,cd] in ky phases :st, gt, oa, ky (q, fluid)

P(kbar)	T(°C)	x(st)	x(gt)	x(oa)	y(oa)
6.0	661	0.831	0.760	0.502	0.332
	58st + 10oa + 217q = 99gt + 431ky + 126H2O				
6.5	658	0.823	0.753	0.488	0.325
	59st + 10oa + 222q = 100gt + 438ky + 128H2O				
7.0	655	0.817	0.745	0.475	0.319
	60st + 10oa + 227q = 102gt + 448ky + 131H2O				
7.5	651	0.810	0.739	0.463	0.312
	62st + 10oa + 233q = 104gt + 459ky + 134H2O				
8.0	646	0.804	0.733	0.451	0.305
	64st + 10oa + 240q = 106gt + 472ky + 137H2O				
8.5	641	0.797	0.727	0.440	0.298
	66st + 10oa + 248q = 109gt + 487ky + 141H2O				
9.0	635	0.791	0.722	0.429	0.291
	68st + 10oa + 257q = 112gt + 505ky + 146H2O				

Appendix A6: Manuscripts arising from Chapter 2

The following two manuscripts have arisen from the investigation of phase diagrams in the FMASH compositional system. Both are reproduced here for convenience.

A6.1 Arnold and Sandiford, 1990

Petrogenesis of cordierite-orthoamphibole assemblages from the Springton Region, South Australia

Jo Arnold and Michael Sandiford

This publication was partly based on work carried out during an honours project in the Department of Geology and Geophysics. The work was expanded upon, refined and published in Contributions to Mineralogy and Petrology (volume 106, pages 100-109) during the early part of candidature for this research and thus has been included here as a representation of the applications of the FMASH petrogenetic grid.

Arnold, J., and Sandiford, M., (1990) Petrogenesis of cordierite-orthoamphibole assemblages from the Springton region, South Australia.
Contributions to Mineralogy and Petrology, v. 106 (1), pp. 100-109.

A6.2 Sandiford et al., (in prep)

Some causes and consequences of high-T, low-P metamorphism in the eastern Mount Lofty Ranges, South Australia

Mike Sandiford, Geoff Fraser, Jo Arnold, John Foden and Trish Farrow

This paper has been submitted to the Australian Journal of Earth Sciences, and accepted for publication. It uses P-T pseudosections calculated for the FMASH system to constrain the metamorphic field gradient in the eastern Mount Lofty Ranges as part of a wider study into the temporal and spatial variations of metamorphism in the area.

Some causes and consequences of high-T, low-P metamorphism in the Eastern Mount Lofty Ranges, South Australia.

MIKE SANDIFORD, GEOFF FRASER*, JO ARNOLD, JOHN FODEN AND TRISH FARROW

Department of Geology and Geophysics, University of Adelaide, GPO Box 498, Adelaide, S.A.

*Present address, Research School of Earth Sciences, Australian National University, Canberra,

Abstract

Andalusite-sillimanite facies series rocks in the eastern Mount Lofty Ranges preserve evidence for mineral equilibration during convergent deformation at temperatures near 550-600°C and pressures of 3-5 kbars, with lateral gradients in peak temperature of about 10°C/km near the first appearance of fibrolitic sillimanite (i.e., the sillimanite-in isograd). The high temperature portion of the metamorphic history appears to have been nearly isobaric and the geometry of folded isograd patterns apparently established during the deformation suggest the duration of deformation to be in the range $0.3^{+0.7}_{-0.2}$ Ma. These factors imply that the thermal perturbation responsible for peak metamorphism resulted primarily from localised, advective heat transfer in the lithosphere. Advection of heat in granitic magma, at least to the presently exposed crustal levels, is suggested by the intimate relationship between the attainment of peak metamorphic temperatures, convergent deformation and intrusion, and, together with the apparently short duration of deformation, suggests that thermal weakening of the lithosphere during magma ascent of heat may have triggered the deformation.

Key words: metamorphism; conduction; advection; magmatism.

INTRODUCTION

Much of the interest in metamorphic rocks stems from their ability to record the effects of orogenic processes during perturbed thermal regimes. Consequently the nature of the heat sources responsible for the thermal regimes attendant with crustal metamorphism have been the subject of intense study in the last few decades (e.g., England & Richardson, 1977). In high-temperature, low-pressure (high-T, low-P) metamorphic terranes the role of advective transport of magmas is of critical importance in the development of the thermal regime (Lux et al., 1986; Sandiford & Powell, 1991; Sandiford et al., 1991), and in this paper we assess the contribution of advective processes to the thermal evolution of a high-T, low-P terrain in the eastern Mount Lofty Ranges, South Australia (see Dymoke & Sandiford, 1992). We conclude with some speculative comments on the causal relationship between advection of magmas, metamorphism and deformation in this region.

GEOLOGICAL BACKGROUND

The Mount Lofty Ranges form part of the southern Adelaide Fold Belt (Fig. 1), an arcuate belt of NeoProterozoic to Early Cambrian sedimentary rocks which were deformed and metamorphosed during the Cambro - Ordovician Delamerian Orogeny (e.g., Preiss, 1987; Jenkins & Sandiford, 1992). Through most of the fold belt the metamorphism has not exceeded biotite grade, however the metasedimentary sequences of the eastern Mount Lofty Ranges have locally experienced much higher grade metamorphism, reaching migmatite-grade in places and it is this region that forms the focus of this paper.

Descriptions of lithologies and comprehensive structural studies of the Mount Lofty Ranges can be found elsewhere (Offler & Fleming, 1968; Mancktelow, 1990), and recent overviews of the tectonic and magmatic evolution of the region are given in Jenkins & Sandiford (1992) and Sandiford et al. (1992), while discussions of various aspects of the metamorphic geology are given in Sandiford et al. (1990), Arnold & Sandiford (1991), and Dymoke & Sandiford (1992). Consequently, we present here only a simple overview of the geology in the vicinity of the Karinya Syncline in the eastern Mount Lofty Ranges (Fig. 1), concentrating on the implications for metamorphic and thermal evolution. This region is characterised by some of the highest grade rocks and steepest lateral temperature gradients in the belt. The metasediments in this region,

including psammites, pelites and carbonates, form part of the Early Cambrian Normanville and Kanmantoo Groups, which record the terminal stages of sedimentation in the Adelaide Fold Belt (Jenkins & Sandiford, 1992). Zircons from a tuffaceous layer in the Normanville Group have been dated at 526 Ma (Cooper et al., 1992).

Previous investigations in the eastern Mount Lofty Ranges have shown that this area provides excellent exposures of a *Buchan Style*, high-T, low-P terrain with particularly well developed andalusite - staurolite bearing assemblages (Offler & Fleming, 1968; Mancktelow, 1990; Dymoke & Sandiford, 1992). Regional mapping of mineral assemblages (Offler & Fleming, 1968; Mancktelow, 1990) shows a concentric zoning of isograds around a NNW-trending belt of deformed intrusives including the Rathjen Gneiss, the Palmer Granite and the Reedy Creek Granodiorite, suggesting these intrusions provided at least some of the heat responsible for the metamorphism (Fig. 1).

The dominant structural fabric in the region of the Karinya Syncline is a steeply dipping schistosity best defined in micaceous schists and axial planar to upright to slightly reclined, tight to isoclinal, N- to NNW-trending folds (Fig. 2). These folds and their associated axial fabrics can be traced down metamorphic grade from the highest grade zones through to biotite grade where the folds are marginally more open in style and the axial planar fabric is less well developed. In the sillimanite and migmatite zones the hinges of upright folds often contain crenulated biotite laminae, implying the existence of an earlier fabric. Hence the upright folds and associated fabric are considered to be a product of the second deformation (D_2) and are here referred to as F_2 and S_2, respectively. In detail, the regional, concentric isograd pattern can be seen to be partly folded around the longest wavelength F_2 folds, a feature which is used here to provide a constraint on the duration of folding. Evidence for the preceding deformation (D_1) is prominent only in the highest grade zones as crenulated early fabrics in F_2 folds or as early, flat lying, migmatitic fabrics in the migmatite zone. Hence structural complexity seems to be directly related to metamorphic grade and proximity to granitic intrusives.

The intrusive rocks in the Eastern Mount Lofty Ranges form two distinct suites recognized on the basis of field relationships, geochronology and geochemistry (Foden et al., 1990; Sandiford et al., 1992; Foden et al., in prep.). The older, dominantly I-type, suite was intruded prior to, and during, D_2 with granite veins either exhibiting F_2 folds or else boudinaged in the S_2 plane. Ion-microprobe ages of zircons believed to represent crystallisation are in the range 515-490 Ma

(Foden et al., in prep). The younger, bimodal suite of dominantly A-type intrusives are always undeformed (i.e., postdate D_2 strain) and have yielded U-Pb zircon ages of 485 Ma (Foden et al., in prep). At Reedy Creek, some 12 km south of the Karinya Syncline, U-Pb analyses of zircons from both members of the older, deformed suite (which preserves the S_2 foliation) and the younger, undeformed suite (which cross-cuts both the older intrusive as well as the S_2 foliation) are interpreted (Foden et al., in prep.) as reflecting virtually identical intrusive ages allowing, within error, for a maximum of no more than about 3 Ma for the development of the S_2 foliation preserved in the older intrusives.

METAMORPHIC GEOLOGY

In this section we concentrate on the distribution and significance of mineral assemblages from the vicinity of the Karinya Syncline in the eastern Mount Lofty Ranges (Fig. 2). The Karinya Syncline, with an estimated wavelength of approximately 15 km and amplitude of the order of 5 km, is a regional scale N-trending, F_2 fold which trends obliquely across the metamorphic zonation over a distance of about 40 km (Fig. 2). In the south, at highest grade, the Karinya Syncline plunges gently north exposing both the stratigraphy and the regional isograd pattern in oblique profile. To the north, in the biotite-zone, the fold axis flattens out eventually becoming essentially horizontal.

As documented by Dymoke & Sandiford (1992), the outcrops in eastern Mount Lofty Ranges are dominated by psammitic metasediments of the Kanmantoo Group consisting of biotite, plagioclase, quartz and muscovite, and containing relatively little useful information for the metamorphic geologist. However, a number of other rock types do provide critical information regarding the spatial and temporal variations in the distribution of temperatures and pressures in this terrain. These are described below.

Pelitic schists

The pelitic schists contain a variety of key index minerals including the aluminosilicates, andalusite and sillimanite, as well as K-feldspar, muscovite, chlorite, garnet and staurolite in addition to ubiquitous biotite, quartz, plagioclase and ilmenite (see Dymoke & Sandiford, 1992). The distribution of isograds marks the progressive increase in metamorphic grade southwards

along the Karinya Syncline. The metamorphic zonation is defined, in order of increasing grade, by the following zones (Offler & Fleming, 1968; Mancktelow, 1990; Dymoke & Sandiford, 1992) :

1. biotite,
2. andalusite + staurolite,
3. fibrolitic sillimanite,
4. prismatic sillimanite,
5. migmatite

According to Offler & Fleming (1968) the first appearance of andalusite and staurolite can be correlated with the disappearance of chlorite throughout much of the Southern Adelaide Fold Belt, although we have not corroborated this observation in the vicinity of the Karinya Syncline. Near the first appearance of fibrolitic sillimanite there is considerable textural evidence for partial replacement of andalusite by sillimanite (Fig. 3a) while at higher grades the aggregated habit of fibrolitic sillimanite in clusters up to 1 cm in diameter is suggestive of its growth being due to the breakdown of andalusite porphyroblasts.

Below the prismatic sillimanite zone garnet is typically spessartine-rich particularly in association with andalusite and staurolite (see Dymoke & Sandiford, 1992). Apart from extensive late muscovitization there is little in the way of important retrograde mineral growth, although we have found one occurrence showing partial replacement of a garnet-sillimanite-biotite assemblage by fine grained staurolite-chlorite-muscovite intergrowths. Because of the general paucity of pelitic outcrops the geometry of the isograd outcrop pattern cannot be precisely defined. Our interpretation of the approximate position of the andalusite–in and staurolite–in isograds (mapped together) as well as the sillimanite–in and sillimanite–k-feldspar–in isograds around the Karinya Syncline is illustrated in Figure 2. We note that this interpretation in which isograds are folded, with a wavelength comparable to, but an amplitude about half, that of the folded metasedimentary layering differs from the interpretation of Mills (1966, and as shown in Sandiford et al., 1990) who regarded all isograds to be NW-trending with significant left-lateral displacement along a N-trending fault immediately east of the axial trace of the Karinya Syncline. Futher support for our interpretation is provided by the distribution of orthoamphibole-bearing assemblages in

K_2O-deficient schists on the eastern limb of the syncline (see below), which define a NE-trend to the isograd sequence.

Aluminosilicate-bearing quartz segregations:

Aluminosilicate-bearing quartz segregations contain all three aluminosilicate polymorphs at the Marne Reserve locality (Sandiford et al., 1990). Textural relations suggest early kyanite has been replaced by andalusite and finally sillimanite (Fig. 3a). These segregations are up to several metres in length and are aligned parallel to the compositional layering and thus we interpret them to have formed prior to the upright D_2 folding.

Orthoamphibole-bearing rocks

Orthoamphibole-bearing rocks occur in scattered pods between the Marne River and Saunders Creek (Arnold & Sandiford, 1990). In these rocks orthoamphibole occurs in association with staurolite, cordierite or garnet as well as quartz, albite and biotite. Staurolite, where present, is rimmed by cordierite (Fig. 3b) in rocks which may also show late growth of orthoamphibole (Fig. 3c). As described by Arnold & Sandiford (1990) these late cordierite-orthoamphibole assemblages are considered a result of the breakdown of biotite and staurolite or andalusite accompanied by metasomatic depletion of potassium at conditions near the peak of metamorphism. However, distinct zonal isograd patterns are recognized in the distribution of assemblages in these K_2O-deficient schists, with the following progression of mineral associations with orthoamphibole is recognized from low to high grade over 5 km of outcrop (all assemblages include quartz, biotite and ilmenite);

1. staurolite + cordierite (± orthoamphibole),
2. orthoamphibole + cordierite,
3. orthoamphibole + cordierite + garnet,
4. orthoamphibole + garnet.

An important aspect of these K_2O-deficient schists is they define the NE-trend of isograds on the eastern limb of the Karinya Syncline (Figure 2), thus corroborating our interpretation of the distribution of pelitic isograds about the fold structure.

P-T conditions and metamorphic field gradient

Dymoke & Sandiford (1992) calculated average pressures (following the method of Powell & Holland, 1988) of between 4 and 4.5 kbars and temperatures between 550 and 600°C for pelitic assemblages in the andalusite-staurolite zone from the Eastern Mount Lofty Ranges. Temperatures reached in the sillimanite zone are indicated by the coexistence of sillimanite and relatively Mn-poor garnet. The T-X_{Fe} relationships in the K_2O-FeO-MgO-Al_2O_3-SiO_2-H_2O (KFMASH) system calculated using the dataset of Holland & Powell (1990) show that at 4.0 kbars a minimum temperature of about 610°C is required for this assemblage (Figs 4 & 5), although considerable sensitivity to even minor amounts of Mn is suspected (Powell, pers. comm.). Conventional garnet - biotite geothermometry on garnet - sillimanite bearing rock, using the calibration of Ferry & Spear (1978) yields temperatures of 600-630°C.

Dymoke & Sandiford (1992) showed that the regional arrangement of isograds in the eastern Mount Lofty Ranges reflects an essentially isobaric metamorphic field gradient with maximum lateral temperature gradients (*grad Tmax*) of about 10°C/km attained in the staurolite and andalusite zones near the sillimanite-in isograd.

The distribution of orthoamphibole-bearing assemblages documented above further corroborates such a metamorphic field gradient. To a first approximation these rocks can be understood by considering the stability of these minerals for a specific bulk rock compositions in the FeO-MgO-Al_2O_3-SiO_2-H_2O (FMASH) system (Figure 6). Note that biotite, ilmenite and albite in these rocks are each stabilised by an additional component (K, Ti, Na respectively) which occurs in negligible amounts in other phases.

As is the case with the mineral assemblages preserved in most rocks, the K_2O-deficient schists described above involve divariant and trivariant assemblages. While the equilibration conditions of these assemblages may be broadly estimated using P-T projections, their reaction relationships are better understood using phase diagrams which display higher variance assemblages, such as P-X or T-X sections or P-T pseudosections. For example, the P-T pseudosection in Figure 6 shows that the sequence of mineral assemblages preserved in K_2O deficient schists results from crossing the univariant reaction [Als] i.e.,

orthoamphibole + staurolite = garnet + cordierite + vapour.

with increasing temperature. This pseudosection (calculated for rocks in the FMASH model system, from thermodynamic data (Holland and Powell, 1985, 1990) using the computer program

THERMOCALC (version 2.2b1, Powell & Holland, 1988) applies to rock compositions with Al_2O_3 : FeO : MgO = 20 : 64 : 16 (or X_{Fe}= 0.8) which contain excess quartz, orthoamphibole and aqueous vapour. For such Fe-rich bulk compositions thedivariant reaction fields involve (1) a staurolite + cordierite field and (2) a staurolite + garnet field on the low temperature side of the [Als] univariant. The high temperature side of the reaction involves a broad cordierite + garnet (+orthoamphibole, quartz, vapour) divariant field.

The magnitude of *grad Tmax* must decline appreciably in the biotite zone in the northern exposures of the Karinya syncline, where no significant changes in mineralogy and texture are observed on scales of 10 kms (Fig. 7a). Since the isograds are concentric about a maximum in the migmatite grade *grad Tmax* must go to zero at the highest grades and the schematic shape defined by a plot of *grad Tmax* against *Tmax* or distance along the axial trace of the Karinya Syncline is shown in Fig. 7b. Of course, peak temperatures recorded in rocks across the terrain do not necessarily represent a temperature gradient that was present at any particular time but they provide important constraints on the nature of the heat source. Such lateral gradients in peak temperature which steepen up-grade along essentially isobaric surfaces are consistent with the expected metamorphic field gradient around a localised, transient heat source.

P-T paths and the duration of deformation

Aluminosilicate phase relations as described above suggest the prograde P-T-t path was essentially isobaric passing beneath the aluminosilicate triple point, reaching the sillimanite field in the highest grade region. Here, sillimanite grows within the S_2 foliation implying that the highest temperatures were attained during the D_2 folding event. Textures in orthoamphibole bearing rocks involving the breakdown of staurolite to cordierite are also consistent with a relatively isobaric prograde heating path for individual rocks, similar in form to the preserved field gradient illustrated in Figure 6. The retrograde P-T path is generally poorly constrained, however, the occurrence of a retrograde staurolite - chlorite assemblage after prograde garnet - sillimanite suggests, by analogy with the KFMASH P-T pseudo-sections from Dymoke & Sandiford (1992), essentially isobaric cooling. For an X_{Fe} appropriate to the bulk rock composition, in this case X_{Fe} of 0.8, the minimum pressure for the staurolite-chlorite assemblage is 3 kbars (Fig. 4). However, the development of retrograde staurolite - chlorite assemblages but not cordierite - chlorite or cordierite - andalusite is suggestive of pressures of 4 kbars or greater during the initial retrograde

P-T interval. At 3 kbars the chlorite - staurolite association is stable at about 570°C (at a(H_2O) = 1.0), with temperatures decreasing with increasing pressures (Dymoke & Sandiford, 1992) .

Distortion of isothermal surfaces by upright folding such as suggested by the partly folded isograd patterns about the Karinya Syncline must induce lateral heat transfer between adjacent fold hinges (Sleep, 1979). Because the isotherms respond to the evolving structure (Fig. 8), the form of isotherms developed during folding can in principal be used to constrain the duration of folding (e.g., Sleep, 1979). Using various simplifying assumptions Sleep (1979) has shown that for an upright fold that amplifies with a (vertical) velocity distribution given by:

$$V = V_z \, sin\left(\frac{2\,\pi\,x}{x_0}\right)$$

where V_z is the maximum velocity, x is the horizontal distance, and x_0 is the wavelength of the fold, the temperature dsitribution, $T_{(x,z)}$, will evolve according to:

$$T_{(x,z)} = G_0 \left(z - z_0\,(1 - exp\,(-t/t_0))\; sin\left(\frac{2\,\pi\,x}{x_0}\right)\right)$$

where G_0 is the initial vertical temperature gradient, and t is time. z_0 and t_0 are given by:

$$z_0 = \frac{V_z x_0^2}{(2\,\pi)^2\,\kappa}$$

$$t_0 = \frac{x_0^2}{(2\,\pi)^2\,\kappa}$$

where κ is the thermal diffusivity. Note that t_0 gives the timescale required to return to the original gradient once folding has ceased. Figure 10 shows that the ratio of the amplitude of folded isotherms to the amplitude of the folded stratigraphy, A', depends only on the wavelength of the fold, the duration of the folding and the thermal diffusivity.

While recognising that isograds and isotherms are not equivalent, we assume that isograd development can be equated with the general form of isothermal surfaces during the development of the Karinya Syncline. Since the mineral textures imply that the preserved isograd pattern in the Karinya Syncline was developed during folding, the geometry of isograds can therefore be used to constrain the duration of folding, with the preservation of partly folded isograd patterns implying that folds amplification occurred at a rate greater than the rate of thermal equilibration over the appropriate length-scale. For a thermal diffusivity of 10^{-6} m^2 s^{-1}, as appropriate to most crustal rocks, and a wavelength of about 15 km, the estimated value of A' of 0.5 implies the duration of folding for the Karinya Syncline was 0.3 Ma. An uncertainty in A' of about 20%

and in the estimated wavelength of the Karinya Syncline of about ± 5 km implies an uncertainty in the duration of folding of the order of $0.3^{+0.7}_{-0.3}$ Ma (Figure 9).

We note that independent evidence to support this result is provided by U-Pb analysis of zircons from both syn-D_2 intrusives (which preserve the S_2 foliation) and post-D_2 intrusives (which cross-cut the S_2 foliation) intrusives at Reedy Creek, as cited above, which shows that the ages of the intrusive events are virtually indistinguishable and allow a maximum time of about 3 Ma for the development of the component of the S_2 foliation preserved in the syn-tectonic intrusives.

SOME MECHANICAL CONSEQUENCES OF METAMORPHISM

The arguments presented in the preceding sections support the notion that the thermal regimes generated during metamorphism of the eastern Mount Lofty Ranges result directly from magmatic advection of heat, and that the magmatism and metamorphism were temporally and spatially associated with a short-lived phase of convergent deformation. In terms of the mechanics of orogenic development the critical questions relate to the processes governing magmatism and whether the process of melt generation, segregation and emplacement significantly modified the way the orogen deformed (e.g., Sandiford et al., 1991; Foden et al., in prep.). Since lithospheric strength is strongly temperature dependent (e.g., Brace & Kholstedt, 1980), the deformation history of an orogen may also be intimately linked to the heat transport processes and will therefore depend on the rates and durations of these processes that modify the thermal regime. In particular, rapid heat transfer into the crust via magma transport may potentially trigger and localise pervasive deformation in metamorphic terrains (Sandiford et al., 1991). That such a relationship between deformation and thermal history is apposite for the high-T, low-P metamorphism in the eastern Mount Lofty Ranges is suggested by the geochemical signatures of magmatic rocks from the Adelaide Fold Belt which suggest that the syn-orogenic granites are crust-mantle mixtures, and not simply the result of crustal melting (Sandiford et al., 1992). We suggest that the metamorphic record in the eastern Mount Lofty Ranges, in which peak temperatures were reached during an extremely short-lived, convergent phase of deformation coeval with magmatism is consistent with such a scenario. The main observations we use to support this

interpretation bear on the temporal and spatial distribution of heat in the metamorphic pile as reflected in the preserved mineral assemblages, isograd patterns and textures. In particular the geometry of isograd patterns developed during folding points to extremely transient deformation. As such we regard the high-T, low-P metamorphism and deformation of the Eastern Mount Lofty Ranges as a consequence of sub-crustal heat input, efficiently transported to mid-upper crustal levels with the attendant thermal weakening providing a trigger for deformation. The resolution of the nature of the mechanisms controlling sub-crustal melting remains to be elucidated.

REFERENCES

Arnold, J. & Sandiford, M., 1990. Petrogenesis of cordierite-orthoamphibole assemblages from the Springton region, South Australia. Contributions to Mineralogy and Petrology. 106, 100-109.

Brace, W.F. & Kholstedt, D.L., 1980. Limits on lithospheric stress imposed by laboratory experiments. Journal of Geophysical Research, 85, 6248-6252.

Cooper, J., Jenkins, R.J.F., Compston, W., Williams, I.S., 1992. Ion-probe zircon dating of a min-Early Cambrian tuff in South Australia. Journal of the Geological Society of London, 149, 185-192.

Dymoke, P. & Sandiford, M., 1992. Phase relations of Buchan facies series pelitic assemblages: calculations and applications to the Mount Lofty Ranges, South Australia. Contributions to Mineralogy and Petrology. 110, 121-132.

England, P. C., & Richardson, S. W., 1977. The influence of erosion upon the mineral facies of rocks from different metamorphic environments. Journal of the Geological Society of London, 134, 201-213.

Ferry, J. M. & Spear, F. S. 1978. Experimental calibration of the partitioning of Fe and Mg between biotite and garnet. Contributions to Mineralogy and Petrology, 13-117.

Foden, J.D. & Turner, S.P, Morrison, R., 1990, The tectonic implications of the Delamerian magmatism in South Australia and western Victoria, In: Proterozoic and Early Palaeozoic geology of the Adelaide Geosyncline, Geological Society of Australia, Special Publication 16 (Daily Volume), pp. 483-495.

Holland, T & Powell, R., 1990, An enlarged and updated internally consistent thermodynamic dataset with uncertainties and correlations: the system K_2O-Na_2O-CaO-MgO-MnO-FeO-Al_2O_3-TiO_2-SiO_2-C-H_2O-O_2, Journal of metamorphic geology, 8, 89-124.

Jenkins, R.F.J., & Sandiford, M., 1992, Observations on the tectonic evolution of the southern Adelaide Fold Belt, Tectonophysics, 214,

Mancktelow, N. S. 1990. The structure of the southern Adelaide Fold Belt, South Australia. In: Proterozoic and Early Palaeozoic geology of the Adelaide Geosyncline, Geological Society of Australia, Special Publication 16 (Daily Volume), pp. 483-495.

Lux , D.R., DeYoreo, J.J., Guidotti, C.V., & Decker, E.R., 1986, Role of plutonism in low-pressure metamorphic belt formation, Nature, 323, 795-797.

Offler, R. & Fleming, P. D. 1968. A synthesis of folding and metamorphism in the Mount Lofty Ranges, South Australia. Journal of the Geology Society of Aust alia , 15, 245-266.

Powell, R. & Holland, T. J. B. 1988 An internally consistent dataset with uncertainties and correlations: 3. Applications to geobarometry, worked examples and a computer program. Journal of Metamorphic Geology, 6, 173-204

Preiss, W. V.(compiler), 1987. The Adelaide Geosyncline- late Proterozoic stratigraphy, sedimentation, palaeontology and tectonics. Geological Survey of South Australia, Bulletin, 53.

Sandiford, M., Foden, J., Zhou, S. & Turner, S., 1992. Granite genesis and the mechanics of convergent orogenic belts with application to the southern Adelaide Fold Belt. Transactions of the Royal Society of Edinburgh: Earth Sciences. 83,

Sandiford, M., Martin, N., Zhou, S. & Fraser, G., 1991. Mechanical consequences of granite emplacement during high-T,low-P metamorphism and the origin of "anticlockwise" PT paths. Earth and Planetary Science Letters, 107, 164-172.

Sandiford, M., Oliver, R. L., Mills, K. J. & Allen, R. V. 1990. A cordierite-staurolite-muscovite association, East of Springton, Mount Lofty Ranges; Implications for the metamorphic evolution of the Kanmantoo Group. In: Proterozoic and Early Palaeozoic geology of the Adelaide Geosyncline, Geological Society of Australia, Special Publication 16 (Daily Volume), pp. 483-495.

Sandiford, M. & Powell, R., 1991. Some remarks on high temperature-low pressure metamorphism in convergent orogens. Journal of Metamorphic Geology, 9, 333-340.

Sleep, N.H., 1979. A thermal constraint on the duration of folding with reference to Acadian geology, New England (USA). Journal of Geology, 87, 583-589.

Figure Captions

Fig. 1. Geological map of the Southern Adelaide Fold Belt showing the concentric metamorphic zonation in the Eastern Mount Lofty Ranges (after Offler and Fleming, 1968 and Mancktelow, 1990). The box east of Springton encloses the area of Fig. 2.

Fig. 2. Geological map of the Karinya Syncline with metamorphic isograds. The folded isograd geometry provides a constraint on the duration of folding in the Karinya Syncline (see text for discussion).

Fig. 3a) Photomicrograph showing early kyanite replaced by andalusite and finally sillimanite in a quartz-rich segregation from near the Marne Reserve. 3b) Photomicrograph showing early staurolite replaced by cordierite in orthoamphibole bearing schist. 3c) late orthoamphibole growing in cordierite-bearing shcist. 3d) orthoamphibole-garnet schist.

Fig.4. PT projection for the KFMASH system, appropriate to the pelitic rocks from the Eastern Mount Lofty Ranges (from Dymoke and Sandiford, 1992). The section pseudo-section for a bulk rock composition of $X_{Fe} = 0.8$ shows the stability field of retrograde staurolite - chlorite assemblages.

Fig. 5. T-X_{Fe} section in the KFMASH system, for pressure of 4.5 kbars. Pelitic rocks from the Eastern Mount Lofty Ranges, with relatively high X_{Fe} values, containing garnet-sillimanite assemblagessuggesting equilibration at temperatures greater than about 610°C (from Dymoke and Sandiford, 1992).

Fig. 6. PT pseudo-section in the FMASH system, appropriate to the orthoamphibole bearing schists, for specific bulk composition. The observed sequence of mineral associations with orthoamphibole (see text) records a near isobaric increase in peak temperature upgrade, shown by the large arrow.

Fig. 7a). Schematic illustration of the variation in *Tmax* as a function of distance along the axial trace of the Karinya syncline. 7b). Schematic illustration of the variation in *grad Tmax* as a function of distance along the axial trace of the Karinya syncline.

Fig. 8. Schematic illustration of the evolving thermal structure around a developing fold.

Fig. 9. Application of Sleep's (1979) analysis to the geometry of isograds around the Karinya Syncline, showing the dependence of the ratio of amplitude of folded isotherms to folded stratigraphy, A', as a function of time for fold wavelengths in the range 5 - 25 kms (assuming a thermal diffusivity of $\kappa = 1 \text{ x } 10^{-6} \text{ m}^2 \text{ s}^{-1}$). For the estimated value of $A' = 0.5 \pm 0.2$ and wavelength of $\lambda = 15 \pm 5$ km, appropriate to tghe Karinya Syncline, we estimate the duration of folding as $0.3^{+0.7}_{-0.2}$ Ma.

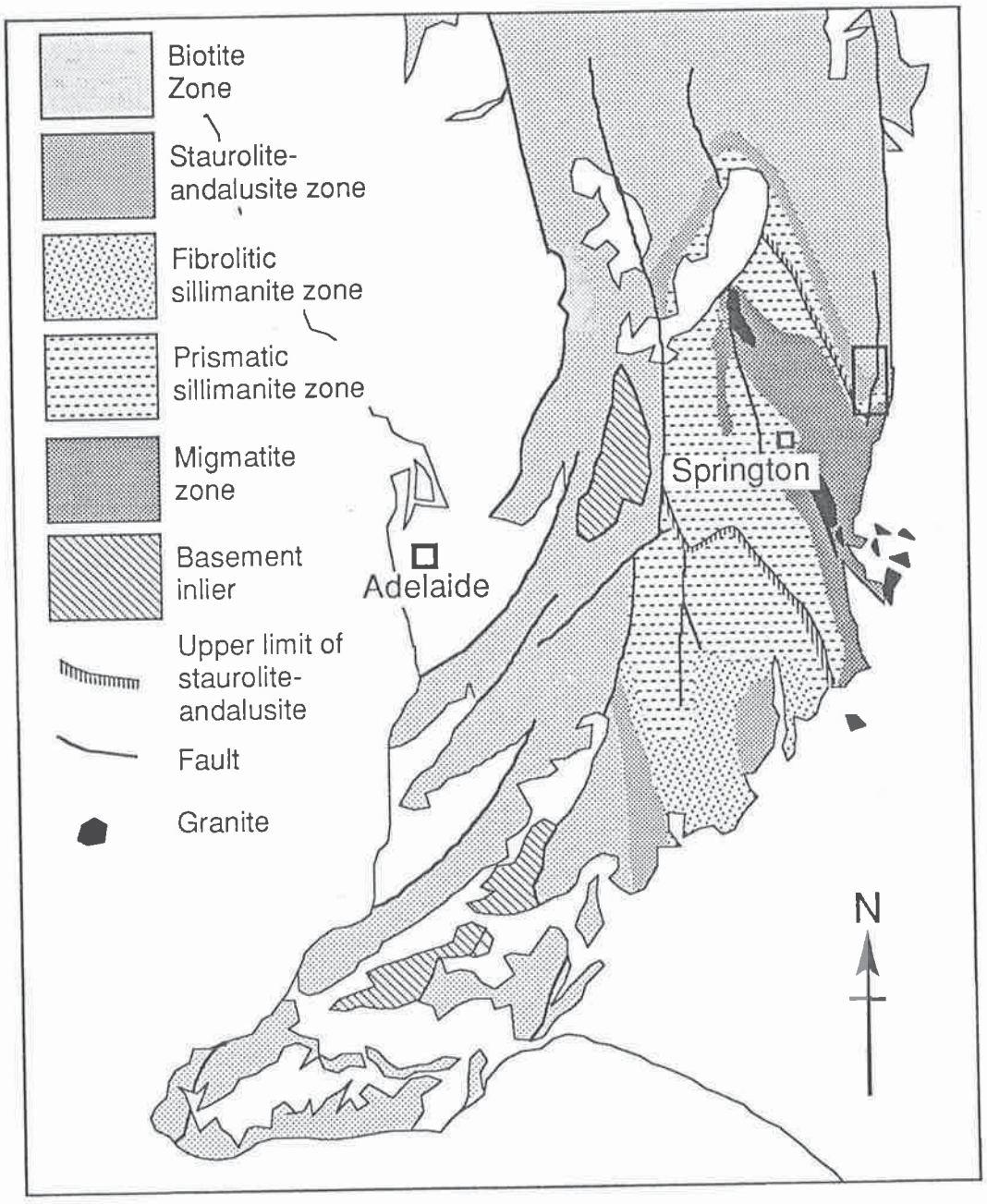
Biotite Zone
Staurolite-andalusite zone
Fibrolitic sillimanite zone
Prismatic sillimanite zone
Migmatite zone
Basement inlier
Upper limit of staurolite-andalusite
Fault
Granite
Adelaide
Springton
N

Figure 1

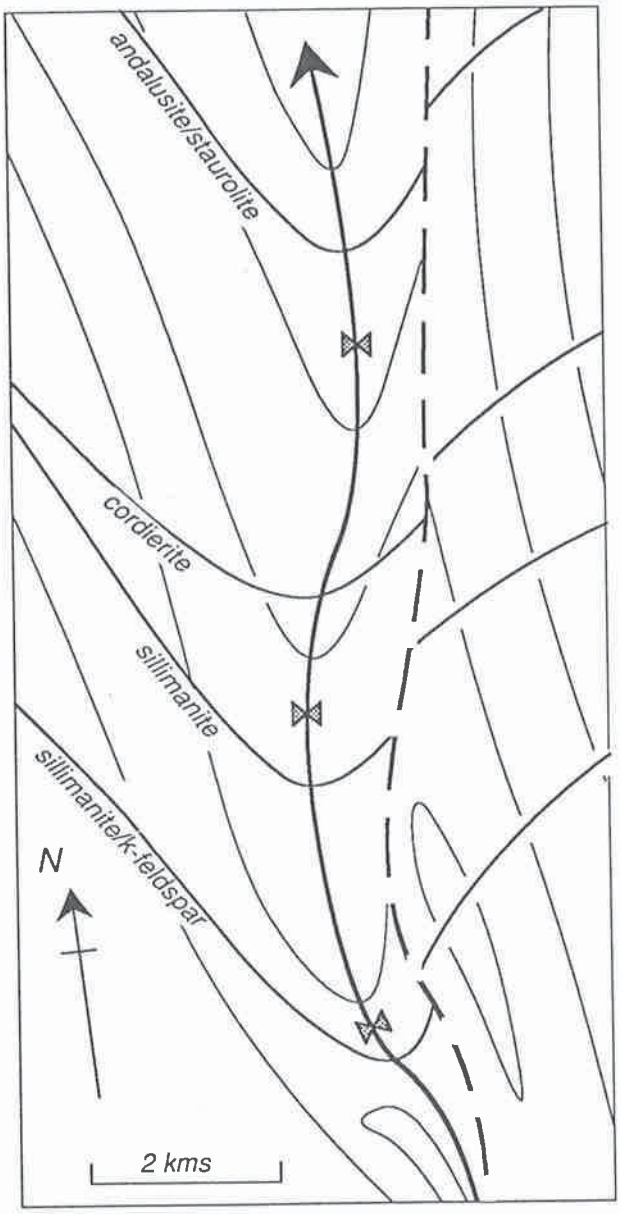
andalusite/staurolite
cordierite
sillimanite
sillimanite/k-feldspar
N
2 kms

Figure 2

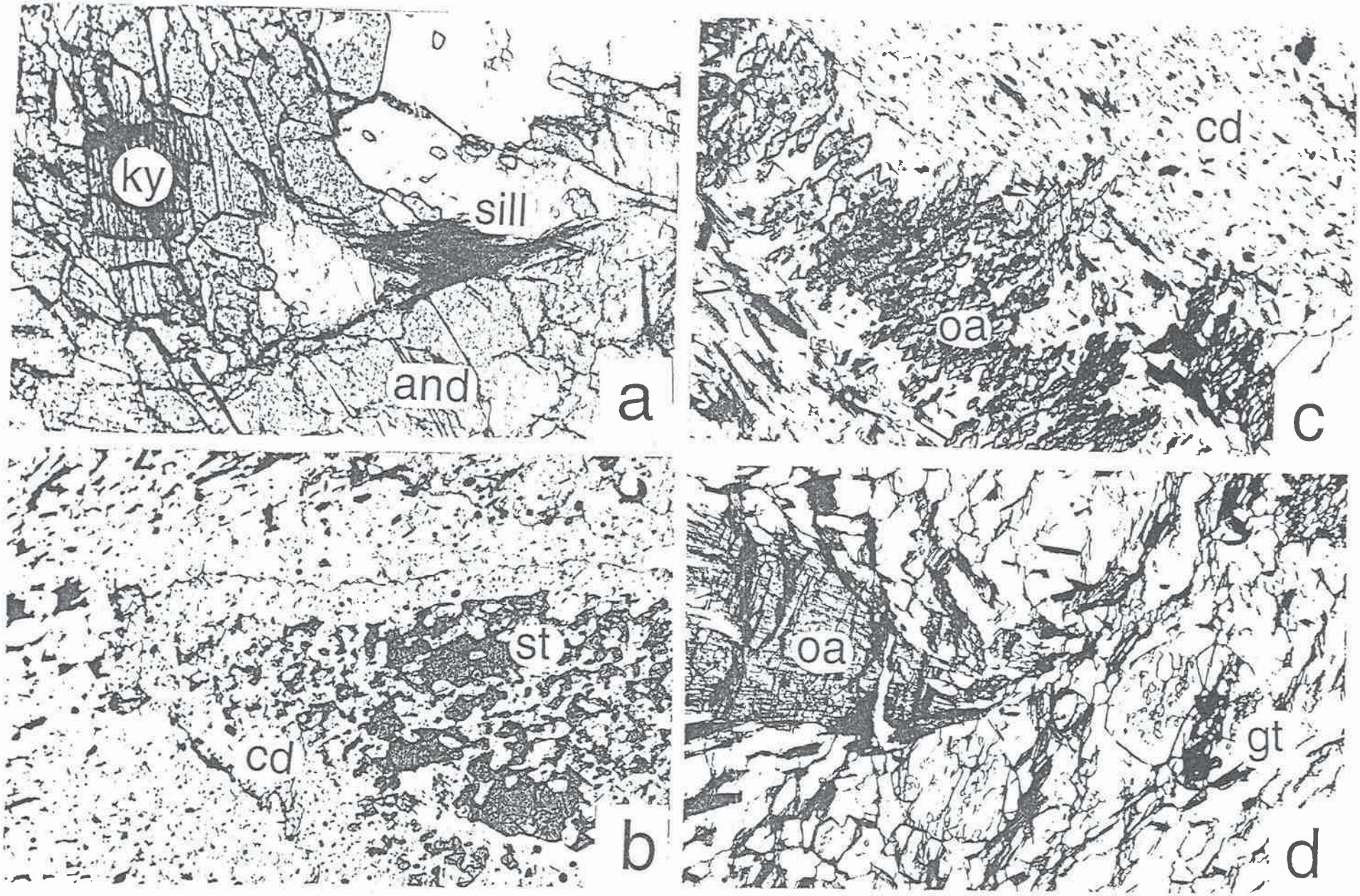

Figure 3

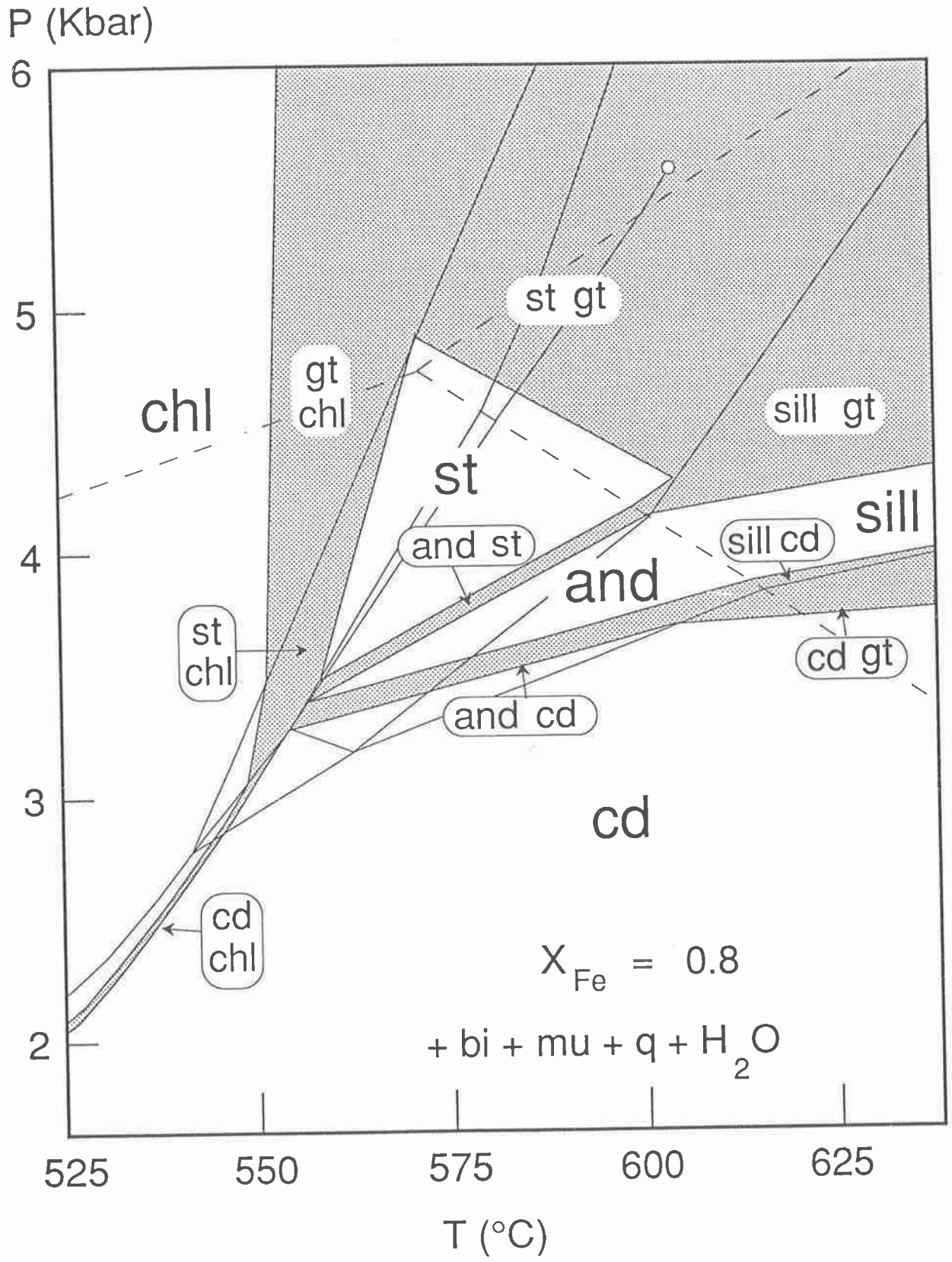
P (Kbar)
6
5
4
3
2
chl
gt
chl
st gt
sill gt
st
sill
and st
sill cd
and
st
chl
cd gt
and cd
cd
cd
chl
X_{Fe} = 0.8
+ bi + mu + q + H_2O
525
550
575
600
625
T (°C)

Figure 4

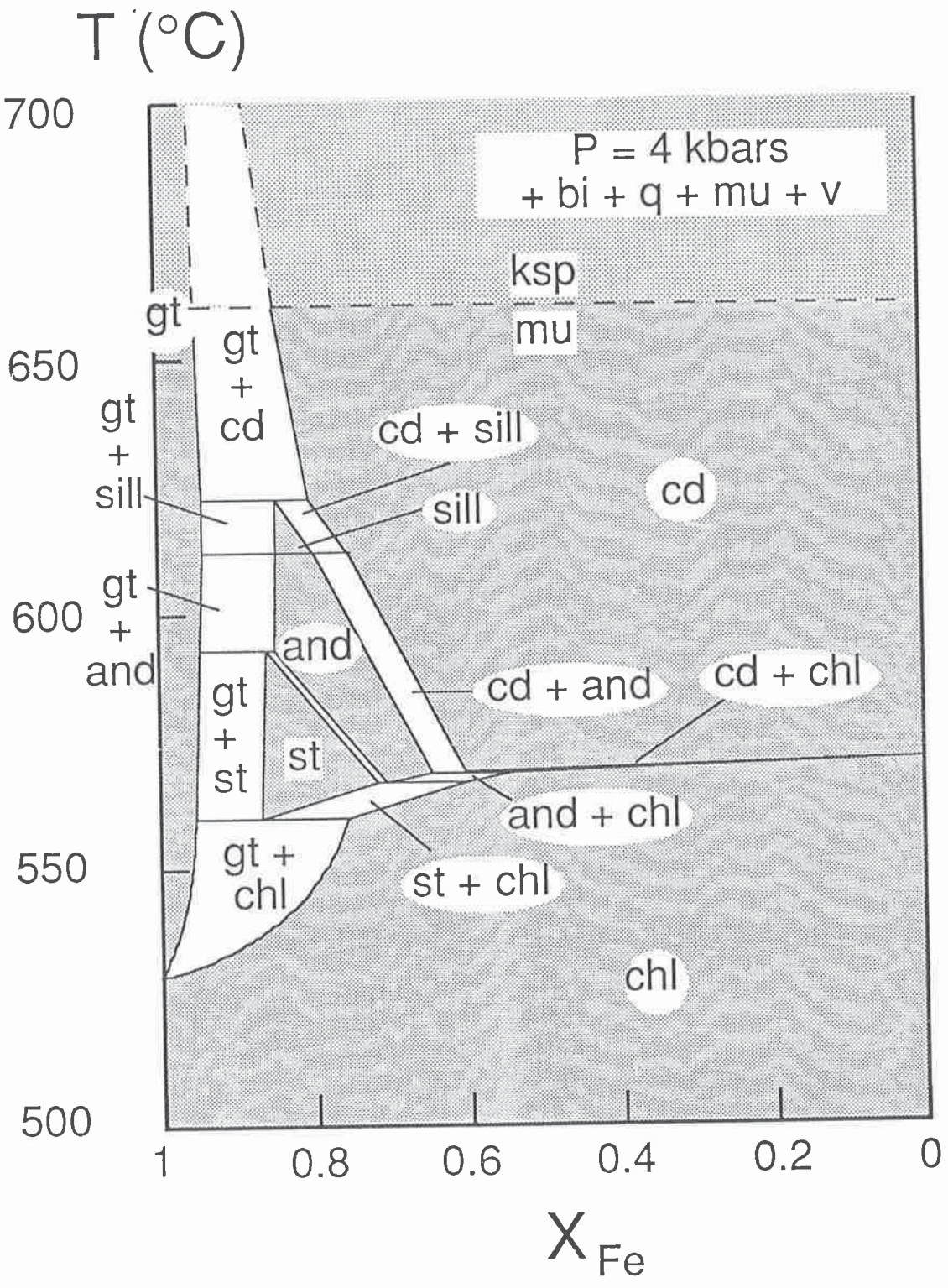
T (°C)
700
650
600
550
500
P = 4 kbars
+ bi + q + mu + v
ksp
mu
gt
gt + cd
gt + sill
gt + and
gt + st
gt + chl
cd + sill
sill
cd
and
cd + and
cd + chl
st
and + chl
st + chl
chl
1
0.8
0.6
0.4
0.2
0
X Fe

Figure 5

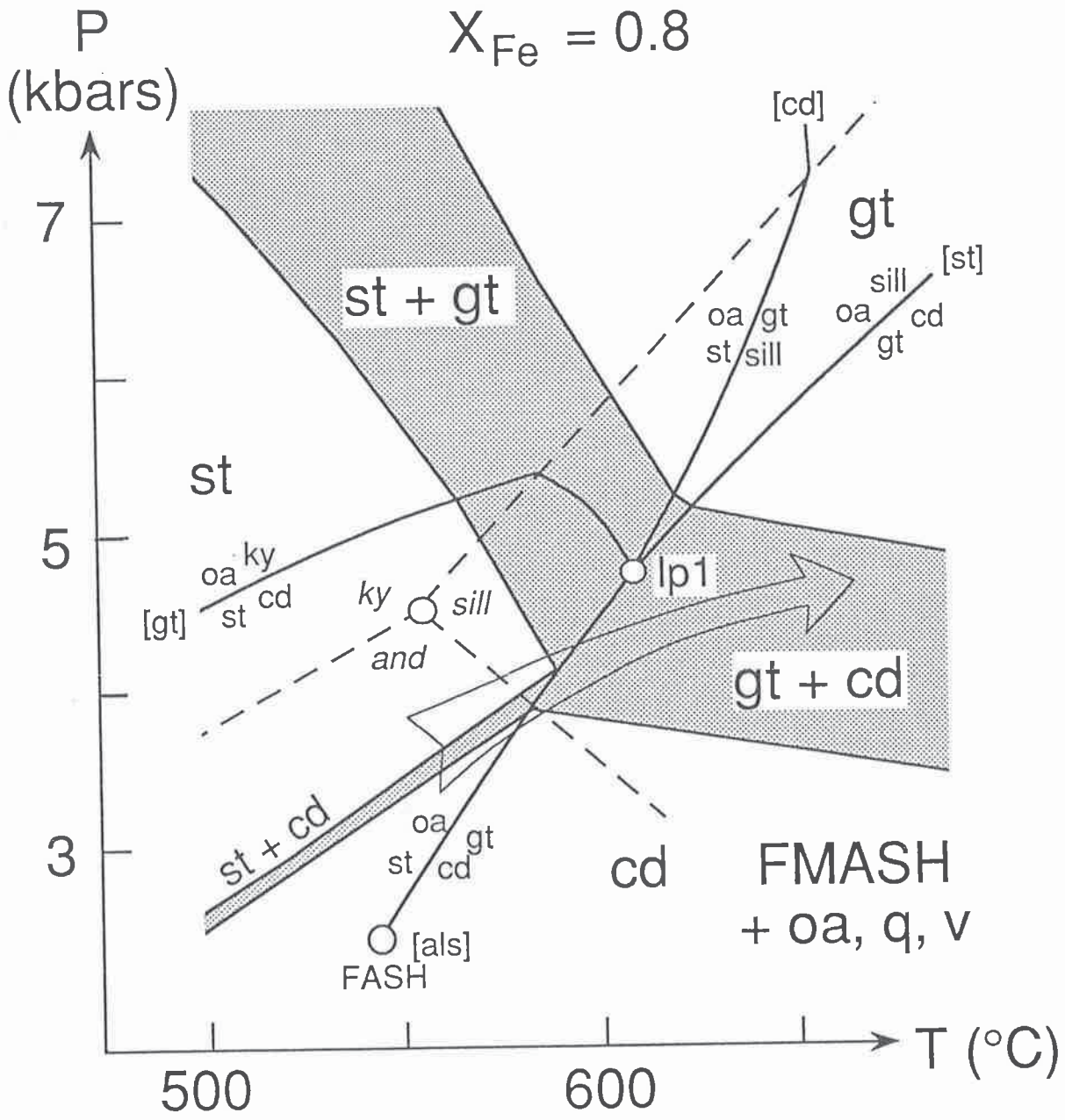
P
(kbars)
X_{Fe} = 0.8
7
5
3
500
600
T (°C)
st + gt
gt
st
gt + cd
st + cd
cd
FMASH
+ oa, q, v
[cd]
[st]
[gt]
[als]
FASH
lp1
oa gt
st sill
sill
oa cd
gt
oa ky
st cd
ky sill
and
oa gt
st cd

Figure 6

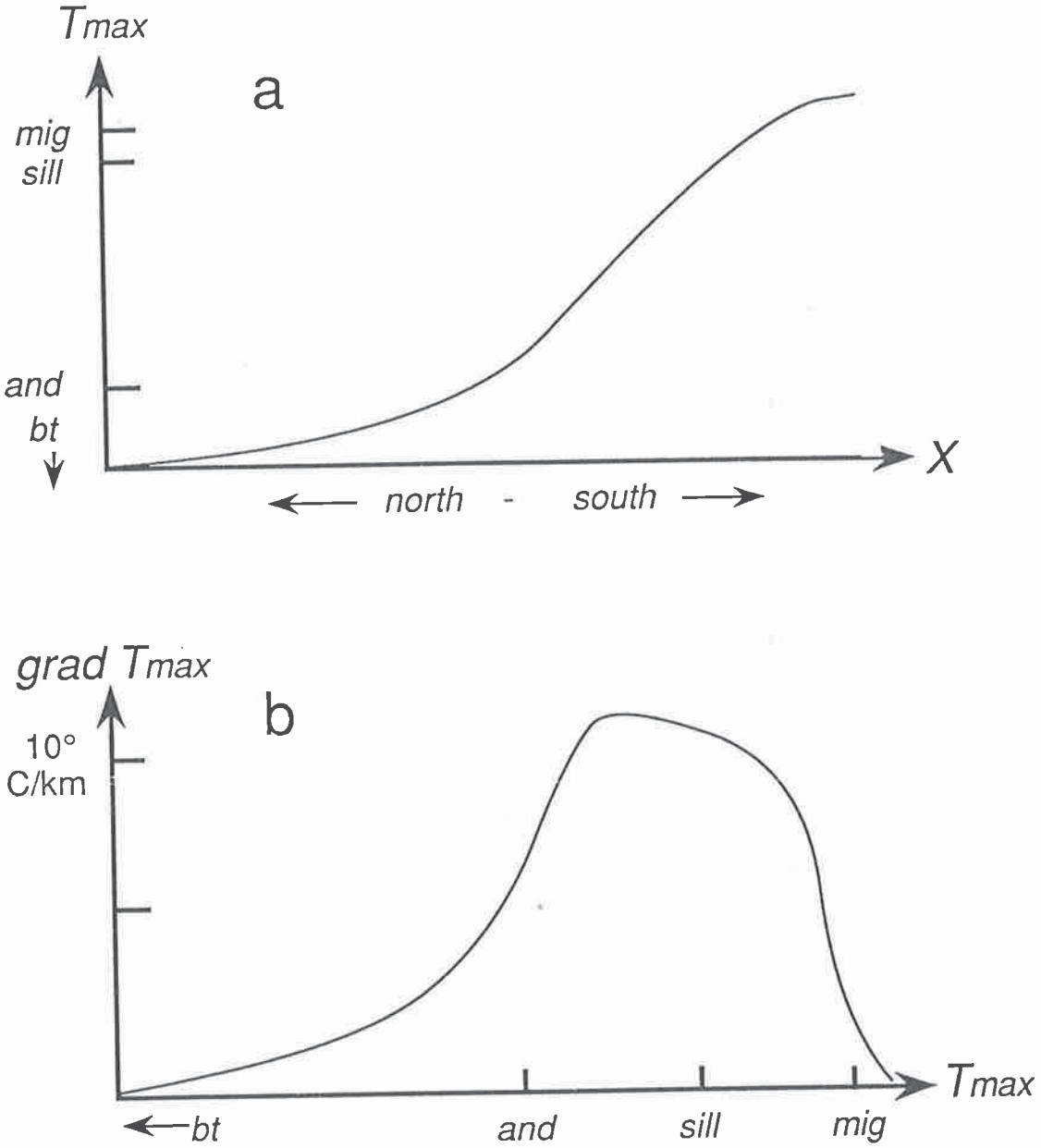
Tmax
a
mig
sill
and
bt
X
north - south
grad Tmax
b
10°
C/km
Tmax
bt
and
sill
mig

Figure 7

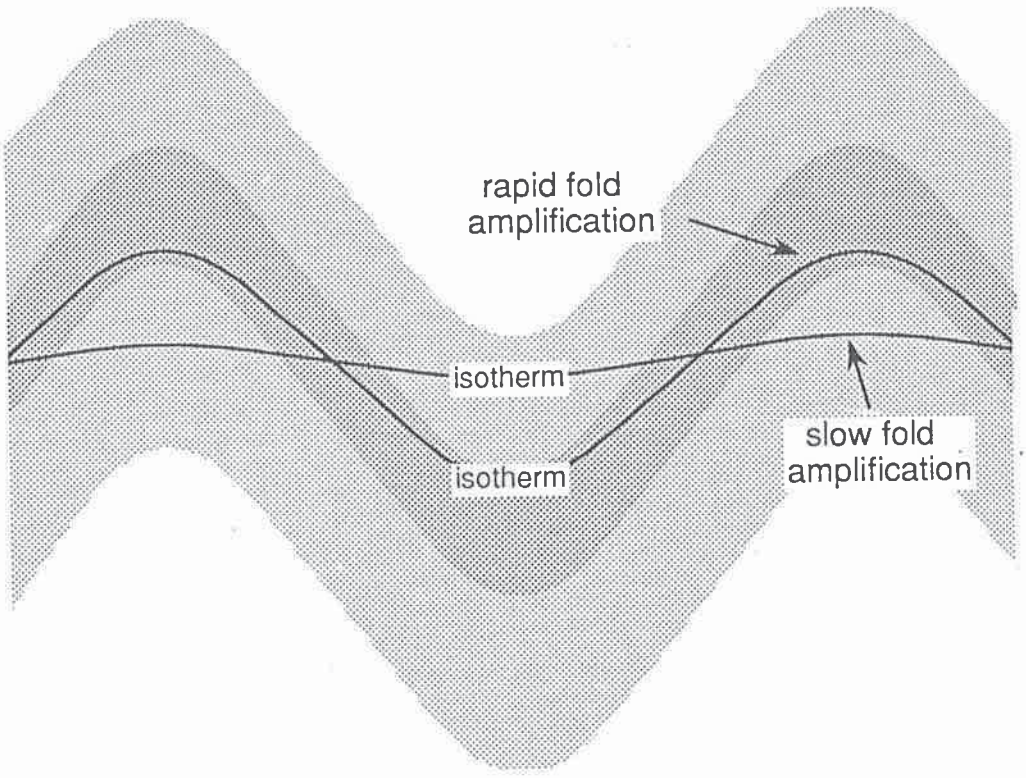
rapid fold
amplification
isotherm
isotherm
slow fold
amplification

Figure 8

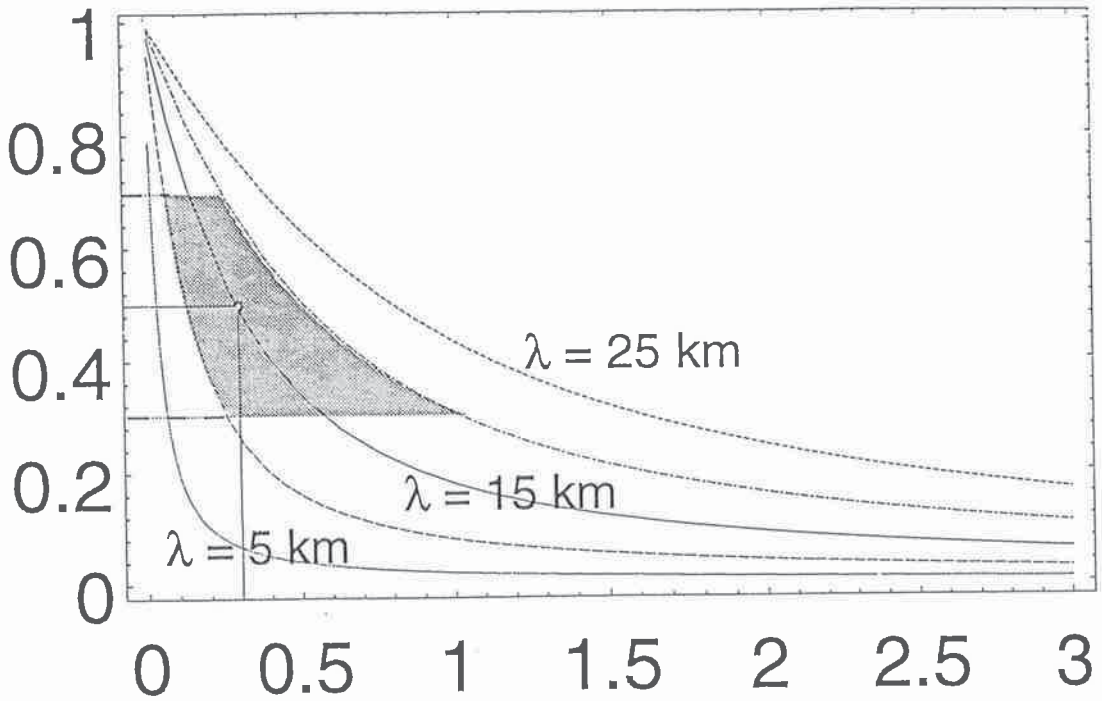

Figure 9

Appendix A7: Permanent data files for CFMASH

This appendix contains a listing of the permanent data files used in the calculation of pressure temperature projections in the CFMASH, CMASH, CFASH and NCFMASH model systems.

A7.1 CFMASH

A7.1.1 Ideal mixing

```
ky      and     sill

st  2           mst     1       1       1  1 -1  1  4
                fst     1       1       0  1  1  1  4
                2       1       1       0  1  1  1
x(st) 0.7

cd  3           crd     1       2       1  1 -1  1  2     1  1 -1  2  1
                fcrd    1       2       0  1  1  1  2     1  1 -1  2  1
                2       1       1       0  1  1  1
                hcrd    1       2       1  1 -1  1  2     0  1  1  2  1
                2       1       1       0  1  1  2
x(cd) 0.1
h(cd) 0.25

gt  3           py      1       2       1  1 -1  1  3     1  1 -1  2  3
                alm     1       2       0  1  1  1  3     1  1 -1  2  3
                2       1       2       0  1  1  1        1  1 -1  2
                gr      1       1       0  1  1  2  3
                2       1       1       0  1  1  2
x(gt) 0.68
z(gt) 0.1

chl 3           clin    16      3       1  1 -1  1  5     1  1 -1  2  2     0  1  1  2  2
                daph    16      3       0  1  1  1  5     1  1 -1  2  2     0  1  1  2  2
                2       0.2     2       0  1  2  1        3  1 -1  2
                ames    1       2       1  1 -1  1  4     0  1  1  2  4
                2       1       1       -1 1  2  2
x(chl) 0.0612
y(chl) 0.623

oa  3           anth    0.0625  3       1  1 -1  1  7     1  1 -1  2  2     2  1 -1  2  4
                fath    0.0625  3       0  1  1  1  7     1  1 -1  2  2     2  1 -1  2  4
                2       0.1429  2       0  1  1  1        7  1 -2  2
                ged     1       3       1  1 -1  1  5     0  1  1  2  4     2  1 -1  2  2
                2       1       1       0  1  1  2
                3       10  0  0        % ged factor
x(oa) 0.3
y(oa) 0.55

hbl  3          tr      0.0625  3       1  1 -1  1  5     1  1 -1  2  2     2  1 -1  2  4
                ftr     0.0625  3       0  1  1  1  5     1  1 -1  2  2     2  1 -1  2  4
                2       0.2     2       0  1  1  1        5  1 -2  2
                hb      2.3704  4       1  1 -1  1  4     1  1 -1  2  1
                                        0  1  1  2  2     2  1 -1  2  3
                2       2       1       0  1  1  2
x(hbl) 0.4
y(hbl) 0.6

an      q       H2O
```

A7.1.1 Non-ideal mixing

Coding for non-ideal garnet in the CFMASH model system, after the model of R. Powell (pers. comm., 1993):

```
gt 3            py                      1   2   1 1 -1  1  3    1  1 -1  2  3
                1 5     1.6 0 0         3   2   0 1  1  1  1    1  1 -1  2  1
                      - 1.6 0 0         3   3   0 1  1  1  1    1  1 -1  1  1    1  1 -1  2  2
                      - 5 0 0           3   3   0 1  1  1  1    0  1  1  2  1    1  1 -1  2  1
                        14.1 0 0        3   1   0 1  1  2  1
                      - 14.1 0 0        3   3   1 1 -1  1  1    0  1  1  2  1    1  1 -1  2  1

                alm                     1   2   1 1 -1  1  3    1  1 -1  2  3
                1 5     1.6 0 0         3   2   1 1 -1  1  1    1  1 -1  2  1
                      - 1.6 0 0         3   3   0 1  1  1  1    1  1 -1  1  1    1  1 -1  2  2
                        5 0 0           3   1   0 1  1  2  1
                      - 5 0 0           3   3   0 1  1  1  1    0  1  1  2  1    1  1 -1  1  1
                      - 14.1 0 0        3   3   1 1 -1  1  1    0  1  1  2  1    1  1 -1  2  1
                2                       1   2   1 1 -1  1  3    1  1 -1  2  3

                gr                      1   1   0 1  1  2  3
                1 3   - 1.6 0 0         3   3   0 1  1  1  1    1  1 -1  1  1    1  1 -1  2  2
                        5 0 0           3   2   0 1  1  1  1    1  1 -1  1  1
                        14.1 0 0        3   2   1 1 -1  1  1    1  1 -1  2  2
                2                       1   1   0 1  1  2

x(gt) 0.68
z(gt) 0.1
```

A7.2 CMASH

```
ky      and     sill

mst

cd 2            crd             1       1       1 1 -1  1  1
                hcrd            1       1       0 1  1  1  1
                2               1       1       0 1  1  1
h(cd) 0.25

gt 2            py              1       1       1 1 -1  1  3
                gr              1       1       0 1  1  1  3
                2               1       1       0 1  1  1
z(gt) 0.1

chl 2           clin            16      2       1 1 -1  1  2    0  1  1  1  2
                ames            1       1       0 1  1  1  4
                2               1       1       -1 1  2  1
y(chl) 0.7

oa 2            anth            0.0625  2       1 1 -1  1  2    2  1 -1  1  4
                ged             1       2       0 1  1  1  4    2  1 -1  1  2
                2               1       1       0 1  1  1
                3               5  0  0         % ΔHged fiddle
y(oa) 0.55

hbl 2           tr              0.0625  2       1 1 -1  1  2    2  1 -1  1  4
                hb              2.3704  3       1 1 -1  1  1    0  1  1  1  2    2  1 -1  1  3
                2               2       1       0 1  1  1

an      q       H2O
```

A7.3 CFASH

```
ky      sill    and

fst

cd 2            fcrd        1       1       1 1 -1 1 1
                fhcd        1       1       0 1 1 1 1
                2           1       1       0 1 1 1
                4           3       1       hcrd 1   crd -1   fcrd 1
h(cd) 0.25

gt 2            alm         1       1       1 1 -1 1 3
                gr          1       1       0 1 1 1 3
                2           1       1       0 1 1 1
z(gt) 0.1

chl     2       daph        16      2       1 1 -1 1 2      0 1 1 1 2
                fame        1       1       0 1 1 1 4
                2           1       1       -1 1 2 1
                4           3       5       ames 5  daph 4  clin -4 % makes fame
y(chl) 0.7

oa 2            fath        0.0625  2       1 1 -1 1 2      2 1 -1 1 4
                fged        1       2       0 1 1 1 4       2 1 -1 1 2
                2           1       1       0 1 1 1
                3           10 0 0                  % ΔHged fiddle
                4           3       7       ged 7  fath 5  anth 5  % makes fged
y(oa) 0.55

hbl 2           ftr         0.0625  2       1 1 -1 1 2      2 1 -1 1 4
                fhb         2.3704  3       1 1 -1 1 1      0 1 1 1 2       2 1 -1 1 3
                2           2       1       0 1 1 1
                4           3       1       hb 1    ftr 0.8   tr -0.8   % makes fhb
y(hbl) 0.6

an      q       H2O
```

A7.4 NCFMASH

Permanent datafile for NCFMASH with plagioclase non ideality calculated for 4T disorder (where Na and Ca and Al and Si mix randomly and the four tetrahedral sites are considered to be equivalent) in the C1 region and ordered in I1 (where mixing of Al and Si does not contribute to the entropy of mixing) (as in Model 4, Holland & Powell, 1992).

```
ky      sill    and

st 2            mst         1       1       1 1 -1 1 4
                fst         1       1       0 1 1 1 4
                2           1       1       0 1 1 1
x(st) 0.719

cd 3            crd         1       2       1 1 -1 1 2      1 1 -1 2 1
                fcrd        1       2       0 1 1 1 2       1 1 -1 2 1
                2           1       1       0 1 1 1
                hcrd        1       2       1 1 -1 1 2      0 1 1 2 1
                2           1       1       0 1 1 2
x(cd) 0.0472
h(cd) 0.815

gt 3            py          1       2       1 1 -1 1 3      1 1 -1 2 3
                alm         1       2       0 1 1 1 3       1 1 -1 2 3
                2           1       2       0 1 1 1         1 1 -1 2
                gr          1       1       0 1 1 2 3
```

```
                2               1       1       0 1 1 2
x(gt) 0.237
z(gt) 0.174

chl 3           clin            16      3       1 1 -1 1 5      1 1 -1 2 2      0 1 1 2 2
                daph            16      3       0 1 1 1 5       1 1 -1 2 2      0 1 1 2 2
                2               0.2     2       0 1 2 1         3 1 -1 2
                ames            1       2       1 1 -1 1 4      0 1 1 2 4
                2               1       1       -1 1 2 2
x(chl) 0.0612
y(chl) 0.623

oa 4            anth            0.003906        4       1 1 -1 3 1      1 1 -1 1 7
                                                        1 1 -1 2 2      4 2 -2 2 -1 3 4
                fath            0.003906        4       1 1 -1 3 1      0 1 1 1 7
                                                        1 1 -1 2 2      4 2 -2 2 -1 3 4
                2               0.14286         2       0 1 1 1         7 1 -2 2
                ged             0.0625          5       1 1 -1 3 1      1 1 -1 1 5      0 1 1 2 2
                                                        0 2 2 2 1 3 2           4 2 -2 2 -1 3 2
                2               1               1       0 1 1 2
                3               0 0 0                   % DQF
                oed             0.0370          4       0 1 1 3 1       1 1 -1 1 7
                                                        0 2 2 2 1 3 1           4 2 -2 2 -1 3 3
                2               1               1       0 1 1 2
                3               9.8 0 0                 % DQF
                4               3               1       ed 1    anth 1  tr -1 % makes oed
x(oa) 0.6
y(oa) 0.1
n(oa) 0.4

hbl 4           tr              0.01563         4       1 1 -1 1 5      1 1 -1 2 2
                                                        1 1 -1 3 1      4 2 -2 2 -1 3 4
                ftr             0.01563         4       0 1 1 1 5       1 1 -1 2 2
                                                        1 1 -1 3 1      4 2 -2 2 -1 3 4
                2               0.2             2       0 1 1 1         5 1 -2 2

                hb              0.14815         6       1 1 -1 1 4      1 1 -1 2 1
                                                        0 1 1 2 1       1 1 -1 3 1
                                                        4 2 -2 2 -1 3 3         0 2 2 2 1 3 1
                2               2               1       0 1 1 2
                ed              0.037037        5       1 1 -1 1 5      1 1 -1 2 2      0 1 1 3 1
                                                        4 2 -2 2 -1 3 3         0 2 2 2 1 3 1
                2               1               1       0 1 1 3
x(hbl) 0.0636
y(hbl) 0.245
n(hbl) 0.264

I1      2       an              1       1       0 1 1 1 1
                1       1       9.8 0 0 1 1     1 1 -1 1 2
                2               1       1       0 1 1 1
                ab              1       1       1 1 -1 1 1
                1       1       9.8 0 0 1 1     0 1 1 1 2
                3               1.72    -0.00395 0              % DQF
anI 0.756

C1      2       an              0.0625  3       0 1 1 1 1       1 1 1 1 2       3 1 -1 1 2
                1       1       5.5 0 0 1 1     1 1 -1 1 2
                2               1       1       0 1 1 1
                3               4.31    -0.00217 0              % DQF
                ab              0.0370  3       1 1 -1 1 1      1 1 1 1 1       3 1 -1 1 3
                1       1       5.5 0 0 1 1     1 1 1 2
anC 0.75

q       H2O
```

Appendix A8: Petrography, mineral chemistry and compatibility relations of amphibolites from the Harts Range, central Australia

A8.1 Introduction

The variable bulk rock chemistry of amphibolites in the Entia gneiss complex of the Harts Range has resulted in a wide range of mineral assemblages which preserve different aspects of the region's metamorphic evolution. The assemblages are dominated volumetrically by high variance assemblages such as hornblende–epidote–plagioclase–quartz, hornblende–garnet–plagioclase–quartz and hornblende–clinopyroxene–plagioclase–quartz which may contain variable but minor proportions of titanite, biotite, oxide phases and other accessory phases. More rarely, the amphibolites contain lower variance assemblages involving kyanite, staurolite, cordierite, garnet or orthoamphibole in addition to hornblende–plagioclase–quartz and accessory phases. Corundum is sometimes present in the absence of quartz. This wide variety of assemblages makes the Harts Range an ideal locality to investigate the compatibility relations in the unusual kyanite–staurolite amphibolites. The petrography and mineral chemistry of amphibolites from the Harts Range are described here with the aim of discerning their compatibility relations. This is utilised in the construction of a P-T history in Chapter 4 and will be combined with information from other areas (Chapters 5 and 6) and the phase diagrams calculated in Chapter 3 in order to develop an understanding of the phase relations in amphibolites (Chapter 6).

This appendix includes a brief summary of the mineralogy and chemistry of the higher variance assemblages including primary assemblages and detailed descriptions of the lower variance amphibolite assemblages. These low variance amphibolites are divided into three groups, Fe-rich amphibolites (e.g. those involving staurolite–garnet–orthoamphibole–hornblende–plagioclase–quartz), intermediate X_{Fe} amphibolites (e.g. kyanite–staurolite–orthoamphibole–hornblende–plagioclase–quartz) and Mg-rich amphibolites (e.g. kyanite–cordierite–orthoamphibole–hornblende–plagioclase–quartz) (Fig. A8.1). Each of these will be discussed in turn.

The Fe-Mg partitioning in the amphibolites was found to be consistent within and between samples and X_{Fe} increased in the order: staurolite > garnet > orthopyroxene > cummingtonite > hornblende ≥ orthoamphibole ≥ clinopyroxene > biotite > cordierite. A petrographic summary of the mineralogy and textures of selected amphibolite assemblages is presented in Chapter 4 (Table 4.2).

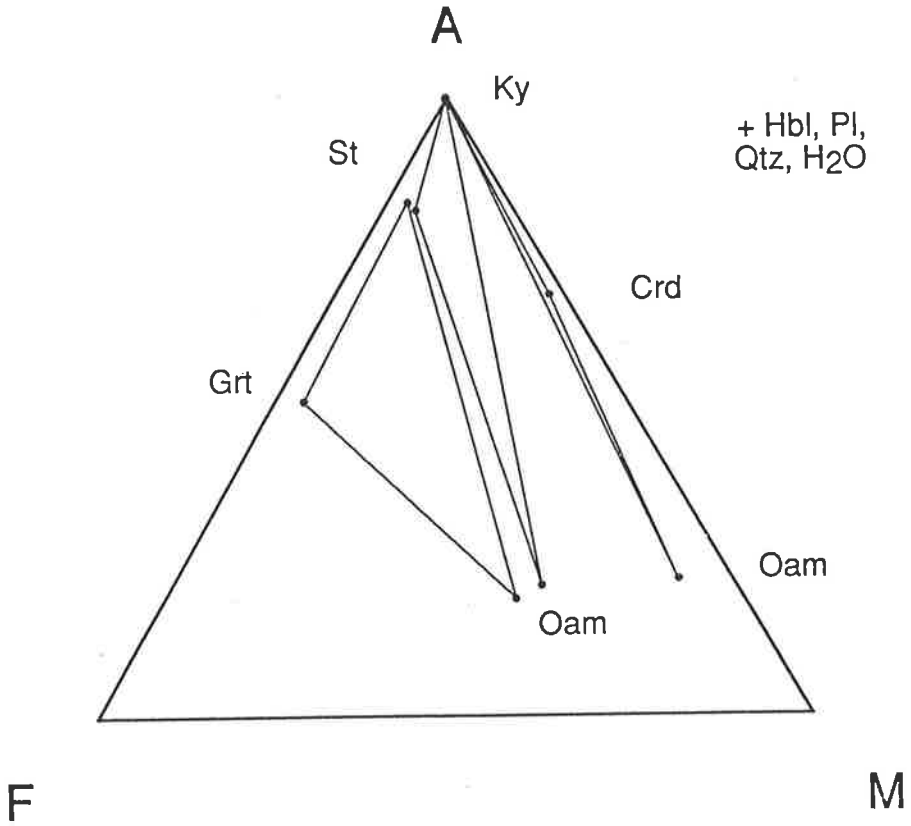

Figure A8.1. Schematic compatibility diagram for low variance assemblages projected from hornblende, plagioclase, quartz and aqueous vapour onto the AFM plane($AlO_{3/2}$, FeO, MgO).

A8.2 Analytical techniques

Mineral analyses were carried out by both energy dispersive (EDS) and wavelength dispersive (WDS) methods using the Jeol 733 SuperProbe at the University of Adelaide and selected analyses are listed throughout the appendix. Data includes analyses of cores and rims, detailed traverses across grains, analyses of adjacent grains and of exsolution lamellae, where present. Amphiboles are named using the classification of Leake (1978) and other minerals are classified using the conventional nomenclature (e.g. Deer et al., 1972). Mineral compositions are plotted on NCAFm ($NaO_{1/2}$-CaO-$AlO_{3/2}$-(FeO+MgO)) tetrahedra projected from quartz and aqueous vapour, and AFM ($AlO_{3/2}$-FeO-MgO) ternary diagrams projected from hornblende, plagioclase, quartz and aqueous vapour.

The bulk chemistry of the amphibolites was analysed by X-Ray Fluorescence in the University of Adelaide. The samples were crushed and ground to a powder in a tungsten carbide ring mill. Major element analyses were carried out using the technique of Norrish and Hutton (1969) and trace element analyses were made on pressed pellets of unignited powder.

A8.3 High variance primary and high grade assemblages

High grade mineral assemblages in the Entia Dome occur in low strain domains or boudins in the highly deformed, dominantly amphibolite-grade Entia gneiss complex (e.g. the Huckitta Mafic Boudin, Mawby, 1991; Foden et al., 1994). The level of hydration and foliation development increases from the centre of the boudins outward and in strongly deformed zones the phases are almost entirely hydrous.

A8.3.1 Textural features

A detailed description of the petrography, mineral chemistry and other aspects of the high grade mafic rocks preserved in the mafic boudins of the Harts Range area is presented by Mawby (1991) and is briefly summarised here. The textures preserved in high grade rocks such as those in the Huckitta Mafic Boudin involve cumulous and intercumulous orthopyroxene, clinopyroxene, olivine and plagioclase. Orthopyroxene–spinel (hercynite) symplectites have developed between cumulous olivine and intercumulous plagioclase in olivine gabbros. Augite lamellae are observed in orthopyroxene and hornblende also occurs as part of a symplectitic texture with spinel surrounding orthopyroxene in pyroxene gabbros (Mawby, 1991). Titaniferous magnetite and ilmenite are observed both as cumulous and intercumulous phases.

In samples collected from the margins of low strain boudins, hornblende mantles surround corroded pyroxene grains. This hornblende is subhedral to anhedral and is elongated to form a weak to strongly developed foliation. Biotite appears to replace hornblende and samples collected from the extremities of the boudins often comprise foliated metamorphic garnet–hornblende–biotite assemblages.

A8.3.2 Mineral Chemistry

The minerals which make up the high grade assemblages rarely show evidence of zoning but the cumulous phases are typically chemically distinct form the intercumulous phases. (Chemical data for the high grade samples is given by Mawby, 1991, and a list of compositional abbreviations is given in Appendix A1.

Cumulous olivine is chrystolite to hyalosiderite in composition (X_{Fe} = Fe/(Fe+Mg) = 25-36) whereas orthopyroxene (enstatite) has X_{Fe} in the range 0.23 in the gabbros to 0.38 in the dolerites and generally contains only a little Ca (1-3 mol %). Zoned phenocrysts and lamellae of augite have proportions Ca_{44-48}:Mg_{42-46}:Fe_{7-11} (Mawby, 1991). Cumulous plagioclase is typically more calcic (labradorite to anorthite An_{64-98} in olivine gabbro and dolerite) than intercumulous andesine (An_{37-48}) (Mawby, 1991) and generally neither variety exhibits zonation.

In more hydrous samples pargasitic hornblende surrounds pyroxene. The chemistry of hornblende is dependent on that of the pyroxene with which it is associated and ranges from approximately X_{Fe} 0.20 to 0.74 (Mawby, 1991). Fe-rich biotite (X_{Fe} 0.59-0.64) and Ca-rich garnet (Mg_{0-7}:Fe_{59-72}:Ca_{24-25}:Mn_{3-10}) are associated with corroded pyroxene and hornblende.

A8.3.3 Interpretation

The correlation of increasingly strongly developed foliation and increasing proportion of hydrous minerals from the interior of the boudins outwards suggests that fluid-flow and deformation were both strongly partitioned around the boudins. Thus the relatively undeformed interiors of the boudins preserve information about the early (igneous) history of the rocks which is not accessible in other rock-types (e.g. Mawby, 1991). The generally large grainsize, the development of exsolution lamellae of augite in orthopyroxene and the presence of orthopyroxene–spinel symplectites between cumulous olivine and intercumulous plagioclase all suggest that the metabasites cooled slowly from their intrusion temperatures, implying that the surrounding country rocks were at high temperatures at the time of intrusion.

The mantle-like texture of hornblende and the dependence of hornblende compositions on those of associated pyroxene suggest that hornblende has only incompletely replaced pyroxene in the cores of boudins whereas in the surrounding highly deformed zones it has obliterated all pyroxene. As the high grade mafic assemblages are generally silica-poor they may not be projected into the same compositional systems as are used later. They are not part of the amphibolite grade metamorphism of primary interest here, however compositional plots are presented by Mawby (1991).

A8.4 High variance amphibolite grade assemblages

Semi-continuous boudinaged and folded layers of amphibolite form long ridges in the dominantly low-lying felsic rocks of the Entia gneiss complex. They typically exhibit gneissic

layering of hornblende-rich layers and more felsic, plagioclase–quartz-dominated layers (0.1-2 cm wide) and may also be grossly banded on a decimetre scale, possibly due to original compositional heterogeneity. The gneissic layered appearance may be reinforced by garnet, epidote or pyroxene-rich bands or quartz-ribbons. Hornblende grains typically define a mineral lineation on the foliation surface. The majority of amphibolites show a variable medium to strongly developed foliation, however isolated outcrops are only weakly foliated.

A8.4.1 Hornblendites

Hornblende-amphibolites are typically darker and more homogeneous than other amphibolites in the area however they often contain lighter epidote-, garnet- or plagioclase-rich bands. The bulk-rock compositions of hornblende amphibolites (i.e. those containing hornblende–plagioclase–quartz ± epidote, pyroxene) are generally Ca-rich (> 5 wt %) and Na-rich (> 1.3 wt %) in comparison to rocks which contain more aluminous assemblages (Table A8.1).

Textural features

The most common mineral assemblage in the amphibolites involves equigranular hornblende–plagioclase–epidote ± relict pyroxene, quartz, biotite and cross-cutting, random chlorite and biotite with accessory allanite, apatite, zircon, rutile, titanite, opaques (magnetite and exsolved ilmenite and titaniferous magnetite-ulvöspinel solid solution).

Hornblende is typically euhedral, elongate and medium grained (usually 1-2 mm in length) and exhibits widely variable colour from pale green to blue-green, brown-green or dark green in thin section. It shares straight grain boundaries with all phases except corroded clinopyroxene, to form a polygonal mosaic with simple triple-point junctions and often defines a mineral lineation within the gneissic layering (Fig. A8.2). Hornblende generally lacks inclusions, but coarse randomly oriented grains may contain anhedral inclusions of zoned plagioclase and epidote group minerals along their central axis.

Optically zoned plagioclase forms equant to slightly elongate subhedral grains which show little twinning (Fig. A8.3). The rarely visible twins show no evidence of kinking or other deformation. Some sericitisation is observed along twin and cleavage planes and in heavily fractured samples or parts of samples plagioclase is almost totally sericitised. Plagioclase occurs in contact with all phases. Polygonal to lobate quartz exhibits undulose extinction, and rarely forms undulose quartz ribbons which help to define the compositional layering.

Euhedral laths (0.1-1 mm) of epidote group minerals are disseminated throughout the samples, and may be included in hornblende. In some samples fine-grained, slightly elongate epidote and opaque grains define a foliation which is cross-cut by coarse grained hornblende (Fig. A8.4). These hornblendes often contain epidote inclusions and are surrounded by an epidote-poor matrix. Epidote is colourless to very weakly pleochroic (colourless to pale green)

Table A8.1. Whole rock analyses.§

	Ep-Hbl	amphib	amphib	amphib	amphib	amphib	Ep-Hbl	calc-silicate	calc-silicate	Hbl
Sample #	962-155	853-180	857-04	857-83	950-045	853-145	962-017r	853-121	853-148	950-042
%										
SiO2	46.42	49.28	50.56	51.00	57.98	58.06	47.78	36.85	51.73	50.73
TiO2	1.06	0.61	0.55	0.65	1.36	0.33	0.57	1.30	0.66	0.33
Al2O3	16.29	14.62	9.32	15.44	13.97	15.05	23.99	26.10	22.77	9.38
Fe2O3*	13.59	9.59	10.56	9.88	6.70	7.31	6.83	11.65	6.01	9.63
MnO	0.20	0.16	0.24	0.19	0.06	0.14	0.10	0.17	0.10	0.17
MgO	7.67	9.91	12.32	8.23	7.40	6.36	5.33	5.02	0.13	15.60
CaO	11.90	14.02	14.40	11.50	9.08	8.32	9.11	18.90	17.49	11.22
Na2O	2.20	1.75	1.28	2.50	2.54	3.45	3.47	0.18	0.66	1.28
K2O	0.48	0.32	0.50	0.84	0.32	1.00	1.12	0.06	0.07	0.29
P2O5	0.16	0.04	0.12	0.07	0.16	0.04	0.42	0.04	0.24	0.07
LOI	0.64	0.71			0.49	0.67	1.59	2.30	1.32	0.66
Total	100.61	101.01	99.85	100.30	100.06	100.73	100.31	102.57	101.18	99.36
ppm										
Cr	156	-	89.0	-	155.0	-	118.0	-	-	1976.0
Ni	82	194.0	61.0	139.0	41.2	107.0	37.0	54.0	8.0	393.8
Sc	47.6	55.0	84.0	47.0	43.5	35.0	22.3	44.0	22.0	40.9
V	281.5	271.0	226.0	255.0	353.5	92.0	170.6	271.0	113.0	152.6
Pb	9.2	-	-	-	3.7		11.7	-	-	2.9
Rb	4	4.4	11.5	6.3	8.9	10.6	41.5	1.8	1.1	3.8
Sr	507.2	90.0	209.0	160.0	381.7	262.0	524.1	1460.0	1036.0	29.8
Ba	113	43.0	173.0	221.0	126.0	165.0	67.0	9.0	116.0	47.0
Ga	18	15.0	14.0	17.0	19.8	20.0	29.1	43.0	35.0	10.7
Nb	3.4	1.2	3.4	2.9	4.7	7.1	7.2	10.1	19.8	3.2
Zr	57.9	24.4	51.0	29.8	108.0	86.0	116.6	79.0	251.0	35.6
Y	23.3	12.6	22.6	14.6	40.8	39.0	30.5	15.6	38.0	14.0
Th	1.1	-	-	-	5.2	-	11.1	-	-	3.6
U	nd	-	-	-	3.6	-	2.4	-	-	nd
ppm										
La	4.0	3.0	15.0	4.0	23.0	22.0	41.0	15.0	77.0	16.0
Ce	10.0	-	47.0	9.0	44.0	49.0	78.0	34.0	122.0	20.0
Nd	4.0	4.0	33.0	1.0	16.0	33.0	33.0	15.0	49.0	10.0
Cu	123	-	-	-	-3.8	-	9	-	-	nd
Zn	105	-	-	-	16.2	-	44	-	-	55.6
Co	67	-	-	-	7.4	-	62.5	-	-	56.6

§ Analysis by X-Ray Fluorescence at University of Adelaide on a Philips PW 1480 X-ray spectrometer.
Major element analysis after Norrish & Hutton (1969).
Trace element analysis: unignited powder mixed with binder and pressed into a pellet.
Elements not analysed are marked (-) those with concentrations below detection limits are marked (nd) and have detection limits of approximately 3.5, 2, 2, 5, 5.5 ppm for Pb, Th, U, Ce, Cr respectively.
Fe2O3* total iron represented as Fe2O3.
Analyses from: 853- Sullivan, 1985; 857- Aouker, 1985; 950-, 962-, HR91- this study.

Table A8.1. Whole rock analyses (continued)

Sample #	Ky-Bt-Oam-Hbl 962-021b	Ky-St-3t-Oam-Hb HR91-6	Ky-St-Ep-Hbl HR91-4	Grt-amphib 950-059	St-Grt Ep-Hbl HR91-8	Grt-Hbl-Bt 853-16	Ky-Bt-schist 853-76	Ky-mu-gt schist 857-30	Ky-mu-gt schist 857-90	migmatite gneiss 853-129	Crd-Oam 853-30
%											
SiO2	61.45	60.07	38.14	39.13	37.92	67.04	42.93	55.67	55.34	70.53	47.18
TiO2	0.95	0.56	1.47	1.22	2.37	1.01	0.31	0.67	0.75	0.41	0.65
Al2O3	16.08	14.06	19.41	23.70	20.78	11.05	34.84	25.99	28.22	13.11	26.53
Fe2O3*	4.91	7.98	16.45	17.34	17.25	9.03	5.23	11.62	7.73	4.8	7.57
MnO	0.04	0.06	0.24	0.19	0.16	0.12	0.05	0.50	0.23	0.06	0.12
MgO	6.07	10.03	8.29	4.18	6.37	3.26	11.8	2.13	1.37	3.28	15.9
CaO	8.44	5.06	11.60	13.21	11.04	6.17	0.55	1.44	0.69	1.21	0.43
Na2O	1.13	0.83	1.86	0.89	1.36	1.09	1.05	0.28	0.63	3.38	0.91
K2O	0.18	0.14	0.76	0.52	0.50	0.27	2.68	0.88	4.78	2.92	0.73
P2O5	0.26	0.04	0.43	0.24	0.04	0.38	0.2	0.62	0.14	0.05	0.07
LOI	0.74	1.03	1.60	0.04	0.91	0.35	3.09			0.84	2.93
Total	100.25	99.86	100.25	100.66	98.70	99.77	99.64	99.80	99.88	99.75	100.09
ppm											
Cr	119.0	178.0	311.0	274.0	38.0	nd	nd	112.0	-	-	5.0
Ni	43.0	148.0	115.0	58.8	40.0	2.0	20.0	27.0	20.0	6.0	13.0
Sc	24.4	22.2	47.4	41.8	54.7	26.0	9.8	28.0	17.8	7.6	26.0
V	182.7	187.7	242.9	328.9	262.0	107.0	75.0	80.0	98.0	44.0	78.0
Pb	3.6	2.0	8.8	11.7	5.6	-	-	-	-	-	
Rb	5.0	4.3	20.9	8.9	14.1	4.9	75.0	24.7	190.0	71.0	21.7
Sr	367.1	54.3	197.5	574.5	363.6	442.0	34.0	17.4	123.0	116.0	14.0
Ba	57.0	54.0	103.0	157.0	162.0	95.0	412.0	123.0	596.0	1049.0	91.0
Ga	22.7	16.2	22.5	45.5	27.2	13.0	28.0	21.0	39.0	15.0	27.0
Nb	9.7	2.0	6.9	16.3	14.3	5.4	7.7	16.9	14.4	7.6	14.4
Zr	140.9	25.0	162.1	285.6	241.8	161.0	190.0	118.0	78.0	203.0	264.0
Y	37.5	11.3	33.2	55.7	52.1	20.1	12.9	73.0	35.0	8.4	14.0
Th	10.6	0.9	6.4	44.9	4.5	-	-	-	-	-	-
U	nd	0.2	2.5	10.7	3.1	-	-	-	-	-	-
ppm											
La	31.0	5.0	32.0	103.0	46.0	46.0	-	82.0	87.0	46.0	2.0
Ce	76.0	13.0	69.0	182.0	87.0	92.0	2.0	110.0	130.0	74.0	20.0
Nd	32.0	6.0	33.0	67.0	46.0	36.0	-	57.0	70.0	24.0	5.0
Cu	3	nd	67	-0.5	529	-	-	-	-	-	-
Zn	21	23	129	30.2	96	-	-	-	-	-	-
Co	55.5	71.5	77.6	10.7	61.8	-	-	-	-	-	-

Figure A8.2. Sketch of euhedral, medium grained hornblende defining a mineral lineation within the gneissic layering in hornblendites (962-177). Width of view 2mm.

Figure A8.3. Photo-micrograph of optically zoned, untwinned plagioclase grains in hornblendite (890-10). Width of view 2mm

Hbl
Pl

Ilm
Hbl
Pl +
Qtz

Figure A8.4. Sketch of coarse grained hornblende cross-cutting a fine epidote-opaque foliatio (parallel to the long edge of the sketch, 962-015a). Width of view 2mm.

Figure A8.5. Sketch of hornblende replacing corroded clinopyroxene (962-202). Width of view 2mm

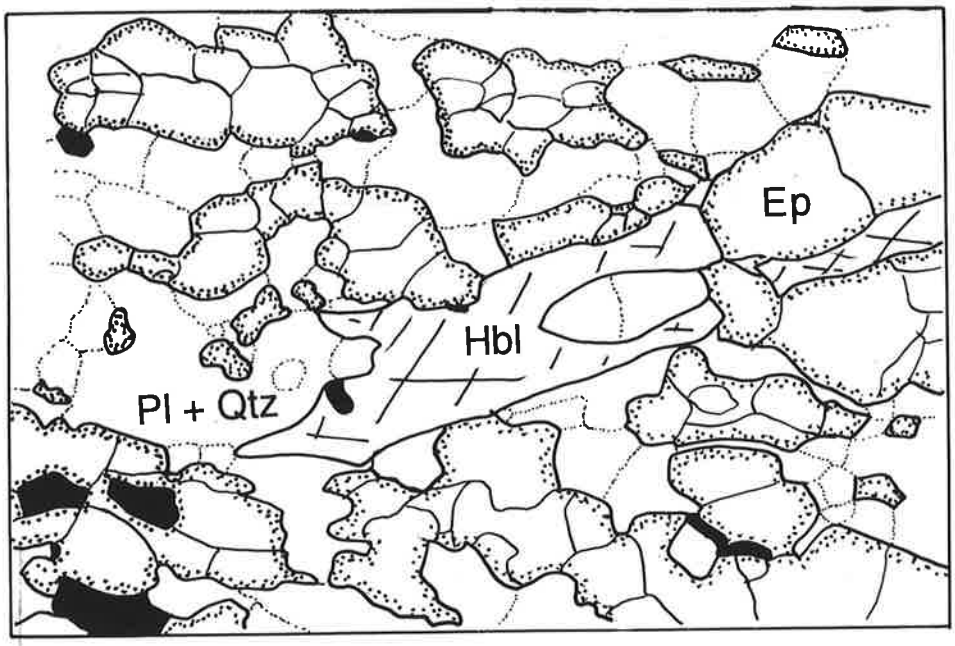
Ep
Hbl
Pl + Qtz

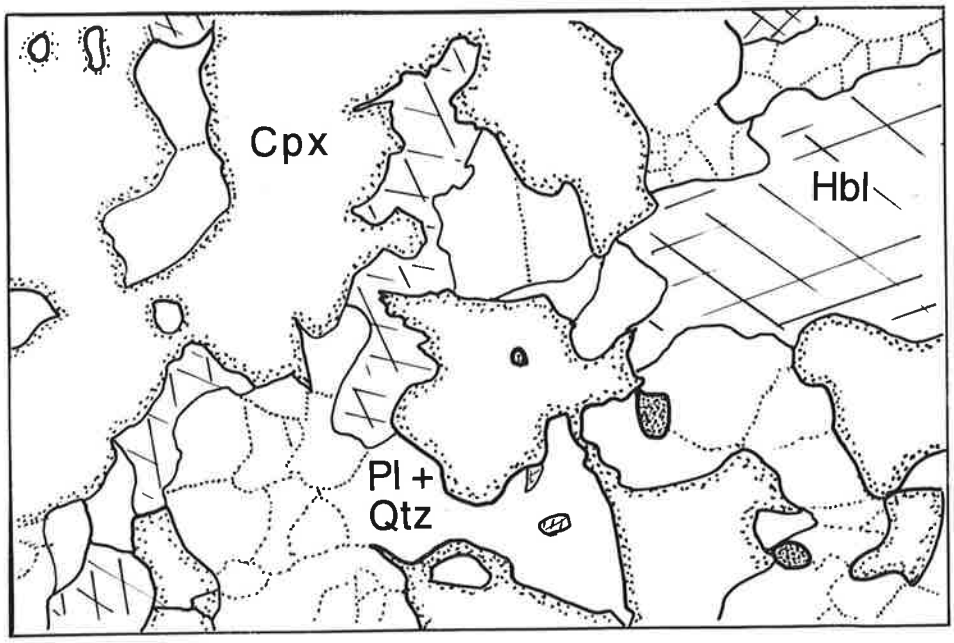
Cpx
Hbl
Pl +
Qtz

and often shows optical zoning. Allanite (cesium-bearing epidote) occurs as an accessory phase and occurs at the centre of radiating fractures through the surrounding phases. In several samples allanite is rimmed by colourless clinozoisite.

Clinopyroxene occurs as relict, corroded, optically continuous grains. It is colourless to very slightly green and is typically partly to entirely mantled or otherwise intergrown with strongly coloured hornblende in a hornblende–plagioclase ± epidote mosaic (Fig. A8.5, Fig A8.6). The relict pyroxene is typically rather ragged in appearance and is heavily altered along fractures and cleavage planes.

Biotite forms dull-brown flakes disseminated through some samples and more greenish biotite occurs with colourless to pale green chlorite around the margins and along fractures in hornblende. Chlorite also pseudomorphs earlier biotite. Some samples contain more than one (often exsolved) oxide phase; rutile, magnetite, ilmenite or exsolved ilmenite and titaniferous magnetite–ulvöspinel-solid solution (Fig. A8.7). Titanite forms rims around rutile or ilmenite in some samples and apatite and zircon occur in trace amounts throughout the samples.

Mineral chemistry

Hornblende (magnesio-hornblende, tschermakitic hornblende or ferro-tschermakitic hornblende, Leake, 1978, Table A8.2) in typical hornblendites is aluminium-poor (Al^{vi} 0.70-1.13) with intermediate to high iron content (X_{Fe} 0.34 to 0.58) and intermediate sodium content (0.21-0.52 atoms of Na per formula unit, pfu) in comparison to that in more complex assemblages. The M_4 site is almost entirely filled with Ca (1.50-1.95 atoms per formula unit (pfu) of 22O+2(OH)). Plagioclase compositions in hornblendites are widely variable between samples (An_{32-65}) but the variation is generally less than 10% within each sample. In magnesio-hornblendites and the more silicious of the tschermakitic hornblendites (which also have lower sodium contents) the plagioclase is typically labradorite, while those in ferro-tschermakitic hornblendites are more calcic andesine (Table A8.2).

Epidote group minerals usually have a solid-solution composition between epidote and clinozoisite (Ps_{12-27}, see Appendix A1 for abbreviations) which is fairly consistent within each sample (± 10%) (Table A8.2). Optically, epidote group minerals often exhibit a pale but obvious green pleochroism, with strong interference colours, implying a generally high proportion of the Fe^{3+}-bearing endmember and this is confirmed by the concentration of analyses in the range Ps_{16-27}. A number of the grains show zonation from intermediate cores (Ps_{16}) to more epidote rich rims (Ps_{19}).

Clinopyroxenes in amphibolites have a wide range of compositions with X_{Fe} 0.21-0.38 (< 5% variation within each sample) which have a positive correlation with $X_{Fe,Hbl}$. The calcium content of clinopyroxenes is near ideal, with 0.92-0.95 atoms of calcium pfu (calculated to 6O).

Hornblendites plot in the NCAFm tetrahedron at relatively Na-poor, Ca-rich compositions and are generally less enriched in aluminium, iron and magnesium than other amphibolites. (Fig. A8.8).

Figure A8.6. Photo-micrograph of hornblende intergrown with corroded clinopyroxene (HR91-24). Width of view 2mm.

Figure A8.7. Photo-micrograph of exsolution of ilmenite from titaniferous magnetite-ilmenite solid solution (950-105). Width of view 2mm.

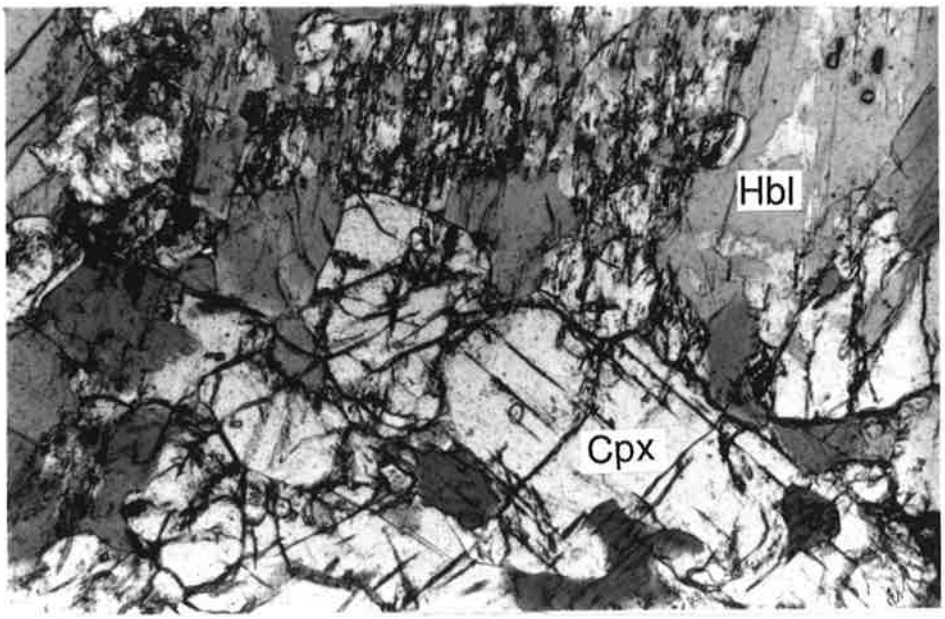
Hbl
Cpx

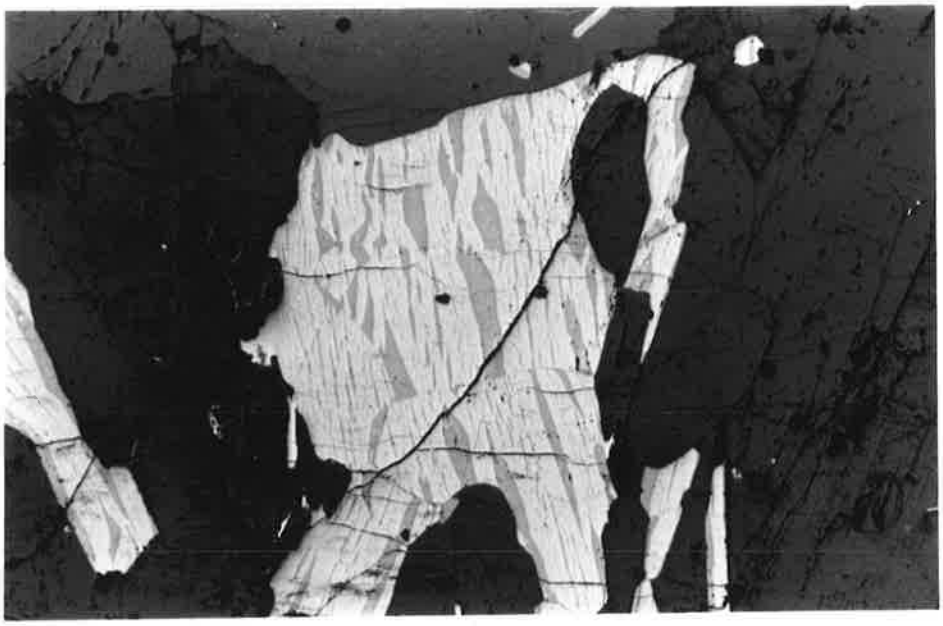

Table A8.2. Selected probe data from hornblendites, recalculated in accordance with Appendix A1

890-10						
	Pl	Hbl	Ep	Pl	Chl	Hbl
SiO2	54.66	41.51	37.76	58.41	24.01	42.01
TiO2	0.00	0.54	0.00	0.00	0.00	0.58
Al2O3	30.64	13.15	22.75	27.29	20.34	13.19
FeO	0.00	19.60	12.61	0.24	26.39	19.25
MnO	0.00	0.22	0.00	0.00	0.00	0.26
MgO	0.00	7.91	0.20	0.00	14.33	8.14
CaO	12.52	11.57	23.53	9.20	0.28	11.80
Na2O	4.70	1.31	0.22	6.47	0.18	1.54
K2O	0.08	0.45	0.07	0.10	0.00	0.58
Cr2O3	n.a.	n.a.	n.a.	n.a.	n.a.	n.a.
ZnO	n.a.	n.a.	n.a.	n.a.	n.a.	n.a.
Total	102.6	96.3	97.1	101.7	85.5	97.4
Si	2.409	6.390	3.104	2.575	2.628	6.391
Ti	0.000	0.063	0.000	0.000	0.000	0.066
Al	1.592	2.387	2.205	1.418	2.625	2.366
Fe2+	0.000	2.523	0.867	0.009	2.416	2.449
Mn	0.000	0.029	0.000	0.000	0.000	0.034
Mg	0.000	1.815	0.025	0.000	2.338	1.846
Ca	0.591	1.908	2.073	0.435	0.033	1.924
Na	0.402	0.391	0.035	0.553	0.038	0.454
K	0.004	0.088	0.007	0.006	0.000	0.113
Cr	-	-	-	-	-	-
Zn	-	-	-	-	-	-
Total	4.998	15.594	8.315	4.995	10.078	15.643
An	0.595			0.440		
XFe		0.582			0.508	0.570
Aliv		1.610			1.372	1.609
Alvi		0.777			1.253	0.757
Xalm						
Xpy						
Xgrs						
Xsps						
ps			26.510			

890-18					
	Hbl	Hbl	Pl	Ilm	Pl
SiO2	41.46	43.15	59.93	0.00	60.42
TiO2	0.56	0.49	0.00	48.96	0.00
Al2O3	15.57	14.68	26.29	0.16	25.80
FeO	16.15	16.54	0.00	47.94	0.00
MnO	0.14	0.18	0.00	0.43	0.00
MgO	9.33	10.46	0.00	0.66	0.00
CaO	10.23	9.36	7.66	0.00	7.29
Na2O	1.77	1.68	7.28	0.21	7.66
K2O	0.24	0.25	0.07	0.00	0.07
Cr2O3	n.a.	n.a.	n.a.	n.a.	n.a.
ZnO	n.a.	n.a.	n.a.	n.a.	n.a.
Total	95.5	96.8	101.2	98.4	101.2
Si	6.288	6.428	2.639	0.000	2.660
Ti	0.064	0.055	0.000	0.957	0.000
Al	2.784	2.578	1.365	0.005	1.339
Fe2+	2.048	2.061	0.000	1.043	0.000
Mn	0.018	0.023	0.000	0.009	0.000
Mg	2.109	2.322	0.000	0.026	0.000
Ca	1.662	1.494	0.361	0.000	0.344
Na	0.520	0.485	0.622	0.000	0.654
K	0.046	0.048	0.004	0.000	0.004
Cr	-	-	-	-	-
Zn	-	-	-	-	-
Total	15.540	15.494	4.991	2.040	5.000
An			0.368		0.345
XFe	0.493	0.470			
Aliv	1.712	1.572			
Alvi	1.072	1.007			
Xalm					
Xpy					
Xgrs					
Xsps					
ps					

890-18					
	Pl	Ep	Hbl	prehnite	Pl
SiO2	52.89	37.59	42.63	43.00	55.34
TiO2	0.00	0.00	0.61	0.00	0.00
Al2O3	30.60	24.52	13.46	22.15	29.60
FeO	0.00	10.07	18.35	3.71	0.00
MnO	0.00	0.00	0.14	0.00	0.00
MgO	0.12	0.14	8.24	1.11	0.15
CaO	12.84	22.89	11.67	25.41	11.55
Na2O	4.43	0.26	1.58	0.18	5.20
K2O	0.21	0.00	0.28	0.00	0.07
Cr2O3	n.a.	n.a.	n.a.	n.a.	n.a.
ZnO	n.a.	n.a.	n.a.	n.a.	n.a.
Total	101.1	95.5	97.0	95.6	101.9
Si	2.374	3.092	6.453	3.006	2.450
Ti	0.000	0.000	0.069	0.000	0.000
Al	1.619	2.378	2.402	1.826	1.545
Fe2+	0.000	0.693	2.323	0.217	0.000
Mn	0.000	0.000	0.018	0.000	0.000
Mg	0.008	0.017	1.859	0.116	0.010
Ca	0.617	2.018	1.893	1.904	0.548
Na	0.385	0.041	0.464	0.024	0.446
K	0.012	0.000	0.054	0.000	0.004
Cr	-	-	-	-	-
Zn	-	-	-	-	-
Total	5.016	8.239	15.535	7.093	5.003
An	0.616				0.551
XFe			0.555		
Aliv			1.547		
Alvi			0.855		
Xalm					
Xpy					
Xgrs					
Xsps					
ps		20.732			

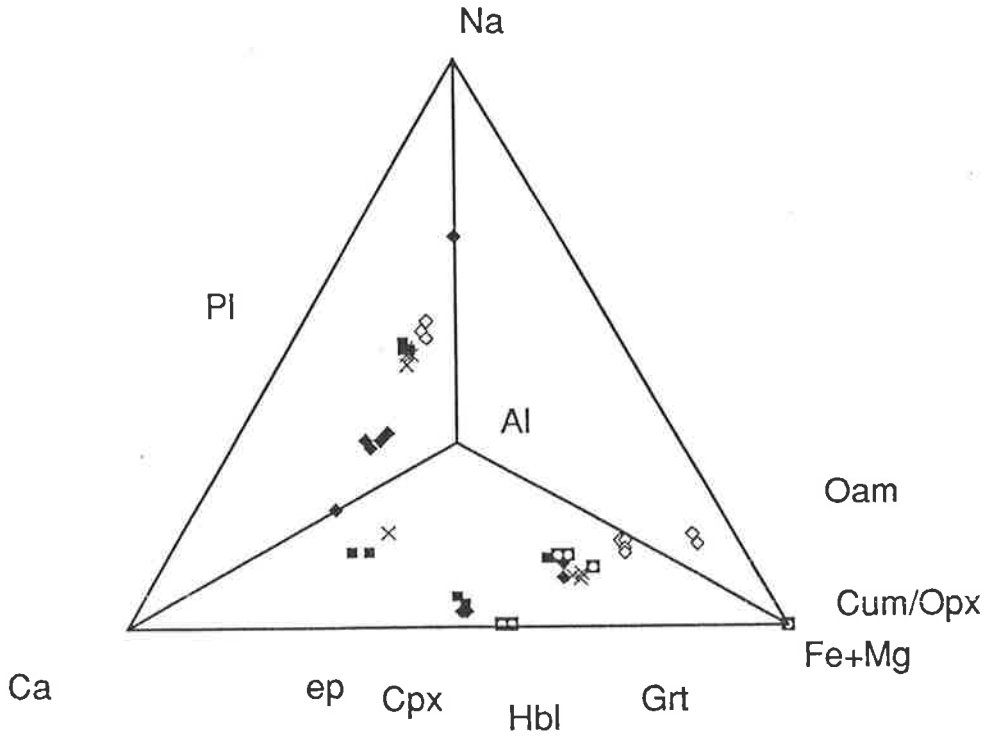

Figure 8.8. Quaternary NCAFm diagram illustrating the compositional space of amphibolites projected from quartz and aqueous vapour; N = $NaO_{1/2}$, C = CaO, A = $AlO_{3/2}$, Fm = FeO+ MgO. Solid squares - sample 852-88 (from Stewart,1985); cross - sample 853-145; open diamonds - 890-13; solid diamonds - 853-180; solid square with circle - HR91-5.

Interpretation

The granoblastic, foliated texture and consistent chemistry of the phases in amphibolites in the Entia gneiss complex suggest that the majority of rocks attained textural equilibration during or after foliation-forming deformation at amphibolite grade. In only a very few samples is there any preservation of pre-existing mineral assemblages in the form of strongly corroded pyroxene which is rimmed by hornblende. The close association of clinopyroxene and hornblende both texturally (as pseudomorphs and intergrowths of hornblende with optically self-continuous clinopyroxene) and chemically implies that clinopyroxene is being replaced by hornblende. The apparently random orientation of the clinopyroxene grains suggests that clinopyroxene may be a relic of the primary igneous assemblage and the presence of hornblende in the foliated matrix implies that the breakdown of pyroxene to form hornblende occurred during foliation development. Low grade alteration is relatively unimportant in most samples.

A8.4.2 Orthoamphibole–hornblende amphibolites

Many of the Harts Range amphibolites contain coarse grained (2-8 mm) orthoamphibole which typically forms planar rosettes of elongate crystals which are coarser than co-existing hornblende. Orthoamphibole is observed both parallel or sub-parallel and cross-cutting the hornblende foliation. The samples dealt with in this section are simple, high variance samples, whereas more complex, lower variance orthoamphibolites containing garnet, staurolite, kyanite or cordierite are described in Section A8.5

Textural features

Pleochroic light grey-brown to clove-brown orthoamphibole occurs in a polygonal mosaic with hornblende, plagioclase and quartz. The coarse, euhedral orthoamphibole grains may be either parallel to the foliation or randomly oriented, cross cutting the hornblende-defined fabric (where developed) and also the hornblende grains themselves (Fig. A8.9). Hornblende often forms inclusions within orthoamphibole grains, while the reverse relationship is never observed. Plagioclase and quartz grains are euhedral to subhedral and show optical zoning and undulose extinction respectively.

Mineral chemistry

Orthoamphibole (gedrite according to the classifications of Leake, 1978) is typically unzoned and unexsolved and straddles the gedrite–anthophyllite miscibility gap with respect to Al^{iv}, Al^{vi} and Na contents (Spear, 1980). Gedrite typically exhibits a large amount of tschermakite and edenite substitution relative to endmember anthophyllite (1.31-1.38 and 0.18-0.34 moles of Al^{vi} and Na pfu, respectively, Table A8.3) however it has a lower Al-content

Figure A8.9. Sketch of gedrite cross cutting hornblende foliation and hornblende grains (890-014). Width of view 2mm.

Figure A8.11. Sketch of garnet porphyroblast containing straight inclusion trails (950-105). Width of view 2mm.

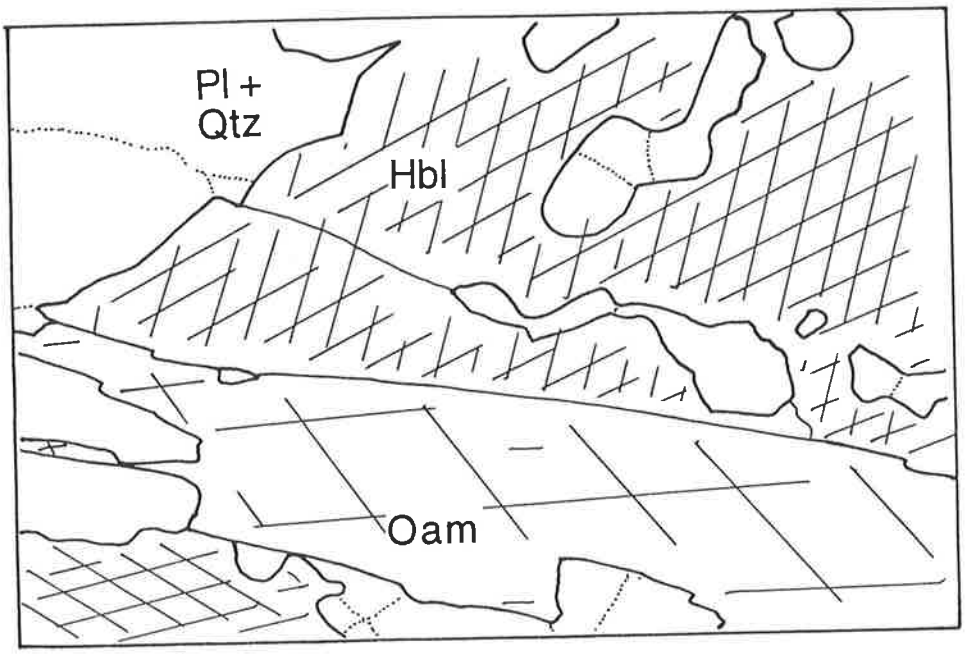
Pl +
Qtz
Hbl
Oam

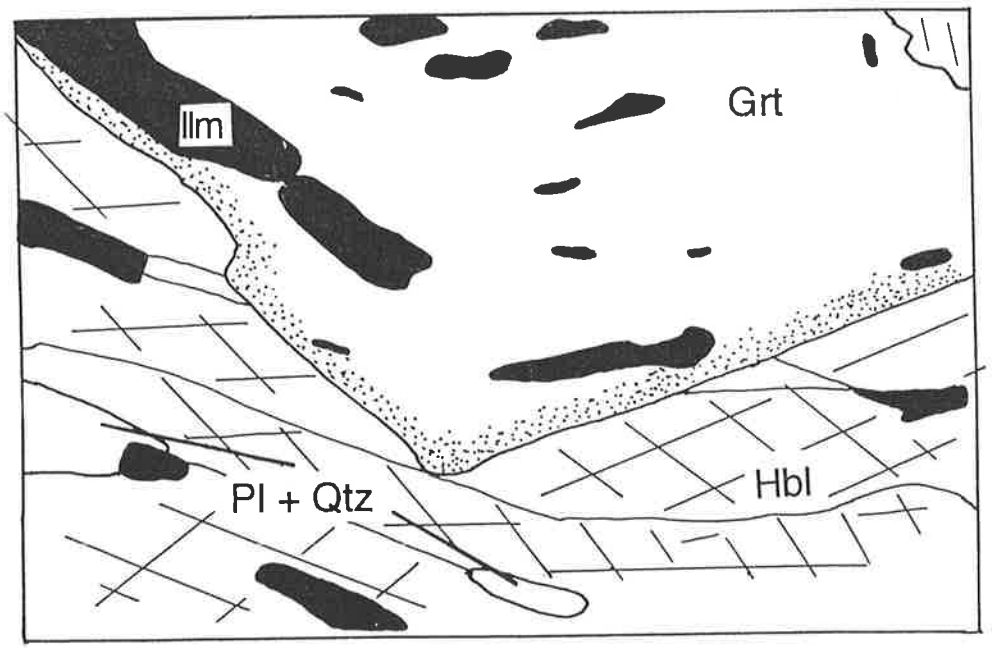
Ilm
Grt
Pl + Qtz
Hbl

Table A8.3. Selected probe data from orthoamphibolite (950-000(1)) and garnet-amphibolite (HR91-5) recalculated according to Appendix A1

950-000(1)							
	Hbl	Pl	Oam	Oam	Pl	Hbl	Pl
SiO2	42.81	56.28	43.07	42.94	55.64	42.37	58.46
TiO2	0.44	0.00	0.15	0.11	0.17	0.45	0.17
Al2O3	16.68	28.13	16.90	16.93	27.79	17.37	27.00
FeO	14.23	0.17	17.39	17.43	0.14	14.68	0.00
MnO	0.14	0.26	0.31	0.12	0.25	0.19	0.00
MgO	10.82	0.00	15.72	15.36	0.00	11.40	0.00
CaO	9.98	9.48	0.79	0.90	9.77	10.04	8.36
Na2O	0.93	6.45	0.62	1.17	5.83	1.35	6.88
K2O	0.15	0.00	0.10	0.00	0.01	0.22	0.09
Cr2O3	n.a.	n.a.	n.a.	n.a.	n.a.	n.a.	n.a.
ZnO	n.a.	n.a.	n.a.	n.a.	n.a.	n.a.	n.a.
Total	96.18	100.8	95.0	94.9	99.6	98.07	101.0
Si	6.327	2.514	6.350	6.345	2.513	6.177	2.589
Ti	0.049	0.000	0.017	0.012	0.006	0.049	0.006
Al	2.906	1.482	2.938	2.950	1.480	2.985	1.410
Fe2+	1.759	0.006	2.145	2.154	0.005	1.790	0.000
Mn	0.018	0.010	0.038	0.015	0.010	0.023	0.000
Mg	2.383	0.000	3.453	3.382	0.000	2.477	0.000
Ca	1.581	0.454	0.125	0.142	0.473	1.568	0.397
Na	0.267	0.559	0.178	0.335	0.511	0.382	0.591
K	0.028	0.000	0.019	0.000	0.001	0.041	0.005
Cr	-	-	-	-	-	-	-
Zn	-	-	-	-	-	-	-
Total	15.318	5.024	15.262	15.335	4.997	15.492	4.998
An		0.448			0.481		0.402
XFe	0.425		0.383	0.389		0.419	
Aliv	1.673		1.650	1.655		1.823	
Alvi	1.234		1.288	1.295		1.162	
Xalm							
Xpy							
Xgrs							
Xsps							
ps							

HR91-5						
	Cum	Opx	Cpx	Hbl	Grt	Hbl
SiO2	51.13	49.16	50.67	43.57	38.14	39.74
TiO2	0.00	0.00	0.06	0.00	0.00	0.12
Al2O3	0.49	0.34	0.87	8.82	22.72	12.84
FeO	35.72	41.96	20.67	26.41	30.80	26.98
MnO	0.36	0.63	0.53	0.35	1.88	0.41
MgO	9.21	9.19	7.35	6.08	1.17	3.89
CaO	1.14	1.03	20.40	10.37	7.49	10.69
Na2O	0.00	0.00	0.08	1.14	0.00	1.50
K2O	0.09	0.029	0.08	1.24	0.00	1.97
Cr2O3	n.a.	n.a.	n.a.	n.a.	n.a.	n.a.
ZnO	n.a.	n.a.	n.a.	n.a.	n.a.	n.a.
Total	98.1	102.3	100.7	98.0	102.2	98.1
Si	7.930	1.975	1.979	6.809	2.980	6.293
Ti	0.000	0.000	0.002	0.000	0.000	0.014
Al	0.089	0.016	0.040	1.625	2.093	2.397
Fe2+	4.633	1.410	0.675	3.451	2.012	3.573
Mn	0.047	0.021	0.018	0.046	0.124	0.055
Mg	2.130	0.550	0.428	1.415	0.137	0.919
Ca	0.189	0.044	0.854	1.737	0.627	1.813
Na	0.000	0.000	0.006	0.345	0.000	0.460
K	0.018	0.001	0.004	0.246	0.000	0.399
Cr	-	-	-	-	-	-
Zn	-	-	-	-	-	-
Total	15.035	4.018	4.004	15.675	7.973	15.923
An						
XFe	0.685	0.719	0.6122	0.709	0.936	0.795
Aliv	0.070			1.191		1.707
Alvi	0.018			0.434		0.690
Xalm					0.694	
Xpy					0.047	
Xgrs					0.216	
Xsps					0.043	
ps						

when co-existing with hornblende alone than when coexisting with other, more aluminous, phases (see later sections). Hornblende co-existing with gedrite (and no other ferromagnesian phases) is typically less aluminous and more sodic than gedrite (with 1.23-1.35 and 0.25-0.43 moles of Al^{vi} and Na, respectively) and has a low Ca-content (1.51-1.62 pfu, Table A8.3). The Fe-content of orthoamphibole ($X_{Fe,Oam}$ 0.38-0.39) varies consistently with that of co-existing hornblende ($X_{Fe,Hbl}$ 0.41-0.43, Fig. A8.10) and in most samples there are examples of orthoamphibole being slightly more Fe-rich than co-exisiting hornblende (in correspondence with the Fe-Mg partitioning reported by James et al., 1978; Spear, 1982; Schumacher & Robinson, 1987). The opposite trend (i.e. $X_{Fe,Hbl} > X_{Fe,Oam}$) may also be observed. This may result from a higher abundance of Fe^{3+} in hornblende than gedrite, however, in view of the large range of values for Fe^{3+} obtained from different methods of estimation (e.g. Robinson et al., 1982), I prefer to present the raw data only. Gedrite has an intermediate iron content when co-existing with hornblende, in comparison to garnet, staurolite or cordierite amphibolites. Plagioclase coexisting with gedrite is generally labradorite (An_{40-48}, Table A8.3) confirming the relatively Ca-poorer nature of orthoamphibole-bearing samples determined from whole rock analyses (Table A8.1, Fig. 4.8).

Interpretation

The absence of orthoamphibole inside porphyroblasts of other phases and its cross-cutting relationship with hornblende suggest that it became stable at some time during or after the hornblende foliation forming event, relatively late in the petrogenetic sequence. However, the dominance of polygonal grains and intergrowths and the lack of any replacement textures along with the consistency of composition of hornblende and orthoamphibole (Fig. A8.10) suggest that these phases developed in equilibrium and that hornblende continued to be stable after orthoamphibole began to form.

A8.5 Low variance amphibolite assemblages

Despite the dominance of high variance, relatively simple amphibolites in the Harts Range area, the lower variance assemblages contain unusual phases and reaction relationships which may allow a deeper understanding of the metamorphic evolution of the area. These lower variance, often more aluminous assemblages are discussed here.

A8.5.1 Fe-rich, garnet-bearing amphibolites

Garnet-bearing amphibolites form semi-continuous bands over hundreds of metres in which garnet is concentrated into decimetre-scale bands parallel to the gneissic layering. Garnet grains typically range in size from 0.25-60 mm and may either cut or be wrapped by the coarse grained hornblende foliation. Very coarse garnets (up to metres in diameter!) are also

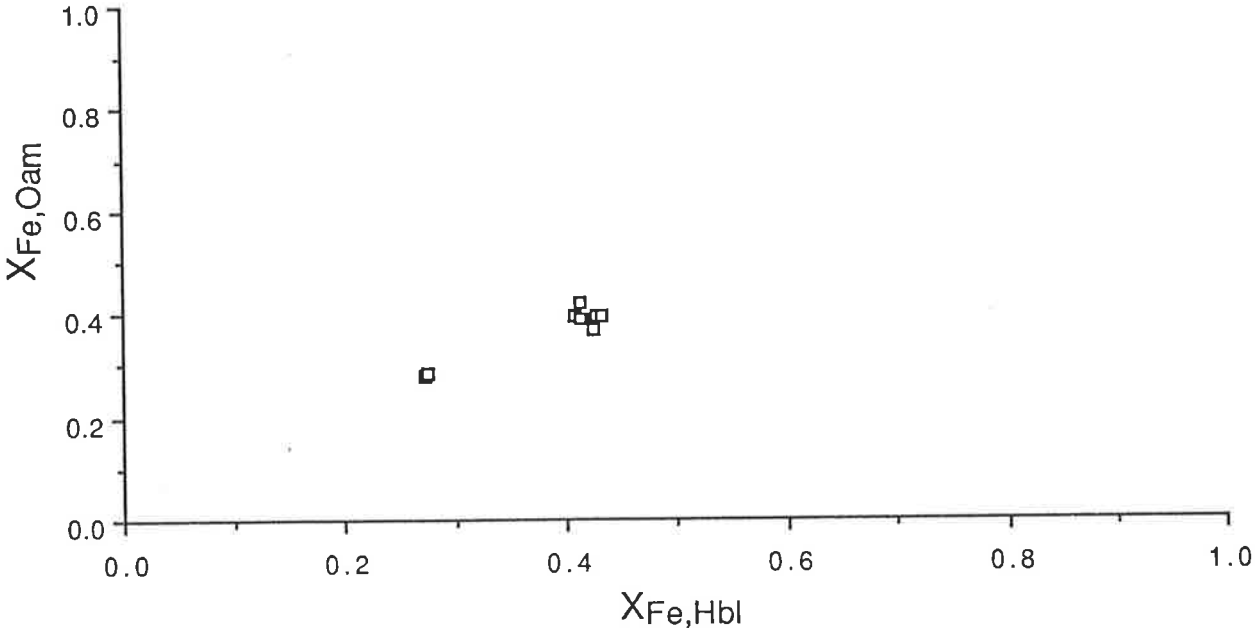

Figure A8.10. Plot of $X_{Fe,Hbl}$ vs $X_{Fe,Oam}$, for the Entia gneiss complex amphibolites.

observed. The discussion below deals first with broad aspects of the textural features and mineral chemistry of garnet amphibolites and later with specific low variance assemblages.

Textural features

Garnet forms porphyroblasts which range from fine to medium grained (from 0.25 mm in diameter) through coarse to very coarse (commonly up to 60 mm) euhedral grains or medium to coarse anhedral grains. Anhedral inclusions of plagioclase, quartz, hornblende (but never gedrite), ilmenite, rutile, biotite or staurolite may be contained in the cores of the euhedral garnets but the inclusions are generally too coarse and scarce to exhibit relict inclusion trails. A few samples contain straight, curved, crenulated or S-shaped inclusion trails usually of matrix material (Fig. A8.11, Fig A8.12). Very fine acicular inclusions of rutile often occur at the cores of garnet grains, aligned with the crystallographic axes of the garnet. These coarsen to more equant inclusions and are joined by ilmenite toward the rim. Very near the rims of garnet porphyroblasts, ilmenite is typically the only titaniferous phase. Garnet porphyroblasts with straight inclusion trails are generally wrapped by the hornblende or hornblende–gedrite foliation where present.

Garnet porphyroblasts may be associated with a partial rim of feldspar which separates the grain from the hornblende–plagioclase–quartz ± gedrite matrix. In a number of instances a symplectitic intergrowth of plagioclase feldspar and hornblende forms partial rims around garnet porphyroblasts (Fig. A8.13). Anhedral garnets are typically dominated by a number of large anhedral inclusions which may extend into the surrounding matrix (Fig. A8.14). More typically, medium to coarse hornblende ± orthoamphibole define a foliation which wraps around the euhedral garnets with sub-parallel inclusion trails. Optically zoned subhedral to euhedral plagioclase grains have curved to lobate grain boundaries and form part of the hornblende–quartz ± gedrite ± epidote even-grained matrix. Plagioclase exhibits little twinning and no deformation features, and is variably sericitised (depending upon the extent of fracturing and the composition of the plagioclase) along cleavage planes. Quartz shows undulose extinction, and occurs as sub-rounded grains within the matrix. The main accessory phases in garnet amphibolites are exsolved titaniferous magnetite-ulvöspinel and ilmenite, zircon and apatite. Some samples also contain rutile and allanite.

Staurolite occurs in three different relationships in garnet amphibolites: (1) as parallel inclusions in garnet porphyroblasts but absent from the surrounding foliated hornblende–plagioclase ± gedrite matrix (e.g. 853-16, 950-077, Fig. A8.12, Fig 4.15), (2) as inclusions of staurolite inside garnet and near its margins, extending into a hornblende-poor part of the matrix (e.g. 950-105, Fig. A8.16), (3) as part of the polygonal matrix (typically surrounded by plagioclase) of a porphyroblastic garnet amphibolite (i.e. HR91-8, Fig. A8.17).

The very Fe-rich sample, HR91-5, contains the assemblage clinopyroxene–orthopyroxene–cummingtonite–hornblende in a garnet–hornblende–plagioclase matrix, and is discussed in detail below.

Figure A8.12. Sketch of garnet porphyroblast containing straight inclusion trails (950-077). Width of view 2mm.

Figure A8.13. Photo-micrograph of garnet porphyroblast with hornblende-plagioclase symplectic partial rim (962-147a). Width of view 2mm.

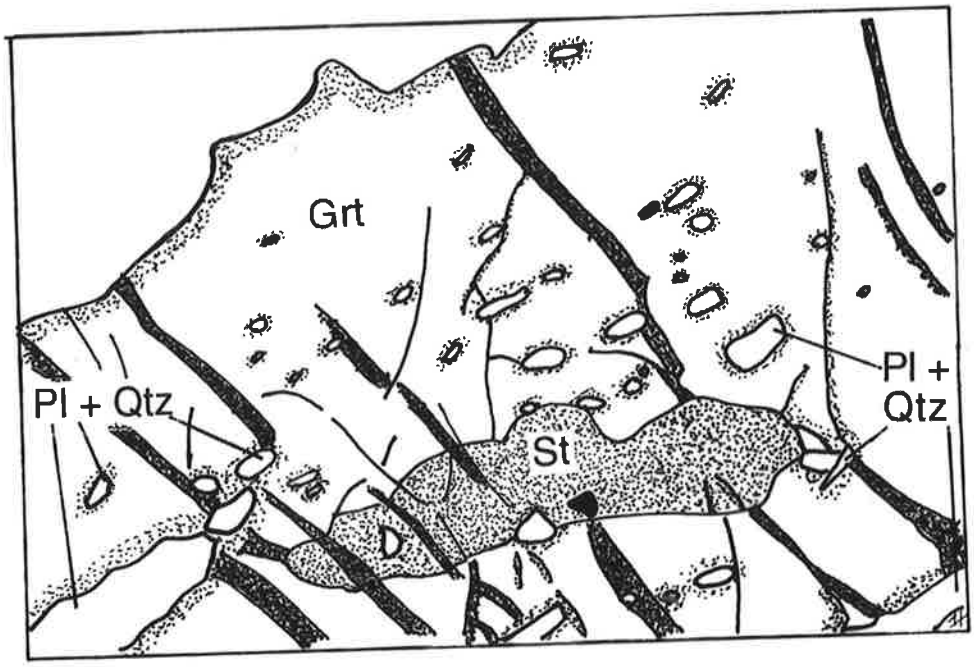
Grt
Pl + Qtz
St
Pl +
Qtz

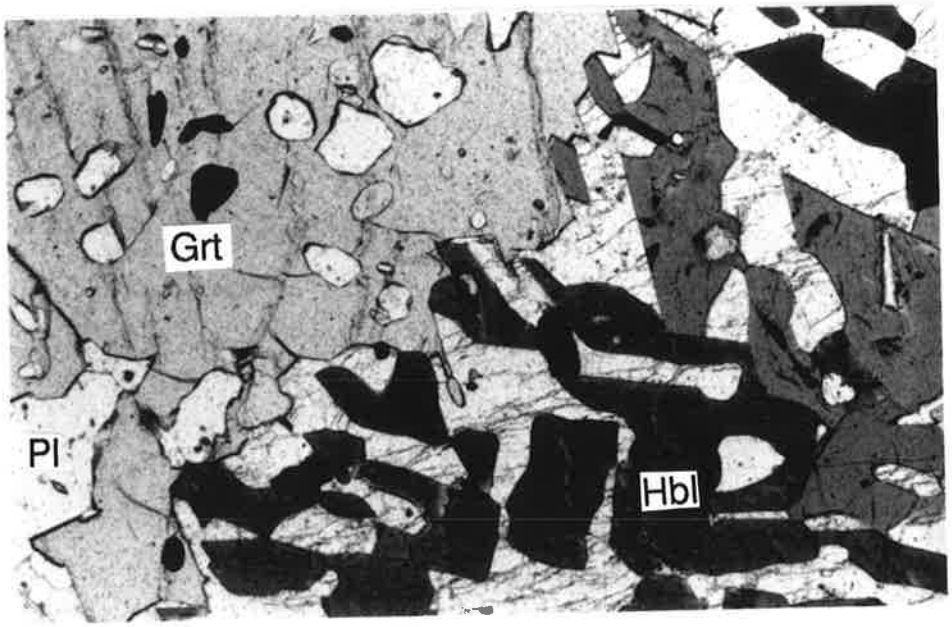
Grt
Pl
Hbl

Figure A8.14. Sketch of anhedral garnet porphyroblast with coarse inclusions (962-214). Width of view 2mm.

Figure A8.15. Sketch of garnet porphyroblast containing staurolite inclusions (950-077). Width of view 2mm.

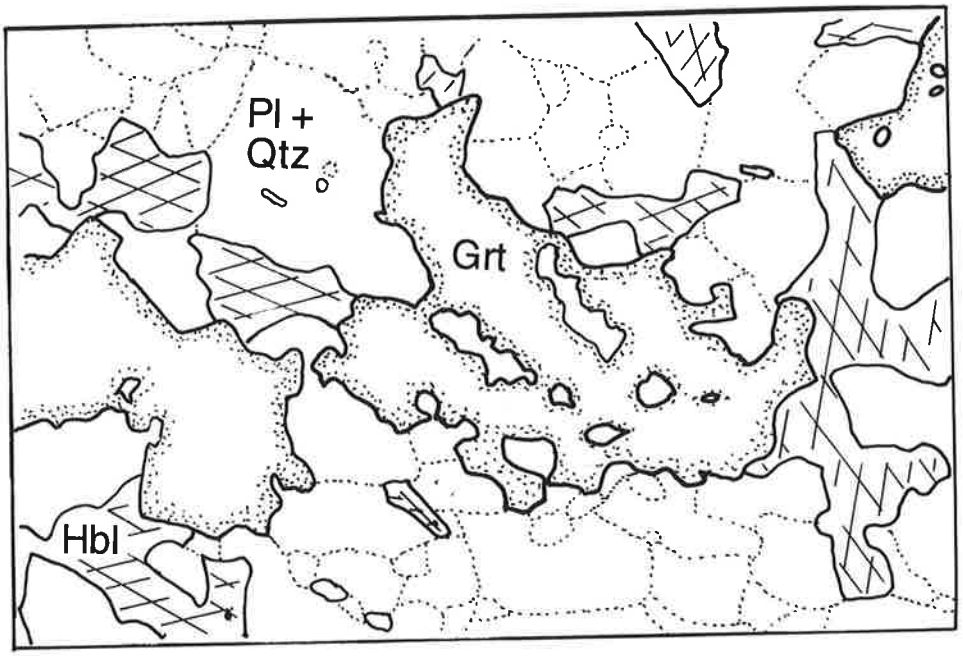
Pl +
Qtz
Grt
Hbl

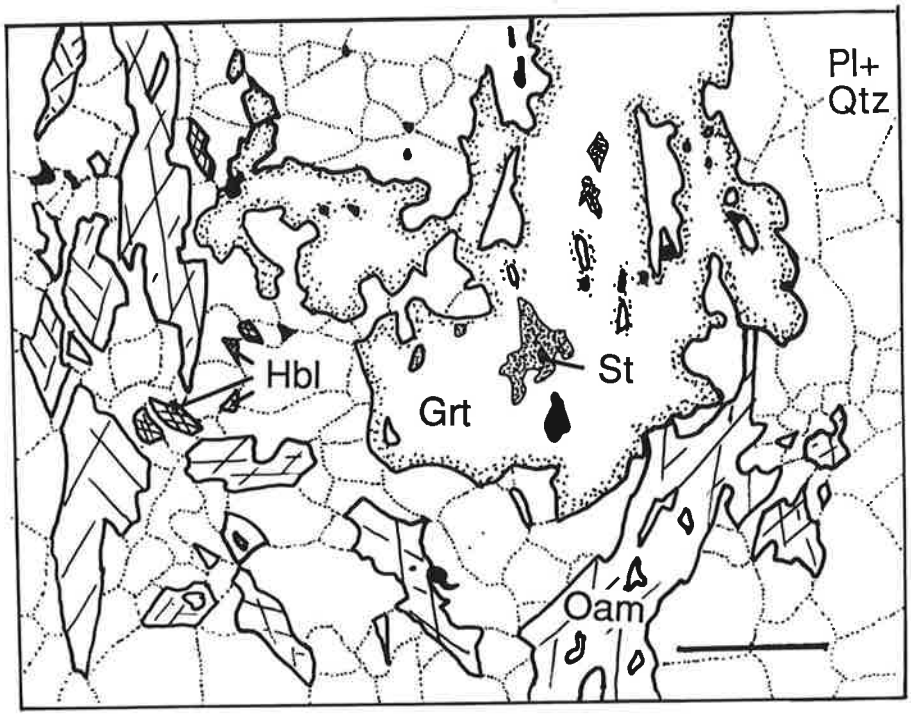
Pl+
Qtz
Hbl
Grt
St
Oam

Figure A8.16. Sketch of staurolite partly included in a garnet porphyroblast (950-105). Width of view 2mm.

Figure A8.17. Sketch of staurolite in the matrix of a garnet-amphibolite (950-105). Width of view 2mm.

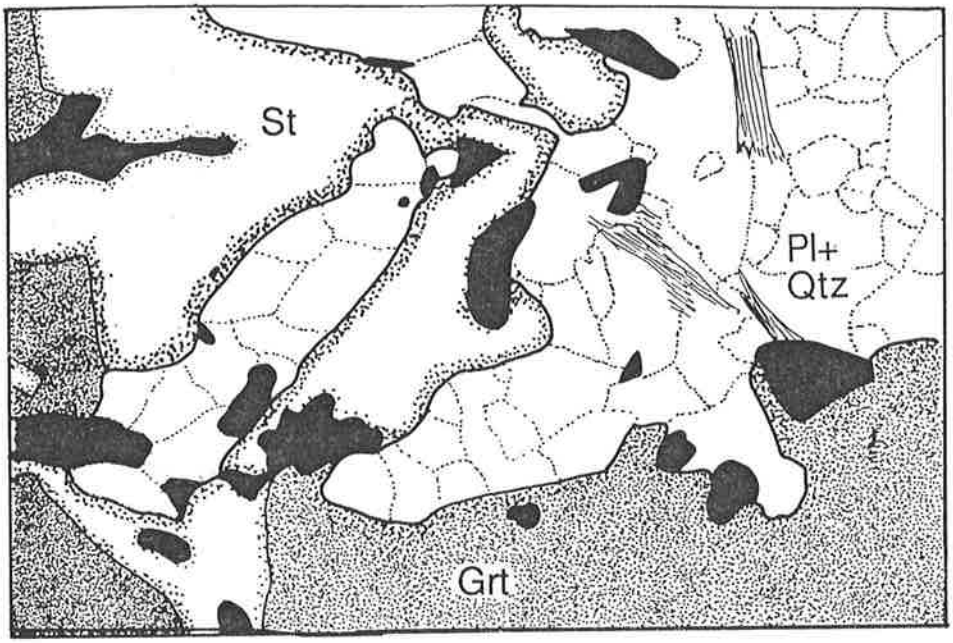
St
Pl+
Qtz
Grt

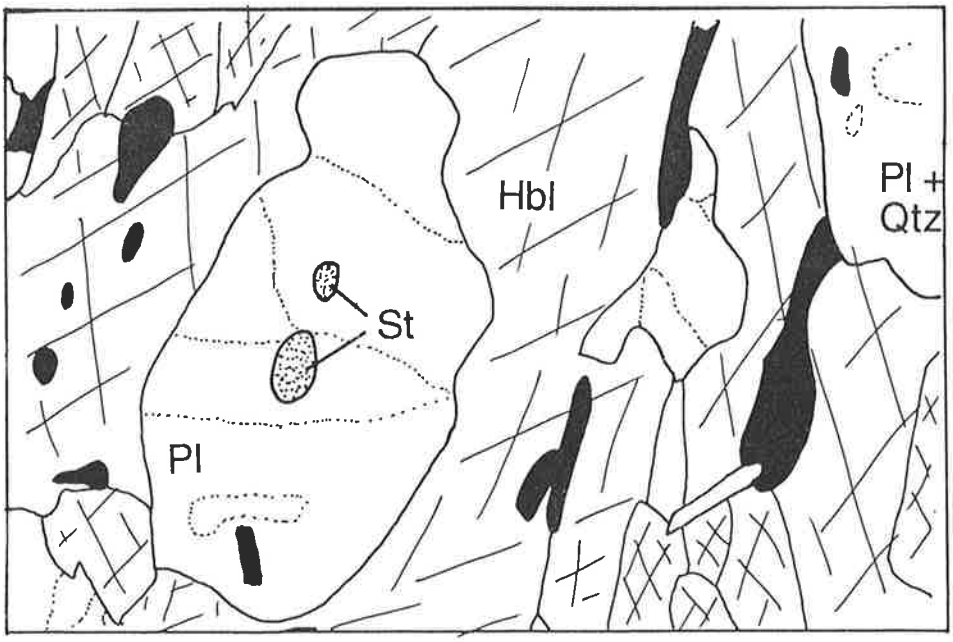
Hbl
Pl +
Qtz
St
Pl

Mineral chemistry

Garnet exhibits little substitution for Al_2O_3 or for SiO_2 (cf. Meagher, 1982) and has a chemistry dominated by almandine-pyrope-grossular solid solution (X_{alm} 0.48-0.71, X_{prp} 0.04-0.36, X_{grs} 0.07-0.37) with only small amounts of the spessartine molecule (X_{sps} 0.01-0.16) (Table A8.4). The most calcium-rich garnets are those which are occur in simple amphibolites (X_{grs} 0.09-0.37) and these are also almandine-rich (X_{alm} 0.48-0.64) and relatively pyrope poor (X_{prp} 0.27-0.26). Garnet is Fe-rich varying between X_{Fe} 0.63 and 0.95 (low with gedrite, high with pyroxene and staurolite), and has an X_{Fe} which is exceeded only by that of staurolite. $X_{Fe,Grt}$ varies sympathetically with $X_{Fe,Bt}$, $X_{Fe,St}$, $X_{Fe,Px}$ and $X_{Fe,Hbl}$ (Fig. A8.18) and analyses across a number of separate garnet grains show that garnets are typically unzoned.

Hornblende (tschermakite, ferro-tschermakite and ferro-tschermakitic hornblende) in garnet amphibolites is aluminous with an intermediate to high sodium content (1.06-1.53, 0.20-0.79 moles Al^{vi} and Na pfu). Hornblende coexisting with garnet is Fe- ($X_{Fe,Hbl}$ 0.38-0.79) and Ca-rich (1.39-1.93 Ca pfu) and gedrite (Leake, 1978) in garnet amphibolites is also Fe-rich ($X_{Fe,Oam}$ 0.40-0.44, Table A8.4).

Plagioclase in garnet amphibolites spans the full compositional range, however analyses from a single sample generally fall into one or two clusterings with less than 15% variation in the proportion of the anorthite endmember. The grossular content of garnet shows a loose positive correlation with the proportion of the anorthite endmember in plagioclase (Fig. A8.19).

The textural and chemical relationships between staurolite and garnet are explored in detail below, however in general staurolite is more Fe-rich than co-existing garnet and has X_{Fe} in the range (0.52-0.83 with a low zinc content of 0.12-0.77 wt % ≡ 0.02-0.15 ZnO pfu (44O+4(OH)).

Interpretation

Although garnet is involved in several different low variance assemblages, each of which will be discussed in detail below, there are some interpretations which apply to the majority of the garnet amphibolites from the area. Garnet may contain a variety of inclusion trail patterns however these are generally more complex, or equally complex in comparison to the matrix texture (e.g. crenulated or curved inclusion trails in garnet in a foliated matrix). This suggests that the garnet porphyroblasts grew relatively early in the deformation history of the rocks. Thus phases included in these porphyroblasts are interpreted to have developed even earlier in the metamorphic and deformation history.

The largely euhedral state of the matrix phases in garnet amphibolites suggests, with the preserved positive correlation between $X_{Fe,Grt}$ and $X_{Fe,Hbl}$, $X_{Fe,Bt}$, $X_{Fe,St}$ that there has

Table A8.4. Selected probe data from garnet-gedrite-amphibolites (950-069, 950-000) recalculated according to Appendix A1

950-069					950-000					HR91-22						
	Oam	Hbl	Grt	Pl	Hbl	Pl	Oam	Ilm	Grt		Grt	Pl	Hbl	Pl	Hbl	Oam
SiO2	45.92	42.97	39.22	57.92	42.16	56.20	41.91	1.33	38.26	SiO2	39.15	57.95	42.99	59.26	42.47	47.35
TiO2	0.23	0.51	0.05	0.00	0.76	0.09	0.21	51.74	0.00	TiO2	0.00	0.19	0.50	0.03	0.58	0.24
Al2O3	14.61	15.76	22.64	26.37	17.02	27.84	16.45	0.86	22.86	Al2O3	23.00	25.79	15.43	25.62	15.24	11.47
FeO	19.51	14.47	28.03	0.36	13.70	0.00	17.71	32.84	27.58	FeO	28.48	0.67	14.85	0.04	15.16	19.40
MnO	0.04	0.16	2.00	0.00	0.24	0.00	0.00	0.39	1.18	MnO	1.98	0.00	0.45	0.05	0.04	0.35
MgO	16.47	11.77	7.13	0.00	11.51	0.00	14.78	0.85	8.69	MgO	7.17	0.00	10.89	0.00	11.23	16.71
CaO	0.75	9.73	3.03	8.31	9.93	9.61	0.80	0.16	2.77	CaO	2.86	7.50	9.81	6.92	10.12	0.78
Na2O	1.73	1.56	0.00	6.94	1.46	6.13	1.15	0.13	0.00	Na2O	0.00	7.13	1.26	7.19	1.72	0.20
K2O	0.00	0.09	0.00	0.00	0.33	0.00	0.00	0.07	0.00	K2O	0.00	0.00	0.14	0.00	0.22	0.00
Cr2O3	n.a.	n.a.	n.a.	n.a.	n.a.	n.a.	n.a.	n.a.	n.a.	Cr2O3	n.a.	n.a.	n.a.	n.a.	n.a.	n.a.
ZnO	n.a.	n.a.	n.a.	n.a.	n.a.	n.a.	n.a.	n.a.	n.a.	ZnO	n.a.	n.a.	n.a.	n.a.	n.a.	n.a.
Total	99.26	97.02	102.10	99.90	97.1	99.9	93.0	88.4	101.3	Total	102.6	99.2	96.3	99.1	96.8	96.5
Si	6.544	6.321	2.987	2.597	6.190	2.526	6.340	0.036	2.926	Si	2.969	2.615	6.384	2.658	6.308	6.901
Ti	0.025	0.056	0.003	0.000	0.084	0.003	0.024	1.048	0.000	Ti	0.000	0.006	0.056	0.001	0.065	0.026
Al	2.455	2.733	2.033	1.394	2.946	1.475	2.934	0.027	2.061	Al	2.057	1.372	2.702	1.355	2.668	1.971
Fe2+	2.325	1.780	1.785	0.014	1.682	0.000	2.241	0.740	1.764	Fe2+	1.806	0.025	1.844	0.002	1.883	2.365
Mn	0.005	0.020	0.129	0.000	0.030	0.000	0.000	0.009	0.076	Mn	0.127	0.000	0.057	0.002	0.005	0.043
Mg	3.498	2.580	0.809	0.000	2.519	0.000	3.332	0.034	0.990	Mg	0.811	0.000	2.411	0.000	2.486	3.629
Ca	0.115	1.534	0.247	0.399	1.562	0.463	0.130	0.005	0.227	Ca	0.232	0.363	1.561	0.333	1.610	0.122
Na	0.478	0.445	0.000	0.603	0.416	0.534	0.337	0.007	0.000	Na	0.000	0.623	0.364	0.625	0.496	0.057
K	0.000	0.017	0.000	0.000	0.062	0.000	0.000	0.002	0.000	K	0.000	0.000	0.027	0.000	0.041	0.000
Cr	-	-	-	-	-	-	-	-	-	Cr	-	-	-	-	-	-
Zn	-	-	-	-	-	-	-	-	-	Zn	-	-	-	-	-	-
Total	15.443	15.487	7.994	5.007	15.491	5.001	15.338	1.907	8.044	Total	8.003	5.004	15.405	4.976	15.562	15.115
An				0.40		0.46			0.964	An		0.368		0.347		
XFe	0.399	0.408	0.688		0.400		0.402			XFe	0.690		0.433		0.431	0.395
Aliv	1.456	1.679			1.810		1.660			Aliv			1.616		1.692	1.099
Alvi	0.998	1.054			1.137		1.274		0.421	Alvi			1.086		0.976	0.873
Xalm			0.601						0.016	Xalm	0.607					
Xpy			0.272						0.202	Xpy	0.272					
Xgrs			0.083						0.361	Xgrs	0.078					
Xsps			0.043							Xsps	0.043					
ps										ps						

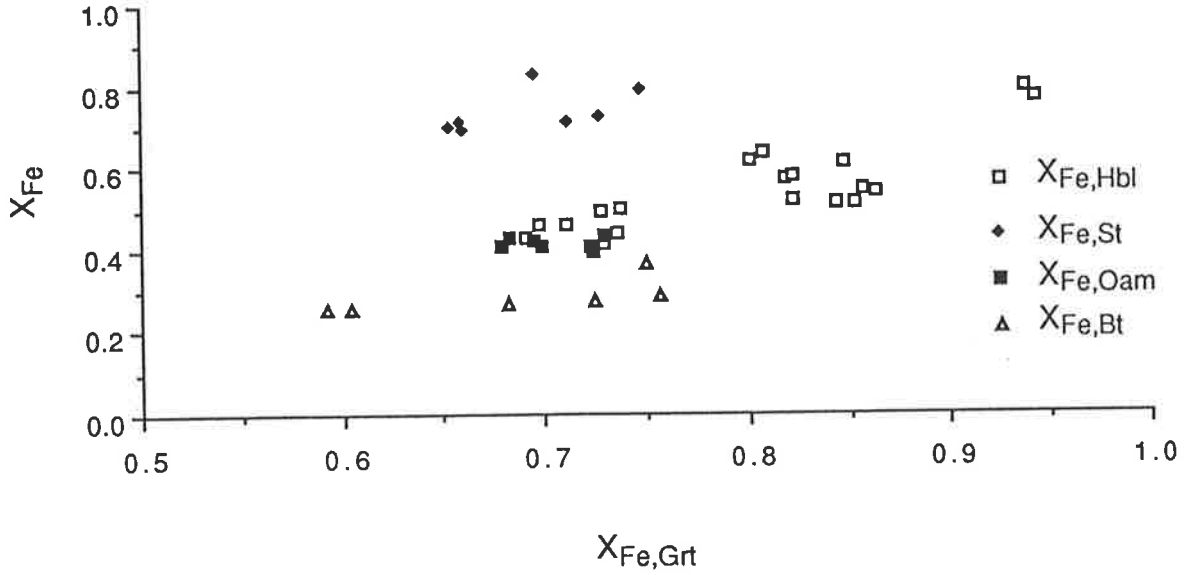

Figure A8.18. Plot of $X_{Fe,Grt}$ vs $X_{Fe,Hbl}$, $X_{Fe,Bt}$, $X_{Fe,Oam}$, $X_{Fe,St}$ for the Entia gneiss complex amphibolites.

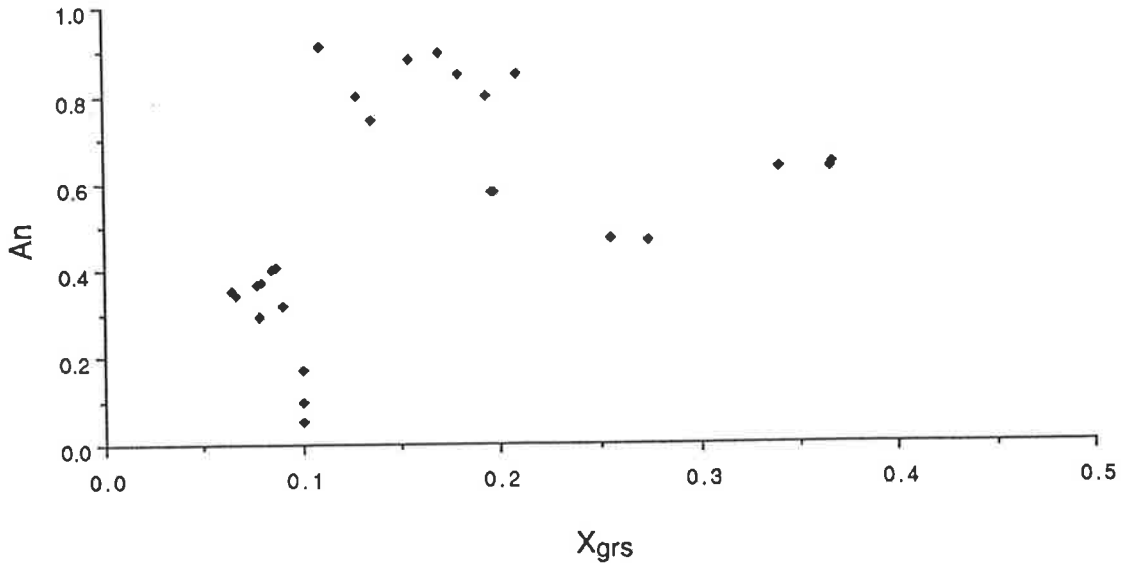

Figure A8.19. Plot of X_{grs} vs An in plagioclase, for the Entia gneiss complex amphibolites.

been little textural or chemical equilibration since the assemblages formed. Garnet-bearing amphibolites are generally more Fe-rich than most amphibolites, however X_{Fe} is also an important factor in the stability of garnet.

A8.5.2 Detailed descriptions of garnet-bearing amphibolites

Two pyroxene-two amphibole-garnet-amphibolite (HR91-5)

The fine grained, low variance equilibrium assemblage clinopyroxene–orthopyroxene–cummingtonite–hornblende–quartz–plagioclase occurs in a small portion of the garnet-amphibolite HR91-5. The Fe:Mg partitioning between the phases is consistent and X_{Fe} increases in the order clinopyroxene (salite-augite, $X_{Fe,Cpx}$ 0.61) < cummingtonite ($X_{Fe,Cum}$ 0.68-69) < hornblende ($X_{Fe,Hbl}$ 0.71-0.80) < orthopyroxene (bronzite, $X_{Fe,Opx}$ 0.72-0.74) < garnet ($X_{Fe,Grt}$ 0.94-0.95, Table A8.3). Clinopyroxene is more abundant than either orthopyroxene or cummingtonite and its X_{Fe} shows a positive correlation with that of hornblende (Fig. A8.20). Orthopyroxene and cummingtonite are both Ca-poor (< 0.05 and 0.19 atoms pfu, respectively).

The ferro-hornblende (Leake, 1978) in this sample shows little tschermakite (Al^{vi} 0.48-0.97) and intermediate edenite (0.30-0.46 moles of Na, pfu) substitution in comparison to more typical amphibolites and has a relatively high Ca content (1.42-1.83 pfu). The garnet porphyroblasts are also calcium rich (X_{grs} 0.19-0.22) and iron-rich (X_{alm} 0.69-0.71, X_{prp} 0.04-0.05) and they contain minimal spessartine (X_{sps} 0.04-0.05). The assemblage and the sample in which it occurs are considerably less sodic and more Fe-rich (reflected in the especially Fe-rich hornblende and garnet compositions) than most other amphibolite assemblages (Fig. A8.8). It is the combination of these factors which results in the unusual mineralogy of the sample.

Garnet–gedrite-amphibolites (e.g. HR91-22, 950-000, 069)

Tschermakitic hornblende occurring in trivariant (in AFM + hornblende, plagioclase, quartz and aqueous vapour) garnet–gedrite amphibolites is typically less Fe-rich than in other garnet amphibolites (X_{Fe} 0.40-0.43) however it contains similar levels of calcium, aluminium and sodium (1.44-1.62, 1.06-1.37, 0.24-.51 moles of Ca, Al^{vi} and Na pfu). Garnet is less Fe-rich (X_{Fe} 0.63-0.69, X_{alm} 0.57-0.61, X_{prp} 0.27-0.33) and contains less grossular than those co-existing with staurolite–hornblende or hornblende alone (X_{grs} 0.07-0.08). Gedrite is more Fe-rich in garnet amphibolites than in other assemblages (X_{Fe} 0.37-0.43), and has intermediate tschermakite and high edenite contents (0.93-1.30, 0-0.51 moles of Al^{vi} and Na, respectively). Plagioclase (andesine) in garnet–gedrite amphibolites has a relatively narrow compositional range (An_{32-47}) and the less calcic chemistry of the phases are reflected in the calcium-poor location of garnet–orthoamphibole assemblages in the NCAFm compatibility diagram (Fig. A8.8).

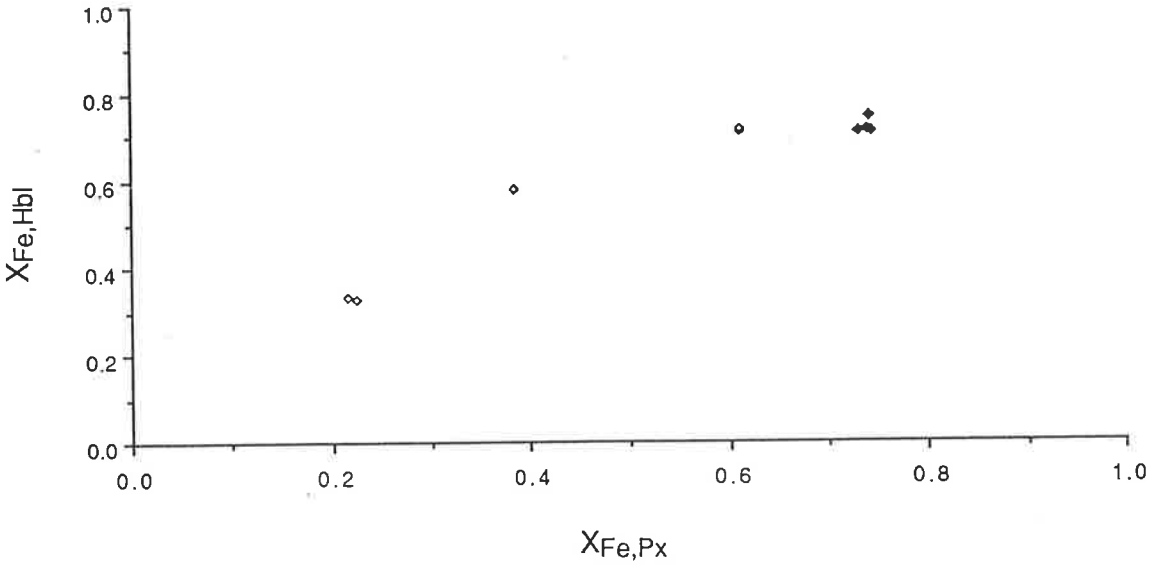

Figure A8.20. Plot of $X_{Fe,Px}$ against $X_{Fe,Hbl}$ in the Entia gneiss complex amphibolites. Cpx are open diamonds, Opx, filled diamonds.

Staurolite–garnet- amphibolites (e.g. 853-16, 950-105, HR91-8)

Staurolite-bearing garnet amphibolites tend to have even higher Fe-contents and are aluminous and Ca-poor than other garnet-bearing amphibolites.

(a) Staurolite included in garnet (853-16)

Anhedral staurolite occurs as mono-minerallic inclusions in poikiloblastic garnet with randomly oriented inclusions of plagioclase, quartz, hornblende and ilmenite. It is completely isolated from the polygonal hornblende–plagioclase–quartz matrix. The staurolite inclusions are very Fe-rich and have an X_{Fe} which is very close to that of the enclosing garnet ($X_{Fe,St}$ = 0.71-0.73, $X_{Fe,Grt}$ = 0.73). The staurolite contains little zinc, though staurolite in this sample is more Zn-rich than those in most other samples from the Harts Range region (0.52-0.69 wt % ≡ 0.11-0.14 pfu ZnO; Tables A8.5 and A8.6). The garnet poikiloblasts have similar compositions to others containing staurolite–garnet assemblages (X_{prp} 0.22-0.23, X_{grs} 0.13-0.14, X_{sps} 0.02-0.03) with only the almandine component being slightly higher than usual (X_{alm} 0.61-0.62). Matrix hornblende is more calcic (1.70-1.77 CaO pfu) and slightly more Fe-rich than in other staurolite–garnet amphibolites ($X_{Fe,Hbl}$ 0.49-0.52), however it is slightly less aluminous (Al^{vi}_{Hbl} 1.18-1.32) and contains only a low proportion of the edenite endmember (0.19-0.38 moles of Na pfu). Plagioclase in sample 853-16 is labradorite-bytownite (An_{63-82}) which is considerably more sodic than in those samples which contain staurolite as a matrix phase. The staurolite–garnet assemblages are plotted in Fig. A8.21. The sodic nature of the plagioclase in sample 853-16 means that hornblende projected from plagioclase has a negative value of Na and that after projection from plagioclase and hornblende, garnet plots in the negative-Mg portion of the AFM ternary compatibility diagram (projected from hornblende, plagioclase, quartz and aqueous vapour).

(b) Staurolite partly included in garnet (950-105)

In sample 950-105 staurolite occurs as inclusions in garnet and also near its margin, extending into the hornblende–plagioclase–quartz matrix (Fig. A8.17). The garnet porphyroblasts exhibit curved inclusion trails of plagioclase, hornblende, exsolved ilmenite and titaniferous magnetite and truncates the matric foliation. In the core, rutile defines straight inclusion trails which are sub-parallel to the hornblende foliation. Staurolite and garnet are less Fe-rich in this sample than in the other staurolite–garnet amphibolites, however they retain their relative Fe-Mg partitioning. Staurolite has X_{Fe} 0.69 whereas co-existing garnet is slightly less Fe-rich ($X_{Fe,Grt}$ 0.67-0.71, Table A8.5). Although the Zn-contents of staurolites in this sample are not known, the amount of "Na" which appears in EDS analyses gives a rough indication of whether the Zn content is significant. (This is due to the close proximity of the $Na_{K\alpha}$ (1.041 keV) and $Zn_{L\alpha}$ (1.009 keV) peaks in EDS spectra.) Sample 950-105 has an apparent "Na" value of 0.49 wt % (from EDS data) suggesting a significant, but not unduly

Table A8.5. Selected probe data from staurolite-garnet amphibolites (853-16, 950-105) recalculated according to Appendix A1

853-16																950-105			
	Hbl	Pl	Grt	St	Grt	Hbl	Pl	Pl-core	Grt	St	St	Hbl	Pl	Hbl	Oam	St	Grt	Pl	Ilm
SiO2	43.03	50.51	39.84	28.17	38.83	42.06	48.97	48.71	40.27	28.35	27.64	42.99	59.26	42.47	47.35	28.02	38.15	45.86	0.05
TiO2	0.74	0.05	0.02	0.68	0.12	0.49	0.00	0.10	0.04	0.61	0.72	0.50	0.03	0.58	0.24	0.57	0.07	0.01	47.71
Al2O3	16.22	33.08	23.68	56.29	22.82	16.70	33.59	33.49	21.59	54.78	54.12	15.43	25.62	15.24	11.47	54.83	22.14	34.22	0.01
FeO	17.35	0.19	29.10	13.65	29.92	17.17	0.00	0.06	27.40	13.10	13.10	14.85	0.04	15.16	19.40	12.72	27.49	0.00	49.21
MnO	0.28	0.05	1.04	0.14	1.11	0.32	0.34	0.11	1.07	0.10	0.11	0.45	0.05	0.04	0.35	0.00	2.21	0.05	0.74
MgO	9.93	0.00	6.09	2.89	6.00	9.41	0.00	0.00	6.20	2.85	2.75	10.89	0.00	11.23	16.71	3.14	6.39	0.15	0.06
CaO	11.26	15.18	5.03	0.24	4.82	11.08	16.15	16.18	4.85	0.10	0.05	9.81	6.92	10.12	0.78	0.06	4.37	17.58	0.00
Na2O	1.36	2.91	0.00	0.33	0.00	1.20	2.25	2.30	0.01	0.01	0.01	1.26	7.19	1.72	0.20	0.49	0.00	1.69	0.00
K2O	0.47	0.00	0.01	0.00	0.03	0.47	0.00	0.00	0.01	0.02	0.02	0.14	0.00	0.22	0.00	0.00	0.00	0.00	0.00
Cr2O3	n.a.	n.a.	n.a.	n.a.	n.a.	n.a.	n.a.	n.a.	0.00	0.02	0.03	n.a.	n.a.	n.a.	n.a.	n.a.	n.a.	n.a.	n.a.
ZnO	n.a.	n.a.	n.a.	n.a.	n.a.	n.a.	n.a.	n.a.	0.00	0.57	0.69	n.a.	n.a.	n.a.	n.a.	n.a.	n.a.	n.a.	n.a.
Total	100.6	102.0	104.8	102.4	103.6	98.9	101.3	100.9	101.4	100.5	99.2	96.3	99.1	96.8	96.5	99.8	100.8	99.6	97.8
Si	6.222	2.259	2.964	7.476	2.944	6.187	2.212	2.208	3.077	7.657	7.575	6.384	2.658	6.308	6.901	7.594	2.961	2.121	0.001
Ti	0.080	0.002	0.001	0.136	0.007	0.054	0.000	0.004	0.002	0.123	0.148	0.056	0.001	0.065	0.026	0.116	0.004	0.000	0.946
Al	2.765	1.744	2.077	17.614	2.040	2.895	1.789	1.790	1.945	17.439	17.489	2.702	1.355	2.668	1.971	17.522	2.026	1.866	0.000
Fe2+	2.098	0.007	1.810	3.031	1.897	2.112	0.000	0.002	1.751	2.958	3.003	1.844	0.002	1.883	2.365	2.884	1.784	0.000	1.086
Mn	0.034	0.002	0.066	0.030	0.071	0.039	0.013	0.004	0.069	0.022	0.025	0.057	0.002	0.005	0.043	0.000	0.145	0.002	0.017
Mg	2.140	0.000	0.676	1.141	0.678	2.062	0.000	0.000	0.706	1.145	1.123	2.411	0.000	2.486	3.629	1.269	0.739	0.010	0.002
Ca	1.744	0.728	0.401	0.068	0.391	1.746	0.782	0.786	0.397	0.029	0.015	1.561	0.333	1.610	0.122	0.017	0.364	0.871	0.000
Na	0.380	0.252	0.000	0.167	0.000	0.343	0.197	0.202	0.001	0.006	0.006	0.364	0.625	0.496	0.057	0.256	0.000	0.152	0.000
K	0.087	0.000	0.001	0.000	0.003	0.088	0.000	0.000	0.001	0.007	0.008	0.027	0.000	0.041	0.000	0.000	0.000	0.000	0.000
Cr	-	-	-	-	-	-	-	-	0.000	0.004	0.006	-	-	-	-	-	-	-	-
Zn	-	-	-	-	-	-	-	-	0.000	0.114	0.139	-	-	-	-	-	-	-	-
Total	15.549	4.994	7.997	29.664	8.031	15.527	4.992	4.995	7.949	29.390	29.398	15.405	4.976	15.562	15.115	29.657	8.023	5.022	2.052
An		0.743					0.799	0.795					0.347					0.852	
XFe	0.495		0.728	0.726	0.737	0.506			0.713	0.721	0.728	0.433		0.431	0.395	0.694	0.707		
Aliv	1.778					1.813						1.616		1.692	1.099				
Alvi	0.986					1.082						1.086		0.976	0.873				
Xalm			0.613		0.625				0.599								0.588		
Xpy			0.229		0.223				0.241								0.244		
Xgrs			0.136		0.129				0.136								0.120		
Xsps			0.022		0.023				0.024								0.048		
ps																			

Table A8.5. Selected probe data from staurolite-garnet amphibolites (950-105, HR91-8) recalculated according to Appendix A1

950-105

	Grt	Hbl	Pl	Ilm
SiO2	38.53	41.27	46.21	2.58
TiO2	0.00	0.65	0.20	20.90
Al2O3	22.70	17.45	34.17	0.00
FeO	27.46	14.63	0.48	67.62
MnO	1.64	0.17	0.33	0.00
MgO	6.23	10.18	0.00	0.00
CaO	4.53	10.76	17.26	0.03
Na2O	0.00	1.73	1.49	0.00
K2O	0.00	0.12	0.00	0.04
Cr2O3	n.a.	n.a.	n.a.	n.a.
ZnO	n.a.	n.a.	n.a.	n.a.
Total	101.1	97.0	100.1	91.2
Si	2.970	6.116	2.127	0.083
Ti	0.000	0.073	0.007	0.506
Al	2.063	3.049	1.854	0.000
Fe2+	1.770	1.813	0.019	1.820
Mn	0.107	0.021	0.013	0.000
Mg	0.716	2.247	0.000	0.000
Ca	0.374	1.708	0.852	0.001
Na	0.000	0.498	0.133	0.000
K	0.000	0.023	0.000	0.002
Cr	-	-	-	-
Zn	-	-	-	-
Total	7.999	15.548	5.005	2.412
An			0.865	
XFe	0.712	0.447		
Aliv		1.884		
Alvi		1.164		
Xalm	0.597			
Xpy	0.241			
Xgrs	0.126			
Xsps	0.036			
ps				

HR91-8

	Hbl	Pl	St	Pl
SiO2	41.26	45.56	28.07	44.33
TiO2	0.48	0.06	0.57	0.07
Al2O3	18.19	35.33	54.66	34.28
FeO	15.32	0.10	13.06	0.19
MnO	0.29	0.22	0.16	0.00
MgO	9.54	0.00	1.55	0.00
CaO	10.68	17.89	0.32	18.13
Na2O	1.55	1.18	0.24	0.81
K2O	0.28	0.00	0.00	0.07
Cr2O3	n.a.	n.a.	n.a.	n.a.
ZnO	n.a.	n.a.	n.a.	n.a.
Total	97.6	100.3	98.6	97.9
Si	6.091	2.091	7.704	2.089
Ti	0.053	0.002	0.118	0.002
Al	3.166	1.912	17.688	1.904
Fe2+	1.892	0.004	2.998	0.008
Mn	0.036	0.009	0.038	0.000
Mg	2.098	0.000	0.632	0.000
Ca	1.690	0.880	0.093	0.915
Na	0.444	0.105	0.125	0.074
K	0.052	0.000	0.000	0.004
Cr	-	-	-	-
Zn	-	-	-	-
Total	15.521	5.003	29.396	4.996
An		0.893		0.925
XFe	0.474		0.826	
Aliv	1.909			
Alvi	1.257			
Xalm				
Xpy				
Xgrs				
Xsps				
ps				

	Hbl	Grt rim	Grt	Grt	Grt	Grt	Grt core
SiO2	41.16	39.45	39.51	39.01	38.88	38.79	38.86
TiO2	0.65	0.02	0.00	0.00	0.27	0.04	0.13
Al2O3	18.39	23.18	23.21	22.70	22.83	22.77	22.54
FeO	15.40	27.80	26.31	27.55	28.01	27.30	26.82
MnO	0.16	1.81	1.84	2.04	2.33	2.10	1.75
MgO	9.86	6.80	6.73	5.37	5.30	5.97	5.73
CaO	10.17	4.02	5.42	5.50	5.65	5.71	5.71
Na2O	0.92	0.00	0.00	0.00	0.00	0.00	0.00
K2O	0.24	0.00	0.05	0.00	0.00	0.00	0.08
Cr2O3	n.a.	n.a.	n.a.	n.a.	n.a.	n.a.	n.a.
ZnO	n.a.	n.a.	n.a.	n.a.	n.a.	n.a.	n.a.
Total	96.9	103.1	103.1	102.2	103.3	102.7	101.6
Si	6.089	2.975	2.973	2.985	2.955	2.955	2.981
Ti	0.072	0.001	0.000	0.000	0.016	0.002	0.008
Al	3.207	2.061	2.059	2.047	2.045	2.045	2.039
Fe2+	1.905	1.753	1.656	1.763	1.781	1.739	1.721
Mn	0.020	0.115	0.117	0.132	0.150	0.135	0.114
Mg	2.174	0.764	0.754	0.613	0.601	0.678	0.655
Ca	1.612	0.325	0.437	0.451	0.460	0.466	0.470
Na	0.265	0.000	0.000	0.000	0.000	0.000	0.000
K	0.045	0.000	0.005	0.000	0.000	0.000	0.008
Cr	-	-	-	-	-	-	-
Zn	-	-	-	-	-	-	-
Total	15.390	7.994	8.000	7.991	8.007	8.020	7.995
An							
XFe	0.467	0.697	0.687	0.742	0.748	0.720	0.724
Aliv	1.911						
Alvi	1.297						
Xalm		0.593	0.559	0.596	0.595	0.576	0.582
Xpy		0.258	0.254	0.207	0.201	0.224	0.221
Xgrs		0.110	0.147	0.152	0.154	0.154	0.159
Xsps		0.039	0.039	0.045	0.050	0.045	0.038
ps							

	Pl	Hbl	Grt	Ep
SiO2	45.15	40.47	39.16	38.17
TiO2	0.09	0.42	0.01	0.27
Al2O3	35.20	18.97	23.01	26.53
FeO	0.39	15.10	25.94	8.91
MnO	0.26	0.34	2.09	0.16
MgO	0.00	9.87	5.95	0.00
CaO	17.92	10.65	5.59	22.41
Na2O	1.30	1.43	0.00	0.00
K2O	0.00	0.31	0.00	0.00
Cr2O3	n.a.	n.a.	n.a.	n.a.
ZnO	n.a.	n.a.	n.a.	n.a.
Total	100.3	97.6	101.8	96.5
Si	2.079	5.976	2.987	3.073
Ti	0.003	0.047	0.001	0.017
Al	1.911	3.303	2.069	2.518
Fe2+	0.015	1.865	1.654	0.600
Mn	0.010	0.043	0.135	0.011
Mg	0.000	2.173	0.676	0.000
Ca	0.885	1.685	0.456	1.933
Na	0.116	0.410	0.000	0.000
K	0.000	0.057	0.000	0.000
Cr	-	-	-	-
Zn	-	-	-	-
Total	5.020	15.559	7.978	8.151
An	0.884			
XFe		0.462	0.710	
Aliv		2.024		
Alvi		1.279		
Xalm			0.566	
Xpy			0.231	
Xgrs			0.156	
Xsps			0.046	
ps				16.061

Table A8.5. Selected probe data from staurolite-garnet (HR91-8) and staurolite-garnet-gedrite amphibolites (950-077) recalculated according to Appendix A1

HR91-8

main	exsolved	St	St	St
0.00	0.11	28.17	27.58	27.59
11.50	46.41	0.89	0.78	0.85
0.00	0.19	54.19	51.84	51.30
78.91	49.33	12.57	12.86	12.27
0.01	0.69	0.12	0.13	0.12
0.00	0.00	2.64	3.40	3.36
0.00	0.19	0.21	0.02	0.03
0.09	0.16	0.00	0.04	0.01
0.00	0.02	0.00	0.03	0.00
n.a.	n.a.	n.a.	0.03	0.04
n.a.	n.a.	n.a.	0.71	0.56
90.5	97.1	98.8	97.4	96.1
0.000	0.003	7.702	7.710	7.784
0.311	0.930	0.183	0.164	0.180
0.000	0.006	17.463	17.082	17.065
2.374	1.100	2.873	3.007	2.895
0.000	0.016	0.027	0.030	0.028
0.000	0.000	1.075	1.416	1.414
0.000	0.006	0.062	0.006	0.008
0.006	0.008	0.000	0.020	0.004
0.000	0.001	0.000	0.009	0.000
-	-	-	0.006	0.009
-	-	-	0.146	0.116
2.692	2.068	29.384	29.596	29.502
		0.728	0.680	0.672

950-077

	Oam	Pl	Pl core	Ilm	Ru	Pl	St	Grt	Oam	Hbl	Grt	Pl	Grt	Pl	St
SiO2	45.42	57.62	57.37	0.50	0.00	56.82	27.84	37.81	46.96	42.91	38.35	56.97	41.03	60.40	28.83
TiO2	0.19	0.00	0.00	45.65	96.08	0.06	0.78	0.00	0.17	0.74	0.08	0.12	0.04	0.03	0.67
Al2O3	13.69	25.60	25.85	0.08	0.22	25.91	54.03	22.34	11.46	15.78	22.49	25.48	23.24	26.80	54.32
FeO	18.36	0.00	0.12	43.33	0.60	0.08	13.01	29.06	19.97	14.52	28.62	0.03	27.50	0.22	11.76
MnO	0.44	0.23	0.09	0.57	0.08	0.01	0.18	2.75	0.37	0.29	2.15	0.02	1.72	0.02	0.12
MgO	15.91	0.00	0.00	0.97	0.09	0.00	1.90	5.50	17.37	11.60	6.15	0.00	8.18	0.01	3.41
CaO	0.60	7.06	7.51	0.00	0.00	8.05	0.18	2.87	0.81	9.91	2.89	7.49	3.29	8.57	0.06
Na2O	0.45	7.07	6.86	0.14	0.30	6.67	0.00	0.00	0.83	1.68	0.00	7.01	0.00	6.90	0.09
K2O	0.03	0.00	0.07	0.00	0.01	0.00	0.00	0.00	0.00	0.08	0.00	0.02	0.02	0.05	0.02
Cr2O3	n.a.	n.a.	n.a.	n.a.	n.a.	n.a.	n.a.	n.a.	n.a.	n.a.	n.a.	n.a.	0.00	0.03	0.06
ZnO	n.a.	n.a.	n.a.	n.a.	n.a.	n.a.	n.a.	n.a.	n.a.	n.a.	n.a.	n.a.	0.10	0.06	0.23
Total	95.1	97.6	97.9	91.2	97.4	97.6	97.9	100.3	97.9	97.5	100.7	97.1	105.1	103.1	99.6
Si	6.702	2.632	2.617	0.014	0.000	2.602	7.695	2.965	6.793	6.294	2.977	2.619	3.012	2.620	7.793
Ti	0.021	0.000	0.000	0.953	0.990	0.002	0.163	0.000	0.018	0.082	0.005	0.004	0.002	0.001	0.137
Al	2.382	1.379	1.390	0.002	0.004	1.399	17.602	2.065	1.955	2.728	2.058	1.380	2.011	1.371	17.313
Fe2+	2.267	0.000	0.005	1.006	0.007	0.003	3.006	1.905	2.416	1.781	1.858	0.001	1.688	0.008	2.659
Mn	0.055	0.009	0.004	0.013	0.001	0.000	0.042	0.183	0.045	0.036	0.141	0.001	0.107	0.001	0.028
Mg	3.499	0.000	0.000	0.040	0.002	0.000	0.783	0.643	3.743	2.536	0.711	0.000	0.895	0.001	1.374
Ca	0.095	0.346	0.367	0.000	0.000	0.395	0.052	0.241	0.125	1.558	0.240	0.369	0.259	0.398	0.017
Na	0.128	0.627	0.607	0.008	0.008	0.592	0.001	0.000	0.233	0.477	0.000	0.625	0.000	0.580	0.045
K	0.005	0.000	0.004	0.000	0.000	0.000	0.000	0.000	0.000	0.015	0.000	0.001	0.001	0.002	0.008
Cr	-	-	-	-	-	-	-	-	-	-	-	-	0.000	0.001	0.014
Zn	-	-	-	-	-	-	-	-	-	-	-	-	0.005	0.002	0.047
Total	15.153	4.992	4.993	2.036	1.012	4.993	29.342	8.002	15.328	15.506	7.990	5.000	7.981	4.985	29.387
An		0.356	0.377			0.400						0.371		0.407	
XFe	0.393						0.793	0.748	0.392	0.413	0.723		0.654		0.659
Aliv	1.298								1.207	1.706					
Alvi	1.084								0.748	1.022					
Xalm								0.641			0.630		0.572		
Xpy								0.216			0.241		0.303		
Xgrs								0.081			0.081		0.088		
Xsps								0.061			0.048		0.036		
ps															

Table A8.6. Selected probe data from kyanite-staurolite (890-5a) and corundum-staurolite (890-009) amphibolites recalculated according to Appendix A1

890-5a

	Hbl	Pl	St	Ep	Pl rim	Pl core	Pl	St	Hbl	Pl	St
SiO2	40.64	55.86	26.10	38.72	56.11	55.54	56.29	24.24	41.42	46.93	28.45
TiO2	0.68	0.00	0.69	0.00	0.00	0.00	0.00	0.62	0.61	0.00	0.65
Al2O3	16.19	26.97	51.55	29.35	27.34	28.36	27.74	53.41	16.97	34.33	54.76
FeO	13.60	0.13	12.81	3.62	0.00	0.00	0.00	12.60	13.15	0.00	12.46
MnO	0.20	0.00	0.00	0.00	0.00	0.00	0.00	0.16	0.13	0.00	0.17
MgO	10.72	0.00	3.63	0.00	0.00	0.00	0.00	3.39	10.58	0.15	3.52
CaO	10.53	9.97	0.00	24.16	10.18	10.88	9.68	0.00	10.57	17.25	0.01
Na2O	2.17	5.91	0.30	0.26	5.82	5.44	5.99	0.48	2.29	1.95	0.00
K2O	0.21	0.00	0.06	0.26	0.15	0.00	0.00	0.00	0.71	0.00	0.00
Cr2O3	n.a.	n.a.	n.a.	n.a.	n.a.	n.a.	n.a.	n.a.	n.a.	n.a.	0.04
ZnO	n.a.	n.a.	n.a.	n.a.	n.a.	n.a.	n.a.	n.a.	n.a.	n.a.	0.24
Total	94.9	98.8	95.1	96.4	99.6	100.2	99.7	94.9	96.4	100.6	100.3
Si	6.151	2.540	7.464	3.050	2.533	2.494	2.533	6.967	6.160	2.143	7.665
Ti	0.077	0.000	0.148	0.000	0.000	0.000	0.000	0.134	0.068	0.000	0.132
Al	2.889	1.446	17.380	2.726	1.455	1.501	1.471	18.097	2.976	1.848	17.392
Fe2+	1.721	0.005	3.064	0.238	0.000	0.000	0.000	3.029	1.636	0.000	2.806
Mn	0.026	0.000	0.000	0.000	0.000	0.000	0.000	0.039	0.016	0.000	0.039
Mg	2.418	0.000	1.547	0.000	0.000	0.000	0.000	1.452	2.345	0.010	1.413
Ca	1.708	0.486	0.000	2.039	0.492	0.523	0.467	0.000	1.685	0.844	0.003
Na	0.637	0.521	0.166	0.040	0.509	0.474	0.523	0.267	0.660	0.173	0.000
K	0.041	0.000	0.022	0.026	0.009	0.000	0.000	0.000	0.135	0.000	0.000
Cr	-	-	-	-	-	-	-	-	-	-	0.007
Zn	-	-	-	-	-	-	-	-	-	-	0.047
Total	15.666	4.998	29.792	8.120	4.999	4.992	4.993	29.985	15.681	5.019	29.46
An		0.48			0.49	0.52	0.47			0.83	
XFe	0.416		0.664					0.676	0.411		0.665
Aliv	1.849								1.840		
Alvi	1.039								1.136		
Xalm											
Xpy											
Xgrs											
Xsps											
ps				9.1395							

890-9

	St	Pl	Hbl	Ilm	2°Ilm	Hbl	Pl	Cor	St
SiO2	23.87	45.16	41.61	0.06	0.00	41.75	47.28	0.00	27.66
TiO2	0.50	0.00	0.38	45.41	13.11	0.52	0.00	0.00	0.52
Al2O3	56.76	36.28	16.57	0.17	0.08	17.76	34.23	99.72	55.18
FeO	12.76	0.00	15.35	49.62	77.84	15.39	0.18	0.84	13.26
MnO	0.31	0.00	0.41	0.60	0.07	0.27	0.22	0.00	0.29
MgO	3.41	0.00	10.50	0.88	0.00	10.43	0.02	0.59	3.57
CaO	0.00	17.71	10.42	0.00	0.00	10.38	17.16	0.00	0.20
Na2O	0.48	1.40	2.07	0.29	0.00	1.88	1.67	0.09	0.17
K2O	0.00	0.00	0.40	0.01	0.00	0.29	0.00	0.00	0.00
Cr2O3	n.a.	n.a.	n.a.	n.a.	n.a.	n.a.	n.a.	n.a.	n.a.
ZnO	n.a.	n.a.	n.a.	n.a.	n.a.	n.a.	n.a.	n.a.	n.a.
Total	98.1	100.6	97.7	97.0	91.1	98.7	100.8	101.2	100.8
Si	6.641	2.067	6.160	0.002	0.000	6.098	2.156	0.000	7.453
Ti	0.105	0.000	0.042	0.912	0.348	0.057	0.000	0.000	0.106
Al	18.616	1.957	2.892	0.005	0.003	3.059	1.840	1.981	17.529
Fe2+	2.969	0.000	1.901	1.108	2.297	1.880	0.007	0.012	2.989
Mn	0.073	0.000	0.051	0.013	0.002	0.033	0.008	0.000	0.067
Mg	1.414	0.000	2.317	0.035	0.000	2.270	0.001	0.015	1.434
Ca	0.000	0.868	1.653	0.000	0.000	1.624	0.838	0.000	0.057
Na	0.259	0.124	0.594	0.015	0.000	0.532	0.148	0.003	0.086
K	0.000	0.000	0.076	0.000	0.000	0.053	0.000	0.000	0.000
Cr	-	-	-	-	-	-	-	-	-
Zn	-	-	-	-	-	-	-	-	-
Total	30.076	5.017	15.686	2.091	2.650	15.607	4.998	2.011	29.720
An		0.87					0.85		
XFe	0.677		0.451			0.453			0.676
Aliv			1.840			1.902			
Alvi			1.052			1.157			
Xalm									
Xpy									
Xgrs									
Xsps									
ps									

Table A8.6. Selected probe data from staurolite amphibolites (890-5b, HR91-3) recalculated according to Appendix A1

890-5b

	Pl	Hbl	Hbl	St	Hbl	Pl	St	Ilm
SiO2	56.75	41.62	41.37	26.71	41.93	57.14	25.00	0.00
TiO2	0.00	0.50	0.63	0.72	0.60	0.00	0.62	42.20
Al2O3	26.97	15.69	16.15	52.72	16.60	28.16	53.84	0.25
FeO	0.19	12.56	12.40	11.89	12.48	0.00	11.80	40.52
MnO	0.00	0.00	0.22	0.18	0.22	0.00	0.00	4.92
MgO	0.00	11.69	11.63	3.49	10.87	0.18	3.82	1.80
CaO	9.63	10.37	10.27	0.00	10.42	9.82	0.00	0.00
Na2O	6.14	2.07	2.06	0.33	2.10	6.16	0.39	0.24
K2O	0.06	0.20	0.25	0.00	0.24	0.06	0.00	0.00
Cr2O3	n.a.	n.a.	n.a.	n.a.	n.a.	n.a.	n.a.	n.a.
ZnO	n.a.	n.a.	n.a.	n.a.	n.a.	n.a.	n.a.	n.a.
Total	99.7	94.7	95.0	96.0	95.5	101.5	95.5	89.9
Si	2.555	6.260	6.207	7.522	6.250	2.527	7.095	0.000
Ti	0.000	0.057	0.071	0.152	0.067	0.000	0.132	0.908
Al	1.432	2.782	2.857	17.503	2.917	1.468	18.014	0.008
Fe2+	0.007	1.580	1.556	2.800	1.556	0.000	2.801	0.969
Mn	0.000	0.000	0.028	0.043	0.028	0.000	0.000	0.119
Mg	0.000	2.621	2.600	1.465	2.415	0.012	1.616	0.077
Ca	0.465	1.671	1.651	0.000	1.664	0.465	0.000	0.000
Na	0.536	0.604	0.599	0.180	0.607	0.528	0.215	0.013
K	0.003	0.038	0.048	0.000	0.046	0.003	0.000	0.000
Cr	-	-	-	-	-	-	-	-
Zn	-	-	-	-	-	-	-	-
Total	4.998	15.613	15.617	29.665	15.550	5.004	29.873	2.095
An	0.46					0.47		
XFe		0.376	0.374	0.657	0.392		0.634	
Aliv		1.740	1.793		1.750			
Alvi		1.043	1.064		1.168			
Xalm								
Xpy								
Xgrs								
Xsps								
ps								

HR91-3

	Ilm	2°Ilm	St	Pl	Pl	Hbl	St	Pl	Hbl	titanite	Ep	Hbl
SiO2	0.00	0.00	27.31	47.66	47.21	39.77	27.64	47.50	39.82	31.884	38.01	39.45
TiO2	10.22	46.06	0.32	0.00	0.05	0.77	0.51	0.00	0.75	27.692	0.11	0.70
Al2O3	0.06	0.12	54.64	33.34	34.21	19.59	54.72	33.81	19.35	8.245	26.69	19.50
FeO	79.31	49.10	12.96	0.07	0.31	14.51	13.39	0.25	14.98	1.095	8.66	14.18
MnO	0.14	0.29	0.19	0.18	0.16	0.40	0.28	0.18	0.20	0.261	0.28	0.34
MgO	0.00	0.45	2.93	0.00	0.00	10.03	2.41	0.00	10.12	0.764	0.00	10.03
CaO	0.00	0.00	0.22	15.91	16.15	10.16	0.17	16.24	10.39	26.875	22.51	10.20
Na2O	0.00	0.46	0.00	2.11	1.72	1.96	0.00	2.07	1.81	0	0.00	1.98
K2O	0.00	0.05	0.00	0.00	0.00	0.19	0.00	0.00	0.41	0	0.00	0.26
Cr2O3	n.a.	n.a.	n.a.	n.a.	n.a.	n.a.	n.a.	n.a.	n.a.	n.a.	n.a.	n.a.
ZnO	n.a.	n.a.	n.a.	n.a.	n.a.	n.a.	n.a.	n.a.	n.a.	n.a.	n.a.	n.a.
Total	89.7	96.5	98.6	99.3	99.8	97.4	99.1	100.0	97.8	96.8	96.3	96.6
Si	0.000	0.000	7.508	2.197	2.166	5.875	7.566	2.177	5.875	1.055	3.065	5.872
Ti	0.281	0.928	0.066	0.000	0.002	0.086	0.106	0.000	0.083	0.689	0.007	0.078
Al	0.003	0.004	17.709	1.811	1.850	3.413	17.661	1.827	3.366	0.322	2.538	3.422
Fe2+	2.429	1.100	2.979	0.003	0.012	1.793	3.066	0.009	1.848	0.030	0.584	1.765
Mn	0.004	0.007	0.044	0.007	0.006	0.049	0.066	0.007	0.024	0.007	0.019	0.042
Mg	0.000	0.018	1.201	0.000	0.000	2.208	0.983	0.000	2.224	0.038	0.000	2.224
Ca	0.000	0.000	0.065	0.786	0.794	1.608	0.048	0.797	1.642	0.953	1.945	1.627
Na	0.000	0.024	0.000	0.188	0.153	0.562	0.000	0.184	0.517	0.000	0.000	0.571
K	0.000	0.002	0.000	0.000	0.000	0.035	0.000	0.000	0.077	0.000	0.000	0.050
Cr	-	-	-	-	-	-	-	-	-	-	-	-
Zn	-	-	-	-	-	-	-	-	-	-	-	-
Total	2.717	2.083	29.571	4.992	4.983	15.631	29.497	5.002	15.657	3.095	8.159	15.650
An				0.81	0.84			0.81				
XFe			0.713			0.448	0.757		0.454			0.442
Aliv						2.125			2.125			2.128
Alvi						1.288			1.241			1.293
Xalm												
Xpy												
Xgrs												
Xsps												
ps											15.396	

Table A8.6. Selected probe data from staurolite-gedrite amphibolites (890-8, 890-16) recalculated according to Appendix A1

890-8

	Pl	St	Hbl	Oam	Ky	Oam	Pl	St	St
SiO2	58.11	24.86	43.90	45.06	38.42	48.01	44.64	28.73	29.12
TiO2	0.00	0.34	0.45	0.10	0.00	0.19	0.01	0.35	0.37
Al2O3	25.96	56.72	14.61	15.15	60.86	15.05	34.43	53.88	55.37
FeO	0.00	11.33	10.87	16.16	1.17	16.06	0.13	11.06	11.29
MnO	0.00	0.12	0.12	0.30	0.00	0.31	0.01	0.15	0.12
MgO	0.00	3.03	13.78	18.36	0.01	18.66	0.00	3.18	3.12
CaO	8.31	0.00	13.61	0.57	0.00	0.54	18.02	0.01	0.01
Na2O	6.74	0.43	2.09	1.76	0.00	1.48	0.80	0.04	0.01
K2O	0.05	0.00	0.24	0.00	0.00	0.00	0.04	0.02	0.03
Cr2O3	n.a.	n.a.	n.a.	n.a.	0.00	0.02	n.a.	0.10	0.03
ZnO	n.a.	n.a.	n.a.	n.a.	0.00	0.12	n.a.	0.19	0.23
Total	99.2	96.8	99.7	97.5	100.5	100.4	98.1	97.7	99.7
Si	2.618	6.929	6.279	6.457	1.036	6.630	2.095	7.881	7.827
Ti	0.000	0.071	0.048	0.011	0.000	0.020	0.000	0.073	0.074
Al	1.379	18.637	2.464	2.559	1.934	2.450	1.906	17.424	17.546
Fe2+	0.000	2.641	1.300	1.937	0.026	1.854	0.005	2.538	2.538
Mn	0.000	0.028	0.015	0.036	0.000	0.036	0.000	0.035	0.027
Mg	0.000	1.259	2.937	3.921	0.000	3.840	0.000	1.298	1.249
Ca	0.401	0.000	2.086	0.088	0.000	0.079	0.907	0.002	0.002
Na	0.589	0.232	0.580	0.489	0.000	0.397	0.073	0.019	0.003
K	0.003	0.000	0.044	0.000	0.000	0.000	0.002	0.006	0.009
Cr	-	-	-	-	0.000	0.002	-	0.021	0.006
Zn	-	-	-	-	0.000	0.013	-	0.038	0.046
Total	4.989	29.798	15.752	15.497	2.997	15.322	4.989	29.34	29.33
An	0.41						0.93		
XFe		0.677	0.307	0.331		0.326		0.662	0.670
Aliv			1.721	1.543		1.370			
Alvi			0.743	1.016		1.081			
Xalm									
Xpy									
Xgrs									
Xsps									
ps									

890-16

	Oam	Pl	St	Hbl	Ilm
SiO2	43.35	55.71	24.53	42.46	0.00
TiO2	0.18	0.00	0.70	0.64	49.34
Al2O3	15.83	29.19	54.19	16.61	0.00
FeO	19.18	0.00	12.38	14.04	49.35
MnO	0.19	0.00	0.00	0.00	0.65
MgO	15.36	0.13	3.60	10.91	0.19
CaO	0.53	10.02	0.00	10.09	0.00
Na2O	1.70	6.28	0.41	1.89	0.17
K2O	0.00	0.00	0.00	0.22	0.00
Cr2O3	n.a.	n.a.	n.a.	n.a.	n.a.
ZnO	n.a.	n.a.	n.a.	n.a.	n.a.
Total	96.3	101.3	95.8	96.9	99.7
Si	6.380	2.475	6.963	6.258	0.000
Ti	0.020	0.000	0.149	0.071	0.957
Al	2.747	1.529	18.134	2.886	0.000
Fe2+	2.361	0.000	2.939	1.731	1.064
Mn	0.024	0.000	0.000	0.000	0.014
Mg	3.369	0.009	1.523	2.397	0.007
Ca	0.084	0.477	0.000	1.594	0.000
Na	0.485	0.541	0.226	0.540	0.000
K	0.000	0.000	0.000	0.041	0.000
Cr	-	-	-	-	-
Zn	-	-	-	-	-
Total	15.469	5.031	29.934	15.518	2.043
An		0.47			
XFe	0.412		0.659	0.419	
Aliv	1.620			1.742	
Alvi	1.127			1.145	
Xalm					
Xpy					
Xgrs					
Xsps					
ps					

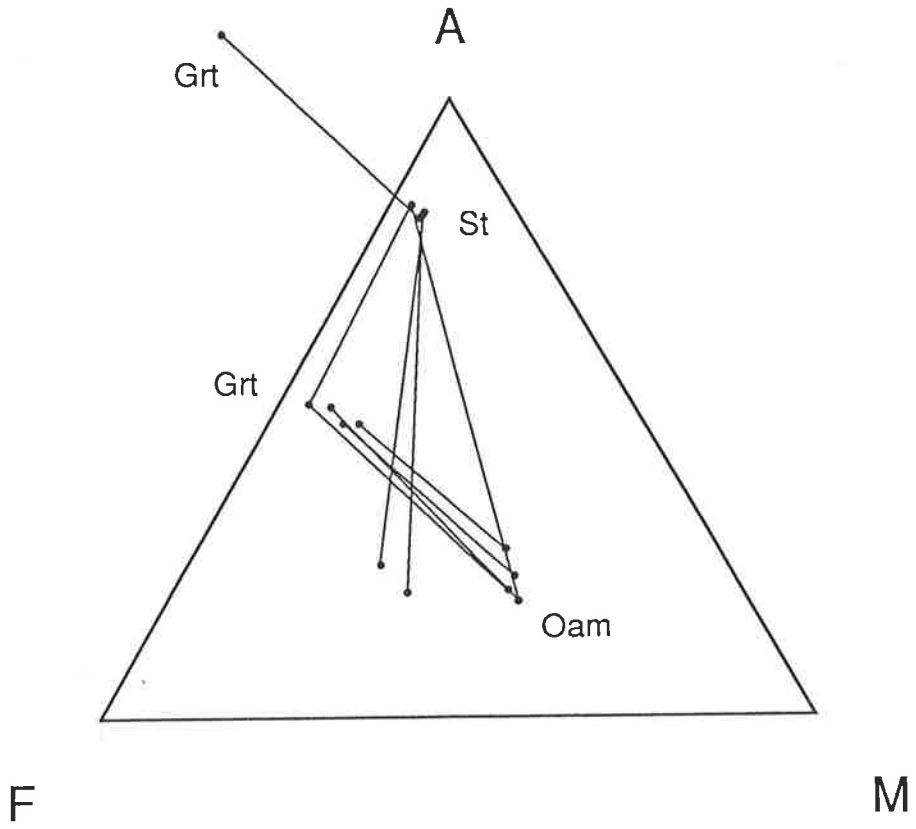

Figure A8.21. Ternary AFM diagram illustrating the compatibility relations in staurolite-garnet amphibolites projected from hornblende, plagioclase, quartz and aqueous vapour onto the AFM plane ($AlO_{3/2}$, FeO, MgO). The unusual plotting positions of some of the garnet analyses is a result of the sodic compositions of the projection plagioclases, and the crossed tie lies reflect the different stages at which the different assemblages equilibrated.

high Zn content. Garnet is more Mg-rich than in other staurolite–garnet bearing samples (cf. 853-16, HR91-8 and 950-077) and is correspondingly Fe-poorer (X_{alm} 0.55-0.62, X_{prp} 0.24-0.36). Garnet in this sample has a grossular content similar to that in other staurolite–garnet amphibolites (X_{grs} 0.10-0.15) and only minor spessartine (X_{sps} 0.03-0.04). Tschermakite hornblende (Al^{vi}_{Hbl} 1.25-1.43) is quite iron-rich with X_{Fe} 0.42-0.50 and also has a relatively high proportion of the edenite end-member (0.33-0.53 moles of Na pfu) and an intermediate Ca-content (1.50-1.73 pfu). Plagioclase is bytownite to anorthitic in composition (An_{85-93}) and overall this sample is less sodic than sample 853-16 in which staurolite is entirely enclosed in garnet and more sodic than sample HR918-8 where garnet and staurolite are both matrix phases.

(c) Staurolite in the garnet–hornblende–plagioclase matrix (HR91-8)

In sample HR91-8 equant staurolite grains occur in the polygonal matrix of a porphyroblastic garnet amphibolite. Garnet and staurolite are slightly more iron rich in this sample than in the above staurolite–garnet amphibolites ($X_{Fe,St}$ 0.72-0.83, $X_{Fe,Grt}$ 0.69-0.75, X_{alm} 0.56-0.6, X_{prp} 0.20-0.25, X_{sps} 0.04-0.05) and garnet is also more grossular-rich (X_{grs} 0.11-0.16) than either of these. Staurolite contains low levels of zinc (0.56-0.71 wt % ≡ 0.02-0.15 Zn pfu) however this staurolite is more Zn-rich than that in other staurolite–garnet amphibolites. Plagioclase is anorthite (An_{94-100}). Tschermakite hornblende has intermediate to high Fe and Na contents ($X_{Fe,Hbl}$ 0.44-0.51, 0.27-0.45 moles of Na, pfu) and is highly aluminous (Al^{vi}_{Hbl} 1.34-1.51) and has a relatively high Ca content (1.61-1.75 pfu, Table A8.5. Overall the chemistry of this sample is more calcic that both of the above staurolite–garnet amphibolites, indicated most effectively by the composition of plagioclase.

(d) Staurolite–garnet–gedrite amphibolite (950-077)

The mineral textures in this sample are similar to those in sample 853-16 (above) with the exception that orthoamphibole occurs as a matrix phase. Straight inclusion trails of anhedral staurolite, plagioclase, ilmenite and rutile are parallel to the foliated orthoamphibole–hornblende matrix. Staurolite has a variable X_{Fe} (0.69-0.81) and a low Zn content (ZnO 0.23-0.39 wt % ≡ 0.05-0.08 Zn pfu) and is slightly more Fe-rich than co-existing garnet ($X_{Fe,Grt}$ 0.65-0.75, X_{alm} 0.57-0.64, X_{prp} 0.22-0.31, Table A8.5). Garnet contains little grossular or spessartine (X_{grs} 0.08-0.11, X_{sps} 0.03-0.09) and is relatively homogeneous in composition. The matrix gedrite (Leake, 1978) and tschermakitic hornblende contain significant proportions of the tschermakite and edenite molecules (Al^{vi}_{Oam} 0.86-1.41, Al^{vi}_{Hbl} 1.13-1.2, 0.13-0.47, 0.26-0.47 moles of Na in orthoamphibole and hornblende, respectively) and both gedrite and hornblende are observed as the more Fe-rich phase in different coexisting mineral pairs ($X_{Fe,Oam}$ 0.39-0.44, $X_{Fe,Hbl}$ 0.40-0.44). Matrix plagioclase is andesine (An_{36-40}), and hornblende and garnet have low calcium contents (1.39-1.60 pfu in hornblende, X_{grs} 0.08-0.11).

Contrary to expectations, the mineral chemistry of this sample is somewhat different to that of 853-16 in which staurolite is also included entirely in garnet. This sample is more Fe-rich than its orthoamphibole-free counterpart and is far less calcic (e.g. An_{36-40} cf. An_{63-82} in sample 853-16). Staurolite us also significantly less Zn-rich than in other staurolite–garnet assemblages. These factors suggests that the assemblage staurolite–garnet–gedrite–hornblende–plagioclase–quartz occurs in rocks which are more Fe-Mg rich and perhaps more sodic than the staurolite–garnet-amphibolites described earlier.

Summary

The relatively consistent temporal relationship between garnet growth and the deformation phase preserved in the rocks implies that these two features provide a relative chronology for the other phases in the garnet amphibolites. Staurolite included in garnet (853-16, 950-077) must have grown relatively early in the rock's metamorphic history, whereas matrix staurolite (HR91-8) grew at some time after garnet and thus the growth of staurolite in 853-16 and 950-077. The staurolite in sample 950-105 is partly included in garnet and partly a matrix phase and is therefore likely to have formed at some stage intermediate to the other two samples. A possible explanation for this variability in the timing of staurolite growth in different samples is that the samples have different chemistry. However, the most obvious cause, X_{Fe}, does not vary coherently with the relative timing of the staurolite growth. Zn is relatively enriched in the latest and least enriched in the earliest staurolite–garnet assemblage. Although is a coherent relationship, since the assemblage is a prograde one (Chapters 3 and 4) staurolite would be expected to be stabilised earlier (at lower pressures and temperatures) in the presence of Zn. The opposite relationship is observed in the samples and so the presence of zinc in staurolite does not seem a valid explanation for the timing of staurolite growth.

The proportion of anorthite in plagioclase does vary coherently with the timing of staurolite growth (X_{An} low with early staurolite and high with later, matrix staurolite) and the loose correspondence between X_{An} and X_{grs} (Fig. A8.19) imply that this change in X_{An} may be due to changing Ca content of the entire assemblage. Figure A8.22 illustrates the relative positions of the different staurolite–garnet–hornblende–plagioclase equilibrium assemblages in the quaternary compatibility diagram NCAFm.

A8.5.3 Intermediate X_{Fe}, kyanite amphibolites

Amphibolites containing aluminous enclaves are typically unfoliated to only weakly foliated and sub-parallel kyanite, hornblende and orthoamphibole are generally the only aligned phases. Kyanite and staurolite form large porphyroblasts up to 1 cm across which, with their rim of pale feldspar, are clearly visible in hand specimen.

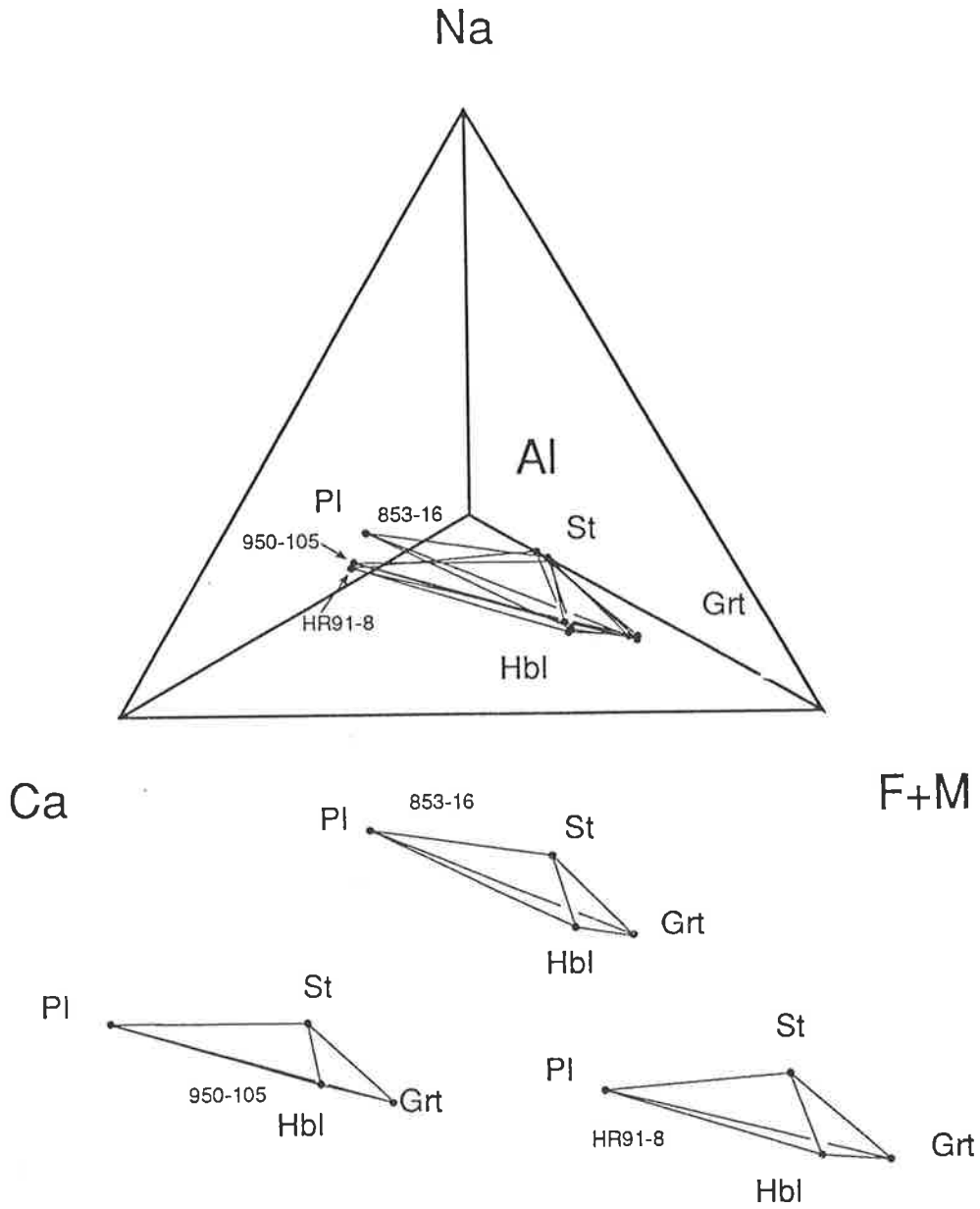

Figure A8.22. Quaternary NCAFm diagram illustrating the different positions of staurolite-garnet and staurolite-garnet-orthoamphibole assemblages in compositional space. Projected from quartz and aqueous vapour; N = $NaO_{1/2}$, C = CaO, A = $AlO_{3/2}$, Fm = FeO+ MgO.

Textural features

Very coarse grains and aggregates (2-10 mm) of kyanite are often embayed with small, relict, optically continuous grains near their margins. The weakly oriented kyanite grains may contain sub-parallel inclusion trails of fine plagioclase, quartz and accessory phases (e.g. rutile, Ti-Fe-ores). Kyanite is typically isolated from the hornblende–plagioclase ± quartz matrix and occurs at the centre of aluminous enclaves rimmed by staurolite–calcic plagioclase coronas. The outline of the aluminous enclaves in the hornblende–plagioclase ± orthoamphibole matrix is mimicked by both the kyanite–staurolite and staurolite grain boundaries (Fig. A8.23). Staurolite occurs as both single-phase aggregates and as part of an aluminous corona surrounding corundum or kyanite. It is generally surrounded by a plagioclase rim in the hornblende–plagioclase ± quartz matrix (Fig. A8.23).

Corundum occurs rarely in association with other highly aluminous phases (kyanite or, more often, staurolite) in silica-poor domains of quartz absent samples. The small grains are generally optically continuous and are surrounded by plagioclase in the hornblende–plagioclase matrix (Fig. A8.24) and in contact with staurolite. Corundum is never observed in contact with the hornblende-bearing matrix.

Hornblende and sometimes orthoamphibole form coarse euhedral grains which are weakly oriented in a polygonal matrix of plagioclase ± quartz. Small inclusions of plagioclase, quartz and accessory phases are typically concentrated toward the cores of hornblende grains to form randomly oriented to poorly defined straight inclusion trails. Hornblende is observed in contact with both matrix and corona plagioclase, quartz (if present) and staurolite. Coarse-grained, euhedral orthoamphibole grains cross-cut hornblende grains and are observed both parallel to and cross-cutting the hornblende foliation. Matrix plagioclase is optically zoned and euhedral. It rarely exhibits poorly developed twinning and where observed, twinning is not disturbed by deformational features. Quartz is also euhedral and generally displays undulose extinction. Accessory phases include rutile, apatite, zircon, ilmenite, magnetite and exsolved Ti-Fe oxides.

Mineral chemistry

Hornblende in kyanite-bearing amphibolites is typically quite Fe-rich, aluminous, sodic and calcium-rich ($X_{Fe,Hbl}$ 0.31-0.47, 0.93-1.43 Al^{vi}_{Hbl}, 0.21-0.90 Na, 1.60-1.93 Ca pfu) and falls into the tschermakitic-hornblende, tschermakite or ferroan pargasite classifications of Leake (1978). Gedrite is slightly less Fe-rich than co-existing hornblende ($X_{Fe,Oam}$ 0.30-0.42) and contains variable amounts of the tschermakite and edenite end-members (0.64-1.59 Al^{vi}_{Oam}, 0.12-0.52 Na pfu). Gedrite is typically less sodic and less aluminous that co-existing hornblende.

The majority of staurolite analyses from the Harts Range fall into the typical compositional ranges suggested by Griffen and Ribbe (1973) (Table A8.6). However, there are a significant number which have lower SiO_2 and higher Al_2O_3 and MgO contents than

Figure A8.23. Sketch of corroded kyanite porphyroblast separated by a staurolite-calcic plagioclase corona from the hornblende-plagioclase-quartz matrix (891-11). Width of view 2mm.

Figure A8.24. Sketch of corroded corundum with staurolite and plagioclase in a hornblende-plagioclase matrix (890-005a). Width of view 2mm.

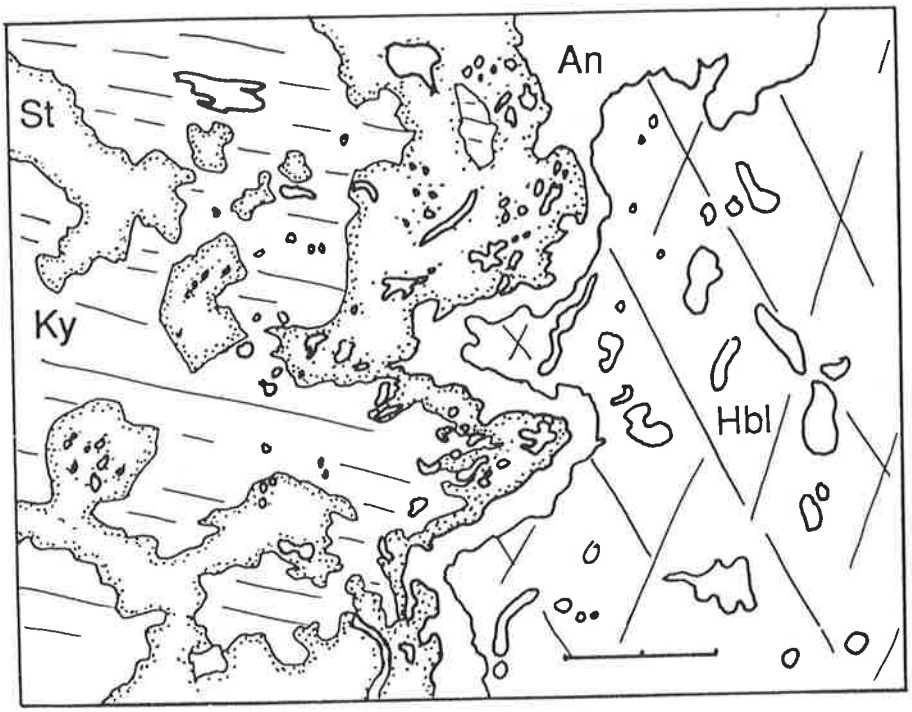
An
St
Ky
Hbl

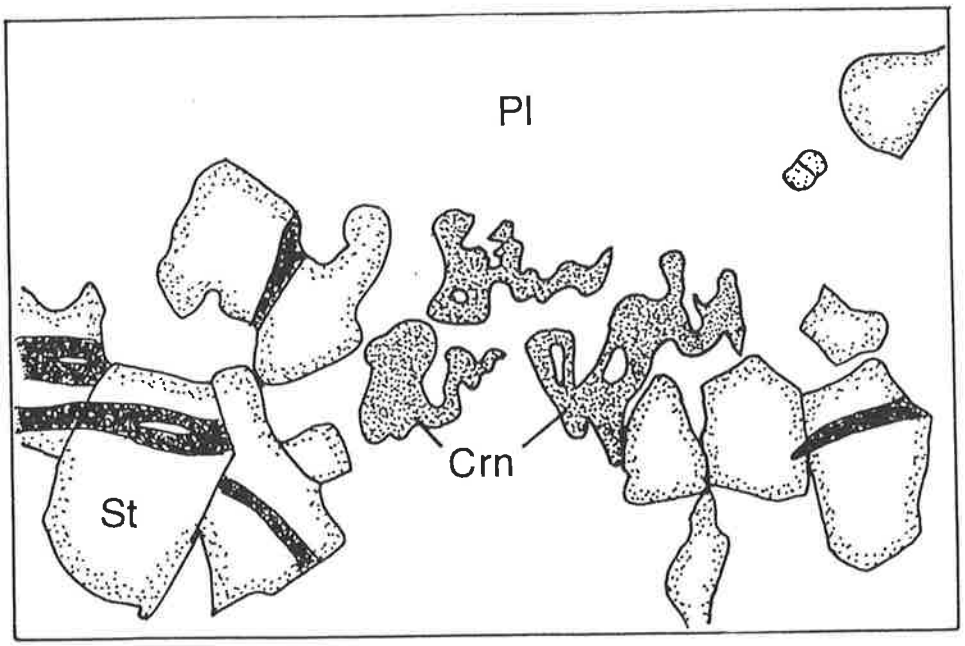
Pl
Crn
St

Griffen and Ribbe's (1973) usual ranges, which were determined mainly from rocks of pelitic affinity. Those more extreme analyses are similar to those of staurolite from amphibolites in Fiordland, New Zealand (Gibson, 1978). Comparison between analyses of staurolites from the Harts Range shows that Al_2O_3 and SiO_2 exhibit a negative correlation, suggesting that there is some substitution of Al for Si within the staurolite structure (Fig. A8.25). WDS Microprobe analyses confirm that the ZnO-content of staurolite from the Entia Dome is low (in the range 0.12-0.77 wt % ≡ 0.02-0.15 atoms pfu) and that sodium is virtually absent (0-0.02 pfu).

Sequences of analyses made across single grains of staurolite confirm that the grains are relatively homogeneous, with only a slight variation in the amount of Al (variation ~ 0.15 atoms pfu) and Si (variation ~ 0.1 atoms pfu) across the grain (Table A8.6). X_{Fe} typically increases *slightly* from core to rim and is in the range 0.60-0.77. Staurolite in kyanite, gedrite or hornblende amphibolites is less iron rich than those in garnet bearing amphibolites.

Plagioclase shows a wide variation in composition (An_{5-92}), though the population in each sample typically consists of two or more distinct ranges, each with compositional variation of ≤ 15%. These generally include a calcic plagioclase associated with staurolite in a corona texture and a more sodic composition in the matrix of the sample. Analyses of kyanite and corundum reveal that those phases contain limited impurities; < 0.01 and < 0.02 atoms per unit formula respectively. Figure A8.26 shows the variation in the compositions of the kyanite–staurolite assemblage projected from hornblende, plagioclase, quartz and aqueous vapour.

Interpretation

The unfoliated to weakly foliated nature of the kyanite-bearing assemblages developed in more Fe-rich, aluminous amphibolites and the preservation of high surface energy corona textures suggest that the foliated phases kyanite–hornblende ± orthoamphibole formed late in or subsequent to a phase of deformation and that the rocks have experienced no local deformation since the formation of the enclaves. As orthoamphibole cross-cuts the hornblende grains it is interpreted to post-date the growth of hornblende, however the lack of reaction textures between those phases suggests that orthoamphibole–hornblende remained a stable assemblage.

The close correspondence between the shape of each corroded kyanite porphyroblast, its staurolite rim and the outline of the aluminous enclaves suggests that the matrix phases (hornblende ± plagioclase ± quartz) were once stable with the inner phase, kyanite, but that reaction between kyanite and hornblende later produced the enclaves of staurolite and plagioclase.

The high surface area to volume ratio of the coronas and the localised growth of the reaction products implies that diffusion of at least one of the components involved in the reaction was insufficiently fast for textural equilibration to occur. The localisation of aluminium-rich phases suggests that it is the slow diffusion of aluminium which controlled the position at which the product phases developed. Staurolite is considered to have formed on the

Figure A8.25. Number of moles of Si per unit formula plotted against number of moles of Al for staurolite from the Entia gneiss complex amphibolites. Formula calculated to 46O.

Figure A8.26. Ternary AFM diagram illustrating the compatibility relations in staurolite-kyanite and staurolite amphibolites projected from hornblende, plagioclase, quartz and aqueous vapour; A = AlO3/2, F = FeO, M = MgO.

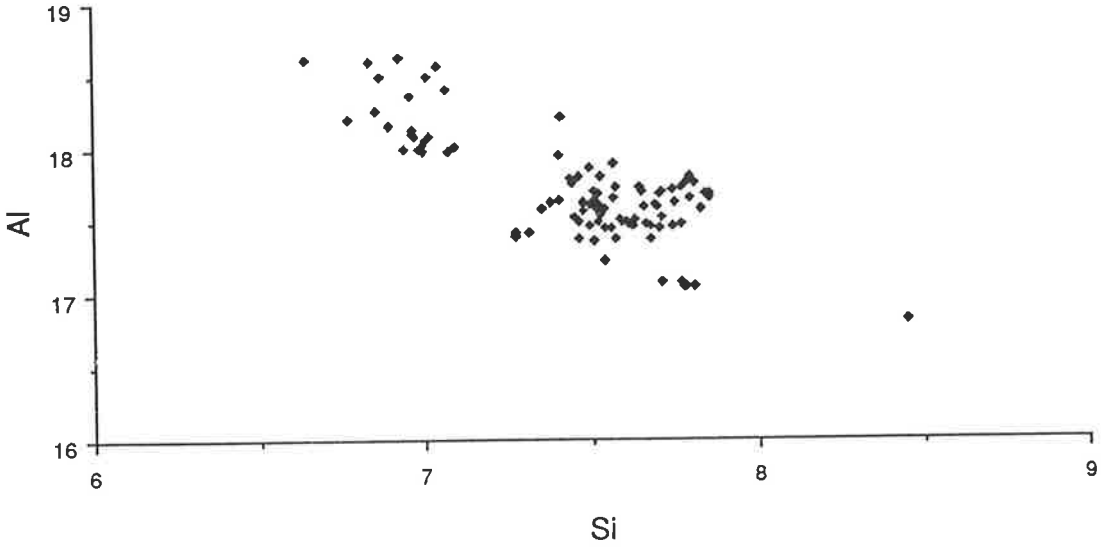
19
18
17
16
Al
6
7
8
9
Si

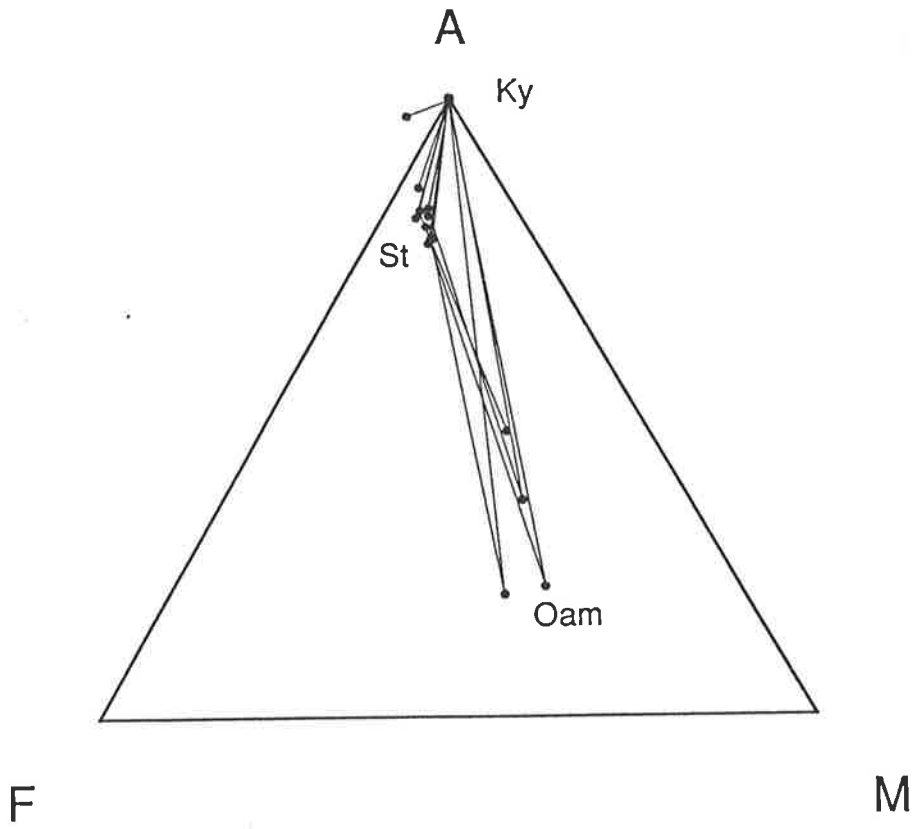
A
Ky
St
Oam
F
M

boundaries of former kyanite hornblende equilibria, where aluminium was released from the kyanite structure. As the kyanite and hornblende were consumed, staurolite would have grown inward, towards the source of Al, while plagioclase developed in place of hornblende ± plagioclase ± quartz. The textures, mineral chemistry and compatibility relations of particular kyanite–staurolite amphibolite assemblages are discussed in the next section.

A8.5.3 Detailed descriptions of kyanite amphibolites

Kyanite–staurolite–anorthite corona amphibolites (e.g. samples 890-5a, 11, 12, 15, 891-11)

Embayed kyanite porphyroblasts form the nucleus of aluminous enclaves which are surrounded by a staurolite corona (X_{Fe} 0.60-0.73; 0.12-0.28 wt % ≡ 0.02-0.05 ZnO pfu) and a calcic plagioclase rim. The composition of plagioclase involved in these corona textures is widely variable between samples (An_{36-49}, An_{50-62}, An_{58-77}, An_{82-92}) but is consistently more calcic than that co-existing with matrix hornblende (An_{23}, An_{38-49}, An_{48-60}). Hornblende in kyanite–staurolite amphibolites is widely variable in composition and covers almost the full range of those observed in the amphibolites.

Corundum–staurolite–anorthite corona amphibolites (e.g. sample 890-009)

In quartz-free samples corundum occupies a similar position to that of kyanite in more siliceous rocks. It occurs as small optically continuous aggregates in quartz-poor amphibolites, rimmed by bytownite plagioclase (An_{85-87}) and in contact with staurolite (X_{Fe} 0.67-0.68; 0.19-0.27 wt % ≡ 0.04-0.06 ZnO pfu), however there are no well-developed staurolite–plagioclase coronas in corundum-bearing amphibolites. Hornblende (tschermakite) in corundum-bearing amphibolites is quite sodic (0.58-0.59 moles of Na pfu) and contains significant proportions of the iron and tschermakite end-members (X_{Fe} 0.45-0.46, Al^{vi} 1.15-1.25). Hornblende also has a relatively low Ca content (1.65-1.67 pfu). The textures in these silica-poor samples are similar to those in the more silica-rich rocks, with the exception that corundum, rather than kyanite, appears to have been stable with the matrix hornblende–plagioclase, early in the metamorphic history. Corundum and hornblende later became metastable and staurolite–plagioclase are the products of this instability. The quartz-free nature of the corundum-bearing samples means that they may not be represented on the NCAFm or AFM compatibility diagrams used so far.

Staurolite–anorthite corona amphibolites (e.g. samples 890-5b, 14, 85-72, HR91-3)

In addition to its presence in coronas surrounding kyanite or corundum, staurolite also occurs as a porphyroblastic phase which is generally separated from the hornblende–plagioclase mosaic by a rim of calcic plagioclase. Several samples contain hornblende in contact with staurolite along smooth, apparently equilibrium grain boundaries. Chemically

these rocks are similar to other corona bearing amphibolites with $X_{Fe,Hbl}$ 0.37-0.45 however staurolite is slightly more Fe-rich ($X_{Fe,St}$ 0.62-0.77) and ZnO levels in staurolite are relatively low in comparison to other samples (0.19-0.30 wt % ≡ 0.04-0.06 ZnO pfu). The tschermakite or ferroan pargasite contains significant proportions of both tschermakite and edenite end-members (Al^{vi} 1.06-1.43, 0.52-0.81 moles of Na pfu) but relatively low Ca (1.65-1.69 pfu). The plagioclase involved in coronas surrounding staurolite is again more calcic (e.g. An_{51-57}, An_{80-90}) than that observed in the hornblende–plagioclase matrix (e.g. An_{39-47}, An_{51-90}, An_{78-83}).

The similarity of the mineral textures in kyanite-bearing and kyanite-absent staurolite amphibolites, most importantly the presence of plagioclase rims surrounding staurolite, implies that the kyanite-absent staurolite assemblages are evidence of a reaction gone to completion. The reactant, probably kyanite, was consumed, leaving the staurolite and plagioclase coronas in the hornblende–plagioclase–quartz matrix.

Kyanite–staurolite–anorthite coronas in gedrite amphibolites (e.g. samples 890-8, 16, 853-93)

Gedrite-bearing kyanite–staurolite amphibolites contain similar reaction textures to other kyanite–staurolite amphibolites. The corroded kyanite porphyroblast are rimmed by a corona of staurolite which is separated from the hornblende–orthoamphibole–plagioclase (An_{26-78})-quartz matrix by a rim of calcium-rich plagioclase (e.g. An_{78}). Both foliated and randomly oriented gedrite cross-cut the foliated hornblende grains however, no disequilibrium textures are observed.

As for other gedrite bearing amphibolites, tschermakitic hornblende (Leake, 1978) has lower aluminium and iron contents than in orthoamphibole-absent samples ($X_{Fe,Hbl}$ 0.31-0.42, Al^{vi}_{Hbl} 0.94-1.38). Hornblende contains high levels of calcium and sodium (1.47-2 CaO pfu, 0.21-0.58 moles Na pfu) and is more Fe-rich and more sodic than gedrite (Leake, 1978) ($X_{Fe,Oam}$ 0.30-0.42, 0.12-0.52 moles Na pfu). Gedrite has a more variable aluminium content (Al^{vi}_{Oam} 0.67-1.59) than co-existing hornblende. The composition of staurolite is also at the more magnesian end of the compositional range exhibited in staurolite-amphibolites from the Entia gneiss complex ($X_{Fe,St}$ 0.65-0.72) and has a low to intermediate ZnO content (0.02-0.05 ZnO pfu, 0.19-0.27 wt %).

The similarity of the textures and mineral compositions of gedrite-bearing kyanite–staurolite amphibolites to those in other kyanite–staurolite amphibolite suggests that despite their compositional differences, the rocks experienced reactions similar to those in gedrite-absent rocks. The divariant assemblage kyanite–staurolite–gedrite plots centrally in the AFM (+hornblende, plagioclase, quartz) compatibility diagram at more aluminous and less Fe-rich compositions than those involving staurolite–garnet–gedrite (described in Section A8.5.2). The assemblage also plots to the Mg-rich side of the trivariant kyanite–staurolite assemblages (Fig. A8.26).

A8.5.4 Magnesium-rich, cordierite amphibolites

Cordierite-rich rocks form rare isolated pods of blue-violet, coarse-grained, unfoliated rocks. Kyanite, anthophyllite, reddish rutile and pale-green hornblende are visible as (relatively) small grains distributed throughout the rocks, while silvery talc and chlorite are most obvious on the surface of small boulders where they have formed a focal point for weathering processes.

Textural features

Kyanite porphyroblasts are heavily embayed, most severely along cleavage planes and have associated optically continuous outliers. Kyanite is surrounded by moats of coarse grained, relatively unaltered cordierite which may exhibit weakly developed twinning. Pale-green, weakly pleochroic clinoamphibole and colourless to pale-brown orthoamphibole are surrounded by cordierite and also exhibit corroded grain boundaries, especially in the vicinity of kyanite (Fig. A8.27). Kyanite, hornblende and orthoamphibole typically define a very weak foliation. Where present, plagioclase shows well developed twinning and is unzoned. Plagioclase may contain inclusions of cordierite, apatite, rutile and zircon. Fine grained randomly oriented talc, chlorite and muscovite are observed to overgrow hornblende, anthophyllite and cordierite. Accessory phases include rutile, apatite and zircon.

Mineral chemistry

The Mg-rich nature of the bulk composition (Fig. A8.1) is reflected in the low X_{Fe} of magnesio-hornblende (Leake, 1978) ($X_{Fe,Hbl}$ 0.15-0.27), anthophyllite (Leake, 1978) ($X_{Fe,Oam}$ 0.07-0.16) and cordierite ($X_{Fe,Crd}$ 0.07-0.13, Table A8.7). Hornblende is much more aluminous and sodic than co-existing orthoamphiboles in cordierite-amphibolites (Al^{vi}_{Hbl} 0.26-1.40, 0.07-0.65 atoms of Na pfu in hornblende and, Al^{vi}_{Oam} 0.06-0.70 with zero Na in orthoamphibole). Hornblende has a particularly high Ca content (1.63-1.80 pfu). Plagioclase exhibits a wide range of compositions both between and within samples. Despite their similar mineral textures, kyanite–cordierite–hornblende, kyanite–cordierite–orthoamphibole–hornblende and cordierite–hornblende rocks have similar but distinct mineral chemistry and this is summarised below.

A8.5.5 Detailed descriptions of cordierite amphibolites

Kyanite–cordierite hornblende rocks (e.g. samples 950-95, 100)

Pale green corroded magnesio-hornblende and corroded kyanite are surrounded by cordierite (Fig. A8.28). The hornblende is much more magnesium-rich than in more typical amphibolites ($X_{Fe,Hbl}$ 0.16-0.20), but retains substantial proportions of the tschermakite and

Figure A8.27. Sketch of corroded anthophyllite and kyanite in cordierite with talc and chlorite (853-74). Scale bar = 2mm.

Figure A8.28. Sketch of corroded hornblende and kyanite in cordierite (950-100). Width of view 2mm.

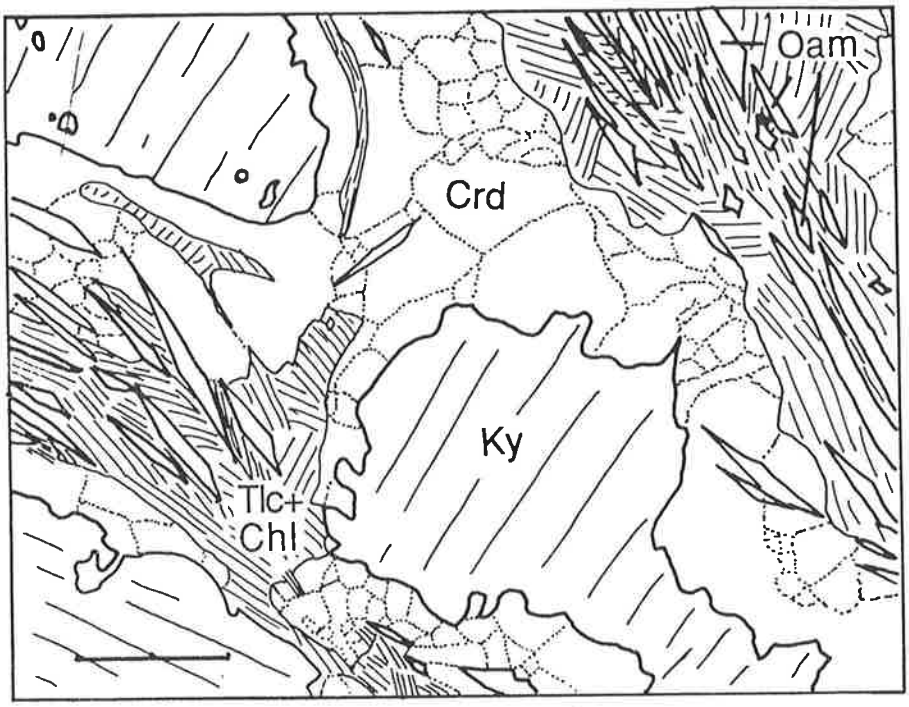
Oam
Crd
Ky
Tlc+
Chl

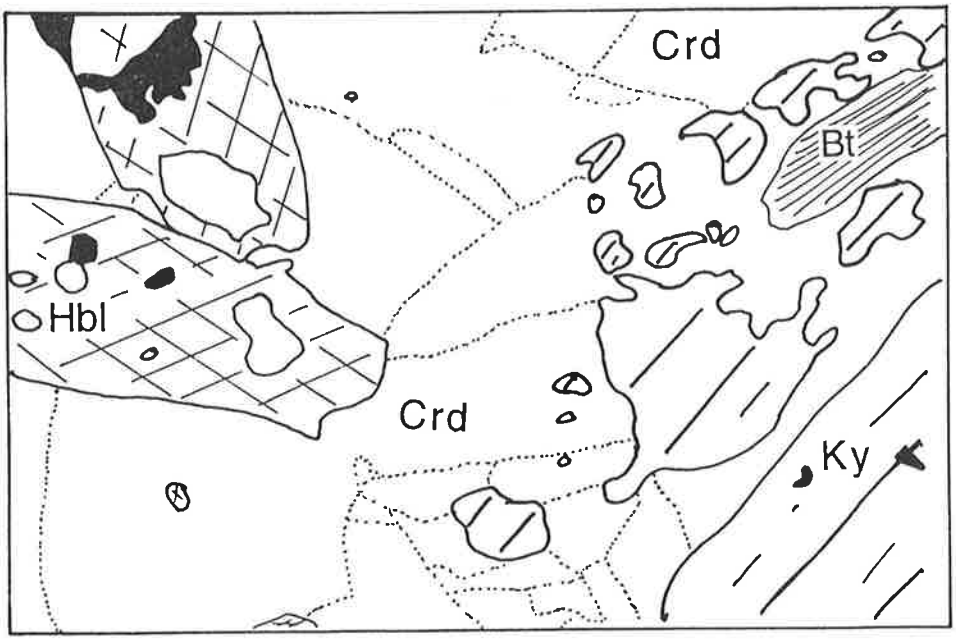
Crd
Bt
Hbl
Crd
Ky

Table A8.7. Selected probe data from kyanite-cordierite (950-95, 950-100) and kyanite-cordierite-anthophyllite-amphibolites (950-047) recalculated according to Appendix A1

950-95				
	Crd	Pl	Hbl	Ky
SiO2	49.41	56.93	45.94	37.22
TiO2	0.05	0.14	0.64	0.00
Al2O3	34.24	27.30	14.54	58.54
FeO	2.05	0.18	7.07	0.72
MnO	0.07	0.00	0.12	0.11
MgO	12.60	0.00	15.78	2.51
CaO	0.28	9.06	10.86	0.33
Na2O	0.26	6.21	1.32	0.00
K2O	0.00	0.29	0.25	0.00
Cr2O3	n.a.	n.a.	n.a.	n.a.
ZnO	n.a.	n.a.	n.a.	n.a.
Total	99.0	100.1	96.5	99.4
Si	4.926	2.553	6.556	1.018
Ti	0.004	0.005	0.069	0.000
Al	4.024	1.443	2.446	1.888
Fe2+	0.171	0.007	0.844	0.016
Mn	0.006	0.000	0.015	0.003
Mg	1.872	0.000	3.356	0.102
Ca	0.030	0.435	1.661	0.010
Na	0.050	0.540	0.365	0.000
K	0.000	0.017	0.046	0.000
Cr	-	-	-	-
Zn	-	-	-	-
Total	11.083	4.999	15.357	3.038
An		0.45		
XFe	0.084		0.201	
Aliv			1.444	
Alvi			1.003	
Xalm				
Xpy				
Xgrs				
Xsps				
ps				

950-100							
	Hbl	Crd	Crd	Ky	Rt	Hbl	Crd
SiO2	47.33	49.67	48.26	35.87	0.00	47.24	50.60
TiO2	0.41	0.00	0.00	0.06	99.75	0.75	0.08
Al2O3	14.51	33.22	32.91	62.00	0.10	13.20	34.65
FeO	6.44	1.99	1.79	0.19	0.00	5.82	1.74
MnO	0.25	0.00	0.21	0.13	0.05	0.32	0.11
MgO	16.68	12.15	12.23	1.73	0.00	16.90	12.22
CaO	11.32	0.35	0.22	0.23	0.00	11.16	0.25
Na2O	0.53	0.04	0.03	0.00	0.00	1.23	0.00
K2O	0.23	0.00	0.00	0.00	0.00	0.10	0.00
Cr2O3	n.a.	n.a.	n.a.	n.a.	n.a.	n.a.	n.a.
ZnO	n.a.	n.a.	n.a.	n.a.	n.a.	n.a.	n.a.
Total	97.7	97.4	95.7	100.2	99.9	96.7	99.6
Si	6.631	5.015	4.967	0.972	0.000	6.687	4.987
Ti	0.043	0.000	0.000	0.001	0.999	0.080	0.006
Al	2.396	3.955	3.993	1.980	0.002	2.203	4.026
Fe2+	0.755	0.168	0.154	0.004	0.000	0.689	0.143
Mn	0.030	0.000	0.018	0.003	0.001	0.038	0.009
Mg	3.482	1.829	1.876	0.070	0.000	3.565	1.796
Ca	1.699	0.038	0.024	0.007	0.000	1.693	0.026
Na	0.144	0.007	0.006	0.000	0.000	0.338	0.000
K	0.041	0.000	0.000	0.000	0.000	0.018	0.000
Cr	-	-	-	-	-	-	-
Zn	-	-	-	-	-	-	-
Total	15.221	11.012	11.039	3.037	1.001	15.310	10.994
An							
XFe	0.178	0.084	0.076			0.162	0.074
Aliv	1.369					1.313	
Alvi	1.027					0.889	
Xalm							
Xpy							
Xgrs							
Xsps							
ps							

950-047					
	Hbl	Pl	Oam	Crd	Rt
SiO2	46.97	50.45	49.19	49.82	0.19
TiO2	0.83	0.00	0.00	0.00	98.96
Al2O3	14.64	32.37	11.46	34.00	0.34
FeO	6.33	0.00	5.40	1.65	0.18
MnO	0.25	0.11	0.31	0.10	0.00
MgO	16.32	0.00	28.64	12.01	0.08
CaO	11.13	14.62	0.04	0.08	0.02
Na2O	0.83	3.48	0.00	0.00	0.27
K2O	0.15	0.00	0.00	0.00	0.02
Cr2O3	n.a.	n.a.	n.a.	n.a.	n.a.
ZnO	n.a.	n.a.	n.a.	n.a.	n.a.
Total	97.45	101.0	95.0	97.66	100.1
Si	6.598	2.277	6.809	5.004	0.003
Ti	0.088	0.000	0.000	0.000	0.990
Al	2.425	1.722	1.871	4.026	0.005
Fe2+	0.744	0.000	0.625	0.139	0.002
Mn	0.030	0.004	0.036	0.009	0.000
Mg	3.417	0.000	5.908	1.798	0.002
Ca	1.675	0.707	0.006	0.009	0.000
Na	0.226	0.305	0.000	0.000	0.007
K	0.027	0.000	0.000	0.000	0.000
Cr	-	-	-	-	-
Zn	-	-	-	-	-
Total	15.228	5.014	15.256	10.983	1.009
An		0.70			
XFe	0.179		0.096	0.072	
Aliv	1.402		1.191		
Alvi	1.023		0.680		
Xalm					
Xpy					
Xgrs					
Xsps					
ps					

edenite molecules and a high Ca content (Al^{vi}_{Hbl} 0.91-1.15, 0.13-0.42 Na pfu, 1.63-1.80 Ca pfu, Table A8.7). Cordierite is very Mg-rich (X_{Fe} 0.07-0.10). The composition of plagioclase is consistent within each sample but, as in most rock-types, varies widely between them (e.g. An_{0-2}, An_{45-49}).

Kyanite–cordierite–anthophyllite hornblende rocks (e.g. sample 950-047)

Corroded magnesio-hornblende, anthophyllite and kyanite are again surrounded by coarse, rarely twinned cordierite. The proportion of the edenite molecule in magnesio-hornblende is substantially higher (0.10-0.65 Na pfu) in anthophyllite-bearing cordierite amphibolites than in anthophyllite-absent samples, despite the lack of any sodium in the anthophyllite. Iron and aluminium contents in both hornblende and anthophyllite are low ($X_{Fe,Hbl}$ 0.17-0.19, Al^{vi}_{Hbl} 0.26-1.11, $X_{Fe,Oam}$ 0.07-0.16, Al^{vi}_{Oam} 0.06-0.70, Table A8.7) and the sample contains three different plagioclase compositions (An_2, An_{42-51}, An_{61-87}) in different sub-domains. Cordierite is the most magnesian phase present, with X_{Fe} in the range 0.07-0.10.

Cordierite–hornblende rocks (e.g. samples 950-092, 083)

In samples where kyanite is not preserved, the corroded magnesio-hornblende is typically significantly more Fe- and Al-rich ($X_{Fe,Hbl}$ 0.15-0.27, Al^{vi}_{Hbl} 0.82-1.40) than in other cordierite-bearing rocks. The hornblende contains less sodium (0.07-0.13 Na pfu) and plagioclase is more anorthite-rich (An_{41-45}, An_{72}) than in kyanite-bearing cordierite amphibolites. The coarse grained, fresh cordierite in these samples has a slightly higher X_{Fe} in the range 0.07-0.13, reflecting the slightly more Fe-rich nature of the samples.

Interpretation

The Mg-rich nature of these cordierite-bearing rocks is well demonstrated by both the Mg-rich mineral compositions and the positions of the assemblages on a compatibility diagram such as that in Fig. A8.29. Slight crossing of the tie-lines of different mineral pairs and three-phase assemblages is thought to be due to slight differences in the timing and hence temperature of equilibration. However, overall the phase relations in these cordierite-bearing Mg-rich amphibolites are consistent (Fig. A8.29). The weak alignment of kyanite, hornblende and anthophyllite porphyroblasts implies that these phases developed during a phase of active deformation. The presence of weak inclusion trails in some plagioclase grains suggests that it too may have been an equilibrium phase at this time. Kyanite is not observed coexisting with either hornblende or anthophyllite in any of the samples collected from the Harts Range and the corroded state of kyanite, hornblende or anthophyllite, the lack of equilibrium grain-boundaries between these phases and the ubiquitous presence of randomly oriented cordierite (± plagioclase) between them suggest that at some time after deformation ceased, kyanite began to

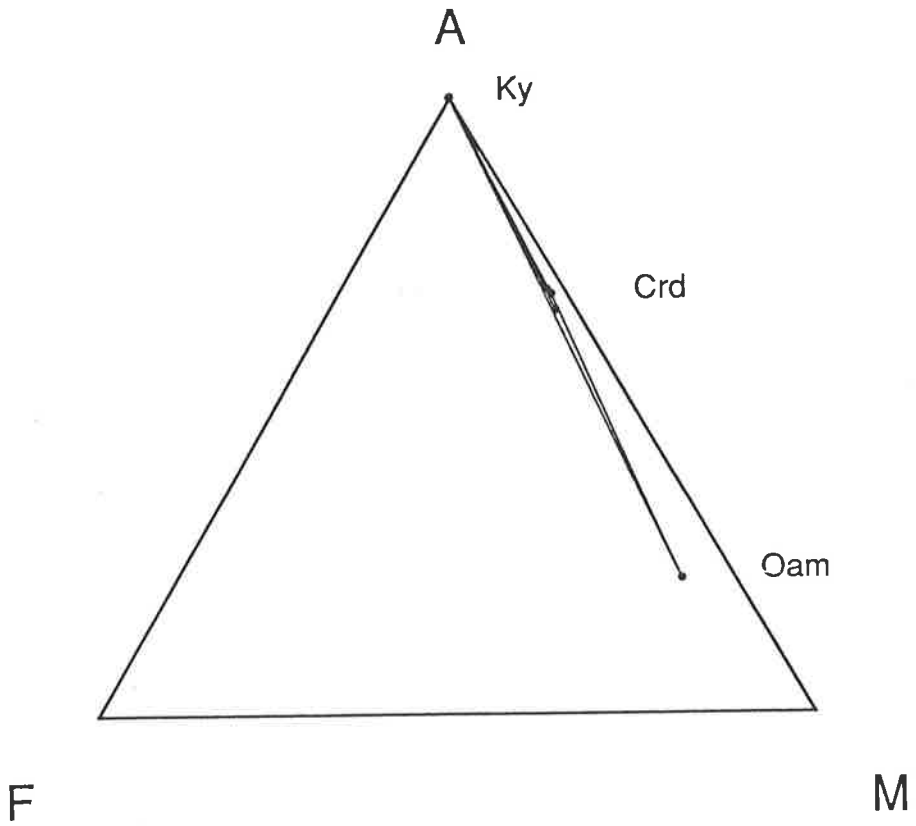

Figure A8.29. Compatibility diagram for Mg-rich aluminous assemblages. AFM, projected from hornblende, plagioclase, quartz and aqueous vapour; A = $AlO_{3/2}$, F = FeO, M = MgO.

react with hornblende and anthophyllite and the cordierite (± plagioclase) produced formed moats separating the reactant phases. As in the kyanite–staurolite corona amphibolites, these corona textures probably result from the slow diffusion of aluminium during reaction and as the reactive assemblage is preserved in some samples, it seems likely that the very slow diffusion of the product components limited the extent of the reaction. In some samples kyanite was exhausted, leaving only cordierite and hornblende ± anthophyllite.

A8.6 Compatibility relations in low variance assemblages

As for all metamorphic rocks, the stability of any particular phase or mineral association is dependent on the bulk-composition of the rock and on the pressure and temperature at which the rock equilibrated. Thus, variations in the abundances of the major elements will cause variation in the mineralogy of the rocks. The amphibolites analysed from the Entia gneiss complex show a wide variation in bulk rock chemistry (Tables A8.2 to A8.7) which is most obvious in the rocks' Si, Ca, Fe, Mg and Na-contents. The variation in the bulk chemistry of amphibolites has allowed several different low variance assemblages to develop. For example, rocks which have more than 5 wt % CaO typically contain hornblende and plagioclase, while the nature of coexisting phases is controlled by the variability of Na_2O, Al_2O_3 and Mg content. More Fe-rich and sodic samples contain garnet and more aluminous phases. Rocks containing significant Na_2O (≥ 1.3 wt %) with intermediate to high Mg# (Mg/(Fe+Mg) (48-66) stabilize hornblende–epidote–plagioclase assemblages to the exclusion of others (Table A8.1). Lower CaO and Na_2O amphibolites with intermediate Mg# (~60) contain gedrite whereas those with relatively high abundances of FeO (Mg# < 38) are often correspondingly Al-rich and tend to contain aluminous phases such as staurolite, kyanite (Table A8.1) or, in rocks with especially low Mg# (< 31), garnet with hornblende. Although their coarse grainsize and inhomogeneous nature does not allow for easy representative sampling of the cordierite-bearing samples for bulk rock analysis, the fairly pure Mg-Al-Si nature of most of the phases implies that these assemblages result from a relatively simple bulk composition with low levels of Ca, Fe and Na.

These simple relationships between bulk composition and mineralogy are mirrored in compatibility diagrams for the rocks (Fig. A8.1). Less aluminous and more aluminous rocks are represented separately in NCAFm (+ quartz and aqueous vapour, Fig A8.30) and AFM (+hornblende, plagioclase, quartz and aqueous vapour, Fig A8.1) and each is discussed below.

A8.6.1 Less aluminous assemblages

A coherent set of trivariant equilibrium volumes is represented in Fig. A8.30 for the quaternary system NCAFm ($NaO_{1/2}$-CaO-$AlO_{3/2}$-FeO+MgO, projected from quartz and aqueous vapour). The central position of hornblende and the variable composition of plagioclase explains the abundance of these phases in rocks of diverse bulk composition.

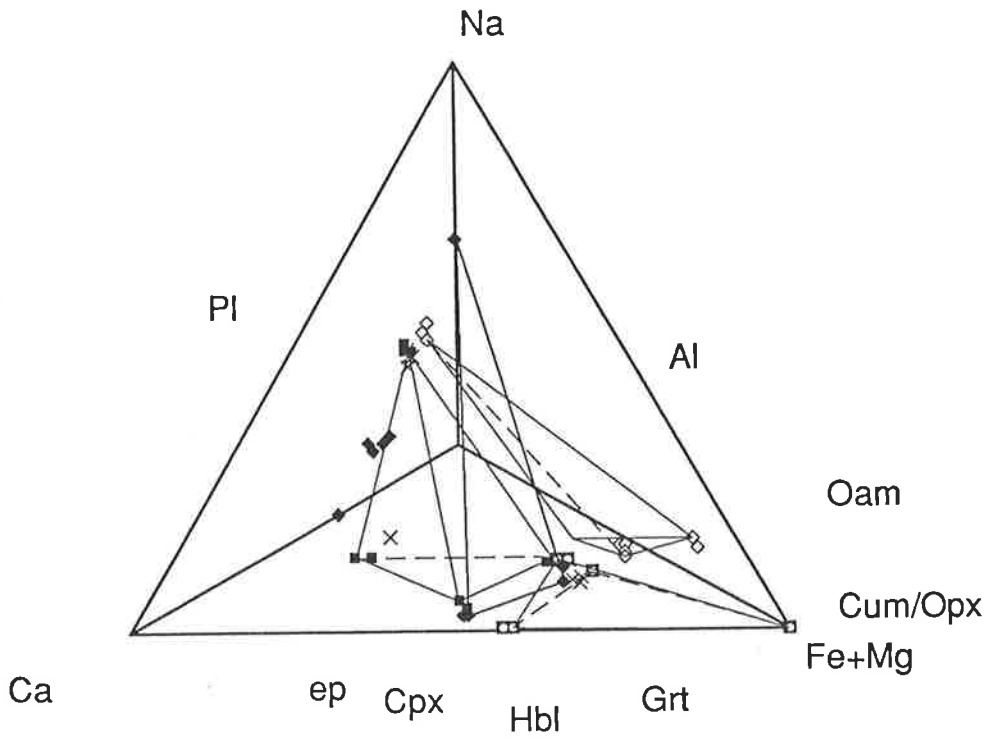

Figure A8.30. Quaternary NCAFm diagram illustrating the relative positions of the less aluminous amphibolite phases in compositional space. Projected from quartz and aqueous vapour; N = $NaO_{1/2}$, C = CaO, A = $AlO_{3/2}$, Fm = FeO+ MgO.Solid squares - sample 852-88 (from Stewart,1985); cross - sample 853-145; open diamonds - 890-13; solid diamonds - 853-180; solid square with circle - HR91-5.

Samples whose bulk composition falls on the calcic side of hornblende and plagioclase contain clinopyroxene and epidote in addition to these phases. Garnet, cummingtonite and orthopyroxene plot near the FeO+MgO apex of the compositional volume and these may co-exist with either hornblende, plagioclase and clinopyroxene for Ca-richer samples or with orthoamphibole, staurolite, cordierite or kyanite for more aluminous amphibolites. Higher variance assemblages such as hornblende–epidote–plagioclase, hornblende–clinopyroxene–plagioclase, garnet–orthoamphibole–plagioclase and hornblende–plagioclase fill out much of the remainder of the volume. Very Ca-rich or Na-rich compositions are not commonly represented in amphibolites.

A8.5.2 More aluminous assemblages

The variable nature of the more aluminous assemblages in the Harts Range amphibolites and the concentration of phases along the A-F-M-rich portion of the amphibolite compositional volume (cf. Fig. A8.30) implies that this portion of compositional space is very reactive. The presence or absence of a particular assemblage in Al-Fe-Mg-rich rocks is strongly dependent on the X_{Fe} of the bulk-composition (Figs. A8.1). Fe-rich samples contain staurolite–garnet–orthoamphibole (+hornblende, plagioclase, quartz and aqueous vapour), more aluminous, or slightly less Fe-rich samples develop kyanite–staurolite–orthoamphibole, whereas Mg-rich samples contain kyanite–cordierite–orthoamphibole assemblages. These assemblages fill the majority of the compositional volume (projected from hornblende, plagioclase, quartz and aqueous vapour), however for less aluminous assemblages, cummingtonite–garnet is observed. The presence of cummingtonite in similar rock-types (e.g. Spear, 1982; Chapter 6) and in the very Fe-rich, partly relict Harts Range sample HR91-5, suggest that cummingtonite might also be stable in more Mg-rich rocks, under metamorphic conditions appropriate to the Harts Range region. Higher grade samples might be expected to develop clinopyroxene or orthopyroxene as μ_{H_2O} decreases. For very Mg-rich rocks chlorite may be stable, however the lack of equilibrium chlorite in any of the Harts Range samples suggests that chlorite is only stable at lower metamorphic grades.

Appendix 9: The construction of compatibility diagrams from mineral composition data

A9.1 Introduction

The chemistry of amphibolites and their constituent phases are exceedingly complex and may involve as many as eleven composition variables (e.g. Na_2O-CaO-FeO-MgO-Al_2O_3-SiO_2-H_2O-TiO_2-O_2-K_2O-CO_2). Even in simplified model compositions, six or seven independent compositional variables are necessary to adequately describe them. As a result of this, understanding the compatibility relations of amphibolites relies heavily on the ability of the petrologist to further simplify the compositional space using the concept of projections. Projection schemes are best known in the pelite system following Thompson (1957) who simplified the KFMASH system to the ternary AFM by "projecting" from muscovite, quartz and H_2O. (In fact Thompson (1957) does not project from water, as such, but rather assumes that the rocks of interest either equilibrated with a free, pure H_2O phase or were under the influence of some externally controlled humidity.) The method used for this "projection" involves writing the phase to be projected in terms of a new set of components defined by the projection phases and the projection plane. This is similar to balancing a reaction between the projected phase to the projection points and projecting phases. For such simple projection phases as quartz, vapour, and even muscovite, this mapping of the phases onto the projection co-ordinate system is relatively simple, however, in the more complex amphibolite case, even the potential projection phases are compositionally complex. Thus, a more generalised, less labour-intensive method is required. Greenwood (1975) has demonstrated the utility of the linear algebraic approach in mapping the phases from a simple set of components to the more complex set involving the projection phases and projection plane. This appendix presents a *Mathematica*^{TM} program which utilises linear algebra to carry out projections and balance reactions even in complex compositonal systems.

A9.2 The linear algebraic approach

Recasting the phases in terms of the new set of components is begun by writing a set of equations for the amount of the simple chemical components (SiO_2, FeO, MgO etc.) involved in the projection. As an illustration, I will assume that we wish to plot clinochlore ($Mg_5Al_2Si_3O_{10}(OH)_8$) onto the binary Al_2O_3-MgO, projected from quartz (SiO_2) and H_2O. The equation listing the nimber of moles of SiO_2 in each of the phases would be:

$$3 * r_{chl} + 0 * r_A + 0 * r_M + 1 * r_q + 0 * r_v = 0.$$

That is, the amount of silica in chlorite (i.e. 3) multiplied by the coefficient of chlorite (which we wish to determine), plus the amount of silica in Al_2O_3 (i.e. 0) multiplied by the coefficient of Al_2O_3, plus the amount of silica in MgO (0) multiplied by the coefficient of MgO, plus the amount of silica in quartz (1) multiplied by the coefficient of quartz, plus the amount of silica in vapour (0) multiplied by the coefficient of vapour . A similar equation can be written for each of the other components: for MgO,

$$5 * r_{chl} + 0 * r_A + 1 * r_M + 0 * r_q + 0 * r_v = 0,$$

for Al_2O_3,

$$1 * r_{chl} + 1 * r_A + 0 * r_M + 0 * r_q + 0 * r_v = 0,$$

for OH,

$$8 * r_{chl} + 0 * r_A + 0 * r_M + 0 * r_q + 2 * r_v = 0.$$

Thus we have four equations in five unknowns, creating the 4 * 5 coefficient matrix, A,

$$A = \begin{bmatrix} 3 & 0 & 0 & 1 & 0 \\ 5 & 0 & 1 & 0 & 0 \\ 1 & 1 & 0 & 0 & 0 \\ 8 & 0 & 0 & 0 & 2 \end{bmatrix}$$

which, when multiplied by the vector r_i of reaction coefficients,

$$r_i = \begin{bmatrix} r_{chl} \\ r_A \\ r_M \\ r_q \\ r_v \end{bmatrix}$$

gives 0. The solution to this equation is given by

$$r_i = \mathbf{N}[A],$$

where $\mathbf{N}[A]$ is the *nullspace* of A.

Note that A is the transpose of the matrix made up of a set of equations which write the composition of each of the phases (and projection phases and projection points) in terms of the components, e.g. for clinochlore;

$$5 * MgO + 1 * Al_2O_3 + 3 * SiO_2 + 8 * OH = 0.$$

The solution of the equation is then

$$r_i = \mathbf{N}[\mathbf{B}^T]$$

because $\mathbf{B} = A^T$.

These matrix manipulations have been utilised in a *Mathematica*™ package, **compatibility.m** which was written by Dr Michael Sandiford in order to simplify the projection of amphibolite phases into compositional space. The package allows the projection of a set of phases from a set of arbitrary points onto an arbitrary line, plane or volume, and gives as its output a binary, ternary or quaternary compatibility diagram. Quaternary diagrams are output as a stereo-pair. The program is written for *Mathematica*™ (version 2.04) in the style recommended by Maeder's (1990) Programming in *Mathematica*™ utilising the concepts of specific contexts and packages to make the program more robust. A copy of the program, an example input file and an example operating file follow.

A9.3 The program, compatibility.m

The program **compatibility.m** consists of 3 parts; Rock, Triplot and Reaction. Rock reads the information contained in the input file and converts it into a table consisting of the mineral formulae and their labels, both of which are used later in the package. Triplot assemblages the matrices **B** (see previous section) from the input information. It includes 2- and 3-dimensional plotting routines (Graph1 and Graph2) and carries out the matrix calculations to determine the coefficients of the projected phases, projection plane apices and projection phases or components for each of the phases to be projected. Triplot also converts this output and information regarding plotting coordinates, labels etc into a form which can be used as input by the plotting routines. Reaction uses linear algebra to solve for the reaction coefficients of a given set of phases and prints it out as a balanced reaction.

compatibility.m

```
BeginPackage["Compatibility`"] ;


Rock::usage =
"Rock[fileName] writes out rock data file information.";

Triplot::usage =
"Triplot[fileName,{projection phases},
        {projection plane}] plots compatibility diagrams.";

React::usage =
"React[fileName] calculates reactions.";


Begin["`Private`"]

Rock[fileName_String] :=
      Module[{},
            ss=ReadList[fileName,Word,RecordLists->True];
            label=ss[[1]];
            phaselist=Map[(#[[1]])&,ss][[Range[2,Length[ss],2]]];
                  phases=Map[ToExpression,ss[[Range[3,Length[ss],2]]]];
            TableForm[{phaselist,label} ]
       ];
```

```
Triplot[fileName_String,proPhases_List,proPoint_List] :=
Module[{pr,pt,phase,data,dim,pts,outline,lines,texta,textb},

                ss=ReadList[fileName,Word,RecordLists->True];
                label=Map[ToExpression,ss[[1]] ];
                phaselist=Map[ToExpression[#[[1]]]&,ss] [[Range[2,Length[ss],2]]];
                phases = Map[ToExpression,ss[[Range[3,Length[ss],2] ]] ];

                Graph1:=Show[Graphics[{GrayLevel[0.3], outline,
                                        GrayLevel[0],
                                         PointSize[0.01],texta,textb,pts},
                                        {AspectRatio -> Automatic}
                                       ]
                             ];
                Graph2:=Block[{},
                             g1 = Graphics3D[{GrayLevel[0.3], outline,
                                        GrayLevel[0],
                                         PointSize[0.01],pts,texta,textb},
                                        {AspectRatio -> Automatic,
                                        Boxed->False,
                                        ViewPoint -> {2,-2,-2}}
                               ];
                             g2 =Graphics3D[{GrayLevel[0.3], outline,
                                        GrayLevel[0],
                                         PointSize[0.01],pts,texta,textb},
                                        {AspectRatio -> Automatic,
                                        Boxed->False,
                                        ViewPoint -> {2.05,-2.05,-1.95}}
                               ];
                                Show[GraphicsArray[{{g1,g2}},GraphicsSpacing -> {0,0}]];
                          ];



                pr = Table[phases[[First[Flatten[Position[phaselist,proPhases[[ii]] ]] ] ]],
                                {ii,Length[proPhases]}
                     ];
                pt = Table[IdentityMatrix[Length[label]][[First[Flatten[Position[label,proPoint[[ii]]]]]]],
                        {ii,Length[proPoint]}
                ];

        phase =phases;
                For[i=1,i<=Length[pr],i++,
                        phase =Drop[phase,Flatten[Position[phase,pr[[i]] ]]]
                ];

                For[i=1,i<=Length[phase],i++,
                        cm[i]=Join[pt,pr,List[phase[[i]]]]
                ];
                data=Table[Take[Flatten[NullSpace[Transpose[cm[ii]]]],Length[proPoint]],
                        {ii,Length[phase]}
                ];

                phaseN=phaselist;
                For[i=1,i<=Length[proPhases],i++,
                        phaseN
=Drop[Flatten[phaseN],Flatten[Position[Flatten[phaseN],proPhases[[i]]]]]
                ];

                dim =Dimensions[data][[1]];

                If[(Length[label] - Length[proPhases])==3,
                        Block[{across,up},
                                For[i=1, i<=dim,i++,
                                        up[i] = data[[i,3]]/(data[[i,1]]+data[[i,2]]+data[[i,3]])
                                ];
```

```
                        For[i=1, i<=dim, i++,
                        If[(data[[i,1]]+ data[[i,2]])==0,across[i]=0,
                                across[i]= data[[i,2]]/(data[[i,1]]+data[[i,2]])
                            ]
                        ];
                        For[i=1, i<=dim, i++,
                            aacross[i]= 0.5 +(up[i]-1)*(across[i]-0.5)
                        ];
                        j =.;
                        pts = Table[Point[{aacross[j],up[j]}],{j,dim}];
                        lines = Table[Line[{{aacross[Mod[j-1,dim]+1],up[Mod[j-1,dim]+1]},
                        {aacross[Mod[j,dim]+1],up[Mod[j,dim]+1]}}],{j,dim}];
                        outline =Line[{{0,0},{1,0},{0.5,1},{0,0}}];
            texta =  List[Text[proPoint[[1]],{1,0},{0,1}],
                                                Text[proPoint[[2]],{0,0},{0,1}],
                                                Text[proPoint[[3]],{0.5,1},{0,-1}]
                                               ];
                        textb=Table[Text[phaseN[[ii]],First[pts[[ii]]],{-
1,0}],{ii,Length[phase]}];
                    Graph1;
                    ],
            ];
    If[(Length[label] - Length[proPhases])==2,
                    Block[{sideways},
                        For[i=1, i<=dim, i++,
                            If[(data[[i,1]]+(data[[i,2]]))==0,
                                sideways[i]=0,
                                sideways[i]=data[[i,2]]/(data[[i,2]]+data[[i,1]])
                            ]
                        ];
                        j =.;
                        pts = Table[Point[{sideways[j],0}],{j,dim}];
                        outline = Table[Line[{{0,0},{1,0}}]] ;
                        texta =  List[Text[proPoint[[1]],{0,0},{1.5,1.5}],
                                                Text[proPoint[[2]],{1,0},{-1.5,1.5}]
                                               ];

                        textb=Table[Text[phaseN[[ii]],First[pts[[ii]]],{0,
-1.5}],{ii,Length[phase]}];
                    Graph1;
                    ],
            ];
            If[(Length[label] - Length[proPhases])==4,
                    Block[{up,right,left,sum},
                        For[i=1,i<=dim,i++,
                            Block[{},
                                b[i]=data[[i,2]]/Apply[Plus,data[[i]]];
                                c[i]=data[[i,3]]/Apply[Plus,data[[i]]];
                                d[i]=data[[i,4]]/Apply[Plus,data[[i]]];
                                ];
                            ];

                        j =.;
                        pts = Table[Point[{b[j],c[j],d[j]}],{j,dim}];
                        outline =
Table[Line[{{0,0,0},{1,0,0},{0,1,0},{0,0,1},{1,0,0},{0,1,0},{0,0,0},{0,0,1}}]] ;
                        texta =  List[Text[proPoint[[1]],{0,0,0},{1.3,0}],
                                                Text[proPoint[[2]],{1,0,0},{-1.3,0}],
                                                Text[proPoint[[3]],{0,1,0},{-1.3,0}],
                                                Text[proPoint[[4]],{0,0,1},{0,-1.3}]
                                               ];
                        textb=Table[Text[phaseN[[ii]],First[pts[[ii]]],{-
1.2,0}],{ii,Length[phase]}];

                    Graph2;
                    ],
            ];
    ];
```

```
React[fileName_String] :=
        Module[{ii,n},
                ss=ReadList[fileName,Word,RecordLists->True];
                label=Map[ToExpression,ss[[1]] ];
                phaselist=Map[ToExpression[#[[1]]]&,ss] [[Range[2,Length[ss],2]]];
                phases = Map[ToExpression,ss[[Range[3,Length[ss],2] ]] ];

        react[phase_List,phaselist1a_List] :=
                Block[{i,j,dropped1,dropped2,phaselist1, phaselist2,reCoef,reCoef1,list,limit,
                  restring},
                table = List[];
                        Do[
                                phaselist1 =Drop[phaselist1a,{j,j}];
                                dropped1 =Complement[phaselist,phaselist1];
                                reCoef=Flatten[NullSpace[Transpose[Drop[phase,{j,j}] ] ] ];
                                limit = 10^-15;
                                Do[If[Abs[reCoef[[i]]]<limit,reCoef[[i]]=0],{i,Length[reCoef]}];
                                gt0[e_] :=Abs[e]>0;
                                reCoef1= Select[reCoef,gt0];
                                list = Table[Flatten[Position[reCoef,reCoef1[[i]] ]
],{i,Length[reCoef1]}];
                                phaselist2=Table[phaselist1[[list[[i,1]] ]],{i,Length[list]} ];
                                dropped2 = Complement[phaselist1,phaselist2];
                                reCoef1 =reCoef1/Min[Abs[reCoef1]];
                                restring =StringForm["``   ",Sort[Flatten[Join[dropped1, dropped2] ] ]
];
                                Do[If[reCoef1[[i]]>0,
                                        restring =      StringForm["`````` " +
",restring,N[reCoef1[[i]],4],Flatten[phaselist2][[i]]
                                                                                                ]
                                   ],{i,Length[reCoef1]}
                                ];
                        restring =      StringForm["`` = ",restring];
                                Do[If[reCoef1[[i]]<0,
                                        restring =      StringForm["`````` " +
",restring,N[Abs[reCoef1[[i]]],4],Flatten[phaselist2] [[i]]
                                          ],
                                        ],{i,Length[reCoef1]}
                                ];
                        table=Append[table,restring],
                {j,Length[phase]}
                ];
                        table1 = Table[ToString[table[[i]]],{i,Length[table]}];
                        table1 =Complement[table1];
                        Print[TableForm[table1]];
                        Print[];Print[];
                ];

                n = Length[phases]-Length[label];
                If[n==2,react[phases,phaselist]];
                If[n==3,
                        Do[
                                Block[{},
                                        Print["[",phaselist[[ii,1]],"]"];
                                        Print[];
                                        react[Drop[phases,{ii,ii}],Drop[phaselist,{ii,ii}]];
                                ],
                        {ii,Length[phases]}
                        ],
                ];
        ];
 End[];
 EndPackage[]
```

```
"Compatibility`Private`"
label::usage =
"label is list of components in data file.";

phaselist::usage =
"phaselist is list of phases in data file.";

phases::usage =
"phases is the list of phases in data file.";
```

A9.4 An example input file

Input files have a standard construction consisting of a list of components followed by a list of phases. The name of each phase is given on one line (the first entry serves as a label in Triplot mode) and thie compostion of the phases to be projected, the projection points and apices of the projection plane or volume written in terms of those components, is given on the next. For example,

```
MFANCSH
cd 563 2
1.5 0.5 4 0 0 5 0
oa 563 4
3.4 2.34 2.65 0.19  0.0 6.48 2
st
1.13 2.86 14.47 0 0 7.74 4
gt
0.89 1.72 2.05  0 .26 2.97 0
ky
0 0 2 0 0 1 0
qtz
0 0 0 0 0 1 0
v
0 0 0 0 0 0 2
pl
0 0 1.38 0.61 0.361 2.627 0
hbe
2.39 1.84 2.83 0.392 1.58 6.3 2
```

A9.5 An example operating file

The operation of **compatibility.m** is carried out in a separate file or notebook. The bold entries in the example below represent input (e.g. In [18]) and those in normal type (e.g. Out[18]) represent output. Examples of the Triplot mode for 1-, 2- and 3-dimensional projections are illustrated.

In[16]:=

?Rock

Rock[fileName] writes out rock data
file information.

In[17]:=

?Triplot

Triplot[fileName,{projection
phases},
{projection plane}] plots
compatibility diagrams.

In[18]:=

Rock["datafile"]

Out[18]//TableForm=

cd	oa	st	gt	ky	qtz	v
	pl	hbe				
M	F	A	N	C	S	H

In[19]:=

Triplot["datafile",{qtz,pl,hbe,ky,v},{M,F}]

In[20]:=

Triplot["datafile",{qtz,pl,hbe,v},{M,F,A}]

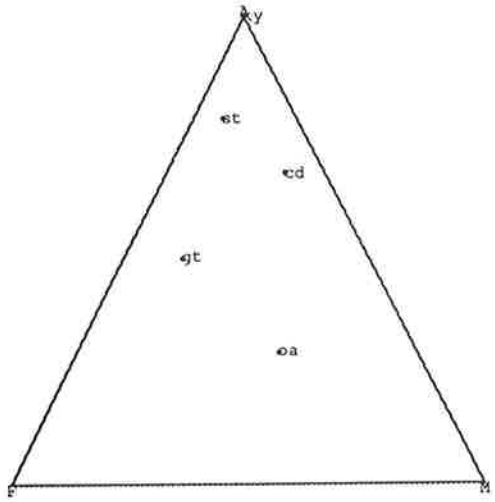

In[21]:=

Triplot["datafile",{gt,hbe,v},{M,C,A,S}]

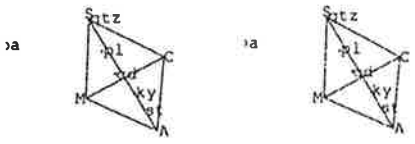

Appendix A10: Detailed petrography of amphibolites from the Zillertaler Alpen

A10.1 Introduction

The following section briefly describes the low-variance assemblages which occur in the hornblende garbenschiefer of the Zillertaler Alpen, western Austria. The geological setting, broad petrography and compatibility relations of the assemblages in these amphibolites are summarised in Chapter 5 and sample localities are given in Fig. A10.1. Selected mineral composition data is presented in Table 5.2. Aluminous kyanite–staurolite-bearing assemblages will be discussed in order of descending Fe-content, and this will be followed by a description of the more Al-poor, cummingtonite–garnet-type amphibolites.

A10.2 Kyanite–staurolite–garnet-amphibolite: sample 938-127

Pale green epidote (Ps_{15-16}), biotite ($X_{Fe,Bt}$ 0.35-0.49), ilmenite and paragonite define a weak foliation which wraps around garnet in a fine to medium grained, foliated matrix of weakly zoned oligioclase to andesine plagioclase (Table 5.2) and undulose quartz. Inclusions of epidote, plagioclase, quartz, ilmenite and magnetite at the cores of sub- to anhedral garnet (0.5-4 mm) do not form any discernible inclusion trails, whereas those contained in the outer parts of garnet grains or in randomly oriented ferro-tschermakitic hornblende are generally weakly to strongly aligned with the matrix foliation (Fig. 5.2). With the exception of epidote, included phases are compositionally similar to their matrix counterparts (epidote inclusions are more Fe-rich than matrix epidote i.e. Ps_{25}). Garnet grains in this sample have a variable composition with $X_{Fe,Grt}$ in the range 0.78-0.90 and coarse grained examples exhibit weak, probably prograde compositional zonation from a calcium-rich, slightly Mn-enriched core (e.g. X_{grs} 0.23, X_{alm} 0.59, X_{prp} 0.07, X_{sps} 0.10) to a Ca-poor, Fe- and Mg-enriched rim (e.g. X_{grs} 0.12, X_{alm} 0.64, X_{pyr} 0.18, X_{sps} 0.06, Table 5.2). A discontinuity at the very rim of the coarse (e.g. ~3.2 mm) garnets (e.g. X_{grs} 0.10, X_{alm} 0.66, X_{pyr} 0.16, X_{sps} 0.08, see also Fig. 5.6) suggests that the possibly prograde zoned garnet has begun to re-equilibrate with the matrix phases during cooling.

Kyanite and Fe-rich staurolite ($X_{Fe,St}$ 0.76-0.82, Table 5.2) form 1-2 mm long optically continuous aggregates in plagioclase. The aggregates are elongate sub-parallel to the foliation and truncate the paragonite-defined foliation. Kyanite is typically intergrown with staurolite, however, staurolite also occurs as small euhedral grains distributed throughout the matrix and is observed in contact with many of the matrix phases.

Randomly oriented hornblende is often slightly corroded and surrounded by a rim of greenish brown biotite (Fig. 5.2) with or without chlorite. Several coarse hornblende grains

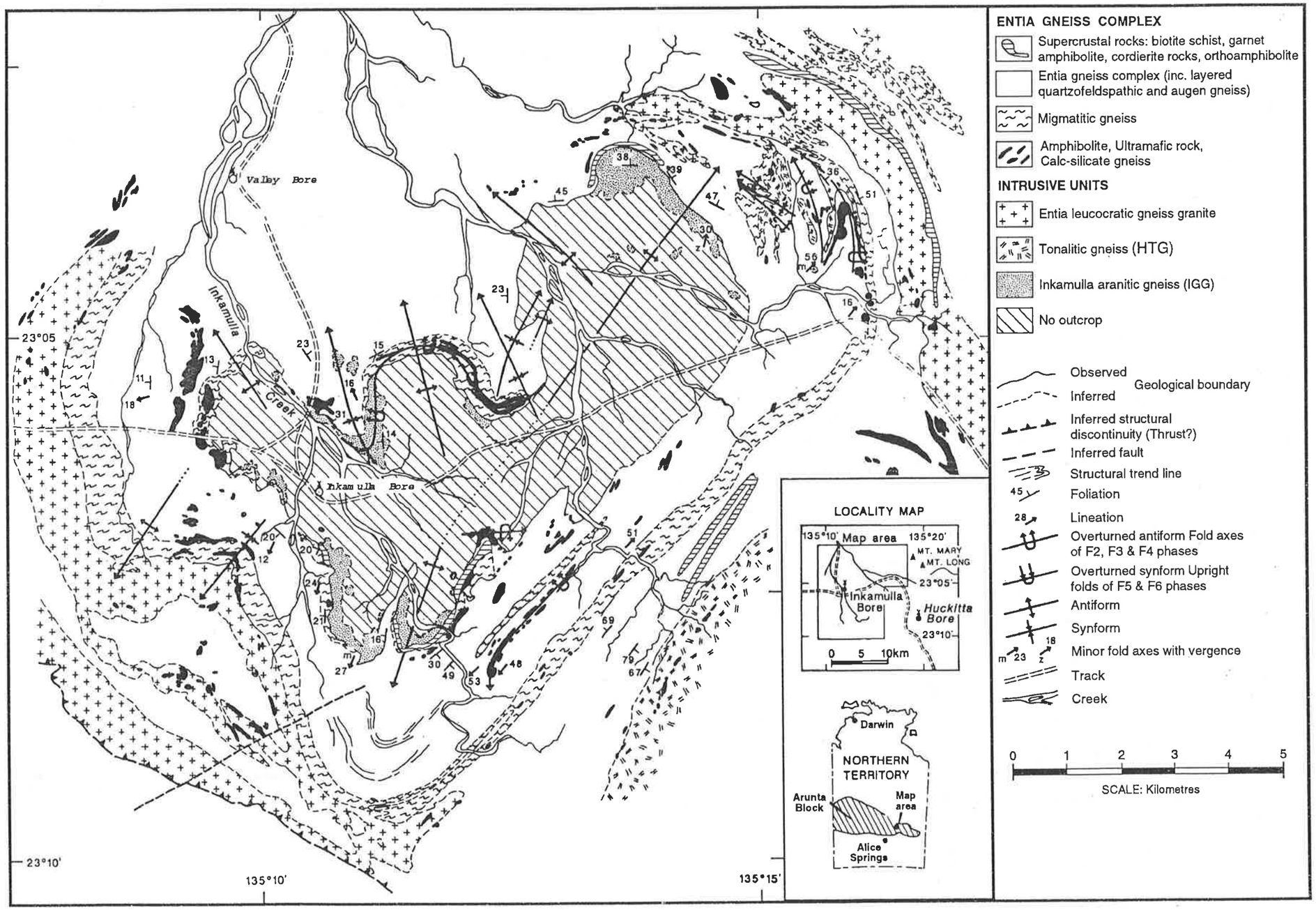
Valley Bore
Inkamulla Creek
Inkamulla Bore
Huckitta Bore
23°05'
23°10'
135°10'
135°15'
135°20'
MT. MARY
MT. LONG
Map area
0 5 10km
Darwin
NORTHERN TERRITORY
Arunta Block
Map area
Alice Springs
LOCALITY MAP
ENTIA GNEISS COMPLEX
Supercrustal rocks: biotite schist, garnet amphibolite, cordierite rocks, orthoamphibolite
Entia gneiss complex (inc. layered quartzofeldspathic and augen gneiss)
Migmatitic gneiss
Amphibolite, Ultramafic rock, Calc-silicate gneiss
INTRUSIVE UNITS
Entia leucocratic gneiss granite
Tonalitic gneiss (HTG)
Inkamulla aranitic gneiss (IGG)
No outcrop
Observed
Inferred
Geological boundary
Inferred structural discontinuity (Thrust?)
Inferred fault
Structural trend line
Foliation
Lineation
Overturned antiform Fold axes of F2, F3 & F4 phases
Overturned synform Upright folds of F5 & F6 phases
Antiform
Synform
Minor fold axes with vergence
Track
Creek
0 1 2 3 4 5
SCALE: Kilometres

are fractured perpendicular to the mica foliation and have been infilled or replaced along these weaknesses by biotite, chlorite, plagioclase and quartz. The dominance of Fe- and Al-rich minerals, the absence of chlorite and the relatively high X_{Fe} of many of the phases observed in this sample (e.g. $X_{Fe,Hbl}$ 0.50-0.58 and $X_{Fe,Bt}$ 0.35-0.49 reflect the Fe-rich, aluminous nature of the bulk-rock.

A10.3 Staurolite–garnet-amphibolite: sample 938-91a

Relatively minor fine biotite and hornblende define a weak foliation in a matrix also comprising zoned oligoclase-andesine plagioclase (An_{21-42}, Table 5.2), undulose quartz, ilmenite and rutile. The foliation is most strongly developed in the vicinity of hornblende and garnet porphyroblasts and wraps around them. Coarse subhedral garnet grains (2-3 mm) consist of a very inclusion-rich core surrounded by a narrow, inclusion poor rim and are compositionally homogeneous ($X_{Fe,Grt}$ 0.84-0.86, X_{alm} 0.65-0.71, X_{prp} 0.10-0.14, X_{grs} 0.11-0.19 and X_{sps} 0.05-0.05, Table 5.2). Epidote (Ps_{18}) inclusions in the core of garnet define linear inclusion trails which are at an angle to the weak matrix foliation. Coarse (up to 8 mm in length), randomly oriented ferro-tschermakitic to ferro-hornblende ($X_{Fe,Hbl}$ 0.52-0.56, Table 5.2) also contains poorly developed inclusion trails which are parallel to those in garnet. Hornblende is often heavily corroded and surrounded by intergrown green Fe-rich biotite ($X_{Fe,Bt}$ 0.45-0.48) and Fe-rich chlorite ($X_{Fe,Chl}$ 0.43), plagioclase and biotite. Fine aggregates of staurolite ($X_{Fe,St}$ 0.81-0.82) are distributed throughout the matrix (Fig. 5.10). The mineralogy of the sample (which does not included kyanite or garnet) and the Fe-rich nature of its phases reflects it's Fe-rich, slightly less Al-rich bulk-composition.

A10.4 Kyanite–staurolite–garnet–chlorite-amphibolite: sample 938-52c

Hornblende forms randomly oriented sheaves (garben) cross-cutting the anastomosing biotite, ankerite, epidote, white mica (paragonite), chlorite ($X_{Fe,Chl}$ 0.31-0.4) foliation. Coarse-grained plagioclase overgrows the foliation and coarse grained tschermakitic to ferro-tschermakitic hornblende ($X_{Fe,Hbl}$ 0.47-0.57, Table 5.2) cross-cuts and includes the crenulated green biotite–ankerite–epidote–white mica–chlorite foliation. The foliation is re-folded with the compositional layering. Hornblende in less micaceous portions of the sample is coarser, more euhedral and is parallel to the foliation. Coarse, compositionally homogeneous euhedral garnets are Fe-rich ($X_{Fe,Grt}$ 0.80-0.86, Table 5.2) and typically consist of a core of linear to S-shaped plagioclase inclusion trails at a high angle to the matrix foliation, with an inclusion-poor euhedral rim of variable width (Fig. 5.3). Rare, foliation-parallel inclusions of andesine (An_{39}, Table 5.2), ilmenite and rutile occur in the outer inclusion-poor rim and some smaller euhedral garnets are entirely inclusion poor. Euhedral garnet is observed in contact with hornblende, biotite, paragonite, kyanite and andesine plagioclase (An_{33-38}) and overgrows the foliation (Fig. 5.3). A single (~4 mm) garnet grain is brecciated and infilled with coarse grained plagioclase. Garnet and hornblende appear to be coeval and the

compositions of garnet and hornblende are relatively consistent and homogeneous, implying that they are part of an equilibrium assemblage. Garnet is similar in composition (X_{alm} 0.65-0.70, X_{prp} 0.11-0.16, X_{grs} 0.12-0.15, X_{sps} 0.04-0.07, respectively, Table 5.2) to those in other garnet-amphibolites.

Mica-rich portions and white mica inclusion trails in coarse grained, untwinned plagioclase appear are crenulated and distorted in the vicinity of garnet and hornblende porphyroblasts (Fig. 5.9). Biotite ($X_{Fe,Bt}$ 0.33-0.37) and paragonite are observed both as fine, foliation-forming and coarse cross-cutting grains in the matrix and biotite is often partially replaced by fine white mica. Small blue kyanite grains are visible in plagioclase at hand specimen scale and kyanite and optically continuous Fe-rich staurolite ($X_{Fe,St}$ 0.76-0.81, Table 5.2) are observed in both hornblende and mica-rich parts of the sample. Both phases are observed in and cross-cutting the foliation (Fig. 5.9). Ilmenite occurs in the cores of coarse garnet where it forms anhedral inclusions, however in the majority of the sample, subhedral rutile is the dominant oxide. Ilmenite often forms a very narrow rims on matrix rutile.

Epidote in mica-rich portions is discontinuously zoned (with decreasing birefringence, and a change in colour from green in the core, Ps_{29-30} to near-colourless at the rims, Ps_{22-23}) but the light green epidote associated with hornblende and garnet is continuously and far less dramatically zoned. Ankerite inclusions in hornblende are typically elongate and may be crenulated, often with a black rim, marking the partial breakdown of ankerite during weathering. Carbonates in the remainder of the sample (mostly in the mica-rich layers) are more equant. The Fe-rich, Al-rich nature of the sample is reflected in both its kyanite–staurolite–garnet mineralogy and its mineral chemistry.

A10.5 Kyanite–staurolite–garnet-amphibolite: sample 938-124c

This sample comprises two texturally distinct layers: a hornblende gneiss in which coarse hornblende defines the foliation, and a more schistose portion where hornblende is more anhedral and corroded and the foliation is defined by fine-grained white mica. In the more schistose parts, euhedral to anhedral garnets (0.5-5 mm in diameter, $X_{Fe,Grt}$ 0.80-0.87, Table 5.2) contain straight inclusion trails of ilmenite, rutile, plagioclase, quartz, hornblende and epidote which are parallel to the anastomosing white mica foliation in the quartz, andesine plagioclase (An_{28-52}, Table 5.2), ankerite, anhedral epidote (Ps_{13-15}) matrix. Several small (< 0.5 mm) grains of randomly oriented subhedral kyanite and staurolite ($X_{Fe,St}$ 0.76-0.77, Table 5.2) are associated with, but not in contact with, garnet and tschermakitic and ferro-tschermakitic hornblende (Table 5.2) porphyroblasts and are observed in contact with the plagioclase–white mica–hornblende matrix which they do not disrupt. Coarser muscovite and green biotite ($X_{Fe,Bt}$ 0.39-0.56) form equant, euhedral grains (< 0.5 mm) which cross-cut the foliation, and form partial to total pseudomorphs after corroded hornblende.

In the gneissic portion, plagioclase, quartz and ilmenite define straight inclusion trails in garnet and hornblende which are parallel to the coarse (1-7 mm) hornblende foliation. Hornblende is often cracked or pulled apart and is infilled with quartz and green biotite (Fig.

5.12). Both garnet and hornblende are compositionally homogeneous ($X_{Fe,Hbl}$ 0.47-0.57, X_{alm} 0.63-0.71, X_{prp} 0.10-0.17, X_{grs} 0.11-0.24, X_{sps} 0.01-0.05, Table 5.2) and are slightly less Fe-rich than other garnet-bearing amphibolites

A10.6 Kyanite–staurolite–chlorite-amphibolite: sample 938-51

Coarse grained equant to slightly elongate hornblende contains parallel inclusion trails of epidote, rutile, ilmenite and ankerite and is sub-parallel to the foliated chlorite, biotite ($X_{Fe,Bt}$ 0.29-0.34), andesine plagioclase (An_{32-55}, Table 5.2), quartz, epidote, ankerite matrix. The tschermakitic- to ferroan pargasitic-hornblende ($X_{Fe,Hbl}$ 0.41-0.48, Table 5.2) occurs in contact with all phases and shares straight grain boundaries with relatively Mg-rich prismatic staurolite ($X_{Fe,St}$ 0.70-0.75, Table 5.2, Fig. 5.7). The magnesian compositions of these phases together with this lack of garnet and the presence of chlorite suggests that this is one of the less Fe-rich staurolite-bearing samples. Fractured hornblende is infilled with chlorite and biotite. Pale green, optically zoned epidote Ps_{26-27} in the cores, Ps_{24-26} in the rims) and ankerite occur as inclusions in all phases and as matrix phases aligned with the foliation. Ankerite is the most Mg-rich phase present with $X_{Fe,Ank}$ in the range 0.19-0.27. Fine-grained white mica forms foliation-parallel inclusion trails in plagioclase in the vicinity of hornblende, but not in chlorite-rich layers. Small grains of kyanite (up to ~1 mm long) and larger ones of staurolite (up to 3 mm long) are observed in contact with hornblende (Fig. 5.7 and 5.8). Kyanite and staurolite are sometimes intimately associated in hornblende-rich, relatively ankerite- and mica-poor parts of the sample. Although they are all subparallel to the foliation, none of hornblende, kyanite or staurolite are consistently oriented and in some cases they truncate the foliation.

A10.7 Kyanite–staurolite-amphibolite: sample 938-61e

Coarse-grained biotite up to 5 mm in length defines a weakly crenulated foliation in an optically zoned plagioclase–quartz matrix and this foliation is rarely cut by very coarse, equant biotite. Sub-parallel coarse (up to 6 mm) hornblende grains are truncated by or included in foliation-parallel biotite. Porphyroblastic sheaves of kyanite are parallel to the foliation and are also crenulated (Fig. 5.11). Staurolite forms euhedral to subhedral grains which are randomly oriented. Kyanite and staurolite are observed in contact with biotite, plagioclase, quartz and in close proximity to hornblende. The absence of more Fe-rich (e.g. garnet) or more Mg-rich phases (e.g. chlorite) phases, along with the presence of kyanite and staurolite implies that this sample is particularly aluminous.

A10.8 Garnet–cummingtonite–chlorite-amphibolite: samples 938-92a, 938-137b, 938-33b;

Hornblende, cummingtonite, oligoclase (An_{16-28}, Table 5.2) and minor biotite define a foliation which is weakly to strongly represented in euhedral (938-137b, 33b) and subhedral garnets (938-92a, 33b) by sub-parallel ilmenite inclusions (Figs. 5.4 and 5.5). Weakly zoned green ferro-hornblende or ferro-tschermakitic hornblende ($X_{Fe,Hbl}$ 0.49-0.53) has cores slightly less sodic and more Fe-rich (e.g. Na 0.42-53 moles, $X_{Fe,Hbl}$ 0.51-0.58) than rims (e.g. Na 0.52-56, $X_{Fe,Hbl}$ 0.49-0.51, Table 5.2). Colourless, multiply-twinned cummingtonite ($X_{Fe,Cum}$ 0.45-0.49, Table 5.2) is often intergrown with hornblende and the two phases exhibit an epitaxial relationship. The sometimes-corroded coarse hornblende grains are often partly surrounded by finer, well-formed, multiply-twinned cummingtonite (Fig. 5.13), both of which may be partly to completely altered to biotite or chlorite. In the vicinity of garnet, the usual matrix assemblage of hornblende–cummingtonite–plagioclase–quartz becomes less hornblende-rich. Garnet is the most Fe-rich phase present($X_{Fe,Grt}$ 0.84-0.85), and garnet in these samples is less manganiferous and less calcic than those in other amphibolites (X_{alm} 0.73-0.74, X_{prp} 0.13-0.14, X_{grs} 0.10-0.11, X_{sps} 0.02, Table 5.2). Chlorite ($X_{Fe,Chl}$ 0.48-0.71) occurs in the matrix as randomly oriented splays and particularly Fe-rich chlorite is associated with highly corroded garnet, hornblende and biotite. The presence of very Al-poor cummingtonite and absence of kyanite and staurolite imply relatively Al-poor bulk compositions.

A10.9 Summary

The composition of common phases such as hornblende and biotite and the presence or absence of kyanite, staurolite, garnet, chlorite and cummingtonite in each of the samples gives an indication of the Fe-Mg and Al-content of the rocks. For example, hornblende is most Fe-rich in garnet-bearing samples, less so in staurolite-bearing samples and most magnesian in rocks which contain chlorite.

Although it has not been possible to develop a definite paragenetic sequence in these rocks, the low-variance assemblages in amphibolites often contain early garnet while kyanite, staurolite and chlorite generally appear to be slightly later. This suggests that the equilibria became more Mg-rich through time Hornblende is stable with both garnet and aluminous phases throughout the high temperature history of the rocks, however in the final stages (presumably during cooling) it breaks down to form fine biotite and chlorite.

References

Ackermand, D., Morteani, G., Raase, P., 1978. Metamorphism of the Penninic Series in the Western Tauern Window (Austria, Italy). In: Closs, H., Roeder, D., Schmidt, K., Alps, Apennines, Helenides - Geodynamic investigation along Geotraverses by an international group of geoscientists. Inter-Union Commission on Geodynamics: Scientific report no 38. E Schweizerbart'sche Verlagsbuchhandlung (Nägele u. Obermiller), Stuttgart, 121-124.

Albee, A.L., 1972. Metamorphism of pelitic schists: reaction relations of chloritoid and staurolite. Geological Society of America Bulletin, 83: 3249-3268.

Arnold, J., Sandiford, M., 1990. Petrogenesis of cordierite-orthoamphibole assemblages from the Springton Region, South Australia. Contributions to Mineralogy and Petrology, 106: 100-109.

Arnold J, Sandiford M, Wetherley S, 1994. Metamorphic events in the eastern Arunta Inlier: Part 1. Metamorphic petrology. Precambrian Research, in press.

Baker, J., Powell, R., Sandiford, M., Muhling, J. 1987. Corona textures between kyanite, garnet and gedrite in gneisses from Errabiddy, Western Australia. Journal of Metamorphic Geology 5: 357-370

Barnicoat, A. C., Fry, N., 1986. High-pressure metamorphism of the Zermatt-Saas ophiolite zone, Switzerland. Journal of the Geological Society, London, 143: 607-618.

Bickle, M.J., Hawkesworth, C.J., England, P.C., Athey, D.R., 1975. A preliminary thermal model for regional metamorphism in the Eastern Alps. Earth and Planetary Science Letters, 26:13-28.

Bowtell, S.A., Cliff, R.A., Barnicoat, A.C., 1994. Sm-Nd isotopic evidence on the age of eclogitization in the Zermatt-Saas Ophiolite. Journal of Metamorphic Geology, 12: 187-196.

Buick, I.S., 1983. The geology, petrology and geochemistry of the Huckitta granodioritic gneiss and associated granitoids, Harts Range, central Australia. University of Adelaide, Australia, Honours Thesis (unpubl.), 28 pp.

Buick, I.S., 1985.The petrology of granitic rocks from the Entia Domal Structure, Eastern Arunta Block. University of Adelaide, Australia, M.Sc. Thesis (unpublished), 149 pp.

Chinner, G.A., Fox, J.S., 1974. The origin of cordierite-anthophyllite rocks in the Land's End aureole. Geological Magazine, 111: 397-408.

Chopin, C., 1984. Coesite and pure pyrope in high-grade blueschists of the Western Alps: a first record and some consequences. Contributions to Mineralogy and Petrology, 86: 107-118.

Clarke, G.L. Collins, W.J., Vernon, R.H., 1990. Successive overprinting granulite facies metamorphic events in the Anmatjira Range, central Australia. Journal of Metamorphic Geology, 8: 65-88.

Cliff, R.A., 1981. Pre-Alpine history of the Pennine Zone in the Tauern Window, Austria: U-Pb and Rb-Sr geochronology. Contributions to Mineralogy and Petrology 77: 262-266

Collins, W.J., Teyssier, C., 1989. Crustal scale ductile fault systems in the Arunta Inlier, Central Australia. Tectonophysics, 158: 49-66.

Collins, W.J., Teyssier, C., 1989b.Crustal scale ductile fault systems in the Arunta Inlier, central Australia - reply. Tectonophysics, 158: 70-73.

Cooper, A. F., 1980. Retrograde alteration of chromian kyanite in metachert and amphibolite whiteschist from the Southern Alps, New Zealand, with implications for uplift on the Alpine Fault. Contributions to Mineralogy and Petrology, 75: 153-164.

Cooper, J.A., Mortimer, G.E., James, P.R., 1988. Rate of Arunta Inlier evolution at the eastern margin of the Entia Dome, central Australia. Precambrian Research, 40/41: 233-259.

Cox, K.G., Bell, J.D., Pankhurst, R.J., 1980. The interpretation of igneous rocks. London, George Allen & Unwin Ltd, 450 pp.

Dal Piaz, G.V., Lomabardo., B., 1986. Early alpine metamorphism in the Penninic Monte Rosa-Gran Paradiso basement nappes. Geological Society of America, Memiors, 164, Blueschists and related eclogites: 249-265.

Darken, L.S., 1967. Thermodynamics of binary metallic solutions. Metallurgical Society of AIME Transactions 239: 80-89

Deer, W.A., Howie, R.A., Zussman, J., 1972. An introduction to the rock-forming minerals. Longman Group Limited, London, 528pp.

Ding, P., James, P.R., 1985. Structural evolution of the Harts Range area and its implication for the development of the Arunta Block, central Australia. Precambrian Research, 27: 251-276.

Dirks, P.H.G.M., Hand, M., Powell, R., 1991. The P-T-deformation path for a mid-Proterozoic, low-pressure terrane: the Reynolds Range, central Australia. Journal of Metamorphic Geology, 9: 641-661.

Droop, G.T.R., 1982. A clinopyroxene paragenesis of albite-epidote-amphibolite facies rocks in meta-syenites from the south-east Tauern Window, Austria. Journal of Petrology, 23: 163-185.

Droop, G.T.R., Bucher-Nurminen, K., 1984. Reaction textures and metamorphic evolution of sapphirine-bearing granulites from the Gruf Complex, Italian Central Alps. Journal of Petrology, 25:766-803.

Droop, G.T.R., Lombardo, B., Pognante, U., 1990. Formation and distribution of eclogite facies rocks in the Alps. In: Carswell, D.A. (Ed.) Eclogite Facies Rocks. Chapman and Hall, New York.

Dunlap, W.J., Teyssier, C., McDougall, I., Baldwin, S., 1991. Ages of deformation from K/Ar and $^{40}Ar/^{39}Ar$ dating of white micas. Geology, 19: 1213-1216.

Dymoke, P., Sandiford, M., 1992. Phase relations of Buchan facies series pelitic assemblages: calculations and applications to the Mount Lofty Ranges, South Australia. Contributions to Mineralogy and Petrology, 110: 121-132.

England, P.C., Holland T.J.B., 1979. Archimedes and the Tauern Eclogites: the role of buoyancy in the preservation of exotic eclogite blocks. Earth and Planetary Science Letters 44: 287-294.

England, P.C., Thompson, A.B., 1984. Pressure-temperature-time paths of regional metamorphism. I: Heat transfer during the evolution of regions of thickened continental crust. Journal of Petrology, 25: 894-928.

Ernst, W.G., 1973. Interpretive synthesis of metamorphism in the Alps. Bulletin of the Geological Society of America. 84: 2053-2078.

Eskola, P., 1914. On the petrology of the Orijävi region in southwestern Finland. Bull Commission Géol Finland 40: 277.

Eskola, P., 1915. On the relation between chemical and minerlogical composition in the metamorphic rocks of the Orijävi region. Bull Commission Géol Finland 44: 109-145.

Etheridge, M.A., Rutland, R.W.R., Wyborn, L.A.I., 1987. Orogenesis and tectonic processes in the early to middle Proterozoic of northern Australia. In: A. Kröner (Editor) Proterozoic Lithospheric Evolution. Geodynamics Series, 17. American Geophysical Union, Washington D.C., pp. 131-147.

Ferry, J.M., Spear, F.S., 1978. Experimental calibration of the partitioning of Fe and Mg between garnet and biotite. Contributions to Mineralogy Petrology, 66: 113-117.

Foden, J.D., Buick, I.S., Mortimer, G.E., 1988. The petrology and geochemistry of granitic gneisses from the East Arunta Inlier, central Australia: Implications for Proterozoic crustal development. Precambrian Research , 40/41: 233-259.

Foden, J., Mawby, J., Arnold, J., Sandiford, M., 1992. Constraints imposed by Nd-Sr isotopic and metamorphic studies on the crustal evolution of the E. Arunta Inlier. In: Collins W.J. (Editor) ,The application of geochronology to field related geological problems (SGGMP Workshop), Abstracts, Alice Springs, NT, Australia. Geological Society of Australia.

Foden, J., Mawby, J., Kelley, S., Turner, S. and Bruce, D., 1994. Metamorphic events in the eastern Arunta Inlier: Part 1. Nd-Sr-Ar isotopic constraints. This volume.

Frank, W., Genser, J., Neubauer, F., 1992. Overview of the Eastern Alps. In: Neubauer, F. (Editor), ALCAPA: Geological evolution of the internal Eastern Alps and Carpathians and of the Pannonian Basin, ALCAPA Field Guide. Graz, pp. 7-16.

Frey, M., Trommsdorff, V., Wenk, E., 1980. Alpine metamorphism of the Central Alps. In: Trümpy, Rudolf (also Homewood, P.W., Ayrton, S., Fischer, H.) and Schweizerische Geologische Kommission. Geology of Switzerland. A guide book. Part B: Geological excursions. Basel, Wepf & Co, 295-316

Froese, E., Hall, R.D., 1983. A reaction grid for potassum-poor pelitic and mafic rocks. Current Research, Part A, Geological survey of Canada, Paper 83-1A: 121-124.

Gibson, G., 1978. Staurolite in amphibolite and hornblendite sheets from the upper Seaforth River, central Fiordland, New Zealand. Mineralogical Magazine, 42: 153-154.

Gibson, G., 1979. Margarite in kyanite- and corundum-bearing anorthosite, amphibolite abd hornblendite from central Fiordland, New Zealand. Contributions to Mineralogy and Petrology, 68: 171-179.

Goscombe, B.D., 1992a. High-grade reworking of central Australian Granulites. Part 1: structural evolution Tectonophysics, 204: 361-399.

Goscombe, B.D., 1992b. High-grade reworking of central Australian Granulites: metamorphic evolution of the Arunta Complex. Journal of Petrology, 33: 917-962.

Graham, C.M., Powell, R., 1984. A garnet-hornblende geothermometer: calibration, testing and application to the Pelona Schist, Southern California. Journal of Metamorphic Geology, 2: 13-31.

Green, T.H., Vernon, R.H., 1974. Cordierite breakdown under high pressure, hydrous conditions. Contributions to Mineralogy and Petrology, 64: 215-226.

Greenwood, H.J., 1975. Thermodynamically valid projections of extensive phase relationships. American Mineralogist, 60: 1-8.

Grew, E.S., Sandiford, M., 1984. A staurolite-talc assemblage in tourmaline-phlogopite-chlorite schist from northern Victoria Land, Antartica, and its petrogenetic significance. Contributions to Mineralogy and Petrology, 87: 337-350.

Grew, E.S., Sandiford, M., 1985. Staurolite in a garnet-hornblende-biotite schist from the Lanterman range, northern Victoria Land, Antarctica. Neues Jahrbuch für Mineralogie: Monatschefte, 9: 396-410.

Grew, E.S., Belakovskiy, D.I., Leskova, N.V., 1988. Phase equilibria in talc-kyanite-hornblende rocks (with andalusite and sillimante) from Kugi-Lal, southwestern Pamirs. Doklady Akademii Nauk SSSR, 299 (5): 1222-1226.

Griffen, D.T., Ribbe, P.H., 1973. The crystal chemistry of staurolite. American Journal of Science, 273A Cooper Volume: 479-495.

Guiraud, M., Powell, R., Holland, T., 1990. Calculated mineral equilibria in the greenschist-blueschist-eclogite facies in Na_2O-FeO-MgO-Al_2O_3-SiO_2-H_2O. Contributions to Mineralogy and Petrology, 104: 85-98.

Harley, S.L., 1985. Paragenetic and mineral-chemical relationships in orthoamphibole-bearing gneisses from Enderby Land, east Antarctica: a record of Proterozoic uplift. Journal of Metamorphic Geology, 3: 179-200.

Helgeson, H.C., Delany, J.M., Nesbitt, W., Bird, D.K., 1978. Summary and critique of the thermodynamic properties of rock-forming minerals. American Journal of Science, 278A: 1-229.

Helms, T.S., McSween, H.Y., Labotka, T.C., Jarosewich, E., 1987. Petrology of a Georgia Blue Ridge amphibolite unit with hornblende + gedrite + kyanite + staurolite. American Mineralogist, 72: 1086-1096.

Hensen, B.J., 1986. Theoretical phase relations involving cordierite and garnet revisited: the influence of oxygen fugacity on the stability of sapphirine and spinel in the system Mg-Fe-Al-Si-O. Contributions to Mineralogy and Petrology, 92: 362-367.

Hietanen, A., 1959. Kyanite-garnet gedritite near Orofino, Idaho. American Mineralogist, 44: 539-564.

Hobbs, B.E., Archibold, N.J., Etheridge, M.A., Wall, V.A., 1984. Tectonic history of the Broken Hill Block, Australia. In: A. Kröner.and R. Greiling (Editors), Precambrian Tectonics Illustrated. E. Schweizerbart'sche Verlagsbuchhandlung (Nägele u. Obermiller), Stuttgart, Germany. pp 353-369.

Hodges, K.V., 1991. Pressure-temperature-time paths. Annual review of Earth and Planetary Science, 19: 207-36.

Hodges, K.V., Spear, F.S., 1982. Geothermometry, geobarometry and the Al_2SiO_5 triple point at Mt Moosilauke, New Hampshire. American Mineralogist, 67: 1118-1134.

Holland, T.J.B., Powell, R., 1985. An internally consistent thermodynamic dataset with uncertainties and correlations: 2. Data and results. Journal of Metamorphic Geology, 3: 343-370.

Holland, T.J.B., Powell, R., 1990. An enlarged and updated internally consistent data set with uncertainties and correlations: the system K_2O-Na_2O-CaO-MgO-MnO-Fe0-Fe_2O_3-Al_2O_3-TiO_2-SiO_2-C-H_2-O_2. Journal of Metamorphic Geology, 8: 89-124.

Holland, T., Powell, R., 1992. Plagioclase feldspars: Activity-composition relations based on Darken's quadratic formalism and Landau theory. American Mineralogist, 77: 53-61.

Howell, N.J., 1991. Calculated metapelitic assemblages. University of Melbourne, Honours thesis (unpublished), 73 pp.

Hudson, N.F.C., Harte, B., 1985. K_2O-poor, aluminous assemblages from the Buchan Dalradian, and the variety of orthoamphibole assemblages in aluminous bulk compositions in the amphibolite facies. American Journal of Science, 285: 224-266.

Humphreys, H.C., 1993. Metamorphic evolution of amphibole-bearing aluminous gneisses from the Eastern Namaqua Province, South Africa. American Mineralogist, 78: 1041-1055.

James, P.R., Ding, P., 1988. "Caterpillar tectonics" in the Harts Range area: a kinship between two sequential Proterozoic extension-collision orogenic belts within the eastern Arunta Inlier of central Australia. Precambrian Research, 40/41: 199-216.

James, R.S., Grieve, R.A.F., Pauk, L., 1978. The petrology of cordierite-anthophyllite gneisses and associated mafic and pelitic gneisses at Manitouwadge, Ontario. American Journal of Science, 278: 41-63.

Laird, J., 1980. Phase equilibria in mafic schist from Vermont. Journal of Petrology, 21: 1-37.

Leake, B., 1978. Nomenclature of amphiboles. American Mineralogist, 63: 1023-1052.

Loosveld, R.J.H., Etheridge, M.A., 1990. A model for low-pressure facies metamorphism during crustal thickening. Journal of Metamorphic Geology, 8: 257-267.

Maeder, R.M. 1990. Programming in Mathermatica. Addison-Wesley Publishing Company, Redwood City, California. 267pp.

Massone, H.J., Schreyer, W., 1983. Stability of the talc-kyanite assemblage revisited. Terra Cognita , 13: 187.

Mawby, J., 1991. Constraints on the protolithic,deformational and metamorphic ages, and geochemical investigation of the Huckitta Bore Mafic Boudin. University of Adelaide Honours thesis (unpublished), 38pp.

McKie, D., 1959. Yoderite, a new hydrous magnesium silicate from Mautia Hill, Tanganyiki. Mineralogical Magazine, 32: 282-307.

Meagher, E.P., 1982. Silicate garnets. In: P.H. Ribbe (Editor), Orthosilicates. Reviews in Mineralogy 5. The Mineralogical Society of America, Washington D.C. pp 335-365.

Miller, C., 1974. On the metamorphism of the eclogites and high-grade blueschists from the Penninic terrane of the Tauern Window, Austria. Schweizerische Mineralogische u Petrographische Mitteilungen, 54: 371-384.

Miller, C., 1977. Mineral parageneses recording the P, T history of Alpine eclogites in the Tauern Window, Austria. Neues Jarbuch für Mineralogie: Abhandlungen, 130: 69-77.

Morteani, G., 1974. Petrology of the Tauern Window. Fortchritte der Mineralogie (Beiheft 1), 52: 195-220.

Mortimer, G.E., Cooper, J.A., James, P.R., 1987. U-Pb and Rb-Sr geochronology and geological evolution of the Harts Range ruby mine area of the Arunta Inlier, central Australia. Lithos, 20: 445-467.

Norrish, K., Hutton, J.T., 1969. An accurate x-ray spectrographic method for the analysis of a wide range of geological samples. Geochimica et Cosmochimica Acta, 33: 431-453.

Percival, J.A., Carmichael, D.M., Helmstaedt, H., 1982. A petrogenetic grid for calcium and alkali-deficient bulk composiitons. Current Research, part A, Geological Survey of Canada, paper 82-1A: 169-173.

Pognante, U., 1991. Petrological constraints on the eclogite- and blueschist-facies metamorphism and P-T-t paths in the Western Alps. Journal of Metamorphic Geology, 9: 5-17.

Powell, R., 1978. Equilibrium thermodynamics in petrology: An intoduction. Harper and Rowe, London, 284 pp.

Powell, R., 1985. Regression diagnostics and robust regression in geothermometer/ geobarometer calibration: the garnet-clinopyroxene geothermometer revisited. Journal of Metamorphic Geology, 3: 231-243.

Powell, R., 1987. Darken's quadratic formalism and thermodynamics of minerals. American Mineralogist, 72 1-11.

Powell, R., 1991. Metamorphic Mineral Equilibria Short Course: Course notes. University of Melbourne (unpublished).

Powell, R., Holland, T.J.B., 1985. An internally consistent thermodynamic dataset with uncertainties and correlations: 1. Methods and a worked example. Journal of Metamorphic Geology, 3: 327-342.

Powell, R., Holland, T.J.B., 1988. An internally consistent dataset with uncertainties and correlations: 3. Applications to geobarometry, worked examples and a computer program. Journal of Metamorphic Geology, 6: 173-204.

Powell, R., Holland, T.J.B., 1990. Calculated mineral equilibria in the pelite system, KFMASH K_2O-FeO-MgO-Al_2O_3-SiO_2-H_2O. American Mineralogist, 75: 367-380.

Powell, R., Sandiford, M., 1988. Sapphirine and spinel phase relationships in the system FeO-MgO-Al2O3-SiO2-TiO2-O2 in the presence of quartz and hypersthene. Contributions to Mineralogy and Petrology, 98: 64-71.

Purtscheller, F., Mogessie, A., 1984. Staurolite in garnet amphibolite from Solden, Otztal Old Crystalline Basement, Austria. Tschermaks Mineral Petrol Mitteilungen, 32:223-233.

Ribbe, P.H., 1982. Staurolite. In: P.H. Ribbe (Editor), Orthosilicates. Reviews in Mineralogy 5. The Mineralogical Society of America, Washington D.C. pp 171-188.

Robinson, P., Jaffe, H.W., 1969a. Aluminous enclaves in gedrite-cordierite gneiss from southwestern New Hampshire. American Journal of Science, 267: 389-421.

Robinson, P., Jaffe, H.W., 1969b. Chemographic exploration of amphibole assemblages from central Massachusetts and southwestern New Hampshire. Mineral Society of America, Special Paper, 2: 251-274.

Robinson, P., Spear, F.S., Schumacher, J.C., Laird, J., Klein, C., Evans, B.W., Doolan, B.L., 1982. Phase relations of metamorphic amphiboles: natural occurrence and theory. Veblen, D.R., Ribbe, P.H. (Eds.). Amphiboles: petrology and experimental phase relations. Reviews in Mineralogy, 9B. Mineralogical Society of America, Michigan. pp 1-228.

Sandiford, M., Oliver, R.L., Mills, K.J., Allen, R.V.A., 1990. A cordierite-staurolite-muscovite association, east of Springton, Mt Lofty Ranges: implications for the metamorphic evolution of the Kanmantoo Group. Special Publication, Geological Society of Australia, 16: 483-494.

Sandiford, M., Powell, R., 1991. Some remarks on high-temperature-low-pressure metamorphism in convergent orogens. Journal of Metamorphic Geology , 9: 330-340.

Sandiford, M., Martin, N., Zhou, S., Fraser, G., 1991. Mechanical consequences of granite emplacement during high-T, low-P metamorphism and the origin of "anticlockwise" PT paths. Earth and Planetary Science Letters, 107: 164-172.

Sandiford, M., Foden, J., Zhou, S., Turner S., 1992. Granite genesis and the mechanics of convergent orogenic belts with application to the southern Adelaide Fold Belt. Transactions of the Royal Society of Edinburgh: Earth Sciences, 83: 83-93.

Sandiford, M., Fraser, G., Arnold, J., Foden, J., Farrow, T. (in prep). Some causes and consequences of high-T, low-P metamorphism in the eastern Mount Lofty Ranges, South Australia. Submitted to Australian Journal of Earth Sciences.

Schreyer, W., 1973. Whiteschist: A high-pressure rock and its geological significance. Journal of Geology, 81: 735-739.

Schreyer, W., 1974. Whiteschist, a new type of metamorphic rock formed at high pressures. Geologische Rundschau, 63: 597-609.

Schreyer, W., 1977. Whiteschists, their compositions and pressure-temperature regimes based on experimental, field and petrographic evidence. Tectonophysics 43: 127-144.

Schreyer, W., Horrocks, P.C., Abraham, K., 1984. High-magnesium staurolite in a sapphirine-garnet rock from the Limpopo Belt, Southern Africa. Contributions to Mineralogy and Petrology, 86: 200-207.

Schreyer, W., Seifert, F., 1969a. Compatibility relations of the aluminum silicates in the systems $MgO-Al_2O_3-SiO_2-H_2O$ and $K_2O-MgO-Al_2O_3-SiO_2-H_2O$ at high pressures. American Journal of Science, 267: 371-388.

Schreyer, W., Seifert, F., 1969b. High pressure phases in the system $MgO-Al_2O_3-SiO_2-H_2O$. American Journal of Science, 267-A: 407-443.

Schreyer, W., Yoder, H.S. Jr., 1964. The system Mg-cordierite-H_2O and related rocks. Neues Jahrbuch Mineralogie: Abhandlungen, 101: 271-342.

Schumacher, J.C., Robinson, P., 1987. Mineral chemistry and metasomatic growth of aluminous enclaves in gedrite-cordierite gneiss from southwestern New Hampshire. Journal of Petrology, 28: 1033-1073.

Scrimgeour, I., Sandiford, M., 1993. Early Proterozoic metamorphism at the Granites Gold Mine, Northern Territory: Implications for the timing of fluid production in the high-T, low-P terrains. Economic Geology, 88:1 099-1133.

Seki, Yôtarô, Yamasaki, Masao, 1957. Aluminian ferroanthophyllite from the Kitakami Mountainland, northeastern Japan. American Mineralogist, 42: 506-520.

Selverstone, J., 1993. Micro- to macroscale interactions between deformational and metamorphic processes, Tauern Window, Eastern Alps. Schweizerische Mineralogische und Petrographische Mitteilungen, 73: 229-239.

Selverstone, J., Munoz, J.L., 1987. Fluid heterogeneities and hornblende stability in interlayered graphitic and non-graphitic schists (Tauern Window, Eastern Alps). Contributions to Mineralogy and Petrology, 96: 426-440.

Selverstone, J., Spear, F.S., 1985. Metamorphic P-T paths from pelitic schists and greenstones from the south-west Tauern Window, Eastern Alps. Journal of Metamorphic Geology, 3: 439-465.

Selverstone, J., Spear, F., Franz, G., Morteani, G., 1984. High pressure metamorphism in the SW Tauern Window, Austria: P-T paths from hornblende-kyanite-staurolite schists. Journal of Petrology, 25: 501-531.

Sharma, R.S., MacRae, N.D., 1981. Paragenetic relations in gedrite-cordierite-staurolite-biotite-sillimanite-kyanite gneisses at Ajitpura, Rajasthan, India. Contributions to Mineralogy and Petrology, 78: 48-60.

Shaw, R.D., Freeman, M.J., 1985. Explanatory notes for Illogwa Creek 1:250 000 sheet, (2nd edition) Bureau of Mineral Resources, Northern Territory Geological Survey, Canberra.

Shaw, R.D., Freeman, M.J., others, 1990. Quartz (1:100 000 scale geological map). Bureau of Mineral Resources, Canberra.

Shaw, R.D., Stewart, A.J., Black, L.P., 1984. The Arunta Inlier: a complex ensialic mobile belt in central Australia. Part 2: tectonic history. Australian Journal of Earth Sciences, 31, 457-484.

Sivell, W.J., Foden, J.D., Lawrence, R.W., 1985. The Entire anorthositic gneiss, eastern Arunta Inlier, central Australia: geochemistry and petrogenesis. Australian Journal of Earth Sciences, 32: 449-465.

Spear, F.S., 1977. Phase Equilibria of amphibolites from the Post Pond Volcanics, Vermont. Carnegie Institution of Washington Yearbook, 76: 613-619.

Spear, F.S., 1978. Petrogenetic grid for amphibolites from the Post Pond and Ammonoosuc Volcanics. Carnegie Institution of Washington Yearbook, 77: 805-808.

Spear, F.S., 1980. The gedrite-anthophyllite solvus and the composition limits of ortoamphibole from the Post Pond Volcanics, Vermont. American Mineralogist, 65: 1103-1118.

Spear, F.S., 1982. Phase equilibria of amphibolites from the Post Pond Volcanics, Mt Cube Quadrangle, Vermont. Journal of Petrology, 23: 383-426.

Spear, F.S., Rumble, D., 1986. Pressure, temperature, and structural evolution of the Ordville Belt, west-central New Hampshire. Journal of Petrology, 27: 1071-1093.

Stewart, A.J., Shaw, R.D., Black, L.P., 1984. The Arunta Inlier: a complex ensialic mobile belt in central Australia. Part 1: Stratigraphy, correlations and origin. Australian Journal of Earth Sciences, 31: 445-455.

Stewart, K.P., 1985. The petrological significance of calc-silicates and associated gneisses, Inkumulla Well area, N.T. University of Adelaide, Australia. Honours Thesis, (unpublished), 31 pp.

Stoddard, E.F., Miller, C.F., 1990; Chemistry and phase petrology of amphiboles and orthoamphibole-cordierite rocks, Old Woman Mountains, SE California, USA. Mineralogical Magazine, 54: 393-406.

Stout, J.H., 1972. Phase petrology and mineral chemistry of coexisting amphibolites from Telemark, Norway. Journal of Petrology, 13: 99-145.

Teyssier, C., 1985. A crustal thrust system in an intracratonic tectonic environment. Journal of Structural Geology, 7: 689-700.

Thompson, A.B., 1976a. Mineral reactions in pelitic rocks:I. Prediction of P-T-X (Fe-Mg) phase relations. American Journal of Science 276: 401-424.

Thompson, A.B., 1976b. Mineral reactions in pelitic rocks: II. Calculation of some P-T-X(Fe-Mg) phase relations. American Journal of Science, 267: 425-454.

Thompson, A.B., England, P.C., 1984. Pressure-temperature-time paths of regional metamorphism II. Their inference and interpretation using mineral assemblages in metamorphic rocks. Journal of Petrology. 25: 929-955.

Thompson, J.B., 1957. The graphical analysis of mineral assemblages in pelitic schists. American Mineralogist, 42: 842-858.

Thompson, J.B., Laird, J., Thompson, A.B., 1982. Reactions in amhibolite, greenschist and blueschist. Journal of Petrology, 23: 1-27.

Tilley, C.E., 1937. Anthophyllite-cordierite granulites of the Lizard. Geological Magazine, 74: 300-309.

Vallance, T.G., 1967. Mafic rock alteration and isochemical development of some cordierite-anthophyllite rocks. Journal of Petrology, 8: 84-96.

Vernon, R.H., 1972. Reactions involving hydration of cordierite and hypersthene. Contributions to Mineralogy and Petrology, 35: 125-137.

Visser, D., Senior, A., 1990. Aluminous reaction textures in orthoamphibole-bearing rocks: the pressure-temperature evolution of the high-grade Proterozoic of the Bamble Sector, South Norway. Journal of Metamorphic Geology, 8: 231-246.

Ward, C.M. 1984a. Magnesium staurolite and green chromian staurolite from Fiordland, New Zealand. American Mineralogist, 69: 531-540.

Ward, C.M., 1984b. Magnesium staurolite and green chromian staurolite from Fiordland, New Zealand. American Mineralogist, 69:531-540.

Warren, R.G., 1983. Metamorphic and tectonic evolution of granulites, Arunta Block, central Australia. Nature, 305: 300-303.

Will, T.M., Powell, R., 1992. Activity-composition relationships in multicomponent amphiboles: An application of Darken's quadratic formalism. American Mineralogist, 77: 954-966.

Will, T.M., Powell, R., Holland, T., 1990a. A calculated petrogenetic grid for ultramafic rocks in the system CaO-FeO-MgO-Al2O3-SiO_2-CO_2-H_2O at low pressures. Contributions to Mineralogy and Petrology, 105: 347-358.

Will, T.M., Powell, R., Holland, T., Guiraud, M., 1990b. Calculated greenschist facies mineral equilibria in the system CaO-FeO-MgO-Al_2O_3-SiO_2-CO_2-H_2O. Contributions to Mineralogy and Petrology, 104: 353-368.

Windrim, D.P., McCulloch, M.T., Chappel, B.W., Cameron, W.E., 1984. Nd isotopic systematics and chemistry of Central Australian sapphirine granulites: an example of rare earth element mobility. Earth and Planetary Science Letters, 70: 27-39.

Wood, B.J., Fraser, D.G., 1984. Elementary thermodynamics for geologists. Oxford, Oxford University Press. 303pp.

Xu, Guowei, Will, T.M., Powell, R., 1994. A calculated petrogenetic grid for the system K_2O-FeO-MgO-Al_2O_3-SiO_2-H_2O, with particular reference to contact-metamorphosed pelites. Journal of Metamorphic Geology, 12: 99-119.

Zen, E-an, 1966. Construction of pressure-temperature diagrams for multicomponent systems after the method of Schreinemakers - a geometric approach. US Geological Survey Bulletin, 1225.

Aouker, N., 1985. A Geological review of the southwest Entia Dome, with emphasis on the Inkamulla Granite Gneiss, Harts Range, eastern Arunta Block, Northern Territory. University of Adelaide, Australia, Honours Thesis (unpubl.).

Sullivan, S.J., 1985. A detailed geological investigation of the Entia Gneiss and Leucocratic Gneiss intrusive, Northern Entia Dome, Harts Ranges, Eastern Arunta Block. University of Adelaide, Australia, Honours Thesis (unpubl.).